Biophysics for the Life Sciences

John Golbeck
Art van der Est *Editors*

The Biophysics of Photosynthesis

Springer

Biophysics for the Life Sciences

Series Editor
Norma M. Allewell

For further volumes:
http://www.springer.com/series/10230

John Golbeck • Art van der Est
Editors

The Biophysics of Photosynthesis

Springer

Editors
John Golbeck
Department of Biochemistry
and Molecular Biology
Department of Chemistry
The Pennsylvania State University
University Park, PA, USA

Art van der Est
Department of Chemistry
Brock University
St. Catharines, ON, Canada

ISBN 978-1-4939-1147-9 ISBN 978-1-4939-1148-6 (eBook)
DOI 10.1007/978-1-4939-1148-6
Springer New York Heidelberg Dordrecht London

Library of Congress Control Number: 2014941447

Printed on acid-free paper

Springer is part of Springer Science+Business Media (www.springer.com)

Preface

Many textbooks treat the topic of photosynthesis as a branch of the biological sciences. The focus is usually on how the electron transport chain and the dark reactions work together to produce carbohydrates and oxygen from carbon dioxide and water. However, the earliest events in this process, including the absorption of light, the act of charge separation, the process of stabilizing the charge-separated state, the buildup of charge to catalyze the oxidation of water, and the movement of protons, are topics that fall more properly under the realm of biophysics and are often not given the attention they deserve. On one hand, the basic laws of physics govern the early events in photosynthesis and place important constraints on how the capture and storage of light energy can occur. On the other hand, living organisms have an enormous degree of flexibility, allowing basic biochemical processes to be optimized through the process of evolution. The result of the eons-long interplay between fundamental physical constraints and evolutionary adaptation is the process of oxygenic photosynthesis.

In this volume, we divide the topic of the biophysics of photosynthesis into five sections. Each of these sections covers a specific aspect of photosynthesis, ranging from light absorption through evolution of the reaction centers. The chapters describe the role that basic physical principles play and give a picture of current research in the area.

Part I deals with the absorption of a photon and the process of energy transfer among the antenna chlorophylls. In Chap. 1, Frank Müh and Thomas Renger use structural information provided by crystallography and spectroscopy to calculate couplings among pigment-protein and excitonic pigment-pigment assemblies. In Chap. 2, Jörg Pieper and Arvi Freiberg describe the technique of hole-burning spectroscopy and how it provides critical information on exciton-phonon coupling in antenna pigments. In Chap. 3, Tjaart Krüger, Vladimir Novoderezhkin, Elisabet Romero, and Rienk van Grondelle offer a fresh view of energy transfer among the pigment array and the initial act of photochemical charge separation.

Part II focuses on the underlying principles of electron transport relevant to photosynthetic reaction centers. In Chap. 4, Christopher Moser discusses how quantum mechanical tunneling among inorganic and organic cofactors governs electron

transport in proteins. In Chap. 5, Isaac F. Céspedes-Comacho and Jörg Matysik describe the often-neglected, but equally important, operation of spin in electron transport. In Chap. 6, David Mauzerall and Steve Mielke provide information on the thermodynamics of energy changes in photosynthesis through the use of pulsed photoacoustic spectroscopy.

Part III is devoted to the charge separation and its stabilization over periods of time that are relevant to physiology. In Chap. 7, Sergei Savikhin and Ryszard Jankowiak show how ultrafast optical spectroscopy and hole-burning spectroscopy provide information on the mechanism of primary charge separation in a variety of photosynthetic reaction centers. In Chap. 8, Stefano Santabarbara, Robert Jennings, and Giuseppe Zucchelli illustrate how the concept of quasi-equilibrium states provides a framework for understanding the kinetics of electron transfer and radical pair stabilization in photosystem I. In Chap. 9, James Allen and JoAnn Williams describe their work on protein cofactor interactions and how they are able to modulate the midpoint potentials of cofactors in the bacterial reaction center.

Part IV is concerned with the description of donor-side intermediates of photosystem II and the process of water splitting. In Chap. 10, K. V. Lakshmi, Christopher Coates, and Ruchira Chatterjee describe the discovery and properties of radical intermediates in photosystem II. In Chap. 11, Jian-Ren Shen outlines structure–function relationships gleaned from the high-resolution structure of the Mn_4CaO_5 water-splitting cluster. In Chap. 12, Serguei Vassiliev and Doug Bruce provide insight obtained from computational studies on water and oxygen diffusion pathways within photosystem II.

Part V attempts to provide a time course of how the flexibility of biology overcame the inflexibility of physics in the evolution of photosynthesis. In Chap. 13, Alexander Melkozernov provides a compelling narrative of how an attempt to protect against ionizing radiation provided the protein framework for what was to become the photosynthetic reaction centers. In Chap. 14, John Allen posits a novel mechanism to describe how anoxygenic type I and type II reaction centers cooperated in space and time to create the process of oxygenic photosynthesis.

We hope that the reader of this volume will come away with a deeper appreciation of the role of biophysics of the early events in photosynthesis and a more in-depth understanding of how light is converted into a stable charge-separated state and, ultimately, into chemical bond energy.

University Park, PA, USA — John H. Golbeck
St. Catharines, ON, Canada — Art van der Est

Contents

Contributors

James P. Allen Department of Chemistry and Biochemistry, Arizona State University, Tempe, AZ, USA

John F. Allen Research Department of Genetics, Evolution and Environment, University College London, London, UK

Doug Bruce Department of Biological Sciences, Brock University, St. Catharines, ON, Canada

Isaac F. Céspedes-Camacho Institut für Analytische Chemie, Universität Leipzig, Leipzig, Germany

Leiden Institute of Chemistry, Universiteit Leiden, Leiden, The Netherlands

Ruchira Chatterjee Physical Sciences Division, Lawrence Berkeley National Laboratory, Berkeley, CA, USA

Christopher S. Coates Department of Chemistry and Chemical Biology, Rensselaer Polytechnic Institute, Troy, NY, USA

The Baruch '60 Center for Biochemical Solar Energy Research, Rensselaer Polytechnic Institute, Troy, NY, USA

Arvi Freiberg Institute of Physics, University of Tartu, Tartu, Estonia

Institute of Molecular and Cell Biology, University of Tartu, Tartu, Estonia

John H. Golbeck Department of Biochemistry and Molecular Biology, Department of Chemistry, The Pennsylvania State University, University Park, PA, USA

Ryszard Jankowiak Department of Chemistry, Kansas State University, Manhattan, KS, USA

Robert Jennings Department of Biology, University of Milano, Milano, Italy

Tjaart P. J. Krüger Department of Physics, Faculty of Natural and Agricultural Sciences, University of Pretoria, Hatfield, South Africa

K. V. Lakshmi Department of Chemistry and Chemical Biology, Rensselaer Polytechnic Institute, Troy, NY, USA

The Baruch ’60 Center for Biochemical Solar Energy Research, Rensselaer Polytechnic Institute, Troy, NY, USA

Jörg Matysik Institut für Analytische Chemie, Universität Leipzig, Leipzig, Germany

David Mauzerall Laboratory of Photobiology, Rockefeller University, New York, NY, USA

Alexander N. Melkozernov Department of Chemistry and Biochemistry, Arizona State University, Tempe, AZ, USA

Steven P. Mielke Laboratory of Photobiology, Rockefeller University, New York, NY, USA

Christopher C. Moser Department of Biochemistry and Biophysics, University of Pennsylvania, Philadelphia, PA, USA

Frank Müh Institute for Theoretical Physics, Johannes Kepler University Linz, Linz, Austria

Vladimir I. Novoderezhkin Department of Photosynthesis, A.N. Belozersky Institute of Physico-Chemical Biology, Moscow State University, Moscow, Russia

Jörg Pieper Institute of Physics, University of Tartu, Tartu, Estonia

Thomas Renger Institute for Theoretical Physics, Johannes Kepler University Linz, Linz, Austria

Elisabet Romero Department of Physics and Astronomy, Faculty of Sciences, VU University Amsterdam, Amsterdam, The Netherlands

Stefano Santabarbara Consiglio Nazionale delle Ricerche, Istituto di Biofisica, Sede di Milano, Milan, Italy

Sergei Savikhin Department of Physics, Purdue University, West Lafayette, IN, USA

Jian-Ren Shen Photosynthesis Research Center, Graduate School of Natural Science and Technology, Okayama University, Okayama, Japan

Stuart Smith Department of Physics, Rensselaer Polytechnic Institute, Troy, NY, USA

The Baruch ’60 Center for Biochemical Solar Energy Research, Rensselaer Polytechnic Institute, Troy, NY, USA

Art van der Est Department of Chemistry, Brock University, St. Catharines, ON, Canada

Rienk van Grondelle Department of Physics and Astronomy, Faculty of Sciences, VU University Amsterdam, Amsterdam, The Netherlands

Serguei Vassiliev Department of Biological Sciences, Brock University, St. Catharines, ON, Canada

JoAnn C. Williams Department of Chemistry and Biochemistry, Arizona State University, Tempe, AZ, USA

Giuseppe Zucchelli Consiglio Nazionale delle Ricerche, Istituto di Biofisica, Sede di Milano, Milano, Italy

Part I
Light Energy Capture and Energy Transfer

Chapter 1
Structure-Based Calculation of Pigment–Protein and Excitonic Pigment–Pigment Coupling in Photosynthetic Light-Harvesting Complexes

Frank Müh and Thomas Renger

Abstract In photosynthesis, specialized pigment–protein assemblies, termed light-harvesting complexes (LHCs) or antenna proteins, absorb solar photons and deliver the excitation energy by exciton transfer (XT) to the photochemically active centers. To understand this process, it has to be linked to molecular structures and spectroscopic properties of LHCs. In this chapter, we show how this link is provided by theoretical modeling. We first describe what excitons are and how the mechanism of XT is influenced by the coupling of excited states to molecular vibrations. This description defines key parameters that are important for a modeling of XT: (1) site energies, (2) excitonic couplings, and (3) exciton-vibrational coupling constants. Next, we discuss how these parameters can be calculated from a crystal structure of the LHC within the framework of an electrostatic model of intermolecular interactions. Finally, we show applications to the Fenna–Matthews–Olson (FMO) protein of green sulfur bacteria and the major LHC of higher plants (LHCII) to illustrate how this approach works and what has already been learned from it.

Keywords Antenna protein • Chlorophyll • Exciton transfer • Excitonic coupling • Frenkel exciton • Normal mode • Reorganization energy • Site energy • Spectral density • Transition density

1.1 Introduction

Photosynthesis starts with the capture of sunlight. This process is referred to as light-harvesting and involves the absorption of photons by pigment molecules (e.g., chlorophylls or carotenoids) that are bound to specialized pigment–protein complexes

F. Müh, Ph.D. (✉) • T. Renger, Ph.D.
Institute for Theoretical Physics, Johannes Kepler University Linz,
Altenberger Strasse 69, 4040 Linz, Austria
e-mail: Frank.Mueh@jku.at

J. Golbeck and A. van der Est (eds.), *The Biophysics of Photosynthesis*,
Biophysics for the Life Sciences 11, DOI 10.1007/978-1-4939-1148-6_1,

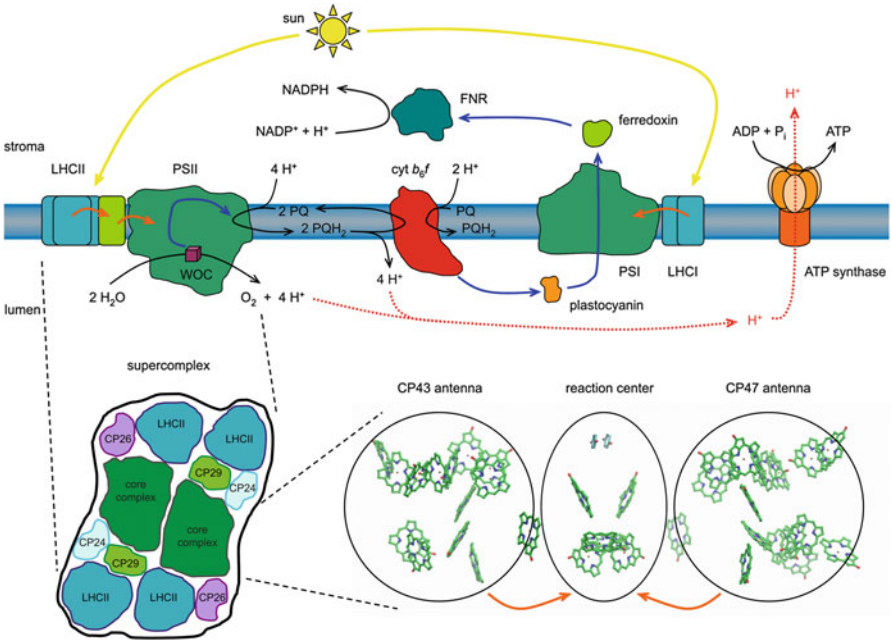

Fig. 1.1 *Upper part*: Overview of processes in and around the thylakoid membrane in oxygenic photosynthesis. Arrow color code: *yellow*, photon flux; *orange*, exciton transfer; *blue*, electron transfer; *red dashed*, proton transport; *black*, chemical reaction. *Lower part, left*: Schematic structure of a photosystem II (PSII) supercomplex of higher plants based on the data of Caffarri et al. [1]. *Lower part, right*: Arrangement of cofactors (chlorophylls, pheophytins, quinones; only π-systems shown) in the cyanobacterial PSII core complex based on the data of Umena et al. [2]; figure made with VMD [3]

(PPCs). The latter are termed light-harvesting complexes (LHCs) or antenna proteins. Their task is twofold. First, they have to deliver the excitation energy (i.e., the energy taken up from the absorbed photons) to other specialized PPCs, the reaction centers (RCs), where the actual photochemical reactions take place. As the LHCs are more abundant and bind more pigments than the RCs, they increase the effective absorption cross section of the RC and thus the number of photons that can be successfully captured. In addition, they often bind a variety of different pigment types absorbing at different wavelengths und thus allow for the exploitation of a wider range of the solar spectrum. Second, the LHCs contribute to a regulation of the energy flow to the RCs. Such a regulation is necessary, because photosynthetic organisms are exposed to varying light intensities, e.g., the changing brightness of the sunlight over a day. While, clearly, darkness hampers photosynthesis, too much light is problematic as well, since it can do harm to the cell, e.g., by production of reactive oxygen species (ROS) as a consequence of photochemical side reactions.

To see how the LHCs are embedded in the photosynthetic apparatus, let us take the thylakoid membrane of higher plants as an example (Fig. 1.1). Here, photosynthesis takes place in organelles of the plant cell known as chloroplasts. The chloroplasts contain in their interior (the stroma) an extended membrane system,

the thylakoids, that enclose a region called lumen. In the upper part of Fig. 1.1 is shown the major proteins of the light reactions of photosynthesis that are either embedded in the thylakoid membrane or soluble in the stroma or the lumen and in contact with the membrane proteins. At the beginning of the chain of events in this apparatus is the splitting of water molecules into oxygen, protons, and electrons at the water-oxidizing complex (WOC) bound to the core complex of photosystem II (PSII). A light-energy driven electron transfer (ET) process within the RC of PSII results in the reduction of plastoquinone (PC) to plastoquinol (PQH_2) that is released into the membrane. The electrons (and protons) stored intermediately in this "quinone pool" are used by the cytochrome (cyt) b_6f complex to reduce the soluble electron carrier plastocyanin in the lumen, which delivers the electrons to photosystem I (PSI). Another light-driven ET in the RC of PSI leads to the reduction of the soluble electron carrier ferredoxin in the stroma, which in turn provides electrons to the ferredoxin:$NADP^+$ reductase (FNR) for the final storage of these electrons in the form of NADPH. Altogether, these processes cause a net transport of protons from the stromal to the lumenal side of the membrane. The resulting electrochemical potential difference is used by the ATP-synthase to form ATP. Thus, the solar energy is ultimately used to transform water into oxygen, reduction equivalents (NADPH), and chemically stored energy (ATP). These are the light reactions of photosynthesis. The oxygen is used by other organisms (e.g., human beings) for their survival, while NADPH and ATP are expended by the plant cell itself to produce sugar from CO_2 in the dark reactions of photosynthesis.

As can be seen from Fig. 1.1, there are two light-powered molecular machines in the photosynthetic apparatus, PSII and PSI. Both contain besides the RC a core antenna system, but are surrounded by additional peripheral LHCs. Let us have a closer look at PSII. The PSII core complex in plant thylakoids is part of a supercomplex that contains various copies of the major light-harvesting complex II (LHCII) and the minor LHCs called CP24, CP26, and CP29 as sketched in the lower left part of Fig. 1.1 [1, 4, 5]. These PPCs deliver energy to the core complex by virtue of a radiationless excitation energy transfer or exciton transfer (XT). Radiationless means that the donor complex does not emit a photon, which is then absorbed by the acceptor complex, but rather that a quantum of excitation energy, an exciton, is transferred directly (orange arrows in Fig. 1.1). This process is further explained below. The PSII core complex itself contains two antenna proteins termed CP43 and CP47 that in turn deliver the energy to the RC (lower right part of Fig. 1.1). Thus, there is a cascade of XT processes between photon capture and the actual photochemistry in the RC. An understanding of light-harvesting implies to unravel the molecular mechanisms of these XT processes and their regulation. One approach to gain information about XT is the application of time-resolved spectroscopic techniques that allow to monitor changes of molecular properties in the course of the process. Another pillar of research is structural biology providing information about the arrangement and conformations of the involved molecular complexes. For example, detailed crystal structures are available for LHCII [6–8] and CP29 [9] of higher plants as well as of the cyanobacterial PSII core complex

that is homologous to that of plants [2, 10, 11]. The arrangement of chlorophylls and RC cofactors in the latter is shown in the lower right part of Fig. 1.1.

The challenge is to find a link between the molecular structures on one hand and the spectroscopic properties and the function of the LHCs on the other hand. Related questions that need to be answered are: (a) Why is light-harvesting so efficient? (The quantum yield is near 100 %, i.e., virtually every photon excitation reaches the RC.) (b) What is the influence of the protein matrix on the embedded pigments that makes them fulfill different tasks at different places? (i.e., XT versus ET) (c) Are there basic building principles of LHCs? (d) How is XT regulated to avoid harmful side reactions? (e) How is XT directed in space? (i.e., towards the RC or an energy sink) (f) What determines the XT rates? (g) What can we learn from nature to create artificial light-harvesting devices? In this chapter, we cannot give an answer to all of these questions, but we shall demonstrate that theoretical modeling of LHCs is pivotal to finding these answers. The modeling is based on a quantum physical treatment of the XT process that allows for a calculation of spectroscopic properties and the determination of XT rates and mechanisms. However, the theory contains parameters that have to be fixed. At this point, information about the molecular structure comes into play. This chapter is devoted to a description of methods that can be used to compute the parameters in question from the crystal structure of a PPC and thus to link structure and function.

The chapter is organized as follows: First, we introduce the basic molecular physics of pigments. Then, we explain what an exciton is and define different kinds of XT based on a quantum physical description. This treatment leads to a definition of the key parameters that we wish to determine on the basis of a crystal structure, i.e., site energies, excitonic couplings, and exciton-vibrational coupling constants (see below). Next, we discuss molecular interactions and how these interactions can be described by computable molecular properties (in particular, atomic partial charges). In the following sections, we demonstrate how these molecular properties can be combined with structural information to determine the requested parameters. Finally, we discuss exemplary applications to illustrate how this approach works and what has already been learned from it. These applications encompass the Fenna–Matthews–Olson (FMO) protein of green sulfur bacteria, which is a suitable model PPC because of its simple, yet not too simple, architecture, and, coming back to Fig. 1.1, the antenna system of PSII.

1.2 States of Photosynthetic Pigments

Light-harvesting requires molecules that absorb photons in a certain wavelength range. As the solar spectrum of sunlight has its largest intensity between 400 and 800 nm [12], the molecules have to absorb in the visible (VIS) or near infrared (NIR) range. If they absorb visible light, they are referred to as dyes or pigments, since they appear colored. The most prominent dye is the one that makes leaves green, the chlorophyll (Chl), whose molecular structure is shown in

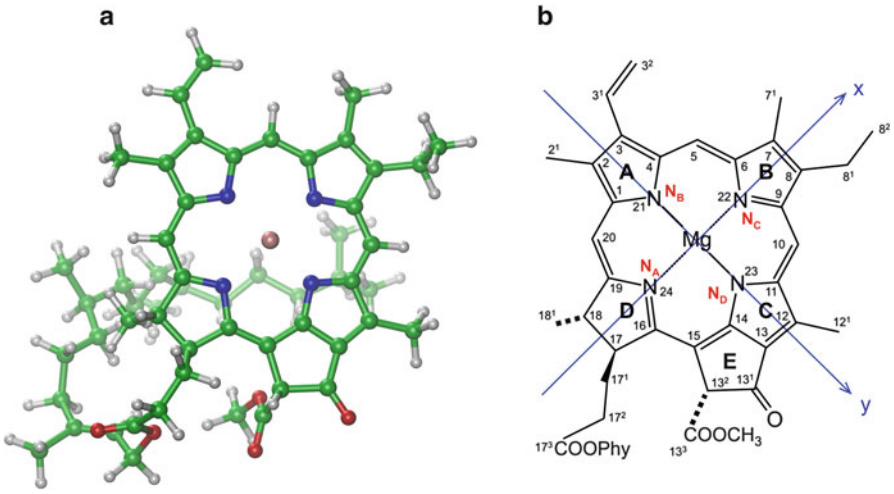

Fig. 1.2 (**a**) Molecular structure of chlorophyll *a* (taken from LHCII, PDB entry 1rwt); hydrogen atoms added by molecular modeling; figure made with VMD [3]. (**b**) Structural formula of Chl *a* with IUPAC numbering scheme. The *blue arrows* correspond to the polarizations of the first (y) and second (x) optical transitions of Chl *a* (Q_y and Q_x, respectively)

Fig. 1.2 (more precisely: Chl *a*; for a review of different Chl types and nomenclature, see [13]). What determines the color of such a pigment?

For concreteness, let us consider a dye molecule with N_{nuc} atoms having atomic numbers z_I, ($I = 1, \ldots\ldots, N_{\mathrm{nuc}}$) and N_{el} electrons (in the case of Chl *a*, $N_{\mathrm{nuc}} = 133$ and $N_{\mathrm{el}} = 478$). The Cartesian coordinates and momenta of the electrons are denoted by $\mathbf{r}_i$ and $\mathbf{p}_i$, respectively, and those of the nuclei by $\mathbf{R}_I$ and $\mathbf{P}_I$. Then, the molecule is characterized by the Hamiltonian [14]

$$H_{\mathrm{mol}} = \underbrace{\sum_{i=1}^{N_{\mathrm{el}}} \frac{\mathbf{p}_i^2}{2m_{\mathrm{el}}} + \frac{1}{2}\sum_{i\neq j} \frac{e^2}{|\mathbf{r}_i - \mathbf{r}_j|} - \sum_{i,I} \frac{z_I e^2}{|\mathbf{r}_i - \mathbf{R}_I|}}_{H_{\mathrm{el}}(\mathbf{R})} + \underbrace{\sum_{i=1}^{N_{\mathrm{nuc}}} \frac{\mathbf{P}_I^2}{2M_I} + \frac{1}{2}\sum_{I\neq J} \frac{z_I z_J e^2}{|\mathbf{R}_I - \mathbf{R}_J|}}_{V_{\mathrm{nuc}}(\mathbf{R})} \tag{1.1}$$

where e is the elementary charge, m_{el} the electron mass, and M_I the mass of the Ith nucleus. The first three terms on the right hand side (rhs) of Eq. (1.1) represent the kinetic energy of the electrons and the potential energy arising from the Coulomb interaction between electrons as well as between electrons and nuclei. The last two terms describe the kinetic energy of nuclei and the potential energy due to Coulomb repulsion between nuclei.[1] Light in the visible range is absorbed by the electrons of the molecule, i.e., the photon energy is used to promote the electrons from their

[1] In Eq. (1.1), spin-orbit coupling and other terms related to spin are neglected.

ground state to a higher energy level. These energy levels are determined by the stationary Schrödinger equation:

$$H_{\mathrm{el}}(\mathbf{R})\phi_a(\mathbf{r},\mathbf{R}) = E_a(\mathbf{R})\phi_a(\mathbf{r},\mathbf{R}) \tag{1.2}$$

where $H_{\mathrm{el}}(\mathbf{R})$ is the electronic Hamiltonian specified in Eq. (1.1) and $\phi_a(\mathbf{r}, \mathbf{R})$ is the wave function characterizing the state a of the electrons. We have introduced the symbols $\mathbf{r}$ and $\mathbf{R}$ to denote collectively the coordinates of all electrons and of all nuclei, respectively. The square of the wave function $|\phi_a(\mathbf{r},\mathbf{R})|^2$ can be interpreted as the probability of finding the electrons in state a at the positions represented by $\mathbf{r}$ given that the nuclei are at the positions represented by $\mathbf{R}$. Apparently, the states of the electrons depend on $\mathbf{R}$, which simply reflects the fact that the chemical structure as well as the conformation of the dye molecule influences the electronic energy levels E_a and their energy differences $E_a - E_b$ and, hence, the type of photons preferentially absorbed by the dye. It follows that the structure of a pigment itself is one important factor that determines its color. The variation of the chemical structure is clearly used in natural photosynthesis to optimize light-harvesting, since there are different types of pigments present in the photosynthetic antenna to exploit a broader range of the solar spectrum (e.g., Chl *a* and *b* and different carotenoids in LHCII), as mentioned above. The role of different conformations of chemically identical pigments in different environments (e.g., different degrees of non-planarity of the tetrapyrrole ring system of Chl *a*) is more difficult to assess. However, as we shall see further below, a key factor for the tuning of the color and for an understanding of XT is the electrostatic interaction of the electrons with the pigment´s environment including the electrons of other pigments.

Due to the huge number of electrons and nuclei, Eqs. (1.1) and (1.2) are difficult to work with, and we need approximations to proceed. The first of these approximation is based on the large mass difference between electrons and nuclei ($m_{\mathrm{el}}/M_I < 10^{-3}$). This fact allows to consider the electrons as moving much faster than the nuclei and as responding instantaneously to changes of the nuclear positions. Then, it makes sense to solve the Schrödinger equation (1.2) for each $\mathbf{R}$ separately, so that $\mathbf{R}$ becomes a parameter. The resulting electronic wave functions $\phi_a(\mathbf{r}, \mathbf{R})$ and states a are called adiabatic. Actually, the total wave function $\psi(\mathbf{r}, \mathbf{R})$ of the molecule in any state, obtained from the Schrödinger equation $H_{\mathrm{mol}}\psi = E\psi$ with H_{mol} given by Eq. (1.1), is a linear combination of all $\phi_a(\mathbf{r}, \mathbf{R})$ that depends on $\mathbf{R}$. However, the problem can be simplified, as in most cases this linear combination is dominated by one $\phi_a(\mathbf{r}, \mathbf{R})$, so that to each state of the molecule can be assigned one adiabatic electronic state. This procedure is referred to as the Born–Oppenheimer approximation. In each adiabatic state, the nuclei move in a potential

$$U_a(\mathbf{R}) = E_a(\mathbf{R}) + V_{\mathrm{nuc}}(\mathbf{R}) \tag{1.3}$$

where $E_a(\mathbf{R})$ is the electronic energy given as solution to Eq. (1.2) and $V_{\mathrm{nuc}}(\mathbf{R})$ is the potential energy due to nuclear repulsion as specified in Eq. (1.1). $U_a(\mathbf{R})$

is termed the potential energy surface (PES) of the molecule in state a. Since $\mathbf{R}$ is a $3N_{\mathrm{nuc}}$-dimensional vector, $U_a(\mathbf{R})$ is a rather complicated hypersurface that cannot be visualized easily. Fortunately, further simplifications can be made. When we study light-harvesting and XT, we are normally interested in excited states of the pigments, but not in photochemical reactions that lead to complicated rearrangements of the nuclei. Thus, for our purposes, it is sufficient to look at the PES in the vicinity of its minimum. This can be accomplished by invoking a Taylor expansion of $U_a(\mathbf{R})$ around the minimum $\mathbf{R}^{(a)}$:

$$U_a(\mathbf{R}) \approx U_a\left(\mathbf{R}^{(a)}\right) + \frac{1}{2}\sum_{\alpha,\beta=1}^{3N_{\mathrm{nuc}}} \left(\frac{\partial^2 U_a}{\partial R_\alpha \partial R_\beta}\right)_{\mathbf{R}=\mathbf{R}^{(a)}} \Delta R_\alpha^{(a)} \Delta R_\beta^{(a)} \tag{1.4}$$

Here, we have introduced the deviation of each of the components R_α of $\mathbf{R}$ ($\alpha = 1, \ldots, 3N_{\mathrm{nuc}}$) from the minimum, $\Delta R_\alpha^{(a)} = R_\alpha - R_\alpha^{(a)}$. Equation (1.4) indicates that we are only interested in small deviations $\Delta R_\alpha^{(a)}$, as we have truncated the Taylor series after the second-order term. In this case, we can further simplify by transforming the nuclear coordinates according to

$$\Delta R_\alpha^{(a)} = \sum_\xi M_\alpha^{-1/2} A_{\alpha\xi}^{(a)} q_{a,\xi} \tag{1.5}$$

In Eq. (1.5), $A_{\alpha\xi}^{(a)}$ is a transformation matrix, and the new coordinates $q_{a,\xi}$ are mass-weighted normal mode coordinates [15, 16]. The nuclear motion is then equivalent to that of $3N_{\mathrm{nuc}} - 6$ independent harmonic oscillators (without translation and rotation of the pigment as a whole), and we have.

$$U_a(\mathbf{q}) \approx U_a(\mathbf{0}) + \frac{1}{2}\sum_{\xi=1}^{3N_{\mathrm{nuc}}-6} \omega_{a,\xi}^2 q_{a,\xi}^2 \tag{1.6}$$

with $\mathbf{q}$ denoting all normal mode coordinates collectively, and with $\omega_{a,\xi}$ and $U_a(\mathbf{0})$ being the frequency of the ξth mode and the energy at the minimum, respectively, of adiabatic state a. For later applications, it is convenient to introduce dimensionless coordinates defined by $Q_{a,\xi} = q_{a,\xi}\ (\hbar/2\omega_{a,\xi})^{-1/2}$. Equation (1.6) then becomes

$$U_a(\mathbf{Q}) \approx U_a(\mathbf{0}) + \frac{1}{4}\sum_{\xi=1}^{3N_{\mathrm{nuc}}-6} \hbar\omega_{a,\xi} Q_{a,\xi}^2 \tag{1.7}$$

The electrons in a molecule can be regarded as a kind of glue that holds the nuclei together and determines their equilibrium positions $\mathbf{R}^{(a)}$ by virtue of $E_a(\mathbf{R})$ in

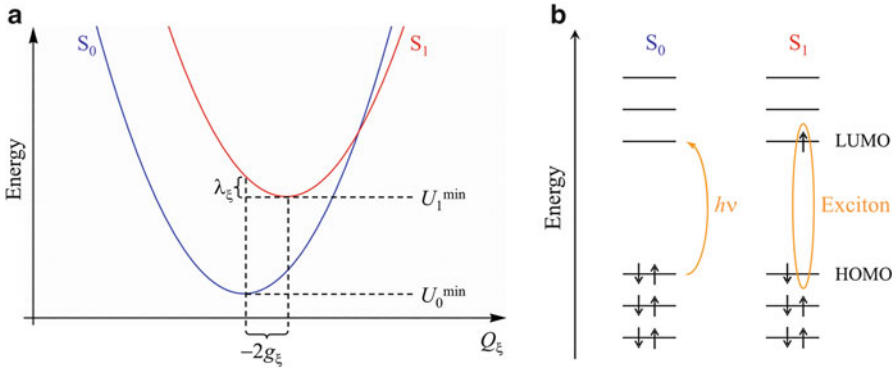

Fig. 1.3 (**a**) Potential energy surfaces (PESs) of the ground state S_0 and the first excited state S_1 of a pigment molecule in the harmonic approximation. Shown is a cut through the PESs along a representative dimensionless vibrational normal coordinate Q_ξ. λ_ξ is the reorganization energy of the mode ξ for the $S_0 \rightarrow S_1$ transition. (**b**) Electron configuration of the S_0 and S_1 states of a pigment within a simple molecular orbital (MO) picture. The transfer of an electron from the highest occupied molecular orbital (HOMO) to the lowest unoccupied molecular orbital (LUMO) due to absorption of a photon ($h\nu$) creates a bound electron–hole pair that is referred to as exciton

Eq. (1.3). Then, one can imagine that a change of the electronic state (e.g., by absorption of a photon) leads to a certain redistribution of the electronic charge density (e.g., from $e\ |\phi_a(\mathbf{r},\mathbf{R})|^2$ to $e\ |\phi_b(\mathbf{r},\mathbf{R})|^2$; we will see an example for this redistribution further below) and, hence, a change of the forces that the electrons exert on the nuclei. As a consequence, the $R_\alpha^{(a)}$, $Q_{a,\xi}$, and $\omega_{a,\xi}$ will in general be different in different adiabatic states a. In what follows, we shall ignore all these changes except for those of the $R_\alpha^{(a)}$. Then, the Q_ξ and ω_ξ are independent of a, and we are allowed to draw a simple 2D sketch of the PES by taking one of the normal mode coordinates as an example. This is done in Fig. 1.3a for those adiabatic states of a pigment that we are mostly interested in here, namely, the electronic ground state ($a = 0$, S_0 state) and the first excited state ($a = 1$, S_1 state). The oscillator potentials pertaining to the two adiabatic states are displaced by an amount $-2g_\xi$ along the coordinate axis due to the change of $\mathbf{R}^{(a)}$ between $a = 0$ and $a = 1$, while they are displaced by ${U_1}^{\min} - {U_0}^{\min}$ along the energy axis. The displacement $-2g_\xi$ plays a crucial role in the coupling of the excited state to the molecular vibrations.[2] This is due to the above-mentioned large mass difference between electrons and nuclei, causing a change of the electronic state to be essentially instantaneous

[2] This coupling is characterized by the coupling constant g_ξ, which is defined as half the displacement of the minima of the two PES for reasons that will become evident below. The negative sign is merely a convention that allows a positive g_ξ (as, e.g., in Eqs. (1.12) and (1.13) below) to shift the excited state PES to the right with respect to the ground state PES as in Fig. 1.3a.

on the time scale of nuclear motion (Franck–Condon principle; [17, 18]).[3] As a consequence, the excited state formed by photon absorption has initially the nuclear positions corresponding to the equilibrium positions of the ground state. However, at these coordinates, the excited state is not in its potential minimum, but at an energy that is higher by an amount λ_ξ, termed the reorganization energy of mode ξ. As can be seen directly from Fig. 1.3a in conjunction with Eq. (1.7), the reorganization energy is connected to the displacement by the mode frequency according to $\lambda_\xi = \hbar\omega_\xi g_\xi^2$. Taking into account all modes, the energy of the absorbed photon with frequency ν is given by

$$h\nu = U_1^{\min} - U_0^{\min} + \sum_{\xi=1}^{3N_{\mathrm{nuc}}-6} \hbar\omega_\xi g_\xi^2 \tag{1.8}$$

Thus, part of the photon energy is deposited in molecular vibrations to an amount depending on the coupling constants g_ξ. Further below, we shall see that this coupling of electronic excitations to vibrations is important for XT in light-harvesting. However, then we have to take into account also vibrations of the protein medium.

After having simplified as far as possible the description of molecular vibrations, we still have to deal with the electronic problem given by Eq. (1.2) at fixed **R**. The first step to a solution is to consider one electron moving in the electric field of the clamped nuclei and the averaged field of the other electrons (Hartree–Fock approximation; see [19]). The resulting wave functions are molecular orbitals (MOs). These MOs can be filled from the bottom up with the N_{el} electrons, putting two electrons with opposite spin in each orbital.[4] In this way, one particular electron configuration can be assigned to each adiabatic state of the pigment, as shown for the S_0 and S_1 states in Fig. 1.3b. While the clarity of such an MO picture is quite appealing, it is an approximation as it neglects the correlation of the motion of different electrons. Taking into account this electron correlation is the central problem to be solved in quantum chemistry and beyond the scope of this chapter (we refer the reader to [16, 19–21]). However, we have to face the fact that the necessary approximations in the treatment of electron correlation limit the accuracy of the calculated wave functions $\phi_a(\mathbf{r}, \mathbf{R})$ and energies $E_a(\mathbf{R})$, which is of concern in the structure-based simulations of PPCs. We come back to this problem below.

[3] The Franck–Condon principle states that during the time of an electronic transition, the nuclear motion can be neglected, so that the nuclei are practically "frozen" during the process of light excitation of the molecule. In a plot of the PESs, this means that the transition occurs at constant Q (valid for all Q). Hence, it is termed a "vertical" transition.

[4] Actually, each electron occupies one *spin orbital*. In the restricted closed-shell Hartree–Fock approach, two of these spin orbitals with different spin functions have the same spatial wavefunction, so that two electrons occupy the same spatial orbital [19]. The energy levels depicted in usual MO schemes (as for example in Fig. 1.3b) refer to these spatial orbitals.

1.3 Excitons and Exciton Transfer

The concept of an exciton originates from solid state physics and was proposed by Frenkel to describe the excitation of atoms in a lattice [22]. The basic idea is that the excitation produces an electron–hole pair that is able to move through the lattice like a particle without a net charge transfer (CT). In the case of dye molecules, the exciton can be visualized best in the approximate MO picture. Absorption of a photon with energy $h\nu$ corresponding to the lowest electronic transition causes an electron in the highest occupied molecular orbital (HOMO) to "jump" into the lowest unoccupied molecular orbital (LUMO) as indicated in Fig. 1.3b. We emphasize again that this view is approximate. Because of the electron–electron interaction in the dye, all electrons are involved to a certain extent, and the $S_0 \rightarrow S_1$ transition is more than simply a HOMO $\rightarrow$ LUMO transition. Nonetheless, the relevant aspects can be discussed on the basis of the simple MO picture. Thus, the photon promotes one electron to a higher energy level, leaving a defect electron (hole) in the lower level. Often, electron and hole are described as a pair of charged particles that attract each other. This bound electron–hole pair is the exciton that stores the photon energy. As the electron and the hole are located on the same molecule, the distance between the two is confined to roughly the diameter of the molecule. Such a "small" exciton corresponds to the situation in insulating solids studied by Frenkel and is, therefore, referred to as Frenkel exciton. The crucial question is: How can a Frenkel exciton move in a PPC?

To answer this question, we have to consider the electron–electron interaction between two adjacent dye molecules. Let us call one of these molecules the donor D and the other the acceptor A. Then the initial state of the XT process is $|\mathrm{D}^*\mathrm{A}\rangle = |\mathrm{S_1S_0}\rangle$, where D is in its first excited state S_1 and A in its ground state S_0, and the final state is $|\mathrm{DA}^*\rangle = |\mathrm{S_0S_1}\rangle$, where A is excited and D in the ground state. The Coulomb interaction between molecules can be represented by the quantum mechanical operator $\hat{V} = e^2/|\mathbf{r}_1 - \overline{\mathbf{r}}_1|$, where $\mathbf{r}_1$ and $\overline{\mathbf{r}}_1$ denote the position of electron no. 1 of D and of A, respectively. Actually, $\hat{V}$ represents the Coulomb interaction of all electrons of D with all electrons of A, but due to the indistinguishability of the electrons, the interaction can be cast in a form, where only one representative electron from each molecule shows up explicitly (see [23]). Then, the interaction energy can be written as the following integral:

$$\langle \mathrm{D}^*\mathrm{A}|\hat{V}\,|\mathrm{DA}^*\rangle = N_{\mathrm{el}}^2 \int d\mathbf{r}_1 \ldots d\mathbf{r}_{N_{\mathrm{el}}} d\overline{\mathbf{r}}_1 \ldots d\overline{\mathbf{r}}_{N_{\mathrm{el}}} \phi_1^{(\mathrm{D})*}(\mathbf{r}) \phi_0^{(\mathrm{A})*}(\overline{\mathbf{r}}) \frac{e^2}{|\mathbf{r}_1 - \overline{\mathbf{r}}_1|} \phi_0^{(\mathrm{D})}(\mathbf{r}) \phi_1^{(\mathrm{A})}(\overline{\mathbf{r}}) \tag{1.9}$$

Here, $\phi_0^{(\mathrm{D})}(\mathbf{r})$ and $\phi_1^{(\mathrm{D})}(\mathbf{r})$ are the many-electron wave functions (solutions of Eq. (1.2)) for the ground and first excited adiabatic states, respectively, of D, and $\phi_0^{(\mathrm{A})}(\overline{\mathbf{r}})$ and $\phi_1^{(\mathrm{A})}(\overline{\mathbf{r}})$ those of A, and we have assumed for simplicity that both molecules have the same number N_{el} of electrons. (The symbol "*" at the wave

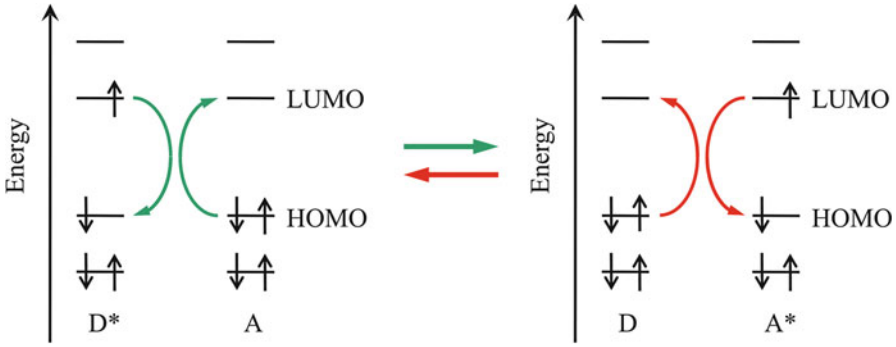

Fig. 1.4 Simple MO picture of radiationless exciton transfer (XT) between two molecules with negligible wave function overlap. The transitions are caused by the intermolecular Coulomb interaction of electrons

functions indicates complex conjugation.) One can distinguish different contributions to the integral $\langle \mathrm{D}^*\mathrm{A}|\hat{V}\,|\mathrm{DA}^*\rangle$ depending on the intermolecular distance. If the distance is sufficiently large (say, >4 Å edge-to-edge), the intermolecular overlap, i.e., the spatial overlap of electronic wave functions on D with those on A, can be neglected. It is this regime of molecular interactions that we will be concerned with in this chapter.[5] Further below, we shall exploit the neglect of intermolecular overlap to derive simple computation schemes. Concerning the coupling $\langle \mathrm{D}^*\mathrm{A}|\hat{V}\,|\mathrm{DA}^*\rangle$, this neglect means that Eq. (1.9) can be written as

$$\langle \mathrm{D}^*\mathrm{A}|\hat{V}\,|\mathrm{DA}^*\rangle = \int d\mathbf{r}_1 d\overline{\mathbf{r}}_1 \frac{\rho_{01}^{(\mathrm{D})}(\mathbf{r}_1)\rho_{01}^{(\mathrm{A})}(\overline{\mathbf{r}}_1)}{|\mathbf{r}_1 - \overline{\mathbf{r}}_1|} \tag{1.10}$$

where we introduced the transition density

$$\rho_{01}^{(\mathrm{X})}(\mathbf{r}_1) = N_{\mathrm{el}} e \int d\mathbf{r}_2 \ldots d\mathbf{r}_{N_{\mathrm{el}}} \phi_1^{(\mathrm{X})*}(\mathbf{r})\phi_0^{(\mathrm{X})}(\mathbf{r}) \tag{1.11}$$

for pigment X = D, A. (The transition density is further explained below in the context of the computation of excitonic couplings.) The kind of process effectuated by such a coupling can be easiest envisaged as a simultaneous excitation–deexcitation of the DA pair as shown in terms of a simple MO picture in Fig. 1.4. Thus, the Coulomb interaction of the electrons on D with those of A disturbs the electron motion such that with a certain probability the electron in the LUMO of D jumps to the HOMO of D, while at the same time one electron of A jumps from the HOMO to the LUMO. The net effect of these jumps is that the exciton has moved

[5] In fact, it is the neglect of electron exchange between the pigments that justifies the use of the term "Frenkel exciton."

from D to A (green arrows in Fig. 1.4). Because this type of radiationless transfer is central to the Förster theory of XT, we refer to the coupling given by Eq. (1.10) as a Förster-type excitonic coupling. One may notice that the electrons on D and A disturb each other in the state $|\mathrm{DA}^*\rangle$ as they do in the state $|\mathrm{D}^*\mathrm{A}\rangle$. Indeed, by virtue of the coupling $\langle \mathrm{D}^*\mathrm{A}|\hat{V}|\mathrm{DA}^*\rangle$, the exciton is as likely moved back from A to D (red arrows) as it is moved from D to A, and the exciton is not really transferred, but merely delocalized between the two pigments. To see, how XT becomes directional, we have to consider molecular vibrations. But before doing that, we briefly comment on situations, where the intermolecular overlap can not be neglected.

If D and A approach each other closer (say, <3.5 Å edge-to-edge, depending on the dimer geometry), there is a non-negligible intermolecular overlap. As a consequence, electron exchange between the two pigments has to be taken into account. Then, the coupling $\langle \mathrm{D}^*\mathrm{A}|\hat{V}|\mathrm{DA}^*\rangle$ gains an overlap-dependent contribution (Dexter-type coupling; [24]), and the exciton states $|\mathrm{DA}^*\rangle$ and $|\mathrm{DA}^*\rangle$ become coupled to charge-transfer (CT) states $|\mathrm{D}^+\mathrm{A}^-\rangle$ and $|\mathrm{D}^-\mathrm{A}^+\rangle$, where literally an electron has moved from one pigment to the other [25]. Clearly, such couplings are important in the RC [26]. However, their role in light-harvesting is not yet well understood and a topic of current research. Here, we only mention that CT states may be relevant to understand the ring-shaped LHCs of purple bacteria [27] and certain features of the core antenna of cyanobacterial PSI.

Turning back to the question of the directionality of XT, we consider now our pair of molecules D and A to be embedded in a protein matrix, i.e., we look at a very simple model PPC with only two pigments. The vibrations of the protein can be characterized approximately by normal modes as explained above for the vibrations of the pigments. By virtue of intermolecular electrostatic interactions, the protein oscillators are coupled to the adiabatic states of the pigments to an extent that depends on the distance and location of the involved atoms relative to the pigments. Then, not only has the PES of a particular pigment state contributions from the protein modes, but also the harmonic function representing one such mode depends on the pigment states. To make this statement more transparent, let us pick out one protein normal mode Q with frequency ω, whose vibrating atoms are in the vicinity of the two pigments D and A. Then, we can assign a parabolic PES along the coordinate Q to each of the three states $|\mathrm{DA}\rangle = |\mathrm{S_0S_0}\rangle$ (electronic ground state of the PPC) as well as $|\mathrm{D}^*\mathrm{A}\rangle = |\mathrm{S_1S_0}\rangle$ and $|\mathrm{DA}^*\rangle = |\mathrm{S_0S_1}\rangle$ (local excited states of the PPC) as shown in the left part of Fig. 1.5a.

Here, we have defined the origin at the equilibrium position of Q in the electronic ground state of the PPC. With this choice, the PESs of both local excited states are shifted along the Q-axis [14]:

$$U_{\mathrm{D}}(Q) = U_{\mathrm{D}}^{\min} + \frac{\hbar\omega}{4}(Q + 2g_{\mathrm{D}})^2 \tag{1.12}$$

$$U_{\mathrm{A}}(Q) = U_{\mathrm{A}}^{\min} + \frac{\hbar\omega}{4}(Q + 2g_{\mathrm{A}})^2 \tag{1.13}$$

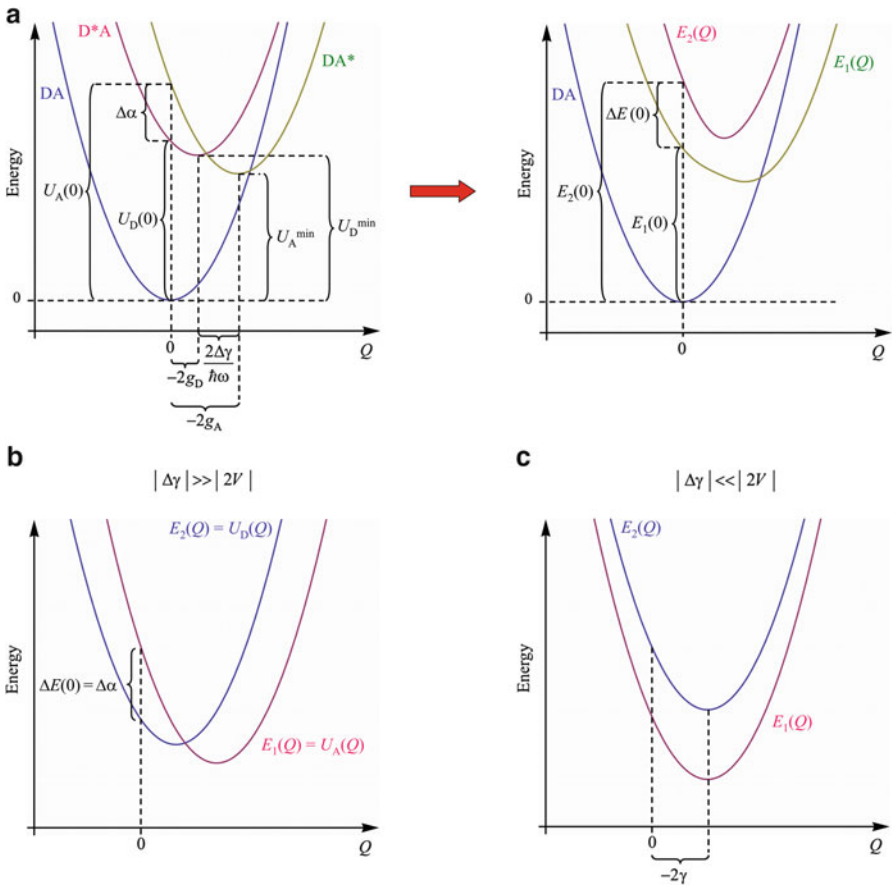

Fig. 1.5 (**a**) *Left*: Harmonic PESs pertaining to a protein vibrational mode Q with frequency ω for the ground state DA and the local excited states D*A and DA* of a pair of pigments bound to a PPC. *Right*: PESs of the DA pair after the excitonic coupling V between the local excited states has been taken into account. (**b**) PESs of the two excited states of the DA pair in the limit $|\Delta\gamma| \gg |2V|$ with $\Delta\gamma = \hbar\omega(g_A - g_D)$. (**c**) PESs of the two excited states of the DA pair in the limit $|\Delta\gamma| \ll |2V|$ with $\gamma = (g_A + g_D)/2$

If the pigments were not coupled excitonically, they would absorb light preferentially at the energies $U_D(0)$ and $U_A(0)$, employing the Franck–Condon principle. The transition energies $U_D(0)$ and $U_A(0)$ are called the *site energies* of the pigments D and A, respectively, and in general, they are different because $U_D^{min} \neq U_A^{min}$ and $g_D \neq g_A$, since

$$\Delta\alpha = U_A(0) - U_D(0) = U_A^{min} - U_D^{min} + \hbar\omega\left(g_A^2 - g_D^2\right) \tag{1.14}$$

Further below, we shall see, how the protein can be made responsible for these differences. In the following, we denote the excitonic coupling by $V = \langle D^*A|\hat{V}|DA^*\rangle$ and assume for simplicity that it does not depend on Q. (This assumption is

justified below in the context of the FMO protein.) If $V \neq 0$, the two states $|\mathrm{D^*A}\rangle$ and $|\mathrm{DA^*}\rangle$ are no longer adiabatic states of the DA dimer. Rather, they are referred to as diabatic states. To find the adiabatic states of the dimer, we have to solve an eigenvalue problem, that is, we have to diagonalize the matrix:

$$\begin{pmatrix} U_\mathrm{D}(Q) & V \\ V & U_\mathrm{A}(Q) \end{pmatrix} \Rightarrow \begin{pmatrix} E_1(Q) & 0 \\ 0 & E_2(Q) \end{pmatrix} \tag{1.15}$$

The resulting adiabatic PESs are shown in the right part of Fig. 1.5a and are given explicitly by

$$E_{1,2}(Q) = \frac{1}{2}\left[U_\mathrm{D}(Q) + U_\mathrm{A}(Q) \pm \sqrt{\Delta E(Q)^2 + 4V^2}\right] \tag{1.16}$$

where we have introduced the abbreviation

$$\Delta E(Q) = U_\mathrm{A}(Q) - U_\mathrm{D}(Q) = \Delta\alpha + Q\Delta\gamma \tag{1.17}$$

with

$$\Delta\gamma = \hbar\omega(g_\mathrm{A} - g_\mathrm{D}) \tag{1.18}$$

The quantity $\Delta\gamma$ can be interpreted as representing the *difference* in coupling of the electronic transition of donor and acceptor to the vibration represented by the mode Q. Introducing, in addition, the two quantities

$$\gamma = \frac{1}{2}(g_\mathrm{A} + g_\mathrm{D}) \tag{1.19}$$

and

$$E^\mathrm{min} = \frac{U_\mathrm{D}^\mathrm{min} + U_\mathrm{A}^\mathrm{min}}{2} + \frac{\Delta\gamma^2}{4\hbar\omega} \tag{1.20}$$

we can rewrite Eq. (1.16) as

$$E_{1,2}(Q) = E^\mathrm{min} + \frac{\hbar\omega}{4}(Q + 2\gamma)^2 \pm \frac{1}{2}\sqrt{(\Delta\alpha + Q\Delta\gamma)^2 + 4V^2} \tag{1.21}$$

where it becomes apparent that the two adiabatic PESs originate from a harmonic oscillator shifted by -2γ that is perturbed by adding or subtracting the square-root term. The two adiabatic states are linear combinations of the two local excited states

$$|1\rangle = s(Q)|\mathrm{D^*A}\rangle + u(Q)|\mathrm{DA^*}\rangle \tag{1.22}$$

$$|2\rangle = -u(Q)|\mathrm{D}^*\mathrm{A}\rangle + s(Q)|\mathrm{DA}^*\rangle \tag{1.23}$$

The probabilities of finding the exciton in state $|1\rangle$ on D or A are $s(Q)^2$ and $u(Q)^2$, respectively, and vice versa for state $|2\rangle$ (implying $s(Q)^2 + u(Q)^2 = 1$). Note that these probabilities depend on Q and, thus, are influenced by nuclear motion. The coefficients $s(Q)$ and $u(Q)$ can be traced back to the parameters $\Delta\alpha$ and $\Delta\gamma$ (contained in $\Delta E(Q)$) as well as V in the following way:

$$s(Q) = \frac{1}{\sqrt{1 + Y(Q)^2}} \tag{1.24}$$

$$u(Q) = \frac{Y(Q)}{\sqrt{1 + Y(Q)^2}} \tag{1.25}$$

with

$$Y(Q) = \frac{u(Q)}{s(Q)} = \frac{\Delta E(Q)}{2V} + \frac{V}{|V|}\sqrt{\left(\frac{\Delta E(Q)}{2V}\right)^2 + 1} \tag{1.26}$$

However, it is yet not clear, how XT from D to A takes place. To see this, it is helpful to look at limiting cases. The two relevant quantities to define these limits are $\Delta\gamma$ and V.

If $|\Delta\gamma| \gg |2\,V\,|$, i.e., the difference in exciton-vibrational coupling between D and A is much larger than the excitonic coupling, we can make the following approximation:

$$E_{1,2}(Q) \approx E^{\min} + \frac{\hbar\omega}{4}(Q + 2\gamma)^2 \pm \frac{1}{2}|\Delta\alpha + Q\Delta\gamma| = \begin{cases} U_{\mathrm{A}}^{\min} + \dfrac{\hbar\omega}{4}(Q + 2g_{\mathrm{A}})^2 \\ U_{\mathrm{D}}^{\min} + \dfrac{\hbar\omega}{4}(Q + 2g_{\mathrm{D}})^2 \end{cases} \tag{1.27}$$

Hence, in this limit, the two adiabatic states are close to the diabatic states (Fig. 1.5b), and the exciton is localized on either the donor D or the acceptor A. The excitonic coupling V can be considered as a small perturbation that causes the transitions between states $|\mathrm{D}^*\mathrm{A}\rangle$ and $|\mathrm{DA}^*\rangle$ with the initial state being in thermal equilibrium. To better see, how the parameters V, $\Delta\alpha$, and $\Delta\gamma$ determine the direction of XT, we have to do further approximations: We have to go into the high-temperature limit, i.e., we assume that $\hbar\omega \ll k_{\mathrm{B}}T$, and we have to consider many modes Q_ξ with a dense distribution of frequencies ω_ξ. Then, the rate for XT from pigment m to pigment n (with $m, n = \mathrm{D}, \mathrm{A}$) can be expressed as [28]:

$$k_{m\to n} = \frac{2\pi}{\hbar^2}|V|^2 \frac{1}{\sqrt{4\pi\lambda k_{\mathrm{B}}T}} \exp\left[-\frac{(\Delta U_{m\to n} + \lambda)^2}{4\lambda k_{\mathrm{B}}T}\right] \tag{1.28}$$

in complete analogy to nonadiabatic ET theory [29]. Here, we have defined the "energy gap" by

$$\Delta U_{m\to n} = U_n^{\min} - U_m^{\min} = \pm\Delta\alpha - \sum_\xi \hbar\omega\left(g_{n,\xi}^2 - g_{m,\xi}^2\right) \tag{1.29}$$

and the reorganization energy by

$$\lambda = \sum_\xi \hbar\omega_\xi \left(g_{m,\xi} - g_{n,\xi}\right)^2 \tag{1.30}$$

In the definition of $\Delta U_{m\to n}$ in Eq. (1.29), the positive sign applies, if $m = \mathrm{A}$, $n = \mathrm{D}$, and the negative sign, if $m = \mathrm{D}$, $n = \mathrm{A}$. Note that $\Delta U_{\mathrm{D}\to\mathrm{A}} = -\Delta U_{\mathrm{A}\to\mathrm{D}}$ and $(g_m - g_n)^2 = \Delta\gamma^2/\hbar^2\omega^2$ for each mode. According to Eq. (1.28), the parameters V, $\Delta\alpha$, and $\Delta\gamma$ (represented by V, $\Delta U_{m\to n}$, and λ) influence the XT rate. To characterize the direction of XT, we introduce the equilibrium constant

$$K = \frac{k_{\mathrm{D}\to\mathrm{A}}}{k_{\mathrm{A}\to\mathrm{D}}} = \exp\left[\frac{(\Delta U_{\mathrm{A}\to\mathrm{D}} + \lambda)^2}{4\lambda k_\mathrm{B}T} - \frac{(\Delta U_{\mathrm{D}\to\mathrm{A}} + \lambda)^2}{4\lambda k_\mathrm{B}T}\right] = \exp\left[-\frac{\Delta U_{\mathrm{D}\to\mathrm{A}}}{k_\mathrm{B}T}\right] \tag{1.31}$$

From Eq. (1.31), we see that the sign of $\Delta U_{\mathrm{D}\to\mathrm{A}}$ determines the direction of XT: If $\Delta U_{\mathrm{D}\to\mathrm{A}} < 0$, $K > 1$, and the exciton is preferentially located on the acceptor. If $\Delta U_{\mathrm{D}\to\mathrm{A}} > 0$, $K < 1$, and the exciton preferentially stays on the donor. For $\Delta U_{\mathrm{D}\to\mathrm{A}} = 0$, we have $K = 1$, and the exciton bounces forth and back between D and A with equal probability. Note that this is a true equilibrium, where the exciton hops between D and A, but at all times is fully localized on either D or A. In order to determine the sign of $\Delta U_{\mathrm{D}\to\mathrm{A}}$, we have to know $\Delta\alpha$ and $\Delta\gamma$. Although V does not show up in Eq. (1.31), it is, of course, a prerequisite for XT, and its magnitude has to be known to determine the XT rate and to decide, whether the limit $|\Delta\gamma| \gg |2\,V\,|$ applies or not.

For completeness, we mention that with an additional assumption we arrive at the Förster theory of XT. For this purpose, we have to assume that $g_m \gg g_n \approx 0$, i.e., each mode is primarily coupled to either the donor or the acceptor. Then, the exponential term in Eq. (1.28) can be expressed in terms of the emission spectrum of the donor and the absorption spectrum of the acceptor [30–32].

Coming back to the one-mode picture, there exists another limit, in which $|\Delta\gamma| \ll |2\,V|$, i.e., the excitonic coupling is much larger than the difference in exciton-vibrational coupling. Then, we can make the following approximation:

$$E_{1,2}(Q) \approx E^{\min} + \frac{\hbar\omega}{4}(Q + 2\gamma)^2 \pm \frac{1}{2}\sqrt{\Delta\alpha^2 + 4V^2} \tag{1.32}$$

Here, the two adiabatic PESs correspond to two harmonic oscillators that are shifted by the same amount -2γ with respect to the ground state (Fig. 1.5c) and

have a Q-independent energy difference given by the square-root term in Eq. (1.32). The adiabatic electronic states are now Q-independent linear combinations of the two localized excited states:

$$|1\rangle = s(0)|\mathrm{D}^*\mathrm{A}\rangle + u(0)|\mathrm{D}\mathrm{A}^*\rangle \tag{1.33}$$

$$|2\rangle = -u(0)|\mathrm{D}^*\mathrm{A}\rangle + s(0)|\mathrm{D}\mathrm{A}^*\rangle \tag{1.34}$$

These are obtained by diagonalizing the matrix in Eq. (1.15) for $Q = 0$. States of this sort are in general referred to as delocalized exciton states. The exciton is delocalized in the quantum physical sense, i.e., the excitation cannot be assigned unequivocally to a particular pigment. All that can be said is that pigment D or A is excited with a certain probability determined by the coefficients $s(0)$ and $u(0)$. However, as these coefficients depend on $\Delta\alpha$ and V, so does the degree of delocalization.

Here, again, two limits can be considered: If $|\Delta\alpha| \gg |2\,V|$, we obtain from Eq. (1.26) that $Y(0)$ either becomes zero or very large depending on the sign of V. In any case, one of the coefficients $s(0)$ or $u(0)$ becomes essentially zero and the other one. This means that the two states $|1\rangle$ and $|2\rangle$ become localized, one on D and the other on A. If, on the other hand, $|\Delta\alpha| \ll |2\,V|$, we obtain $Y(0) \approx \pm\,1$ depending on the sign of V, resulting in $s(0) = 2^{-½}$ and $u(0) = \pm\,2^{-½}$. In this case, the exciton is found with equal probability on either D or A. For most pigment pairs in real PPCs, the situation is between these two extremes.

Let us assume that $V > 0$. Then, we can still distinguish the three basic cases $\Delta\alpha < 0$, $\Delta\alpha = 0$, and $\Delta\alpha > 0$ (Fig. 1.6). To understand, how XT takes place in this limit, we first have to answer the question of how a transition from the energetically higher exciton state $|1\rangle$ to the lower exciton state $|2\rangle$ (red arrows in Fig. 1.6) can happen. The origin of such a transition is a small perturbation that couples the two states $|1\rangle$ and $|2\rangle$. However, in contrast to the limit discussed before, this perturbation is not of electronic origin, but due to nuclear motion. Performing the diagonalization in Eq. (1.15) for $Q = 0$ is an approximation, and the exciton states are not exactly the adiabatic states of the DA dimer for $Q \neq 0$. Thus, nuclear motion results in a coupling of the states, i.e., it contributes an off-diagonal matrix element to the Hamiltonian in the basis of exciton states. This can be seen by rewriting the PES of the local excited states in Eqs. (1.12) and (1.13) as

$$U_\mathrm{D}(Q) = U_\mathrm{D}^\mathrm{min} + \hbar\omega g_\mathrm{D}^2 + \hbar\omega g_\mathrm{D} Q + \frac{\hbar\omega}{4} Q^2 \tag{1.35}$$

$$U_\mathrm{A}(Q) = U_\mathrm{A}^\mathrm{min} + \hbar\omega g_\mathrm{A}^2 + \hbar\omega g_\mathrm{A} Q + \frac{\hbar\omega}{4} Q^2 \tag{1.36}$$

where $U_\mathrm{D}(0)$ and $U_\mathrm{A}(0)$ were used to define the exciton states in Eqs. (1.33) and (1.34). Transforming the Q-dependent terms in Eqs. (1.35) and (1.36) into the exciton basis then results in diagonal and off-diagonal Q-dependent matrix elements, where the latter read

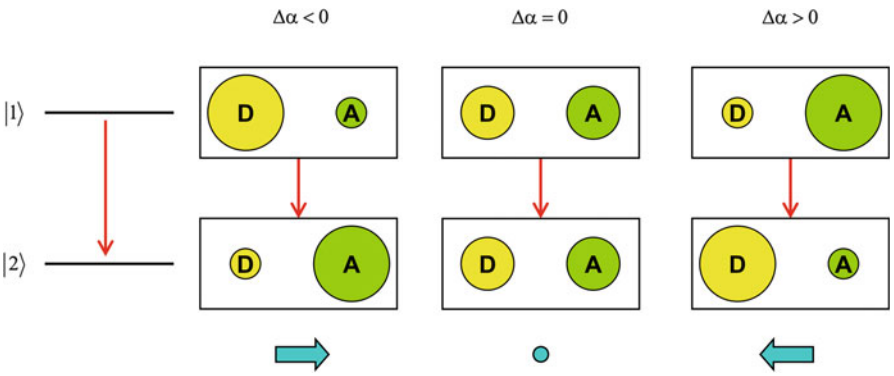

Fig. 1.6 Relationship between thermal relaxation (*red arrows*) from a higher exciton state $|1\rangle$ to a lower state $|2\rangle$ (both delocalized over two pigments D and A) and XT between D and A. The size of the circles symbolizes the probability to find the exciton on either pigment in the respective exciton state. The sign of the site energy difference $\Delta\alpha$ determines the direction of probability transfer (*blue symbols*) due to the relaxation process

$$J_{12} = s(0)u(0)Q\Delta\gamma \tag{1.37}$$

We see that in this limit, all the relevant parameters $\Delta\gamma$, $\Delta\alpha$, and V (with the latter two hidden in $s(0)$ and $u(0)$) contribute to the residual coupling between the two adiabatic states of the DA dimer. (Note that J_{12} does not imply a Q-dependence of V, but originates solely from the Q-dependence of $U_D(Q)$ and $U_A(Q)$.) In a real PPC, there is not just one mode, so that the states $|1\rangle$ and $|2\rangle$ can be regarded as being coupled to a bath of harmonic oscillators. If, then, the state $|1\rangle$ is initially populated, thermal relaxation results in a transition to state $|2\rangle$ with the excess energy $\sqrt{\Delta\alpha^2 + 4V^2}$ being dissipated in the bath. How is this energetic relaxation related to XT?

The answer to the latter question depends on $\Delta\alpha$. If $\Delta\alpha = 0$, the transition from $|1\rangle$ to $|2\rangle$ does not affect the probability of finding the exciton on either D or A. However, if $\Delta\alpha < 0$, the probability of finding the exciton on A is higher in state $|2\rangle$ than in state $|1\rangle$, so that energetic relaxation results in a net transfer of probability from D to A, and vice versa for $\Delta\alpha > 0$ (blue arrows in Fig. 1.6). Thus, the sign of $\Delta\alpha$ determines the direction of XT. Note, however, that in this case the exciton is always delocalized. XT is complete only, if, for example, A further transfers the exciton to another pigment.

It should be clear now, that knowledge of the parameters $\Delta\alpha$, $\Delta\gamma$, and V is important for an analysis of XT mechanisms. In a real PPC, there are normally more than two pigments and significantly more than one vibrational mode to consider. For example, one monomeric subunit of the FMO protein has almost 19,400 normal modes [33]. A further complication arises from the fact that in most cases the two limits discussed above do not really apply, but rather $|\Delta\gamma| \approx |2\,V\,|$. Nonetheless, the parameters $\Delta\alpha$, $\Delta\gamma$, and V have to be known for computations of XT rates and optical spectra. In the following, we shall see how this information can be extracted from a crystal structure of the PPC.

1.4 Molecular Interactions and Charge Distributions

We now exploit the neglect of intermolecular electron exchange to partition the PPC into building blocks that mutually interact only via non-bonded interactions, i.e., without covalent bonds. The neglect of intermolecular overlap of electronic wave functions is also referred to as the "long-range approximation" [34]. For simplicity of notation, we consider only two building blocks explicitly. The building blocks are a pigment denoted A and an arbitrary second building block denoted B. The latter could be another pigment, cofactor or protein subunit. In the following, these building blocks are simply referred to as "molecules." We presume that the Schrödinger equation for each of the two molecules has been solved within the approximations discussed above, so that we can write for the electronic states at the equilibrium geometry

$$H^{(\mathrm{A})}|a\rangle = E_a^{(\mathrm{A})}|a\rangle \tag{1.38}$$

$$H^{(\mathrm{B})}|b\rangle = E_b^{(\mathrm{B})}|b\rangle \tag{1.39}$$

Here, the quantum numbers a and b count the adiabatic electronic states of A and B, respectively. The two equations correspond to Eq. (1.2) with $\mathbf{R}$ representing the nuclear coordinates at the energy minimum of the ground state PES, i.e., $\mathbf{Q} = \mathbf{0}$ in the normal mode representation. The long-range approximation allows for the use of perturbation theory.[6] According to perturbation theory, the Hamiltonian of the combined system of the two molecules is written as

$$H = H^{(0)} + H' \tag{1.40}$$

with the zeroth-order Hamiltonian $H^{(0)} = H^{(\mathrm{A})} + H^{(\mathrm{B})}$ representing the non-interacting molecules and the perturbation H' being the electrostatic interaction between the molecules. As each adiabatic state of A can be combined with each adiabatic state of B, a suitable basis for the representation of the states of the combined system are product states of the form $|ab\rangle = |a\rangle|b\rangle$ (also referred to as Hartree products; [30]). If molecule A is originally in state $|a\rangle$ and B in state $|b\rangle$, the perturbative approximation to the energy of the state $|ab\rangle$, after the interaction between the molecules has been switched on, is

$$W_{ab} = W_{ab}^{(0)} + W_{ab}^{(1)} + W_{ab}^{(2)} + \cdots \tag{1.41}$$

[6] We have to be careful, however, if B is another pigment. Below, we shall focus on the $S_0 \rightarrow S_1$ transitions of A ($a = 0,1$). Then, we have to exclude the $S_0 \rightarrow S_1$ transitions of the other pigments. This is no restriction, since the couplings between these transitions are treated explicitly in the exciton formalism and do not require a perturbative approximation; see [30].

where the superscript indicates the order of the perturbation. The zeroth-order contribution is simply the energy of the non-interacting molecules, since

$$H^{(0)}|ab\rangle = \left(H^{(\mathrm{A})} + H^{(\mathrm{B})}\right)|ab\rangle = \left(E_a^{(\mathrm{A})} + E_b^{(\mathrm{B})}\right)|ab\rangle = W_{ab}^{(0)}|ab\rangle \tag{1.42}$$

The first-order correction reads

$$W_{ab}^{(1)} = \langle ab|H'|ab\rangle \tag{1.43}$$

and is the electrostatic interaction energy between the permanent charge densities of the two molecules in states $|a\rangle$ and $|b\rangle$. These charge densities have contributions from the electrons and the nuclei. Because of the neglect of intermolecular wave function overlap, we can define the electronic charge density for each molecule X in state $|x\rangle$ separately as

$$\rho_{xx}^{(\mathrm{X})}(\mathbf{r}_1) = -N_{\mathrm{el}} e \int d\mathbf{r}_2 \ldots d\mathbf{r}_{N_{\mathrm{el}}} \phi_x^{(\mathrm{X})*}(\mathbf{r}) \phi_x^{(\mathrm{X})}(\mathbf{r}) \tag{1.44}$$

which is analogous to the definition of the transition density in Eq. (1.11), but with the two wave functions referring to the same adiabatic state. Let the atomic numbers and positions of the nuclei be z_K and $\mathbf{R}_K$, respectively, as above (cf. Eq. (1.1)), and denote by $\mathbf{x}$ a general position in space. Then, the whole charge density of molecule X in state $|x\rangle$ is

$$\widetilde{\rho}_{xx}^{(\mathrm{X})}(\mathbf{x}) = \rho_{xx}^{(\mathrm{X})}(\mathbf{x}) + \sum_K e z_K \delta(\mathbf{x} - \mathbf{R}_K) \tag{1.45}$$

The electrostatic potential due to this charge distribution, evaluated outside the molecule, can be written as

$$\phi_{xx}^{(\mathrm{X})}(\mathbf{x}) = \int d\mathbf{x}' \frac{\rho_{xx}^{(\mathrm{X})}(\mathbf{x}')}{|\mathbf{x} - \mathbf{x}'|} + \sum_K \frac{e z_K}{|\mathbf{x} - \mathbf{R}_K|} \tag{1.46}$$

It is then possible to write the first-order interaction energy between molecules A and B as

$$W_{ab}^{(1)} = \int d\mathbf{x} \widetilde{\rho}_{aa}^{(\mathrm{A})}(\mathbf{x}) \phi_{bb}^{(\mathrm{B})}(\mathbf{x}) \tag{1.47}$$

This equation is still unhandy, but there is a procedure to arrive at a practical scheme for the explicit computation of $W_{ab}^{(1)}$. The trick is to assign to each atom K of molecule X an atomic partial charge $q_K^{(\mathrm{X})}(x,x)$ in a way that the electrostatic potential of all these charges mimics the potential $\phi_{xx}^{(\mathrm{X})}(\mathbf{x})$. This can be accomplished by suitable fitting algorithms [23]. Then, the first-order interaction energy

can simply be obtained by summing up the Coulomb interactions of all the atomic partial charges belonging to different molecules, i.e.,

$$W_{ab}^{(1)} = \sum_{I,J} \frac{q_I^{(\mathrm{A})}(a,a) q_J^{(\mathrm{B})}(b,b)}{\left|\mathbf{R}_I - \overline{\mathbf{R}}_J\right|} \tag{1.48}$$

where I counts the atoms of A, J those of B, and $\mathbf{R}_I$ and $\overline{\mathbf{R}}_J$ are the respective atom positions.

The second-order correction to the interaction energy is somewhat more complicated:

$$W_{ab}^{(2)} = \overbrace{-\sum_{a'\left(a'\neq a\right)} \frac{\langle ab|H'|a'b\rangle\langle a'b|H'|ab\rangle}{W_{a'b}^{(0)} - W_{ab}^{(0)}}}^{U_{\mathrm{ind}}^{(\mathrm{A})}} \overbrace{-\sum_{b'\left(b'\neq b\right)} \frac{\langle ab|H'|ab'\rangle\langle ab'|H'|ab\rangle}{W_{ab'}^{(0)} - W_{ab}^{(0)}}}^{U_{\mathrm{ind}}^{(\mathrm{B})}} \underbrace{-\sum_{\substack{a'\left(a'\neq a\right),\\ b'\left(b'\neq b\right)}} \frac{\langle ab|H'|a'b'\rangle\langle a'b'|H'|ab\rangle}{W_{a'b'}^{(0)} - W_{ab}^{(0)}}}_{U_{\mathrm{disp}}} \tag{1.49}$$

Here, one has to distinguish two principally different types of interaction energies: inductive and dispersive. In $U_{\mathrm{ind}}^{(\mathrm{A})}$, the permanent charge density of molecule B in state $|b\rangle$ *induces* a change of the electron density in molecule A (hence inductive), i.e., it polarizes the electron cloud of A. The polarization can be expressed as a sum over all excitations, which is why there is a sum over $a' \neq a$. Similarly, $U_{\mathrm{ind}}^{(\mathrm{B})}$ originates from the polarization of molecule B by the permanent charge distribution of molecule A in state $|a\rangle$. In addition, in U_{disp}, there is a mutual polarization of the electron clouds of the two molecules originating from the intermolecular electron–electron interaction. This mutual polarization is also known as London dispersive interaction [35] or van der Waals interaction.[7]

In principle, the matrix elements occurring in the numerators of Eq. (1.49) can be recast in terms of atomic partial charges. (Note that then, besides charge distributions, one also needs transition densities for the cases $a' \neq a$ and $b' \neq b$ that likewise can be expressed with atomic partial charges as shown below.) However, there is a

[7] The term "van der Waals interaction" is sometimes used to subsume inductive and dispersive interactions.

complication due to the energy differences occurring in the d enominators. A closed expression for the dispersive interaction in terms of molecular polarizabilities can be deduced [34, 36], but then these polarizabilities have to be calculated with quantum chemistry. For molecules as large as chlorophylls, such calculations are not only computationally demanding but also not necessarily accurate enough. A similar problem appears, if one abandons perturbation theory altogether and tries to calculate the molecular interactions directly with quantum chemistry or combinations of quantum chemistry with classical molecular dynamics simulations. Therefore, in the following, we shall stick on the simplest possible approximation, in which only the first-order correction to the interaction energy is treated explicitly in terms of atomic partial charges, while second- and higher-order effects are effectively taken into account by introducing dielectric continua. In other words, we model the PPC as a collection of atomic partial charges that are situated on the atom positions (inferred from a crystal structure for heavy atoms and from molecular modeling for hydrogen atoms) and are embedded in a polarizable continuum (which is not necessarily homogeneous, see below). Although this approach is approximative, it turns out to work quite well for ordinary PPCs in photosynthesis.[8]

1.5 Site Energies

Above, we have already introduced the site energy as the energy difference between first excited and ground state of a pigment in site m at the equilibrium positions of the nuclei in the ground state. If we take into account not just one, but all relevant vibrational modes of the PPC, the site energy is

$$\Delta U_m(\mathbf{0}) = \underbrace{U_{m,1}^{\min} - U_{m,0}^{\min}}_{\Delta U_m^{\min}} + \underbrace{\sum_{\zeta} \hbar\omega_\zeta g_\zeta^2}_{\lambda_{\text{int}}} + \underbrace{\sum_{\xi} \hbar\omega_\xi g_{m,\xi}^2}_{\lambda_m} \tag{1.50}$$

with the difference between energy minima of the PES of the $S_0 \rightarrow S_1$ transition of pigment m, $\Delta U_m^{\min}$, the reorganization energy of intramolecular pigment modes ζ, λ_{intra} (assumed for simplicity to be pigment-, but not site-specific) and the reorganization energy of environmental modes ξ, λ_m, (depending on the site m due to specific interactions of the pigment with the local environment consisting of protein, other pigments etc.). On the other hand, for a pigment in vacuum, we would have just the transition energy

[8] Readers interested in alternative approaches that go beyond this level will find information in Renger and Müh [30] and the references therein.

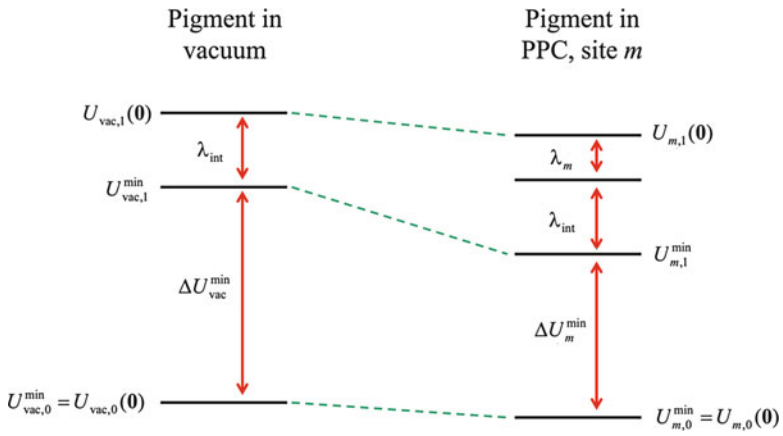

Fig. 1.7 Energy level shifts resulting from transferring a pigment from vacuum to the binding site m in a PPC. $U_{vac,0}(\mathbf{0})$ and $U_{vac,1}(\mathbf{0})$ are the energies of the S_0 and S_1 state, respectively, of the pigment in vacuum at the equilibrium structure of the ground state. $U_{m,0}(\mathbf{0})$ and $U_{m,1}(\mathbf{0})$ are the corresponding quantities of the protein-bound pigment in site m. The superscript "min" indicates an energy of the PES minimum, and "Δ" indicates a difference between S_1 and S_0 state. λ_{int} is the reorganization energy of intramolecular pigment modes assumed, for simplicity, to be not affected by pigment–protein interactions. λ_m is the additional reorganization energy due to coupling of the $S_0 \rightarrow S_1$ transition of the pigment to protein vibrations in site m

$$\Delta U_{vac}(\mathbf{0}) = \underbrace{U^{min}_{vac,1} - U^{min}_{vac,0}}_{\Delta U^{min}_{vac}} + \lambda_{int} \tag{1.51}$$

which is the same we already considered above in Eq. (1.8). Thus, if we transfer a pigment from vacuum to site m in the PPC, the transition energy changes due to a shift of the difference in energy minima and the additional contribution from λ_m (Fig. 1.7). The site energy difference $\Delta\alpha_{mn}$ between two pigments in different sites m and n that are chemically identical and have the same conformation, then is

$$\Delta\alpha_{mn} = \Delta U_n(\mathbf{0}) - \Delta U_m(\mathbf{0}) = \Delta U^{min}_n - \Delta U^{min}_m + \lambda_n - \lambda_m \tag{1.52}$$

similar to Eq. (1.14).

Within the framework of perturbation theory described above, the change from $\Delta U_{vac}(\mathbf{0})$ in vacuum to $\Delta U_m(\mathbf{0})$ in the PPC is obtained to first order from Eq. (1.48). The pigment A is now our pigment in site m, so we replace A with m, and the "second molecule" is in fact the whole environment of the pigment, which we call "background" (bg) and replace B with bg. Equation (1.48) has to be applied twice, namely, for $a = 0$ (electronic ground state of the pigment) and $a = 1$ (first excited state). The background is always in its electronic ground state ($b = 0$). Thus we have

$$\begin{aligned}\Delta U_m(\mathbf{0}) - \Delta U_{\mathrm{vac}}(\mathbf{0}) &= U_{m,1}(\mathbf{0}) - U_{m,0}(\mathbf{0}) - U_{\mathrm{vac},1}(\mathbf{0}) + U_{\mathrm{vac},0}(\mathbf{0}) \\ &= W_{10}^{(1)} - W_{00}^{(1)} - (U_{\mathrm{vac},1}(\mathbf{0}) - U_{\mathrm{vac},0}(\mathbf{0})) \\ &= \sum_{I,J} \frac{q_I^{(m)}(1,1)\ q_J^{(\mathrm{bg})}(0,0)}{\left|\mathbf{R}_I^{(m)} - \overline{\mathbf{R}}_J\right|} \\ &\quad - \sum_{I,J} \frac{q_I^{(m)}(0,0)\ q_J^{(\mathrm{bg})}(0,0)}{\left|\mathbf{R}_I^{(m)} - \overline{\mathbf{R}}_J\right|} - \Delta U_{\mathrm{vac}}(\mathbf{0}) \end{aligned} \tag{1.53}$$

that is,

$$\Delta U_m(\mathbf{0}) = \sum_{I,J} \frac{\left(q_I^{(m)}(1,1) - q_I^{(m)}(0,0)\right) q_J^{(\mathrm{bg})}(0,0)}{\left|\mathbf{R}_I^{(m)} - \overline{\mathbf{R}}_J\right|} \tag{1.54}$$

Here, we have used the atomic partial charges $q_I^{(m)}(1,1)$ and $q_I^{(m)}(0,0)$ that represent the charge distribution of the pigment in the first excited and the ground state, respectively, and the charge distribution of the environment in its ground state is represented by the charges $q_J^{(\mathrm{bg})}(0,0)$. The sum over I goes over all atoms of the pigment that carry different partial charges in the excited and the ground state, and the sum over J is over all environmental atoms.

We believe that Eq. (1.54) represents the dominant mechanism of color tuning for protein-bound pigments, namely, the charge density coupling between pigment and environment. This mechanism also provides a descriptive explanation for the site energy shifts. To see this, we recast Eq. (1.54) in the form

$$\Delta U_m(\mathbf{0}) = \sum_J \Delta\phi_m(\overline{\mathbf{R}}_J) q_J^{(\mathrm{bg})}(0,0) \tag{1.55}$$

where we have introduced the electrostatic difference potential of the pigment in site m as

$$\Delta\phi_m(\mathbf{x}) = \sum_I \frac{\left(q_I^{(m)}(1,1) - q_I^{(m)}(0,0)\right)}{\left|\mathbf{x} - \mathbf{R}_I^{(m)}\right|} \tag{1.56}$$

In the left part of Fig. 1.8 is shown the difference potential for a typical Chl *a* molecule. The figure is a contour plot showing only a cut through the potential in the π-plane of the molecule. Nonetheless it illustrates the aforementioned redistribution of electrons in a dye molecule upon light excitation. The regions of positive and negative difference potential $\Delta\phi_m$ are represented by blue and red color, respectively.

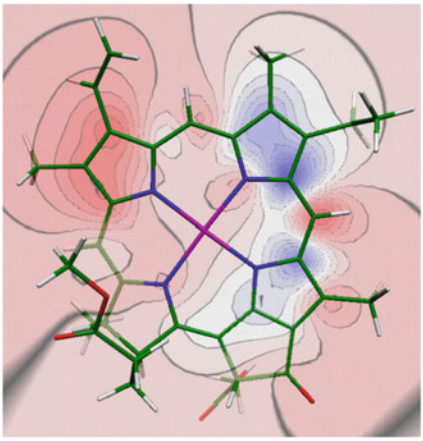

Background partial charge	$\Delta\phi_m$	Resulting site energy shift
>0	>0	>0
>0	<0	<0
<0	>0	<0
<0	<0	>0

Fig. 1.8 *Left*: Electrostatic potential $\Delta\phi_m$ of Chl *a* (contour plot in the π-plane of the molecule; *blue*: $\Delta\phi_m > 0$, *red*: $\Delta\phi_m < 0$) representing the difference in charge distribution between first excited and ground state. The difference potential has been obtained with quantum chemistry [23, 37] employing time-dependent density functional theory implemented in Q-Chem [38]. *Right*: Contribution of a background partial charge to the resulting site energy shift of a pigment in site *m* of a PPC depending on the relative sign of the background partial charge and the difference potential $\Delta\phi_m$

Thus, electrons are redistributed from the blue to the red regions. In an alternative view, the contour plot can be interpreted as illustrating directly the exciton being localized on the pigment. With the exciton being seen as an electron–hole pair, the red and blue colors indicate the spatial regions where the electron and the hole, respectively, is predominant. Apparently, the exciton is characterized by a certain degree of electron–hole separation resulting in an electrostatic potential ($\Delta\phi_m$) that interacts with the permanent charge distribution of the surrounding PPC (represented by the partial charges $q_J^{(\mathrm{bg})}(0,0)$). It is this interaction that determines the site energy shift. Then, it depends on the relative sign of an environmental partial charge and the difference potential ($\Delta\phi_m$) at the position of this charge (Eq. (1.55)), whether the contribution of the background charge to the site energy is a blueshift (>0, higher transition energy) or a redshift (<0, lower transition energy) as summarized in the right part of Fig. 1.8. Since Coulomb interactions are effective at long distance, a fairly large portion of the PPC will contribute to the total site energy of a pigment. For example, most of the 96 site energies of Chl *a* in one monomeric subunit of cyanobacterial PSI [39] were found to be significantly influenced by more than 20 amino acid residues [40].

The simple picture drawn so far seems to indicate that the calculation of site energy shifts is easy. However, the situation is in fact more complicated. Besides the higher-order effects to be discussed below, there are at least two problems that are not yet solved satisfactorily and are topics of current research. The first problem concerns the approximate treatment of the many-electron system of the pigment.

The "shape of the exciton" as represented by the contour plot in Fig. 1.8 depends somewhat on the quantum chemical method used to calculate the electronic wave functions [23, 37]. Hence, different methods in general yield different atomic partial charges and different site energy shifts. At present, there is no faithful method to directly evaluate the reliability of the calculated charge sets. The only way to test the charge sets is to simulate optical spectra of PPCs and compare with experiment. Although this procedure works, it is rather empirical and provides no systematic route to improved atomic partial charges.

The second problem is due to conformational variations between chemically identical pigments in different sites. For example, the macrocycle of a chlorophyll may become nonplanar because of interactions with the protein. If the degree of nonplanarity varies from site to site, the site energy difference $\Delta\alpha$ between two pigments can no longer be calculated solely on the basis of Eq. (1.54), but obtains an additional contribution that has to be determined by quantum chemical methods.[9] The limited accuracy of the latter then is again an issue. For chlorophylls, it seems that quantum-chemistry based methods so far have overestimated the contributions of conformational variations to site energy shifts, and further work is required to better quantify these effects.

We now turn to the higher-order site energy shifts. The simplest way to include these is to place the atomic partial charges of pigment and background in a homogeneous dielectric with an effective dielectric constant $\varepsilon_{\mathrm{eff}}$. The site energy shift then becomes

$$\Delta U_m(\mathbf{0}) = \frac{1}{\varepsilon_{\mathrm{eff}}} \sum_{I,J} \frac{\left(q_I^{(m)}(1,1) - q_I^{(m)}(0,0)\right) q_J^{(\mathrm{bg})}(0,0)}{\left|\mathbf{R}_I^{(m)} - \overline{\mathbf{R}}_J\right|} \tag{1.57}$$

In this charge density coupling (CDC) method [40, 42, 43], the dielectric constant accounts for all polarization effects. However, employing a homogeneous dielectric continuum implies to neglect polarizability differences between molecules. Further, $\varepsilon_{\mathrm{eff}}$ has to be determined from a comparison of simulated and measured optical spectra of the PPC. Thus, it is essentially an adjustable parameter that not only serves to describe medium polarization in an averaged form, but also to compensate for possible errors in the charge sets. Therefore, one has to be careful with a physical interpretation of this parameter.

A somewhat more differentiated approach is to distinguish between the protein volume, the surrounding aqueous medium and eventually a membrane region, and to assign different dielectric constants ε_{p}, $\varepsilon_{\mathrm{solv}}$, and $\varepsilon_{\mathrm{mem}}$, respectively, to these regions. This is done in the Poisson–Boltzmann/quantum chemical (PB/QC) method [37, 42, 44, 45]. The name of this method originates from the fact that besides the

[9] We note that there are other types of light-harvesting complexes that contain more flexible pigments (e.g., bilins, see [41]). In these cases, the contribution from conformational variations may become dominant.

atomic partial charges originating from quantum chemistry, one also needs to calculate variants of the electrostatic potentials $\phi_{00}^{(m)}(\mathbf{x})$ and $\phi_{11}^{(m)}(\mathbf{x})$ of the ground and excited state of the pigment that take into account the polarization induced by these charges in the dielectric environment. This is accomplished by solving the so-called linearized Poisson–Boltzmann equation. We shall not go into further details of this method, but refer the interested reader to a recent review [30]. There, it is also shown that by similar means another problem concerning the charge distribution of the PPC can be solved: Certain groups in the protein can take up or release a proton. Examples are the acidic or basic side chains of amino acids. Since the change of the protonation state of such a group implies that it loses or gains a full elementary charge, the protonation state can have a profound influence on the site energy of a nearby pigment. Therefore, it is important to know the probability of such a group to be protonated. Because the protein environment influences the stability of the protonated relative to the deprotonated form, electrostatic methods are used to evaluate the protonation probability (for further details, see [46, 47]). The atomic partial charges corresponding to the most probable states of the protonatable groups then contribute to the background charges in both the CDC and the PB/QC method.

1.6 Excitonic Couplings

Next, we consider two pigments in the PPC situated at sites m and n and ask for the excitonic coupling V, which has been shown above to be one of the crucial parameters. We call this coupling now V_{mn} to specify the involved sites. Based on Eq. (1.10), we can write

$$V_{mn} = \int d\mathbf{r}_1 d\bar{\mathbf{r}}_1 \frac{\rho_{01}^{(m)}(\mathbf{r}_1)\rho_{01}^{(n)}(\bar{\mathbf{r}}_1)}{|\mathbf{r}_1 - \bar{\mathbf{r}}_1|} \tag{1.58}$$

where $\mathbf{r}_1$ and $\bar{\mathbf{r}}_1$ are the spatial coordinates pertaining to the transition density of the pigment in site m and n, respectively. The transition density as defined in Eq. (1.11) has no simple classical interpretation. Nonetheless, we can handle it formally as if it was a charge density. Note that the transition density, in contrast to the charge density, is defined only up to a factor of ± 1, which is, however, of no concern for the calculation of optical spectra and XT. The next logical step is to introduce the counterpart of an electrostatic potential:

$$\phi_{01}^{(m)}(\mathbf{x}) = \int d\mathbf{x}' \frac{\rho_{01}^{(m)}(\mathbf{x}')}{|\mathbf{x} - \mathbf{x}'|} \tag{1.59}$$

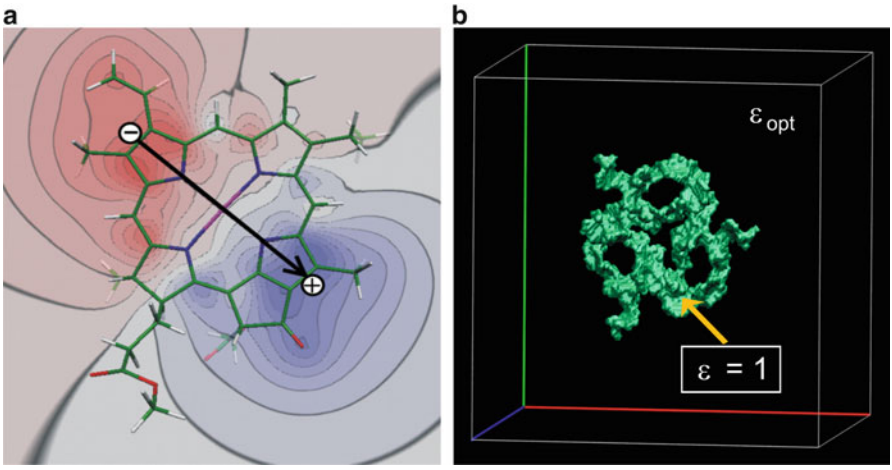

Fig. 1.9 (**a**) Electrostatic potential $\phi_{01}^{(m)}$ of Chl *a* (contour plot in the π-plane of the molecule; *blue*: $\phi_{01}^{(m)} > 0$, *red*: $\phi_{01}^{(m)} < 0$) representing the transition density between first excited and ground state. The transition density has been obtained with quantum chemistry [23] employing time-dependent density functional theory implemented in Q-Chem [38]. (**b**) Dielectric boundary between chlorophylls and protein in trimeric LHCII and assignment of dielectric constants used in the calculation of excitonic couplings with the Poisson-TrEsp method; figure made with VMD [3]

By analogy to Eq. (1.47), we can then write

$$V_{mn} = \int d\mathbf{x} \rho_{01}^{(m)}(\mathbf{x}) \phi_{01}^{(n)}(\mathbf{x}) \tag{1.60}$$

Note that there is no contribution from the nuclei. It is probably not surprising that the next step is to represent the potential $\phi_{01}^{(m)}(\mathbf{x})$ in terms of atomic partial charges $q_I^{(m)}(0,1)$. Then, the excitonic coupling is simply

$$V_{mn} = \sum_{I,J} \frac{q_I^{(m)}(0,1) q_J^{(n)}(0,1)}{\left| \mathbf{R}_I^{(m)} - \mathbf{R}_J^{(n)} \right|} \tag{1.61}$$

The spatial coordinates $\mathbf{R}_I^{(m)}$ and $\mathbf{R}_J^{(n)}$ are those of the atoms of the two pigments. This way of calculating the excitonic couplings is denoted the Transition charge from Electrostatic potential (TrEsp) method [23]. The transition charges are also referred to as "transition monopoles" based on the pioneering work of Weiss [48] and Chang [49], who derived them in a different way.

The potential $\phi_{01}^{(m)}(\mathbf{x})$ is shown for a typical Chl *a* molecule in Fig. 1.9a (again as a contour plot of a cut through the potential in the π-plane of the molecule). It can be seen that the potential has a strongly dipolar character. Thus, instead of using all the

monopoles $q_I^{(m)}(0,1)$ placed at the atom positions, it may be approximated by just two partial charges of opposite sign placed at the positions indicated in Fig. 1.9a.[10] Within this extended-dipole approximation, the excitonic coupling between the $S_0 \rightarrow S_1$ transitions of two chlorophylls can be calculated from just four Coulomb interactions. Even for pigments that are close to each other, this approximation is often very accurate and provides a suitable alternative to the TrEsp or other more sophisticated methods [23]. Note that the dipole is oriented along the axis joining the nitrogen atoms N_B and N_D (according to the crystallographer's nomenclature), which is defined as the y-axis (see Fig. 1.2b) according to the Gouterman model of transitions in tetrapyrroles [51, 52]. Based on this model, the $S_0 \rightarrow S_1$ transition is also referred to as Q_y transition. We note that there is some discussion about the possibility that this dipole is not exactly oriented along this axis (see [53], and references therein).

A further approximation is obtained by replacing the extended dipole with a point dipole. The latter is formally derived by letting the two charges of the extended dipole approach each other until they meet in one point, while the magnitudes of the charges are changed such that the magnitude of the dipole moment remains constant [54]. The resulting vector is the transition dipole or transition dipole moment $\boldsymbol{\mu}_{01}^{(m)}$ that can be calculated from the first moment of the transition density:

$$\boldsymbol{\mu}_{01}^{(m)} = \int d\mathbf{x}\ \mathbf{x}\ \rho_{01}^{(m)}(\mathbf{x}) = \sum_I \mathbf{R}_I^{(m)} q_I^{(m)}(0,1) \tag{1.62}$$

Within this point-dipole approximation, the excitonic coupling is given as

$$V_{mn} \approx \frac{\boldsymbol{\mu}_{01}^{(m)} \cdot \boldsymbol{\mu}_{01}^{(n)}}{R_{mn}^3} - 3\frac{\left(\boldsymbol{\mu}_{01}^{(m)} \cdot \mathbf{R}_{mn}\right)\left(\boldsymbol{\mu}_{01}^{(n)} \cdot \mathbf{R}_{mn}\right)}{R_{mn}^5} \tag{1.63}$$

where $\mathbf{R}_{mn}$ is a vector joining the centers of the two pigments and R_{mn} is the corresponding center-to-center distance. Equation (1.63) is quite popular. However, it should be applied with care, since it corresponds to the first non-vanishing term in a multipole expansion of the interaction between the two transition densities. As such, it is a crude approximation and at best valid, if the extension of the pigments does not exceed their center-to-center distance. This condition is often violated by the rather densely packed pigments in PPCs. Nonetheless, the transition dipole is an important quantity, as its square is proportional to the dipole strength or absorption cross section of the $S_0 \rightarrow S_1$ transition. This brings us to the question of how well the dipole strength can be calculated.

The application of different quantum chemical methods to calculate the Q_y transition density of chlorophylls shows that the overall shape of the potential

[10] A systematic procedure for finding these positions is described in [50].

$\phi_{01}^{(m)}(\mathbf{x})$ does not depend significantly on the chosen method. However, the magnitude of the transition dipole moment does, and it is usually overestimated. To solve this problem, the transition charges are rescaled with a correction factor χ chosen such that the dipole strength obtained from the first moment of the transition charges matches the experimental value, i.e., we have for the corrected transition charges

$$\widetilde{q}_I^{(m)}(0,1) = \chi\, q_I^{(m)}(0,1) \tag{1.64}$$

However, the vacuum dipole strength of large molecules is normally not available. Rather, these molecules are investigated in organic solvents. Knox and Spring [55] provided an important analysis to relate the dipole strengths of chlorophylls in solution to those in vacuum.

The interaction between transition densities is influenced by a polarizable medium similar to that between charge densities. An important difference is that in the case of excitonic couplings only the optical (fast) polarization of the environment needs to be taken into account, since there is no time for the nuclei to react during an electronic transition. To consider screening and local field corrections in the TrEsp method, an additional scaling constant f is introduced, so that with transition charges properly scaled to the vacuum value of the dipole strength, the excitonic coupling becomes:

$$V_{mn} = f \sum_{I,J} \frac{\widetilde{q}_I^{(m)}(0,1)\widetilde{q}_J^{(n)}(0,1)}{\left|\mathbf{R}_I^{(m)} - \mathbf{R}_J^{(n)}\right|} \tag{1.65}$$

Of course, one can subsume $f\chi^2$ in one correction factor and use unscaled charges in Eq. (1.65). The distinction between f and χ^2 has its roots in a more differentiated way to investigate the influence of the polarization as explained in the following.

In an extension of the TrEsp method, referred to as Poisson-TrEsp [40, 42, 56, 57], different dielectric constants are assigned to the volumes inside and outside the pigments. More precisely, pigment-shaped cavities are defined based on overlapping spheres representing the atoms of the chromophores as shown for trimeric LHCII in Fig. 1.9b. The transition charges are placed within the cavities on the atom positions. The dielectric constant becomes position-dependent, $\varepsilon = \varepsilon(\mathbf{x})$, in that $\varepsilon(\mathbf{x}) = 1$ is used for the space inside the cavities, and $\varepsilon(\mathbf{x}) = \varepsilon_{\text{opt}}$ otherwise. Here, $\varepsilon_{\text{opt}} = n^2$, where n is the refractive index of the medium. For each pigment, a potential $\phi_{01}^{(m)}(\mathbf{x})$ is calculated numerically as the solution to the Poisson equation:

$$\nabla\left(\varepsilon(\mathbf{x})\nabla\phi_{01}^{(m)}(\mathbf{x})\right) = -4\pi\sum_I \widetilde{q}_I^{(m)}(0,1)\delta\left(\mathbf{x} - \mathbf{R}_I^{(m)}\right) \tag{1.66}$$

This potential not only takes into account the potential due to the transition charges as in Eq. (1.59), but also that due to the polarization that the transition charges induce in the surrounding dielectric medium. The resulting excitonic coupling is then:

$$V_{mn} = \sum_J \phi_{01}^{(m)}\left(\mathbf{R}_J^{(n)}\right)\tilde{q}_J^{(n)}(0,1) \tag{1.67}$$

The tilde on the transition charges in Eqs. (1.66) and (1.67) indicates that transition charges have to be employed that are scaled with reference to the vacuum dipole strength of the pigments. Normally, $\varepsilon_{\text{opt}} = 2$ is used. This value is suggested by microscopic simulations [58] as well as by an estimate [53] that is based on a comparison of the dipole strengths of protein-bound and solvent-extracted Chl *a* [59].

A comparison of excitonic couplings obtained with Poisson-TrEsp to those obtained with TrEsp in vacuum ($f = 1$) allows to estimate an effective value of f for use with the TrEsp method in a medium. Application to various PPCs resulted in values of f between 0.6 and 0.8 [30]. The result $1/f < \varepsilon_{\text{opt}}$ is reasonable, as in the Poisson-TrEsp method the pigment interior is assumed to be non-polarizable, and there is a local field enhancement of the transition density by the polarizability of the environment. The assumption of a non-polarizable interior of the pigments is physically motivated, since the $S_0 \rightarrow S_1$ transition, which makes a major contribution to the polarizability of the volume occupied by the pigment, is already accounted for in the exciton simulation, for which V_{mn} is determined. On the other hand, higher transitions of the pigments contribute to the polarizability of the pigment volume, which thus has a residual polarizability neglected so far. This problem has not been further analyzed yet.

Application of the Poisson-TrEsp method shows that the medium surrounding the pigments does not always diminish V_{mn}, but in rare cases may even enhance it [57] in agreement with earlier model calculations [56, 60]. This result calls in question the general applicability of screening factors. Other methods have been employed, in which the dielectric environment is directly incorporated in the quantum chemistry of the pigments (for a review, see [61]). The results from these methods suggest on the one hand that the heterogeneity of the protein is ultimately important to understand excitonic couplings in detail. On the other hand, they also arrive at a value of $\varepsilon_{\text{opt}} = 2$ for a reasonable description of the average dielectric properties of a PPC.

1.7 Exciton-Vibrational Coupling

The CDC method for the calculation of site energies also provides a means to get information about the exciton-vibrational coupling constants $g_{m,\xi}$ that underlie the reorganization energy λ_m. To see this, we write down again the PES of the ground

state of the PPC, $U_{m,0}(Q_\xi)$, and of the state, in which pigment m is locally excited to its S_1 state, $U_{m,1}(Q_\xi)$:

$$U_{m,0}(Q_\xi) = U_{m,0}^{\min} + \frac{\hbar\omega_\xi}{4} Q_\xi^2 \tag{1.68}$$

$$U_{m,1}(Q_\xi) = U_{m,1}^{\min} + \frac{\hbar\omega_\xi}{4} \left(Q_\xi + 2g_{m,\xi}\right)^2 \tag{1.69}$$

Then, the energy difference between first excited and ground state as a function of the normal mode coordinate Q_ξ, $\Delta U_m(Q_\xi) = U_{m,1}(Q_\xi) - U_{m,0}(Q_\xi)$, is given by

$$\begin{aligned}\Delta U_m(Q_\xi) &= U_{m,1}^{\min} + \frac{\hbar\omega_\xi}{4} \left(Q_\xi + 2g_{m,\xi}\right)^2 - U_{m,0}^{\min} - \frac{\hbar\omega_\xi}{4} Q_\xi^2 \\ &= \Delta U_m^{\min} + \hbar\omega_\xi g_{m,\xi} Q_\xi + \hbar\omega_\xi g_{m,\xi}^2\end{aligned} \tag{1.70}$$

Thus, $g_{m,\xi}$ is related to the first derivative of $\Delta U_m(Q_\xi)$ with respect to the normal mode coordinate:

$$\frac{\partial \Delta U_m(Q_\xi)}{\partial Q_\xi} = \hbar\omega_\xi g_{m,\xi} \tag{1.71}$$

If we recall that the normal modes originate from a transformation of the Cartesian coordinates of the nuclei according to Eq. (1.5), we can write [33]:

$$g_{m,\xi} = (2\hbar)^{-1/2} \omega_\xi^{-3/2} \sum_J M_J^{-1/2} \mathbf{A}_{J\xi} \cdot \nabla_J (\Delta U_m(\mathbf{R}))|_{\mathbf{0}} \tag{1.72}$$

Here, $\mathbf{A}_{J\xi}$ is the transformation matrix, ∇_J the gradient with respect to the Cartesian coordinates of atom J (taken at the ground state equilibrium positions of the nuclei), and the sum goes over all environmental atoms that contribute to the mode ξ. Now, we make the assumption that the permanent charge distributions of either electronic state of pigment m and of the environment do not change appreciably due to small displacements of the nuclei. Then, the atomic partial charges can be considered constant, and the gradient of the CDC expression for $\Delta U_m(\mathbf{R})$ (Eq. (1.57)) can be calculated to give:

$$\begin{aligned}g_{m,\xi} = &\frac{1}{\widetilde{\varepsilon}_{\text{eff}} (2\hbar)^{1/2} \omega_\xi^{3/2}} \sum_{I,J} \frac{\left(q_I^{(m)}(1,1) - q_I^{(m)}(0,0)\right) q_J^{(\text{bg})}(0,0)}{\left|\mathbf{R}_{m,I}^{(0)} - \overline{\mathbf{R}}_J^{(0)}\right|^{-3}} \\ &\times \left(\overline{\mathbf{R}}_J^{(0)} - \mathbf{R}_{m,I}^{(0)}\right) \cdot \left(M_I^{-1/2} \mathbf{A}_{I\xi} - M_J^{-1/2} \mathbf{A}_{J\xi}\right)\end{aligned} \tag{1.73}$$

Here, I counts the atoms of the pigment and J those of the environment. $\mathbf{R}_{m,I}^{(0)}$ and $\overline{\mathbf{R}}_J^{(0)}$ are the respective Cartesian coordinates of the equilibrium positions of the

nuclei in the ground state of the PPC. Thus, $g_{m,\xi}$ can be calculated directly from the crystal structure, if the atomic partial charges are known. The effective dielectric constant $\widetilde{\varepsilon}_{\text{eff}}$ differs from ε_{eff} used in Eq. (1.57), however, since the latter has to account for electronic and nuclear polarization, whereas the former has to describe only the electronic part. Note that in the present calculations, only information about λ_m is obtained, but not about λ_{int}. The latter requires a quantum chemical treatment of the pigment.

In a similar way, coupling constants $g_{mn,\xi}$ that eventually lead to a Q_ξ-dependence of the excitonic coupling V_{mn} can be calculated, since

$$\frac{\partial V_{mn}(Q_\xi)}{\partial Q_\xi} = \hbar\omega_\xi g_{mn,\xi} \tag{1.74}$$

(Note that this coupling is different from J_{12} discussed before.) By invoking the TrEsp method, we obtain [33]:

$$g_{mn,\xi} = \frac{f}{(2\hbar)^{1/2}\omega_\xi^{3/2}} \sum_{I,J} \frac{\widetilde{q}_I^{(m)}(0,1)\widetilde{q}_J^{(n)}(0,1)}{\left|\mathbf{R}_{m,I}^{(0)} - \mathbf{R}_{n.,J}^{(0)}\right|^3} \left(\mathbf{R}_{m,I}^{(0)} - \mathbf{R}_{n,J}^{(0)}\right) \cdot \left(M_J^{-1/2}\mathbf{A}_{J\xi} - M_I^{-1/2}\mathbf{A}_{I\xi}\right) \tag{1.75}$$

where I counts the atoms of pigment m and J those of pigment n, and $\mathbf{R}_{m,I}^{(0)}$ and $\mathbf{R}_{n,J}^{(0)}$ are the respective ground state equilibrium positions of the nuclei.

1.8 Application to the FMO Protein

The FMO protein is a small water-soluble PPC occurring in green sulfur bacteria that is situated between the outer antenna system (chlorosome/baseplate) and the RC complex [62]. Thus, it acts as a kind of XT mediator. The crystal structure of the FMO protein is known for quite some time [63, 64]. It is a trimer with each monomer being a shell-like structure holding seven bacteriochlorophyll (BChl) *a* pigments in its interior and eventually binding an eighth BChl *a* per monomer at the monomer–monomer interface [65]. The presence of the latter pigment has been confirmed only recently [66].

Because of its relatively simple structure, the FMO protein is a suitable model system for experimental and theoretical research on PPCs. Nonetheless, it took a long time to arrive at a suitable set of site energies and excitonic couplings to describe the optical spectra of the FMO protein with the seven inner pigments (*apo*-form) and to model exciton dynamics [67]. A major obstacle in earlier theoretical analyses was the use of a rather high value for the dipole strength of the Q_y transition of BChl *a*. Louwe et al. [68] used a value of 68.9 D^2, but considered dielectric screening by the protein with $\varepsilon_{\text{eff}} = 2.4$, resulting in a relatively low value

for the effective dipole strength[11] of ~30 D^2. The latter value was later confirmed by application of the Poisson-TrEsp method [56]. More precisely, the analysis by Knox and Spring [55] suggests a value for the dipole strength in vacuum of 37.1 D^2. Combined with $\varepsilon_{opt} = 2.0$, the Poisson-TrEsp method provides excitonic couplings that can be compared with TrEsp calculations to yield $1/f = \varepsilon_{eff} = 1.25$ and hence again 30 D^2.

The lower values of V_{mn} paved the way for finding realistic site energies from fits of optical spectra, but the fits did not provide a structure-based explanation for the assignment of site energies. A first step in this direction was to consider the influence of charged amino acids, which together with the fits resulted in the assignment of the lowest site energy (i.e., the "energy sink") to BChl *a* 3 (in the numbering scheme of *Prosthecochloris aestuarii* according to [64]). Consequently, it was proposed that the FMO protein is oriented in such a way that BChl *a* 3 faces the RC complex for efficient XT [56]. This orientation was later confirmed experimentally by a combination of chemical labeling with mass spectrometry [69]. A more detailed structure-based rationale for the assignment of site energies was provided by application of the PB/QC method [44] and later the CDC method [42, 43]. It was stressed that besides amino acid side chains, the backbone architecture of a PPC has to be taken into account, as the dipoles of the peptide bonds can make a significant contribution to site energy shifts. In this respect, two α-helices were found important in the determination of the energy sink at BChl *a* 3 in the FMO protein [44], and site energy differences turned out to be the major mechanism for the direction of XT in this system. Thus, it is the inhomogeneous charge distribution within the PPC that guides the exciton to a particular site. An advantage of the electrostatic calculation scheme is that certain parts of the PPC can easily be tested for their influence by just setting the respective atomic partial charges to zero. In this way, it was found that without the dipole fields of the two aforementioned α-helices, XT through the FMO protein gets stuck in the center of the PPC instead of reaching BChl *a* 3 at the interface to the RC complex [44]. This is a clear illustration of how the methods described in this chapter work and how they provide information about structure–function relationships in PPCs.

The eighth BChl *a* in the FMO protein (*holo*-form) is located at the side opposite to BChl *a* 3 [66]. This finding led to the proposal that BChl *a* 8 faces the chlorosome/baseplate and serves as entrance site for the exciton coming from the outer antenna. Indeed, application of the CDC method to the *holo*-form showed the eighth pigment to have the highest site energy [43]. The origin of the blueshift is a conglomerate of negatively charged amino acid side chains in a negative region of the $\Delta\phi_8$ potential (cf. Fig. 1.8). Since these groups can principally be protonated and lose their negative net charge, the influence of the medium dielectric constant on the protonation states was tested. For example, contact with the chlorosome/baseplate could lower the polarizability of the environment of the eighth BChl *a*.

[11] We define the effective dipole strength as vacuum dipole strength divided by ε_{eff}.

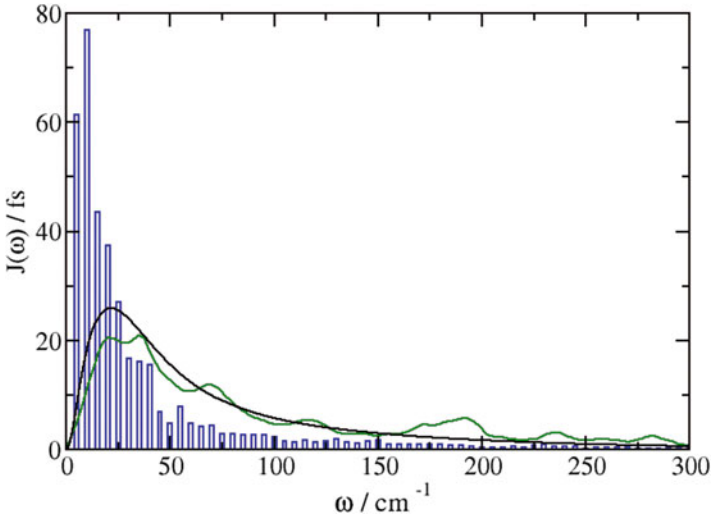

Fig. 1.10 Averaged NMA-based spectral density $\overline{J}(\omega)$ (Eq. (1.78), *blue histogram*) compared to spectral densities inferred from experimental data. The *black curve* was obtained [72] from an analysis of fluorescence line narrowing (FLN) spectra of the B777-complex of purple bacteria [73] and the *green curve* from FLN spectra of the FMO protein [70]. The latter two have been rescaled to the averaged Huang–Rhys factor 0.39 of $\overline{J}(\omega)$

It was found that only one group loses its net charge, and BChl *a* 8 remains the most blueshifted pigment in the FMO protein.

Recently, a normal mode analysis (NMA) of one monomeric subunit of the *apo*-form of the FMO protein has been carried out and combined with the CDC and TrEsp methods to obtain the coupling constants $g_{m,\xi}$ and $g_{mn,\xi}$, respectively [33]. A suitable measure for the strength of the exciton-vibrational coupling characteristic for a local excited state is the Huang–Rhys factor

$$S_m = \sum_{\xi} g_{m,\xi}^2 \tag{1.76}$$

These factors were found to vary between 0.19 and 0.54 between the seven sites with an average value of 0.39 in excellent agreement with experimental estimates [70, 71]. The variations of S_m suggest that the reorganization energies λ_m for the local $S_0 \rightarrow S_1$ transitions are indeed site-dependent. However, as the accuracy of the NMA-based data is presently unclear, it is too early to say anything about the significance of this variation. A possibility to test the accuracy is to calculate the spectral density and compare with experiment. The spectral density is defined as

$$J_m(\omega) = \sum_{\xi} g_{m,\xi}^2 \delta(\omega - \omega_{\xi}) \tag{1.77}$$

In Fig. 1.10 is shown a comparison of the averaged NMA-based spectral density

$$\overline{J}(\omega) = \frac{1}{7}\sum_{m=1}^{7} J_m(\omega) \tag{1.78}$$

with data inferred from experiment. Apparently, the calculation overestimates the spectral density in the low-frequency region and underestimates it in the high-frequency range. The latter discrepancy is due to the inevitable lack of the contributions from λ_{int} in the calculation of intermolecular coupling constants. The overestimation of the low-frequency region may have its roots in the harmonic approximation of nuclear motion, which is probably inadequate for soft protein modes contributing to this frequency range. This problem is currently under further investigation. Nonetheless, the NMA-based spectral density is closer to experiment than any other structure-based spectral density. In particular, methods have been applied, in which the environment is directly incorporated in the quantum chemistry of the pigments. Although these methods have, in principle, the potential to also yield information about the intramolecular coupling constants, they failed so far at arriving at a balanced description of λ_{int} and λ_m (for a further discussion and references, see [33]).

The concept of the Huang–Rhys factor can be generalized to fluctuations of excitonic couplings:

$$S_{mn} = \sum_{\xi} g^2_{mn,\xi} \tag{1.79}$$

The NMA of the FMO protein shows that the values of S_{mn} are about one order of magnitude smaller than the values of S_m [33]. This result suggests that the excitonic couplings are much less sensitive to nuclear motion than are the site energies. Therefore, it is a reasonable approximation to neglect the dependence of V_{mn} on the Q_ξ in calculations of exciton states as we did above.

Another important result of the NMA is that the coupling constants pertaining to one mode ξ are usually different for different sites, which is a consequence of the inhomogeneous distribution of charges and vibrating atoms in the PPC [33]. As a result, coherent superpositions of exciton states decay fast, which is a prerequisite for fast XT and an efficient dissipation of the excess energy during the relaxation to the energy sink.

1.9 The Antenna System of PSII

Although significant progress has been made in characterizing the structure of PSII in higher plants [1, 4, 5], crystal structures of sufficient resolution are available only for LHCII [6, 7] and CP29 [9]. The computational methods described herein have been applied so far only to LHCII [37, 74, 75]. In addition, high-resolution structures of the PSII core complex from cyanobacteria have been published

[2, 11], but rigorous structure-based calculations of site energies are in an early stage [45]. Therefore, we concentrate on LHCII in the following overview.

LHCII is a trimeric complex that binds eight Chl *a* and six Chl *b* pigments as well as four carotenoid cofactors and one structurally important phospholipid molecule per monomer [8]. Based on the crystal structure by Liu et al. [6], Novoderezhkin et al. [76] determined the 14 different Chl site energies of trimeric LHCII from a simultaneous fit of steady-state and time-resolved optical spectra using an exciton model with excitonic couplings obtained from the point-dipole approximation. They assumed $n = 1.54$ for the refractive index of the protein and dipole strengths of 33.1 D^2 and 24 D^2 for Chl *a* and *b*, respectively. The latter values originate from the analysis by Knox and Spring [55] for the implied refractive index. The effective dipole strengths are then 14 D^2 and 10 D^2 for Chl *a* and *b*, respectively. The same values for the effective dipole strengths were used as reference by Frähmcke and Walla [77] to scale the transition densities in a quantum chemical computation of excitonic couplings. Their data confirm that the point-dipole approximation is a reasonable approximation for the excitonic coupling between Q_y transitions of Chls in LHCII with the exception of the Chl *b*606/*b*607 pair (in the numbering scheme of [6]), for which the coupling is overestimated by ~30 cm^{-1}. A similar conclusion follows from the application of the Poisson-TrEsp method with vacuum dipole strengths of 21.0 D^2 and 14.7 D^2 for Chl *a* and *b*, respectively, and $\varepsilon_{opt} = 2$ [37]. In addition, very similar couplings are obtained from the two crystal structures with the exception of the Chl *a*611/*a*612 pair, which shows the largest structural variation and a difference in the excitonic coupling of 21 cm^{-1} [37].

Application of the PB/QC method to LHCII resulted in site energies that allow for a good match between simulated and measured low-temperature optical spectra with the exception of circular dichroism in the Chl *b* region [37, 75]. This implies that the optical spectra can in principle be understood on the basis of the crystal structure within the approximations of the electrostatic model. However, this analysis also clearly demonstrates the sensitivity of the computed site energies to the quantum chemical method underlying the determination of the charge distributions. It should be emphasized again that neither the PB/QC nor the CDC method use quantum chemically calculated transition energies. Other approaches applied to LHCII, that use quantum chemistry more directly [78, 79], so far failed at the description of low-temperature optical spectra. This indicates that the electrostatic approach, despite its approximations and limitations, is presently a very efficient route to a structure-based understanding of PPCs.

Regarding the direction of XT in LHCII, there are three main aspects to be considered: (1) the heterogeneous charge distribution in the PPC causes site energy differences between chemically identical pigments. These differences contribute to directing XT as in the FMO protein. (2) Some strong excitonic couplings cause exciton delocalization and corresponding shifts of energy levels. For example, the two Chls *a*611 and *a*612 have site energies that would result in absorption peaks centered at ~670 nm. Due to their relatively strong excitonic coupling of ~100 cm^{-1}, two new bands appear at ~665 and 675 nm. XT then occurs by exciton

relaxation as described above for the limit $|\Delta\gamma| \ll |2V|$. (3) There are two different types of Chl (*a* and *b*) absorbing in different wavelength regions with the Chl *b* S_1 states having higher energies than the Chl *a* states. Thus, XT occurs preferentially from Chl *b* to Chl *a*.

The energy sink is found at Chl *a*610 in LHCII [37]. This result is in agreement with the earlier fits [76] and experimental studies that apply site-directed mutagenesis to knock out specific Chls from LHCII and report the resulting spectral changes [80]. However, this assignment applies strictly only to cryogenic temperatures. At elevated temperatures that are closer to physiological conditions, an exciton level seems to shift to lower energies, in which Chl *a*612 (strongly coupled to Chl *a*611) is involved as known from studies on mutants [81]. Thus, the energy sink (i.e., the terminal emitter domain) of LHCII is believed to encompass Chls *a*610, *a*611, and *a*612. These Chls are located at the periphery of the LHCII trimer in a layer of pigments facing the stroma, so that excitons are guided to the stromal side of the thylakoid membrane (cf. Fig. 1.1). The further track of the exciton is presently unknown, but ongoing research on the structures of CP29 and other antennae will likely uncover it in the future together with a further insight into the regulation of XT.

1.10 Summary and Outlook

In this chapter, we use theoretical physics—simplified as far as possible—to link structure and function in photosynthetic LHCs. The basic idea underlying our approach is that despite the close packing of molecules in biological systems, intermolecular wave function overlap can be neglected to arrive at a building block principle. The complicated treatment of many-electron systems being inherent in quantum chemistry then can be restricted to the building blocks, while interactions between building blocks are treated with classical electrostatics. Although approximative, this approach works reasonably well and allows us to cope with the complexity of the involved molecular structures. Nonetheless, the electrostatic approach reaches its limits. A future refinement of structure-based simulations of PPCs will have to put more emphasis on quantum chemistry and quantum dynamics. Given the limited accuracy of quantum chemical methods particularly as regards excited states, this remains a challenge.

Acknowledgement Financial support by the Austrian Science Fund (FWF): P 24774-N27 is gratefully acknowledged.

References

1. Caffarri S, Kouril R, Kereiche S, Boekema EJ, Croce R. Functional architecture of higher plant photosystem II supercomplexes. EMBO J. 2009;28:3052–63.
2. Umena Y, Kawakami K, Shen JR, Kamiya N. Crystal structure of oxygen-evolving photosystem II at a resolution of 1.9 Å. Nature. 2011;473:55–60.
3. Humphrey W, Dalke A, Schulten K. VMD: visual molecular dynamics. J Mol Graphics. 1996;14:33–8.
4. Croce R, van Amerongen H. Light-harvesting and structural organization of photosystem II: from individual complexes to thylakoid membrane. J Photochem Photobiol B. 2011;104:142–53.
5. Kouril R, Dekker JP, Boekema EJ. Supramolecular organization of photosystem II in green plants. Biochim Biophys Acta. 2012;1817:2–12.
6. Liu ZF, Yan HC, Wang KB, Kuang TY, Zhang JP, Gui LL, An XM, Chang WR. Crystal structure of spinach major light-harvesting complex at 2.72 Å resolution. Nature. 2004;428:287–92.
7. Standfuss J, Terwisscha van Scheltinga AC, Lamborghini M, Kühlbrandt W. Mechanism of photoprotection and nonphotochemical quenching in pea light-harvesting complex at 2.5 Å resolution. EMBO J. 2005;24:919–28.
8. Barros T, Kühlbrandt W. Crystallization, structure and function of plant light-harvesting complex II. Biochim Biophys Acta. 2009;1787:753–72.
9. Pan X, Li M, Wan T, Wang L, Jia C, Hou Z, Zhao X, Zhang J, Chang W. Structural insights into energy regulation of light-harvesting complex CP29 from spinach. Nat Struct Mol Biol. 2011;18:309–15.
10. Müh F, Renger T, Zouni A. Crystal structure of cyanobacterial photosystem II at 3.0 Å resolution: a closer look at the antenna system and the small membrane-intrinsic subunits. Plant Physiol Biochem. 2008;46:238–64.
11. Guskov A, Gabdulkhakov A, Broser M, Glöckner C, Hellmich J, Kern J, Frank J, Müh F, Saenger W, Zouni A. Recent progress in the crystallographic studies of photosystem II. ChemPhysChem. 2010;11:1160–71.
12. Gueymard CA, Myers D, Emery K. Proposed reference irradiance spectra for solar energy systems testing. Sol Energy. 2002;73:443–67.
13. Scheer H. An overview of chlorophylls and bacteriochlorophylls: biochemistry, biophysics, functions and applications. In: Grimm B, Porra RJ, Rüdiger W, Scheer H, editors. Chlorophylls and bacteriochlorophylls – biochemistry, biophysics, functions and applications. Dordrecht: Springer; 2006. p. 1–26.
14. May V, Kühn O. Charge and energy transfer dynamics in molecular systems. Berlin: Wiley-VCH; 2011.
15. Wilson EB, Decius JC, Cross PC. Molecular vibrations – the theory of infrared and Raman vibrational spectra. New York, NY: McGraw-Hill; 1955. Dover edition 1980.
16. McQuarrie DA. Quantum chemistry. Sausalito, CA: University Science; 2008.
17. Franck J. Elementary processes of photochemical reactions. Trans Faraday Soc. 1926;21:536–42.
18. Condon EU. Nuclear motions associated with electron transitions in diatomic molecules. Phys Rev. 1928;32:858–72.
19. Szabo A, Ostlund NS. Modern quantum chemistry – introduction to advanced electronic structure theory. New York, NY: McGraw-Hill; 1989. Dover edition 1996.
20. Koch W, Holthausen MC. A chemist's guide to density functional theory. New York, NY: Wiley-VCH; 2001.
21. Dreuw A, Head-Gordon M. Single-reference ab initio methods for the calculation of excited states of large molecules. Chem Rev. 2005;105:4009–37.
22. Frenkel J. On the transformation of light into heat in solids. I. Phys Rev. 1931;37:17–44.

23. Madjet ME, Abdurahman A, Renger T. Intermolecular Coulomb couplings from ab initio electrostatic potentials: application to optical transitions of strongly coupled pigments in photosynthetic antennae and reaction centers. J Phys Chem B. 2006;110:17268–81.
24. Dexter DL. A theory of sensitized luminescence in solids. J Chem Phys. 1953;21:836–50.
25. Harcourt RD, Scholes GD, Ghiggino KP. Rate expressions for excitation transfer. II. Electronic considerations of direct and through–configuration exciton resonance interactions. J Chem Phys. 1994;101:10521–5.
26. Madjet ME, Müh F, Renger T. Deciphering the influence of short-range electronic couplings on optical properties of molecular dimers: application to "special pairs" in photosynthesis. J Phys Chem B. 2009;113:12603–14.
27. Scholes GD, Gould IR, Cogdell RJ, Fleming GR. *Ab initio* molecular orbital calculations of electronic couplings in the LH2 bacterial light-harvesting complex of *Rps. acidophila*. J Phys Chem B. 1999;103:2543–53.
28. Renger T. Absorption of light, excitation energy transfer and electron transfer reactions. In: Renger G, editor. Primary processes of photosynthesis – principles and apparatus, part 1. Cambridge: RSC Publishing; 2008. p. 39–97.
29. Marcus RA, Sutin N. Electron transfer in chemistry and biology. Biochim Biophys Acta. 1985;811:265–322.
30. Renger T, Müh F. Understanding photosynthetic light-harvesting: a bottom up theoretical approach. Phys Chem Chem Phys. 2013;15:3348–71.
31. Beljonne D, Curutchet C, Scholes GD, Silbey RJ. Beyond Förster resonance energy transfer in biological and nanoscale systems. J Phys Chem B. 2009;113:6583–99.
32. Ito A, Mayer TJ. The golden rule: application for fun and profit in electron transfer, energy transfer, and excited state decay. Phys Chem Chem Phys. 2012;14:13731–45.
33. Renger T, Klinger A, Steinecker F, Schmidt am Busch M, Numata J, Müh F. Normal mode analysis of the spectral density of the Fenna-Matthews-Olson light-harvesting protein: how the protein dissipates the excess energy of excitons. J Phys Chem B. 2012;116:14565–80.
34. Stone AJ. The theory of intermolecular forces. Oxford: Clarendon; 1996.
35. London F. The general theory of molecular forces. Trans Faraday Soc. 1937;33:8–26.
36. Casimir HBG, Polder D. The influence of retardation on the London-Van der Waals forces. Phys Rev. 1948;73:360–72.
37. Müh F, Madjet ME, Renger T. Structure-based identification of energy sinks in plant light-harvesting complex II. J Phys Chem B. 2010;114:13517–35.
38. Shao Y, et al. Advances in methods and algorithms in a modern quantum chemistry program package. Phys Chem Chem Phys. 2006;8:3172–91.
39. Jordan P, Fromme P, Witt HT, Klukas O, Saenger W, Krauss N. Three-dimensional structure of cyanobacterial photosystem I at 2.5 Å resolution. Nature. 2001;411:909–17.
40. Adolphs J, Müh F, Madjet ME, Schmidt am Busch M, Renger T. Structure-based calculations of optical spectra of photosystem I suggest an asymmetric light-harvesting process. J Am Chem Soc. 2010;132:3331–43.
41. Curutchet C, Novoderezhkin VI, Kongsted J, Munoz-Losa A, van Grondelle R, Scholes GD, Mennucci B. Energy flow in the cryptophyte PE545 antenna is directed by bilin pigment conformation. J Phys Chem B. 2013;117:4263–73.
42. Adolphs J, Müh F, Madjet ME, Renger T. Calculation of pigment transition energies in the FMO protein – from simplicity to complexity and back. Photosynth Res. 2008;95:197–209.
43. Schmidt am Busch M, Müh F, Madjet ME, Renger T. The eighth bacteriochlorophyll completes the excitation energy funnel in the FMO protein. J Phys Chem Lett. 2011;2:93–8.
44. Müh F, Madjet ME, Adolphs J, Abdurahman A, Rabenstein B, Ishikita H, Knapp EW, Renger T. α-Helices direct excitation energy flow in the Fenna-Matthews-Olson protein. Proc Natl Acad Sci U S A. 2007;104:16862–7.
45. Müh F, Madjet ME, Renger T. Structure-based simulation of linear optical spectra of the CP43 core antenna of photosystem II. Photosynth Res. 2012;111:87–101.

46. Ullmann GM, Knapp EW. Electrostatic models for computing protonation and redox equilibria in proteins. Eur Biophys J. 1999;28:533–51.
47. Bashford D. Macroscopic electrostatic models for protonation states in proteins. Front Biosci. 2004;9:1082–99.
48. Weiss Jr C. The Pi electron structure and absorption spectra of chlorophylls in solution. J Mol Spectrosc. 1972;44:37–80.
49. Chang JC. Monopole effects on electronic excitation interactions between large molecules. I. Application to energy transfer in chlorophylls. J Chem Phys. 1977;67:3901–9.
50. Renger T, Grundkötter B, Madjet ME, Müh F. Theory of solvatochromic shifts in nonpolar solvents reveals a new spectroscopic rule. Proc Natl Acad Sci U S A. 2008;105:13235–40.
51. Gouterman M, Wagniere G, Snyder L. Spectra of porphyrins Part II. Four orbital model. J Mol Spectrosc. 1963;11:108–27.
52. Scheer H. Chlorophylls. In: Renger G, editor. Primary processes of photosynthesis – principles and apparatus, part 1. Cambridge: RSC Publishing; 2008. p. 101–49.
53. Renger T, Madjet ME, Müh F, Trostmann I, Schmitt FJ, Theiss C, Paulsen H, Eichler HJ, Knorr A, Renger G. Thermally activated superradiance and intersystem crossing in the water-soluble chlorophyll binding protein. J Phys Chem B. 2009;113:9948–57.
54. Böttcher CJF. Theory of electric polarization, vol. 1. Amsterdam: Elsevier; 1973.
55. Knox RS, Spring BQ. Dipole strengths in the chlorophylls. Photochem Photobiol. 2003;77:497–501.
56. Adolphs J, Renger T. How proteins trigger excitation energy transfer in the FMO complex of green sulfur bacteria. Biophys J. 2006;91:2778–97.
57. Renger T, Müh F. Theory of excitonic couplings in dielectric media – foundations of Poisson-TrEsp method and application to photosystem I trimers. Photosynth Res. 2012;111:47–52.
58. Simonson T, Perahia D. Microscopic dielectric properties of cytochrome *c* from molecular dynamics simulations in aqueous solution. J Am Chem Soc. 1995;117:7987–8000.
59. Müh F, Zouni A. Extinction coefficients and critical solubilisation concentrations of photosystems I and II from *Thermosynechococcus elongatus*. Biochim Biophys Acta. 2005;1708:219–28.
60. Hsu CP, Head-Gordon M, Head-Gordon T, Fleming GR. Excitation energy transfer in condensed media. J Chem Phys. 2001;114:3065–72.
61. Mennucci B, Curutchet C. The role of the environment in electronic energy transfer: a molecular modeling perspective. Phys Chem Chem Phys. 2011;13:11538–50.
62. Hauska G, Schoedl T, Remigy H, Tsiotis G. The reaction center of green sulfur bacteria. Biochim Biophys Acta. 2001;1507:260–77.
63. Fenna RE, Matthews BW. Chlorophyll arrangement in a bacteriochlorophyll protein from *Chlorobium limicola*. Nature. 1975;258:573–7.
64. Tronrud DE, Schmid MF, Matthews BW. Structure and X-ray amino-acid-sequence of a bacteriochlorophyll-*a* protein from *Prosthecochloris aestuarii* refined at 1.9 Å resolution. J Mol Biol. 1986;188:443–54.
65. Ben-Shem A, Frolow F, Nelson N. Evolution of photosystem I – from symmetry through pseudosymmetry to asymmetry. FEBS Lett. 2004;564:274–80.
66. Tronrud DE, Wen JZ, Gay L, Blankenship RE. The structural basis for the difference in absorbance spectra for the FMO antenna protein from various green sulfur bacteria. Photosynth Res. 2009;100:79–87.
67. Milder MTW, Brüggemann B, van Grondelle R, Herek JL. Revisiting the optical properties of the FMO protein. Photosynth Res. 2010;104:257–74.
68. Louwe RJW, Vrieze J, Hoff AJ, Aartsma TJ. Toward an integral interpretation of the optical steady-state spectra of the FMO-complex of *Prosthecochloris aestuarii*. 2. Exciton simulations. *J. Phys*. Chem B. 1997;101:11280–7.
69. Wen J, Zhang H, Gross ML, Blankenship RE. Membrane orientation of the FMO antenna protein from *Chlorobaculum tepidum* as determined by mass spectrometry-based footprinting. Proc Natl Acad Sci U S A. 2009;106:6134–9.

70. Wendling M, Pullerits T, Przyjalgowski MA, Vulto SIE, Aartsma TJ, van Grondelle R, van Amerongen H. Electron-vibrational coupling in the Fenna-Matthews-Olson complex of *Prosthecochloris aestuarii* determined by temperature-dependent absorption and fluorescence line-narrowing measurements. J Phys Chem B. 2000;104:5825–31.
71. Rätsep M, Freiberg A. Electron-phonon and vibronic couplings in the FMO bacteriochlorophyll *a* antenna complex studied by difference fluorescence line narrowing. J Lumin. 2007;127:251–9.
72. Renger T, Marcus RA. On the relation of protein dynamics and exciton relaxation in pigment-protein complexes: an estimation of the spectral density and a theory for the calculation of optical spectra. J Chem Phys. 2002;116:9997–10019.
73. Creemers TMH, De Caro CA, Visschers RW, van Grondelle R, Völker S. Spectral hole burning and fluorescence line narrowing in subunits of the light-harvesting complex LH1 of purple bacteria. J Phys Chem B. 1999;103:9770–6.
74. Renger T, Madjet ME, Knorr A, Müh F. How the molecular structure determines the flow of excitation energy in plant light-harvesting complex II. J Plant Physiol. 2011;168:1497–509.
75. Müh F, Renger T. Refined structure-based simulation of plant light-harvesting complex II: linear optical spectra of trimers and aggregates. Biochim Biophys Acta. 2012;1817:1446–60.
76. Novoderezhkin VI, Palacios MA, van Amerongen H, van Grondelle R. Excitation dynamics in the LHCII complex of higher plants: modeling based on the 2.72 Å crystal structure. J Phys Chem B. 2005;109:10493–504.
77. Frähmcke JS, Walla PJ. Coulombic couplings between pigments in the major light-harvesting complex LHC II calculated by the transition density cube method. Chem Phys Lett. 2006;430:397–403.
78. Linnanto J, Martiskainen J, Lehtovuori V, Ihalainen J, Kananavicius R, Barbato R, Korppi-Tommola J. Excitation energy transfer in the LHC-II trimer: a model based on the new 2.72 Å structure. Photosynth Res. 2006;87:267–79.
79. König C, Neugebauer J. First-principles calculation of electronic spectra of light-harvesting complex II. Phys Chem Chem Phys. 2011;13:10475–90.
80. Remelli R, Varotto C, Sandona D, Croce R, Bassi R. Chlorophyll binding to monomeric light-harvesting complex – a mutation analysis of chromophore-binding residues. J Biol Chem. 1999;274:33510–21.
81. Rogl H, Schödel R, Lokstein H, Kühlbrandt W, Schubert A. Assignment of spectral substructures to pigment-binding sites in higher plant light-harvesting complex LHC-II. Biochemistry. 2002;41:2281–7.

Chapter 2
Electron–Phonon and Exciton–Phonon Coupling in Light Harvesting, Insights from Line-Narrowing Spectroscopies

Jörg Pieper and Arvi Freiberg

Abstract In photosynthetic antenna complexes, apart from defining the positions and orientations of the pigment molecules, the protein matrix plays an important role in excitation energy transfer dynamics. The low-frequency protein vibrations—often referred to as phonons—serve as acceptor modes in nonadiabatic excitation energy transfer between energetically inequivalent electronic or excitonic energy states, assuring a spatially and energetically directed flow of excitation energy within an antenna complex. Due to electron–phonon and electron–vibrational coupling, the purely electronic or excitonic transitions of pigment molecules are usually accompanied by a broad and asymmetric low-frequency sideband spreading a few hundred wavenumbers and, in addition, by a number of distinct lines covering the frequency range between ~200 and 1,700 cm^{-1}. The low-frequency sideband peaking at 20–30 cm^{-1} is typically identified with a continuous distribution of widely delocalized protein vibrations. The narrow lines at higher frequencies can mostly be attributed to localized pigment vibrations of (bacterio-) chlorophyll molecules, which are only slightly modified by the surrounding protein matrix. In conventional absorption or fluorescence spectra measured at cryogenic temperatures this substructure is usually hidden by significant inhomogeneous broadening due to the heterogeneity of the amorphous protein matrix. Line-narrowing spectroscopies like spectral hole burning and (difference) fluorescence line-narrowing have been proved to be powerful experimental tools for unraveling the hidden homogeneous spectral features from the inhomogeneously broadened spectra. This contribution focuses on electron–phonon

J. Pieper (✉)
Institute of Physics, University of Tartu, Ravila 14c, 50411 Tartu, Estonia
e-mail: pieper@ut.ee

A. Freiberg
Institute of Physics, University of Tartu, Ravila 14c, 50411 Tartu, Estonia

Institute of Molecular and Cell Biology, University of Tartu, Riia 23, 51010 Tartu, Estonia
e-mail: arvi.freiberg@ut.ee

J. Golbeck and A. van der Est (eds.), *The Biophysics of Photosynthesis*,
Biophysics for the Life Sciences 11, DOI 10.1007/978-1-4939-1148-6_2,

and exciton–phonon coupling in photosynthetic pigment–protein complexes. It also discusses the underlying concepts of electron–phonon and electron–vibrational coupling starting from the Franck–Condon principle and the general composition of homogeneously and inhomogeneously broadened spectra of pigment–protein complexes. The advantages and limitations of different spectroscopic techniques in revealing the electron–phonon and electron–vibrational coupling parameters are discussed based on model calculations. The chapter concludes with a discussion of recent results on electron–phonon and electron–vibrational coupling for isolated (bacterio-) chlorophyll molecules as well as for selected photosynthetic pigment–protein complexes.

Keywords Photosynthesis • Pigment–protein complex • Electron–phonon coupling • Electron–vibrational coupling • Huang–Rhys factor • Spectral density • Spectral hole burning • Fluorescence line-narrowing

Abbreviations

BChl	Bacteriochlorophyll
Chl	Chlorophyll
FLN	Fluorescence line narrowing
FWHM	Full-width-at-half-maximum
IDF	Inhomogeneous distribution function
LH1	Light harvesting complex 1 (of purple bacteria)
LH2	Light harvesting complex 2 (of purple bacteria)
LHC II	Light harvesting complex II (of green plants)
PSB	Phonon sideband
SHB	Spectral hole burning
SMS	Single-molecule spectroscopy
ZPL	Zero-phonon line

2.1 Introduction

For efficient light-harvesting nature has developed specialized pigment–protein complexes referred to as “antennae” whose electronic absorption spectra span broad energy ranges of several hundreds to two thousand wavenumbers and are well adapted to the maximum of the solar radiation reaching the earth’s surface. Since in many cases photosynthetic antenna complexes consist of arrays of closely spaced pigment molecules, excitonic interactions have to be taken into account (see Sect. 1.1). The exciton, a bound state of an electron and a hole, is regarded as an elementary excitation of condensed matter that can transfer energy without transporting net electric charge. Relevant for photosynthesis are short range Frenkel excitons where an electron and a hole reside on the same molecule and propagate

together [1]. Excitons in the context of photosynthesis have already been discussed since 1938 [2]; a modern overview of photosynthetic excitons can be found in [3]. Within the recent years, much effort has been invested to unravel the excitonic energy level structure and excitation energy transfer dynamics in photosynthetic antenna complexes as well as the underlying pigment–pigment and pigment–protein interactions (see Sects. 1.1 and 1.2) by different experimental approaches like time-resolved spectroscopy [4], spectrally selective techniques [5] or single-molecule spectroscopy (SMS) [6], and more recently, by two-dimensional electronic spectroscopy [7]. The wealth of experimental information has initiated detailed theoretical simulations of excitation energy transfer, specifically, in the major antenna complexes LHC II of green plants (see, e.g., Müh et al. [8] and references therein) and LH2 from purple bacteria (see, e.g., Novoderezhkin and van Grondelle [9], Freiberg and Trinkunas [10]).

In addition to the pigment–pigment interactions discussed above, photosynthetic antenna complexes are also characterized by electron–vibrational coupling, which refers to the interaction between a molecular electronic transition and intramolecular nuclear vibrations determining the vibronic structure of optical spectra of individual pigments (chromophores) [11]. A special case of electron–vibrational coupling is the chromophore–host interaction, which gives rise to the electron–phonon structure of the spectra. Strictly speaking, phonons are collective vibrational modes (standing waves) in perfectly periodic lattices, in which all the lattice particles simultaneously participate. Here, the term phonon is more loosely used to distinguish delocalized low-frequency protein vibrations in pigment–protein complexes (and amorphous lattices in general) from the higher-frequency intramolecular vibrations localized on the (bacterio)chlorophyll ((B)Chl) and other pigment molecules bound to the photosynthetic antenna complex. The electron–phonon and electron–vibrational (vibronic) interactions together shape the so-called homogeneously broadened spectra of the photosynthetic pigment molecules surrounded by an optically transparent dielectric medium, here consisting of the native protein scaffold and buffer solution. In case of non-negligible excitonic coupling between the pigment molecules of a given photosynthetic complex, one has to refer to exciton–phonon coupling. In either regime, the purely electronic/excitonic transitions of photosynthetic pigments embedded into amorphous protein environments are thus typically accompanied by a large number of vibrational replicas due to electron–phonon and vibronic coupling. The energetic difference between the purely electronic/excitonic origin and a given vibrational line generally reflects the corresponding vibrational frequency.

This is illustrated in Fig. 2.1 by showing vibrational spectra of the ground state of a Chl*a*-containing water soluble chlorophyll-protein (Chl*a*-WSCP) complex [12], obtained by spectrally selective low-temperature difference fluorescence line-narrowing technique at 4.5 K (delta-FLN, see below). The Chl*a*-WSCP complex is well suited for studies of pigment–pigment and pigment–protein interactions, because it binds only two Chl*a* molecules, which are excitonically coupled with moderate interaction energy of roughly ~100 cm^{-1}, and which in the simplest approximation [13] form only two excitonic energy levels denoted by E_1^+ and E_1^-.

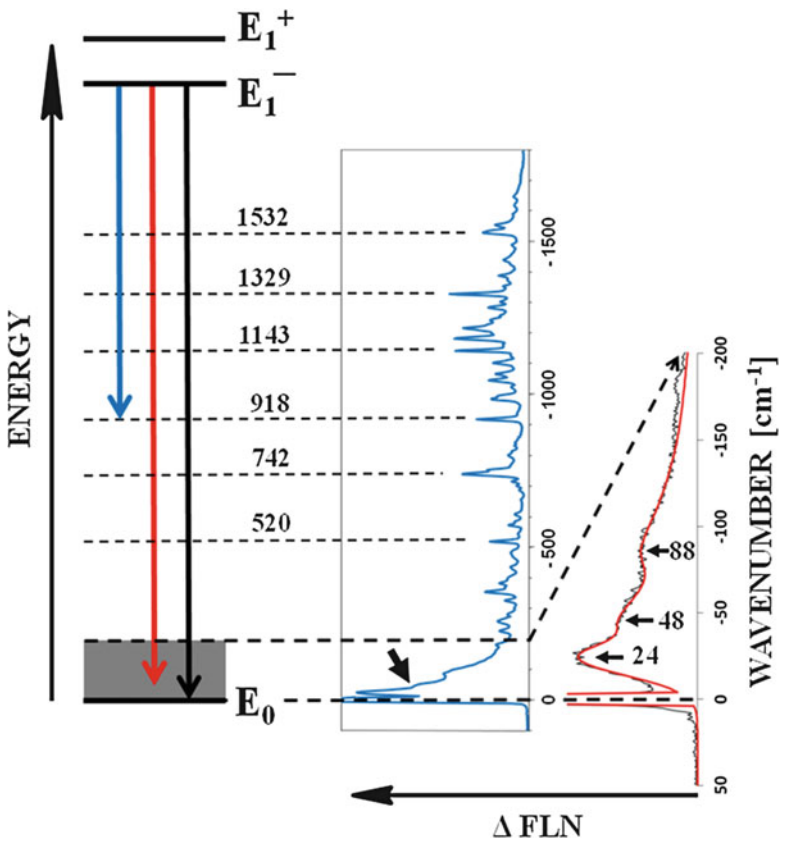

Fig. 2.1 Schematic vibrational energy level diagram of Chl*a*-WSCP derived from high-resolution delta-FLN spectroscopy at 4.5 K. A 4.5 K delta-FLN spectrum of Chl*a*-WSCP is shown as a *blue line*; selected vibronic lines are labeled by their frequencies in wavenumbers (data taken from [12]). The ZPL is cut off for clarity. A magnification of the phonon region (labeled by a *thick black arrow*) is shown to the right (*black noisy line*); the magnified wavenumber region is indicated by a *dashed arrow*. The peaks in the phonon sideband are also labeled by their frequencies. A simulation of the phonon region (*red line*) is calculated using a Huang–Rhys factor S of 0.81 and three one-phonon profiles with peak frequencies of 24, 48, and 88 cm^{-1}, respectively. In the energy level diagram (see *left* side), the ground state as well as lower and higher exciton level of Chl*a*-WSCP are given by thick black lines and labeled by E_0, E_1^-, and E_1^+, respectively. The ground state ($E_1^- \rightarrow E_0$) vibrational levels are indicated by *dashed lines*, the phonon region by *grey color*. The *black arrow* represents a zero-phonon (purely excitonic) transition, while the *blue* and *red arrows* correspond to transitions involving Chla vibrations and phonons, respectively

The delta-FLN spectrum shown in the center of Fig. 2.1 generally consists of three parts: (1) the intense and narrow purely excitonic line at the excitation frequency of $\omega = (E_1 — E_0)/\hbar$. As follows, this frequency is for convenience taken as zero point and considered as an origin of the delta-FLN spectrum. The readers familiar with many spectroscopic techniques might recognize the analogy with Raman

spectroscopy (see, e.g., Aartsma and Matysik [4]); (2) a broad, asymmetric phonon sideband adjacent to the purely excitonic line on its low-energy side and spreading up to ~200 cm^{-1}; and (3) around 50 distinct vibrational lines covering the frequency range between ~200 and 1,700 cm^{-1}. The phonon sideband peaking at ~24 cm^{-1} is shown in more detail in the rightmost spectrum of Fig. 2.1. It is typically identified with a broad and continuous distribution of widely delocalized low-frequency protein vibrations and their multi-quantum transitions, while the narrow vibrational lines at frequencies higher than ~200 cm^{-1} can mostly be attributed to localized Chl*a* vibrations, only slightly modified by the environment (see Rebane [11] and Kühn et al. [14] for reviews). Since the coupling between the excitonic transition and the intramolecular vibrational degrees of freedom is weak [12], the vibrational replicas represent in a good approximation just single-quantum transitions for the local vibrational modes of Chl*a*. Figure 2.1 also shows a schematic energy level diagram of the ground state $E_1^- \rightarrow E_0$ phonon and vibrational transitions indicated by grey color and dashed lines, respectively. The black arrow represents a zero-phonon (purely excitonic) transition, while the blue and red arrows correspond to transitions involving Chl*a* vibrations and phonons, respectively. The complementary excited state vibrational frequencies can be observed in hole burned spectra at 4.5 K and typically show little variation [15].

It is apparent from Fig. 2.1 that even the spectrum of a simplest pigment–protein complex is rather complicated and extends over a significant range of frequencies. Therefore, detailed knowledge of the parameters of electron–phonon and electron–vibrational coupling is essential for a proper understanding and theoretical simulations of optical spectra as well as energy transfer rates in photosynthetic systems. Furthermore, the example of WSCP underlines that photosynthetic pigment–protein complexes often feature excitonic rather than localized electronic states, so that exciton–phonon and exciton–vibrational couplings also have to be considered (see below). The rich vibrational structure characteristic for homogeneously broadened spectra is, however, not apparent in conventional absorption and fluorescence spectra even at low temperatures, which are widely structureless due to significant heterogeneity of the pigment microenvironments and ensemble averaging, as will be discussed in some detail below. This observation constitutes the need for experimental techniques which are capable of revealing phonon and vibrational substructures at least at low temperatures such as spectral hole burning (SHB) [16, 17], FLN [18], and delta-FLN [19–21]. In principle, the low-temperature SMS [6, 22, 23] also belongs to this list. However, as is well known, the single-molecule spectra suffer from poor signal to noise ratio, rendering investigation of weak vibronic and phonon structures a rather difficult task. Therefore, in the present chapter we will limit ourselves to providing an overview on the analysis of phonon structure in line-narrowed (SHB, FLN, delta-FLN) optical spectra. Electron–vibrational coupling will be addressed in parallel, because of the many analogies to the case of phonons.

The present chapter is organized as follows: In Sect. 2.2 we will introduce the homogeneous lineshape of an isolated pigment molecule embedded into a protein matrix and explain the origin of the electron–phonon and electron–vibrational

coupling. The meaning of the frequently used terms in the corresponding literature, such as the Huang–Rhys factor and reorganization energy, will be clarified. Effects of excitonic coupling on the electron–phonon coupling parameters will be shortly commented. In Sect. 2.3 we will follow with a discussion of the origin of inhomogeneous spectral broadening and its effect on conventional absorption and fluorescence spectra. In Sect. 2.4 the different types of line-narrowing spectroscopies (SHB, FLN, and delta-FLN) will be introduced. Their similarities and differences will be illustrated by model calculations. Finally, in Sect. 2.5, we will provide a short overview and critical discussion of some experimental results related to electron/exciton–phonon and electron/exciton–vibrational coupling for (B)Chl*a* pigment molecules either in isolation or when embedded into the major photosynthetic light-harvesting complexes of green plants (LHC II) and purple bacteria (LH2).

2.2 Conceptual Basis of Electron–Phonon and Electron–Vibrational Coupling: Homogeneously Broadened Spectra

A quantitative description of electron–phonon coupling requires a number of simplifying assumptions to be made about the complex macromolecular pigment–protein system, including the adiabatic, harmonic, and Franck–Condon approximations (see Rebane [11] and references therein). For simplicity, the theory of electron–phonon coupling discussed below is strictly valid for highly localized electronic transitions only, e.g., for isolated (B)Chl molecules at large distance from other chromophores in a given photosynthetic complex. A short overview of the excitonic coupling effects is provided at the end of this Section.

Within the adiabatic approach, the motions of the heavy nuclei of a macromolecule are assumed to be uncorrelated with the faster motions of the much lighter electrons so that the two types of motions can be separated. This assumption is the prerequisite for the description of a macromolecule in terms of a potential energy diagram as shown in Fig. 2.2 depicting the motion of the system of heavy nuclei along one selected conformational coordinate q_k for each the two electronic states E_i and E_f. More generally, a macromolecular system of N atoms is characterized by 3N motional degrees of freedom including three translational and three rotational components so that we arrive at a total of 3N-6 vibrational eigenmodes characterized by their eigenfrequencies ω_k. A realistic assumption for E_i is a Lennard-Jones potential [11] with an attractive and a repulsive component at large and small values of the conformational coordinate, respectively. In thermal equilibrium at low temperature, however, one can assume that the nuclei perform only small fluctuations around the respective potential energy minima. Within the harmonic approximation, it is then presumed that these fluctuations can be described by parabolic potentials, i.e., the motion of the nuclei along one conformational coordinate is equivalent to that of a harmonic oscillator moving around an equilibrium position.

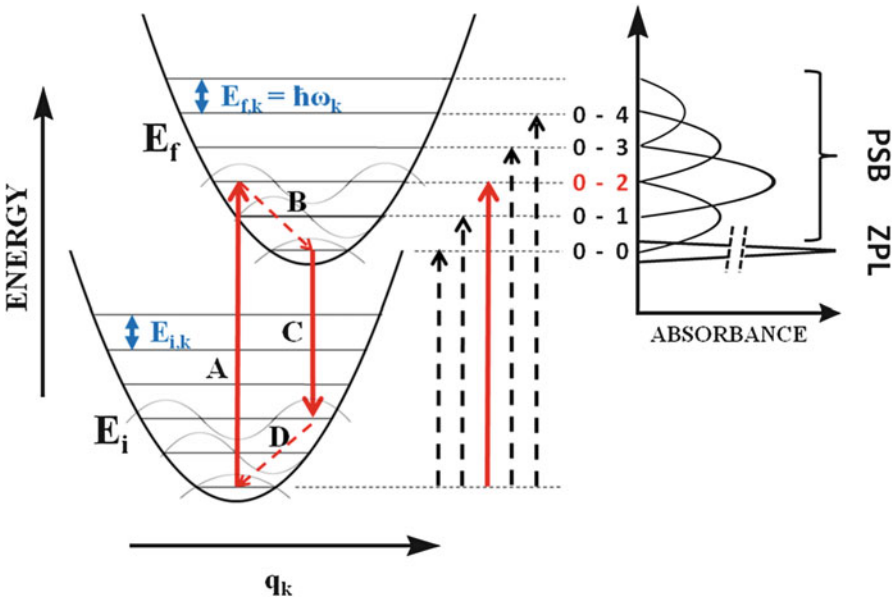

Fig. 2.2 Schematic potential energy diagram of a pigment embedded into an amorphous protein matrix for the case of linear harmonic Franck–Condon coupling (*left side*) and the corresponding absorption spectrum (*right side*) in the low temperature limit where k_BT is much smaller than the vibrational energy $\hbar\omega_k$ of the considered nuclear motion. The potential energy curves of a selected nuclear motion are plotted as a function of its conformational coordinate q_k in the electronic ground and excited states E_i and E_f, respectively. The most probable transitions are given by *red full arrows* for the cases of absorption (A) and fluorescence (C). Schematic vibronic wavefunctions are given by grey lines for selected vibrational energy levels to illustrate the principle of the overlap integral in Eq. (2.1). *Red dashed arrows* (B, D) indicate fast vibrational relaxation following the initial electronic transition. The energy level diagram to the right of the potential energy curves illustrates the different (multi-) quantum transitions of the selected vibrational frequency ω_k in absorption. The corresponding spectral features are qualitatively shown in the right diagram, where 0–0 transitions constitute the ZPL (not in scale) and all transitions involving phonons (0–1, 0–2, etc.) constitute the PSB. Note that in contrast to the different quantum transitions of a single vibrational frequency ω_k shown here, the vibronic energy levels depicted in Fig. 2.1 correspond to one-quantum transitions of different vibrational eigenfrequencies

The various harmonic oscillators characterized by a frequency ω_k and the corresponding discrete energy levels with an energetic spacing of $\hbar\omega_k$ (as shown in Fig. 2.2) are independent from each other. Upon electronic excitation due to absorption of a light quantum the system of nuclei generally undergoes a rearrangement leading to a shift of the equilibrium position and change of curvature of the harmonic potential in the excited electronic state E_f. These changes determine the Franck–Condon type of vibronic coupling [24, 25]. As a first approximation, however, the parabolic potentials in the ground and the excited electronic state are usually taken identical, except for the shift of the equilibrium position, resulting in an identical phonon frequency ω_k in both electronic states [11]. This is the

situation also illustrated by the shifted potentials E_i and E_f of the ground and excited electronic states shown in Fig. 2.2.

The transition probabilities between a given vibrational level in the electronic ground state and any vibrational level in the excited electronic state as shown in Fig. 2.2 are given by the Franck–Condon principle. Within the classical Franck–Condon approach, the heavy nuclei do not react during a fast electronic transition upon light absorption, i.e., the latter transition is vertical in the potential energy diagram shown in Fig. 2.2. A detailed quantum mechanical description is beyond the scope of this contribution; a comprehensive derivation can be found in [11]. Briefly, the transition probability between the vibrational levels n and m in the initial and the final electronic states E_i and E_f, respectively, is given by the square of the product of electronic transition probability $D_{f,i}$ and the overlap integral of the respective vibrational wave functions of each oscillator k [11]

$$W_{fm,in} = \left| D_{f,i} \prod_k \langle m_k | n_k \rangle \right|^2 . \tag{2.1}$$

Equation (2.1) is at the heart of the electron–phonon and electron–vibrational coupling. Strictly speaking, the electronic transitions between the initial and final electronic states are almost always coupled to the vibrations and the quantum mechanical formulation of the Franck–Condon principle provides a probability for each vibrational transition coupled to an optical excitation by evaluation of the overlap integral in Eq. (2.1). As an illustration, schematic wavefunctions are shown for selected vibrational levels in Fig. 2.2. For brevity, we will consider here only the case of sufficiently low temperatures, i.e., at $k_B T \ll \hbar\omega_k$, where k_B is the Boltzmann constant. In this case only the lowest vibrational level of the electronic ground state is thermally populated and serves as the starting point of an electronic transition in absorption. Generally, the final vibrational level in the excited electronic state depends on the shift of the equilibrium position of the harmonic potential in the excited electronic state. The situation depicted in Fig. 2.2 shows the largest overlap of ground and excited state wavefunctions in case of a transition from the lowest vibrational level in the electronic ground state E_i to the second vibrational level in the excited electronic state E_f, i.e., the absorption process leads to creation of two vibrational quanta or phonons and thus requires higher light energy than the purely electronic or zero-phonon transition. Therefore, the schematic absorption spectrum on the right side of Fig. 2.2 exhibits the most intense feature at the position of the two-quantum/two-phonon (0–2) transition. All other quantum transitions shown are less probable and appear with smaller intensity. We distinguish transitions with and without participation of the vibrational quanta/phonons that form the phonon sideband (PSB) and the zero-phonon line (ZPL), respectively, as also shown in Fig. 2.2. The reason for the different linewidths of ZPL and PSB components is discussed below. Following light absorption, the macromolecular system depicted in Fig. 2.2 is in nonequilibrium state (again assuming that $k_B T \ll \hbar\omega_k$), so that it subsequently relaxes to the lowest vibrational

level in the excited electronic state E_f (see dashed arrow labeled with B). The energy released upon this nonradiative equilibration process is called the reorganization energy. Then, following the Franck–Condon principle, de-excitation occurs via a radiative transition into the second vibrational level of the electronic ground state E_i, again followed by vibrational relaxation into the ground state in thermal equilibrium (dashed arrow labeled with D). In contrast to absorption, the average light quantum emitted as fluorescence is smaller than that of a zero-phonon transition, so that in this simple case the electron–phonon coupling leads to mirror symmetry between the absorption and fluorescence transition probabilities/spectra. The energetic difference between the absorption and fluorescence spectral maxima is called Stokes shift; it is numerically equal to twice the reorganization energy (see Eq. (2.7) below). Qualitatively, the above potential energy model applies to both localized vibrations of (B)Chl molecules and delocalized protein vibrations (phonons).

The complexities rapidly amount in the more general cases of arbitrary potential surfaces in the ground and excited electronic state, and especially, when the electronic transition probability $D_{f,i}$ in Eq. (2.1) depends on nuclear coordinates resulting in a breakdown of mirror symmetry [24, 25]. This latter effect in relation with the Chl*a* and BChl*a* spectra will be discussed in the last part of this chapter. At higher temperatures with $k_BT \ll \hbar\omega_k$, thermal population of higher vibrational levels has to be considered so that transitions with annihilation of vibrations/phonons become available. This generally leads to a redistribution of the electron–vibrational band intensity in favor of the PSB. Also, in absorption, the PSB components at the low-energy side of the ZPL are observed, in addition to those present at the high-energy side. The latter and former are referred to as Stokes and anti-Stokes parts of the PSB [11, 26].

We will now discuss the spectral lineshape of an isolated pigment molecule whose electronic transition is coupled to a distribution of delocalized protein phonons as well as to intramolecular localized vibrations. As discussed above, this spectrum consists of a narrow purely electronic ZPL, a broad PSB, and a series of narrow vibrational lines lying towards higher energy in absorption (see red line in Frame A of Fig. 2.3, where for clarity only the ZPL and PSB parts are reproduced). We assume that the shape of the latter spectrum is the same for all chemically equivalent molecules in a bulk sample, so that it can be referred to as the homogeneously broadened single site absorption spectrum. Furthermore, as is frequently done, we apply a "mean frequency approximation" for phonons, i.e., the distribution of 3N-6 eigenmodes of the protein shall be represented by a single band of mean frequency ω_m and a lineshape that accounts for the whole ensemble of energetically closely spaced protein vibrations. The analytical expression for the low-temperature single site absorption and fluorescence spectra of a chromophore embedded into an amorphous protein matrix within the approximation of Eq. (2.1) is given by [27]

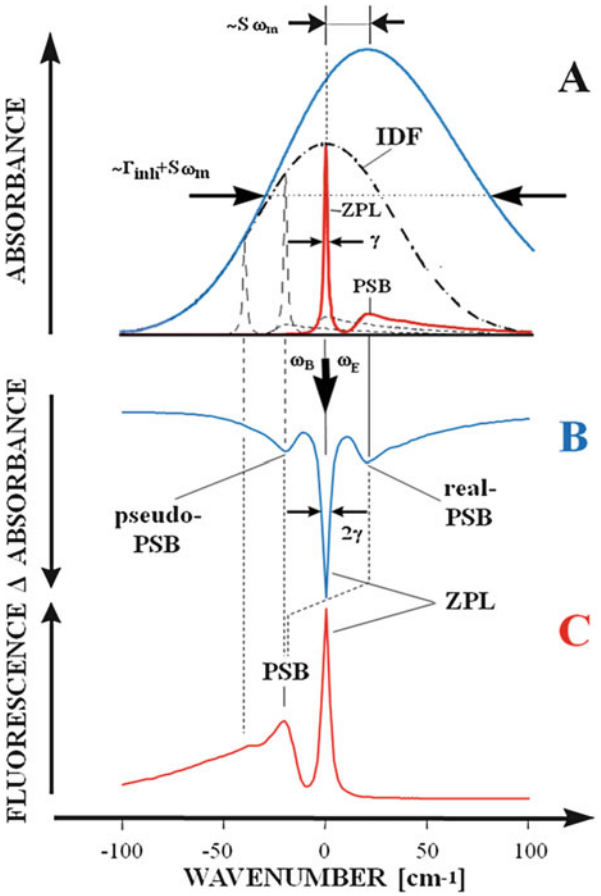

Fig. 2.3 Schematic illustration of conventional (Frame **A**) and line-narrowing spectroscopies (Frames **B** and **C**). Frame **A**: The homogeneously broadened absorption spectrum of a model pigment–protein complex shown as a *red line* consists of ZPL and an asymmetric PSB towards higher energies at low temperature. The homogeneously broadened spectrum is directly accessible only by SMS and delta-FLN spectroscopies, see text. In conventional absorption spectroscopy, however, inhomogeneous broadening has to be considered so that the resulting ensemble spectrum (*blue line*) is the convolution of the homogeneously broadened absorption spectrum with a Gaussian IDF (see *dashed dotted line*). The calculations were performed assuming an inhomogeneous width of 80 cm^{-1}, a Huang–Rhys factor of 1.0, and a phonon profile with a peak at 20 cm^{-1} and a width of $\Gamma = 20\ cm^{-1}$ ($\Gamma_G = 10\ cm^{-1}$, $\Gamma_L = 30\ cm^{-1}$). Frame **B** shows a SHB spectrum of the model pigment–protein complex introduced in Frame **A** (*blue line*). It consists of ZPL (or ZPH) and real-PSB towards the high-energy side of the ZPL. The latter features correspond to the homogeneously broadened absorption spectrum and appear due to resonant burning of pigment molecules, whose ZPL are resonant with the burn frequency ω_B (indicated by the *red spectrum* in Frame **A**). The additional pseudo-PSB lying towards the low-energy side of the ZPL is the result of nonresonant burning of pigment molecules whose PSB are resonant with the burn frequency ω_B (indicated by the *dashed spectra* in Frame **A**). Correspondences between features shown in Frames **A** and **B** are indicated by *full* and *dashed lines* for the cases of resonant and nonresonant burning, respectively. Frame **C** shows a FLN spectrum of the model pigment–protein complex introduced in Frame **A** (*red line*) consisting of ZPL and only a single PSB towards the low-energy side of the ZPL, because both, real-and pseudo-PSB, are found at the same side of the ZPL in the case of FLN. Adapted from [82]. Copyright 2000 J. Pieper

$$L(\omega) = e^{-s} l_0(\omega - \Omega) + \sum_{R=1}^{\infty} S^R \frac{e^{-S}}{R!} \; l_R(\omega - \Omega \mp R\omega_m). \tag{2.2}$$

In Eq. (2.2), the − and + signs correspond to absorption and fluorescence, respectively. The first term describes the ZPL with a Lorentzian shape l_0 at a frequency position Ω. The phonon sideband consists of all one-phonon and multi-phonon transitions forming the l_R-terms with ($R \geq 1$). Here, the terms for $R = 1$, $R = 2$, $R = 3$, ... correspond to one-quantum, two-quantum, three-quantum, ... and further multi-quantum transitions, respectively. This means that in case of a one-quantum transition peaking at ω_m, the two-quantum transition is found at $2\omega_m$, the three-quantum transition at $3\omega_m$, and any multi-quantum transition at $R\omega_m$. In order to account for the frequency dependence of absorption and fluorescence, Eq. (2.2) would have to be multiplied by ω and ω^3, respectively [11]. However, this effect is relatively small in the case of electron–phonon coupling given the relatively low phonon frequencies.

The one-quantum lineshape l_1 has a special meaning and is referred to as the spectral density, generally representing the distribution of all (delocalized protein as well as localized chromophore) vibrational modes, and their coupling strength to the electronic transition. Referring to electron–phonon coupling only, the shape l_1 is also denoted as the one-phonon profile. Comparing the protein and the chromophore vibrations, the 3N-6 chromophore frequencies collectively lie at higher energies than the delocalized protein vibrations, because of the smaller effective mass of the moving entities. Therefore, the chromophore vibrations are observed as individual narrow lines at higher energies than the phonon sideband.

The dynamics of energy transfer and relaxation processes is mostly determined by the quasi-continuum phonon part of the spectral density. Therefore, the total coupling strength of phonons to an electronic transition, governing the intensity distribution between the ZPL and the PSB, has a special interest [28]. It is characterized by a single dimensionless number, the Huang–Rhys factor S. The Huang–Rhys factor is associated with the displacement of the equilibrium positions of the nuclei upon a photoexcitation of the chromophore as illustrated in Fig. 2.2. Therefore, S is a measure for the strength of the linear electron–phonon coupling and characterizes the average number of phonons accompanying a particular electronic transition. It follows from Eq. (2.2) that the intensity share of ZPL (I_{ZPL}) yields the value of exp(−S), being equivalent to

$$\exp(-S) = \alpha = I_{ZPL}/(I_{ZPL} + I_{PSB}). \tag{2.3}$$

In addition, the strength of electron–phonon coupling is often expressed in terms of the Debye–Waller factor α that is also defined in Eq. (2.3). Typically, one distinguishes weak electron–phonon coupling with S-factors smaller than 1 and strong coupling with S-factors larger than 1. Although the Huang–Rhys factor has a rigorous meaning only within the Franck–Condon interaction model, it is widely used in a much broader context, even in case of excitons, as a general indicator of

Table 2.1 Huang–Rhys factor S obtained by SHB, FLN, and delta-FLN for the lowest energy states of different photosynthetic pigment–protein complexes[a]

Complex	S-factor	Method	Reference
Chl*a* in 1-propanol	0.56	Delta-FLN[b]	[60]
BChl*a* in triethylamine	0.46	Delta-FLN[b]	[61]
FMO from green sulphur bacteria	0.46	Delta-FLN[b]	[52]
LH1 from Rb. sphaeroides	1.6	Delta-FLN[b]	[73]
B850 band of LH2 from Rb. sphaeroides	2.0	Delta-FLN[b]	[73]
B800 band of LH2 from Rb. sphaeroides	0.1–0.9	SMS	[46]
CP43	0.30	SHB	[83]
			[84]
CP47	0.7	SHB	[85]
	1.0	SHB	[86]
CP29	0.50–0.68	Delta-FLN[b]	[54]
LHC I	2.9	FLN	[87]
LHC II monomer	0.62	Delta-FLN[b]	[69]
LHC II trimer	0.9	SHB/FLN	[50]
Chl*a* dimers In WSCP	0.81	Delta-FLN	[12]
Chl*b* dimers In WSCP	0.88	Delta-FLN	[12]
PS I core from cyanobacteria	2.0	SHB	[88]
P680 from PS II RC	1.9	SHB	[89]

[a]Obtained at the excitation/burn frequency corresponding to the half height of the IDF from the long-wavelength side
[b]Corrected values, see text

the exciton–phonon coupling strength. This operational approach based on Eq. (2.3) is also followed in the present text. An overview of the experimentally determined S-factors in case of isolated (B)Chls and several photosynthetic complexes, obtained by different line-narrowing techniques, is given in Table 2.1. The characteristic vibrational frequencies and corresponding coupling constants S for Chl*a* and Chl*b* are summarized in Table 2.2.

The phonon part of the one-quantum profile l_1 is within the mean frequency approximation represented by a product of the phonon density of states g(ω) and of a frequency-dependent electron–phonon coupling term s(ω). The one-phonon profiles determined for various photosynthetic complexes are typically broad and asymmetric lineshapes with a major peak at about 20–30 cm^{-1}. The shape l_1 can often be well approximated by a Gaussian at its low-energy side according to

$$l_R = \frac{2}{\Gamma_R \sqrt{\Pi/\ln 2}} \exp\left(- \left[\frac{\omega - \nu \mp R\omega_m}{\Gamma_R / 2\sqrt{\ln 2}} \right]^2 \right) \tag{2.4}$$

and a Lorentzian at its high-energy side according to

Table 2.2 Vibrational frequencies ν_j (± 2 cm^{-1}) and Huang–Rhys factors, S_j (± 0.0005) of Chl*a*-WSCP and Chl*b*-WSCP obtained by delta-FLN spectroscopy at 4.5 K [12]

Chl*a*-WSCP, ν_j (cm^{-1}) [12]	Chl*a*-WSCP, S_j [12]	CP29, ν_j (cm^{-1}) [54]	Chl*b*-WSCP, ν_j (cm^{-1}) [12]	Chl*b*-WSCP, S_j [12]	Chl*b*, ν_j (cm^{-1}) [58]
183	0.0078	192	181	0.0173	
228	0.0082		221	0.0246	
			240	0.0182	245
259	0.0160	262	269	0.0064	255
283	0.0052	287	283	0.0036	
			298	0.0104	310
327	0.0055		325	0.0112	
356	0.0245	350	352	0.0249	345
384	0.0147	386	366	0.0112	375
402	0.0088	401	405	0.0061	405
435	0.0085	425	430	0.0050	
			470	0.0075	465
481	0.0137	467	488	0.0061	
520	0.0157	517	515	0.0045	515
547	0.0042	545	537	0.0157	
574	0.0072	573	572	0.0132	560
584	0.0049		598	0.0036	595
609	0.0075	607	620	0.0047	625
656	0.0013		641	0.0033	
690	0.0013	701	700	0.0019	680
703	0.0019				700
718	0.0039		713	0.0025	
			734	0.0107	732
742	0.0353	745	746	0.0112	742
754	0.0212		757	0.0229	750
803	0.0101	800	800	0.0022	
816	0.0066				
840	0.0072	842	834	0.0140	832
			863	0.0033	
			887	0.0019	885
920	0.0251	918	922	0.0291	923
985	0.0158	989	977	0.0110	980
993	0.0129		998	0.0036	1,003
1,024	0.0068		1,023	0.0022	
1,047	0.0215	1,049	1,045	0.0056	1,040
1,067	0.0170	1,070	1,068	0.0050	1,070
1,104	0.0176	1,109	1,108	0.0087	1,087
			1,128	0.0011	1,120
1,144	0.0303	1,145	1,150	0.0244	1,140
1,184	0.0460	1,186	1,172	0.0121	
		1,227	1,186	0.0226	1,190
1,217	0.0502		1,227	0.0249	1,217
1,243	0.0176		1,243	0.0090	1,253
1,259	0.0101	1,262	1,264	0.0126	1,275

(continued)

Table 2.2 (continued)

Chl*a*-WSCP, ν_j (cm^{-1}) [12]	Chl*a*-WSCP, S_j [12]	CP29, ν_j (cm^{-1}) [54]	Chl*b*-WSCP, ν_j (cm^{-1}) [12]	Chl*b*-WSCP, S_j [12]	Chl*b*, ν_j (cm^{-1}) [58]
1,285	0.0193	1,286	1,288	0.0224	
1,304	0.0107	1,307	1,305	0.0093	
1,329	0.0389	1,329	1,326	0.0509	1,330
1,354	0.0105	1,353	1,360	0.0093	1,270
1,375	0.0094	1,374			
1,390	0.0173	1,387	1,393	0.0328	1,390
1,441	0.0232	1,439	1,443	0.0121	
1,490	0.0088	1,490	1,484	0.0107	1,480
1,532	0.0330	1,537	1,522	0.0185	1,515
1,556	0.0212	1,556	1,550	0.0241	1,540
1,591	0.0058		1,573	0.0182	
1,620	0.0091	1,610	1,628	0.0081	
1,649	0.0114	1,665	1,654	0.0135	
			1,681	0.0067	
Sum	0.80		Sum	0.74	

The vibrational frequencies are compared to those determined for Chl*a* in CP29 of green plants [54] and isolated Chl*b* in solution [58]

$$l_R = \frac{\Gamma_R/_{2\Pi}}{\left[\omega - \nu \mp R\omega_m\right]^2 + \left[\Gamma_R/_2\right]^2}, \tag{2.5}$$

where the width Γ_R is defined as $\Gamma^R_{gauß} = \sqrt{R}\Gamma^0_{gauß}$ and $\Gamma^R_{lorentz} = R\Gamma^0_{lorentz}$ in the case of a Gaussian and Lorentzian, respectively [27].

The two terms g(ω) and s(ω) cannot be determined individually by optical line-narrowing techniques; however, the density of phonon states, which represents the 3N-6 eigenfrequencies of the protein matrix, can be directly obtained using inelastic neutron scattering [29]. Based on neutron studies, the density of phonon states appears to be rather similar for many different proteins with broad and asymmetric lineshapes peaking at about 20–30 cm^{-1} [30–32]. However, its spectral form was shown to vary with protein size (see, e.g., [30]) and due to interaction with the solvent (see, e.g., [32]). More recent, temperature-dependent inelastic neutron scattering experiments indicated that the shape of the one-phonon profile may change with temperature increase and shift towards lower frequencies above the dynamical transition of the protein matrix at about 240 K [33]. The shape of the one-phonon profile can in principle be predicted by normal mode analysis and molecular dynamics simulations based on the crystal structure of a given protein [29, 32] and has recently been reported for the Fenna–Matthews–Olson complex [34]. Individual one-phonon profiles for several photosynthetic pigment–protein complexes are listed in Table 2.3.

Similar concepts as for isolated chromophores are applicable to exciton–phonon coupling in the photosynthetic complexes that bind the excitonically coupled

Table 2.3 One-phonon profiles l_1 obtained for the lowest energy states of different photosynthetic pigment–protein complexes assuming a Gaussian and Lorentzian lineshape at the low- and high-energy side of the mean phonon frequency ω_m

Complex	Mean phonon frequency, ω_m (cm^{-1})	FWHM of the Gaussian wing of the one-phonon profile l_1 (cm^{-1})	FWHM of the Lorentzian wing of the one-phonon profile l_1 (cm^{-1})	Reference
FMO from green sulphur bacteria	21	21	56	[52]
LH1 from Rb. sphaeroides	26	26	130	[73]
B850 band of LH2 from Rb. sphaeroides	28	28	80	[73]
CP29	22	20	130	[54]
LHC II trimer	18	16	160	[31]
Chl*a* dimers in WSCP[a]				[12]
Profile 1	24	25	25	
Profile 2	48	20	50	
Profile 3	88	24	60	

[a]A proper description of the highly structured PSB of WSCP delta-FLN spectra required the assumption of three individual one-phonon profiles, [12] for details

pigments with the following modifications. According to Davydov [13], within the adiabatic approximation, the exciton–bath interaction can be separated into two, diagonal and non-diagonal, parts. The diagonal part describes the modulation of the molecular (site) transition energies by spatial and orientational coordinates of the molecule and is primarily responsible for the phonon and vibrational/vibronic sidebands of the exciton spectra. Its physical origin is the change in dispersion interactions between the chromophores when one of the chromophores is electronically excited. The non-diagonal part of the interaction is due to variation of the inter-pigment (excitonic) coupling energies by nuclear motions. This term is mostly accountable for the phonon-assisted exciton relaxation. Assuming for simplicity only diagonal coupling (the dispersion force coupling limit [35]), a picture of mutually shifted excitonic potential energy surfaces arises, qualitatively similar to the one for individual chromophores shown in Fig. 2.3. However, due to delocalized nature of excitons as well as vibrations the Huang–Rhys factor (and the respective reorganization energy) corresponding to the specific exciton state is modified compared with that of individual chromophores. For equivalent diagonal coupling strength the electron–phonon coupling for an exciton state will be reduced relative to that for a localized excitation. This effect will be larger, the wider (the more spread) is the exciton band [35, 36]. Furthermore, since the extent of delocalization of different exciton states may be different, the reorganization energy and the Huang–Rhys factor may also vary from state to state [37]. The value of the Huang–Rhys factor for a selected exciton state can be accessed from the experimental phonon sideband using the same procedure (see Eq. 2.3) as in case

of localized excitations. Also similar criteria of weak ($S < 1$) and strong ($S > 1$) coupling apply. However, their physical meaning is different. In case of excitons the strength of the electron–phonon coupling involves a propagation aspect. At $S \ll 1$ excitons are free, almost not disturbed by lattice vibrations. In contrast, when $S \gg 1$ the exciton is completely localized (self-trapped) by the on-site or local electron–phonon coupling. Various situations in between can be described as excitons propagating in the form of an exciton polaron, i.e., of an electronic excitation, which is accompanied by lattice phonons [38]. The exciton polaron effects discovered in bacterial light-harvesting complexes will be briefly introduced in the last Section of this treatise. Vibrational sidebands of excitonic transitions in dye aggregates and biological light-harvesting complexes are presently a matter of active study. The physical insights and computational methodologies of this research area can be found in [10, 39–43].

2.3 Encounter with the Reality: Inhomogeneous Broadening

As already noted in Introduction, a direct experimental determination of single site spectra of photosynthetic pigment–protein complexes (illustrated by red line in Frame A of Fig. 2.3) can only be achieved by low-temperature SMS, which remains a challenging task, although a number of successful single-molecule studies have been reported since 1999 ([44–48]). On the other hand, conventional absorption and fluorescence spectra are widely structureless because of significant inhomogeneous broadening of optical transitions of the pigments embedded in amorphous protein matrices [5].

Generally speaking, broadening mechanisms are considered to be *homogeneous* when affecting an optical transition of all molecules in an ensemble in the same way. Therefore, single-molecule spectra are by definition homogeneously broadened spectra. Ensemble spectra may be *inhomogeneously* broadened, because the specific environment of a pigment embedded into an amorphous matrix (including proteins) may differ from protein to protein in a bulk sample, affecting the transition frequency of that molecule. Static inhomogeneous broadening of photosynthetic pigment–protein complexes is usually well approximated by a nearly Gaussian distribution with full widths Γ_{inh} in the order of 80–200 cm^{-1} [5], which is referred to as inhomogeneous distribution function (IDF). Here, Γ_{inh} can be viewed as a measure for the inherent heterogeneity of the protein matrix. Sometimes, the IDF is also called site distribution function (SDF); however, this notation might occasionally interfere with the term *pigment binding site* in photosynthetic complexes. Therefore, we stick with a unique IDF, which does not include contributions from different pigment sites, but denotes a distribution of transition frequencies for the pigments at one and the same binding site in a bulk sample due to different protein conformations.

Based on the above considerations, the absorption and fluorescence spectra for an ensemble of pigments in an amorphous protein host at low temperatures are obtained through a convolution of the homogeneously broadened spectrum of Eq. (2.2) with a Gaussian IDF denoted as N (Ω_0-ω_C)

$$L(\omega) = \sum_{R=0}^{\infty} \left(S^R \frac{e^{-S}}{R!} \right) \int d\Omega_0 N(\Omega_0 - \omega_C) l_R(\omega - \Omega_0 \mp R\omega_m). \tag{2.6}$$

In Eq. (2.6), the $-\mathrm{R}\omega_\mathrm{m}$ and $+\mathrm{R}\omega_\mathrm{m}$ terms correspond to absorption and fluorescence, respectively, and the IDF function N ($\Omega_0-\omega_C$) of full width of Γ_inh peaks at ω_C.

The mutual relationships between the homogeneously and inhomogeneously broadened spectra are illustrated by model simulations presented in Fig. 2.3, Panel A. Due to the main focus of this chapter on electron–phonon coupling, these and the subsequent simulations include only phonon modes. The homogeneously broadened absorption spectrum (bold red line) is calculated according to Eq. (2.2). The intensities of the ZPL are distributed according to a Gaussian IDF with $\Gamma_\mathrm{inh} = 80\ \mathrm{cm}^{-1}$ (dashed-dotted line). The resulting inhomogeneously broadened absorption spectrum is calculated according to Eq. (2.6) (bold blue line). As known from the experiments performed under non-line-narrowing conditions, the latter spectrum appears to be widely structureless. When $\omega_\mathrm{m} < \Gamma_\mathrm{inh}$, the separate ZPL and PSB features are wholly masked by the relatively broad IDF, which determines the spectral resolution of conventional spectroscopy. The only apparent signature of the electron–phonon coupling is a slight asymmetry of the inhomogeneously broadened spectrum towards higher energies as well as a shift between the purely electronic transition at the center of the IDF and the absorption maximum, denoted as $\mathrm{S}\omega_\mathrm{m}$. Assuming mirror symmetry between the absorption and fluorescence spectra around the ZPL, the shift between the absorption and fluorescence maxima, referred to as *Stokes shift*, can in the mean phonon frequency approximation be estimated to be equal to twice the reorganization energy [27]

$$\Delta\omega_\mathrm{Stokes} \sim 2\ \mathrm{S}\omega_\mathrm{m}. \tag{2.7}$$

On the same footing, the width of the non-line-narrowed absorption spectrum is approximately [27]

$$\Gamma_\mathrm{non\text{-}line} \sim \Gamma_\mathrm{inh} + \mathrm{S}\omega_\mathrm{m}. \tag{2.8}$$

Equations (2.7) and (2.8) hold the better the narrower is the one-phonon profile, i.e., the better validated is the mean phonon approximation.

In summary, it is apparent from the simulations presented in Fig. 2.3 that any phonon structure is hidden by inhomogeneous broadening in conventional spectra, so that spectrally selective experimental techniques are necessary to unravel information on electron–phonon coupling in photosynthetic pigment–protein complexes. The static fluctuations of the environment, believed to be the main cause of

inhomogeneous broadening of optical spectra, can formally be looked at as a kind of a random noise that modulates the molecular transition energies, i.e., spectral positions of ZPL. Possible modifications of the homogeneous shapes of the spectra, which are related to electron–phonon and/or vibronic couplings, are ignored by this approach. As will be shown in the final part of the chapter, this view turns out to be too simplistic. In reality the total electron–phonon coupling strength depends on the excitation frequency both for localized excitations and for excitons.

2.4 Phonon Structure in Selectively Excited Spectra

In general, all line-narrowing techniques (SHB, FLN, delta-FLN) are based on selective laser excitation within an inhomogeneously broadened absorption profile at low temperatures, which selects information from only a subset of pigment molecules absorbing at a certain burn/excitation frequency. In SHB experiments, the transition frequency of those molecules/states selected by the burn laser is altered, so that the difference between pre- and post-burn absorption spectra reveals a hole at the burn frequency and a concomitant increase of absorption at another frequency. The latter gain in absorption is referred to as anti-hole or photoproduct depending on the mechanism of hole burning. For details on the different SHB mechanisms see Jankowiak et al. [5] and references therein.

A SHB spectrum for a model pigment–protein complex is shown in Frame B of Fig. 2.3. This spectrum exhibits a sharp zero-phonon hole (ZPH) at the burn frequency ω_B and different PSB holes on the low- and high-energy sides of the ZPH, respectively. Comparison with the single site absorption spectrum in Frame A of Fig. 2.3 shows that the ZPH is due to resonantly burned electronic transitions overlapping the burn frequency ω_B. The width of the ZPH is twice the homogeneous linewidth γ, because the burn laser does not only select perfectly resonant ZPL, but also those absorbing via their Lorentzian wings. Here, it is assumed that the laser linewidth is much narrower than the ZPL width γ. The feature at the high-energy side of the ZPH is the real-PSB, which is due to the phonon sidebands of the resonantly burned ZPH. Therefore, ZPH and real-PSB correspond directly to ZPL and PSB of the homogeneously broadened absorption spectrum, respectively, shown by the bold red line in Frame A of Fig. 2.3. In addition, there are electronic transitions within the IDF, which are nonresonantly overlapping the burn frequency ω_B via their phonon sidebands (see dashed lines in Frame A of Fig. 2.3). Following fast relaxation into the zero-phonon energy levels, the burn process becomes effective at the ZPL positions of those nonresonantly selected pigment molecules. As a result, these transitions form an additional feature named pseudo-PSB, which in ideal case forms the mirror image of the real-PSB. Electronic transitions at higher energy than ω_B do not contribute to the hole-burned spectrum. The corresponding FLN spectrum is shown in Frame C of Fig. 2.3. The latter spectrum exhibits a ZPL and only a single PSB feature. The reason for this observation is that the real-PSB

lies on the low-energy side of the ZPL in fluorescence and is, therefore, superimposed on the pseudo-PSB.

In a next step, expressions for the line-narrowed spectra of a pigment–protein system shall be developed. As for SHB, the pre-burn (absorption) spectrum A ($\tau = 0$, ω) at the burn time $\tau = 0$ is given by Eq. (2.6) [27]. SHB produces a persistent loss of absorption for a distinct electronic transition selected by the burn laser frequency. Upon exposure to the burn frequency ω_B during time τ the IDF is modified as given by [27]

$$N(\tau, \Omega_0 - \omega_C) = N(\Omega_0 - \omega_C)\exp[-\sigma I \Phi \tau L(\omega_B - \Omega_0)], \tag{2.9}$$

where the exponential term describes the hole growth due to the burn process. The lineshape $L(\omega_B\text{-}\Omega_0)$ corresponds to the homogeneously broadened absorption spectrum as given by Eq. (2.2). ZPL and PSB of this lineshape represent those electronic transitions within the IDF that are bleached resonantly and nonresonantly, respectively. Each of the purely electronic transitions burned according to Eq. (2.9) carries a finite width γ of the ZPL and is accompanied by a PSB. Therefore, the homogeneously broadened absorption spectrum (Eq. 2.2) has to be convoluted with the modified IDF (Eq. 2.9) to yield the entire absorption spectrum after a burn time τ, which is given by [27]

$$\begin{aligned} A(\tau, \omega) = \sum_{R=0}^{\infty} \left(S^R \frac{e^{-S}}{R!} \right) \int d\Omega_0 N(\Omega_0 - \omega_C) \times \\ \exp[-\sigma I \Phi \tau L(\omega - \Omega_0)] l_R(\omega - \Omega_0 - R\omega_m). \end{aligned} \tag{2.10}$$

The total SHB spectrum is then obtained as the difference between the absorption spectrum at the burn frequency ω_B at the burn time τ and the pre-burn absorption spectrum at the start of the experiment, i.e.,

$$\Delta A(\omega) = A(\tau, \omega) - A(\tau = 0, \omega) \tag{2.11}$$

In order to be concise, we will not discuss effects of arbitrary burn fluence in the present chapter. Rather, the reader is referred to comprehensive reviews for further information (e.g., Jankowiak et al. [5]). In the low-fluence limit expanding the exponential in Eq. (2.10) into a Taylor series and neglecting second and higher order terms one obtains the SHB spectrum:

$$\begin{aligned} \Delta A(\omega) = \sum_{R,P=0}^{\infty} \left(S^R \frac{e^{-S}}{R!} \right) \left(S^P \frac{e^{-S}}{P!} \right) \int d\Omega_0 N(\Omega_0 - \omega_C) \times \\ l_P(\omega_B - \Omega_0 - P\omega_m) l_R(\omega - \Omega_0 - R\omega_m), \end{aligned} \tag{2.12}$$

where l_P represents the electronic transitions bleached during the burn process. For simplicity, the pre-factor $\sigma P \phi \tau$ was set to unity here. In the low-fluence limit, this

has no effect on the shape of the spectrum. The FLN spectrum can be expressed in a rather similar form, if the term $-R\omega_m$ in the homogeneously broadened lineshape l_R is replaced by $+R\omega_m$ to account for fluorescence.

All the above considerations as well as the model calculations presented in Fig. 2.3 assume that real- and pseudo-PSB are mirror symmetric, which is valid only in cases where the inhomogeneous width is much larger than the width of the one-phonon profile Γ, i.e., $\Gamma_{inh} \gg \Gamma$. In this regard it is important to note that SHB and FLN results obtained for the antenna complex LHC II of green plants [49, 50] have established a width of the phonon sideband of ~ 100 cm^{-1} comparable or even broader than the inhomogeneous width of only ~80 cm^{-1}. Therefore, following [51], we will now consider the different PSB contributions in the $\Gamma_{inh} \approx \Gamma$ regime. The simulated FLN and SHB spectra are shown by dashed curves in Frame A and Frame B of Fig. 2.4, respectively. Specific parameters of these calculations are provided in the figure caption. It is obvious from Fig. 2.4 that the real- (contribution b) and pseudo-PSB (contribution c) exhibit clearly different shapes in both SHB and FLN spectra. The PSB of the dashed FLN spectrum and the real-PSB of the dashed SHB spectrum show features at 15 and 26 cm^{-1} that correspond to one- and two-quantum transitions of phonons with $\omega_m = 15$ cm^{-1}. The two-quantum transition and the slight tailing towards higher phonon frequencies, however, are not observed in the pseudo-PSB of the dashed spectrum in Frame B, i.e., the mirror symmetry between real- and pseudo-PSB breaks down in the $\Gamma \approx \Gamma_{inh}$ regime. This is because the pseudo-PSB is governed by the quickly tailing Gaussian IDF rather than by the slowly tailing Lorentzian wing of the one-phonon profile. The latter point is nicely illustrated in frame A of Fig. 2.4 where it is obvious that the IDF determines the shape of the pseudo-PSB (c) on its low-energy side. These findings suggest that accurate extraction of Huang–Rhys factors from SHB spectra requires a careful analysis, especially for systems in which the width of the PSB is similar to or larger than that of the IDF. Although SHB in principle provides real- and pseudo-PSBs as separate features (see above), the real-PSB is often interfered with by the anti-hole, so that the one-phonon profile is routinely obtained from the more intense pseudo-PSB.

In the limit of an infinitely wide IDF and low-fluence, this approximation would be perfectly justified since the real- and pseudo-PSB terms, being mirror symmetric, provide exactly the same information. Based on the argumentation above, however, it can be expected that in real systems, the one-phonon profile determined this way will not reflect the correct tailing at its high-energy side, particularly for systems in which the IDF is narrow relative to the PSB. As a result, Huang–Rhys factors calculated from the areas of ZPL and pseudo-PSB would generally be artificially lowered, with the extent of lowering depending on the burn wavelength and the relative widths of the IDF and PSB.

More recently, a new method for obtaining electron–phonon coupling parameters called delta-FLN spectroscopy [52] emerged, which is capable of overcoming the shortcomings of SHB and FLN spectroscopy discussed above. Earlier realizations of this technique [19, 20] have been applied to enhance spectral selectivity of FLN mainly in the range of vibronic lines. The approach of Rätsep and Freiberg,

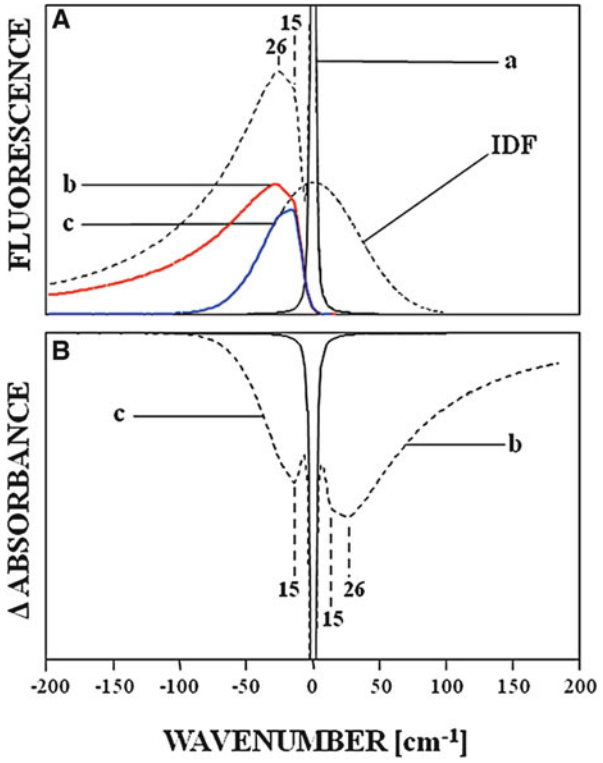

Fig. 2.4 Low-temperature line-narrowed fluorescence (Frame **A**) and hole-burned (Frame **B**) spectra (*dashed lines*) simulated according to Eq. (2.12), respectively, for illustration of the $\Gamma_{inh} \sim \Gamma$ regime. The calculations were performed assuming an inhomogeneous width of 80 cm^{-1}, a Huang–Rhys factor of 1.0, and a phonon profile with a peak at 15 cm^{-1} and a width of $\Gamma = 57.5$ cm^{-1} ($\Gamma_G = 15$ cm^{-1}, $\Gamma_L = 100$ cm^{-1}), i.e., in contrast to the simulations shown in Fig. 2.3, the Lorentzian tailing of the one-phonon profile does exceed Γ_{inh}. In Frame **A**, the *full black line* represents the ZPH (a), the *red line* is the real-PSB (b), and the *blue line* is the pseudo-PSB (c). In Frame **B**, the real-PSB and the pseudo-PSB contributions are labelled by b and c, respectively. The multi-PSBs are omitted for clarity and the zero-phonon lines are cut off at 4 % of their peak intensity value. The *dashed-dotted line* represents the profile of the IDF. Note the breakdown of mirror symmetry between the real-PSB and the pseudo-PSB contributions visible in both frames and the high-energy tailing of the pseudo-PSB determined by the shape of the IDF. Reprinted with permission from Pieper et al. [51]. Copyright 1999 Elsevier B.V.

however, readily yields the ZPL together with the phonon and vibrational structure building on it so that electron–phonon and electron–vibrational coupling strengths can be uniquely determined.

A delta-FLN spectrum is obtained as the difference between FLN spectra recorded before and after an intermediate hole-burning step. This technique provides two important advantages over traditional SHB and FLN spectroscopy: first, the scattered laser light which otherwise obscures the ZPL in FLN spectra can be

effectively eliminated in the difference spectrum, allowing direct measurement of the ZPL; second, the "double selection" via both SHB and FLN suppresses the pseudo-PSB term in the low-fluence limit, so that the final delta-FLN spectrum becomes identical to the homogeneously broadened spectrum [19, 20, 53].

Theoretically, the delta-FLN spectrum is obtained by subtracting pre- and post-burn FLN spectra according to delta-FLN(ω) = FLN(τ,ω) − FLN(τ = 0, ω). Here, the pre-burn spectrum FLN(τ = 0, ω) is identical to Eq. (2.12), while the post-burn FLN spectrum FLN(τ,ω) is best derived from Eq. (2.6) by replacing the IDF term by N (Ω_0-ω_C) modified by the burn process. Accordingly, the post-burn FLN spectrum can be written as

$$\Delta FLN(\tau,\omega) = \sum_{R,P=0}^{\infty} S^R \frac{e^{-S}}{R!} S^P \frac{e^{-S}}{P!} \int N(\Omega_0 - \omega_C) \times \exp[-\sigma I \Phi \tau L(\omega - \Omega_0)] \times l_R(\omega_E - \Omega_0 - R\omega_m)\, l_P(\omega - \Omega_0 \mp P\omega_m)\, d\Omega_0 \tag{2.13}$$

Note in this regard that Eq. (2.13) contains two absorption lineshapes: first, L due to the hole-burning process, and second, l_R due to the selective excitation of the post-burn FLN spectrum. This difference leads to the "double selection effect" in delta-FLN [19, 20, 53], which is more apparent when Eq. (2.13) is specified for the low-fluence limit:

$$\Delta FLN(\omega) = k\, e^{-3S} \sum_{R,P=0}^{\infty} \frac{S^Q}{Q!} \frac{S^R}{R!} \frac{S^P}{P!} \int d\Omega_0 N(\Omega_0 - \omega_C) \times l_Q(\omega_E - \Omega_0 - Q\omega_m)\, l_R(\omega_B - \Omega_0 - R\omega_m)\, l_P(\omega - \Omega_0 + P\omega_m) \tag{2.14}$$

Except for writing down all terms explicitly, this equation is identical to that of Reppert et al. [53]. To discuss the difference between delta-FLN on one hand and FLN/SHB on the other in the low-fluence limit, this equation has to be compared to Eq. (2.12). It emerges that Eq. (2.14) contains the absorption lineshape describing the selective excitation twice as l_R and l_Q (identical to the quadratic term in [53]), while this term appears only once in the comparable expression for FLN (Eq. 2.12). Since the ZPL and PSB of the latter term represent resonant and nonresonant excitation, respectively, the multiplication of l_R with l_Q leads to an enlargement of the ZPL and a suppression of the PSB in the expression for delta-FLN and thus to a suppression of the nonresonantly excited pseudo-PSB. Some of the earlier delta-FLN results have, unfortunately, been analyzed in terms of Eq. (2.12) so that the S-factors obtained were somewhat underestimated by a maximum of 20 % in the case of CP29 [54]. Table 2.1 contains the corrected values of S assuming that the delta-FLN spectrum in the low-fluence limit reflects the homogeneously broadened fluorescence spectrum.

2.5 Results for Selected Photosynthetic Systems

Chlorophylls are ubiquitous photosynthetic chromophores in plants and algae, similar to BChls in bacterial systems [55]. The useful functioning of these molecules is based on their unique quantum-optical and redox properties. Being the lowest-energy electronic transitions in the visible range, the Q_y singlet electronic transitions are instrumental in all photophysical and photochemical processes these pigments are involved in. Their properties in dependence on solvent polarity, axial coordination of the central magnesium atom, pigment aggregation, temperature, pressure, electric and magnetic field, etc. have experimentally been studied using almost all conceivable spectroscopic techniques. Despite this intensive scrutiny, optical spectroscopy of the (B)Chl molecules is still not fully understood, neither experimentally nor theoretically [42, 56, 57]. Avarmaa and co-workers [58] were the first to obtain high-resolution spectra related to the Q_y electronic state of the impurity Chl*a* and BChl*a* molecules. Yet these low-temperature results had rather qualitative than quantitative value, since experimental limitations prohibited determination of the coupling strengths for both the bath phonons and individual intramolecular vibrations. As follows we will discuss a few basic experimental results, achieved by the delta-FLN method on the (B)Chl*a* pigment molecules either in isolation or when bound by the major photosynthetic light-harvesting complexes of green plants (LHC II) and purple bacteria (LH2).

*2.5.1 Isolated Photosynthetic Chromophores: Chl**a** and BChl**a***

Mirror symmetry between the conjugate absorption and emission spectra is theoretically expected within the model framework of the crude adiabatic, Condon, and harmonic approximations, assuming linear electron–phonon and vibronic coupling (this set of approximations is known as the basic model [11]), together with postulation of a fast excited state relaxation (the Kasha–Vavilov rule [59]). Whether or not asymmetry exists between the (B)Chl Q_y absorption and emission spectra has for a long time been an unsettled question. The experimental data concerning this problem were not only scarce but also controversial. While quantitative quantum chemical modeling of the absorption and emission spectra should in principle reveal the nature of the electronic transitions and the origin of any spectral asymmetry, without proper experimental guiding this is a challenging task for the chlorophyll type molecules owing to their relatively large size and extended conjugation.

The deviations from mirror symmetry in optical absorption and fluorescence emission spectra of Chl*a* and BChl*a* molecules were experimentally studied in [60, 61] using different solvents to induce either penta- or hexa-coordination of the central Mg atom. Based on the data obtained at different temperatures, one can

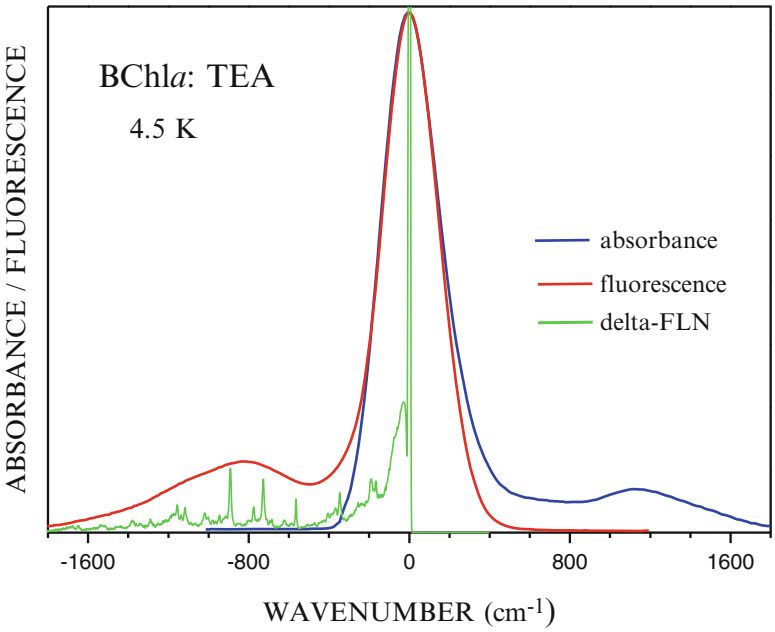

Fig. 2.5 Comparison of the frequency-weighted absorption (intensity/ω, *blue*) and (intensity/ω^3, *red*) spectra of BChl*a* in triethylamine (TEA) recorded at 4.5 K. The fluorescence was nonselectively excited at 405 nm. Revealed from the inhomogeneously bradened fluorescence lineshape is the homogeneously broadened delta-FLN spectrum (*green*), which comprises a narrow ZPL at zero frequency together with its phonon and vibrational sidebands extending towards lower frequency. See text for further details

safely conclude that mirror symmetry does not hold at any temperature between 4.5 K and ambient temperature neither in Chl*a* nor in BChl*a* molecules. In the BChl*a* emission (see Fig. 2.5), for example, the low-resolution vibronic sideband structure is centered on modes at ~900 cm^{-1}, while in absorption this band moves out to 1,100–1,200 cm^{-1}. In environments with sixfold-coordinated Mg, the emission sideband is considerably stronger, resulting in the corresponding reorganization energy being slightly larger than the reorganization energy in absorption. In fivefold-coordinated environments, however, the absorption value is 50 % larger than the emission value. Most computational methods predict the spectral asymmetry to be very much larger than that actually observed [62]; only the long-range corrected density functional CAM-B3LYP reproduced detailed experimental results for BChl*a* and predicted asymmetry of the correct magnitude. These simulations also revealed that the spectral asymmetry arises primarily through Duschinsky rotation [61]. In the case of the Chl*a* molecule the deviation from the mirror symmetry between the conjugated absorption and fluorescence spectra was assigned to a combined effect of Franck–Condon and Herzberg–Teller interactions [60]. A detailed analysis of the breakdown of mirror symmetry between fluorescence and fluorescence excitation spectra of arylpolyene molecules dissolved in the

n-octane matrix in terms of Franck–Condon and Herzberg–Teller interactions can be found in [63]. In case of Chl*a*, however, the most recent analyses [64] exposed a fundamentally new mechanism for the spectral asymmetry, which may overshadow the above Franck–Condon and Herzberg–Teller mechanisms. This is the strong coupling between the energetically closely spaced Q_y and Q_x excited electronic states, mediated by high-frequency intramolecular vibrations.

2.5.2 LHC II Antenna Complex of Green Plants

LHC II is the major light harvesting complex of higher plants and green algae. Its importance is underlined by the fact that it accounts for approximately 65 % of the Chl of photosystem II. LHC II is believed to occur in trimeric form, where each monomeric subunit binds 8 Chl*a* and 6 Chl*b* molecules [65, 66]. Electron–phonon coupling of the lowest energy level of trimeric LHC II has been intensively studied by all the selective spectroscopy techniques described in this chapter: SHB [49, 67], FLN [50, 68], and delta-FLN [69]. Initially, however, the results derived from the different techniques appeared to be rather diverse. SHB results suggested weak electron–phonon coupling with $S = 0.8$ and a rather narrow one-phonon profile with a peak at ~18 cm^{-1} and a width of only ~25 cm^{-1} [49]. In contrast, FLN data yielded slightly higher mean phonon frequencies of 22–24 cm^{-1} and systematically wider and more asymmetric one-phonon profiles with a width of ~65 cm^{-1} [68]. In the latter study, the S factor could not be directly obtained, because the ZPL is typically hidden by intense scattered laser light in FLN spectra. The different shapes of the PSBs obtained by SHB and FLN, respectively, are directly visible in Fig. 2.6 (data taken from Pieper et al. [49] and Pieper et al. [50]).

In this regard it is important to recall that the width of the widely asymmetric phonon sideband revealed by FLN is of the same order of magnitude as the inhomogeneous width of ~80 cm^{-1}, determined by constant fluence SHB spectroscopy [49]. As demonstrated by the model calculations for the $\Gamma_{inh} \sim \Gamma$ regime above (see Fig. 2.4), a breakdown of the mirror symmetry between the real- and pseudo-PSB contributions can be expected in this case even in the limit of linear Franck–Condon coupling. Consequently, the SHB and FLN data shown in Fig. 2.6 can be simultaneously modeled assuming a Huang–Rhys factor of ~0.9 and one and the same broad and strongly asymmetric one-phonon profile peaking at ~15 cm^{-1}. In the case of SHB, however, analysis had been based on the pseudo-PSB, which is cut off by the narrow IDF found for the lowest Q_y-state of LHC II at ~680.0 nm. This is further illustrated in Fig. 2.6, where the pseudo-PSB contributions to SHB and FLN are plotted individually and labeled by full arrows in Frames A and B. It is apparent that the pseudo-PSB contribution simulated for FLN is similar to the one directly visible in SHB. In the case considered here, the advantage of FLN lies in the accessibility of the real-PSB, which is undisturbed by the narrow IDF. The same feature is hardly visible in SHB (see Frame B of Fig. 2.6), because as described above it is refilled by the anti-hole produced during the burn process. These results

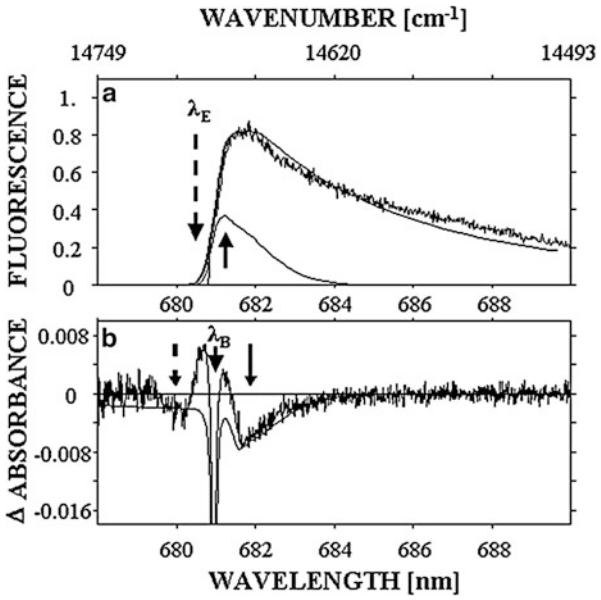

Fig. 2.6 Analysis of phonon structure in SHB and FLN spectra of trimeric LHC II at 4.2 K. Frame **a**: FLN spectrum (*noisy line*) experimentally obtained by selective laser excitation within the lowest energy state of LHC II with $\lambda_E = 680.5$ nm (see *dashed arrow*). The ZPL contaminated with scattered laser light has been subtracted for clarity. The fit of the FLN spectrum was calculated according to Eq. (2.13) (*smooth line*). The feature labeled by a *full arrow* is the simulated pseudo-PSB, whose shape differs significantly from the entire phonon sideband, but proves to be rather similar to pseudo-PSB observed directly by SHB in Frame **b**. Data are taken from Pieper et al. [51]. Frame **b**: Experimental SHB spectrum (*noisy line*) experimentally obtained with $\lambda_B = 681.0$ nm and a burn fluence of 15 J/cm^2. The real- and pseudo-PSB are indicated by *full* and *broken arrows*, respectively. The fit was calculated according to Eq. (2.12) with $\gamma = 0.2$ cm^{-1} and $\sigma I \Phi \tau = 0.003$ (*smooth line*). Reprinted with permission from Pieper et al. [51]. Copyright 1999 Elsevier B.V.

indicate that the apparent breakdown of mirror symmetry between real- and pseudo-PSB in the case of LHC II is a purely technical effect and not comparable to the spectral subtleties discussed in the previous paragraph for (B)Chl. In summary, a simultaneous modeling of SHB and FLN spectra of LHC II is necessary to obtain the correct parameters of electron–phonon coupling [21, 51].

The parameters of electron–phonon coupling of trimeric LHC II reviewed above have been further corroborated by delta-FLN spectroscopy [69]. In Fig. 2.7 a pre-burn FLN spectrum selectively excited within the fluorescence origin band of LHC II is shown as a black curve for a representative excitation wavelength of 682 nm. As expected, the spectrum is composed of a sharp ZPL located at the excitation wavelength and the broad phonon sideband peaking about 22 cm^{-1} to the red of the ZPL. In this spectrum the ZPL is still contaminated with scattered light originating from the excitation laser. An additional FLN spectrum (blue curve) was recorded after hole burning at the excitation wavelength with a burn fluence of 32 mJ/cm^2 shown as a blue curve in Fig. 2.8. The delta-FLN spectrum (red curve) is

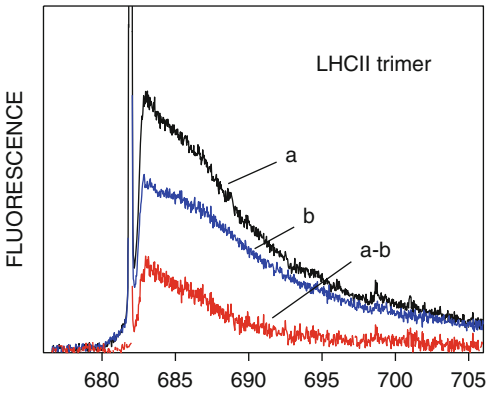

Fig. 2.7 Experimental 4.5 K delta-FLN spectra of trimeric LHC II excited/burned at 682.0 nm (*lower red curve*). The ZPL is cut off at 3.7 % of its full intensity for ease of inspection. The *black* (a) and *blue curves* (b) show the corresponding pre- and post-burn FLN spectra, respectively. FLN spectra were recorded with a fluence of 0.4 mJ/cm^2, while the fluence applied for hole burning was 32 mJ/cm^2. Reprinted with permission from Pieper et al. [69]. Copyright 2009 American Chemical Society

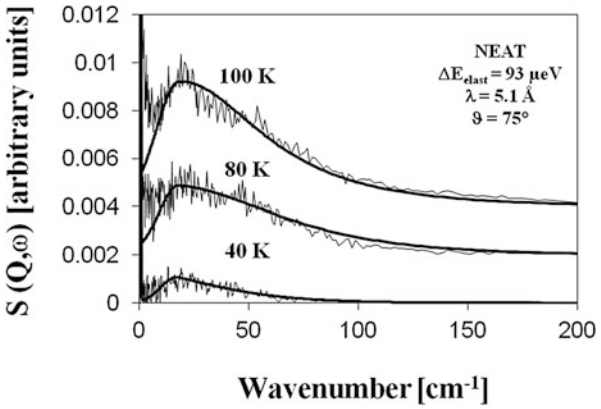

Fig. 2.8 Temperature dependence of INS spectra of trimeric LHC II obtained with an incident neutron wavelength of 5.1 Å and an elastic resolution of ~0.75 cm^{-1}. The spectra are given equidistant offsets of 0.002 for ease of inspection. The smooth, full lines correspond to theoretical fits (see text for details). Reprinted with permission from Pieper et al. [31]. Copyright 2004 American Chemical Society

readily obtained by subtracting the post-burn FLN spectrum from the pre-burn spectrum. The latter spectrum now consists of both the ZPL and PSB, because the subtraction procedure widely eliminates the scattering contribution and thus provides a reliable measure of the ZPL intensity. A Huang–Rhys factor S of 0.88 can be directly obtained from the delta-FLN spectrum, which turns out to be practically the same value reported above from the simultaneous fits of SHB and FLN spectra [51].

To the best of our knowledge, LHC II is the only isolated photosynthetic antenna complex that has been investigated by inelastic neutron scattering (INS) in order to directly obtain the phonon density of states [31]. Low-temperature INS spectra of LHC II are presented in Fig. 2.8. The data can be well described by a one-phonon function $S_1(\omega)$ with a maximum at 18.4 cm^{-1} as well as Gaussian and Lorentzian widths of 16 and 160 cm^{-1} at their low- and high-energy sides, respectively. Widely similar parameters were employed before to model the SHB and FLN results shown in Fig. 2.6 under the reasonable assumption that the electron–phonon coupling strength $s(\omega)$ is quite uniform in the investigated range of vibrational frequencies. This finding is a further proof for a rather broad and asymmetric distribution of phonon frequencies in LHC II as derived before from SHB and FLN.

2.5.3 *Strong Exciton–Phonon Coupling in the LH2 Antenna Complexes of Purple Bacteria*

The idealized exciton states in deformable (soft) lattices interact with the local vibrations of the molecular units themselves as well as with the collective phonons of the surroundings, leading (like in individual molecules albeit more complex ways) to dissipation of excitations as well as to vibronic and electron–phonon spectral structures, respectively. The same interactions, which increase with temperature, also govern decoherence and transport dynamics of excitons. To envision the latter effects, one could picture a moving exciton dragging behind a cloud of phonons, an exciton polaron. The thicker the cloud, the slower moves the exciton. In the limiting scenario the exciton may stop moving altogether localizing on a small region of the lattice. "This latter phenomenon is called exciton "self trapping" [38]."

A strong ($S > 2$) exciton–phonon coupling has been found [70–73] in fluorescence spectra of the ring-shaped B850 aggregates of BChl*a*, which is a part of the LH2 bacterial antenna complex, several times greater than observed for the monomeric BChl*a* chromophores in similar protein environments [52]. This is unexpected, since coupling in case of excitons should be several times smaller than in case of respective localized excitations due to "motional reduction" [38]. A visible consequence of such a strong exciton–phonon interaction is a broad multi-phonon PSB.

The Frenkel exciton model [1] as well as its various modifications such as the Redfield theory, which assume negligible exciton–lattice interactions, cannot capture strong coupling effects. A theoretical model involving dynamic exciton polaron formation in the spirit of Holstein [74], Heeger [75], and others has, therefore, been developed by us to explain the conflicting observations in case of the LH2 complexes [71, 73, 76, 77]. The fundamental nature of this model is that due to strong exciton–phonon interaction a structural reorganization of the immediate environment is induced by the exciton, thereby lowering the exciton energy and causing its localization. In the one-dimensional electronic systems this kind of

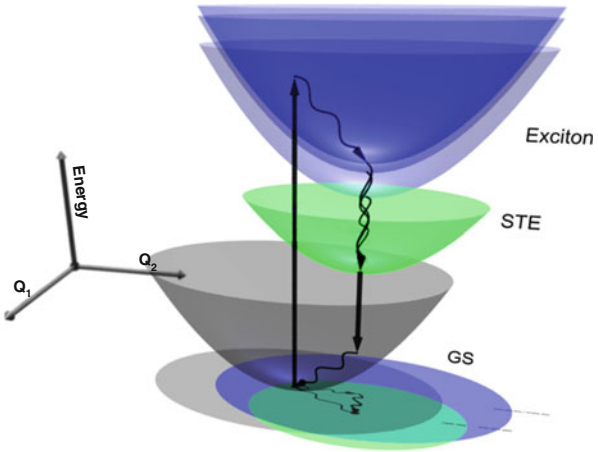

Fig. 2.9 The configuration coordinate model with two (off-diagonal Q1 and diagonal Q2) interaction coordinates for the excitons in the B850 aggregate of LH2. The colored surfaces counted from the bottom of the figure towards the growing potential energy (not in scale) correspond to the ground state (GS, *gray*), self-trapped exciton (STE, *green*), and Frenkel exciton states $k = 0$ and $k = \pm 1$ (Exciton, *blue* of different shades). *Upward* and *downward bold arrows* indicate the photon absorption and fluorescence emission transitions, respectively. The *curly arrows* designate relaxation channels

exciton self-trapping is taking place at all nonvanishing couplings [78], being thus unavoidable in any real structure. The situation is rather different in higher dimensional organizations, where the free and self-trapped excitons, being separated by an energetic barrier, can co-exist. Since the B850 ring can be considered with certain reservations a one-dimensional crystal made from the BChl*a* molecules that strongly couple with their environment, exciton polarons rather than Frenkel excitons are generic photoexcitations of the LH2 antenna complex.

A configuration coordinate diagram (Fig. 2.9) illustrates this issue. Shown in the figure are the adiabatic potential energy surfaces that correspond to the ground state (GS, gray), the three lowest ($k = 0, \pm 1$) light-absorbing Frenkel exciton states (Exciton, blue of different shades), and the relaxed self-trapped exciton state (STE, green). The transitions between the ground and the excited states are linearly coupled via two interaction coordinates. The horizontal Q2 coordinate accounts for the diagonal (energetic) coupling, while the Q1, for the off-diagonal (structural) interaction. The straight and curly arrows represent the optical transitions and relaxation channels, respectively. The reorganization energy related to the diagonal exciton–phonon bath couplings in the LH2 complexes from *Rps. acidophila* is 285 cm^{-1}. The same parameter for the off-diagonal couplings is 73 cm^{-1} [77]. Since just the ground state and the Frenkel exciton states from one side and the self-trapped exciton state and the ground state from another side are directly coupled by photon transitions, it should be clear from Fig. 2.9 that the absorption and emission spectra in such a system deliver different information about the excited states of the matter. While the absorption spectra characterize the exciton

immediately after its creation, the emission spectra describe the exciton behavior immediately before its annihilation [38]. This situation is qualitatively different from that for localized impurities in condensed matter.

2.5.4 *Excitation Energy Dependence of Electron–Phonon Coupling*

As it was already noted above, the basic models ignore possible variations of electron–phonon and/or vibronic couplings, i.e., homogeneous lineshapes, through the IDF. This view is too simplistic, especially for amorphous host materials, where significant dispersion of the solvent shift has been predicted and observed [79, 80]. Strong color effects in the linear electron–phonon coupling strength S [54, 60] were also reported. Figure 2.10 demonstrates a large increase of the Huang–Rhys factor with increasing excitation wavelength across the inhomogeneously broadened absorption band in the low-temperature spectra of glassy samples of Chl*a* and BChl*a* [60, 81]. The observed quasi-linear increase of S suggests a strong correlation between the electron–phonon coupling strength and the solvent shift. Such a correlation can be rationalized within a two-particle Lennard-Jones model of intermolecular interactions [81]. The same model also allows changes of the quadratic couplings, which affect the widths of ZPLs. The latter effect is yet to be shown experimentally.

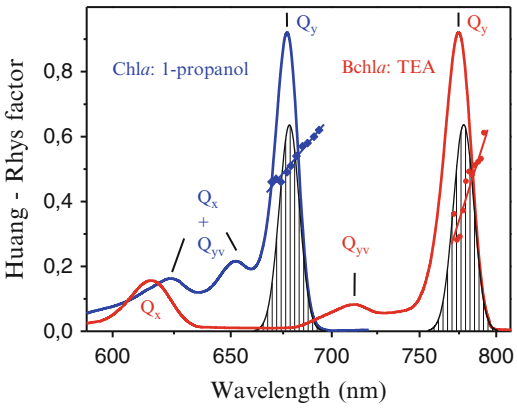

Fig. 2.10 Wavelength dependence of the electron–phonon coupling strength S for the Chl*a*-doped 1-propanol (*blue rhombs*) and for the BChl*a*-doped TEA (*red rings*) solutions at 4.5 K. The lines connecting the scattered data points present linear fits of the data. Plotted on the background with continuous coloured curves are the corresponding absorption spectra. The areas with *drop lines* denote IDF of the ZPL related to the Q_y electronic transitions. A reciprocal (linear in energy) presentation of the wavelength scale is used. Q_y and Q_x refer to the two lowest-energy singlet electronic transitions; Q_{yv} indicates vibronic sidebands related to the Q_y transition

Apparently similar increase of the coupling strength as in Chl*a* and BChl*a* impurity spectra is observed for excitons in the CP29 antenna complex of green plants [54], and the LH2 and LH1 bacterial antenna complexes [73]. While the weakly coupled CP29 excitons in the protein environment are quite expected to act in a similar way as the localized Chl*a* and Bchl*a* molecular excitations in common solvents, the case of strongly coupled as well as self-trapped excitons in bacterial antennas is more complex. A detailed analysis of this situation is beyond the scope of this chapter. We only remark that the latter excitons appear to exhibit strong color effects even without involvement of any solvent shift dispersion [10, 73]. To conclude this paragraph, it is of notice that opposite tendency, i.e., a decrease of S with increasing excitation wavelength, has also been reported in various pigment–protein complexes such as FMO [52] and WSCP [12]. Due to this color effect, the data for the Huang–Rhys factor presented in Table 2.1 are all obtained at the excitation/burn frequency corresponding to the half height of the IDF from the long-wavelength side.

Acknowledgements J. Pieper gratefully acknowledges support by the European Social Fund's Internationalisation Programme DoRa. Furthermore, Estonian Research Council (Grant IUT02-28) and Estonian Science Foundation (Grant No. 9453) supported this work. We are grateful to M. Rätsep, R. Jankowiak, and M. Reppert for stimulating discussions. M. Rätsep and M. Pajusalu designed Figs. 2.5 and 2.9, respectively.

References

1. Frenkel J. Phys Rev. 1931;37:1276.
2. Franck J, Teller E. Migration and photochemical action of excitation energy in crystals. J Chem Phys. 1938;6:861–72.
3. Van Amerongen H, Valkunas L, Van Grondelle R. Photosynthetic excitons. Singapore: World Scientific; 2000.
4. Aartsma TJ, Matysik J, editors. Biophysical techniques in photosynthesis. Dordrecht: Springer; 2008.
5. Jankowiak R, Reppert M, Zazubovich V, Pieper J, Reinot T. Chem Rev. 2011;111(8):4546.
6. Osadko IS. Selective spectroscopy of single molecules. Berlin: Springer; 2003.
7. Ishizaki A, Calhoun TR, Schlau-Cohen GS, Fleming GR. Phys Chem Chem Phys. 2010;12:7319.
8. Müh F, Madjet ME, Renger T. J Phys Chem B. 2010;114:13517.
9. Novoderezhkin V, van Grondelle R. Phys Chem Chem Phys. 2006;8:793–807.
10. Freiberg A, Trinkunas G. In: Laisk A, Nedbal L, Govindjee, editors. Photosynthesis in silico: understanding complexity from molecules to ecosystems. Netherlands: Springer; 2009. p. 55–82.
11. Rebane KK. Impurity spectra of solids. New York: Plenum Press; 1970.
12. Pieper J, Rätsep M, Trostmann I, Paulsen H, Renger G, Freiberg A. J Phys Chem B. 2011;115 (14):4042.
13. Davydov AS. Theory of molecular excitons. NewYork: Plenum Press; 1971.
14. Kühn O, Renger T, May V, Voigt J, Pullerits T, Sundström V. Trends Photochem Photobiol. 1997;4:213.
15. Pieper J, Rätsep M, Trostmann I, Schmitt F-J, Theiss C, Paulsen H, Freiberg A, Renger G. J Phys Chem B. 2011;115(14):4053.

16. Gorokhovskii AA, Kaarli RK, Rebane LA. J Exp Theor Phys Lett. 1974;20:216.
17. Kharlamov BM, Personov RI, Bykovskaya LA. Opt Commun. 1974;12:191.
18. Szabo A. Phys Rev Lett. 1970;25:924.
19. Jaaniso R. Proc Acad Sci Estonian SSR Phys Math. 1985;34:277.
20. Fünfschilling J, Glatz D, Zschokke-Gränacher I. J Lumin. 1986;36:85.
21. Rätsep M, Freiberg A. Chem Phys Lett. 2003;377:371.
22. Moerner WE, Kador L. Phys Rev Lett. 1989;62:2535.
23. Cogdell RJ, Gall A, Köhler J. Quart Rev Biophys. 2006;39:227.
24. Osadko IS. Sov Phys Usp. 1979;22:311.
25. Osadko IS. Theory of light absorption and emission. In: Agranovich VM, Hochstrasser RM, editors. Spectroscopy and excitation dynamics of condensed molecular systems. Amsterdam: Elsevier/North-Holland; 1983. p. 437–512.
26. Hayes JM, Lyle PA, Small GJ. J Phys Chem. 1994;98:7337.
27. Hayes JM, Gillie JK, Tang D, Small GJ. Biochim Biophys Acta. 1988;932:287.
28. Lax M. J Chem Phys. 1952;20:1752.
29. Smith JC. Q Rev Biophys. 1991;24(3):227–91.
30. Orecchini A, Paciaroni A, Bizzarri AR, Cannistraro S. J Phys Chem B. 2002;106:12150.
31. Pieper J, Irrgang K-D, Renger G, Lechner RE. J Phys Chem B. 2004;108:10556.
32. Kurkal V, Smith JC. J Am Chem Soc. 2006;128:2356.
33. Pieper J, Trapp M, Skomorokhov A, Natkaniec I, Peters J, Renger G. Temperature dependent vibrational and conformational dynamics of photosystem II membrane fragments from spinach investigated by elastic and inelastic neutron scattering. Biochim Biophys Acta. 2012;1817:1213.
34. Renger T, Klinger A, Steinecker F, Schmidt am Busch M, Numata J, Müh F. J Phys Chem B. 2012;116:14565.
35. Hochstrasser RM, Prasad PN. J Chem Phys. 1972;56:2814.
36. Hanson DM. Chem Phys Lett. 1976;43:217.
37. May V, Kühn O. Charge and energy transfer dynamics in molecular systems. Berlin: Wiley-VCH; 2000.
38. Toyozawa Y. Optical processes in solids. Cambridge: Cambridge Univ. Press; 2003. p. 149–91.
39. Lu N, Mukamel S. J Chem Phys B. 1991;95:1588.
40. Renger T, Marcus RA. J Chem Phys. 2002;116(22):9997.
41. Kelley AM. J Chem Phys. 2003;119:3320.
42. Laisk A, Nedbal L, Govindjee, editors. Photosynthesis in silico. Understanding complexity from molecules to ecosystems. Heidelberg: Springer; 2009
43. Olbrich C, Jansen TLC, Liebers JR, Aghtar M, Strümpfer J, Schulten K, Knoester J, Kleinekathöfer U. J Phys Chem B. 2011;115:8609.
44. van Oijen AM, Ketelaars M, Köhler J, Aartsma TJ, Schmidt J. Science. 1999;285:400–2.
45. Tietz C, Cheklov O, Dräbenstedt A, Schuster J, Wrachtrup J. J Phys Chem B. 1999;103:6328.
46. Hofmann C, Michel H, van Heel M, Köhler J. Phys Rev Lett. 2005;94:195501.
47. Brecht M, Studier H, Radics V, Nieder JB, Bittl R. J Am Chem Soc. 2008;130:17487.
48. Kunz R, Timpmann K, Southall J, Cogdell RJ, Freiberg A, Köhler J. Single-molecule spectroscopy unmasks the lowest exciton state of the B850 assembly in LH2 from Rps. Acidophila. Biophys J. 2014;106:2008–16.
49. Pieper J, Rätsep M, Jankowiak R, Irrgang K-D, Voigt J, Renger G, Small GJ. J Phys Chem A. 1999;103:2412.
50. Pieper J, Schödel R, Irrgang K-D, Voigt J, Renger G. J Phys Chem B. 2001;105:7115.
51. Pieper J, Voigt J, Renger G, Small GJ. Chem Phys Lett. 1999;310:296.
52. Rätsep M, Freiberg A. J Lumin. 2007;127:251.
53. Reppert M, Naibo V, Jankowiak R. Chem Phys. 2010;367:27.
54. Rätsep M, Pieper J, Irrgang KD, Freiberg A. J Phys Chem B. 2008;112:110.
55. Blankenship RE. Molecular mechanisms of photosynthesis. Oxford: Blackwell Science; 2002.

56. Grimm B, Porra RJ, Rüdiger W, Scheer H, editors. Chlorophylls and bacteriochlorophylls. Dordrecht: Springer; 2006.
57. Renge I, Mauring K. Spectrochim Acta A: Mol Biomol Spectros. 2013;102:301.
58. Avarmaa RA, Rebane KK. Spectrochim Acta A. 1985;41:1365.
59. Lakowicz JR. Principles of fluorescence spectroscopy. New York: Springer; 2010.
60. Rätsep M, Linnanto J, Freiberg A. J Chem Phys. 2009;130:194501.
61. Rätsep M, Cai Z-L, Reimers JR, Freiberg A. J Chem Phys. 2011;134:024506.
62. Dahlbom MG, Reimers JR. Mol Phys. 2005;103:1057.
63. Naumova NL, Vasil'eva IA, Naumov AV, Osad'ko IS. J Lumin. 2005;111:37.
64. Reimers JR, Cai Z-L, Kobayashi R, Rätsep M, Freiberg A, Krausz E. Sci Rep. 2013;3:2761.
65. Liu Z, Yan H, Wang K, Kuang T, Zhang J, Gui L, An X, Chang W. Nature. 2004;428:287.
66. Standfuss J, Lamborghini M, Kühlbrandt W, van Scheltinga ACT. EMBO J. 2005;24:919.
67. Gibasiewicz K, Rutkowski M, van Grondelle R. Photosynthetica. 2009;47:232.
68. Peterman EJG, Pullerits T, van Grondelle R, van Amerongen H. J Phys Chem B. 1997;101:4448.
69. Pieper J, Rätsep M, Irrgang K-D, Freiberg A. J Phys Chem B. 2009;113:10870.
70. Timpmann K, Katiliene Z, Woodbury N, Freiberg A. J Phys Chem B. 2001;105:12223.
71. Freiberg A, Rätsep M, Timpmann K, Trinkunas G, Woodbury NW. J Phys Chem B. 2003;107:11510.
72. Timpmann K, Rätsep M, Hunter CN, Freiberg A. J Phys Chem B. 2004;108:10581.
73. Freiberg A, Rätsep M, Timpmann K, Trinkunas G. Chem Phys. 2009;357:102.
74. Holstein T. Ann Phys. 1959;8:325–42.
75. Heeger AJ, Kivelson S, Schrieffer JR, Su W-P. Rev Mod Phys. 1988;60:781.
76. Trinkunas G, Freiberg A. J Lumin. 2006;119-120:105.
77. Pajusalu M, Rätsep M, Trinkunas G, Freiberg A. Chem Phys Chem. 2011;12:634.
78. Sumi H, Sumi A. J Phys Soc Japan. 1994;63:637.
79. Sesselmann T, Kador L, Richter W, Haarer D. Europhys Lett. 1988;5:361.
80. Kador L, Jahn S, Haarer D, Silbey R. Phys Rev B. 1990;41:12215.
81. Renge I, Rätsep M, Freiberg A. J Lumin. 2011;131:262.
82. Pieper J. Application of high-resolution spectroscopy investigating the energy level structure and electron-phonon-coupling of the light-harvesting complex II of green plants. Ph.D. thesis, Humboldt University Berlin, Berlin, Germany; 2000.
83. Hughes JL, Picorel R, Seibert M, Krausz E. Biochemistry. 2006;45:12345.
84. Dang NC, Zazubovich V, Reppert M, Neupane B, Picorel R, Seibert M, Jankowiak R. J Phys Chem B. 2008;112:9921.
85. den Hartog FTH, Dekker JP, van Grondelle R, Völker S. J Phys Chem B. 1998;102:11007.
86. Neupane B, Dang NC, Acharya K, Reppert M, Zazubovich V, Picorel R, Seibert M, Jankowiak R. J Am Chem Soc. 2010;132:4214.
87. Ihalainen JA, Rätsep M, Jensen PE, Scheller HV, Croce R, Bassi R, Korppi-Tommola JEI, Freiberg A. Red spectral forms of chlorophylls in green plant PS I – a siteselective and high-pressure spectroscopy study. J Phys Chem B. 2003;107:9086–93.
88. Hayes JM, Matsuzaki S, Rätsep M, Small GJ. J Phys Chem B. 2000;104:5625.
89. Chang H-C, Small GJ, Jankowiak R. Chem Phys. 1995;194:323.

Chapter 3
Photosynthetic Energy Transfer and Charge Separation in Higher Plants

Tjaart P.J. Krüger, Vladimir I. Novoderezhkin, Elisabet Romero, and Rienk van Grondelle

Abstract In this chapter we introduce the physical models at the basis of photosynthetic light harvesting and energy conversion (charge separation). We discuss experiments that demonstrate the processes of light harvesting in the major plant light-harvesting complex (LHCII) and charge separation in the photosystem II reaction center (PSII RC) and how these processes can be modeled at a quantitative level. This is only possible by taking into account the exciton structure of the chromophores in the pigment–protein complexes, static (conformational) disorder, and coupling of electronic excitations and charge-transfer (CT) states to fast nuclear motions. We give examples of simultaneous fitting of linear and nonlinear (time-dependent) spectral responses based on modified Redfield theory that resulted in a consistent physical picture of the energy- and electron-transfer reactions. This picture, which includes the time scales and pathways of energy and charge transfer, allows for a visualization of the excitation dynamics, thus leading to a deeper understanding of how photosynthetic pigment-proteins perform their function in the harvesting and efficient conversion of solar energy. We show that LHCII has the intrinsic capacity to switch between different light-harvesting and energy-dissipating (quenched) states. We introduce the conformational "switching" model

T.P.J. Krüger, Ph.D. (✉)
Department of Physics, Faculty of Natural and Agricultural Sciences, University of Pretoria, Private bag X20, Hatfield, 0028, South Africa
e-mail: tjaart.kruger@up.ac.za

V.I. Novoderezhkin, Ph.D.
Department of Photosynthesis, A.N. Belozersky Institute of Physico-Chemical Biology, Moscow State University, Leninskie Gory, 119992 Moscow, Russia
e-mail: novoder@belozersky.msu.ru

E. Romero, Ph.D. • R. van Grondelle, Ph.D. (✉)
Department of Physics and Astronomy, Faculty of Sciences, VU University Amsterdam, De Boelelaan 1081, 1081 HV Amsterdam, The Netherlands
e-mail: eli@few.vu.nl; r.van.grondelle@vu.nl

J. Golbeck and A. van der Est (eds.), *The Biophysics of Photosynthesis*, Biophysics for the Life Sciences 11, DOI 10.1007/978-1-4939-1148-6_3,

for the LHCII protein to explain its role both in light harvesting and in photoprotection. This model explains how the local environment of the protein controls its intrinsic conformational disorder to serve a functional role. Finally, we demonstrate that the PSII RC performs charge separation via two competing pathways of which the selection depends on the conformational disorder induced by slow protein motions. Therefore, we show that the pigment–protein interactions play a decisive role in controlling the functionality of the pigment–protein complexes at work in photosynthesis.

Keywords Photosynthetic light harvesting • Single-molecule spectroscopy • Femtosecond spectroscopy • Quantum coherence • Conformational dynamics • Fluorescence blinking • Charge separation • Electron transfer • Energy transfer • Two-dimensional electronic spectroscopy

Abbreviations

2DES	Two-dimensional electronic spectroscopy
CD	Circular dichroism
Chl	Chlorophyll
Chl_Z	Additional chlorophylls bound at the periphery of the photosystem II reaction center
CS	Charge separation
CT	Charge transfer, D1/D2/Cytb_{559}—reaction center of photosystem II
FL	Fluorescence
FLN	Fluorescence line-narrowing
LD	Linear dichroism
LHCII	Major light-harvesting complex II of plants
NPQ	Nonphotochemical quenching of chlorophyll *a* fluorescence
OD	Optical density (absorption)
P	Special pair of chlorophylls in reaction center
Phe	Pheophytin
PR	Participation ratio
PSI, PSII	Photosystem I, photosystem II
qE	Major, energy-dependent component of NPQ
Q_y, Q_x	Lowest electronic transitions of Chl and Phe
RC	Reaction center
RC5	RC6, reaction center of photosystem II lacking one peripheral Chl, and containing all peripheral Chls
SMS	Single-molecule spectroscopy
TA	Transient absorption
ZPL	Zero-phonon line

3.1 Introduction

In the primary steps of photosynthesis, solar photons are absorbed by pigments associated to protein domains. These pigment–protein complexes are embedded and organized in the photosynthetic membrane. The pigments (chlorophylls and carotenoids) serve to absorb the incoming photons (lending the pigment-proteins the term "light-harvesting antennas") and very efficiently transfer the ensuing electronically excited state to a photoactive pigment-protein complex, the reaction center (RC). Upon excitation of the RC, an ultrafast charge separation (CS) is initiated, leading to the formation of a transmembrane electrochemical potential difference that drives all the subsequent chemical processes [1–4]. In plant photosynthesis, antenna complexes consist of chlorophylls (Chls) as the main light-harvesting pigments, carotenoids with both light-harvesting and photoprotective functions, and other cofactors bound to the proteins. Crystallography studies have revealed intermediate- and high-resolution structures of the major plant light-harvesting complex LHCII [5, 6] and the core complexes of cyanobacterial photosystem I (PSI) [7] and photosystem II (PSII) [8–13]. Due to the large number of pigments bound in these complexes, the effective concentration may easily be about 0.5 M, the distance between nearest-neighbor pigments being as short as 9–10 Å, thus giving rise to strong ($>10\ cm^{-1}$) pigment–pigment interactions. As a result, the antenna and the RC are generally characterized by a complicated manifold of excited states, including collective electronic excitations (excitons) with a high degree of delocalization, and more localized excitations on weakly coupled pigments.

In this chapter we discuss the process of excitation energy transfer and trapping in the context of the major light-harvesting complex of plants, LHCII, and the PSII RC. Figure 3.1 shows the structure of LHCII [5], which, being part of the lhc multigenic family, is a trimeric pigment–protein complex, where each monomer is characterized by three transmembrane helices binding eight Chls *a*, six Chls *b*, and four carotenoids. The Chls are arranged in strongly coupled clusters, with the different clusters being weakly coupled to each other. Energy transfer occurs on a multitude of time scales from the carotenoids and the Chls *b* to the Chls *a*. Once located on the lower-energy Chls *a* the excitation either migrates within the trimeric complex or jumps to an adjacent light-harvesting complex. Eventually the core of PSII is excited and CS in the RC is initiated. The Chl arrangement in LHCII can be divided into two layers: a stromal and a lumenal layer, with the lowest energy states located in the latter.

LHCII has the surprising property that it can switch between a light-harvesting state and a quenched state [14]. In the light-harvesting state the complex delivers excitation energy with a high efficiency to a neighboring light-harvesting complex and eventually to the RC; in the quenching, photoprotective state excitation energy is efficiently converted into heat. We will demonstrate that this functionality works like a switch between conformational states that are naturally available to the complex and is controlled by its biological environment. The complex has "learned" to control its own disordered energy landscape [15].

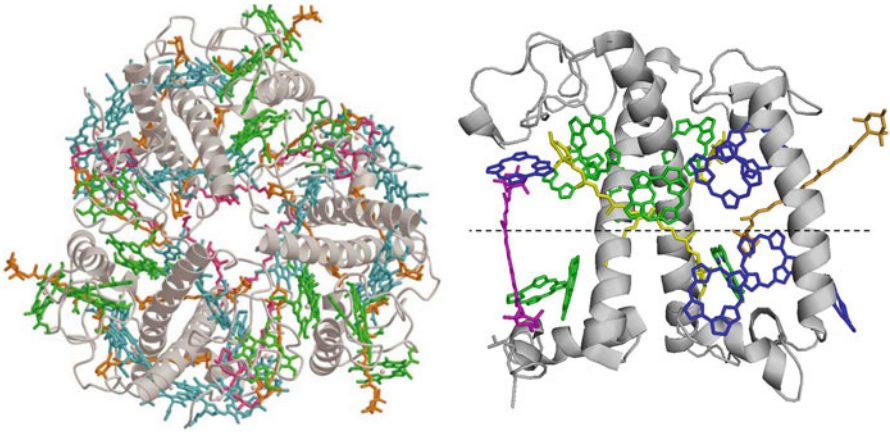

Fig. 3.1 Pigment–protein organization in the plant light-harvesting complex II (LHCII), viewing the whole trimer along the membrane from the stromal side (*left*) and viewing one monomeric subunit parallel to the membrane plane (*right*). The protein is shown in a *ribbon*-representation and the pigments as *sticks*. For clarity, the Chl phytyl chains and lipids are omitted. The separation between stromal- and lumenal-side Chls is indicated by *dashed line*. X-ray structure adapted from the following reference [5]. Colors: *gray*—protein; *green*—Chl *a*; *blue*—Chl *b*; *yellow*—lutein; *orange*—neoxanthin; *magenta*—violaxanthin or zeaxanthin

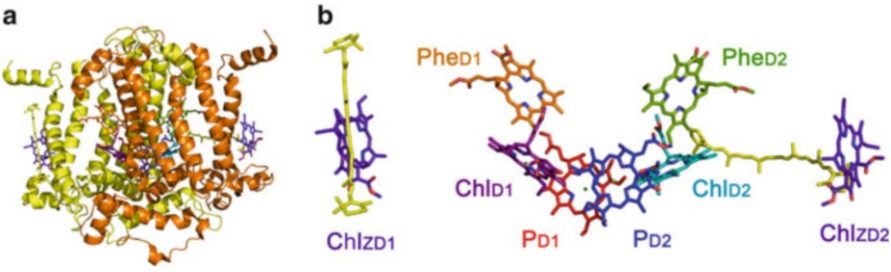

Fig. 3.2 Pigment–protein arrangement in the photosystem II reaction center (PSII RC), viewed perpendicular to the membrane normal. (**a**) The protein is represented as *ribbons* with D1 in *yellow* and D2 in *orange*. The pigments are represented as *sticks*. (**b**) Expanded view and labeling of the pigments. X-ray structure adapted from the following reference [12]

The pigment organization in the isolated PSII RC is shown in Fig. 3.2. The complex contains ten pigments: four Chl *a* and two pheophytin *a* (Phe) in the center (P_{D1}, P_{D2}, Chl_{D1}, Chl_{D2}, Phe_{D1}, Phe_{D2}, the RC core), two additional Chls ($Chls_Z$) located at opposite sides on the periphery of the complex and two β-carotenes situated between the $Chls_Z$ and the RC core. CS takes place in the RC core, where the Chls and Phes are arranged in two quasi-symmetric branches (D1 and D2), selectively along the so-called active branch (D1) [16]. After a series of energy- and electron-transfer events, the final charge-separated state $P_{D1}{}^{+}Phe_{D1}{}^{-}$ is created. We show how the mixing of excitonic and charge-transfer states in combination with

the intrinsic disorder of pigment-proteins produce a complex but highly efficient way of separating charges.

In LHCII and the PSII RC, each Chl binding site is characterized by its own specific protein microenvironment, giving rise to a set of "site" energies. Each of these site energies is modulated by slow conformational motion of the protein matrix, which results in "static" disorder of the site energies within a single complex (thus producing more localized exciton wave functions). Different disorder patterns determined by conformational changes are viewed in conventional bulk spectroscopy (with ensemble averaging) as inhomogeneous broadening. However, the conformational dynamics can be monitored directly using single-molecule techniques [17–19].

The exciton states also couple to the fast, collective nuclear vibrational modes of the protein (known as phonons) as well as to intra- and interpigment vibrations. These couplings give rise to a number of processes: (1) homogeneous broadening of the electronic transition spectra; (2) redshifting of these spectra due to reorganization effects (which are associated with changes in the equilibrium position of the nuclear modes after electronic excitation); (3) a further decrease in the delocalization size due to polaron effects; and (4) transfer of electronic excitations within the excited-state manifold, including fast (fs) relaxation between exciton states within strongly coupled clusters and slower (ps) energy migration between clusters or monomeric sites. Thus, the coupling between the excitons and this vibrational "bath" allows for energy transfer between excited states belonging to the same or to different spectral bands. This energy transfer is the basic mechanism of photosynthetic light harvesting, producing an ultrafast energy cascade from higher to lower levels, a process which contributes to the effective energy migration in the antenna and delivery of excitation energy to the RC.

Since the biochemical isolation of antenna complexes and the discovery of their structures, the fast energy-transfer and primary CS events have been studied using a variety of advanced laser spectroscopic methods, including time-resolved (sub-100 fs) nonlinear techniques that are interpreted together with theoretical modeling (see for a review [1, 2, 16, 20–27]). In this chapter we discuss a number of important experimental results and show how the light harvesting in plant LHCII and the CS process in PSII RCs can be modeled at a quantitative level by taking into account the exciton structure, static (conformational) disorder, and coupling of electronic excitations and charge-transfer (CT) states to fast nuclear motions in a pigment–protein complex. Simultaneous fittings of linear and nonlinear (dependent on excited-state evolution) spectral responses of the LHCII complex and the isolated RC complex of PSII have been done at a quantitative level using modified Redfield theory [18, 27–29]. The consistent physical picture of energy and electron transfer emerging from these models allows for a visualization of the excitation dynamics. The picture also allows for a physical view on how LHCII can switch between a light-harvesting and a quenching state, thereby providing a molecular explanation for the important, regulatory property known as nonphotochemical quenching in plant photosynthesis.

3.2 Physical Models of Energy Transfer

3.2.1 Collective Electronic Excitations: Excitons

Photosynthetic light-harvesting complexes have three important physical properties that enable effective light harvesting: relatively long-living (ns) excited states of their pigments, a high cross section for light absorption, and a sufficiently high pigment density to give rise to a phenomenon known as "coherence" [1, 27, 30–35]. The latter property can be understood in the following context. Let the wave function $|n\rangle$ denote the elementary excitation of the n-th Chl in the antenna. Quantum mechanics allows for a superposition of such wave functions, i.e., $c_1|n_1\rangle + c_2|n_2\rangle + \ldots$, for constants c_1, c_2, ..., where one elementary excitation is shared among a number of pigments. Such a collective excitation is known as an "exciton" and is different from the independently excited pigments n_1, n_2, ... due to correlations ("coherences") between them. These correlations are given by the terms $c_i{}^* c_j$, $i \neq j$, appearing due to the off-diagonal elements of the electronic Hamiltonian, i.e., $H \sim |n_i\rangle\langle n_j|$, $i \neq j$. In this coherent state a pigment "knows" about the excitation of its neighbors. This dramatically changes the spectrum of the light-harvesting pigment–protein as well as its energy-transfer dynamics. In natural light-harvesting systems these features produce more efficient light absorption, faster conversion from short- to long-wavelength spectral bands, and more irreversible trapping of excitations by the RC.

The Hamiltonian of the antenna in the basis of the local excited-state wave functions $|n\rangle$ is given by

$$H = \sum_{n=1}^{N} E_n |n\rangle\langle n| + \sum_{n \neq m}^{N} M_{nm} |n\rangle\langle m|, \tag{3.1}$$

where N is the number of Chls in the antenna, E_n is the electronic transition energy of the n-th Chl, and M_{nm} is the interaction energy between the n-th and m-th Chls. For simplicity we consider only the lowest Chl excited states, corresponding to the Q_y transition. The off-diagonal couplings M_{nm} produce new, collective eigenstates that are delocalized over a number of Chls instead of excitations localized on individual pigments. The energies ω_k and wave functions $|k\rangle$ of the exciton eigenstates can be obtained by diagonalizing the Hamiltonian in Eq. (3.1):

$$H = \sum_{k=1}^{N} \omega_k |k\rangle\langle k|; \qquad |k\rangle = \sum_{n=1}^{N} c_n^k |n\rangle, \tag{3.2}$$

where the collective exciton states $|k\rangle$ contain a coherent superposition of the original individual molecular excitations $|n\rangle$. The wave function amplitudes c_n^k reflect the participation of the n-th site in the k-th exciton state.

Generally the energies ω_k of the exciton states exhibit some shifts from the site energies E_n due to exciton splitting, the extent of which is determined by the couplings M_{nm}. The resulting exciton band consists of a manifold of N discrete exciton transitions. In addition, interaction with phonons induces a homogeneous broadening and a further energy shift of the corresponding spectral lines. This will be elaborated on in the next section.

3.2.2 Exciton–Phonon Coupling and Spectral Line Shapes

We consider the k-th exciton state from the manifold of N one-exciton levels. The corresponding line shape is given by the coupling of this level to fast nuclear modes. These phonon modes are determined by the collective modes of the pigment–protein matrix and the intra-pigment high-frequency vibrations. The absorption (OD) and fluorescence (FL) spectra of the whole pigment–protein complex are then given by the sum of the contributions from all exciton components:

$$\begin{aligned} \mathrm{OD}(\omega) &= \omega \sum_k d_k^2 \mathrm{Re} \int_0^\infty A_k(t)dt \\ \mathrm{FL}(\omega) &= \omega \sum_k P_k d_k^2 \mathrm{Re} \int_0^\infty F_k(t)dt \\ &\text{where } A_k(t) = e^{i(\omega-\omega_k)t - g_{kkk}(t)} \\ &\text{and } F_k(t) = e^{i(\omega-\omega_k)t + 2i\lambda_{kkkk}t - g^*_{kkkk}(t)} \end{aligned} \tag{3.3}$$

In Eq. (3.3) d_k represents the transition dipole moment of the k-th exciton state, P_k denotes the steady-state population, $g_{kkkk}(t)$ determines the line broadening of the k-th exciton state due to exciton–phonon coupling, and λ_{kkkk} is the corresponding reorganization energy. These quantities relate to the exciton–phonon spectral density C(ω) as follows [36–38]:

$$\begin{aligned} g_{kk'k''k'''}(t) &= -\int_{-\infty}^{\infty} \frac{d\omega}{2\pi\omega^2} C_{kk'k''k'''}(\omega) \left[\coth\frac{\omega}{2k_BT}(\cos\omega t - 1) - i(\sin\omega t - \omega t) \right] \\ \lambda_{kk'k''k'''} &= \int_{-\infty}^{\infty} \frac{d\omega}{2\pi\omega} C_{kk'k''k'''}(\omega) \\ C_{kk'k''k'''}(\omega) &= \sum_n c_n^k c_n^{k'} c_n^{k''} c_n^{k'''} C_n(\omega) \end{aligned} \tag{3.4}$$

where T is the temperature, k_B the Boltzmann constant, and $C_n(\omega)$ the spectral density in the site representation, corresponding to phonon-induced modulation of

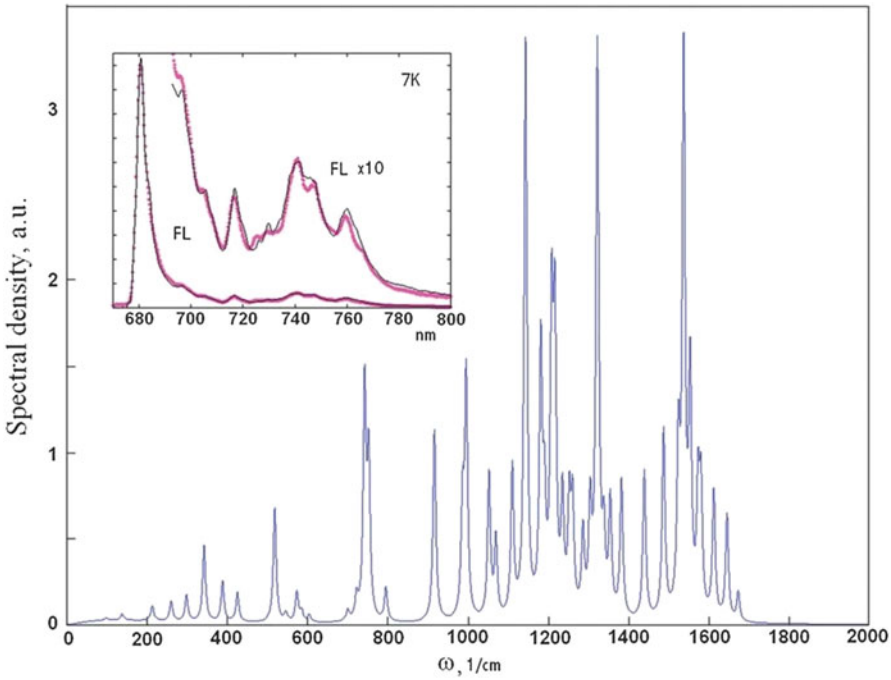

Fig. 3.3 Experimental exciton–phonon spectral density $C_n(\omega)$ for Chl *a* obtained using low-temperature FLN spectra of LHCII trimers [119]. The spectral density is modeled as a sum of an over-damped Brownian oscillator and 48 high-frequency modes with Huang–Rhys factors taken from FLN experiments [46] and adjusted from the fit of non-selective FL profiles [40]. The *inset* shows the 7 K non-selective (inhomogeneously broadened) FL spectrum for LHCII calculated with this spectral density (*thin line*) together with the measured one (*points*)

the transition energy of the n-th site. Here it is supposed that modulations of different sites are uncorrelated and modulations of the pigment–pigment interaction energies are excluded.

In the presence of static disorder, i.e., disorder of the site energies E_n and couplings M_{nm}, the homogeneous FL profiles (Eq. 3.3) should be averaged over a random distribution of E_n and M_{nm} that will perturb the energies and eigenfunctions of the exciton states. The nonlinear spectral responses can also be expressed in terms of the line-broadening functions (Eq. 3.4), as shown for pump–probe spectra [29, 38–42], Stark spectra [28], photon echoes [36], and 2D echoes [43].

The spectral density needed to evaluate the spectral responses can either be obtained from molecular-dynamics simulations [44] or extracted from experiments, such as hole-burning [45] or fluorescence line-narrowing (FLN) [46, 47]. Figure 3.3 shows the spectral density for the Chl *a* molecules in the LHCII complex, as obtained from FLN data [40, 46].

3.2.3 Modified Redfield and Generalized Förster Theories

When the spectral density $C_n(\omega)$ is known, Eq. (3.4) can be used to calculate not only the spectral shapes (Eq. 3.3) but also the energy-transfer rates. As such, the rate of population transfer from the state k′ to the state k is given by [38, 48]

$$R_{kkk'k'} = 2\mathrm{Re}\int_0^\infty dt A_k(t) F^*_{k'}(t) V_{kk'}(t)$$

$$\begin{aligned} V_{kk'}(t) = \exp\bigl(&2g_{k'k'kk}(t) + 2i\lambda_{k'k'kk}t\bigr) \\ &\times \bigl[\ddot{g}_{kk'k'k}(t) - \bigl\{\dot{g}_{k'kk'k'}(t) - \dot{g}_{k'kkk}(t) + 2i\lambda_{k'kk'k'}\bigr\} \\ &\times \bigl\{\dot{g}_{k'k'kk'}(t) - \dot{g}_{kkkk'}(t) + 2i\lambda_{k'k'kk'}\bigr\}\bigr] \end{aligned} \tag{3.5}$$

where F(t) and A(t) are defined by Eq. (3.3) and denote line-shape functions, corresponding to the fluorescence of the donor state and absorption of the acceptor state, respectively, and V describes the electrostatic interaction between the donor and acceptor. Note that Eq. (3.5) is valid for an arbitrary delocalization of the donor and acceptor states and arbitrary strong coupling to phonons when polaron effects are neglected. (The polaron-induced localization length is supposed to be larger than the disorder-induced localization size.) This approach, which is valid when the wave functions defined by the coefficients $c_m^{k'}$ and c_n^k exhibit significant spatial overlap, is generally referred to as modified Redfield [48].

If the donor and acceptor states are localized at the m-th and n-th sites, respectively (i.e., $c_m^{k'} = c_n^k = 1$) these two states are only weakly coupled. In terms of the interaction energy M_{nm}, V is then given by

$$V_{kk'}(t) = |M_{nm}|^2. \tag{3.6}$$

For such weak coupling, the original Förster equation [49] can be recovered by employing the Fourier transforms of F(t) and A(t) and writing the integral in Eq. (3.5) in a form of donor-acceptor spectral overlap [48].

The standard Förster formula can be generalized to the case of energy transfer between two weakly connected clusters [50–54]. In this context, the energy-transfer rate from the k′-th exciton state of one cluster to the k-th state of the other cluster is

$$V_{kk'}(t) = \left|\sum_{n,m} c_n^k M_{nm} c_m^{k'}\right|^2, \tag{3.7}$$

where n and m designate pigments belonging to different clusters. In this formulation the donor and acceptor states, k′ and k, correspond to arbitrarily strong excitonic interactions within each cluster, whereas the intercluster interactions

M_{nm} are restricted to be weak. This gives rise to a small spatial overlap between the k' and k wave functions.

In the Förster formula, the pigment interactions M_{nm} are treated perturbatively, as in Eqs. 3.6 and 3.7. In contrast, for the modified Redfield expression, the energy-transfer rates are calculated on the basis of the exciton states of the whole system (Eq. 3.5). In particular, this approach treats the diagonal part of exciton–phonon coupling in the exciton representation non-perturbatively.

The difference between the Förster and modified Redfield approaches is demonstrated in Fig. 3.4. Here the energy-transfer rates between two Chl molecules as a function of the energy gap E_1–E_2 between them are compared for calculations based on the Förster (Eq. 3.6) and modified Redfield (Eq. 3.5) expressions. In both cases, a realistic spectral density, as given by Fig. 3.3, was employed. The difference between the two rates is compared with the delocalization length (N_{del}), calculated as the inverse participation ratio that varies from 1 (in the localized limit) to 2 (in the limit of uniform delocalization over two molecules).

In the case of strong coupling ($M_{12} = 255\ cm^{-1}$), Redfield theory predicts overall higher rates than Förster theory. Note that the difference between the two rates is proportional to the deviation of the delocalization length from its value in the localized limit. In the limit of small delocalization lengths ($1 < N_{del} < 1.1$), which corresponds to large energy gaps (E_1–$E_2 > 5\ M_{12}$), Förster and Redfield theories give comparable rates.

For moderate coupling ($M_{12} = 55\ cm^{-1}$) the two theories give the same results everywhere, except in the delocalization limit. In this limit, which corresponds to small gaps (E_1–$E_2 < 5\ M_{12} = 275\ cm^{-1}$), Redfield theory again predicts higher rates.

For both strong and moderate couplings, the transfer rates given by Redfield theory in the isoenergetic limit (E_1–$E_2 = 0$) are 2–5 times faster as a result of delocalization. This deviation of the Redfield rates from the Förster limit becomes anomalously and unrealistically high in the weak-coupling limit, i.e., up to 2–3 orders of magnitude (see the lower frame of Fig. 3.4)! In principle, such a fast transfer is possible if the excitation is delocalized over two isoenergetic molecules, even if these molecules are spatially well separated and weakly interacting. However, in reality such a delocalization will be destroyed by the dynamic localization and polaron effects, features that are not included in the Redfield approach. Evidently, Förster theory, for which localization is assumed a priori, predicts more accurate rates in this limit.

A combined Redfield–Förster theory can be used to avoid the weak-coupling artifact of Redfield theory [55]. In this approach modified Redfield theory is employed to calculate the relaxation dynamics within strongly coupled clusters (where the intracluster interactions dominate the coupling cutoff value, i.e., $M_{nm} > M_{cr}$), while generalized Förster theory is used to model the energy transfer among these clusters (with $M_{nm} < M_{cr}$). The coupling cutoff value M_{cr} was found to be in the range 15–30 cm^{-1} [43, 55–57].

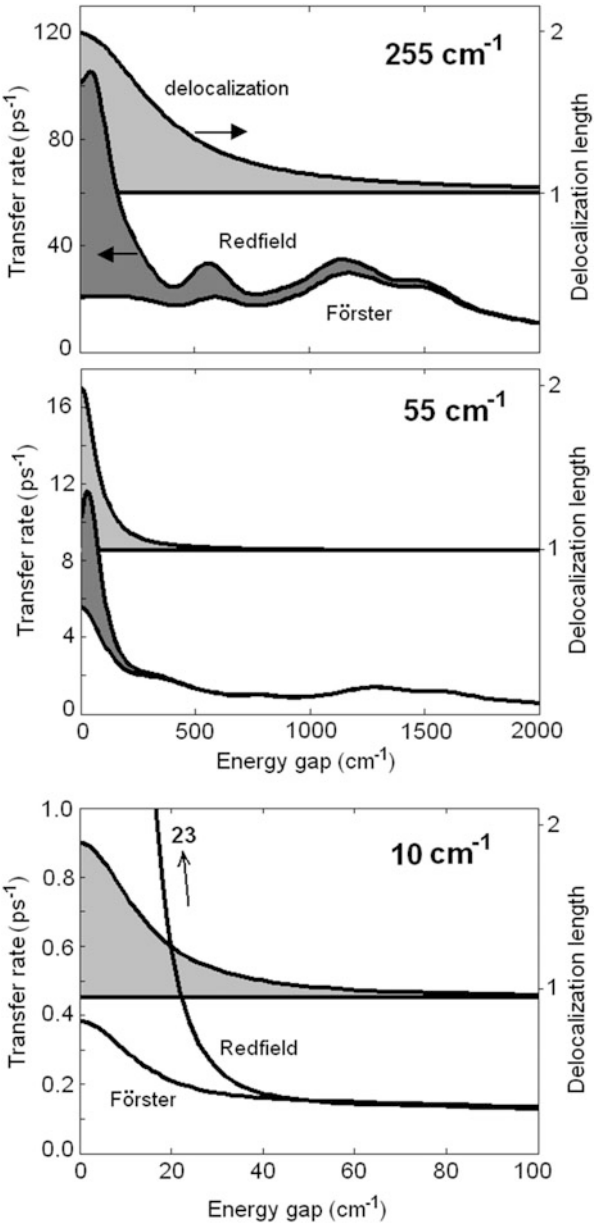

Fig. 3.4 The energy-transfer rate as a function of the energy gap between two molecules calculated with Förster and modified Redfield theory [119]. Only downhill rates are shown. The delocalization length N_{del} is calculated as the inverse participation ratio of the exciton wave functions. The $N_{del} = 1$ line is shown to highlight the deviations from the localized limit. The three frames correspond to strong, moderate and weak coupling, i.e., $M_{nm} = 255$, 55, and 10 cm^{-1}, respectively. The energy-gap range is 0–2,000 cm^{-1} for strong and moderate coupling and 0–100 cm^{-1} for weak coupling. We use the exciton–phonon spectral density of Fig. 3.3. The relaxation rates were calculated for 77 K. The specific non-monotonous dependence of the rates on the energy gap is determined by the shape of the phonon wing

3.2.4 Mixing of Excited and Charge-Transfer States

When two or more pigments are sufficiently closely separated, a situation that exists in RCs, charge-transfer (CT) states can be formed. The energy of these states is generally close to some of the exciton states, in which case mixing between the CT and exciton states occurs [58, 59]. The generally strong coupling of CT states to phonons gives rise to large displacements along the nuclear coordinates as compared to the excited states. Any pair of exciton and CT states is thus represented by two potential energy surfaces with different displacements along the effective nuclear coordinates. The mixing of the two surfaces near their intersection point will produce a redistribution of the dipole moments of the two states. This gives rise to some borrowing of the transition dipole strength from the exciton state (making the CT state weakly allowed), and borrowing of the static dipole from the CT state (thereby increasing the amplitude of the Stark signal). This mixing will also induce forward and backward transfer between the exciton and CT states. Relaxation along the nuclear coordinates within the exciton and CT potentials causes a dynamic localization of the exciton-CT state near the bottom of the corresponding surfaces.

In the limit of complete localization of the two states, Förster theory allows for a calculation of the exciton-CT transfer rates. In that case, all spectral features that would result from mixing, such as the shape of the red wing of the absorption spectrum, the broadening of the FL profile, and the increase in the Stark amplitude, are excluded.

In the opposite limit, the coupling between the two states is independent of the nuclear coordinates, giving rise to a uniform mixing of the two potential surfaces. In this case modified Redfield theory can be employed to calculate the relaxation rates between the mixed eigenstates as well as the spectral features that are induced by such mixing. This is done by including the CT state as an additional state to the excited states in Eq. (3.1). This approach is valid if the reorganization energy associated with the relative displacements of the excited and CT states is smaller than that of their coupling. Otherwise the degree of mixing is overestimated, in particular in the case of a small energy gap between the two states.

Extrapolation between these two limiting cases (localization and strong mixing, described by the Förster and modified Redfield theories, respectively) is possible by including explicitly the dynamics along a limited number of effective nuclear coordinates. In such a system the relaxation dynamics can be described more accurately by using Redfield theory on the basis of electron-vibrational eigenstates [60–62].

3.3 Excitation Dynamics in the Major Light-Harvesting Complex II (LHCII)

3.3.1 Simultaneous Fit of Linear Spectra and Nonlinear Transient Absorption Kinetics in LHCII

The crystal structure of the LHCII complex (Fig. 3.1) resolved the orientations of all the Chls, which allows for determination of the effective dipole moments of the pigments. In addition, knowledge of the spectral density of their exciton–phonon coupling enables a quantitative calculation of the spectral and dynamic properties of the complex using one unified physical picture. Only the site energies of the Chls remained unspecified and had to be determined from spectroscopic data. Following the discovery of the structure it was demonstrated that the unperturbed transition energies of the 14 Chls of each monomeric subunit can be extracted from a simultaneous fit of the linear spectra and transient absorption (TA) kinetics upon different excitation conditions using the modified Redfield approach [29] and later with the combined Redfield–Förster theory [56].

The Chl arrangement within the LHCII trimer is shown in Fig. 3.5a, b. On the stromal side (Fig. 3.5a) the Chls are arranged in two tightly packed Chl *a* clusters (*a*610–*a*611–*a*612 and *a*602–*a*603), which are in close proximity to three Chls *b* (*b*601, *b*608, and *b*609). In addition, the structure suggests that the Chls *b*601 and *b*609 from adjacent monomeric subunits are significantly coupled. Hence, the *b*601–*b*608–*b*609 group may be considered as a Chl *b* cluster, which is expected to have a short excited-state lifetime due to excitation energy transfer to the two Chl *a* clusters in each of the two related monomeric subunits. Within each *a*-cluster, fast exciton relaxation is expected, and between these clusters, a slower hopping.

On the lumenal side (Fig. 3.5b) there are two groups of pigments, viz., the *a*613–*a*614 dimer and the *b*605–*b*606–*b*607–*a*604 tetramer. The four sites of the tetramer are weakly connected to the rest of the complex. The excited-state dynamics within this cluster are therefore expected to be dominated by fast downhill energy transfer from the three Chls *b* to the Chl *a*604. The latter pigment is weakly coupled to the other Chls *a* in the complex, and therefore is the most likely site for a long-living "bottleneck" state in the Chl $b \rightarrow$ Chl *a* energy transfer. The presence of a bottleneck state was suggested by TA experiments upon excitation at 660–670 nm [63–65].

The site energies of LHCII were determined by simultaneously fitting the linear spectra (OD, LD, and FL), using an evolutionary-based search [29]. Figure 3.5c shows an example of the fit for the OD and LD spectra. Here, Chls *b* and *a* are responsible for the two main absorption bands, peaking at 650 and 675 nm, respectively. Although only a relatively small number of free parameters were employed (the 14 site energies, which were assumed to be the same for all three monomeric subunits of the trimer), the fit is not unique: 20–30 suitable models with different site energies were found. However, by calculating the best fits to the TA

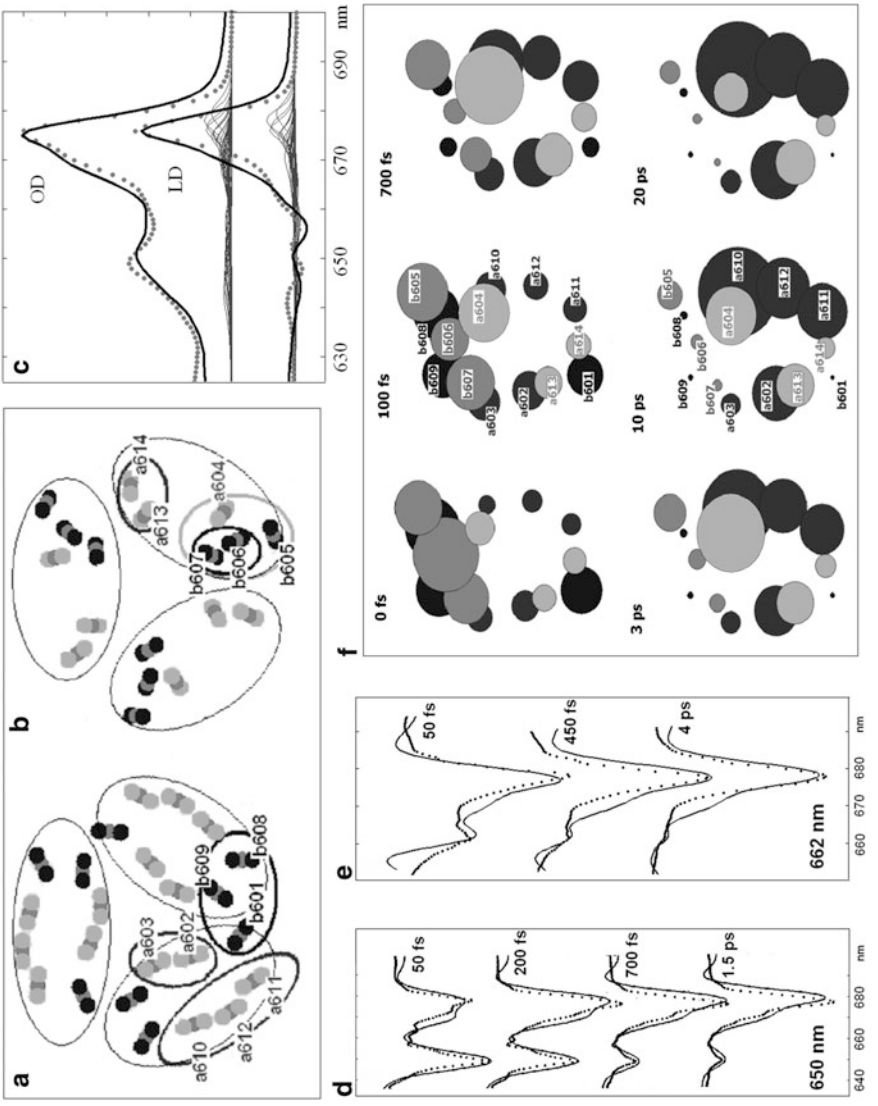
a
b
a610
a612
a611
a603
a602
b609
b601
b608
a614
a613
a604
b607
b606
b605
c
OD
LD
630
650
670
690
nm
d
50 fs
200 fs
700 fs
1.5 ps
650 nm
640
660
680
nm
e
50 fs
450 fs
4 ps
662 nm
660
670
680
nm
f
0 fs
100 fs
700 fs
3 ps
10 ps
20 ps

Fig. 3.5 Simultaneous fit of steady-state and time-dependent spectra for LHCII trimers with modified Redfield theory and visualization of the excitation dynamics in the complex [29]. (**a** and **b**) Arrangement of Chls within the LHCII trimer on the stromal (**a**) and lumenal (**b**) sides. Labeling of Chls corresponds to the following reference [5]. Chls are represented by *three filled circles*, the *middle one* denoting the Mg atom and the *two* on the sides corresponding to the two nitrogen atoms N_B and N_D, the positions of which define the directions of the Q_y transition dipole. Clusters of Chls *a*, Chls *b*, and a mixed group containing long-living intermediate sites are encircled and denoted by *red*, *blue*, and *green*, respectively. (**c**). Experimental absorption (OD), and linear-dichroism (LD) spectra of LHCII, measured at 77 K (*points*) and calculated (*solid lines*). Calculated spectra are shown together with individual exciton components (*thin lines*). (**d**). Evolution of the transient-absorption (TA) spectra upon excitation of Chls *b* (excitation wavelength 650 nm, pulse duration 90 fs, pump–probe delays of 50, 200, 700, and 1,500 fs). Measured spectra (*points*) are shown together with the calculated ones (*solid lines*). (**e**). Dynamics of the TA spectra following selective excitation of the intermediate region (662-nm, 180-fs pulses, and 50-, 450-, and 4,000-fs delays), shown for the experimental values (*points*) and the simulation (*solid lines*). (**f**). Dynamics of the site populations (averaged over disorder) during 0–20 ps upon 650 nm excitation at 77 K. The Chl sites within one monomeric subunit are shown by *circles*. The time-dependent area of the circle is proportional to the population of the corresponding site. The monomeric subunit is viewed from the lumenal to the stromal side, i.e., Chls from lumenal side (shown in *gray*) are on the top, and stromal-side Chls (shown in *black*) are behind them

spectra upon 650- and 662-nm excitation, the number of suitable models could be reduced considerably: A simultaneous fit of the 650- and 662-nm TA was possible with only one model (shown in Fig. 3.5d, e). Whereas the 650-nm excitation reflects fast (sub-ps) energy transfer from an initially populated Chl *b* band to the Chl *a* region around 670–680 nm (Fig. 3.5d), the narrow 662-nm excitation band could selectively excite the intermediate blueshifted Chl *a* states, giving rise to kinetics that are much more sensitive to the fine structure of the blue wing of the Chl *a* band (Fig. 3.5e).

3.3.2 Visualization of the Excitation Dynamics Within a Monomeric Subunit

The time scales and pathways of energy transfer can be calculated using the model parameters that were determined from the fit of the spectroscopic data. This enables a visualization of the complete excitation dynamics in a monomeric subunit of the LHCII complex. The dynamics in the Chl *a* region are determined by fast (50–200 fs) exciton relaxation within the *a*-clusters (*a*610–*a*611–*a*612, *a*602–*a*603, and *a*613–*a*614), whereas the coupling between these clusters produces slower (250–600 fs) intercluster transfers. The Chl *b* region is characterized by a fast relaxation (100 fs) within the *b*601–*b*608–*b*609 cluster at the stromal side and sub-ps transfer from this cluster to the neighboring *a*-clusters, i.e., *a*610–*a*611–*a*612 and *a*602–*a*603.

At the lumenal side there is first a fast population of the *b*605 and *a*604 sites due to equilibration within the *b*606–*b*607–*b*605–*a*604 group, followed by a slow depopulation of the *b*605 site by means of ps transfer to *a*604 or to the stromal *b*601–*b*608–*b*609 cluster. As a result, *b*605 serves as a "bottleneck" site that is responsible for a slow (few ps) component in the $b \rightarrow a$ transfer. Chl *a*604 is another, "bottleneck" site which lives even longer and is characterized by a very slow flow of energy to the remaining *a*-sites, with time constants of 40–50 ps, giving a total lifetime of the *a*604 site of about 13 ps.

Figure 3.5f provides a visualization of the site-population dynamics related to the positions within a monomeric subunit. The first three frames (0–700 fs) show the excitation-energy flow from the stromal-side Chls *b* (*b*601, *b*608, and *b*609) to the *a*-sites and the subsequent redistribution of the energy within the *a*-clusters. At the lumenal side the energy redistribution within the *b*606–*b*607–*b*605–*a*604 group occurs via transfer from *b*606 to *b*607 and *b*605 as well as a predominant population of the intermediate *a*604 site. The next three frames (3–20 ps) show a slow transfer from *a*604 (and from the *b*606–*b*607–*b*605 cluster) to the quasi-equilibrated *a*-sites. The *a*610–*a*611–*a*612 cluster (mostly *a*610) is predominantly populated when the energy has been fully equilibrated. This cluster is located on the outer side of the LHCII trimer, thereby likely providing a good connection with the other PSII subunits.

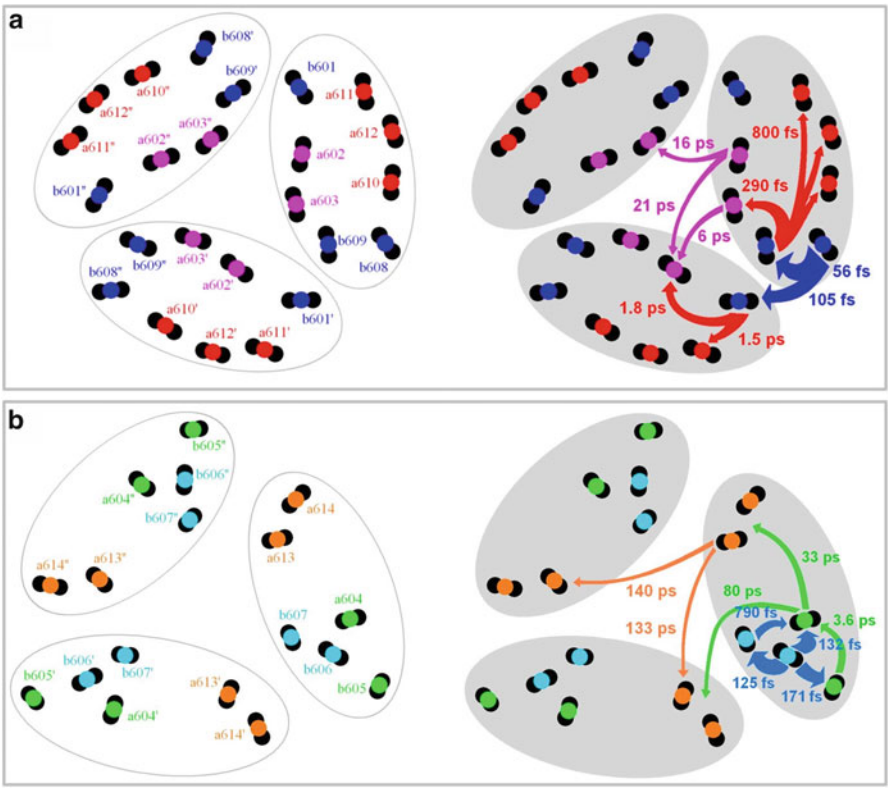

Fig. 3.6 Inter- and intra-monomeric energy transfer within the LHCII trimer at the stromal (**a**) and lumenal (**b**) sides [56]. *Left*: Chl arrangement and labeling corresponding to [5], except that the designations ′ and ″ are used to differentiate the pigments in the second and third monomeric subunits from the first. Each monomeric subunit is encircled and each Chl is represented by three overlapping, *filled circles* as defined in Fig. 3.5. *Right*: Main energy-transfer pathways following excitation of *b*608 (**a**) and *b*606 (**b**). Indicated in (**a**) are the relaxation within the *b*608–609–601′ cluster (*thick*, *dark blue arrows*), energy-transfer pathways from this cluster to the nearest Chl *a* clusters (*red arrows*), and the inter-monomeric transfer pathways in the Chl *a* region, the latter of which starts at the *a*602–603 dimer (*thin magenta arrows*). In (**b**) are shown the fast intra-cluster relaxation within the *a*604–*b*605–*b*606–*b*607 cluster (*thick*, *light blue arrows*), and the main inter-monomeric pathways of energy transfer that start from this cluster, including a slower migration between the intermediate long-living *a*604 and *b*605 sites and migration from the "bottleneck" *a*604 site (all shown by *thin*, *green arrows*), and transfers between the Chl *a* clusters (*orange arrows*)

3.3.3 *Inter-Monomeric Transfer in LHCII Trimers*

The competition between the intra- and inter-monomeric energy transfer in the whole LHCII trimer has been studied using the combined Redfield–Förster theory [56]. Figure 3.6a shows the energy-transfer scheme within the stromal layer of the LHCII trimer, following the hypothetical excitation of the stromal blue-most

*b*608 site. After excitation of the *b*608–*b*609–*b*601′ cluster, energy is transferred on a sub-ps time scale to the *a*602–*a*603 and *a*610–*a*611–*a*612 clusters within the same subunit as *b*608. The fastest transfer (290 fs) occurs from the lower exciton level of the *b*608–*b*609 dimer (*b*609 having a stronger participation) to the higher exciton level of the *a*602–*a*603 dimer (which is localized at *a*603). This transfer pathway is expected, considering the small distance between *b*609 and *a*603. Furthermore, *b*601′ being located in the second subunit, energy transfer takes place from this pigment to the two neighboring clusters, i.e., *a*602′–*a*603′ and *a*610′–*a*611′–*a*612′. The total effective time constant of the latter transfer is ~700 fs. Thus, the strong coupling within the *b*601′–*b*608–*b*609 cluster results in fast sub-ps conversion to the stromal-side Chl *a* clusters from the two monomeric subunits connected to this Chl *b* cluster.

The initial, fast $b \rightarrow a$ transfer is followed by a slower inter-monomeric transfer from the *a*602–*a*603 cluster to the same clusters in the other two subunits, i.e., *a*602′–*a*603′, and *a*602″–*a*603″. The higher and lower exciton states of these clusters are localized at the *a*603 and *a*602 pigments, respectively. Excitation of the higher level (localized at *a*603) gives rise to a relatively fast (6.3 ps) transfer to the nearest *a*602′ site, but the largest fraction of energy from *a*603 flows to the lower *a*602 site or to the *a*610–*a*611–*a*612 trimer. From *a*602, the dominant (fastest) inter-monomeric pathway is uphill to *a*603″ (occurring within 16 ps), while isoenergetic transfers take place to both *a*602′ and *a*602″ with time constants of 21 and 26 ps, respectively. Hence, an exchange between the subunits in quasi-equilibrium must be temperature dependent, determined by isoenergetic and uphill energy transfer from the higher *a*602 site.

On the lumenal side of LHCII (see Fig. 3.6b), *b*606 is the blue-most site. This pigment is part of the *a*604–*b*605–*b*606–*b*607 cluster, which contains the long-living, "bottleneck" *a*604 site (see Sect. 3.3.2). After rapid equilibration within this cluster, only slow migration takes place from *a*604, including a 33- and 80-ps transfer to the *a*613–*a*614 and *a*613′–*a*614′ dimers, respectively.

Energy transfer obviously also occurs between the lumenal and stromal layers of the LHCII trimer. The inter-monomeric stromal-lumenal transfer in the Chl *a* region is mostly determined by migration between the *a*602–*a*603 and *a*613–*a*614 clusters. There is a 12-ps transfer from the higher energy state of *a*613–*a*614 (localized at *a*614) to the *a*602″–603″ dimer, and 18- and 62-ps transfers from the higher and lower states of *a*602–*a*603 (localized at *a*603 and *a*602, respectively) to *a*613′–614′.

Combination of the above-mentioned intra- and inter-monomeric pathways produces complicated dynamics within the LHCII trimer (for more details see [56]). The complete energy-transfer dynamics in the LHCII trimer include the following:

1. Fast (sub-ps) conversion from Chls *b* to Chls *a* at the stromal side, followed by fast (sub-ps) equilibration between the Chl *a* clusters on the stromal side.
2. Slower (10 ps or more) equilibration within each monomeric subunit between the Chl *a* clusters at the stromal side and those at the lumenal side.
3. Even slower (20 ps and more) migration between the Chl *a* clusters from different monomeric subunits.

The slow energy-transfer channels through the "bottleneck" *a*604 site at the lumenal side give rise to additional dynamics, including

1. Fast (sub-ps to 3.6 ps) migration from the Chls *b* at the lumenal side to the "bottleneck" *a*604 site.
2. Slow (33 ps) transfer from *a*604 to the lumenal-side Chls *a*.
3. Reasonably slow (21 ps) transfer from *a*604 to the stromal-side Chl *a* clusters.

Interestingly, the total decay of the *a*604 "bottleneck" (with time constants of 13 ps and more) is still faster than the inter-monomeric equilibration between the Chl *a* clusters.

3.3.4 Comparing the Exciton Model and Single-Molecule Spectra

The spectral responses and dynamics simulated in Figs. 3.5 and 3.6 are averaged over many realizations of the static disorder. These realizations are associated with the passage of the antenna protein through a number of conformational substates that are characterized by various disorder patterns (i.e., a distribution of the site energies). The conformational dynamics give rise to dynamically changing spectra, i.e., spectra with different peak positions and shapes. These spectral fluctuations on the microsecond to second time scale have for the first time been observed in bacterial antenna complexes [66–72]. Recently, similar data have been obtained for single, trimeric LHCII complexes [18].

The strength of single-molecule spectroscopy (SMS) lies in its strong selectivity and sensitivity by revealing properties that are generally obscured by ensemble averaging. The FL dynamics from a single fluorescing quantum unit (i.e., a pigment–protein complex in our context) are typically investigated. This condition is fulfilled by firstly using a sufficiently low concentration of solubilized complexes such that the probability to find more than one complex within the laser excitation focal volume at a given instant is very small. Secondly, the fluorescence emitted by one complex should be sufficiently larger than the background signal for a reasonable averaging time. This condition obviously puts severe demands on the experimental setup and the photophysical properties of the sample. The complexes are usually immobilized to enable sufficiently long measuring times (seconds to tens of minutes per complex), and surface immobilization by means of electrostatic interactions is commonly employed for photosynthetic light-harvesting complexes studied near room temperature. When a monolayer of well-separated complexes is obtained, the surface is raster-scanned in the two lateral directions, which is used to locate the complexes.

Figure 3.7 shows FL spectra of single, immobilized LHCII complexes near room-temperature. The peak position of the measured FL spectra is fluctuating around the FL maximum of the bulk spectrum. Moreover, a shift of the FL peak is accompanied

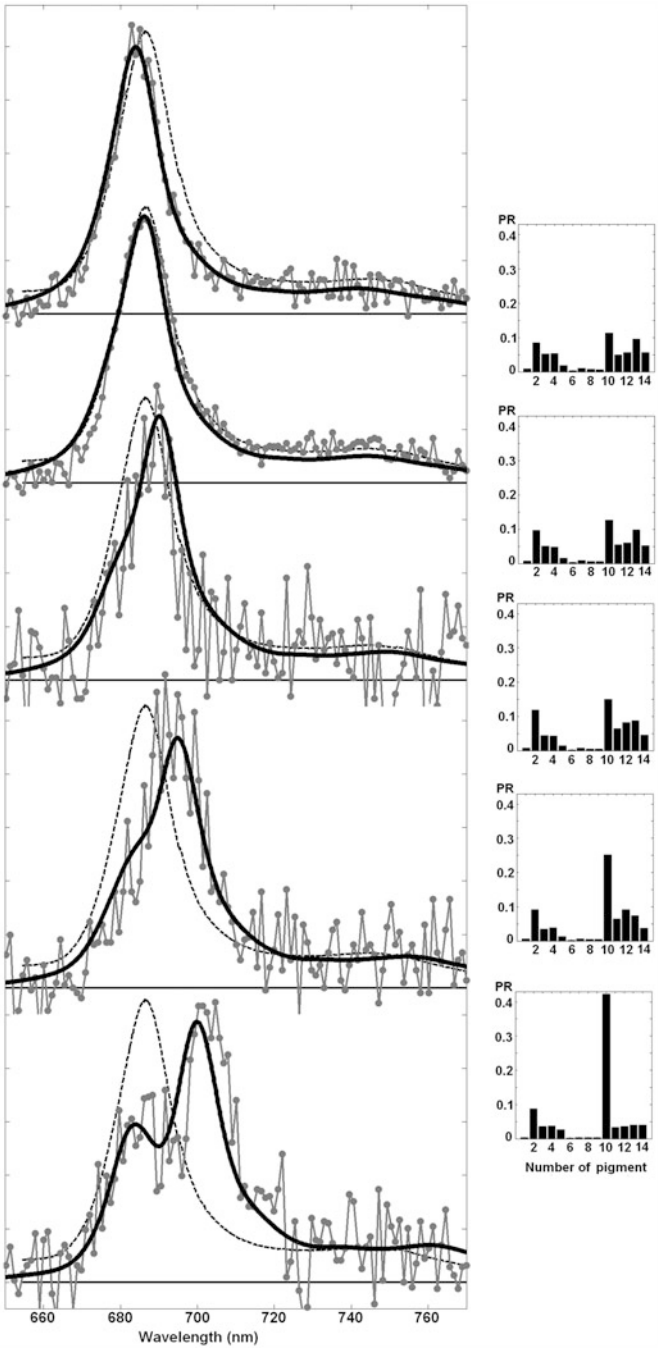

Fig. 3.7 Selected experimental (*points* connected by *lines*) and modeled (*thick*, *solid lines*) room-temperature FL spectral profiles from single LHCII complexes [18]. Measured profiles shown from top to bottom display different shifts from the ensemble-averaged spectrum (*dashed lines*),

by specific changes in the line shape. Explanation of these features is a challenging problem, which is one more test for the disordered-exciton model that emerged from the interpretation of the bulk spectra of the LHCII complex (Fig. 3.5).

Remarkably, a large percentage of the observed FL spectral fluctuations can be reproduced with the same model (i.e., with the same site energies, phonon couplings, and disorder value) as used for the calculation of the bulk spectra [18]. In Fig. 3.7 a few measured FL profiles, each with a different peak position, are compared with different calculated spectra. The latter are obtained from the ensemble of FL spectra that were calculated for different realizations of the disorder. Note that the calculated spectra have essentially the same characteristic line shape as the measured FL profiles with the same peak position.

The insets in Fig. 3.7 show that the redshift of the spectrum corresponds to an increasingly more non-uniform distribution of the participation ratio, with predominant localization at Chl *a*602 or *a*610. A disorder-induced redshift of the *a*602 or *a*610 sites breaks the delocalization within the Chl *a* clusters at the stromal side (i.e., within the *a*610–*a*611–*a*612 and *a*602–*a*603 clusters), thus increasing a reorganization shift accompanied by a further redshifting of the lowest exciton states. As a result, the emission on the red side is significantly increased. In realizations with strong disorder the FL spectrum appears to consist of two components: one from the strongly redshifted lowest exciton state and one from the next level.

Thus, we conclude that each single-molecule spectrum is determined by a specific localization pattern, controlled by the disorder of the site energies that is induced by protein conformational disorder.

3.4 LHCII as a Switch

3.4.1 Single-Molecule Spectra of LHCII

Although the intrinsic conformational disorder of the protein can explain most of the spectral dynamics of LHCII complexes (see Sect. 3.3.4), some of their spectral fluctuations require another explanation [18]. In Fig. 3.8a the spectral peak

Fig. 3.7 (continued) i.e., from a small blueshift (top spectrum) to increasingly bigger redshifts (three lower spectra). Measured spectra are averages of spectral profiles with similar shapes, and calculated spectra are taken from the ensemble of FL spectra calculated for different realizations of the disorder using the same exciton model of LHCII as in Fig. 3.4. *Insets on the right* show the thermally averaged participation ratio (PR) of the pigments corresponding to the same realizations as the calculated FL spectra. The PR values of the nth pigment are defined as $PR_n = \sum_k p_k (c_n^k)^4$, where p_k is the steady-state population of the kth exciton state, and c_n^k is the wave function amplitude (Eq. 3.2). Numbers from $n = 1$ to 14 correspond to pigments from 601 to 614 in the notation of the following reference [5]

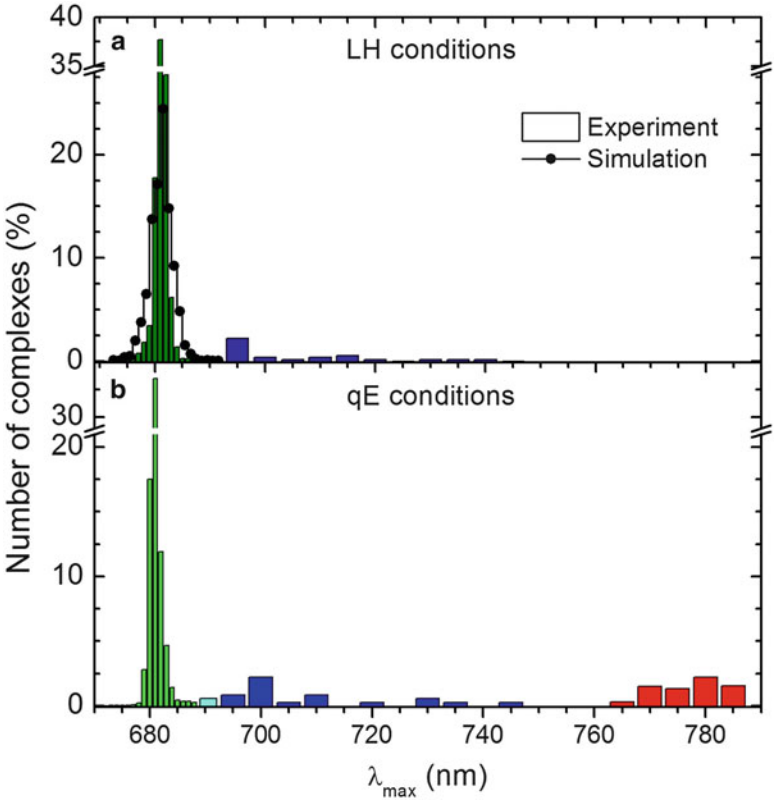

Fig. 3.8 FL spectral peak distributions of ~2,000 individually measured LHCII trimers in two different environments [15, 18]. (**a**) Complexes in light-harvesting (LH) environment (*bars*) as compared to the modeled distribution (*points* connected by *lines*). Calculations were performed by taking 2,000 different realization of the static disorder, using the same exciton model of LHCII as for Fig. 3.5 and a disorder of 90 cm^{-1}. 5-nm bars indicate spectral states that were not reproduced by the calculations. 1-nm bars denote the weighted frequency of occurrence of single-band spectral peaks, while the 5-nm bars represent the fraction of complexes exhibiting double-band spectra, where the peak position of the redder band is displayed. (**b**) Similar as (**a**) but for the qE-mimicking environment

distribution of a large number of individually measured LHCII complexes near room temperature is compared with the calculated distribution, using the modified Redfield model as explained in the previous section. The calculated distribution is somewhat broader than the measured one, which signifies that the pure exciton model can explain the spectral profiles with peak maxima up to ~695 nm and that the modeled disorder may even be an overestimation. Larger redshifts require the presence of special protein conformations. These low-energy states can be best explained by mixing between a CT state and an exciton manifold of two or more closely separated pigments within the complex. The most probable site of this mixing can be identified by considering the structurally and compositionally similar

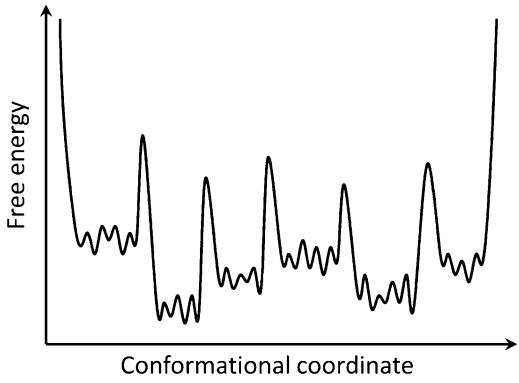

Fig. 3.9 Cartoon of the energy landscape of a protein, projected onto one conformational coordinate, illustrating the hierarchical arrangement of barrier heights which separate local energy minima

peripheral antenna complexes of PSI. These complexes characteristically fluoresce at wavelengths longer than 700 nm, reminiscent of the far-red emission of LHCII, and is known to originate from the CT-exciton coupling of a Chl dimer in the L2 site of these complexes [73, 74] (nomenclature of Liu et al. [5]). The corresponding Chl dimer in LHCII (*a*603–*b*609) is therefore the most probable site of this complex's low-energy emission states.

The protein conformational energy landscape model [75–77] provides a feasible context to explain the spectral fluctuations of photosynthetic light-harvesting complexes [78]. Such an energy landscape describes all the possible protein conformations and the associated free energy of each conformation (see Fig. 3.9). As such the energy landscape constitutes a hypersurface in the high-dimensional space where each degree of freedom of the protein corresponds to another coordinate. An energy landscape is typified by hierarchically ordered conformational substates (local minima), where the substates belonging to a particular tier are in dynamic equilibrium. The heights of the free energy barriers separating different substates reflect the activation energy required for a protein to escape from a particular substate and acquire another conformation. Perturbations of the protein conformation increase the probability to cross relatively large energy barriers. If the corresponding substates correspond to distinct emissive states, a spectral jump is observed.

3.4.2 Nonphotochemical Quenching (NPQ)

When the harvested energy delivered to the RCs saturates the electron-transfer chain connecting PS2 and PS1 to the reduction of $NADP^+$, the lumenal pH decreases and the resulting transmembrane pH gradient triggers a phenomenon known as nonphotochemical quenching (NPQ), during which excess excitation energy is harmlessly dissipated as heat (see [14] for a recent review). Although the site and molecular mechanism of qE, the main component of NPQ, are inconclusive at present, there are strong indications that LHCII plays an important role.

Protein conformational changes associated to qE redistribute the energy levels of particular pigments in the complex, thereby opening energy dissipating channels. In particular, one important molecular mechanism for qE that was proposed identifies the energy transfer from a low-lying Chl exciton state to the optically forbidden carotenoid S_1 state and the subsequent rapid dissipation of the energy as heat upon relaxation of the carotenoid excited state [79]. The carotenoid was identified as the lutein L1 in the atomic structure [5] of LHCII, indicating that the closely coupled exciton state is associated with the *a*610–*a*611–*a*612 cluster. In addition, the crystal form of LHCII manifests fast FL decay, accompanied by a characteristic Raman signal, and redshifted FL [80]. Similar spectroscopic properties were observed for isolated, quenched LHCII complexes immobilized in a gel matrix [81, 82] as well as for aggregates, chloroplasts, and leaves under NPQ conditions [79, 83–87]. Since in the crystals and gel-immobilized complexes no strong interactions between neighboring complexes are present, it was concluded that the energy dissipation and the accompanying reversible conformational changes are intrinsic features of each LHCII trimer [80, 81].

The molecular processes underlying the switching capability of LHCII between the light-harvesting and the quenched state could earlier only be hypothesized on the basis of ensemble techniques [88]. However, using SMS the intrinsic intensity switching capability of this complex has recently been demonstrated [89]. The FL intensity was found to switch rapidly and reversibly between different quasi-stable quenched and unquenched states, the switches occurring at apparently random times, which reflects significant disorder in these complexes. This phenomenon is generally known as fluorescence intermittency or blinking and is a common feature of intrinsically fluorescent quantum units [90]. However, the fluorescence blinking of LHCII complexes has demonstrated some unique features. For example, three conditions generally associated with qE were mimicked in a single-molecule environment. For LHCII, each of these three qE-related conditions affected the fluorescence blinking such that the time- and population-averaged FL intensities decreased [15], while a distinctly different behavior was found for the structurally homologous minor antenna complexes [91]. These findings strongly suggest the idea of an explicit relationship between the mechanism(s) underlying fluorescence blinking in LHCII and the qE switch. This relationship is supported by a conformational diffusion model that was used to reproduce the experimental blinking behavior of LHCII on a quantitative level [92].

These observations indicate that the environmental control over the intrinsic dynamic disorder in LHCII that gives rise to fluorescence blinking provides a molecular basis for qE. In addition, this particular environmental control is highly specific for LHCII, based on its finely tuned structure. In a more general view, the variability of the FL spectra of single LHCII complexes can be considered a direct manifestation of their self-regulatory ability in response to external conditions.

3.4.3 *A Physical Model for Functional Switching: Controlled Disorder*

While on the level of a single complex the quenching capability of LHCII features as a switch, on an ensemble level the functionality is reflected by a population redistribution. This can again be understood well in the context of the protein landscape model. The populations of the conformational substates follow statistical thermodynamic distributions. Proteins respond to environmental changes by redistributing the populations of these preexisting substates, an idea commonly known as "conformational selection" or "population shift" [93]. Recent spectroscopic studies on numerous proteins, employing in particular SMS, have demonstrated that functional changes can be explained in the same framework, by associating two or more such protein substates with different functional characteristics [94]. In many proteins, the intermolecular interactions associated with the new functional state are optimized by additional conformational changes taking place after the conformational population shift [94].

By considering qE in this framework, the dissipative states associated with qE are not induced by particular environmental conditions, but are intrinsic to LHCII under any environmental conditions, albeit with a different probability. The biological environment of an LHCII complex changes the forward and backward switching probabilities between the light-harvesting and quenching states by means of subtle conformational changes. As such, the complex environmentally controls its own disordered energy landscape.

Figure 3.8b shows the spectral peak distribution of individually measured, isolated LHCII complexes under conditions that mimic qE. Replacing the light-harvesting environment with the qE environment did not notably affect the spectral peak populations below 760 nm. However, a significant population shift occurred for spectral peaks above 760 nm. While the quenched states described in Sect. 3.4.2 generally correspond to small or negligible spectral changes, the population above 760 nm included only quenched conformations. This indicates the presence of at least two distinct qE mechanisms in LHCII, characterized by different spectral signatures. In a recent Stark fluorescence study, two distinct sites of energy dissipation in LHCII were also found [95], supporting the notion that different competing quenching pathways are simultaneously present in this complex.

The scheme in Fig. 3.10 illustrates how LHCII exists in a dynamic equilibrium between a small number of different quenched and spectral conformations and shows the most likely sites associated to the different spectroscopic states. In this model, the protein structural disorder is responsible for frequent switching between the different quasi-stable states, while the local environment of the complex determines which of these states are favored, i.e., controlling the intrinsic switching capability. Hence, LHCII exists as a natural, environmentally controlled, conformational nanoswitch.

Another example of environmentally controlled protein disorder in light-harvesting complexes of plants was demonstrated by comparing the spectral switches of LHCII complexes with those of PSI peripheral antenna complexes [96].

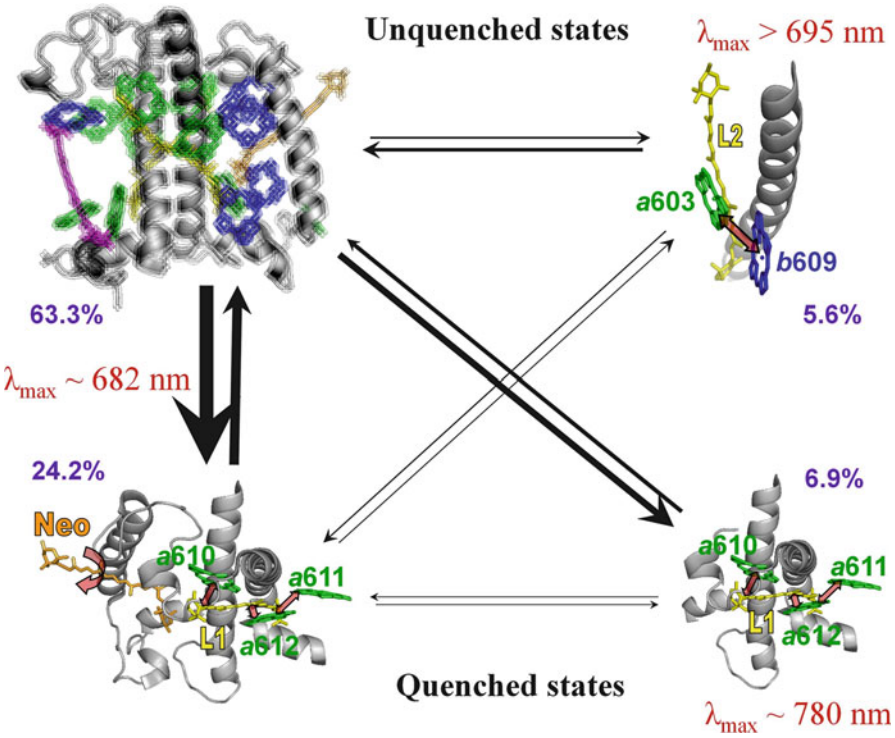

Fig. 3.10 Model illustrating the switching mechanism of LHCII to redshifted and two types of energy-dissipating states [15]. *Top left*: LHCII monomeric structure [5] in an unquenched state, exhibiting emission at ~682 nm. The induced uncertainty in the molecular positions indicates the subtle structural difference between the unquenched structure and the resolved quenched structure. *Top right*: Key pigments involved in the establishment of the unquenched, redshifted states [18, 96]. *Bottom left*: Key pigments involved in the spectrally non-shifted, quenched states [79]. *Bottom right*: Key pigments involved in the spectrally shifted, quenched states. The *straight*, *red arrows* signify strong interactions, the *curved arrow* indicates a configurational twist, and the *black arrows* represent transitions between different states, with the thickness giving a qualitative indication of the frequency of occurrence. The percentages in *purple* denote the approximate time spent on average in each state under qE-mimicking conditions

While LHCII generally fluoresces at around 680 nm and occasionally switches to states characterized by emission above 695 nm, the exact opposite spectral behavior was observed for the PSI antenna complexes. These complexes are structurally homologous to LHCII, suggesting that all the PSI and PSII peripheral antenna complexes can be approximated by a single generic protein structure. The "blue" and "red" spectroscopic states can then be considered to be intrinsic to the disordered energy landscape of this protein. As a result, the intrinsic structural disorder of the protein gives rise to switching between the "blue" and "red" spectroscopic states at random times and for random durations. Furthermore, this disorder is controlled by the

direct protein environment by shifting the population distribution between the two conformations, explaining why the "blue" conformation is more stable for LHCII and the "red" more stable for the PSI antenna complexes.

3.5 Energy Transfer and Primary Charge Separation in the Photosystem II Reaction Center (PSII RC)

3.5.1 The PSII RC and the Charge Separation Process

The primary steps of solar energy conversion in oxygenic photosynthesis take place in the reaction center of Photosystem II (PSII RC), also known as D1/D2/Cytb_{559} with near-unity quantum efficiency [16, 20, 97, 98]. The isolated PSII RC is a photoactive pigment–protein complex that contains six Chls *a*, two pheophytins (Phes) *a*, and two β-carotenes associated to the D1 and D2 transmembrane proteins, where only the D1 branch is active in charge separation (CS) [16]. The crystal structure [8–13] shows that four Chls and two Phes are arranged in two quasi-symmetric branches in the center of the complex (P_{D1}, P_{D2}, Chl_{D1}, Chl_{D2}, Phe_{D1}, Phe_{D2}, the RC core). The remaining two Chls, known as $Chls_Z$, are located at the periphery of the complex on opposite sides, while each carotene is situated between one Chl_Z and the center of the complex. CS takes place within the RC core and leads to the oxidation of P_{D1} and the reduction of Phe_{D1}, producing the final charge-separated state $P_{D1}{}^{+}Phe_{D1}{}^{-}$.

The short distance of around 10–11 Å between neighboring pigments in the center of the PSII RC complex [8–13] gives rise to exciton states that are delocalized over several pigments [20, 99]. These exciton states and the monomeric $Chls_Z$ interact with light at a similar wavelength (around 675 nm), producing a highly congested absorption spectrum. In addition, the dynamics in this low-energy spectral region (Q_y) reflect ultrafast energy equilibration among the core pigments, radical-pair formation, and excitation energy transfer from the $Chls_Z$ to the RC core. The combination of these processes and the spectral congestion greatly complicates the interpretation of the spectroscopic data. Furthermore, the complex exhibits considerable structural disorder: fast nuclear motions (intra- and inter-pigment and protein vibrations), constituting dynamic disorder; and slow conformational motions of the protein, which are known as static disorder. The slow protein motions create many different protein configurations (i.e., realizations of the static disorder) with different relative distances and orientations of the pigments and protein residues. As a result, the sample ensemble consists of a large collection of energetically different reaction centers.

The CS process in the PSII RC consists in the conversion of solar excitation energy into a transmembrane electrochemical potential. The exciton states are converted into a primary charge-transfer (CT) state (or radical pair), which evolves further into a secondary CT state, yielding the following path: exciton $\rightarrow CT_1 \rightarrow CT_2$ state.

3.5.2 The Model: Simultaneous Fit of Linear and Nonlinear Spectra

In order to gain insight into the mechanism(s) of CS, theoretical models have been developed. These models are constantly extended and improved. The first model that provided an explanation for the spectra and kinetics in the PSII RC is known as the "multimer model." In this model it is assumed that all the Chls and Phes are spectroscopically equivalent, i.e., having equal site energies, giving rise to exciton states that are delocalized over two or three pigments [99, 100]. Redfield relaxation theory was then used to model the dynamics within the excited-state manifold and the associated spectral signatures, such as pump–probe [42, 101] and photon-echo responses [102], but failed to give a reasonable quantitative fit of the spectral shapes due to the restrictions of the multimer model. That model was later replaced by more realistic models based on modified Redfield theory. These models employed the site energies extracted from a simultaneous evolutionary-based fit of linear spectra (OD, CD, LD, and FL) over a wide temperature range [41] and nonlinear spectra (time-resolved OD and FL at room temperature) [39]. In a later work, a CT state, which was strongly mixed with the exciton states, was included in the excitonic manifold [28]. Therefore, in the following we will refer to this model as the "disordered exciton–CT model." The site energies were verified by modeling the absorption spectra of modified RCs, such as RCs with (1) modified Phe_{D2}, (2) modified Phe_{D1} and Phe_{D2}, and (3) complexes that lack one of the peripheral Chls (the so-called "RC5 complexes"). In addition, the triplet-minus-singlet (T-S) and the Stark spectra were calculated. The line shapes were obtained using the exciton–phonon spectral density taken from the FLN data for the PSII RC [47].

Figure 3.11 shows an example of a simultaneous fit of various spectral types by employing the disordered exciton–CT model of Novoderezhkin et al. [28]. The main absorption band in the 660–690 nm region is determined by the Q_y transitions of the eight chlorin pigments. The sub-bands at 670 and 680 nm are explained by the differences in the pigment site energies, in combination with exciton splitting and phonon-induced reorganization shifts. The broad absorption at 620 nm originates from coupling between the Q_y transitions and high-frequency vibrations. The low-temperature FL has its main peak at 680 nm and displays a broad vibrational wing with a maximum at 740 nm.

The lowest exciton state with an absorption peak near 682 nm (see Fig. 3.11i, j) corresponds to a charge-transfer (CT) state. Due to mixing between this state and the pure exciton states, the CT state borrows some dipole strength and becomes weakly dipole-allowed. This mixing produces relatively small changes in the absorption-type spectra (OD, CD, and LD) but has a dramatic effect on the FL line shape. This is explained by the latter being mostly determined by contributions from the two lowest energy states, which constitute a mixed exciton-CT state (peaking around 682 nm)

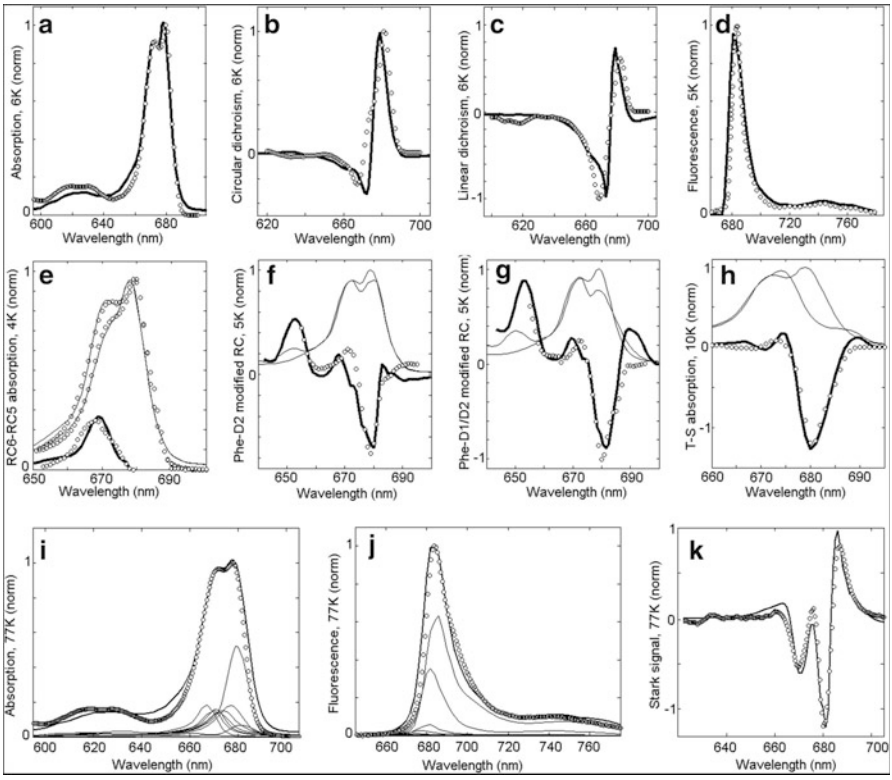

Fig. 3.11 Simultaneous fit of the low-temperature spectra of isolated PSII RC [28]. *Open circles* show the experimental data, while *solid lines* represent the calculated spectra. (**a**–**c**) OD, CD, and LD spectra at 6 K. (**d**) Non-selective FL profile at 5 K. (**e**) Absorption spectra at 6 K for normal 6-Chl RC complexes (RC6) and for modified RC complexes lacking one of the peripheral $Chls_Z$ (RC5). The calculated RC6, RC5, and difference RC6 − RC5 spectra are shown together with the measured ones. (**f** and **g**) Absorption changes at 5 K induced by modification of Phe_{D2} (**f**) or of both Phe_{D2} and Phe_{D1} (**g**). *Thin solid lines* show absorption spectra calculated for normal and modified RCs. The latter display a bleaching near 680 nm and a new absorption peak near 650 nm due to the blueshift of the modified Phes. (**h**) Triplet-minus-singlet (T − S) spectra measured at 10 K. The calculated T − S spectrum (*thick line*) is obtained as the difference between the ground-state absorption (*thin line*) and absorption without contribution of the Chl_{D1} (*thin line*), implying localization of the triplet state on Chl_{D1} at 10 K. (**i**–**k**) Simultaneous fit of the 77 K spectra including OD, FL, and Stark spectra. The calculated OD (**i**) and FL (**j**) spectra are shown together with contributions from the individual exciton states (*thin lines*)

and a superradiant "multimeric" exciton state (delocalized over the D1 branch and peaking at 680 nm). This indicates that the FL profile is extremely sensitive to the precise energy of the CT state. However, the degree of mixing between the CT state, with its large static dipole, and the exciton states is the determining factor for the shape and amplitude of the Stark spectrum (Fig. 3.11k).

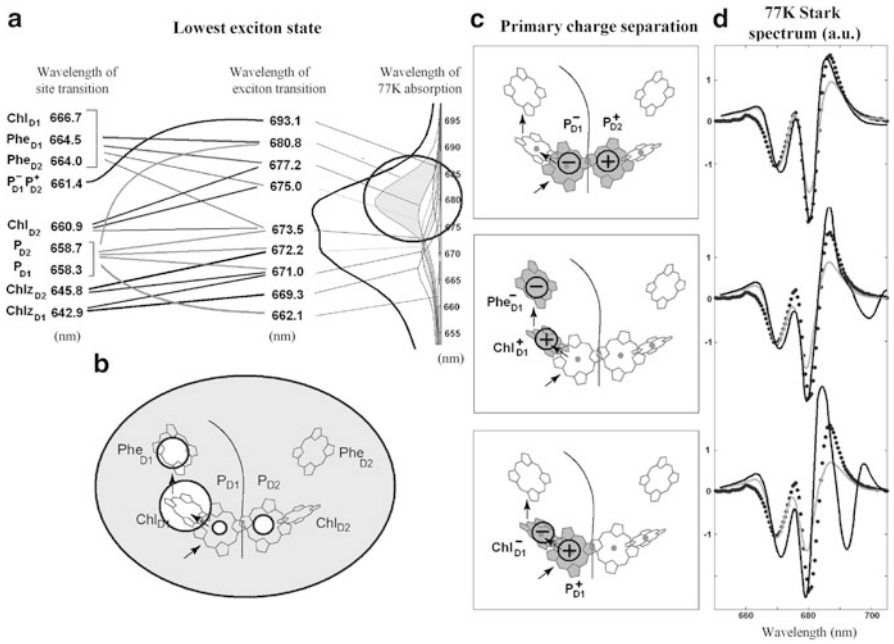

Fig. 3.12 (**a**) Exciton structure of the PSII RC [28]. Wavelengths corresponding to the unperturbed site energies of the eight pigments and the first CT intermediate $P_{D2}^{+}P_{D1}^{-}$, without including the reorganization shift (*left*); wavelengths of the zero-phonon lines of the exciton eigenstates averaged over disorder (*middle*); 77 K absorption spectrum (*thick line*) with the individual exciton components (*thin lines*) (*right*); the *connecting lines* indicate the participation of the pigments in the exciton states. (**b**) Structure of the lowest exciton state, where the *circles* show the pigments that on the average are coherently mixed in the lowest exciton state. The area of the circle is proportional to the population of the corresponding site. (**c**) Possible pathways for primary charge separation in the PSII RC. *Circles* show the localization of the electron and hole in the CT states (i.e., $P_{D2}^{+}P_{D1}^{-}$, $Chl_{D1}^{+}Phe_{D1}^{-}$, and $P_{D1}^{+}Chl_{D1}^{-}$) that can be coupled to the lowest exciton state. (**d**) Stark spectra calculated with the CT states shown in (**c**). Experimental data are displayed (*points*), together with the Stark signal calculated with (*black line*) and without (*gray line*) coupling to the CT state

3.5.3 *Mixing with CT States: Multiple Charge Separation Pathways*

In the model presented by Novoderezhkin et al. [28], the lowest excited state from which the CS is initiated consists of a coherent superposition of four pigments, viz., Chl_{D1}, Phe_{D1}, P_{D1}, and P_{D2} (Fig. 3.12). Participation of these sites in the multimeric exciton state is not uniform: *on average* the excitation is predominantly localized at Chl_{D1}, the population of Phe_{D1} is about two times less, and the population of the P_{D1} and P_{D2} pigments is even smaller (see Fig. 3.12b). Due to the strong coherence between these four sites, a CT state coupled with any of these four pigments will be effectively mixed with the whole set of exciton states, the degree of mixing

depending on the energy gap between the exciton and the CT state. Hence, the primary electron transfer toward Phe_{D1} could, in principle, start from P_{D2}, Chl_{D1}, or P_{D1}, producing the first charge-separated configuration $P_{D2}^{+}P_{D1}^{-}$, $Chl_{D1}^{+}Phe_{D1}^{-}$, or $P_{D1}^{+}Chl_{D1}^{-}$, respectively, indicating that CS can occur via different pathways.

In principle, the predominant population of Chl_{D1} provides a strong ground for considering this pigment as the primary electron donor, producing the CT state $Chl_{D1}^{+}Phe_{D1}^{-}$. However, P_{D1} and P_{D2} have overlapping electronic wave functions, which creates a better mixing between their excited states and the $P_{D2}^{+}P_{D1}^{-}$ CT state. Both factors favor the CS reaction and, therefore, are in competition. According to the model, the factor that determines the success of a charge separation pathway is the specific realization of the disorder. The specific protein conformation determines the participation of each of the pigments in the lowest exciton state as well as the mixing between this state and the corresponding CT state. In this view, the pigment–protein interactions control the way the RC functions.

In summary, the disordered exciton–CT model predicts the presence of multiple CS pathways in the PSII RC which are strongly disorder controlled [28]. A particular realization of the disorder can favor one of the two possible charge separation pathways. The measured kinetics, which are averaged over the disorder, therefore contain a superposition of components corresponding to different pathways. As a result, various experimental methods sensitive to different aspects of the electron transfer produce a large distribution in the estimated "time constants" of primary CS.

3.5.4 Multiple Charge Separation Pathways: Experimental Evidence

The hypothesis of the disorder-induced CS pathways has recently been tested experimentally by performing a TA study [103]. The complexity of the CS dynamics in the PSII RC due to the spectral congestion and the similar timescales predicted for the proposed CS pathways requires a careful experimental design. The following experimental conditions were used: (1) cryogenic temperatures (77 K) to enhance spectral resolution, freeze the slow protein motions, and reduce back reactions and uphill energy transfer; (2) a series of excitation conditions that expand the Q_y region in order to photoselect subpopulations that follow the different pathways in different proportions; (3) probing the absorption changes over the whole visible range and during an extensive time range in order to investigate all absorption bands and all timescales of CS.

Combining the results obtained from numerous experiments and applying global and target analysis according to a kinetic scheme [104], we have demonstrated that at least two different excited states, $(Chl_{D1}Phe_{D1})^*$ and $(P_{D1}P_{D2}Chl_{D1})^*$, give rise to two different pathways for ultrafast CS, viz., the so-called Chl_{D1} and P_{D1} paths, respectively [103]. These results are in agreement with the theoretical model [28] and indicate that the energetic differentiation among the RC complexes caused by

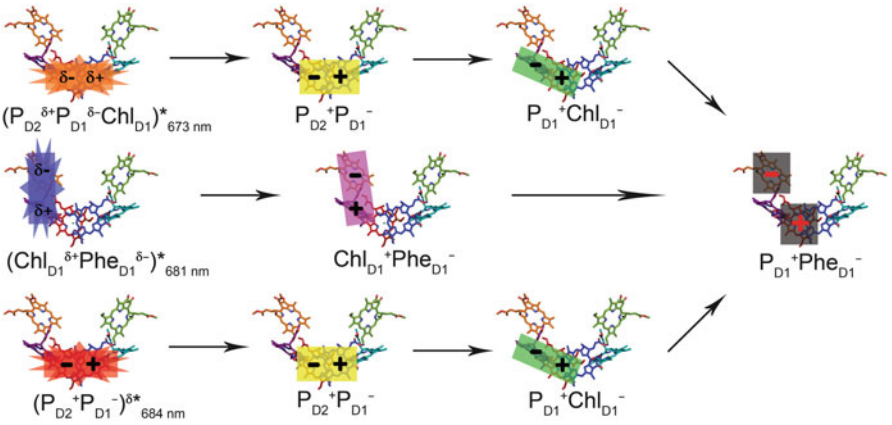

Fig. 3.13 Two charge-separation pathways scheme. Two different pathways for charge separation in the PSII RC: excitation energy and charge distribution of the electronic states involved in charge separation. *Top* and *bottom*: Charge separation via the P_{D1} path. *Center*: Charge separation via the Chl_{D1} path. The excited states are represented as *stars*, the radical pairs are represented as *rectangles*. X-ray structure adapted from the following reference [12]

the slow protein motions (i.e., their static disorder) enables the complexes to follow different pathways for CS (see Fig. 3.13).

The modeling of this experimental data allowed for a further verification (and refinement) of the exciton model [105]. That work shows that the model including two CS pathways is in much better agreement with the experimental data than the model with a single pathway.

3.5.5 Mixing with CT States: Experimental Evidence

The efficiency of the first CS step depends on the electronic characteristics of the exciton states. The efficiency is high if the electron-density distribution of the exciton is similar to that of the CT state. The most sensitive spectroscopic technique to investigate the presence and properties of CT states is Stark spectroscopy [106]. However, due to the spectral congestion in the PSII RC, this technique has to be applied to site-directed mutants, which allows for an unambiguous assignment of the absorption spectral bands [107]. Using this approach, it has recently been demonstrated that the configuration and transition energy of the excited states of the PSII RC can be unraveled [108]. In that study, each of the utilized mutants contained a single amino-acid mutation near one of the chlorins involved in CS (P_{D1}, P_{D2}, Chl_{D1}, Phe_{D1}), thereby inducing an energy shift in the transition energy with respect to that of the wild-type complex. By comparing the Stark spectra of the wild-type complex with that of eight different mutants it was demonstrated that the excited states that initiate CS are mixed exciton-CT states. These mixed states are

$(P_{D2}{}^{\delta+}P_{D1}{}^{\delta-}Chl_{D1})^*_{673nm}$ and $(Chl_{D1}{}^{\delta+}Phe_{D1}{}^{\delta-})^*_{681nm}$, where the superscripts δ+ and δ− indicate the partial CT character, the subscripts indicate the approximate center wavelength of the electronic transition for each mixed state and the cofactor sequence reflects the order of participation in the excitonic wave function. Moreover, the CT state $P_{D2}{}^{+}P_{D1}{}^{-}$ acquires an excited-state character due to its mixing with the $(P_{D1}P_{D2}Chl_{D1})^*$ exciton, producing the $(P_{D2}{}^{+}P_{D1}{}^{-})^{\delta*}_{684\ nm}$ CT-exciton state, where the superscript δ* indicates the partial exciton character, which is also able to initiate CS [108].

In conclusion, these results show that the pigment–protein interactions in the PSII RC fine-tune the energy of the exciton and CT states and hence the mixing between these states, a process which ultimately controls the selection and efficiency of a specific CS pathway. In this view, the protein is not just a passive spectator of the electron transfer reactions, but the active director of the action [109–111].

Combining the conclusions obtained by TA, Stark spectroscopy and theoretical modeling, we obtain the following CS pathways (see Fig. 3.13) [108]:

P_{D1} path	$(P_{D2}{}^{\delta+}P_{D1}{}^{\delta-}Chl_{D1})^*_{673\ nm} \rightarrow P_{D2}{}^{+}P_{D1}{}^{-} \rightarrow P_{D1}{}^{+}Chl_{D1}{}^{-} \rightarrow P_{D1}{}^{+}Phe_{D1}{}^{-}$
Chl_{D1} path	$(Chl_{D1}{}^{\delta+}Phe_{D1}{}^{\delta-})^*_{681\ nm} \rightarrow Chl_{D1}{}^{+}Phe_{D1}{}^{-} \rightarrow P_{D1}{}^{+}Phe_{D1}{}^{-}$
P_{D1} path	$(P_{D2}{}^{+}P_{D1}{}^{-})^{\delta*}_{684\ nm} \rightarrow P_{D2}{}^{+}P_{D1}{}^{-} \rightarrow P_{D1}{}^{+}Chl_{D1}{}^{-} \rightarrow P_{D1}{}^{+}Phe_{D1}{}^{-}$

3.5.6 Quantum Coherence and Charge Separation in the PSII RC

The CS process in the PSII RC is extremely efficient, with near-unity quantum efficiency, despite the strong energetic disorder present in the system. One strategy to overcome disorder is the functional flexibility of the PSII RC, i.e., the possibility to follow different CS pathways (see Sect. 3.5.4 and [103]). However, is this strategy enough to explain such an efficiency? Or are there more effects at play? One plausible answer is the presence of quantum effects which have previously been observed in bacterial RCs [112, 113] and antenna complexes [30–35].

In order to investigate the presence and the possible role of quantum effects in the PSII RC, the system has recently been studied by two-dimensional electronic spectroscopy (2DES) [114]. 2DES is an emerging nonlinear spectroscopic technique to study quantum effects in photosynthetic complexes [115–117]. Briefly, in these experiments the sample is excited with a pair of temporally ultrashort and spectrally broad excitation laser pulses, while the photon echo stimulated by a third laser pulse is measured. The 2D spectra, which are obtained by a double Fourier transform of the measured signal, correlate excitation and emission events as a function of the delay time (i.e., the population time). The spectra of the PSII RC are very rich in information, in particular the cross-peaks which reflect energy transfer and/or coherences between exciton states [30].

The dynamics of quantum coherences are visualized as amplitude oscillatory features in the spectral traces [31–33, 118]. The presence of electronic and/or vibrational coherences as well as the interplay between them are currently under investigation. Our disordered exciton–CT model predicts that the degree of coherent mixing between exciton-CT states (determined by energetic disorder, which is induced by slow conformational changes of the complex) is related to the high speed and efficiency of the CS process. Nevertheless, the role of quantum coherence in the CS process in the PSII RC has to be confirmed by an exhaustive analysis and modeling of the 2DES experimental data.

3.6 Concluding Remarks

We show that nonlinear spectroscopy in combination with modeling that is based on high-resolution crystal structures have unveiled the pathways of energy transfer in the major plant light-harvesting complex LHCII and in the reaction center of plant Photosystem II (PSII RC). In these complexes a strong coupling within pigment clusters is present together with weak coupling between the clusters and separated monomeric sites, giving rise to a complicated interplay of fast exciton relaxation and slow migration. Obviously, the traditional Förster theory for excitation energy transfer among weakly coupled chromophores does not work in this case. A self-consistent description of the dynamics and steady-state spectra can only be obtained using a unified physical model valid for an arbitrary degree of delocalization, like modified Redfield or modified Redfield–Förster theory. However, a description of mixing with CT states requires even more sophisticated approaches, where dynamics along nuclear coordinates can be treated explicitly.

A combination of increasingly realistic physics with new experimental results provides the unique possibility to reveal the exact nature of elementary events and their interplay in the excitation dynamics of photosynthetic pigment–protein complexes. Simultaneous quantitative fittings of the steady-state spectra and nonlinear kinetics, using a global systematic model, have been done successfully for the LHCII complex and the PSII RC. On the other hand, modeling of the whole core complexes, different interacting complexes within PSII and regulatory processes such as NPQ remains a challenge due to the complexity of the system.

Acknowledgments This work was supported by the EU FP6 Marie Curie Early Stage Training Network via the Advanced Training in Laser Sciences project (T.P.J.K.); a visitor's grant from the Netherlands Organization for Scientific Research (NWO) (V.N.), the Russian Foundation for Basic Research (12-04-01085) (V.N.); TOP grant (700.58.305) from the Foundation of Chemical Sciences (CW), part of the NWO (T.P.J.K. and R.v.G.), and the Advanced Investigator Grant (267333, PHOTPROT) from the European Research Council (ERC) (T.P.J.K., E.R., and R.v.G.).

References

1. Novoderezhkin VI, van Grondelle R. Physical origins and models of energy transfer in photosynthetic light-harvesting. Phys Chem Chem Phys. 2010;12(27):7352–65.
2. van Amerongen H, Valkunas L, van Grondelle R. Photosynthetic excitons. Singapore: World Scientific Publishing; 2000.
3. van Grondelle R, Dekker JP, Gillbro T, Sundstrom V. Energy-transfer and trapping in photosynthesis. Biochim Biophys Acta Bioenerg. 1994;1187(1):1–65.
4. Renger G, Renger T. Photosystem II: the machinery of photosynthetic water splitting. Photosynth Res. 2008;98(1–3):53–80.
5. Liu Z, Yan H, Wang K, Kuang T, Zhang J, Gui L, et al. Crystal structure of spinach major light-harvesting complex at 2.72 A resolution. Nature. 2004;428(6980):287–92.
6. Standfuss J, Terwisscha van Scheltinga AC, Lamborghini M, Kuhlbrandt W. Mechanisms of photoprotection and nonphotochemical quenching in pea light-harvesting complex at 2.5 A resolution. EMBO J. 2005;24(5):919–28.
7. Jordan P, Fromme P, Witt HT, Klukas O, Saenger W, Krauss N. Three-dimensional structure of cyanobacterial photosystem I at 2.5 angstrom resolution. Nature. 2001;411(6840):909–17.
8. Ferreira KN, Iverson TM, Maghlaoui K, Barber J, Iwata S. Architecture of the photosynthetic oxygen-evolving center. Science. 2004;303(5665):1831–8.
9. Guskov A, Kern J, Gabdulkhakov A, Broser M, Zouni A, Saenger W. Cyanobacterial photosystem II at 2.9-Angström resolution and the role of quinones, lipids, channels and chloride. Nat Struct Mol Biol. 2009;16(3):334–42.
10. Kamiya N, Shen JR. Crystal structure of oxygen-evolving photosystem II from *Thermosynechococcus vulcanus* at 3.7-angstrom resolution. Proc Natl Acad Sci U S A. 2003;100(1):98–103.
11. Loll B, Kern J, Saenger W, Zouni A, Biesiadka J. Towards complete cofactor arrangement in the 3.0 Å resolution structure of photosystem II. Nature. 2005;438:1040–4.
12. Umena Y, Kawakami K, Shen JR, Kamiya N. Crystal structure of oxygen-evolving photosystem II at a resolution of 1.9Å. Nature. 2011;473:55–60.
13. Zouni A, Witt HT, Kern J, Fromme P, Krauss N, Saenger W, et al. Crystal structure of photosystem II from *Synechococcus elongatus* at 3.8 Angström resolution. Nature. 2001;409 (6821):739–43.
14. Ruban AV, Johnson MP, Duffy CDP. The photoprotective molecular switch in the photosystem II antenna. Biochim Biophys Acta Bioenerg. 2012;1817(1):167–81.
15. Krüger TPJ, Ilioaia C, Johnson MP, Ruban AV, Papagiannakis E, Horton P, et al. Controlled disorder in plant light-harvesting complex II explains its photoprotective role. Biophys J. 2012;102(11):2669–76.
16. Diner BA, Rappaport F. Structure, dynamics, and energetics of the primary photochemistry of photosystem II of oxygenic photosynthesis. Annu Rev Plant Biol. 2002;53:551–80.
17. Barkai E, Jung YJ, Silbey R. Theory of single-molecule spectroscopy: beyond the ensemble average. Annu Rev Phys Chem. 2004;55:457–507.
18. Krüger TPJ, Novoderezhkin VI, Ilioaia C, van Grondelle R. Fluorescence spectral dynamics of single LHCII trimers. Biophys J. 2010;98(12):3093–101.
19. Moerner WE. A dozen years of single-molecule spectroscopy in physics, chemistry, and biophysics. J Phys Chem B. 2002;106(5):910–27.
20. Dekker JP, Van Grondelle R. Primary charge separation in photosystem II [Review]. Photosynth Res. 2000;63(3):195–208.
21. Gobets B, van Grondelle R. Energy transfer and trapping in photosystem I. Biochim Biophys Acta Bioenerg. 2001;1507(1–3):80–99.
22. Renger T, May V, Kuhn O. Ultrafast excitation energy transfer dynamics in photosynthetic pigment-protein complexes. Phys Rep. 2001;343(3):138–254.

23. Renger T, Schlodder E. Modeling of optical spectra and light harvesting in photosystem I. In: Golbeck JH, editor. Photosystem I: the light-driven plastocyanin: ferredoxin oxidoreductase, Advances in photosynthesis and respiration. Dordrecht: Springer; 2006. p. 595–610.
24. Savikhin S, Golbeck JH. Ultrafast optical spectroscopy of Photosystem I. In: Golbeck JH, editor. Photosystem I: the light-driven plastocyanin: ferredoxin oxidoreductase. Dordrecht: Springer; 2006. p. 155–75.
25. van Amerongen H, Dekker JP. Light-harvesting antennas in photosynthesis. Dordrecht: Kluwer Academic Publishers; 2003.
26. Van Grondelle R, Gobets B. Transfer and trapping of excitations in plant photosystems. In: Papageorgiou CC, Govindjee, editors. Chlorophyll a fluorescence, a signature of photosynthesis. Heidelberg: Springer; 2005. p. 107–32.
27. van Grondelle R, Novoderezhkin VI. Energy transfer in photosynthesis: experimental insights and quantitative models. Phys Chem Chem Phys. 2006;8(7):793–807.
28. Novoderezhkin VI, Dekker JP, Van Grondelle R. Mixing of exciton and charge-transfer states in photosystem II reaction centers: modeling of stark spectra with modified Redfield theory. Biophys J. 2007;93(4):1293–311.
29. Novoderezhkin VI, Palacios MA, van Amerongen H, van Grondelle R. Excitation dynamics in the LHCII complex of higher plants: modeling based on the 2.72 Å crystal structure. J Phys Chem B. 2005;109(20):10493–504.
30. Brixner T, Stenger J, Vaswani HM, Cho M, Blankenship RE, Fleming GR. Two-dimensional spectroscopy of electronic couplings in photosynthesis. Nature. 2005;434:625–8.
31. Collini E, Wong CY, Wilk KE, Curmi PMG, Brumer P, Scholes GD. Coherently wired light-harvesting in photosynthetic marine algae at ambient temperature. Nature. 2010;463 (7281):644–7.
32. Engel GS, Calhoun TR, Read EL, Ahn TK, Mancal T, Cheng YC, et al. Evidence for wavelike energy transfer through quantum coherence in photosynthetic systems. Nature. 2007;446(7137):782–6.
33. Panitchayangkoon G, Hayes D, Fransted KA, Caram JR, Harel E, Wen J, et al. Long-lived quantum coherence in photosynthetic complexes at physiological temperature. Proc Natl Acad Sci U S A. 2010;107:12766–70.
34. Read EL, Engel GS, Calhoun TR, Mancal T, Ahn TK, Blankenship RE, et al. Cross-peak-specific two-dimensional electronic spectroscopy. Proc Natl Acad Sci U S A. 2007;104 (36):14203–8.
35. Scholes GD, Fleming GR, Olaya-Castro A, van Grondelle R. Lessons from nature about solar light harvesting. Nat Chem. 2011;3(10):763–74.
36. Meier T, Chernyak V, Mukamel S. Femtosecond photon echoes in molecular aggregates. J Chem Phys. 1997;107(21):8759–80.
37. Mukamel S. Principles of nonlinear optical spectroscopy. Oxford: Oxford University Press; 1995.
38. Zhang WM, Meier T, Chernyak V, Mukamel S. Exciton-migration and three-pulse femtosecond optical spectroscopies of photosynthetic antenna complexes. J Chem Phys. 1998;108 (18):7763–74.
39. Novoderezhkin VI, Andrizhiyevskaya EG, Dekker JP, Van Grondelle R. Pathways and timescales of primary charge separation in the photosystem II reaction center as revealed by a simultaneous fit of time-resolved fluorescence and transient absorption. Biophys J. 2005;89:1464–81.
40. Novoderezhkin VI, Palacios MA, van Amerongen H, van Grondelle R. Energy-transfer dynamics in the LHCII complex of higher plants: modified Redfield approach. J Phys Chem B. 2004;108(29):10363–75.
41. Raszewski G, Saenger W, Renger T. Theory of optical spectra of photosystem II reaction centers: location of the triplet state and the identity of the primary electron donor. Biophys J. 2005;88(2):986–98.

42. Renger T, Marcus RA. On the relation of protein dynamics and exciton relaxation in pigment-protein complexes: an estimation of the spectral density and a theory for the calculation of optical spectra. J Chem Phys. 2002;116(22):9997–10019.
43. Cho MH, Vaswani HM, Brixner T, Stenger J, Fleming GR. Exciton analysis in 2D electronic spectroscopy. J Phys Chem B. 2005;109(21):10542–56.
44. Damjanovic A, Kosztin I, Kleinekathofer U, Schulten K. Excitons in a photosynthetic light-harvesting system: a combined molecular dynamics, quantum chemistry, and polaron model study. Phys Rev E. 2002;65(3):031919–43.
45. Pieper J, Voigt J, Renger G, Small GJ. Analysis of phonon structure in line-narrowed optical spectra. Chem Phys Lett. 1999;310(3–4):296–302.
46. Peterman EJG, Gradinaru CC, Calkoen F, Borst JC, van Grondelle R, van Amerongen H. Xanthophylls in light-harvesting complex II of higher plants: light harvesting and triplet quenching. Biochemistry. 1997;36(40):12208–15.
47. Peterman EJG, van Amerongen H, van Grondelle R, Dekker JP. The nature of the excited state of the reaction center of photosystem II of green plants: a high-resolution fluorescence spectroscopy study. Proc Natl Acad Sci U S A. 1998;95(11):6128–33.
48. Yang MN, Fleming GR. Influence of phonons on exciton transfer dynamics: comparison of the Redfield, Forster, and modified Redfield equations. Chem Phys. 2002;275(1–3):355–72.
49. Förster T. Delocalized excitation and excitation transfer. In: Sinanoglu O, editor. Modern quantum chemistry. New York: Academic; 1965. p. 93–137.
50. Jang S, Newton MD, Silbey RJ. Multichromophoric Forster resonance energy transfer. Phys Rev Lett. 2004;92:218301(1–4).
51. Novoderezhkin VI, Razjivin AP. Exciton states of the antenna and energy trapping by the reaction center. Photosynth Res. 1994;42:9–15.
52. Novoderezhkin VI, Razjivin AP. The theory of Förster-type migration between clusters of strongly interacting molecules: application to light-harvesting complexes of purple bacteria. Chem Phys. 1996;211:203–14.
53. Scholes GD, Fleming GR. On the mechanism of light harvesting in photosynthetic purple bacteria: B800 to B850 energy transfer. J Phys Chem B. 2000;104(8):1854–68.
54. Sumi H. Theory on rates of excitation-energy transfer between molecular aggregates through distributed transition dipoles with application to the antenna system in bacterial photosynthesis. J Phys Chem B. 1999;103(1):252–60.
55. Yang M, Damjanovic A, Vaswani HM, Fleming GR. Energy transfer in photosystem I of cyanobacteria *Synechococcus elongatus*: model study with structure-based semi-empirical Hamiltonian and experimental spectral density. Biophys J. 2003;85(1):140–58.
56. Novoderezhkin VI, Marin A, van Grondelle R. Intra- and inter-monomeric transfers in the light harvesting LHCII complex: the Redfield-Förster picture. Phys Chem Chem Phys. 2011;13:17093–103.
57. Renger T, Madjet ME, Knorr A, Muh F. How the molecular structure determines the flow of excitation energy in plant light-harvesting complex II. J Plant Physiol. 2011;168:1497–509.
58. Parson WW, Warshel A. Spectroscopic properties of photosynthetic reaction centers. 2. Application of the theory to Rhodopseudomonas-viridis. J Am Chem Soc. 1987;109 (20):6152–63.
59. Warshel A, Parson WW. Spectroscopic properties of photosynthetic reaction centers. 1. Theory. J Am Chem Soc. 1987;109(20):6143–52.
60. Jean JM, Fleming GR. Competition between energy and phase relaxation in electronic curve crossing processes. J Chem Phys. 1995;103(6):2092–101.
61. Novoderezhkin VI, Yakovlev AG, Van Grondelle R, Shuvalov VA. Coherent nuclear and electronic dynamics in primary charge separation in photosynthetic reaction centers: a Redfield theory approach. J Phys Chem B. 2004;108:7445–57.
62. Renger T, May V. Theory of multiple exciton effects in the photosynthetic antenna complex LHC-II. J Phys Chem B. 1997;101(37):7232–40.

63. Gradinaru CC, Ozdemir S, Gulen D, van Stokkum IHM, van Grondelle R, van Amerongen H. The flow of excitation energy in LHCII monomers: implications for the structural model of the major plant antenna. Biophys J. 1998;75(6):3064–77.
64. Kleima FJ, Gradinaru CC, Calkoen F, van Stokkum IHM, van Grondelle R, van Amerongen H. Energy transfer in LHCII monomers at 77K studied by sub-picosecond transient absorption spectroscopy. Biochemistry. 1997;36(49):15262–8.
65. Visser HM, Kleima FJ, van Stokkum IHM, van Grondelle R, van Amerongen H. Probing the many energy-transfer processes in the photosynthetic light-harvesting complex II at 77 K using energy-selective sub-picosecond transient absorption spectroscopy. Chem Phys. 1996;210(1–2):297–312.
66. Bopp MA, Sytnik A, Howard TD, Cogdell RJ, Hochstrasser RM. The dynamics of structural deformations of immobilized single light-harvesting complexes. Proc Natl Acad Sci U S A. 1999;96(20):11271–6.
67. Novoderezhkin VI, Rutkauskas D, van Grondelle R. Dynamics of the emission spectrum of a single LH2 complex: interplay of slow and fast nuclear motions. Biophys J. 2006;90 (8):2890–902.
68. Rutkauskas D, Cogdell RJ, van Grondelle R. Conformational relaxation of single bacterial light-harvesting complexes. Biochemistry. 2006;45(4):1082–6.
69. Rutkauskas D, Novoderezkhin V, Cogdell RJ, van Grondelle R. Fluorescence spectral fluctuations of single LH2 complexes from *Rhodopseudomonas acidophila* strain 10050. Biochemistry. 2004;43(15):4431–8.
70. Rutkauskas D, Olsen J, Gall A, Cogdell RJ, Hunter CN, van Grondelle R. Comparative study of spectral flexibilities of bacterial light-harvesting complexes: structural implications. Biophys J. 2006;90(7):2463–74.
71. Tietz C, Chekhlov O, Drabenstedt A, Schuster J, Wrachtrup J. Spectroscopy on single light-harvesting complexes at low temperature. J Phys Chem B. 1999;103(30):6328–33.
72. van Oijen AM, Ketelaars M, Kohler J, Aartsma TJ, Schmidt J. Unraveling the electronic structure of individual photosynthetic pigment-protein complexes. Science (New York, NY). 1999;285(5426):400–2.
73. Croce R, Chojnicka A, Morosinotto T, Ihalainen JA, van Mourik F, Dekker JP, et al. The low-energy forms of photosystem I light-harvesting complexes: spectroscopic properties and pigment-pigment interaction characteristics. Biophys J. 2007;93(7):2418–28.
74. Romero E, Mozzo M, van Stokkum IHM, Dekker JP, van Grondelle R, Croce R. The origin of the low-energy form of photosystem I light-harvesting complex Lhca4: mixing of the lowest exciton with a charge-transfer state. Biophys J. 2009;96(5):L35–7.
75. Elber R, Karplus M. Multiple conformational states of proteins—a molecular-dynamics analysis of myoglobin. Science. 1987;235(4786):318–21.
76. Frauenfelder H, Petsko GA, Tsernoglou D. Temperature-dependent X-ray-diffraction as a probe of protein structural dynamics. Nature. 1979;280(5723):558–63.
77. Frauenfelder H, Sligar SG, Wolynes PG. The energy landscapes and motions of proteins. Science. 1991;254(5038):1598–603.
78. Hofmann C, Aartsma TJ, Michel H, Kohler J. Direct observation of tiers in the energy landscape of a chromoprotein: a single-molecule study. Proc Natl Acad Sci U S A. 2003;100(26):15534–8.
79. Ruban AV, Berera R, Ilioaia C, van Stokkum IHM, Kennis JTM, Pascal AA, et al. Identification of a mechanism of photoprotective energy dissipation in higher plants. Nature. 2007;450(7169):575–U22.
80. Pascal AA, Liu ZF, Broess K, van Oort B, van Amerongen H, Wang C, et al. Molecular basis of photoprotection and control of photosynthetic light-harvesting. Nature. 2005;436 (7047):134–7.
81. Ilioaia C, Johnson MP, Horton P, Ruban AV. Induction of efficient energy dissipation in the isolated light-harvesting complex of photosystem II in the absence of protein aggregation. J Biol Chem. 2008;283(43):29505–12.

82. Ilioaia C, Johnson MP, Liao P-N, Pascal AA, van Grondelle R, Walla PJ, et al. Photoprotection in plants involves a change in lutein 1 binding domain in the major light-harvesting complex of photosystem II. J Biol Chem. 2011;286(31):27247–54.
83. Bilger W, Björkman O. Relationships among violaxanthin deepoxidation, thylakoid membrane conformation, and nonphotochemical chlorophyll fluorescence quenching in leaves of cotton (*Gossypium-hirsutum* L). Planta. 1994;193(2):238–46.
84. Bode S, Quentmeier CC, Liao PN, Hafi N, Barros T, Wilk L, et al. On the regulation of photosynthesis by excitonic interactions between carotenoids and chlorophylls. Proc Natl Acad Sci U S A. 2009;106(30):12311–6.
85. Horton P, Ruban AV, Walters RG. Regulation of light harvesting in green plants. Annu Rev Plant Physiol Plant Mol Biol. 1996;47:655–84.
86. Johnson MP, Ruban AV. Photoprotective energy dissipation in higher plants involves alteration of the excited state energy of the emitting chlorophyll(s) in the light harvesting antenna II (LHCII). J Biol Chem. 2009;284(35):23592–601.
87. Ruban AV, Horton P. Mechanism of [Delta]pH-dependent dissipation of absorbed excitation energy by photosynthetic membranes. I. Spectroscopic analysis of isolated light-harvesting complexes. Biochim Biophys Acta Bioenerg. 1992;1102(1):30–8.
88. Horton P, Johnson MP, Perez-Bueno ML, Kiss AZ, Ruban AV. Photosynthetic acclimation: does the dynamic structure and macro-organisation of photosystem II in higher plant grana membranes regulate light harvesting states? FEBS J. 2008;275(6):1069–79.
89. Krüger TPJ, Ilioaia C, Van Grondelle R. Fluorescence intermittency from the main plant light-harvesting complex: resolving shifts between intensity levels. J Phys Chem B. 2011;115 (18):5071–82.
90. Kulzer F, Orrit M. Single-molecule optics. Annu Rev Phys Chem. 2004;55:585–611.
91. Krüger TPJ, Ilioaia C, Johnson MP, Belgio E, Ruban AV, Horton P, Van Grondelle R. The specificity of controlled protein disorder in the photoprotection of plants. Biophys J. 2013;105(4):1018–26.
92. Valkunas L, Chmeliov J, Krüger TPJ, Ilioaia C, van Grondelle R. How photosynthetic proteins switch. J Phys Chem Lett. 2012;3(19):2779–84.
93. Tsai CJ, Kumar S, Ma BY, Nussinov R. Folding funnels, binding funnels, and protein function. Protein Sci. 1999;8(6):1181–90.
94. Boehr DD, Nussinov R, Wright PE. The role of dynamic conformational ensembles in biomolecular recognition. Nat Chem Biol. 2009;5(11):789–96.
95. Wahadoszamen M, Berera R, Ara AM, Romero E, van Grondelle R. Identification of two emitting sites in the dissipative state of the major light harvesting antenna. Phys Chem Chem Phys. 2012;14(2):759–66.
96. Krüger TPJ, Wientjes E, Croce R, van Grondelle R. Conformational switching explains the intrinsic multifunctionality of plant light-harvesting complexes. Proc Natl Acad Sci U S A. 2011;108(33):13516–21.
97. Barber J. Photosystem II: the engine of life. Q Rev Biophys. 2003;36(1):71–89.
98. Yoder LM, Cole AG, Sension RJ. Structure and function in the isolated reaction center complex of photosystem II: energy and charge transfer dynamics and mechanism. Photosynth Res. 2002;72(2):147–58.
99. Durrant JR, Klug DR, Kwa SLS, Van Grondelle R, Porter G, Dekker JP. A multimer model for P680, the primary electron-donor of photosystem-II. Proc Natl Acad Sci U S A. 1995;92 (11):4798–802.
100. Barter LMC, Durrant JR, Klug DR. A quantitative structure-function relationship for the photosystem II reaction center: supermolecular behavior in natural photosynthesis. Proc Natl Acad Sci U S A. 2003;100(3):946–51.
101. Leegwater JA, Durrant JR, Klug DR. Exciton equilibration induced by phonons: theory and application to PS II reaction centers. J Phys Chem B. 1997;101(37):7205–10.
102. Prokhorenko VI, Holzwarth AR. Primary processes and structure of the photosystem II reaction center: a photon echo study. J Phys Chem B. 2000;104(48):11563–78.

103. Romero E, van Stokkum IHM, Novoderezhkin VI, Dekker JP, van Grondelle R. Two different charge separation pathways in photosystem II. Biochemistry. 2010;49:4300–7.
104. van Stokkum IHM, Larsen DS, van Grondelle R. Global and target analysis of time-resolved spectra. Biochim Biophys Acta. 2004;1657(2–3):82–104.
105. Novoderezhkin VI, Romero E, Dekker JP, van Grondelle R. Multiple charge separation pathways in photosystem II: modeling of transient absorption kinetics. ChemPhysChem. 2011;12:681–8.
106. Boxer SG. Stark spectroscopy of photosynthetic systems. In: Amesz J, Hoff AJ, editors. Biophysical techniques in photosynthesis. Dordrecht: Kluwer Academic Publishers; 1996. p. 177–89.
107. Diner BA, Schlodder E, Nixon PJ, Coleman WJ, Rappaport F, Lavergne J, et al. Site-directed mutations at D_1-His198 and D_2-His197 of photosystem II in *Synechocystis* PCC 6803: sites of primary charge separation and cation triplet stabilization. Biochemistry. 2001;40:9265–81.
108. Romero E, Diner BA, Nixon PJ, Coleman WJ, Dekker JP, van Grondelle R. Mixed exciton-charge-transfer states in photosystem II: Stark spectroscopy on site-directed mutants. Biophys J. 2012;103:185–94.
109. Brecht M, Radics V, Nieder JB, Bittl R. Protein dynamics-induced variation of excitation energy transfer pathways. Proc Natl Acad Sci U S A. 2009;106(29):11857–61.
110. Lin JP, Balabin IA, Beratan DN. The nature of aqueous tunneling pathways between electron-transfer proteins. Science. 2005;301:1311–3.
111. Wang H, Lin S, Allen JP, Williams JC, Blankert S, Laser C, et al. Protein dynamics control the kinetics of initial electron transfer in photosynthesis. Science. 2007;316(5825):747–50.
112. Lee H, Cheng Y-C, Fleming GR. Coherence dynamics in photosynthesis: protein protection of excitonic coherence. Science. 2007;316(5830):1462–5.
113. Westenhoff S, Palecek D, Edlund P, Smith P, Zigniantas D. Coherent picosecond exciton dynamics in a photosynthetic reaction center. J Am Chem Soc. 2012;134(40):16484–7.
114. Romero E, Augulis R, Novoderezhkin VI, Ferretti M, Thieme J, Zigmantas D, et al. Photosynthesis exploits quantum coherence for efficient energy conversion. Manuscript in preparation.
115. Ginsberg NS, Cheng YC, Fleming GR. Two-dimensional electronic spectroscopy of molecular aggregates. Acc Chem Res. 2009;42(9):1352–63.
116. Read EL, Lee H, Fleming GR. Photon echo studies of photosynthetic light harvesting. Photosynth Res. 2009;101:233–43.
117. Schlau-Cohen GS, Dawlaty JM, Fleming GR. Ultrafast multidimensional spectroscopy: principles and applications to photosynthetic systems. IEEE J Sel Topics Quant Electron. 2012;18(1):283–95.
118. Cheng YC, Fleming GR. Coherence quantum beats in two-dimensional electronic spectroscopy. J Phys Chem A. 2008;112:4254–60.
119. Van Grondelle R, Dekker JP, Novoderezhkin VI. Modeling light-harvesting and primary charge separation in photosystem I and photosystem II. Photosynthesis in silico: understanding complexity from molecules to ecosystems. Dordrecht: Springer; 2009.

Part II
Underlying Principles of Electron Transport

Chapter 4
Tunneling in Electron Transport

Christopher C. Moser

Abstract Light excitation of chlorophylls and bacteriochlorophylls creates strong reductants to initiate guided electron transfer through chains of redox centers, converting light energy into electrostatic and chemical redox energy and largely avoiding the threat of charge recombination unless useful. Most electron-transfer reactions of photosynthesis are single-electron transfers between well-separated redox centers via electron tunneling through the insulating intervening protein medium. Tunneling rates are dominated by an exponential dependence on the edge-to-edge distance between cofactors. There is an approximately Gaussian dependence of rate on driving force, with a peak rate at the reorganization energy, as defined by classical Marcus theory and modified to include quantum effects. Complex quantum theoretical rate dependencies are well approximated by a simple empirical expression with three parameters: distance, driving force, and reorganization energy. Natural selection exploits distance and driving force to speed desirable electron transfers or slow undesirable electron transfer. Redox centers engaged in productive electron transfer are placed less than 14 Å apart. Natural photosynthetic proteins are far from ideal: they have high yields but a superabundance of cofactors and relatively large energy losses.

Keywords Electron-transfer chains • Electron tunneling • Marcus theory • Photosynthesis • Reaction centers • Reorganization energy

C.C. Moser, Ph.D. (✉)
Department of Biochemistry and Biophysics, University of Pennsylvania,
422 Curie Blvd, Philadelphia, PA 19104-6059, USA
e-mail: moserc@mail.med.upenn.edu

J. Golbeck and A. van der Est (eds.), *The Biophysics of Photosynthesis*,
Biophysics for the Life Sciences 11, DOI 10.1007/978-1-4939-1148-6_4,

Abbreviations

ADP	Adenosine diphosphate
ATP	Adenosine triphosphate
NADH	Reduced nicotinamide adenine dinucleotide
PSI	Photosystem I
PSII	Photosystem II
λ	Reorganization energy
ΔG	Free energy of reaction
$\hbar\omega$	Characteristic frequency of vibration coupled to electron transfer

4.1 Concept 1: Light Excitation of Chlorophylls and Bacteriochlorophylls Creates Strong Reductants for Charge Separation

The act of exciting a photosynthetic pigment promotes an electron to a higher energy level and leaves an empty orbital behind. This simultaneously creates a good reductant in the excited electron, and a good oxidant in the empty orbital or "hole" left behind. While the light-activated flavoproteins such as photolyase or cryptochrome [1, 2] use the excited state as a photo-oxidant, filling the emptied orbital with an electron from a nearby reductant such as tryptophan or tyrosine, the chlorophylls and bacteriochlorophylls of photosynthesis are biased to act as photo-reductants such that the initial electron transfer is the reduction of a nearby redox cofactor by the excited pigment.

The chlorins and bacteriochlorins of photosynthesis are tetrapyrrole rings with extensive conjugation of two dozen nitrogen and carbon p-orbitals that leads to large molecular orbitals about 10 Å across. This means that light absorption will be red-shifted from the typical ultraviolet absorption of smaller organic molecules into the red and infrared regions, respectively. The lowest excited-state energies associated with these electronic transitions are around 1.8–1.1 eV (deep red 680 nm to infrared 1,100 nm). With an oxidation/reduction potential of the ground-state chlorophyll of +1.26 (vs. the standard hydrogen electrode) in PSII [3], the absorbed photon lowers the reducing potential of the excited singlet state to ~ −0.57 V. The protein environment of the P700 chlorophyll of PSI lends the ground-state pigment considerably more reducing power at ~0.45 V [4]; even though the absorbed photon has nearly the same energy, the excited singlet state is also much more reducing, ~−1.32 V. These excited state redox potentials are low enough to reduce most biological redox centers.

4.2 Concept 2: Photosynthesis Uses Light-Activated Charge Separation and Guided Electron Transfer to Convert Light Energy into Electrostatic and Chemical Redox Energy

In natural photosynthetic proteins, redox centers are placed relatively close together so that electrons are guided by proximity through a series of redox cofactors assembled across a bioenergetic membrane (Fig. 4.1) that are, to first approximation, progressively more oxidizing. This results in the loss of reducing power, but converts the electrostatic energy of charge separation into a transmembrane electric field. When the electron reaches a quinone redox center in PSII and purple sulfur bacterial reaction centers, reduction may be accompanied by the uptake of a proton, contributing to transmembrane proton gradients. The transmembrane electric field and proton gradient represent an electrochemical proton gradient. This distributed energy currency can be used to power other transmembrane events such as the pumping of molecules across the membrane counter to their concentration gradients or into the energetically uphill chemical reaction of phosphorylating ADP to ATP using the transmembrane ATPase protein. The redox energy of the original charge separation is preserved in relatively stable form in chemical oxidants and reductants. In the case of plant photosynthesis, this is molecular oxygen, the product of water splitting in PSII, and chemically reduced species such as NADH or glucose.

4.3 Concept 3: Charge Recombination Poses the Threat of Energy Loss, Though Sometimes This Is Useful

The progressive charge separation along the chain of redox cofactors competes with charge recombination to either an excited state or the low-energy ground state. Electron spins are important in the both the time scale and energetics of charge recombination. At first, the light-excited electron maintains the same spin state as in the ground state; both are called singlets. Charge recombination to the excited state can occur before electron spins rephase, recreating the excited singlet state, which can again engage in productive electron transfer or return to the ground state by emitting a photon in fluorescence. Alternatively, charge recombination can short-circuit to the ground state, which has the net effect of turning light energy into heat. Normal fluorescence of chlorins and bacteriochlorins occurs on the nanosecond time scale [8]. Emission from this thermally assisted return of the electron to the singlet state is called delayed fluorescence. During the time of charge separation, magnetic interactions can rephase the electron spin from singlet to triplet; in this case charge recombination occurs to a generally lower energy-excited triplet state. As the spins must flip to recreate the singlet ground state, return to the ground state is considerably slower,

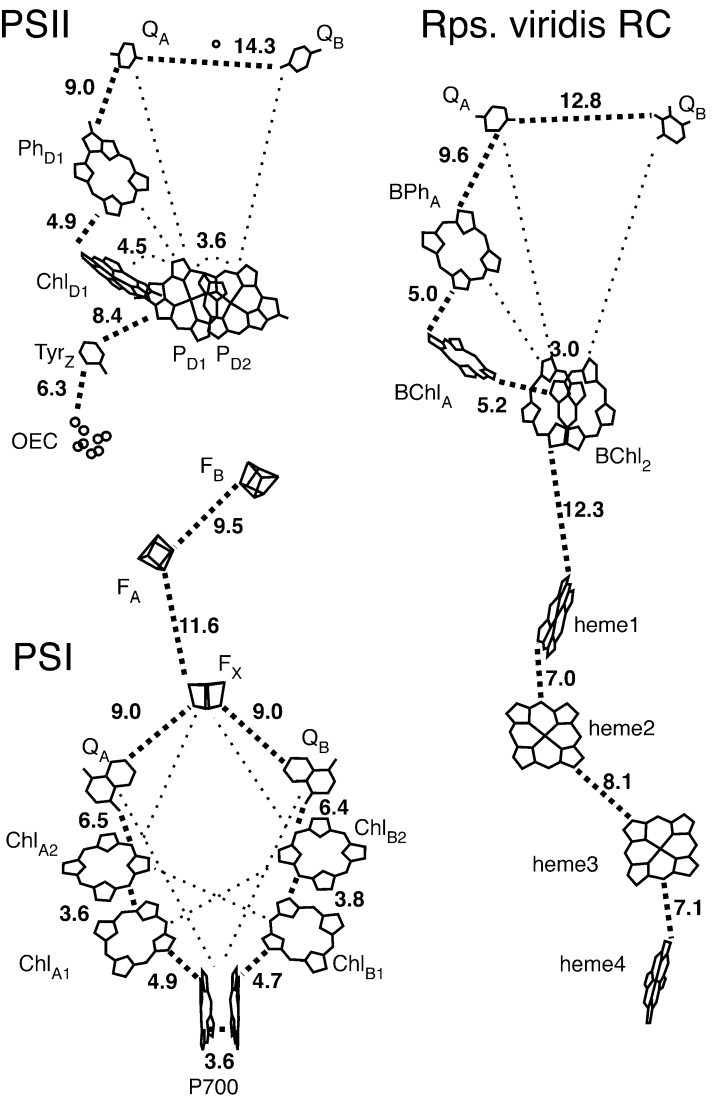

Fig. 4.1 Productive electron transfer is guided across the membrane (vertical direction) in natural photosynthetic reaction centers by the proximity of the redox cofactors. Productive reactions are *thick dashed lines*, unproductive short circuits are *thin*. Photosystem I and II use chlorophylls ChlD1 and P700 as light-activated centers and the photosynthetic bacteria use a bacteriochlorophyll $BChl_2$. Edge-to-edge distances between cofactors are given by crystal structures available in the PDB database 1JBO [5], 1S5L [6], and 1PRC [7]

emitting a lower energy photon in phosphorescence. Magnetic sensitivity allows flavoproteins in some organisms to sense the earth's magnetic field direction.

Although loss of the light energy in the form of lower energy photons and heat due to charge recombination is not bioenergetically productive, it can nevertheless

have important survival value. Under high-light conditions, or when assembly of the photosystems are incomplete, charges can be separated faster than they can be consumed by the rest of the photosynthetic machinery. The powerful oxidizing and reducing radicals created by light excitation can create unintended and destructive side reactions, compromising the protein structure or the pigment and redox cofactors themselves. Triplet states can also react with triplet molecular oxygen to create singlet oxygen, which is aggressively chemically reactive and can destroy nearby pigments [9]. The half-life of singlet oxygen is only about 200 ns in cells [10] allowing reactions within 10 nm of the site of production [11]. Indeed, the central subunit of PSII is replaced with regularity during normal operating conditions, presumably because of just such destructive reactions [12].

4.4 Concept 4: Most Electron-Transfer Reactions of Photosynthesis Are Single-Electron Transfers Between Well-Separated Redox Centers via Electron Tunneling Through the Insulating Intervening Protein Medium

Only a minority of electron transfers in photosynthesis occur by direct contact between diffusing oxidants and reductants. One such example is the collisional interaction between reduced NADH and oxidized flavin that can transfer a two-electron-carrying hydride group from the nicotinamide to the flavin. In the majority of electron-transfer reactions, rather than group transfer of pairs of electrons, electrons are delivered one at a time from reductants to oxidants [13, 14]. Single-electron transfer is the general rule even in cases of coupled two-electron-transfer reactions, where the second following electron transfer may be so much faster than the first that the single-electron-transfer intermediate cannot be separately observed [13]. Because the amino acids and occasional water molecules that make up the protein medium are relatively difficult to oxidize or reduce, protein acts as an electrical insulator. The single-electron transfers between redox centers that are not in direct contact must traverse the electrically insulating gap between redox centers by electron tunneling [15].

According to classical physics, the electron does not have the energy to exist in the medium between donor and acceptor, far from the donor. But quantum physics describes the electron as a wave function that can extend into this barrier region. That tunneling was indeed a central part of biology was first clearly demonstrated in photosynthetic systems, as revealed by the temperature independence of electron-transfer rates at cryogenic temperatures in photosynthetic reaction centers [16]. This temperature independence at low temperatures eliminates the possibility that some sort of thermally activated classical reaction might be taking place.

4.5 Concept 5: Electron-Tunneling Rates Are Dominated by an Exponential Dependence on the Distance Between Cofactors

Electron tunneling between well-separated redox centers in proteins is dependent upon the extent of overlap of the relevant orbitals for the electron in the donor and the acceptor—the better the overlap, the faster the rate. The wave functions tail off approximately exponentially with the distance between the cofactors, with the result that the maximum electron-tunneling rate trends to a steep exponential decay with edge-to-edge distance between cofactors (Fig. 4.2). In proteins, this coefficient of exponential decay is around 1.4 $Å^{-1}$ on a natural log scale or 0.6 $Å^{-1}$ on a common log scale [17]. This means that the electron tunneling will be ten times slower for every 1.7 Å added to the donor-to-acceptor edge-to-edge distance. The maximal electron-tunneling rate is around 10^{13} s^{-1} at distances approaching van der Waals contact, which is essentially the same as the pre-exponential term k_BT/h in Eyring's 1935 absolute reaction rate theory [18, 19], in which k_B is Boltzmann's constant, T absolute temperature, and h Planck's constant. The protein medium acts as a condensed phase that propagates wave functions better than a vacuum but not as well as a direct covalent link between redox cofactors [17].

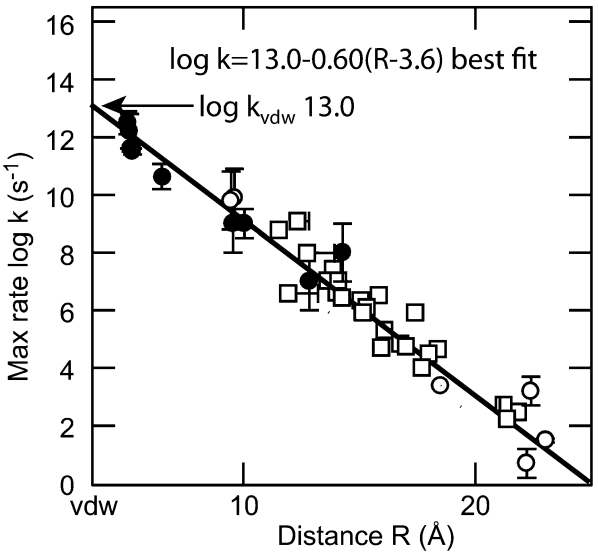

Fig. 4.2 Free energy-optimized rates of electron tunneling in proteins show an exponential dependence with edge-to-edge distance between cofactors [20]. Productive and unproductive electron transfers in photosynthetic reaction centers shown as *filled* and *open circles*, respectively [17]. *Open squares* represent electron transfers in non-photosynthetic and modified protein systems

4.6 Concept 6: Reorganization Energy Dictates the Driving Force Dependence of Electron-Tunneling Rates

Although electron tunneling is an essentially quantum mechanical phenomenon, in order for an electron to tunnel from one center to another, the donor and acceptor orbitals must be at least temporarily at equal energies, even if the overall electron-transfer reaction is energetically favorable and the equilibrium energy of the electron on the donor will be greater than the equilibrium energy on the acceptor. As the atomic nuclei fluctuate in thermal motion, the relative energies of the electron on the donor and acceptor will change for certain atomic motions that are said to be "coupled" to electron transfer. In the 1950s Marcus applied a classical harmonic oscillator viewpoint to these motions [21]. Simple harmonic oscillators have a parabolic dependence of their energy as the nuclei vibrate on either side of an equilibrium, low-energy geometry. The generalized energy surface of the reactant donor/acceptor pair with the electron on the donor is shown as the thick curve in Fig. 4.3. A similar surface applies to the energy of the product donor/acceptor pair (thin curves), with the electron now on the acceptor, but with a different equilibrium nuclear geometry and free energy at the bottom of the product parabola.

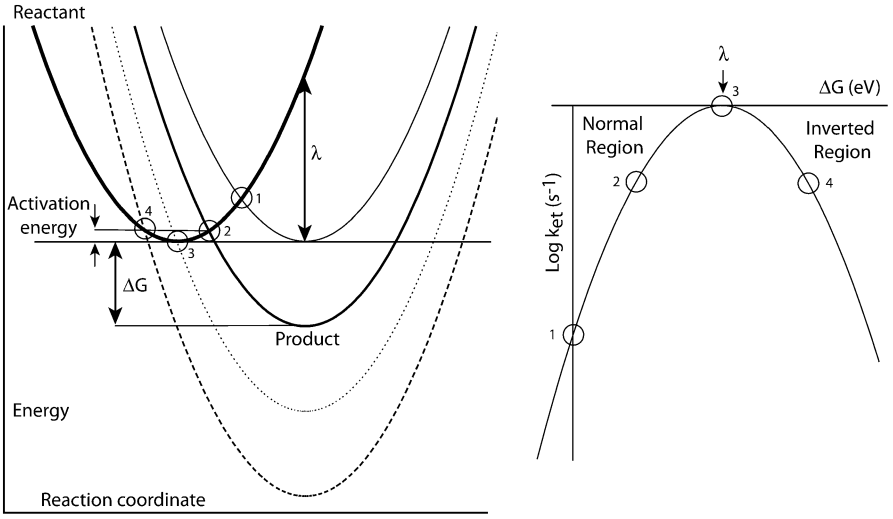

Fig. 4.3 Marcus theory considers the intersection of the energy surfaces of classical simple harmonic oscillators (*parabolas*) along a generalized reaction coordinate (*left*). The intersection of the reactant (with the tunneling electron on the donor) with the product (electron on the acceptor) takes place at different activation energies depending on the driving force for electron transfer ($-\Delta G$). Four different ΔG values are shown (1–4), all with the same reorganization energy (λ); for convenience only one ΔG and one activation energy are labeled that associated with product energy surface 2. On a log rate scale (*right*), this gives a parabolic dependence of rate on driving force with "normal" and "inverted" regions where increased driving force speeds or slows the reaction, respectively

For simplicity, we assume that there is a roughly similar frequency for the vibrational wells of the reactants and products, differing mainly in nuclear and energetic displacement. If we follow the thick energy curve of the reactant to the right as its nuclei are vibrationally moved to resemble the equilibrium geometry of the reactant, but without allowing the electron to be transferred, we would need to add energy lambda, called the reorganization energy.

This reorganization energy λ can be combined with the overall driving force for the electron transfer, $-\Delta G$, to give a classical activation energy for the electron-transfer reaction, that is, the amount of thermal energy that must be added to the equilibrium reactants in order to reach the intersection of the reactant and product surfaces: $E^{\ddagger} = (\Delta G + \lambda)^2/4\lambda$. These intersections are circled and numbered in Fig. 4.3. The activation energy for an electron transfer will begin at λ/4 when there is no net driving force for the reaction (thin curve in Fig. 4.3), and decrease to zero, for an activationless electron transfer, when the driving force matches the reorganization energy (dotted curve). In other words, the reactant ground state is the transition state. All other factors, such as the edge-to-edge distance between donor and acceptor, being the same, this will be the maximal rate at which the electron transfer can occur. If the driving force for electron transfer is even greater than the reorganization energy (dashed curve), then the activation energy will begin to rise again. Counterintuitively, Marcus theory predicts that providing more driving force for a reaction can actually slow the reaction rate. This situation in which the driving force is greater than the reorganization energy is called the Marcus inverted region, and has important significance for the design of photosynthetic systems.

The driving force and reorganization energy dependence of the electron-tunneling rate according to classical Marcus theory is as follows:

$$\text{ket} \propto \frac{1}{\sqrt{4\pi\lambda k_B T}} e^{-(\Delta G+\lambda)^2/4\lambda k_B T} \tag{4.1}$$

Classical Marcus theory predicts a Gaussian dependence of the electron-transfer rate as a function of the driving force with a peak value at λ. This Gaussian curve appears parabolic on a log rate scale (Fig. 4.4). Typical reorganization energies for biological electron-transfer reactions are around 0.7–1 eV. Larger reorganization energies, up to about 1.4 eV, are found for systems in relatively polarizable or mobile polar environments (often near protein surfaces) and with smaller cofactors for donors and acceptors. Under these conditions the change in the distribution of electric charge on moving from donor to acceptor will be more concentrated, which generally leads to a larger reorganization of the electric dipoles in the cofactor environments. Conversely, smaller reorganization energies are associated with larger cofactors and relatively immobile and low dielectric environments (often deeply buried), as the charge changes are more diffuse and the protein environment around the cofactors is less subject to reorganization on electron transfer. The most reliable way to experimentally estimate the reorganization energy of any protein

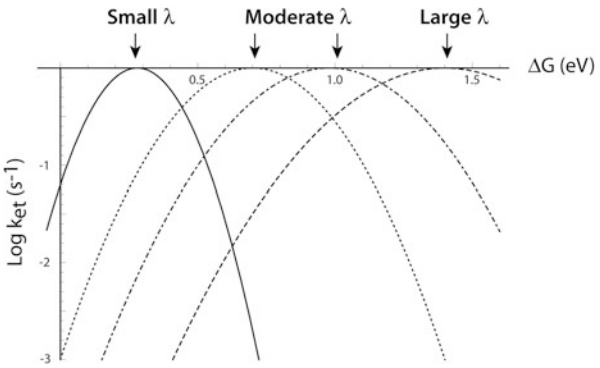

Fig. 4.4 The classical Marcus theory model for the free energy dependence of electron tunneling on driving force is parabolic on a log rate scale with a maximum when the driving force matches the reorganization energy (λ). The reorganization energies shown cover the typical biological range. A comparison can be made with Fig. 4.3: smaller reorganization or larger reorganization energies would correspond movement of the product parabola to the *left* or the *right* (smaller or larger change in nuclear coordinates) in that figure

electron-tunneling reaction is to make progressive changes in the driving force by chemical substitution of the donor or the acceptor and look for a Marcus-like dependence. This has been done for a number of different photosynthetic electron-transfer reactions [22–26].

4.7 Concept 7: The Initial Charge Separation of Photosynthesis Exploits the Marcus Inverted Region to Make Charge Recombination Slower than Charge Separation

After light excitation of a photosynthetic reaction center pigment and the initial reduction of the nearby acceptor molecule, there is a competition between electron transfer to another acceptor to further separate charges and charge recombination to the ground state. With a modest, energy-conserving driving force for the initial electron transfer compared to the exciting photon energy, the driving force for the charge recombination to the ground state is large. When the reorganization energy for the electron transfer between the excited pigment and the acceptor is less than half the photon energy, then the initial electron transfer will be in the "normal" Marcus region and the charge recombination in the "inverted" region (Fig. 4.5). This has the effect of slowing down the charge recombination by many orders of magnitude and allows time for a second, productive electron transfer to take place further separating charges. Without exploiting the Marcus inverted region, is it difficult to construct light-activated charge-separating systems that have both high

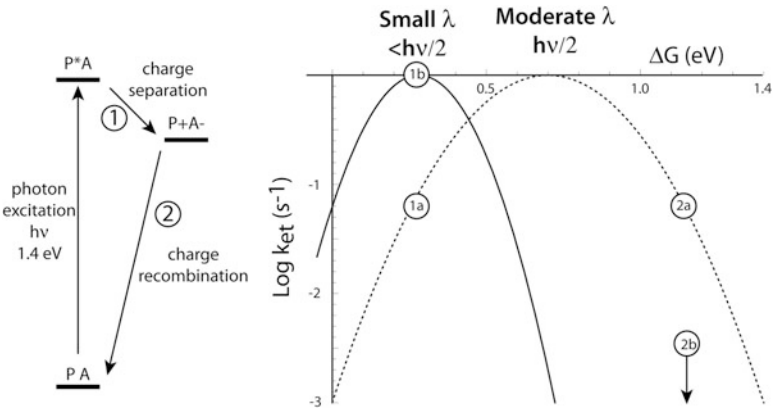

Fig. 4.5 For light-activated charge separations, the productive initial charge separation (*left*) competes with the loss reaction of charge recombination to ground state over the same distance. If the reorganization energy is half the energy of the excited state, both these electron-transfer steps will have the same rate (*1a* and *2a* at *right*) and the net loss can be high. If the reorganization energy is less than half the excited state energy, then the charge separation will be slower than the charge recombination (*1b* and *2b*), because the former is in the normal region, and the latter in the inverted region

quantum efficiency of charge separation and good conservation of the photon energy in the form of the redox energy difference between product oxidants and reductants. This can be seen in a survey of the present generation of synthetic photochemical dyads and triads.

4.8 Concept 8: For Biological Cofactors, Classical Marcus Theory Needs to Be Modified to Include Quantum Effects on the Driving Force Dependence

While classical Marcus theory is roughly applicable to biological electron-transfer systems, a closer look at the temperature dependence of those systems in which the driving force has been systematically changed by altering the redox properties of the donors and acceptors shows that the classical approach must be modified to include quantum terms not only for the tunneling electron but also for the vibrating nuclei.

The most obvious demonstration of this effect is seen when photosynthetic reactions are followed at cryogenic temperatures. The classical Marcus theory predicts an increasingly sharp falloff of the rate as the driving force departs from the optimum at $-\Delta G = \lambda$ as the temperature is lowered (Fig. 4.6). Essentially, lower temperatures make it harder to thermally surmount the Marcus activation energy barrier and only nearly activationless reactions can proceed at the lowest temperatures.

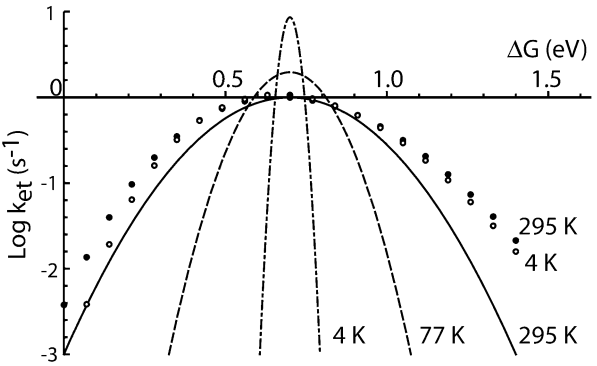

Fig. 4.6 The temperature modulation of classical Marcus (*lines*) and quantum single (*dots*) harmonic oscillator models of the driving force dependence of electron-tunneling rates. The lack of strong temperature dependency for many biological electron transfers indicates that relatively high-energy quantum nuclear vibrations are coupled to electron transfer

As seen in the original DeVault and Chance experiments [16] and in the extensive quinone substitution experiments of Gunner et al. [22, 25], the Marcus curve sharpening fails to materialize at cryogenic temperatures. It is clear that there are vibrations that are coupled to electron transfer that are comparable to or greater than the Boltzmann thermal energy k_BT at room temperature, and that these high-energy vibrations must be treated in a quantum tunneling rather than classical manner. These same experiments show that the driving force dependence of the rate, even at room temperature, is noticeably broader than that implied by the classical Marcus treatment.

There are several approaches to introducing the quantum effects of relatively large energy vibrations to electron tunneling in proteins [15]. Hopfield [27] presents a mathematically simple, semiclassical method which uses a trigonometric Coth term that reverts to the Marcus classical expression at high temperatures, but merges into a temperature-independent form at thermal energies below the characteristic quantum frequency of vibration coupled to the electron transfer, $\hbar\omega$:

$$ket \propto \frac{1}{\sqrt{2\pi\lambda\hbar\omega \mathrm{Coth}[\hbar\omega/2k_BT]}} e^{-(\Delta G+\lambda)^2/2\lambda\omega \mathrm{Coth}[\hbar\omega/2k_BT]} \tag{4.2}$$

The Hopfield expression maintains the Marcus simplicity of a Gaussian dependence of rate on driving force, but yields a broader Gaussian when vibrational modes larger than room temperature k_BT are coupled to electron transfer.

A fully quantum treatment of an electron transfer coupled to a quantized simple harmonic oscillator of energy $\hbar\omega$ requires a modified Bessel function [28]. This is a discrete function that is only defined at energy intervals of $\hbar\omega$, corresponding to

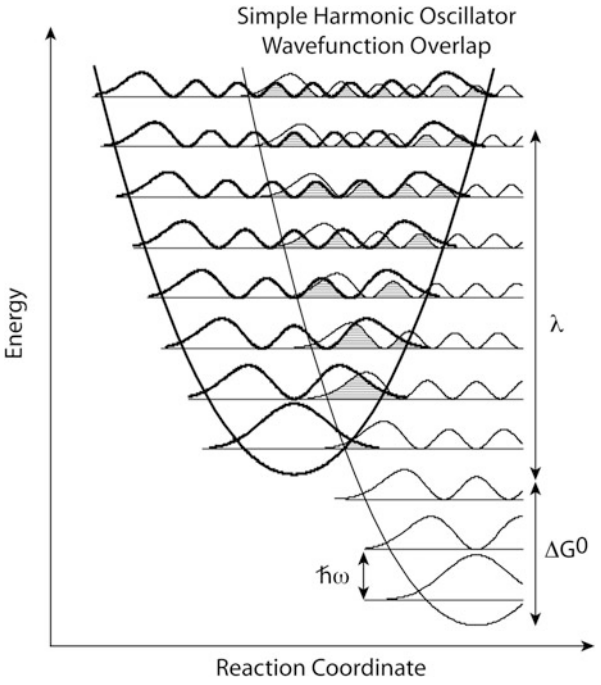

Fig. 4.7 To capture the nuclear dependent terms in electron tunneling, a simple quantum harmonic oscillator picture describes the overlap (hatching) of reactant and product wave functions (approximated here as the square of the wave functions in *wavy lines*) at various energy levels separated by the quantum of vibrational energy $\hbar\omega$

the overlap of vibrational wave functions shown in Fig. 4.7, because only at these ΔG values can the reactant and product be at the same energy at the same nuclear coordinates. An example of this function is plotted in Fig. 4.7 as the separate points:

$$\text{ket} \propto \exp[-(\lambda/\hbar\omega)(2n_k+1)]\left(\frac{(n_k+1)}{n_k}\right)^{\Delta G/2\hbar\omega} I_{\Delta G/\hbar\omega}\left[2(\lambda/\hbar\omega)\sqrt{n_k(n_k+1)}\right] \tag{4.3a}$$

where

$$n_k = 1/\left(\exp[k_B\hbar\omega]-1\right] \tag{4.3b}$$

Practically, electron transfer in proteins takes place smoothly at all driving forces, combining harder high-energy and softer low-energy vibrations to equalize donor and acceptor energies for electron tunneling. The quantum expression of Eq. (4.4) sums all these wave function overlaps. In this equation, S_k is the reorganization energy of the hard vibration in units of $\hbar\omega$; m is the change in the quantum number of the vibration; n_k is the same as in Eq. (4.3b), an expression of the temperature-dependent population of higher vibrational levels; and λ_s

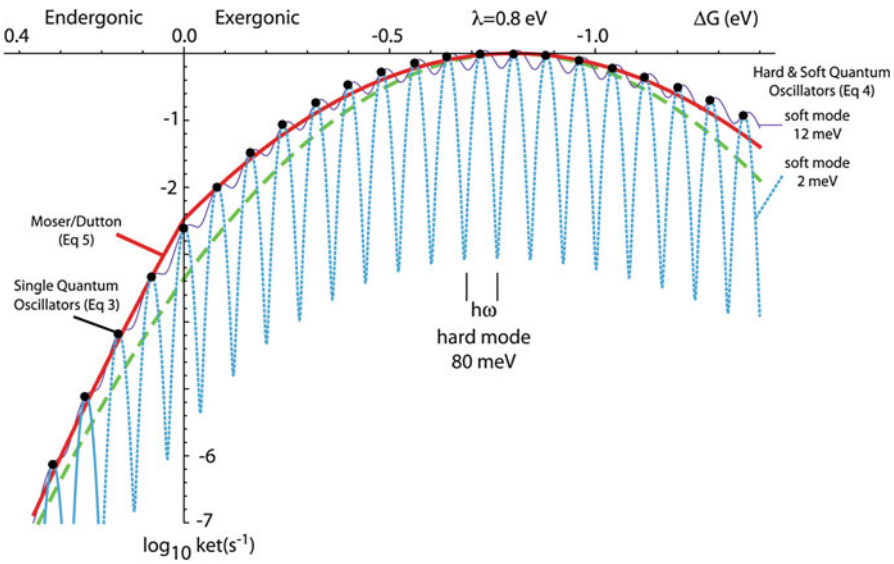

Fig. 4.8 Examples of classical and quantum approaches to the driving force dependence of the rate of electron tunneling. *Dashed line*: The classical Marcus expression at room temperature with a reorganization energy of 0.7 eV. *Black dots*: A single quantized harmonic oscillator with characteristic frequency of 80 meV; in this extreme view the reaction will only occur when ΔG is an integer multiple of this vibration and so is undefined at other ΔG values, defined only at quantized energies. *Dotted line*: Coupled quantized hard (80 meV) and soft (2 meV) energy harmonic oscillators for a continuous curve. *Thin solid line*: Same but with a 12 meV soft mode. *Thick solid line*: The Moser-Dutton simple approximation to quantized harmonic oscillators dominated by a hard vibration

the reorganization energy associated with the soft vibrational modes. Examples of this function are shown as the wavy curves in Fig. 4.8:

$$\text{ket} \propto \frac{\exp[-S_k(2n_k+1)]}{\sqrt{4\pi\lambda_s k_B T}} \sum_{m=-\infty}^{+\infty} \left(\frac{(n_k+1)}{n_k}\right)^{m/2} I_m\left[2S_k\sqrt{n_k(n_k+1)}\right] \exp\left[-\frac{(\lambda_s + m\hbar\omega_k - \Delta E)^2}{4\lambda_s k_B T}\right] \tag{4.4}$$

4.9 Concept 9: The Quantum Dependence on Driving Force Can Be Approximated by a Simple Empirical Expression

The more complex exact quantum expressions are calculation overkill for matching any practical experimental system of electron tunneling in protein. The experimental measurements and parameters are just not precise enough. While appropriate

distances can be reasonably estimated from X-ray crystal structures, driving forces are often poorly known and have significant uncertainties when estimated from equilibrium redox potentials. Reorganization energies are even more uncertain and there is no clear way to measure the characteristic vibrational frequencies coupled to electron transfer, leaving it to be a fit parameter. Furthermore, biological electron-transfer rates themselves are often not well fit by a single exponential time course, but cover a range of rates.

A simple empirical expression [17] that successfully estimates protein electron-tunneling rates with less than an order of magnitude of uncertainty and comparable to experimental errors combines the observed exponential falloff of rate with distance of Fig. 4.1 with a room-temperature version of the Hopfield expression for an exergonic electron-transfer reaction that uses just the three most important parameters:

$$\log k_{et}^{exer} = 15 - 0.6(R - 3.6) - 3.1(\Delta G + \lambda)^2/\lambda \tag{4.5a}$$

where R is the edge-to-edge distance between redox cofactors in Å, ΔG is the free energy of electron transfer, and λ is the reorganization energy, both in units of eV. For the corresponding endergonic electron transfer of the reverse reaction, we use a Boltzmann ratio of rates:

$$\log k_{et}^{ender} = \log k_{et}^{exer} - \Delta G/.06. \tag{4.5b}$$

While the fusion of Eqs. (4.5a) and (4.5b) introduces an esthetically distracting inflection point at zero driving force, we can see from Fig. 4.8 that it presents a remarkably good approximation, well within experimental error, of the much more complex discrete fully quantum simple harmonic oscillator equation, without any of the driving force oscillations that are part of the even more complex quantum high and low vibrational energy model. There is no clear evidence for this type of oscillation in the biological experimental literature. Contrary to some reports [29], there is no inconsistency or mathematical error that arises from using these coupled equations exclusively for the exergonic domain on one hand, and the endergonic domain on the other as an approximation to more unwieldy quantum mathematical expressions. Obviously, it is inappropriate to use the endergonic expression for an exergonic reaction, and vice versa. Equations (4.5a) and (4.5b) are enough to understand the basic engineering and operation of natural electron-transfer proteins and to provide a reliable rule of thumb when modifying natural proteins or designing artificial electron-transfer proteins.

Indeed, with edge-to-edge distances provided by a protein structure and a rough idea of the redox potentials of the redox cofactors and hence the driving force for electron transfer, using this expression with a generic reorganization energies of around 0.9 eV estimates the rate of all the electron-tunneling reactions with an accuracy of about an order of magnitude, enough to understand how the intraprotein

electron-transfer network operates. Or, if there is no structure but intraprotein electron-transfer rates and redox potentials of cofactors are known, then it is possible to predict the distances between redox centers and gain a fair idea of the structure of the protein.

4.10 Concept 10: Natural Selection Has Used Distance and Driving Force to Speed Desirable Electron Transfers or Slow Undesirable Electron Transfer, Not Modification of the Intervening Protein Medium

The distance that an electron can tunnel through a surrounding medium depends on the height of the energetic barrier the electron must tunnel through. The lower the barrier, the faster the electron tunneling for any given distance. It has been shown in many chemical synthetic systems that a direct covalent link between donor and acceptor speeds the electron-transfer rate compared to donors and acceptors separated by solvent [17]. The presence of a dense array of atomic orbitals connecting the donor and acceptor effectively lowers the barrier the electron must tunnel through. In principle, nature could have selected the amino acid structure making the protein medium between a donor and acceptor to resemble a more covalent, bridge-like connection in order to speed useful electron transfers, or to resemble more solvent like or even vacuum like to slow short-circuiting or unproductive electron transfers. The free energy-optimized electron-tunneling rates of Fig. 4.1, representing a collection of both productive charge-separating reactions of photosynthesis and unproductive charge recombinations, as well as a collection of unphysiological rates achieved by introducing extraneous redox centers to natural proteins, show that this is not the case [30].

Natural selection appears to have favored using distance and driving force as the principle means to direct electron transfers in productive directions and avoid unproductive directions. This is likely due to the profound effect that even small changes in distance can have on electron-transfer rates, speeding or slowing by a 100-fold with just a 3.3 Å change in distance. Typically, natural protein scaffolds fix redox centers with relatively little wiggle although, in rare cases, large conformational changes in the protein effectively move redox centers into and out of electron transfer distance. It is apparently much more difficult for natural selection to secure structural changes in the effective tunneling barrier between redox centers over a sufficient distance to achieve a comparable effect on the rate. Instead, donors and acceptors in productive reactions are closer than in unproductive reactions.

Changes in driving force, through mutational changes in redox midpoint potentials, can also be effective in slowing unproductive reactions. All else being equal, a near-zero driving force electron-tunneling reaction is slowed a 100-fold by lowering the redox midpoint of the acceptor by 0.12 V. Much smaller changes will be seen if the driving force more nearly matches the reorganization energy, as is the case for several productive electron transfers in photosynthetic reaction centers.

4.11 Concept 11: Nature Guides the Path of Electron Transfer Mainly Through Placing Redox Centers Close Together, Less than 14 Å

A survey of structures of natural electron-transfer proteins shows conspicuous chains of redox centers, with nearly all redox partners separated by 4–14 Å [31]. This assures that electron-tunneling rates for low-driving-force reactions with typical reorganization energies are in the range of 0.3 ns to 0.3 ms. What this means is that electron tunneling is generally fast enough to not limit the enzymatic turnover of electron-transfer proteins, which are typically in the range of 10^3 s^{-1}, a rate that seems to be limited by protein and substrate diffusion as well as proton transfers that are common in catalysis. There seems to be no pressure for natural selection to achieve faster electron-tunneling rates when the overall performance of catalytic turnover in an electron-transfer system will be unchanged. A corollary of this observation is that if two redox centers in a protein are separated by more than 14 Å, then they are likely not natural redox partners.

While distances towards the long end of this range may be acceptable for most electron transfers of respiration and photosynthesis, the initial light-induced charge separation reactions compete with the usually unproductive decay of the excited state of the ns time scale. Natural selection has favored initial charge separations at the short end of this distance scale and fast enough to assure a high quantum yield of charge separation.

4.12 Concept 12: Natural Photochemical Systems Are Not Ideal. They Have High Yields, but a Superabundance of Cofactors and Relatively Large Energy Losses

In spite of a common belief that many millions of years of natural selection must have created protein systems in which each component has been optimized and that natural designs are near perfect and cannot be improved, photosynthetic systems are not perfect but simply good enough to work in a biological context. In many ways natural photosystems are a poor model for molecular designers to mimic while attempting to create artificial systems to harvest sunlight. Using the empirical electron-tunneling expressions (4.5a) and (4.5b) it is a simple matter to demonstrate that photochemical triads embedded in protein, with donor, light-activated pigment and acceptor in an approximately linear arrangement, can preserve significantly more of the energy of the absorbed photon in the redox difference between the photo-oxidized donor and photo-reduced acceptor, at any selected time scale, than is seen in any natural photosystem. For example, such a triad could have greater than 80 % efficiency on a millisecond time scale, while natural photosystems operate at closer to 50 % energetic efficiency.

Lowered overall energetic efficiency presumably reflects the evolution of natural photosystems in a bioenergetic legacy that could make little use of more energetically efficient designs. For example, reliance on membrane-diffusible quinones with redox midpoint potentials around 0 mV to connect photosynthetic protein modules means that there is no effective way to preserve the low redox potential of the highly reducing light-activatable donors in purple bacterial reaction centers or PSII. Instead these systems have much larger driving force drops between cofactors than are needed to achieve rapid enough charge separation through electron tunneling to avoid unproductive charge recombination reactions. More than half the energy of the photon is lost as heat. It is true that the quantum efficiency of natural photosystems is high, approaching 100 %, but this comes along with significant loss of redox energy that could otherwise be harnessed in designed artificial systems.

PSI is designed to reach lower redox potentials in the reduction of the terminal iron sulfur cluster (~−0.5 V) [32] but it achieves this by using a lower redox potential oxidizing terminal in P700 (~+0.45 V) [4]. Once again, nearly half the energy of the photon is consumed in the charge separation. There is enough energy available in the 1.8 eV of the 680–700 nm red photons absorbed by the chlorophylls of PSI and PSII to activate millisecond-long charge separation in an artificial photochemical triad with a donor oxidizing enough to split water into O_2, +1.0 V, in the oxygen-evolving Mn cluster of PSII [3], and an acceptor reducing enough to reduce protons to H_2, −0.42 V at pH 7. Yet natural photosystems are designed to use two red photons to span the H_2O/O_2 and $H+/H_2$ redox gap and they use many more than three redox cofactors to do so. With a basic understanding of the distance scales appropriate for electron tunneling, synthetic chemists and designers of artificial proteins can be expected to step into this design gap.

Acknowledgments This didactic account is the result of the development of engineering for man-made oxidoreductases of the kind proposed in Office of Basic Energy Sciences, Division of Materials Sciences and Engineering [DE-FG02-05ER46223], and the US National Institutes of Health, General Medical Institutes [RO1 GM 41048]. The support from each is nearly equal.

References

1. Byrdin M, Lukacs A, Thiagarajan V, Eker APM, Brettel K, Vos MH. Quantum yield measurements of short-lived photoactivation intermediates in DNA photolyase: toward a detailed understanding of the triple tryptophan electron transfer chain. J Phys Chem A. 2010;114 (9):3207–14.
2. Zeugner A, Byrdin M, Bouly JP, Bakrim N, Giovani B, Brettel K, et al. Light-induced electron transfer in Arabidopsis cryptochrome-1 correlates with in vivo function. J Biol Chem. 2005;280(20):19437–40.
3. Rappaport F, Guergova-Kuras M, Nixon PJ, Diner BA, Lavergne J. Kinetics and pathways of charge recombination in photosystem II. Biochemistry. 2002;41(26):8518–27.
4. Krabben L, Schlodder E, Jordan R, Carbonera D, Giacometti G, Lee H, et al. Influence of the axial ligands on the spectral properties of P700 of photosystem I: a study of site-directed mutants. Biochemistry. 2000;39(42):13012–25.

5. Jordan P, Fromme P, Witt HT, Klukas O, Saenger W, Krauss N. Three-dimensional structure of cyanobacterial photosystem I at 2.5 angstrom resolution. Nature. 2001;411(6840):909–17.
6. Ferreira KN, Iverson TM, Maghlaoui K, Barber J, Iwata S. Architecture of the photosynthetic oxygen-evolving center. Science. 2004;303(5665):1831–8.
7. Deisenhofer J, Epp O, Sinning H, Michel H. Crystallographic refinement at 2.3 Å resolution and refined model of the photosynthetic reaction centre from rhodopseudomonas viridis. J Mol Biol. 1995;246:429–57.
8. Kee HL, Kirmaier C, Tang Q, Diers JR, Muthiah C, Taniguch M, et al. Effects of substituents on synthetic analogs of chlorophylls. Part 1: synthesis, vibrational properties and excited-state decay characteristics. Photochem Photobiol. 2007;83(5):1110–24.
9. Rutherford AW, Osyczka A, Rappaport F. Back-reactions, short-circuits, leaks and other energy wasteful reactions in biological electron transfer: Redox tuning to survive life in O-2. FEBS Lett. 2012;586(5):603–16.
10. Gorman AA, Rodgers MAJ. Current perspectives of singlet oxygen detection in biological environments. J Photochem Photobiol B. 1992;14(3):159–76.
11. Sies H, Menck CFM. Singlet oxygen induced DNA damage. Mutat Res. 1992;275(3–6):367–75.
12. Trebst A, Depka B, Hollander-Czytko H. A specific role for tocopherol and of chemical singlet oxygen quenchers in the maintenance of photosystem II structure and function in Chlamydomonas reinhardtii. FEBS Lett. 2002;516(1–3):156–60.
13. Pross A. The single electron shift as a fundamental process in organic chemistry: the relationship between polar and electron-transfer pathways. Acc Chem Res. 1985;18:212–9.
14. Eberson L. Electron transfer reactions in organic chemistry. New York: Springer-Verlag; 1987. 234 p.
15. Devault D. Quantum-mechanical tunnelling in biological-systems. Q Rev Biophys. 1980;13 (4):387–564.
16. Devault D, Chance B. Studies of photosynthesis using a pulsed laser. I Temperature dependence of cytochrome oxidation rate in Chromatium. Evidence for tunneling. Biophys J. 1966;6 (6):825–47.
17. Moser CC, Keske JM, Warncke K, Farid RS, Dutton PL. Nature of biological electron-transfer. Nature. 1992;355(6363):796–802.
18. Eyring H. The activated complex in chemical reactions. J Chem Phys. 1935;3:107–15.
19. Zwolinski BJ, Marcus RJ, Eyring H. Inorganic oxidation-reduction reactions in solution-electron transfers. Chem Rev. 1955;55(1):157–80.
20. Moser CC, Anderson JLR, Dutton PL. Guidelines for tunneling in enzymes. Biochim Biophys Acta. 2010;1797(8):1573–86.
21. Marcus RA. On the theory of oxidation-reduction reactions involving electron transfer: I. J Chem Phys. 1956;24:966–78.
22. Gunner MR, Dutton PL. Temperature and -delta-G-degrees dependence of the electron-transfer from Bph.- to Qa in Reaction center protein from rhodobacter-sphaeroides with different quinones as Qa. J Am Chem Soc. 1989;111(9):3400–12.
23. Iwaki M, Kumazaki S, Yoshihara K, Erabi T, Itoh S. Delta G(0) dependence of the electron transfer rate in the photosynthetic reaction center of plant photosystem I: Natural optimization of reaction between chlorophyll a (A(0)) and quinone. J Phys Chem. 1996;100(25):10802–9.
24. Lin X, Williams JC, Allen JP, Mathis P. Relationship between rate and free-energy difference for electron-transfer from cytochrome C(2) to the reaction-center in rhodobacter-sphaeroides. Biochemistry. 1994;33(46):13517–23.
25. Woodbury NW, Parson WW, Gunner MR, Prince RC, Dutton PL. Radical-pair energetics and decay mechanisms in reaction centers containing anthraquinones, naphthoquinones or benzoquinones in place of ubiquinone. Biochim Biophys Acta. 1986;851(1):6–22.
26. Lin X, Murchison HA, Nagarajan V, Parson WW, Allen JP, Williams JC. Specific alteration of the oxidation potential of the electron-donor in reaction centers from rhodobacter-sphaeroides. Proc Natl Acad Sci U S A. 1994;91(22):10265–9.

27. Hopfield JJ. Electron transfer between biological molecules by thermally activated tunneling. Proc Natl Acad Sci U S A. 1974;71:3640–4.
28. Jortner J. Temperature-dependent activation-energy for electron-transfer between biological molecules. J Chem Phys. 1976;64(12):4860–7.
29. Crofts AR, Rose S. Marcus treatment of endergonic reactions: a commentary. Biochim Biophy Acta. 2007;1767(10):1228–32.
30. Moser CC, Chobot SE, Page CC, Dutton PL. Distance metrics for heme protein electron tunneling. Biochim Biophy Acta. 2008;1777(7–8):1032–7.
31. Page CC, Moser CC, Chen XX, Dutton PL. Natural engineering principles of electron tunnelling in biological oxidation-reduction. Nature. 1999;402(6757):47–52.
32. Evans MCW, Heathcote P. Effects of glycerol on the redox properties of the electron-acceptor complex in spinach photosystem-I particles. Biochim Biophy Acta. 1980;590(1):89–96.

Chapter 5
Spin in Photosynthetic Electron Transport

Isaac F. Céspedes-Camacho and Jörg Matysik

Abstract Photosynthetic charge separation also leads to electron spin separation. The two separated electron spins form a spin-correlated radical pair initially in a pure singlet state. This high electron spin order can be detected by EPR spectroscopy as CIDEP (chemically induced dynamic electron polarization). The radical pair undergoes spin evolution leading to periodic intersystem crossing. Interactions with nuclear spins lead to CIDNP (chemically induced dynamic nuclear polarization), which is often referred to as "photo-CIDNP" if it is of photochemical origin. NMR spectroscopy is able to observe such nuclear spin hyperpolarization. Both CIDEP EPR and CIDNP NMR allow for the early steps of photosynthesis to be studied in great detail. History and examples of these studies are presented. Finally, the question whether the occurrence of the spin-polarization is simply a by-product of the charge separation is discussed. Concepts for a possible functional relevance are proposed.

Keywords Electron transfer • Hyperpolarization • Spin dynamics • CIDEP • CIDNP

I.F. Céspedes-Camacho, Dr.
Leiden Institute of Chemistry, Leiden University, Einsteinweg 55, 2300 RA Leiden, The Netherlands

Fakultät für Chemie und Mineralogie, Institut für Analytische Chemie, Universität Leipzig, Linnéstr. 3, 04103 Leipzig, Germany
e-mail: isaac.cespedes@uni-leipzig.de

J. Matysik, Dr. rer. nat. (✉)
Fakultät für Chemie und Mineralogie, Institut für Analytische Chemie, Universität Leipzig, Linnéstr. 3, 04103 Leipzig, Germany
e-mail: joerg.matysik@uni-leipzig.de

J. Golbeck and A. van der Est (eds.), *The Biophysics of Photosynthesis*, Biophysics for the Life Sciences 11, DOI 10.1007/978-1-4939-1148-6_5,

Abbreviations

B	Magnetic field strength
B_L	Local magnetic field strength
BChl	Bacteriochlorophyll
C.	*Chlorobium*
Chl	Chlorophyll
CIDEP	Chemically induced dynamic electron polarization
CIDNP	Chemically induced dynamic nuclear polarization
DD	Differential decay
DR	Differential relaxation
EPR	Electron paramagnetic resonance
ESR	Electron spin resonance
ESEEM	Electron spin echo envelope modulation
ET	Electron transport
g	g- or Landé value of an electron
G-pair	Geminate radical pair
Hb.	*Heliobacillus*
hfc, hfi	Hyperfine coupling or interaction
ISC	Intersystem crossing
J	Exchange coupling
MAS	Magic-angle spinning
MFE	Magnetic field effects
m_S	Spin quantum number
NMR	Nuclear magnetic resonance
OMAR	Organic magnetoresistance effect
RC	Reaction center
P	Primary electron donor
PSI	Photosystem I
PSII	Photosystem II
Q	Quinone
r	Inter-radical distance
Rb.	*Rhodobacter*
Rps.	*Rhodopseudomonas*
RPM	Radical pair mechanism
S	Singlet spin state of a radical pair
S	Spin quantum number
SCRP	Spin-correlated radical pair
T	Triplet spin state of a radical pair
TSM	Three spin mixing
Φ	Bacteriopheophytin

5.1 Primary Photoreaction Leads to Electron Hyperpolarization

Much effort has been devoted to analyzing photosynthetic electron transport (ET). Investigations on ET focus mostly on the *charge* of the electron. Indeed, the light driven charge separation processes lead to the buildup of the membrane potentials that drive the chemiosmotic processes. However, in addition to charge, electrons also possess the fundamental property of the *spin*. Hence, ET results in both charge and spin transfer, and a full understanding of the conversion of light energy into chemical energy requires an analysis of the spin transport. Here we summarize spectroscopic studies of spin transport and discuss the role of spin in photosynthetic systems.

In photosynthetic reaction centers (RC), the initial step of electron transfer occurs in a few picoseconds between the primary electron donor P and the first electron acceptor. In RCs of *Rhodobacter* (*Rb.*) *sphaeroides*, experimental evidence has shown that the primary (P) donor is a bacteriochlorophyll (BChl) dimer, called the "special pair," and the primary acceptor is a bacteriopheophytin Φ_A with an accessory BChl monomer as a spectroscopically observable transient [1–4]. The electron transfer continues via the two quinones Q_A and Q_B. Higher plants require two photosynthetic protein complexes, photosystem I (PSI) and photosystem II (PSII), operating in series to provide sufficient electric potential to pump electrons from water to carbon dioxide. The photoreaction in RCs of *Rb. sphaeroides* can be expressed as:

$$P\Phi_A Q_A Q_B \xrightarrow{h\nu} P^+\Phi_A{}^- Q_A Q_B \rightarrow P^+\Phi_A Q_A{}^- Q_B \rightarrow P^+\Phi_A Q_A Q_B{}^-$$

EPR experiments have shown that the cation radical of the primary donor ($P^{+\bullet}$) in PSI is also a chlorophyll (Chl) dimer [5]. X-ray crystallographic data have supported this observation [6]. The primary donors in PSII and PSI contain plant Chl *a* cofactors. In solution, Chl *a* has a higher oxidation potential than BChl *a* [7]. The primary donor in PSII (P680) shows an oxidation potential sufficient to oxidize tyrosine, H_2O, and other chlorophylls. X-ray studies on PSII confirm that there are no strongly coupled chlorophylls in the RC [8]. In the case of the primary donor in PSI (P700), a low oxidation potential for a Chl *a* is observed. These highly symmetric dimeric species were also identified by spectroscopic and crystallographic data [9].

Photochemical reactions are often initiated from triplet states and occur on the nanosecond and microsecond timescale. In contrast, the photochemical reaction and ET in photosynthesis occur from the excited singlet state on the picosecond timescale, which relates to the high efficiency of the photosynthetic primary reaction. If the forward reaction is blocked, however, photo-excitation forms Chl and BChl molecules in their triplet states ($S = 1$) that present a potential danger for the photosystems because they react with molecular oxygen forming singlet oxygen, i.e., an extremely reactive compound that can damage the protein. Therefore, the formation of Chl triplet

states is avoided in all photosystems. To that end, two reaction steps are highly optimized and fast: (1) the singlet energy transfer in the antennae and (2) the charge separation in the RC [10]. Also, a natural protection is provided by the presence of carotenoids close to the Chl molecules, enabling efficient triplet energy transfer from Chl to the carotenoids. The carotenoid triplet states decay to the singlet ground state by energy dissipation [11].

The photochemical charge and spin separation in the primary reactions creates radical pairs that can be detected by Electron Paramagnetic Resonance (EPR). During the first several microseconds after the charge separation, the EPR spectra of such radical pairs show strong electron spin-hyperpolarization, which is often called either CIDEP (chemically induced dynamic electron polarization) or ESP (electron spin polarization). The term "spin-hyperpolarization" refers to a non-Boltzmann spin polarization, which can be detected as a change in signal intensity by magnetic resonance techniques. CIDEP is electron spin-hyperpolarization occurring transiently during a chemical process. Research on CIDEP has been very active and is summarized in several review articles [12–15].

The origin of CIDEP in photosynthetic systems can be explained with the concept of a spin-correlated radical pair (SCRP), an important class of species with non-equilibrium initial spin-state (*vide infra*) [16–19]. In the dynamics of the SCRP, the following interactions of electrons and nucleus must be taken into account to describe the observed CIDEP: hyperfine coupling (hfc) (electron–nucleus), electron (electron field) and nuclear (nucleus field) Zeeman interactions, exchange (J) and dipolar interactions (electron–electron) as well as the thermal motion. An analysis of the CIDEP based on the SCRP model can help to obtain information about structure, dynamics, and energetics. The group spin $S = S_1 + S_2$ for the two radicals remains the same as the total spin of the precursor molecule: $S = 0$ for an excited singlet precursor and $S = 1$ for a triplet precursor. This spin correlation occurs because both bond rupture and ET are spin-conserving processes [20–22]. On the other hand, bond-formation between two radicals or recombination to the ground state requires group spin $S = 0$, i.e., only a singlet radical pair can recombine to the ground state. That is in contrast to the traditional concept widespread among chemists in which radical recombination in solution is nearly activationless at short distances. We have seen, however, that recombination requires the right electron spin state of the radical pair.

Figure 5.1 shows a vector model of the four possible electron spin states of a radical pair with their corresponding total spin state, S, and the spin quantum number, m_S. One singlet sate (S) and three triplet (T_+, T_0, T_-) states are formed. None of the four combinations of the quantum numbers S and m_S are identical, and hence, the four states are quantum theoretically distinguishable. The exchange interaction J causes an energy difference between the T_0 and S states by an amount of $2J(r)$, such that T_0 is higher in energy when J is positive. If $J(r)$ is much larger than the difference in the precession frequency of the two spins, i.e., at short inter-radical distance r, S, T_+, T_0 and T_- form stationary eigenstates. For larger distances S and T_0 are neither stationary nor eigenstates. At very large distance r, $J(r)$ is close to zero and S and T_0 are nearly degenerate. Under this condition, the S and T_0 states can

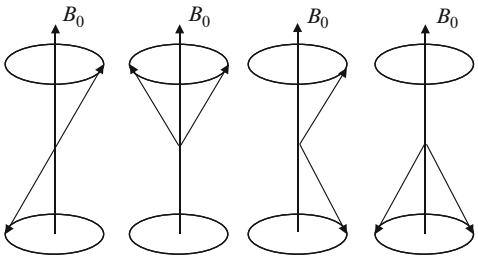

	Singlet S	Triplet T_+	Triplet T_0	Triplet T_-
Total spin number, S	0	1	1	1
Magnetic quantum number, m_S	0	+1	0	–1

Fig. 5.1 Vector model of electron spin states formed by a spin-correlated radical pair (SCRP)

interconvert coherently, i.e., undergo intersystem crossing (ISC), if the two electrons have different precession frequencies. Hence, the S and T states are mixed by hyperfine couplings (due to different local magnetic fields B_L) and different g-values of the two radicals (due to their electron Zeeman interactions) within a few nanoseconds. At medium distance r, $J(r)$ can become involved into the spin dynamics.

The precession frequency (also called Larmor frequency) depends on the g-value of the electron, which reflects the chemical environment of the electron. For organic molecules, the value is usually slightly above 2 but occurs over a large range for metal-centered radicals. A typical difference in the g values (Δg) in an organic radical pair is ~0.001. These deviations from the free electron g-value are caused by an interaction of ground and excited states, which combine the orbital angular momentum from the excited states into the ground state. The closer the excited states to the ground state and larger the spin–orbit coupling, the larger the deviation of the g principal values from g_e [23]. A thorough interpretation of the g-values is provided by quantum electrodynamics. Furthermore, the hyperfine interaction (hfi) is caused by magnetic nuclei and affects the precession frequency (*vide infra*). While external fields (B) in EPR and NMR experiments are in the range of a few T, hyperfine fields provide local modifications in the mT range leading to the so-called local magnetic fields (B_L). At earth's magnetic field (~50 μT), the local field is dominated by the hyperfine fields.

At "zero field," i.e., in the absence of an external magnetic field, the S and T states are separated by the exchange coupling J, and the three triplet states are almost degenerate but symmetry-dependent electron–electron interactions might cause the so-called zero-field splitting (Fig. 5.2). The three triplet states are labeled T_x, T_y and T_z which correspond to the principal axes directions of the zero-field splitting tensor.

At high magnetic fields, the electron Zeeman splitting separates energetically the three triplet states. While the T_0 states remains energetically close to the singlet state (only separated by J), T_+ is increased in energy and T_- is lowered. Hence, T_+

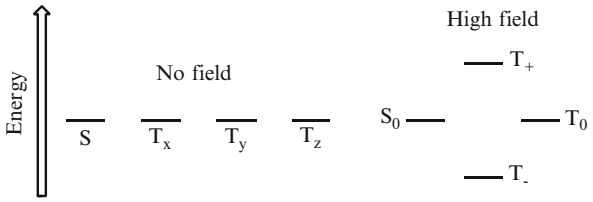

Fig. 5.2 Diagram of the energy levels of the four spin states of an SCRP. *Left*: without magnetic field, *right*: at high magnetic field

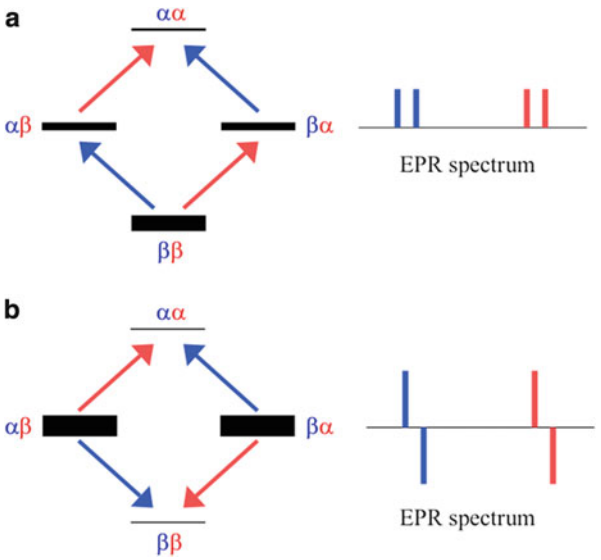

Fig. 5.3 A two-electron spin system shows four collective spin states. Populations and EPR spectra are shown for a sample at Boltzmann equilibrium (**a**) as well as for an SCRP (**b**)

and T_- have a pure triplet character and do not mix with S. Spin–lattice relaxation (i.e., the energy transfer between the spins and the lattice is mediated by fluctuating local magnetic fields, which are induced by lattice vibrations) can cause transitions between the spin states; however, this process is usually too slow (a few microseconds for organic radicals in solution) to interfere with the coherent S–T_0 spin dynamics.

SCRPs can be identified by EPR spectroscopy based on their particular line-shape pattern, which is related to the hyperpolarization. Figure 5.3 shows a two-electron system having four possible electron spin states: $\alpha\alpha$ and $\beta\beta$ refer to T_+ and T_-, respectively. Combinations of the states $\alpha\beta$ and $\beta\alpha$ form the S ($[\alpha\beta - \alpha\beta]/\sqrt{2}$) and the T_0 ($[\alpha\beta + \beta\alpha]/\sqrt{2}$) states. At thermal equilibrium conditions (Fig. 5.3a), the populations are distributed according to the Boltzmann function, and all signals show positive ("absorptive") lines of similar intensity in the EPR spectrum. In an SCRP, which is at non-equilibrium, hyperpolarization leads to a different spectral shape (Fig. 5.3b). If the SCRP is generated from a singlet precursor, only the central $\alpha\beta$ and $\beta\alpha$ states are populated. Hence, the transitions from these two states to T_+ give enhanced positive ("absorptive") signals and transitions to T_- give negative

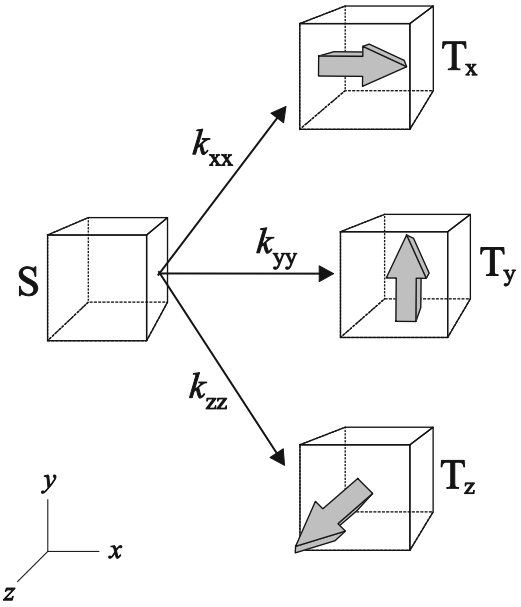

Fig. 5.4 The generation of electron magnetization in the molecular frame

("emissive") signals. The overall shape, showing positive and negative lines, is reminiscent of anti-phase coherences in pulse NMR and EPR experiments. Such SCRP-CIDEP features can only be observed during the lifetime of the SCRP. In solution the lifetime is limited by diffusion processes, and in a solvent of normal viscosity the lifetime of such germinate radical pairs (the so-called G-pairs) is about 500 ps and therefore challenging to be observed. In fact, CIDEP of SCRP have been initially observed in micellar solutions where the G-pair can function as molecular supercage allowing for SCRP lifetimes of hundreds of nanoseconds or even microseconds [24]. In contrast, in photosynthetic systems the radicals are bound to the protein and the SCRP lifetimes are determined by the forward and reverse electron transfer rates.

Alternatively to radical pairs, also molecular triplet states can be a source of electron spin hyperpolarization leading to CIDEP. In this case, the electron polarization occurs during the ISC from the initially formed excited singlet state into the three triplet states. In particular if the symmetry of the chromophore is low, the populations of the triplet sublevels (Fig. 5.4) can be highly unequal leading to a non-Boltzmann distribution of electron spins [25–27].

As we saw, ET, bond breaking and bond formation are spin conserving processes, and recombination of a radical pair to the singlet-ground state is only possible for a singlet radical pair. This spin selectivity also implies that the reaction products are distinguished by the spin state of the radical pair. While in the singlet state of the SCRP, recombination to the ground state is spin-allowed, this process is spin-forbidden during the triplet state (Fig. 5.5). Hence, chemical reaction dynamics are spin-controlled and periodically modulated with time. This spin-dynamics

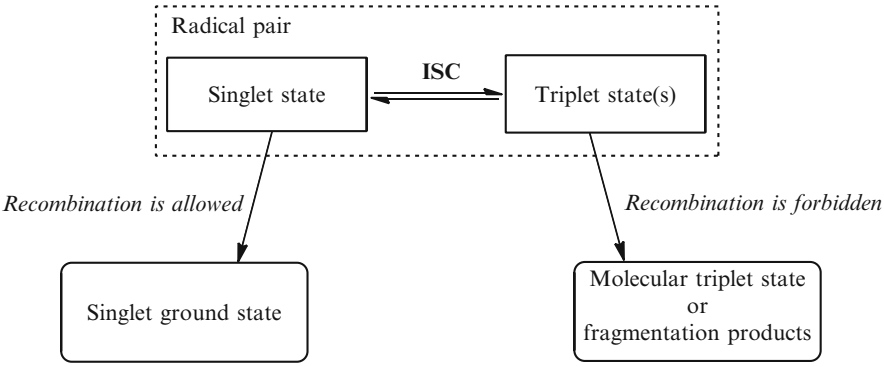

Fig. 5.5 Schematic view of the formation and decay of the SCRP

opens the possibility of coherent chemistry with nanosecond waves (the so-called quantum beats) of product formation [28, 29].

Since the electron Zeeman energy in typical EPR experiments is small (~50 J mol^{-1}) compared to the thermal energy (~5 kJ mol^{-1} at room temperature) and in particular to chemical reaction energies (~500 kJ mol^{-1}), a purely energetic view of the reaction process tends to underestimate the role of spin dynamics. As we will see below, even smaller nuclear spin energies (<0.2 J mol^{-1}) can decide the fate of the chemical reaction. Hence, the concepts of SCRPs and spin-selective population of triplet states demonstrate the effect of small spin energies on chemical kinetics and reaction dynamics. In fact, the field of spin chemistry was born with the discovery of the CIDEP effect by EPR spectroscopy in 1963 [30].

In addition to its relevance for chemical processes, spin hyperpolarization allows for the sensitivity and selectivity of EPR and NMR spectroscopy as analytical techniques to be improved. Spin polarization studies provide information about the identity of both radicals of the pair. The excited state that is the precursor to the radical-pair formation can be determined from the sign (emission or enhanced absorption) of the polarization if the sign of J is known [31]. Furthermore, the dependence of the spectrum on membrane orientation provides information on the anisotropy of the magnetic interactions and the orientation of the radical species [32]. As we will see, spin-hyperpolarization plays a significant role in photosynthesis, for both its functional mechanism and the analytical research on it [33].

5.2 CIDEP Studies on Photosynthetic Systems

Chronologically, CIDEP effects in radical ESR spectra were detected in 1963 prior to CIDNP when Schuler observed unusual ESR spectra of hydrogen and deuterium atoms in methane [30]. In 1968, Smaller et al. founded that those unusual spectra were due to electron spin polarization (i.e., CIDEP) [34]. In 1974, Harbour and

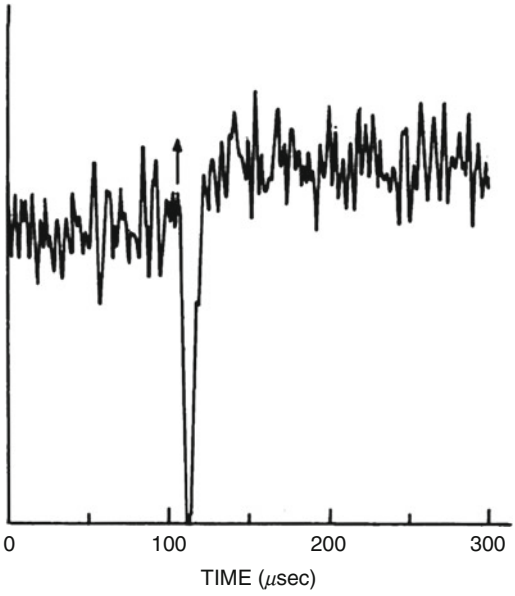

Fig. 5.6 The first example of CIDEP in a photosynthetic organism obtained from green plants. Reproduced with permission from Blankenship et al. [36]

Tollin irradiated BChl with red light in the presence of Q at low temperatures and observed the first example of CIDEP effect in a biological system [35]. One year later, the first reported observation of the CIDEP phenomenon in a photosynthetic organism was presented by Sauer and coworkers showing strongly polarized transient EPR signals from spinach chloroplasts at room temperature in the $g = 2.0$ region of the EPR field profile (Fig. 5.6) [36].

The theoretical explanation of the CIDEP phenomenon in radical pair reactions was developed by Closs and Closs and by Kaptein and Oosterhoff [20, 37] by introducing the classical radical-pair mechanism (RPM, *vide infra*). Later, the theory was extended within the framework of a radical pair model by Adrian, Atkins, and others [38–43]. At the same time, Atkins and Wong proposed the idea that CIDEP can also arise in the triplet precursors of radical pairs [44, 45].

CIDEP experiments allow for information on the relative orientation of the dipolar and g-tensor axes between radicals to be obtained. Hence, this technique enables the structure of cofactor organization in RCs to be determined or the changes in orientation and distance of cofactor during charge separation to be studied. For example, it has been possible to obtain the ESP spectrum of perdeuterated Zn^{2+}-reconstituted RCs from *Rb. sphaeroides* R26 at X- and K-band, showing the influence of the orientation of the g-tensor in the radical pair spectrum [46]. CIDEP has also been helpful in studying possible changes in conformation after charge separation and stabilization of the radical pair. When the Q_B-depleted RCs are frozen under illumination, the decay of the radical pair by recombination is slower than when it is created by illumination at cryogenic temperatures [47]. This difference in kinetics suggests that reorientation of Q_A

may occur when the charge separation occurs at room temperature. However, studies of the spin-polarized EPR signals indicate that reorientation of Q_A does indeed occur for light frozen samples [48–50], results that have been confirmed on deuterated RCs [51]. The spin–spin interactions in SCRPs results in deep out-of-phase electron spin echo envelope modulation (ESEEM) which allows for the distance between the radicals to be determined. This has been applied to radical pairs in Zn^{2+}-reconstituted RCs of *Rb. sphaeroides* R26, PSI and PSII (see [52] for a review).

Although almost all of the initial observations of CIDEP were explained by either the RPM or the triplet mechanism, in the early theory, ISC was not explicitly considered to be a coherent process. Studies on several photosynthetic organisms however could not be interpreted in the original framework [53–56]. To explain the unusual "anti-phase" (i.e., a dispersive band shape) CIDEP patterns observed in some free radicals trapped in micelles, Closs, Hoff, Hore, McLauchlan, Norris, and others introduced the concept of SCRPs based on *coherent* spin-dynamics [16–18, 31, 57, 58]. SCRPs, born in a pure state, either S or T_0, *oscillate* between both states. The SCRP is the geminate radical pair (also called "G-pair") from the time that it is formed until it ceases to exist. In solution, the coherence might be lost by a diffusion and re-encounter, by a chemical reaction or by a relaxation process. In the solid state, diffusion cannot occur, and only the last two processes can destroy the coherence.

Hence, the formalism of the SCRP theory allows for the quantum beats observed in the transient EPR signals to be described [59, 60]. Quantum beat EPR spectroscopy allows for the spectral resolution to be improved and has been applied to bacterial RCs [61, 62]. It has been demonstrated that when foreign quinones are introduced into bacterial RCs no major difference in the orientation of Q_A occurs [63, 64]. On the other hand, drastic changes of the CIDEP spectrum of some PSI preparations upon replacement of the acceptor Q by naphthoquinone were observed. The results were attributed to a weaker binding of Q in PSI, compared to the bacterial RCs [64]. Thurnauer's group found that CIDEP can also develop in the P^+ $BPhe^-$ radical pair of the bacterial RC [65, 66]. Spectra of native RCs containing the non-heme iron have been recorded for *Rb. sphaeroides* and *Rhodopseudomonas* (*Rps.*) *viridis*. Those experiments, together with spectra simulations, demonstrated that the CIDEP spectrum is mainly due to the P^+ part of the SCRP $[P^+(Q_A^{\bullet -}\ Fe^{2+})]$ and the rapid decay of the spin-polarized signal is due to spin–lattice relaxation of the $Q_A^{\bullet -}\ Fe^{2+}$ complex [67, 68].

5.3 Magnetic Field Effects (MFE)

The first convincing observation of a MFE on a chemical reaction was in the late 1960s by Johnson in the triplet-exciton annihilation luminescence of anthracene crystals [69] and the results were evaluated using a spin-Hamiltonian approach [70].

An early theoretical prediction of the MFE was based on thermodynamics pointing out that chemical changes should be enhanced by a magnetic field if the reaction leads from diamagnetic to paramagnetic states, or vice versa. However, the magnetic contributions to ΔG turned out to be too minor to induce significant effects on the yields. Concerning kinetics, in the case of adiabatic reactions (i.e., strong coupling between initial and final electronic states), it is possible to exclude any significant MFE on the chemical reaction rate. For diabatic reactions there exists a large dynamic range for MFE [71, 72].

The MFE has been used to study the effect on the lifetime of radical intermediates and also to determine the exchange interaction between the components of the radical pair and the decay rates of the singlet and triplet radical pair states. In addition, the MFE allows for triplet-singlet absorbance difference spectra to be recorded, for example for photosynthetic preparations [73, 74].

After the discovery of the MFE on the triplet yield in RCs of photosynthetic bacteria [2, 75, 76], a relation between the MFE and CIDEP has been recognized. Both triplet yield and CIDEP were traced back to magnetic field dependent interactions of the electrons with nuclei [77, 78]. Hence, new investigations on RCs that use photochemically induced dynamic nuclear polarization (photo-CIDNP) have been foreseen [79].

However, the exact mechanism involving the interaction between electron and nuclei that induced the MFE was not known. In 1967, CIDNP in dark organic radical reactions was observed for the first time by solution NMR [80, 81]. This phenomenon was initially interpreted to be due to a transfer of spin polarization from radical electron spins to nuclear spins by the Overhauser effect. The alternative concept of the RPM, which was later shown to be correct, was suggested in 1969 independently by Gerhard and Liselotte Closs as well as by Kaptein and Oosterhoff [20, 37]. The proposed process is based on spin sorting, ruled by the state of the nuclear spin, and leads to equal intensities of emissive and absorptive NMR lines. Closs initially treated the S–T_0 transitions in the radical pair with two nuclear spin states ($I = +½$ and $-½$) in a non-coherent fashion. Meanwhile, Kaptein and Oosterhoff introduced the notion of coherent spin motion, where the hyperfine coupling energies are comparable to J in a radical pair. At the same time, Gerhart demonstrated the role of g-factor difference (Δg) in a radical pair for inducing singlet-triplet transitions, generating net nuclear spin polarization [82]. It was subsequently noted by Adrian and Kaptein that the diffusive separation and possible re-encounters of the two radicals play a significant role in the mechanism in the liquid state [38, 83, 84]. Thus, soon after the discovery of CIDNP phenomena, all the essential parts of the RPM had been assessed. Subsequently, the RPM has been a very helpful tool for kinetic modeling in bacterial photosynthesis [85, 86].

5.4 Electron–Nuclear Interactions

5.4.1 The Radical Pair Mechanism (RPM)

In its simplest form, the theory of the classical RPM is built on the radical pair Hamiltonian [87], as expressed in the following equation:

$$H = -J(\mathrm{R})\left(2S_1S_2 + \frac{1}{2}\right) + \mu_B \mathbf{B}_0(g_1S_1 + g_2S_2) + \sum_{\mathrm{n}} a_{1\mathrm{n}}I_{1\mathrm{n}}S_1 + \sum_{\mathrm{m}} a_{2\mathrm{m}}I_{2\mathrm{m}}S_2 \tag{5.1}$$

The first term corresponds to the exchange interaction, where $J(\mathrm{R})$ is a short range function of the inter-radical distance R. The other terms are the magnetic interactions within the individual radicals, where μ_B is the Bohr magneton, S_1 and S_2 are the electron spins of the two radicals, g_1 and g_2 are the electronic g-factors of radicals 1 and 2, $a_{1\mathrm{n}}$ and $I_{1\mathrm{n}}$ are the isotropic hyperfine constant and nuclear spin, respectively, and $a_{2\mathrm{m}}$ and $I_{2\mathrm{m}}$ are the analogous quantities for the second radical. The anisotropic terms are omitted under conditions of solution state because they average to zero by molecular tumbling of the radicals during the slow S–T_0 mixing process.

In order to see the influence of the classical RPM for the production of nuclear polarization consider the pair $R_1^{\bullet}H + R_2^{\bullet}$, where $R_1^{\bullet}H$ has one nucleus of spin ½ and R_2 has no magnetic nuclei (Fig. 5.7). Shown is an example in which the hyperfine splitting leads to two cases depending on the nuclear spin state. While in the case $I = -½$ the frequency of the Zeeman precession of both radicals is similar and the original electron spin state of the radical pair remains, in case $I = +½$ the radical pair undergoes rapid ISC transitions.

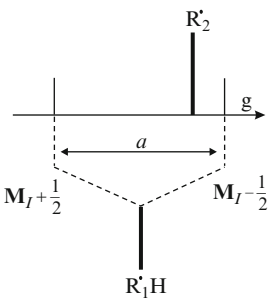

Fig. 5.7 The g-values of two radicals $R_1^{\bullet}$ and $R_2^{\bullet}$ of different chemical constitution may differ. In radical $R_1^{\bullet}$, interaction with nucleus H leads to hfi splitting with the hfi-constant a. Since the nucleus can be in two different nuclear spin states, in a magnetic field $R_1^{\bullet}H$ has two different Zeeman frequencies

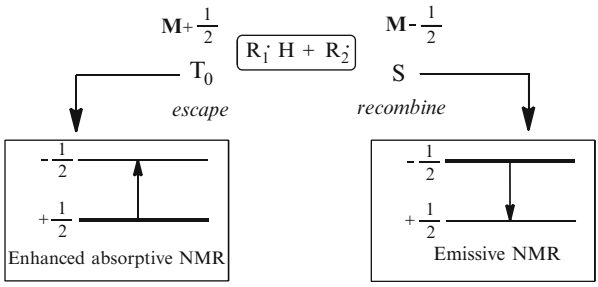

Fig. 5.8 RPM causes spin-sorting. The *solid arrows* indicate favored states

Figure 5.8 illustrates the mechanism of spin-sorting if the pair is formed as an electronic triplet and the nuclear magnetic moment is positive (i.e., ground nuclear Zeeman state has a nuclear spin parallel to the external field). For this case, the S–T_0 mixing rate is greater in the nuclear spin state ½ than in the −½ state. Hence, the former state will acquire S character faster than the latter and will be favored in the recombination product, giving enhanced absorptive signals for the product. Conversely, the other nuclear spin state will favor products formed from the escaped $R_1^{\bullet}H$ radical, which thus have emissive signals. Starting with an S instead of a T pair (or changing the sign of Δg or a_1) will reverse this pattern, giving emissive signals for recombination products and absorption signals for the escape products.

For a qualitative prediction of the sign of the polarization effects (Γ_n) by spin sorting, it is possible to apply the following rules, developed by Kaptein [88]:

$$\Gamma_n = \mu \cdot \varepsilon \cdot \Delta g \cdot a_i \begin{cases} +\text{A} \\ -\text{E} \end{cases} \tag{5.2}$$

Where A stands for enhanced absorption, E for emission, Δg and a_i have been established previously and the other symbols are defined as follows:

$$\mu \begin{cases} +\text{for T precursor} \\ -\text{for S precursor} \end{cases}$$

$$\varepsilon \begin{cases} +\text{for recombination products} \\ -\text{for escape products} \end{cases}$$

This sign rules provide an extremely valuable tool for the classical RPM and interpreting the CIDNP observations.

Hence, the classical RPM explains very well spin-sorting in solution and provided a sound basis for interpretation of CIDEP and CIDNP experimental data obtained under these conditions. Later, the classical RPM was extended to include the production of net nuclear polarization in cyclic reactions of, for example, biradicals [89]. In such systems, nuclear spin states control the formation of a long-living electronic triplet state. Since this highly paramagnetic electronic triplet

extinguishes nuclear polarization on the triplet reaction pathway, more nuclear polarization on the singlet reaction pathway survives and net nuclear polarization is created. This variation of the RPM is called "cyclic reactions" for liquid-state photo-CIDNP and "differential relaxation" (DR) for solid-state photo-CIDNP (*vide infra*). Several excellent review articles on the RPM have been published [90–94].

5.4.2 Solid-State Photo-CIDNP Effect

Encouraged by the success of the RPM to explain CIDEP data, researchers started to search for CIDNP signals in particular in photosynthetic systems. In 1979, Hoff and Kaptein recognized that photo-CIDNP cannot be observed in bacterial RCs by ^{1}H solution NMR. The discovery of the anisotropy of the MFE as well as technical progress in solid-state NMR shifted the attention to the solid state [95]. The development of magic-angle spinning (MAS) solid-state NMR and its application to proteins paved the way for the advent of photo-CIDNP MAS NMR. A solid-state photo-CIDNP effect was reported for the first time by Zysmilich and McDermott in 1994 in quinone-depleted (or prereduced) and frozen ^{15}N-labeled bacterial RCs of the purple bacteria *Rb. sphaeroides* R26 [96]. A huge enhancement of the ^{15}N MAS NMR signals was observed upon continuous illumination with white light (Fig. 5.9). Subsequently, the effect has been observed in various frozen RCs of

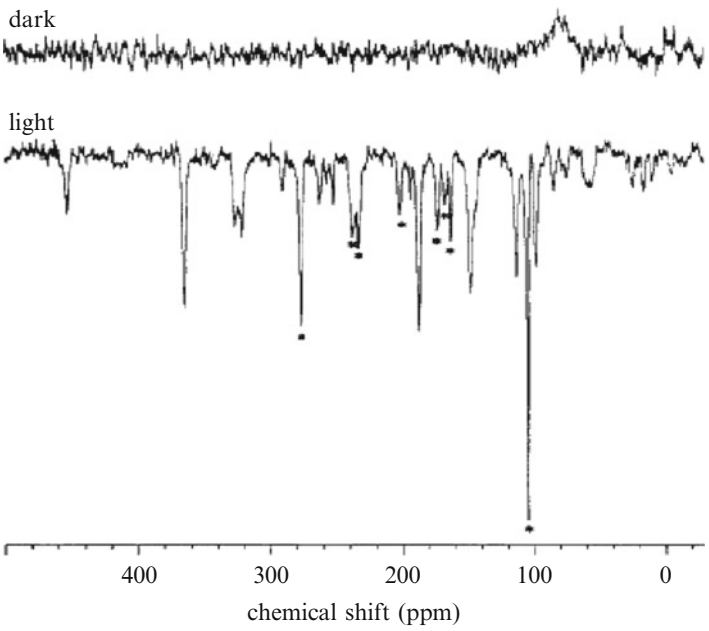

Fig. 5.9 The first photo-CIDNP MAS NMR experiment reported by Zysmilich and McDermott using ^{15}N-labeled RCs of *Rb. sphaeroides* R26. Reproduced with permission from Zysmilich and McDermott [96]. Copyright (1996) American Chemical Society

different photosynthetic organisms as well as in a blue-light photoreceptor, the mutant C57S of the phototropin LOV1 domain from the green alga *Chlamydomonas reinhardtii*, by ^{13}C and ^{15}N MAS NMR (*vide infra*) [97]. Obviously, the sample state rules out that the enhancement of NMR signal intensities is related to molecular diffusion.

The very strong enhancement in the ^{13}C photo-CIDNP MAS NMR spectra makes it possible to observe the effect in whole photosynthetic systems like membranes, chromatophores, and cells [98, 99]. The solid-state photo-CIDNP effect has been observed in all natural photosynthetic RCs studied so far and it appears to be an intrinsic property of efficient photosynthetic electron transfer. It is safe to say that systems showing photo-CIDNP originate from very different branches of the evolutionary tree. It appears that the solid-state photo-CIDNP effect is highly conserved in the evolution of photosynthetic organisms [100]. That correlation between the solid-state photo-CIDNP effect and the unsurpassed efficiency of photosynthetic electron transfer might be due to the fact that the short radical pair lifetime is related to both the selectivity of the chemical process and the lifetime broadening of the parameters allowing for the observation of the effect. That would imply that other electron transfer systems, having longer radical pair lifetimes and lower quantum yield for electron transfer, have smaller matching windows for observation of the effect making its detection more demanding. In any case, the effect allows for development of a sensitive analytical technique to study the electronic structure the photochemically active cofactors of RCs in great detail. The chemical shifts of the light-induced signals provide information about the electronic structure of diamagnetic ground state after the photocycle. Similarly, the light-induced signal intensities reveal the electron spin density distribution at atomic resolution. Photo-CIDNP intensities observed in steady state experiments refer to the electron spin densities in the p_Z-orbitals [101], while intensities obtained in the initial phase of time-resolved experiments is related to electron spin densities of s-orbitals [102, 103].

An explanation of the origin of the solid-state photo-CIDNP effect has been provided [104]. In particular, experiments on the field dependence [105, 106] as well as on the kinetic development allowed for a deeper insight [102, 107]. The classical RPM machinery of spin sorting is also active in the photoprocess of quinone-blocked RC. However, only time-resolved experiments are able to detect the RPM polarization [102]. In continuous illumination experiments, the RPM spin-sorting contribution is cancelled and up to three mechanisms are involved in building up photo-CIDNP under continuous illumination. In all three mechanisms, which might work in parallel, the breaking of the balance of the nuclear spin populations in the two decay branches (see Fig. 5.10) of the radical pair state leads to net steady-state nuclear polarization, which is detected in the NMR experiment after completion of the photocycle.

As shown in Fig. 5.10, upon birth of the photosynthetic radical pair, a pure singlet state is created having a high electron spin order associated with zero-quantum

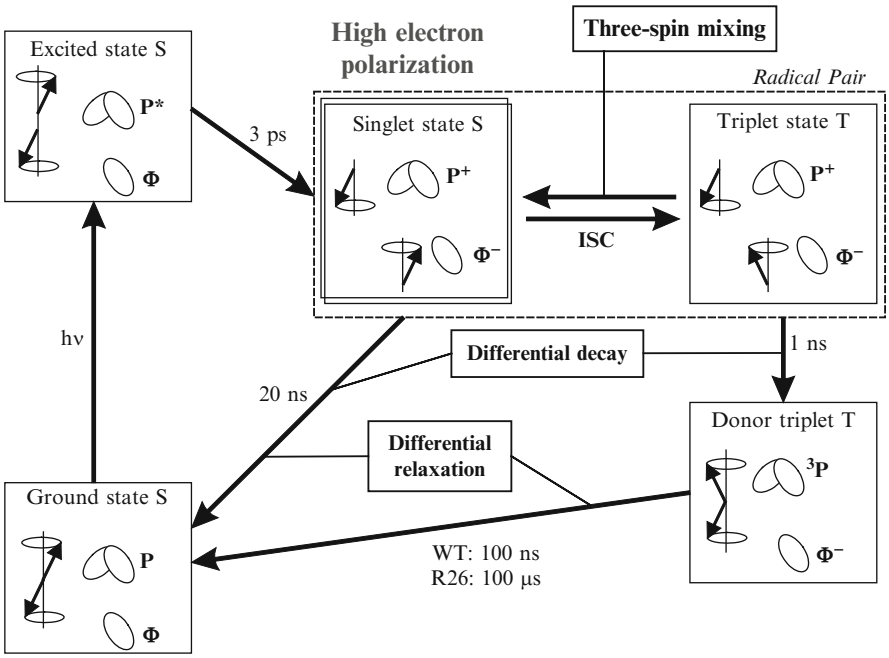

Fig. 5.10 Kinetics and spin-dynamics of solid-state photo-CIDNP effect in *Rb. sphaeroides* wild-type (WT) and R26

coherence between the electron spin states of the radical pair. There are two transfer mechanisms which transfer this electron polarization to nuclear polarization:

1. Three spin mixing (TSM). As stated above, photo-induced ET in the RCs leads to an SCRP that is highly electron-polarized. The evolution of the T_0 state is accompanied by a transfer of polarization to the nuclei. The electron–electron–nuclear model system for TSM, proposed by Jeschke in 1997 [108], consists of two electron spins $S_1 = ½$, $S_2 = ½$ and one nuclear spin $I = ½$. Since at high magnetic fields, the T_+ and T_- are energetically too distant to become involved, the spin dynamics occur selectively on the S–T_0 subsystem at the zero-quantum transition of the two electron spins (Fig. 5.11).

   The anti-symmetry of the coherent spin evolution in the correlated radical pair between the S and T_0 states is broken by state mixing due to anisotropic pseudo-secular hf coupling and electron–electron dipolar coupling. The symmetry breaking concerning the nuclear states is caused by the pseudo-secular hf coupling, which tilts the quantization axes of nuclear spins with respect to the external magnetic field. The tilt angles and tilt direction differ in the electron spin $S_{1\alpha}$ and $S_{1\beta}$ manifold. This tilt converts part of the electron–electron zero-quantum coherence that exists in a singlet-born radical pair to electron–electron–nuclear zero/single quantum coherence. A further tilt of the electron spin

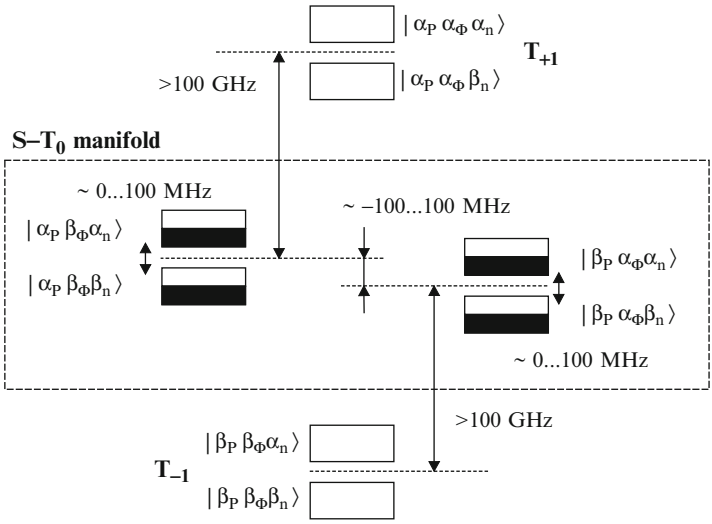

Fig. 5.11 Energy levels of the radical pair

quantization axes by the exchange coupling or by the pseudo-secular component of the electron–electron dipole–dipole coupling converts part of this three-spin coherence to nuclear antiphase coherence. This corresponds to a symmetry breaking with respect to the singlet and triplet state of the radical pair. The antiphase nuclear coherence further evolves to nuclear coherence during the lifetime of the radical pair. On recombination of the pair, part of this coherence is projected to polarizations, since the tilt of the nuclear spin quantization axes due to the pseudo-secular hyperfine field suddenly vanishes.

A maximum of net nuclear polarization through the TSM is generated when the double matching condition is fulfilled:

$$2|\Delta\Omega| = 2|\omega_I| = |A_z| \tag{5.3}$$

The nuclear polarization by TSM vanishes when the absolute pseudo-secular hyperfine contribution approaches zero, $B = 0$, and persists at $\Delta\Omega = 0$ and $A_z = 0$. The contribution of TSM to nuclear polarization is maximum at $\Delta\Omega = 0$. The relevant conditions for TSM are explained in Fig. 5.12. The TSM mechanism creates significant polarization only if the product of the electron–electron coupling d and the radical pair lifetime is of the order of unity or larger. On the other hand, the contribution vanishes if d is so large that the S and T_0 states become eigenstates of the pair. TSM contributions are thus observed only for moderate electron–electron couplings. Further, the sign of photo-CIDNP effect by TSM contribution is depended on the sign of d.

2. Differential decay (DD). This mechanism explains the polarization transfer in the solid-state photo-CIDNP effect in the absence of the electron–electron

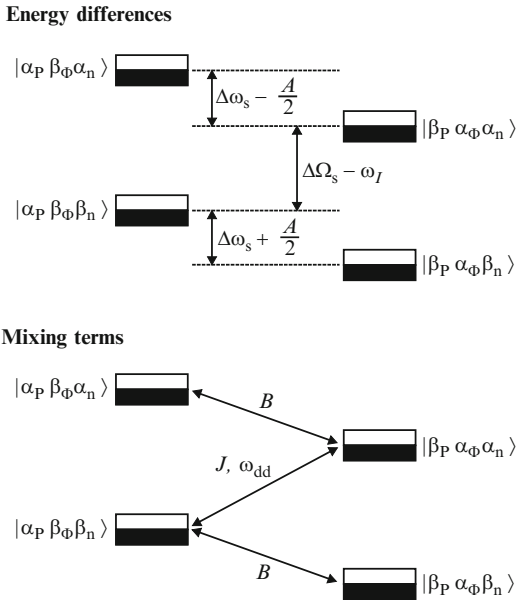

Fig. 5.12 Energy diagram (*top*) and mixing terms (*bottom*) allowing for electron–electron–nuclear three spin mixing

coupling d [109]. The evolution of nuclear polarization from the electron polarization occurs owing to the different lifetimes of singlet (T_S) and triplet radical pairs (T_T). This means that in the two radical pair spin states different fractions of polarization flow from the electrons to the nuclei. The DD mechanism requires only a single matching of interactions.

$$2|\omega_I| = |A_z| \tag{5.4}$$

However, note that the timescales of radical pair recombination and hyperfine-induced spin evolution must also match. Similar to TSM, the Zeeman interaction and the pseudo-secular hyperfine interaction are essential for polarization transfer in this mechanism. The nuclear polarization by DD vanishes if $T_S = T_T$, $\Delta\Omega = 0$ or $A = 0$. For polarization transfer in photo-CIDNP via the DD mechanism, both the secular part of hyperfine interaction and the difference between g values of the two electron spins are required. On the other hand, the DD contribution persists when the electron–electron coupling vanishes ($d = 0$). The efficiency of this mechanism depends on the ratio of both lifetimes.

It is remarkable that nature has chosen the time constants and magnetic parameters of the radical pair in bacterial RCs in such a way that the DD runs at its optimum allowing TSM and DD to make contributions of similar magnitude to the nuclear polarization (Fig. 5.13).

In addition to the two polarization transfer mechanisms TSM and DD, in samples having a long lifetime of the triplet donor (^{3}P), as in the carotenoid-less

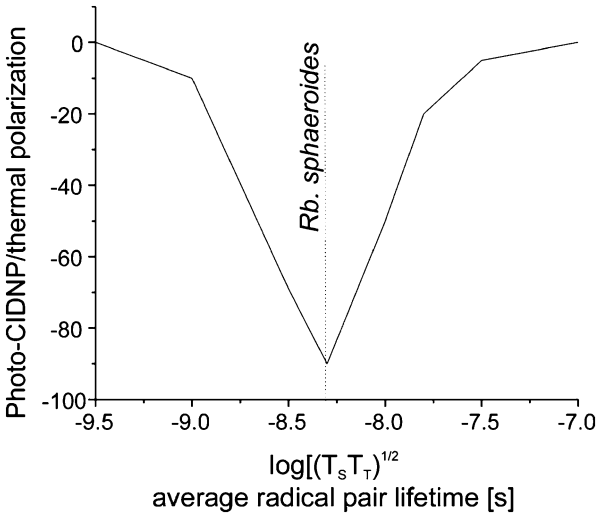

Fig. 5.13 Dependence of the DD mechanism of the solid-state photo-CIDNP effect on the lifetime of the radical pair. Reproduced with permission from Matysik et al. [100]. Copyright (2009) Springer

R26 mutant of RCs of *Rb. sphaeroides* [98, 106], a third mechanism might occur creating nuclear polarization:

3. Differential relaxation (DR). During this mechanism, the breaking of the anti-symmetry of the polarization in the singlet and triplet branch occurs in a non-coherent way. The enhanced relaxation of nuclear spins in the proximity of the highly paramagnetic donor partially cancels the nuclear polarization on nuclei of the donor cofactors. When the ^{3}P lifetime is comparable to or exceeds the paramagnetically enhanced longitudinal relaxation time, net polarization occurs due to partial extinction of nuclear polarization of the triplet state of the radical pair [110]. This extinction of polarization also leads to a significant enhanced recovery rate of the polarization in steady-state experiments [111].

5.5 Solid-State Photo-CIDNP MAS NMR Experiments

The solid-state photo-CIDNP effect opens the possibility for an efficient method to analyze the electronic structures of cofactors in RC proteins of different photosynthetic organisms. As an analytical tool to study structure and function of different RCs in various photosynthetic organisms, solid-state photo-CIDNP MAS NMR has been developed into a fully fledged analytical method [112]. Combination with selective isotope labeling adds further to selectivity and sensitivity. The new developments of this technique as two-dimensional photo-CIDNP MAS NMR

and nanosecond flash photo-CIDNP MAS NMR allows for exploring not only the aromatic cofactors but also their surroundings as the protein pocket. Here we provide an overview about the photosynthetic systems studies so far.

5.5.1 Rhodobacter sphaeroides *WT and R26*

Although RCs of *Rb. sphaeroides* WT are well-studied systems, two central functional aspects are still under debate [1, 2, 113]: (1) While the cofactor arrangement is highly symmetric, the electron transfer occurs selectively into one of the two branches (see Chap. 9). (2) The quantum yield for light-induced long range electron transfer is close to unity and it is not clear what makes natural photosynthetic systems so exceptionally efficient.

The asymmetry of the special pair P in its cationic state has been investigated by experimental techniques like EPR, ENDOR, TRIPLE, and photo-CIDNP MAS NMR. These studies show that a greater electron density is located on cofactor P_L than in P_M [52, 114]. This asymmetry has been attributed to either the different structure of two BChls in P_L and P_M or due to the effect of environment around the special pair [115]. This asymmetry might be interpreted in terms of differences in orbital factors which lead to more efficient orbital overlap in the active branch. Since theoretical calculations on the isolated special pair excellently reproduce the experimental data, we conclude that the electronic properties of the special pair are determined by internal factors, and the role of the protein is limited to stabilize these properties of the special pair [103].

Photo-CIDNP MAS NMR also allows for the ground-state electronic properties of the neutral state to be explored by comparing chemical shift values. The data show very significant chemical shift differences between the cofactors of the special pair [103, 116]. The data demonstrate that P_L contains more ground-state density than P_M which is in particular concentrated in the overlap region of P_L and P_M. Although both the electron spin density in the cation state and the electron density in the neutral ground state refer to the same molecular orbital, the HOMO, the appearance of the patterns is rather different. In particular, the central part of the special pair, the overlapping area of the two cofactors, which contains especially high amount of ground-state electron density, is emptied in the radical cation. That observation suggests that electric polarization effects of the matrix stabilize the radical cation and thus prevent electron back-transfer during charge separation [103]. In contrast to the asymmetric electron density distribution in the ground state and the radical cation state, it is very symmetric in the donor triplet state [106], suggesting that the LUMO is mainly on P_M.

There are several lines of evidence from photo-CIDNP MAS NMR, for example the linewidths of the signals, that the special pair is very rigid and highly ordered [105, 106, 116]. Comparing chemical shifts of the special pair from dark MAS NMR and photo-CIDNP MAS NMR, no light-induced change is revealed [116]. Hence, it appears that well-designed internal coordinates, which are well maintained and stabilized by the matrix, control the properties of the special pair.

5.5.2 Other Bacteria

Also RCs of other photosynthetic bacteria have been studied. Those, for which isolated RC are not available, were studied directly in membranes or whole cells. In the RC of *Rps. acidophila*, the solid-state photo-CIDNP effect was observed in ^{13}C labeled LH1-RC complexes [117]. The light induced ^{13}C MAS NMR signals in aromatic region of the spectrum show emissive peaks very similar to those obtained in *Rb. sphaeroides* WT RC. Both of them have similar distribution of electron spin density in the radical pair state.

An emissive light-induced spectrum, detected by ^{13}C MAS NMR, was also observed in purified Fenna-Matthews-Olson (FMO) RC particles of *Chlorobium* (*C.*) *tepidum* [118]. This green sulfur bacterium is an anoxygenic photosynthetic organism with the type I RCs and with the Fe-S clusters acting as terminal electron acceptor. The photo-CIDNP MAS NMR spectrum of this organism is comparable to that in *Rb. sphaeroides* WT RCs.

Another bacterium in which the solid-state photo-CIDNP effect has been observed is *Heliobacillus* (*Hb.*) *mobilis* [119]. This heliobacterium is characterized by the presence of a unique BChl-*g* pigment that acts as an antenna and as the primary donor in the electron transfer chain. The RC of *Hb. mobilis* belongs to type-I RCs which possesses Fe-S clusters as terminal electron acceptors. The cell samples can be prepared in an anoxygenic brown and in an oxygenic green form. The color change is due to oxygenation of BChl *g* to Chl *a*. Photo-CIDNP MAS NMR has shown that this primary donor, a symmetric dimer and the acceptors of the two active branches remain unchanged while the accessory cofactors undergo the transformation [99].

5.5.3 Photosystems of Plants

In plants and algae, photosynthesis is driven by two coupled photosystems, PSI and PSII. While PSI is a strong reductant, PSII is a very powerful oxidant. The ^{13}C photo-CIDNP MAS NMR spectra of the two plant photosystems indeed are well distinguished in their sign patterns. In PSI preparations of PSI-110 particles all signals are emissive [120]. On the other hand, the spectrum of a D1D2-preparation of PSII appears to have a sign pattern similar to R26 (Fig. 5.14) [121, 122], suggesting occurrence of the DR mechanism and absence of carotenoids close to the donor. In PSI spectrum, all signals can be assigned to a single undisturbed Chl *a* cofactor or a symmetric pair of Chl *a* cofactors. The PSII spectrum shows a monomeric Chl *a* showing, compared to an isolated Chl *a* molecule in organic solution, an inversion in its electron spin density. Additional signals suggest an involvement of the axial histidine [101].

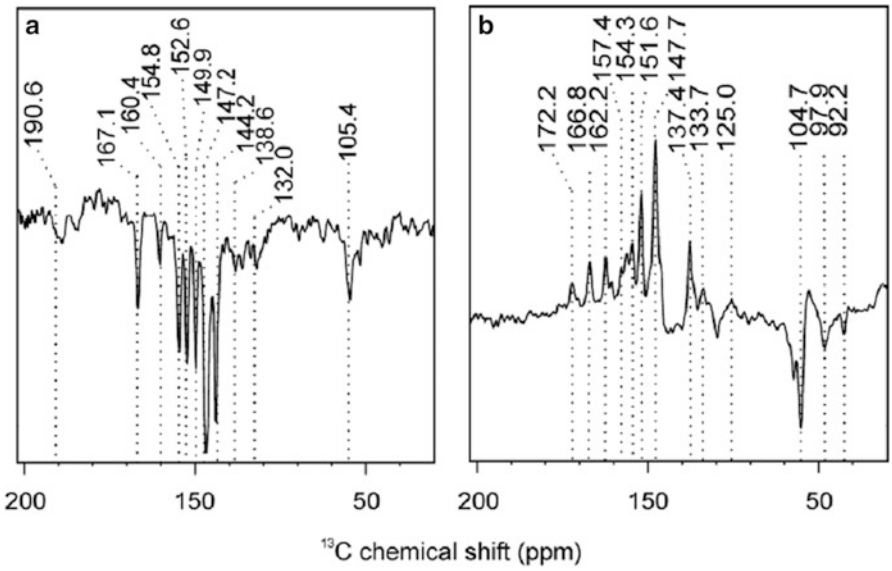

Fig. 5.14 ^{13}C photo-CIDNP MAS NMR spectra of (**a**) PSI and (**b**) PSII at a magnetic field of 9.4 T and a MAS frequency of 9.0 kHz. Reproduced with permission from Diller et al. [122]. Copyright (2005) Springer

5.6 Possible Functional Relevance of Nuclear Spin-Hyperpolarization

Presently, photochemically induced spin dynamics in radical pairs in blue-light photoreceptors is expected to play a prominent role in animal navigation in the earth's magnetic field [123–128]. The question whether photosynthesis also might be influenced by magnetic fields arises. It has already been proposed, esp. by Thurnauer, that spin-correlated radical pairs are a hallmark of efficient electron transfer [129–132]. Indeed, various and complex magnetic field effects are documented on plant growth [133, 134]. As we have seen, photosynthetic ET is linked to spin transport and electron and nuclear spin hyperpolarization. The TSM theory predicts that photosynthetic systems also produce high nuclear spin-hyperpolarization at earth's magnetic field conditions [135].

There are two hints that photo-CIDNP might play a role in the functioning of RCs:

1. All RCs investigated, although from very different branches of the evolutionary tree show the solid-state photo-CIDNP effect implying that the effect is correlated to functional relevance [98]. Efficiency of electron transfer and the general observability of the solid-state photo-CIDNP effect have indeed one common feature: the short lifetime of the radical-pair, which reflects an optimized reaction channel avoiding side-reactions as well as which leads to broadening of the excitation field curve of the effect [136] Since most of the systems other than

natural photosynthetic RCs forming light-induce radical pairs have longer radical pair lifetimes, the observation of the effect is more difficult.
2. It appears that the ratio of radical-pair lifetimes of radical pairs in the singlet and in the triplet state in RCs of *Rb. sphaeroides* is optimized to produce maximum nuclear polarization (Fig. 5.13) [104]. That might suggest that nuclear hyperpolarization plays an active role in optimizing the efficiency of photosynthetic ET. Here the question whether the high spin-order might be related to function rises. Could it be that efficient ET also relies on nuclear spin order?

Now we shortly want to introduce three ideas how one could imagine that high nuclear spin-order produced in photosynthetic charge separation might improve the efficiency of ET:

1. Spin catalysis by observer spin. A third radical interacting with a radical pair is called "observer spin." If the radical pair is spin-polarized, the observer spin obtains polarization from the radical pair. On the other hand, the observer spin might act as spin catalyst in radical pair processes [137]. One might consider the strongly coupled nuclear spin pool of the RC protein as such observer spin receiving hyperpolarization from the radical pair and directing the electron transfer process.
2. Coupling of spins, charges and heat by the Onsager equation. During the photochemical event, the protein is not in equilibrium and energy is dissipating and charges and spins are moving. According to non-equilibrium thermodynamics these currents are not independent but coupled. To that end, the Onsager equation provides a mathematical tool to describe these couplings [138]. Such a non-equilibrium treatment might allow for directionality for the ET process.
3. Organic magnetoresistance effect (OMAR) as a dynamic spin-valve. An analogue to the giant magnetoresistance effect, in which ordered electron spins affect the transport of electrons through the semiconductor, in which nuclear spins control the ET in organic semiconductors has been discovered by Wohlgenannt and coworkers in 2004 [139–142]. One could imagine that in proteins, highly organized nuclear spins, for example a proton pool, could take over such function.

Hence, in non-equilibrium thermodynamics order is created spontaneously. In photosynthesis, the first order is due to charge and spin separation. To what extent these processes interrelate will require further studies.

Acknowledgments The authors thank Profs. P.A. Bobbert, P. Hore, G. Jeschke, B. Koopmans, A. van der Est and M. Wohlgenannt for the stimulating discussions. This work has been financially supported by the Netherlands Organization for Scientific Research (NWO) through an ECHO grant (713.012.001).

References

1. Hunter CN, Daldal F, Thurnauer MC, Beatty JT, editors. Advances in photosynthesis and respiration, The purple phototropic bacteria, vol. 28. Dordrecht: Springer; 2009.
2. Hoff AJ, Deisenhofer J. Photophysics of photosynthesis. Structure and spectroscopy of reaction centers of purple bacteria. Phys Rep. 1997;287(1–2):1–247.

3. Holzwarth AR, Müller MG. Energetics and kinetics in reaction centers from Rhodobacter sphaeroides. A femtosecond transient absorption study. Biochemistry. 1996;35(36):11820–31.
4. Arlt T, Schmidt S, Kaiser W, Lauterwasser C, Meyer M, Scheer H, Zinth W. The accessory bacteriochlorophyll: a real electron carrier in primary photosynthesis. Proc Natl Acad Sci U S A. 1993;90(24):11757–61.
5. Norris JR, Uphaus RA, Crespi HL, Katz JJ. Electron spin resonance (ESR) of chlorophyll and the origin of signal I in photosynthesis. Proc Natl Acad Sci U S A. 1971;68(3):625–8.
6. Jordan P, Fromme P, Witt HT, Klukas O, Saenger W, Krauss N. Three-dimensional structure of cyanobacterial photosystem I at 2.5 Å resolution. Nature. 2001;411(6840):909–17.
7. Watanabe T, Kobayashi M. Electrochemistry of chlorophylls. In: Scheer H, editor. Chlorophylls. Boca Ratón, FL: CRC Press; 1991. p. 287–364.
8. Zouni A, Witt HJ, Kern J, Fromme P, Krauss N, Saenger W, Orth P. Crystal structure of photosystem II from *Synechococcus elongates* at 3.8 Å resolution. Nature. 2001;409 (6821):739–43.
9. Webber AN, Lubitz W. P700: the primary electron donor of photosystem I. Biochim Biophys Acta. 2001;1507(1–3):61–79.
10. Woodbury NW, Allen JP. The pathway, kinetics and thermodynamics of electron transfer in wild-type and mutant reaction centers of purple nonsulfur bacteria. In: Blankenship RE, Madigan MT, Bauer CE, editors. Anoxygenic photosynthetic bacteria. Dordrecht: Kluwer; 1995. p. 527–57.
11. Cogdell RJ, Howard TD, Bittl R, Schlodder E, Geisenheimer I, Lubitz W. How carotenoids protect bacterial photosynthesis. Philos Trans R Soc Lond B Biol Sci. 2000;335(1402):1345–9.
12. Hore PJ, Joslin CG, McLauchlan KA. Chemically induced dynamic electron polarization. In: Ayscough PB, editor. Electron spin resonance, Volume 5. London: The Chemical Society; 1979.
13. Salikhov KM. Magnetic isotope effect in radical reactions: an introduction. Wien: Springer; 1996.
14. Salikhov KM, Molin YN, Sagdeev RZ, Buchachenko AL. Spin polarization and magnetic effects in radical reactions. Amsterdam: Elsevier; 1984.
15. Möbius K, Lubitz W, Savietsky A. Photo-induced electron spin polarization in chemical and biological reactions: probing structure and dynamics of transient intermediates by multifrequency EPR spectroscopy. Appl Magn Reson. 2011;41(2–4):113–43.
16. Closs GL, Forbes MDE, Norris JR. Spin-polarized electron paramagnetic resonance spectra of radical pairs in micelles: observation of electron spin-spin interaction. J Phys Chem. 1987;91(13):3592–9.
17. Buckley CD, Hunter DA, Hore PJ, McLauchlan KA. Electron spin resonance of spin-correlated radical pairs. Chem Phys Lett. 1987;135(3):307–12.
18. Hore PJ, Hunter DA, McKie CD, Hoff AJ. Electron paramagnetic resonance of spin-correlated radical pairs in photosynthetic reactions. Chem Phys Lett. 1987;137(6):495–500.
19. McLauchlan KA, Steiner UE. The spin-correlated radical pair as a reaction intermediate. Mol Phys. 1991;73(2):241–63.
20. Kaptein R, Oosterhoff JL. Chemically induced dynamic nuclear polarization II (Relation with anomalous ESR spectra). Chem Phys Lett. 1969;4(4):195–7.
21. Closs GL. Mechanism explaining nuclear spin polarizations in radical combination reactions. J Am Chem Soc. 1969;91(16):4552–4.
22. Brocklehurst B. Formation of excited states by recombining organic ions. Nature. 1969;221 (5184):921–3.
23. Schweiger A, Jeschke G. Principles of pulse electron paramagnetic resonance. New York: Oxford University Press; 2001.
24. Turro NJ, Weed GC. Micellar systems as supercages for reactions of geminate radical pairs. Magnetic effects. J Am Chem Soc. 1983;105(7):1861–8.
25. Atkins PW, Evans GT. Chemically induced electron spin polarization: the rotating triplet model. Chem Phys Lett. 1974;25(1):108–10.

26. Atkins PW. The triplet mechanism. In: Muus LT, Atkins PW, McLauchlan KA, Pedersen JB, editors. Chemically induced magnetic polarization. Dordrecht: Reidel Publishing; 1977.
27. van der Waals JH. EPR of photo-excited triplet states: a personal account. Appl Magn Reson. 2001;20(4):541–61.
28. Anisimov OA, Bizyaev VL, Lukzen NN, Grigoryants VM, Molin YN. The induction of quantum beats by hyperfine interactions in radical-ion pair recombination. Chem Phys Lett. 1983;101(2):131–5.
29. Usov OM, Grigoryants VM, Tajikov BM, Molin YN. Determination of a fraction of spin-correlated radical ion pairs in irradiated alkanes by quantum oscillation technique. Radiat Phys Chem. 1997;49(2):237–43.
30. Fessenden RW, Schuler RH. Electron spin resonance studies of transient alkyl radicals. J Chem Phys. 1963;39(9):2147–95.
31. Hoff AJ. Electron spin polarization of photosynthetic reactants. Q Rev Biophys. 1984;17(2):153–282.
32. Dismukes GC, McGuire A, Blankenship R, Sauer K. Electron spin polarization in photosynthesis and the mechanism of electron transfer in photosystem I. Biophys J. 1978;21(3):239–56.
33. Möbius K. Primary processes in photosynthesis: what do we learn from high-field EPR spectroscopy? Chem Soc Rev. 2000;29(2):129–39.
34. Smaller B, Remko JR, Avery EC. Electron paramagnetic resonance studies of transient free radicals produced by pulse radiolysis. J Phys Chem. 1968;48(11):5174–81.
35. Harbour JR, Tollin G. Photoinduced one-electron transfer between bacteriochlorophyll and quinone in acetone. Photochem Photobiol. 1974;19(2):163–7.
36. Blankenship R, McGuire A, Sauer K. Chemically induced dynamic electron polarization in chloroplasts at room temperature: evidence for triplet state participation in photosynthesis. Proc Natl Acad Sci U S A. 1975;72(12):4943–7.
37. Closs GL, Closs LE. Induced dynamic nuclear spin polarization in reactions of photochemically and thermally generated triplet diphenylmethylene. J Am Chem Soc. 1969;91(16):4549.
38. Adrian FJ. Theory of anomalous electron spin resonance spectra of free radicals in solution. Role of diffusion-controlled separation and reencounter of radical pairs. J Chem Phys. 1971;54(9):3918–23.
39. Adrian FJ. Contribution of $S \leftrightarrow T_{\pm 1}$ intersystem crossing in radical pairs to chemically induced nuclear and electron spins polarization. Chem Phys Lett. 1971;10(1):70–4.
40. Adrian FJ. Singlet-triplet splitting in diffusing radical pairs and the magnitude of the chemically induced electron spin polarization. J Chem Phys. 1972;57(12):5107–13.
41. Pedersen JB, Freed JH. Theory of chemically induced dynamic electron polarization I. J Chem Phys. 1973;58(7):2746–62.
42. Atkins PW, Gurd RC, McLauchlan KA, Simpson AF. Electron spin resonance emission spectra in solution. Chem Phys Lett. 1971;8(1):55–8.
43. Atkins PW. Chemically induced electron spin polarization and radical pair re-encounters. Chem Phys Lett. 1973;18(2):290–4.
44. Atkins PW, McLauchlan KA. Electron spin polarization. In: Lepley AR, Closs GL, editors. Chemically induced magnetic polarization. New York: Wiley; 1973.
45. Wong SK, Hutchinson DA, Wan JKS. Chemically induced dynamic electron polarization II. A general theory for radicals produced by photochemical reactions of excited triplet carbonyl compounds. J Chem Phys. 1973;58(3):985–9.
46. van der Est A, Bittl R, Abresch EC, Lubitz W, Stehlik D. Transient EPR spectroscopy of perdeuterated Zn-substituted reaction centers of *Rhodobacter sphaeroides* R26. Chem Phys Lett. 1993;212(6):561–8.
47. Kleinfeld D, Okamura MY, Feher G. Electron-transfer kinetics in photosynthetic reaction centers cooled to cryogenic temperatures in the charge-separated state: evidence of light induced structural changes. Biochemistry. 1984;23(24):5780–6.

48. van den Brink JS, Hulsebosch RJ, Gast P, Hore PJ, Hoff AJ. Q_A binding in reaction centers of photosyntethic purple bacterium *Rhodobacter sphaeroides* R26 investigated with electron spin polarization spectroscopy. Biochemistry. 1994;33(46):13668–77.
49. Savitsky A, Dubinskii AA, Flores M, Lubitz W, Möbius K. Orientation-resolving pulsed electron dipolar high-field EPR spectroscopy on disordered solids: I. Structure of spin-correlated radical pairs in bacterial photosynthetic reaction centers. J Phys Chem B. 2007;111(22):6245–62.
50. Heinen U, Utschig LM, Poluektov OG, Link G, Ohmes E, Kothe G. Structure of the charge separated state $P_{865}^{+}Q_A^{-}$ in the photosynthetic reaction centers of *Rhodobacter sphaeroides* by quantum beat oscillations and high-field electron paramagnetic resonance: evidence for light-induced Q_A^{-} reorientation. J Am Chem Soc. 2007;129(51):15935–46.
51. Bittl R, Zech SG, Lubitz W. Light-induced changes in transient EPR spectra of $P_{865}^{+}Q_A^{-}$. In: Michel-Beyerle ME, editor. The reaction center of photosynthetic bacteria: structure and dynamics. Berlin: Springer; 1996.
52. Lubitz W, Lendzian F, Bittl R. Radicals, radical pairs and triplet states in photosynthesis. Acc Chem Res. 2002;35(5):313–20.
53. McIntosh AR, Bolton JR. Triplet state involvement in primary photochemistry of photosynthetic photosystem II. Nature. 1976;263(5576):443–5.
54. McIntosh AR, Bolton JR. CIDEP in the photosystems of green plant photosynthesis. Res Chem Interm. 1979;3(1–2):121–9.
55. McIntosh AR, Manikowski H, Wong SK, Taylor CPS, Bolton JR. CIDEP observations in photosystem I of green plants and algal photosynthesis. Biochem Biophys Res Commun. 1979;87(2):605–12.
56. McIntosh AR, Manikowski H, Bolton JR. Observations of chemically induced dynamic electron polarization in photosystem I of green plants and algae. J Phys Chem. 1979;83 (26):3309–13.
57. Norris JR, Morris AL, Thurnauer MC, Tang J. A general model of electron spin polarization arising from the interactions within radical pairs. J Chem Phys. 1990;92(7):4239–49.
58. Hore PJ. Analysis of polarized electron paramagnetic resonance spectra, Chapter 12. In: Hoff AJ, editor. Advanced EPR: applications in biology and biochemistry. Amsterdam: Elsevier; 1989. p. 405–40.
59. Salikhov KM, Boch CH, Stehlik D. Time development of electron spin polarization in magnetically coupled, spin correlated radical pairs. Appl Magn Reson. 1990;1(2):195–211.
60. Bittl R, Kothe G. Transient EPR of radical pairs in photosynthetic reaction centers: prediction of quantum beats. Chem Phys Lett. 1991;177(6):547–53.
61. Kothe G, Weber S, Ohmes E, Thurnauer MC, Norris JR. High time resolution electron paramagnetic resonance of light-induced radical pairs in photosynthetic bacterial reaction centers: observation of quantum beats. J Am Chem Soc. 1994;116(17):7729–34.
62. Dzuba SA, Bosch MK, Hoff AJ. Electron spin echo detection of quantum beats and double-quantum coherence in spin-correlated radical pairs of protonated photosynthetic reaction centers. Chem Phys Lett. 1996;248(5–6):427–33.
63. Feezel LL, Gast P, Smith UH, Thurnauer MC. Electron spin polarization of P^{+}-870Q^{-} observed in the reaction center protein of the photosynthetic bacterium *Rhodobacter sphaeroides* R26. The effect of selective isotopic substitution at X- and Q-band microwave frequencies. Biochim Biophys Acta. 1989;974(2):149–55.
64. van der Est A, Sieckmann I, Lubitz W, Stehlik D. Differences in the binding of the primary quinone acceptor in photosystem I and reaction centers of *Rhodobacter sphaeroides* R26 studied with transient EPR spectroscopy. Chem Phys. 1995;194(2–3):349–59.
65. Snyder SW, Morris AL, Bondeson SR, Norris JR, Thurnauer MC. Electron spin polarization in sequential electron transfer. An example from iron-containing photo-synthetic bacterial reaction center proteins. J Am Chem Soc. 1993;115(9):3774–5.
66. Morris AL, Snyder SW, Zhang Y, Tang J, Thurnauer MC, Dutton PL, Robertson DE, Gunner MR. Electron spin polarization model applied to sequential electrons transfer in

iron-containing photosynthetic bacterial reaction centers with different quinones as Q_A. J Phys Chem. 1995;99(11):3854–66.
67. Proskuryakov II, Klenina IB, Shkuropatov AY, Shkuropatova VA, Shuvalov VA. Free-radical and correlated radical-pair spin-polarized signals in *Rhodobacter sphaeroides* R26 reaction centers. Biochim Biophys Acta. 1993;1142(1–2):207–10.
68. van den Brink JS, Hermolle TEP, Gast P, Hore PJ, Hoff AJ. Electron spin polarization of the oxidized primary electron donor in reaction centers of photosynthetic purple bacteria. J Phys Chem. 1996;100(6):2430–7.
69. Johnson RC, Merrifield RE, Avakian P, Flippen RB. Effects of magnetic fields on the mutual annihilation of triplet excitons in molecular crystals. Phys Rev Lett. 1967;19(6):285–7.
70. Merrifield RE. Theory of magnetic field effects on the mutual annihilation of triplet excitons. J Chem Phys. 1968;48(9):4318–9.
71. Steiner UE, Ulrich T. Magnetic field effects in chemical kinetics and related phenomena. Chem Rev. 1989;89(1):51–147.
72. Zagdeev RZ, Molin YN, Salikhov KM, Leshina TV, Kamha MA, Shein SM. Effects of magnetic field on chemical reactions. Org Magn Res. 1973;5(12):603–5.
73. Hoff AJ. Magnetic field effects on photosynthetic reactions. Q Rev Biophys. 1981;14(4):599–665.
74. Boxer SG, Chidsey ED, Roelofs MG. Magnetic field effects on reaction yields in the solid state: an example from photosynthetic reaction centers. Annu Rev Phys Chem. 1983;34:389–417.
75. Hoff AJ, Rademaker R, van Grondelle R, Duysens LNM. On the magnetic field dependence of the yield of the triplet state in reaction centers of photosynthetic bacteria. Biochim Biophys Acta. 1977;460(3):547–54.
76. Blankenship RE, Schaafsma TJ, Parson WW. Magnetic field effects on radical pair intermediates in bacterial photosynthesis. Biochim Biophys Acta. 1977;461(2):297–305.
77. Hoff AJ, Rademaker H. Light-induced magnetic polarization in photosynthesis. In: Muus LT, Atkins PW, McLauchlan KA, Pedersen JB, editors. Chemically induced magnetic polarization. Dordrecht: Reidel Publishing; 1977. p. 399.
78. Werner HJ, Schulten K, Weller A. Electron transfer and spin exchange contributing to the magnetic field dependence of the primary photochemical reaction of bacterial photosynthesis. Biochim Biophys Acta. 1978;502(2):255–68.
79. Goldstein RA, Boxer SG. Effects of nuclear spin polarization on reaction dynamics in photosynthetic bacterial reaction centers. Biophys J. 1987;51(6):937–46.
80. Bargon J, Fischer H, Johnsen U. Kernresonanz-Emissionslinien während rascher Radikalreaktionen I. Aufnahmeverfahren und Beispiele. Z Naturforsch. 1967;22:1551–5.
81. Ward HR, Lawer RG. Nuclear magnetic resonance emission and enhanced absorption in rapid organometallic reactions. J Am Chem Soc. 1967;89(21):5518.
82. Gerhart F. Chemically induced nuclear polarization: dependence on Landé factors in radical recombination reactions. Tetrahedron Lett. 1969;10(58):5061–6.
83. Adrian FJ. Role of diffusion-controlled reaction in chemically induced nuclear spin polarization. J Chem Phys. 1970;53(8):3374.
84. Kaptein R. Chemically induced dynamic nuclear polarization. VIII: Spin dynamics and diffusion of the radical pairs. J Am Chem Soc. 1972;94(18):6251–62.
85. Haberkorn R, Michel-Beyerle ME. On the mechanism of magnetic field effects in bacterial photosynthesis. Biophys J. 1979;26(3):489–98.
86. Haberkorn R, Michel-Beyerle ME, Marcus RA. On spin-exchange and electron-transfer rates in bacterial photosynthesis. Proc Natl Acad Sci U S A. 1979;76(9):4185–8.
87. Adrian FJ. Principles of the radical pair mechanism of chemically induced nuclear and electron spin polarization. Res Chem Interm. 1979;3(1–2):3–43.
88. Kaptein R. Simple rules for the chemically induced dynamic nuclear polarization. J Chem Soc D. 1971;14:732–3.

89. Closs GL, Doubleday CE. Chemically induced dynamic nuclear spin polarization derived from biradicals generated by photochemical cleavage of cyclic ketones, and the observation of a solvent effect on signal intensities. J Am Chem Soc. 1972;94(26):9248–9.
90. Kaptein R. Chemically induced dynamic nuclear polarization: theory and applications in mechanistic chemistry. In: Williams GH, editor. Advances in free radical chemistry. London: Elek Science; 1975.
91. Closs GL, Miller RJ, Redwine OD. Time-resolved CIDNP: applications to radical and biradical chemistry. Acc Chem Res. 1985;18(7):196–202.
92. Hore P, Broadhurst RW. Photo-CIDNP of biopolymers. Prog Nucl Magn Reson Spectrosc. 1993;25(4):345–402.
93. Roth HD. Chemically induced dynamic nuclear polarization. In: Grant DM, Harris RK, editors. Encyclopedia of nuclear magnetic resonance. Chichester: Wiley; 1996.
94. Wan JKS. Theory and application of chemically induced magnetic polarization in photochemistry. In: Pitts JN, Hammond GS, Gollnick K, Grosjean D, editors. Advances in photochemistry, vol. 12. Toronto: Wiley; 1980. p. 283–346.
95. Boxer SG, Chidsey CED, Roelofs MG. Anisotropic magnetic interactions in the primary radical ion-pair of photosynthetic reaction centers. Proc Natl Acad Sci U S A. 1982;79 (15):4632–6.
96. Zysmilich MG, McDermott A. Photochemically induced dynamic nuclear polarization in the solid-state ^{15}N spectra of reaction centers from photosynthetic bacteria *Rhodobacter sphaeroides* R26. J Am Chem Soc. 1994;116(18):8362–3.
97. Thamarath SS, Heberle J, Hore PJ, Kottke T, Matysik J. Solid-state photo-CIDNP effect observed in phototropin LOV1-C57S by ^{13}C magic-angle spinning NMR spectroscopy. J Am Chem Soc. 2010;132(44):15542.
98. Prakash S, Alia A, Gast P, de Groot HJM, Matysik J, Jeschke G. Photo-CIDNP MAS NMR in intact cells of *Rhodobacter sphaeroides* R26: molecular and atomic resolution at nanomolar concentration. J Am Chem Soc. 2006;128(39):12794–9.
99. Thamarath SS, Alia A, Daviso E, Mance D, Golbeck JH, Matysik J. Whole-cell NMR characterization of two photochemically active states of the photosynthetic reaction center in heliobacteria. Biochemistry. 2012;51(29):5763–73.
100. Matysik J, Diller A, Roy E, Alia A. The solid-state photo-CIDNP effect. Photosynth Res. 2009;102(2–3):427–35.
101. Diller A, Roy E, Gast P, van Gorkom HJ, de Groot HJM, Glaubitz C, Jeschke G, Matysik J. ^{15}N photo-CIDNP MAS NMR analysis of the electron donor of photosystem II. Proc Natl Acad Sci U S A. 2007;104(31):12767–71.
102. Daviso E, Alia A, Prakash S, Diller A, Gast P, Lugtenburg J, Jeschke G, Matysik J. Electron-nuclear spin dynamics in a bacterial photosynthetic reaction center. J Phys Chem C. 2009;113 (23):10269–78.
103. Daviso E, Alia A, Prakash S, Gast P, Neugebauer J, Jeschke G, Matysik J. The electronic structure of the primary electron donor of reaction centers of purple bacteria at atomic resolution as observed by photo-CIDNP ^{13}C NMR. Proc Natl Acad Sci U S A. 2009;106 (52):22281–6.
104. Jeschke G, Matysik J. A reassessment of the origin of photochemically induced dynamic nuclear polarization effects in solids. Chem Phys. 2003;294(3):239–55.
105. Prakash S, Alia A, Gast P, de Groot HJM, Jeschke G, Matysik J. Magnetic field dependence of Photo-CIDNP MAS NMR on photosynthetic reaction centers of *Rhodobacter sphaeroides* WT. J Am Chem Soc. 2005;127(41):14290–8.
106. Thamarath SS, Bode BE, Prakash S, Sai Sankar Gupta KB, Alia A, Jeschke G, Matysik J. Electron spin density distribution in the special pair triplet of *Rhodobacter sphaeroides* R26 revealed by magnetic field dependence of the solid-state photo-CIDNP effect. J Am Chem Soc. 2012;134(13):5921–30.

107. Daviso E, Diller A, Alia A, Matysik J, Jeschke G. Photo-CIDNP MAS NMR beyond the T_1 limit by fast cycles of polarization extinction and polarization generation. J Magn Reson. 2008;190(1):43–51.
108. Jeschke G. Electron-electron-nuclear three spin mixing in spin-correlated radical pairs. J Chem Phys. 1997;106(24):10072–86.
109. Polenova T, McDermott AE. A coherent mixing mechanism explains the photoinduced nuclear polarization in photosynthetic reaction centers. J Phys Chem B. 1999;103(3):535–48.
110. McDermott AE, Zysmilich MG, Polenova T. Solid state NMR studies of photoinduced polarization in photosynthetic reaction centers: mechanism and simulations. Solid State Nucl Magn Reson. 1998;11(1–2):21–47.
111. Diller A, Prakash S, Alia A, Gast P, Matysik J, Jeschke G. Signals in solid-state photochemically induced dynamic nuclear polarization recover faster than with the longitudinal relaxation time. J Phys Chem B. 2007;111(35):10606–14.
112. Bode B, Thamarath SS, Sai Sankar Gupta KB, Alia A, Jeschke G, Matysik J. The solid-state photo-CIDNP effect and its analytical application. In: Kuhn L, editor. Hyperpolarization methods in NMR spectroscopy. Springer; in press.
113. Feher G, Allen JP, Okamura MY, Rees DC. Structure and function of bacterial photosynthetic reaction centres. Nature. 1989;339(6220):111–6.
114. Rautter J, Lendzian F, Lubitz W, Wang S, Allen JP. Comparative study of reaction centers from photosynthetic purple bacteria: electron paramagnetic resonance and electron nuclear double resonance spectroscopy. Biochemistry. 1994;33(40):12077–84.
115. Lendzian F, Huber M, Isaacson RA, Endeward B, Plato M, Bönigk B, Möbius K, Lubitz W, Feher G. The electronic structure of the primary donor cation radical in *Rhodobacter sphaeroides* R26: ENDOR and TRIPLE resonance studies in single crystals of reaction centers. Biochim Biophys Acta. 1993;1183(1):139–60.
116. Schulten EAM, Matysik J, Alia A, Kiihne S, Raap J, Lugtenburg J, Gast P, Hoff AJ, de Groot HJM. ^{13}C MAS NMR and photo-CIDNP reveal a pronounced asymmetry in the electronic ground state of the special pair of *Rhodobacter sphaeroides* reaction centers. Biochemistry. 2002;41(27):8708–17.
117. Diller A, Alia A, Gast P, Jeschke G, Matysik J. ^{13}C photo-CIDNP MAS NMR on the LH1-RC complex of *Rhodopseudomonas acidophila*. In: Allen JF, Gantt E, Golbeck JH, Osmond B, editors. Photosynthesis. Energy from the sun. 14th International Congress on Photosynthesis. Dordrecht: Springer; 2008. p. 55–8.
118. Roy E, Alia A, Gast P, van Gorkom JH, de Groot HJM, Jeschke G, Matysik J. Photochemically induced dynamic nuclear polarization in the reaction center of the green sulfur bacterium *Chlorobium tepidum* observed by ^{13}C MAS NMR. Biochim Biophys Acta. 2007;1767(6):610–5.
119. Roy E, Rohmer T, Gast P, Jeschke G, Alia A, Matysik J. Characterization of the primary radical pair in reaction centers of *Heliobacillus mobilis* by ^{13}C photo-CIDNP MAS NMR. Biochemistry. 2008;47(16):4629–35.
120. Alia A, Roy E, Gast P, van Gorkom JH, de Groot HJM, Jeschke G, Matysik J. Photochemically induced dynamic nuclear polarization in photosystem I of plants observed by ^{13}C magic-angle spinning NMR. J Am Chem Soc. 2004;126(40):12819–26.
121. Matysik J, Alia A, Gast P, van Gorkom JH, Hoff AJ, de Groot HJM. Photochemically induced nuclear spin polarization in reaction centers of photosystem II observed by ^{13}C solid-state NMR reveals a strongly asymmetric electronic structure of the $P680^+$ primary donor chlorophyll. Proc Natl Acad Sci U S A. 2000;97(18):9865–70.
122. Diller A, Alia A, Roy E, Gast P, van Gorkom JH, Zaanen J, de Groot HJM, Glaubitz C, Matysik J. Photo-CIDNP solid-state NMR on photosystems I and II: what makes P680 special? Photosynth Res. 2005;84(1–3):303–8.
123. Mouritsen H, Hore PJ. The magnetic retina: light-dependent and trigeminal magnetoreception in migratory birds. Curr Opin Neurobiol. 2012;22(2):343–52.

124. Hore PJ. Are biochemical reactions affected by weak magnetic fields? Proc Natl Acad Sci U S A. 2012;109(5):1357–8.
125. Wiltschko W, Wiltschko R. Magnetic orientation in birds. J Exp Biol. 1996;199(1):29–38.
126. Rodgers CT, Hore PJ. Chemical magnetoreception in birds: the radical pair mechanism. Proc Natl Acad Sci U S A. 2009;106(2):353–60.
127. Chaves I, Pokorny R, Byrdin M, Hoang N, Ritz T, Brettel K, Essen L, van der Horst GTJ, Batschauer A, Ahmad M. The cryptochromes: blue light photoreceptors in plants and animals. Annu Rev Plant Biol. 2011;62:335–64.
128. Solov'yov IA, Schulten K. Reaction kinetics and mechanism of magnetic fields effects in cryptochrome. J Phys Chem B. 2012;116(3):1089–99.
129. Wasielewski MR. Photogenerated, spin-correlated radical ion pairs in photosynthetic model systems. Spectrum. 1995;8(1):8–12.
130. Thurnauer MC, Dimitrijevic NM, Poluektov OG, Rajh T. Photoinitiated charge separation: from photosynthesis to nanoparticles. Spectrum. 2004;17(1):10–5.
131. Thurnauer MC, Poluektov OG, Kothe G. High-field EPR studies of electron transfer intermediates in photosystem I. In: Golbeck JH, editor. Photosystem I: the light-driven plastocyanin-ferredoxin oxidoreductase. Advances in photosynthesis and respiration, vol. 24. Dordrecht: Springer; 2006. p. 339–60.
132. Kothe G, Thurnauer M. What you get out of high-time resolution electron paramagnetic resonance: example from photosynthetic bacteria. Photosynth Res. 2009;102(2–3):349–65.
133. Belyavskaya NA. Biological effects due to weak magnetic field on plants. Adv Space Res. 2004;34(7):1566–74.
134. Galland P, Pazur A. Magnetoreception in plants. J Plant Res. 2005;118(6):371–89.
135. Closs GL. Low field effects and CIDNP of biradical reactions. In: Muus LT, Atkins PW, McLauchlan KA, Pedersen JB, editors. Chemically induced magnetic polarization. Dordrecht: Reidel Publishing; 1977. p. 225–56.
136. Jeschke G, Anger B, Bode BE, Matysik J. Theory of solid-state photo-CIDNP in earth magnetic field. J Phys Chem A. 2011;115(35):9919–28.
137. Ivanov KL. Net and multiplet CIDEP of the observer spin in recombination of radical-biradical pair. J Phys Chem A. 2005;109(23):5160–7.
138. Bauer GEW, Bretzel S, Brataas A, Tserkovnyak Y. Nanoscale magnetic heat pumps and engines. Phys Rev B. 2010;81(2):024427.
139. Francis TL, Mermer Ö, Veeraraghavan G, Wohlgenannt M. Large magnetoresistance at room temperature in semiconducting polymer sandwich devices. New J Phys. 2004;6:185.
140. Bobbert PA, Nguyen TD, van Oost FWA, Koopmans B, Wohlgenannt M. Bipolaron mechanism for organic magnetoresistance. Phys Rev Lett. 2007;99(21):216801.
141. Bobbert PA, Wagemans W, van Oost FWA, Koopmans B, Wohlgenannt M. Theory for spin diffusion in disordered organic semiconductors. Phys Rev Lett. 2009;102(15):156604.
142. Kersten SP, Schellekens AJ, Koopmans B, Bobbert PA. Magnetic-field dependence of the electroluminescence of organic light-emitting diodes: a competition between exciton formation and spin mixing. Phys Rev Lett. 2011;106(19):197402.

Chapter 6
Energy Changes in Photosynthetic Electron Transport: Probing Photosynthesis by Pulsed Photoacoustics

David Mauzerall and Steven P. Mielke

Abstract Pulsed photoacoustics (PPA) is the ideal method for determining the thermodynamics and energy-storage (E-S) efficiency of photosynthesis. In particular it is applicable to whole cells, and so allows direct study of in vivo energy storage by PSI and PSII, avoiding artifacts resulting from damage to isolated photosystems and disruption of linear electron flow. It is the in vivo efficiency that ultimately limits energy storage at limiting light intensities. In this chapter, after discussing advantages of separating the enthalpic and entropic contributions to free energy changes of photochemistry, we describe PPA methodology in detail, and discuss information available from the enthalpies it provides. To illustrate the use of PPA to obtain E-S efficiencies in vivo, we then describe a comprehensive study of cyanobacterial whole cells in the far-red spectral region. This study has resulted in the clear differentiation of the contributions of PSI and PSII to the observed efficiency; the first identification of the trap energies of both systems directly from enthalpy measurements; and quantification of the thermodynamically required decay in storage for excitations below these energies. This unique and elegant biophysical method can additionally provide such key information as volume changes resulting from electron transfer, optical cross sections, quantum yields, and turnover times.

Keywords Thermodynamics • Electron transfer • Photoacoustics • Enthalpy • Energy-storage efficiency • Oxygenic photosynthesis • *Acaryochloris marina* • Chlorophyll *d*

D. Mauzerall (✉) • S.P. Mielke
Laboratory of Photobiology, The Rockefeller University,
1230 York Avenue, 10065 New York, NY, USA
e-mail: mauzera@mail.rockefeller.edu

J. Golbeck and A. van der Est (eds.), *The Biophysics of Photosynthesis*,
Biophysics for the Life Sciences 11, DOI 10.1007/978-1-4939-1148-6_6,

Abbreviations

Am	*Acaryochloris marina*
Chl	Chlorophyll
E-S	Energy-storage
PA	Photoacoustics
PPA	Pulsed photoacoustics
PSI	Photosystem I
PSII	Photosystem II
Sl	*Synechococcus leopoliensis*

6.1 Introduction

Full understanding of a process requires knowledge of both its thermodynamics and its kinetics. Extensive spectroscopic investigations have led to good knowledge of the intermediates and kinetics of photosystem I (PSI) and photosystem II (PSII) (see Chaps. 8 and 10 of this volume). Further, the successful determination of the structure of reaction centers and antenna proteins (see Chaps. 1 and 11 of this volume) has added much to our understanding of electron transport in both photosystems. However, knowledge of the thermodynamics of this process is far less advanced.

Since the early photosynthetic reactions are electron-transfer processes, focus has been placed on the redox potentials of the intermediates. As discussed below, values of these potentials are not known at all well. There are two principal reasons for wishing to know redox potentials of the electron-transport cofactors more accurately. One is the far greater understanding obtained by separating the free energy change into its bonding (enthalpic) and structural (entropic) components. Aside from the concentration term, the latter is small in many chemical reactions at normal temperature, ~300 K. However, in structured environments such as proteins in the particular solvent, water, the contribution of entropy can be the determining factor. (This is exemplified by protein denaturation, where the massive configuration entropy determines the irreversible thermal reaction.) From the viewpoint of statistical mechanics, a further breakdown of the free energy into the change in heat capacity at each reaction step is the most useful. Unfortunately, we are still quite a ways from the precise measurements required for such detailed knowledge of the intermediates. Nevertheless, knowledge of the enthalpy and entropy from accurate thermodynamic measurements provides important insights into the processes involved in electron transfer.

The second reason to accurately know the thermodynamics of electron transfer is that it provides information on the efficiency. In the context of photosynthesis, the word “efficiency” is used with several different meanings [1, 2]. It often refers to the “solar-energy conversion efficiency,” or that fraction of incident solar energy that is absorbed by the system and ultimately stored in chemical form [1, 3]. This is

a small and variable number. It is variable because incident photon flux densities are affected by the diurnal cycle, changes in cloud cover, physical differences among local environments, etc. It is small because about half the solar spectrum is in the infrared region, and therefore not used in photosynthesis. Moreover, for absorbed shorter wavelength photons that are used, all energy exceeding that of the reaction center traps is rapidly degraded to heat. (This fast degradation of surplus energy is a characteristic of all photon-driven systems, including photocells. Photothermal devices maximize this effect by converting all the photon energy to heat.) Thus, only a small fraction of incident solar energy is captured and converted by the reaction centers—perhaps 1 or 2 % in higher plants under typical conditions [4].

This chapter focuses on the "energy-storage efficiency," ε_{ES}, or that fraction of the *absorbed* energy that is converted and stored. This quantity is a function of time, reaching a minimum when the final products of photosynthesis are reached. Our primary subject is the determination of ε_{ES} from enthalpies obtained using pulsed photoacoustics (PPA). PPA is unique among biophysical methods of photosynthesis research in that, rather than providing spectroscopic or kinetic information from which the details of photochemistry must be inferred, it measures changes in *energy* (enthalpy) resulting from electron-transfer reactions, directly providing detailed thermodynamic and other basic information that is difficult to obtain by other means. Examples include changes in volume and entropy [5–7], turnover times and quantum yields [7, 8], optical cross sections and energy-storage efficiencies [8], and, from the latter, trap energies and spectral dependence of uphill energy transfer [9].

In Sect. 6.2, we discuss what is currently known of the free energies of electron transport. Biophysical methods of measuring the enthalpy are discussed in Sect. 6.2.1, and what can be learned from knowledge of enthalpy and entropy changes is discussed in Sect. 6.2.2. In Sect. 6.3, we concentrate on PPA—one of only a few available methods for directly obtaining the enthalpy—emphasizing accurate in vivo measurements that allow determination of the millisecond time scale ε_{ES} and other key photosynthetic quantities. PPA methodology and what can be learned by this method are discussed in Sect. 6.3.1. An example of determining several useful parameters of photosynthesis in the Chl *d*-utilizing organism *Acaryochloris marina*, as well as in the Chl *a* species *Synechococcus leopoliensis*, is given in Sect. 6.3.2. Finally, in Sect. 6.4, we offer some concluding remarks.

6.2 Decomposition of Free Energy into Enthalpy and Entropy

The redox potentials (free energies, ΔG) of the steps in the PSI and PSII electron-transfer pathways are in general not very accurately known, because of the limitations of methodology and variability of the preparations. We previously

concluded that for PSI the potentials are known only to within ±0.05 V (eV) [10]. The uncertainties arise primarily because of mismatch of time scales—minutes for measurements (typically standard-state redox titrations) and less than microseconds for the actual reactions. This mismatch opens the possibility that equilibrium measurements do not accurately capture non-equilibrium in vivo processes. In addition, the measurements allow only one of the pair of products to be measured. The range of values observed for the intermediates allows a compromise between maximizing the energy-use efficiency and preserving adequate forward electron flow to products. In vivo measurements of ΔG are preferable to in vitro measurements, but, when possible, require more difficult methods.

The Gibbs free energy is given by the well-known expression

$$\Delta G = \Delta H - T\Delta S, \tag{6.1}$$

where T is the absolute temperature and ΔG, ΔH, and ΔS are changes in free energy, enthalpy, and entropy for reactions in a closed system at constant pressure. Given Eq. (6.1) (and that entropy meters are hard to come by!), a simple method for determining the change in entropy is to measure ΔH, and then calculate ΔS by difference with ΔG. The justification for treating the measured values as standard-state values is given in [11]. Before discussing specific methods for obtaining ΔH, we make the following comments:

1. The photosynthetic system is obviously "open"; that is, energy flows into and out of the system throughout the sequence of reaction steps. Yet we are treating it as a closed system at equilibrium. This is a fair approximation for light intensities well below saturation or for single-turnover flashes, where only one electron per unit is being transferred. The electron flow will lead to a potential drop across the organized system, the components of which span a biological membrane in their in vivo state. For liposomal or in vivo systems, the resulting transmembrane potential must be included in the estimated potential. More importantly, there is the question of whether the "completely relaxed" (equilibrium) state of the protein is achieved between each electron-transfer step. If equilibrium is reached, then all is well. If not, then a new state must be defined. Since the thermalization time of small molecules in condensed phases is very fast, any step that lasts beyond a few picoseconds can be defined as a "thermal equilibrium" state; however, if it is not the completely relaxed state, as in reactions with proteins, then it must be carefully distinguished from the true equilibrium state [12–16]. At the moment this issue is not resolved.
2. It is important to remember that it is changes of the thermodynamic parameters that are relevant, and that these changes are a function of temperature, pH, ionic strengths, and, unfortunately, the preparation from which they are obtained. This is another reason why in vivo measurements are particularly useful (Sect. 6.3.1).
3. All the thermodynamic parameters in Eq. (6.1) can be related to changes in heat capacity, ΔC_P. Unfortunately, the time resolution of current heat capacity measurements is insufficient for the transient intermediates under discussion; thus, obtaining the corresponding parameters from their relationship to ΔC_P is not yet feasible.

6.2.1 Methods of Measuring Enthalpy

Indirect method. The temperature dependence of the yield of delayed light from previously excited reaction centers of *R. sphaeroides* has been used by Arata and Parson [17] to estimate the enthalpy of the charge-separation reaction. The basic assumption is that the ion pair is in equilibrium with the singlet excited state. However, there are many other states involved, such as triplets, and the detailed kinetics are always observed to be rather complex. This approach has been criticized on these grounds by Brettel [18] and by McMahon et al. [19].

Direct methods: Photoacoustics. The only available methods for directly measuring the heat evolved (ΔH) in photochemical processes are photoacoustics (PA) and the related thermal deflection [20] and transient grating [21] methods. Here we concentrate on PA, since it is the method with which we have experience, and with which most of the information on photosynthetic systems has been obtained. PA methodology is well described in the literature [22–28]; therefore, in the following section we focus on *pulsed* photoacoustics (PPA), emphasizing in vivo methods for obtaining the enthalpy—and thereby the energy-storage efficiency—of oxygenic photosynthesis on the millisecond time scale.

6.2.2 Information from Enthalpy and Entropy

As stated in Sect. 6.1, the ΔH and $T\Delta S$ terms in Eq. (6.1) define the basic driving force of the reaction. If ΔH is larger, the driving force is bonding. If $T\Delta S$ is larger, it is the number of states, or the occupation of low-frequency modes, i.e., structural changes from weak intermolecular interactions. For simple chemical reactions, ΔH usually predominates. However, for reactions in the complex solvent, water, or those involving proteins, with their many conformational and ionization states, $T\Delta S$ can compete with or even exceed enthalpic contributions to ΔG. Comparison of ΔG and ΔH therefore immediately distinguishes simple and complex reactions. If $\Delta G \approx \Delta H$ then $T\Delta S \approx 0$, and there is little structural change in the system. If $\Delta G \neq \Delta H$, then the reaction may be complex, possibly involving significant structural change.

Reactions with small ΔG are often considered to be trivial: nothing much happens, one is near equilibrium. However, if in this case one finds a large ΔH (of either sign) then there must be a corresponding large $T\Delta S$ of the same sign. Thus the small observed ΔG may hide large bonding and structural changes that would be missed without this additional information. An example of this is the A_1^--to-$F_{A/B}$ reaction in PSI [29].

In the next section, we discuss PPA and its application to obtain key information on in vivo photosynthesis from direct knowledge of the thermodynamics of photochemistry.

6.3 Pulsed Photoacoustics (PPA) and Photosynthesis

Pulsed PA methods and photosynthesis seem almost to be tailor-made for each other. The typical photosynthetic unit has a very large antenna, consisting of hundreds of photon-collecting molecules that funnel energy to the much smaller reaction center, where photochemistry takes place. Thus the system is easily saturated—i.e., maximally excited with minimal continuous light—and its absorption does not change upon excitation. These intrinsic properties allow the sample used in a PPA measurement to be its own reference [7, 22]. Specifically, PPA requires measuring the total amount of incident pulse energy absorbed by the sample. This can always be done by replacing the sample with a reference that has the same pulsed light absorption, but degrades all the absorbed energy to heat within the resolving time of the apparatus. Photosynthetic samples with the abovementioned properties do just this by themselves when saturated by continuous light in combination with the actinic flashes. A reference is thereby provided without the need for even touching the sample—clearly ideal from an experimental point of view. Isolated reaction centers, or systems with less than a dozen or so antenna molecules, require a separate reference.

We now present an overview of PPA methodology (Sect. 6.3.1) and discuss what can be learned from its application, emphasizing information provided by the energy-storage (E-S) efficiency, ε_{ES}. We then describe a study in which PPA was used to obtain the trap energies and efficiencies of both a common Chl *a* cyanobacterium and the unique Chl *d* species, *A. marina* (Sect. 6.3.2).

6.3.1 PPA Methodology

In PPA, a short (ns–μs) pulse of light shaped as a sheet is directed onto a simple cuvette [30] or a uniform beam into a front-face cell [31] containing a photoactive sample. Following illumination, heat dissipated by the sample generates in the suspending medium a plane sound wave that is detected by a piezoelectric film in a hydrophone (liquid medium) or by a microphone in the air surrounding the sample (air medium). The time scale of measurement is determined by the thickness of the sample, the medium-dependent speed of sound, and the dimensions of the PA cell. Liquid-phase PPA probes 10 ns to 10 μs processes, and air-coupled PPA 100 μs to 100 ms processes.

6.3.1.1 Light Pulses

The required duration of the light pulse depends on the chosen time resolution of the measurement. To measure the complete electron-transfer path of photosynthesis, a few millisecond pulse from a flash lamp is adequate. However, much

more information is available if a spectrally well-defined, shorter duration pulse is used. A Nd:YAG-pumped OPO system is ideal, as the pulse time is a few nanoseconds, and wavelength resolution can be <1 nm (i.e., <0.002 eV). Difficulties with this system include its instability and delicacy of alignment; one can easily spend more time tuning the YAG and aligning the OPO than running the experiment. This problem is now being solved by the availability of pulsed diode lasers with resolution near 1 nm. Obtaining a few μJ pulse in ~10 μs with these lasers requires an output of ≥1 W. Their ease of operation is far superior to that of the YAG-OPO system. However, pulsed diode lasers are currently monochromatic, and thus a new "head" is needed for each experimental wavelength. As the cost of these lasers decreases, multiple-wavelength units will likely become increasingly available.

6.3.1.2 Fast Hydrophone: Liquid-Phase PPA

In fast time-scale PPA, a liquid sample is placed in a front-face PA cell [31] in which the detector is a hydrophone, consisting of a piezoelectric film following a highly reflective mirror at the rear of the cell (Fig. 6.1a). This construction doubles the light path length and isolates the piezo film from the light pulse. The delay of a few μs determined by the speed of sound within the thick mirror usefully isolates electrical artifacts from the pulsed laser or flash lamp. Use of a front-face cell or a light sheet in a simple cuvette ensures a plane acoustic wave and linearity of measurements, which allows deconvolution of the signal and isolation of time-dependent components. The liquid-phase apparatus is highly sensitive and thermostated to accommodate controlled changes in temperature, allowing separation of enthalpic and inherent contributions to observed volume changes [17] (see next section).

Photochemistry-Induced Volume Changes

In PPA, the pressure wave following the light pulse is produced by the volume change (ΔV) of the system, and is therefore proportional to dV/dt. In fast PPA, ΔV has two sources. One is the thermal expansion caused by the heat flux, or ΔH of photochemistry. The other is the volume change inherent to the reactions themselves—notably, in photosynthetic primary reactions, the shrinkage caused by electrostriction on charge separation [17, 32]. By taking advantage of the unique physical properties of water, liquid-phase PPA allows separation of the two components of ΔV. At the temperature of its maximum density (≈4 °C), the thermal expansivity (α) of water is zero, so only inherent volume changes are observed. Assuming that inherent contributions to the total ΔV are constant over a small (≈20 °C) temperature range, additional measurements within this range allow the thermal contributions to be easily obtained from the observed total. To optimize signal-to-noise, one averages many signals following weak flashes and plots the

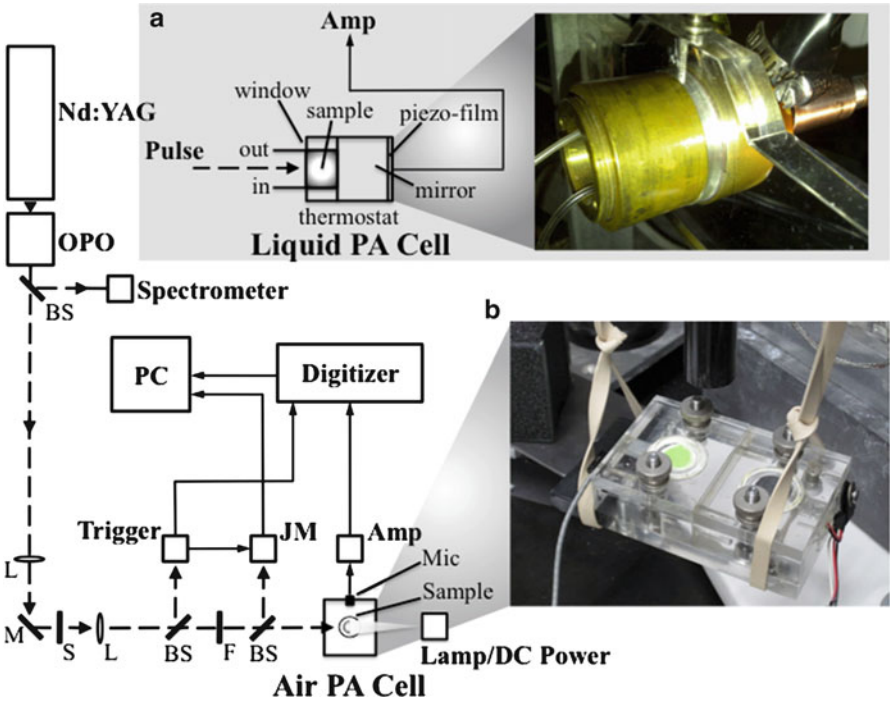

Fig. 6.1 *Fast and slow PPA experimental setups.* (**a**) Setup for ns–μs (solution) PPA. *Nd:YAG* pulsed laser source, *OPO* optical parametric oscillator, *BS* beam splitter, *L* lens, *PD-Trig* (pulsed) diode trigger. Elements of the thermostated hydrophone cell described in the text (Sect. 6.3.1.2) are indicated. (**b**) Setup for millisecond (air) PPA. *M* mirror, *S* shutter, *F* filters, *JM* joulemeter, *Lamp/DC Power* continuous (saturating) light source. Elements of the microphone cell described in the text (Sect. 6.3.1.3) are indicated. The photograph shows the PA cell used in the experiments described in Sect. 6.3.2.1. The cell is suspended by a viscoelastic medium (rubber bands in the setup shown), which absorb external vibrations at least as effectively as costly isolation tables. The black end piece of the optical guide from the saturating lamp is visible at top center. A sample consisting of *A. marina* whole cells on Millipore filter paper is also visible (*green circle*). Measurements of whole cells using this setup provide the enthalpy of in vivo reactions yielding millisecond time-scale products

data—corrected for any changes in compressibility—versus the thermal expansivity of the particular medium used. By normalizing to the reference, the slope of the resulting line is $\Delta H/E_{h\nu}$, and the intercept is $\Delta V/\alpha \times E_{h\nu}$. Details and possible sources of error are discussed in [7, 33].

Knowledge of inherent volume changes can provide important information on the underlying photochemistry. For example, our analysis of electrostriction in bacterial reaction centers using the Drude equation allows an estimation of the dielectric constant of the surrounding protein [34]. Other sources of inherent volume change include conformational changes that create or destroy internal space in the protein. An example of this is seen in the photocycle of bacteriorhodopsin, where such changes make a positive (expansive) contribution to ΔV [35].

Fast PPA In Vivo

Since so much is now known of the kinetics of PSI and PSII, one can use whole cells and PA to determine not only the energetics of "total" photosynthesis but also that of its individual steps. The enormous advantage is that the information is of the interacting photosystems in their natural context, without disruption or addition of deleterious reagents.

The use of intact cells with liquid-phase PPA requires a correction for their internal medium [5]. Depending on the size of the cell, the prompt thermal expansion differs from that of the surrounding water, so two further measurements are required. The time resolution depends on the thickness of the wave-forming volume; it is about 1 μs for a 1 mm thickness. However, data deconvolution procedures allow measurement at 10 % of this resolution [25], and have enabled us to resolve, for instance, the 10 ns formation of the triplet state from B_{860} cation–Bacteriopheophytin anion in quinone-less bacterial reaction centers in a 0.1 mm cell [Edens and Mauzerall, unpublished]. We have determined that the same signal is obtained from light-saturated photosynthetic cells as from a reference material [7]; thus, samples used for fast PPA measurements in vivo can be used as their own reference, as described above.

The long time-range for in vivo liquid-state experiments is limited to about 10 μs, because of the aforementioned proportionality between the acoustic signal and dV/dt; for a given ΔV, a microvolt signal in 1 μs becomes a nanovolt signal in 1 ms. In addition, reflections from any air boundaries in a reasonably sized apparatus lead to a confused signal within a few tens of μs.

6.3.1.3 Slow Microphone: Air PPA

Air PPA employs a simple plexiglass cell where samples are placed in an airtight receptacle, and photoacoustic waves are channeled to a microphone embedded in the cell wall [36] (see Fig. 6.1). The loss of sensitivity on the slower time scale is compensated by the much larger thermal expansivity of air. But this adds the complication of thermal diffusivity in the sample, and thus a depth-dependent signal. Therefore, use of thin samples—such as a leaf, or cells deposited on a thin substrate—is ideal. One can then measure photochemistry of the entire sample in the 10–100 ms time available to commercial microphones. The time resolution can be as high as ≈50 μs [36]. Only heat changes are measured since the large thermal expansivity of air overwhelms the small inherent volume changes. An advantage of ms-time scale PA is that it provides information on complete photosynthesis, at least from oxygen to further than ferrodoxin. Since the detectors are essentially noisy capacitors, a high-impedance FET input amplifier is best. Some air microphones have a built-in FET, allowing the output to be used directly. With low-energy light pulses, essential for obtaining the maximum efficiency of photosynthetic systems (Sect. 6.3.2), averaging of the signal is required. The pulse rate must be checked to ensure that it is not too large a

fraction of the turnover time of the system; however, for very-low-energy light pulses this is less of a problem, because the time required for saturation increases as the fraction of excitation decreases.

This method can be used for in vivo measurements in the 10 ms range. It is principally sensitive to surface effects and thus is ideal for leaves, either real or synthetic. Synthetic leaves consisting of whole-cell cultures affixed to Millipore filter paper have been used to obtain energy-storage efficiencies for the alga *Chlorella vulgaris* [37], and the cyanobacteria *Synechococcus* sp. PCC 7002 [8] and *A. marina* [9, 38] (Sect. 6.3.2.1).

We have developed a robust PA cell that measures the pressure change directly and is useful in the 50 μs-to-1 s time range [39, 40]. This cell has been used to obtain the enthalpy and volume changes of intermediates in the photocycle of bacteriorhodopsin [35]. Arata and Parson [17] used a capacitor cell to make similar measurements, but their results could not be repeated, most likely because the cell was highly sensitive to vibration and electrical interference.

6.3.2 *An Example of the Application of PPA: Determination of the Maximal Energy Yield and Trap Energies of Photosynthesis*

The determination of the quantum yield or the quantum requirement of photochemistry was a major hurdle on the path to understanding photosynthesis [41]. The formidable problem was, and still is, the determination of the absolute light absorption by the heavily light-scattering sample. Photoacoustics bypasses this problem by directly determining the light absorbed, and *only* the light absorbed, by the system. The effect of light scattering is only to reduce and homogenize the incident light intensity. As long as it is the same for the dark measurement (sample is in the dark) and the reference light measurement (sample is saturated by continuous light), the scattered light is irrelevant.

Photoacoustics determines the energy efficiency, not the quantum efficiency. If the enthalpies of the products of the photosynthetic system are known, a given efficiency is easily converted to the other. However, there are two significant advantages to the photoacoustic method. First, one determines *all* the energy stored in the system up to the time of measurement. Thus, in addition to the energy stored in products of photochemistry, that stored in proton gradients and protein conformational changes is measured. In principle, even the formation of ATP can be measured by PA; detection of the pressure wave would be difficult in this case because of the slowness of the reaction, but is likely achievable with the aforementioned pressure cell, which measures into the many-second time range [39, 40]. By contrast, quantum yield experiments measure energy stored in a specific product, such as oxygen or “fixed” carbon dioxide, and so do not capture complete photosynthesis.

A second advantage of PPA over quantum yield experiments is that it has already achieved an accuracy of 99 % [9, 38]. The accuracy of quantum yield measurements is typically no higher than 95 % [42–44]. As discussed in Sect. 6.3.2.1, the combination of accuracy and ability to employ many well-defined excitation wavelengths has allowed PPA measurements of energy-storage efficiencies in vivo that provide unprecedented additional information, including the trap energies and specific efficiencies of PSI and PSII directly from energy measurements [9].

The E-S efficiency at chosen pulse energy and wavelength, ε_{ES}, is defined as that fraction of the absorbed energy that is stored by the sample on the time scale of the PPA measurement:

$$\varepsilon_{ES} \equiv E_{sto}/E_{abs}, \tag{6.2}$$

where E_{sto} and E_{abs} are the energy stored and absorbed. Following a pulse in the dark, the unstored portion of E_{abs} is dissipated as heat (E_{dis}), generating the acoustic wave detected by the microphone within the PA cell. Eq. (6.2) can then be written as

$$\varepsilon_{ES} = (E_{abs} - E_{dis})/E_{abs} = 1 - E_{dis}/E_{abs}. \tag{6.3}$$

When the same sample is continuously illuminated during the experiment, $E_{sto} = 0$ because photochemistry is saturated. Following a pulse in this case, all the absorbed energy is dissipated by the sample ($E_{dis} = E_{abs}$). Thus, as noted above, the reference energy E_{abs} needed to calculate ε_{ES} can be obtained simply by illuminating the sample and repeating the measurement. Moreover, because the pressure waves are proportional to E_{dis}, the PA signals themselves can be directly used to calculate the efficiency:

$$\varepsilon_{ES} = 1 - E_{dis,Dk}/E_{dis,Lt} = 1 - S_{Dk}/S_{Lt}, \tag{6.4}$$

where $E_{dis,Dk}$ and $E_{dis,Lt} = E_{abs}$ are the energies dissipated from the dark (Dk) and illuminated (Lt) sample following a laser pulse, and S_{Dk} and S_{Lt} are the amplitudes (or integrals) of the corresponding signals from the detector (Fig. 6.2).

The observed ε_{ES} at chosen wavelength decreases with increasing flash energy, E, because the flashes themselves saturate the sample. At low (~10 μJ) energies, this decrease is linear [8, 38], allowing the maximal or the ideal (zero-energy) E-S efficiency, $\varepsilon_{ES,max}$, to be obtained from a linear fit to low-E measurements of $\varepsilon_{ES}(E)$ (Fig. 6.2b); that is, $\varepsilon_{ES,max} \equiv \lim_{E_{abs} \to 0} \varepsilon_{ES}$.

The wavelength dependence of ε_{ES} is determined by the trapping energies of the photosystems, $E_t = hc/\lambda_t$, where the trap wavelength λ_t is the photon wavelength corresponding to E_t. When $\lambda < \lambda_t$, absorbed photons are degraded to E_t in subpicoseconds, with the excess energy being dissipated as heat. Then, with the trap at E_t, photochemistry ensues, with a fraction ε_t of E_t being stored and the remainder, corresponding to ΔH, being dissipated. Because the overall efficiency is the stored fraction of the total absorbed energy, the ε_{ES} measured by PPA is

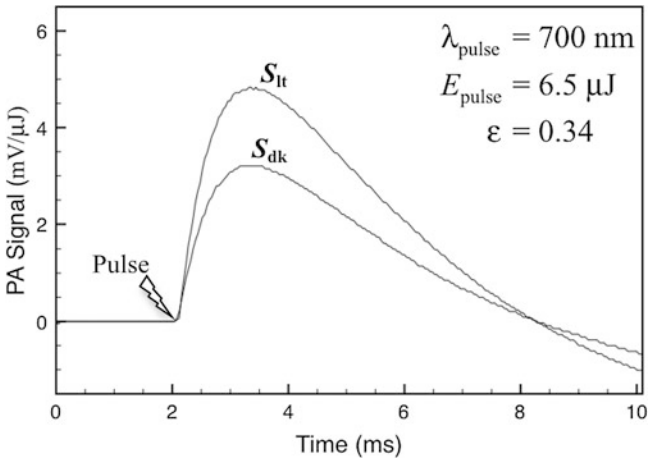

Fig. 6.2 Representative ms-timescale PPA signals, which are the time derivative of the pressure, dP/dt, following illumination of the sample with a laser pulse (Sect. 6.3.1, 6.3.2). S_{dk} and S_{lt} are the amplitudes of averaged signals from an active, dark-adapted *A. marina* sample (0.8 cm^2), and the same sample under continuous saturating light, respectively. The pulse energy (E) is 6.5 μJ and the pulse wavelength (λ_{pulse}) 700 nm. The pulse flashes the sample at 2.05 ms, and the peak of the resulting pressure wave, S_{dk} or S_{lt}, is detected by the microphone at 3.4 ms. The energy-storage efficiency at this flash energy and wavelength, calculated from the amplitudes (Eq. 6.4), is $\varepsilon = 34\,\%$

expected to increase linearly as λ increases to λ_t, and contributions to the observed E_{dis} from light harvesting decrease to zero. For oxygenic photosynthesis, the observed ε_{ES} is usefully complicated by the simultaneous contributions to storage by two photosystems with differing E_t [9] (see below); however, for a given system, one can write

$$\varepsilon_{ES}(\lambda) = (\lambda/\lambda_t)\varepsilon_t. \tag{6.5}$$

Thus, when the pulse wavelength equals the trap wavelength ($\lambda = \lambda_t$), one obtains the E-S efficiency intrinsic to the trap and specific to photochemistry, i.e., the trap efficiency, $\varepsilon_t = \varepsilon_{ES}(\lambda_t)$. For simplicity we are neglecting small losses by fluorescence. The complete equations are given in [37].

When $\lambda > \lambda_t$ ($E < E_t$), excitation of the trap requires uphill energy transfer driven by the thermal bath. In this case, the efficiency actually increases. However, thermodynamics requires an increase of the activation energy of the uphill reaction for increasing $\lambda > \lambda_t$, leading to an exponential slowing. Correspondingly, one expects a drop in energy storage, and therefore in the observed efficiency.

PPA applied at well-resolved wavelengths over a sufficient range provides the detailed spectral behavior of ε_{ES}. It is therefore the ideal—if not the only—methodology for directly identifying the crucial photosystem trap energies of which this behavior is a consequence.

6.3.2.1 Spectral Dependence of the In Vivo Energy-Storage Efficiency in the Chl *d* Cyanobacterium, *Acaryochloris marina*

We recently reported results of PPA measurements of the ms-time scale E-S efficiency in cyanobacterial intact cells over a 90 nm range of pulse wavelengths [9]. As noted, the unprecedented accuracy (1 % error) and wavelength resolution (1 nm or 0.002 eV) of these measurements, combined with the differing efficiencies of PSI and PSII, allow unique fits of a simple model to the data, and thereby provide the trap efficiencies and spectrally dependent fractional absorption of the photosystems. Results include the first direct observation of the PSI and PSII trap energies, which to date have been inferred from other information, typically absorption difference spectra [45]. We next briefly review this effort in order to illustrate both the application of PPA and the information it is able to provide.

The main objective of the study reported in [9] was to obtain the in vivo, wavelength-dependent E-S efficiency (specifically, the maximal wavelength-dependent efficiency, $\varepsilon_{ES,max}(\lambda)$) in the cyanobacterium *Acaryochloris marina*. This species is the only photosynthetic organism known to utilize chlorophyll (Chl) *d* as its primary photopigment [46]. In Chl *d*, a vinyl-to-formyl substitution redshifts the Q_Y absorption peak of Chl *a* by ≈40 nm (i.e., to ≈710 nm) in vivo, enabling *A. marina* to perform oxygenic phototrophy in niche environments enhanced in far-red/near-IR light [46–48]. *A. marina*'s viability in these low-photon-energy environments, and the presence of Chl *d* in its reaction centers [49], indicate that Chl *a*—otherwise ubiquitous among oxygenic species—is not a categorical requirement of water-utilizing photosynthesis. Determining $\varepsilon_{ES,max}(\lambda)$ in *A. marina* and comparing with that in Chl *a* species address the extent to which photochemistry in the former is thermodynamically limited by its use of Chl *d*, and potentially elucidate fundamental constraints on electron transfer in oxygenic photosynthesis. This question of the "long-wavelength limit" for O_2 formation by water-utilizing photochemistry [3, 9, 38, 50] is of considerable interest to a broad range of research areas, including basic photosynthesis, evolutionary biology, renewable energy, and astrobiology.

PPA employing an air microphone (Sect. 6.3.1.3) was used to obtain reaction enthalpies from *A. marina* whole-cell samples on a time scale of ≈3 ms (see Fig. 6.2). By referencing to the enthalpies measured when the same samples were saturated by continuous light, we obtained the in vivo E-S efficiency of photochemistry from formation of oxygen to beyond formation of ferrodoxin [51]. The λ dependence of the efficiency is directly determined by the wavelengths (exciting photon energies) of the photosystem traps, $\lambda_{t,I}$ (PSI) and $\lambda_{t,II}$ (PSII). If (and only if) these have different efficiencies, they can be directly identified from accurate measurements of $\varepsilon_{ES,max}$ at well-resolved wavelengths in the spectral region encompassing $\lambda_{t;I,II}$. For *A. marina*, we determined $\varepsilon_{ES,max}$ at 5 nm intervals from $\lambda = 670$ to 760 nm. By then fitting to the data a model that contains the dependence of $\varepsilon_{ES,max}(\lambda)$ on the absorption of each photosystem, and also on

the absorbed pulse wavelength relative to the trap wavelengths (Sect. 6.3.2), we obtained the trap energy, E_t, and efficiency, ε_t, for both photosystems. By incorporating an exponential factor to accommodate uphill energy transfer, the model also captures observed decays in the efficiency following both $\lambda_{t,II}$ and $\lambda_{t,I}$. For comparison, we additionally determined $\varepsilon_{ES,max}(\lambda)$ at 5 nm intervals from $\lambda = 670$ to 725 nm in whole cells of the Chl *a* cyanobacterium, *Synechococcus leopoliensis*.

The principal conclusions of [9] include the following: (1) The efficiency in *A. marina* (*Am*) exceeds that in *S. leopoliensis* (*Sl*) by ≈5 % at the respective peak absorption wavelengths, consistent with the higher efficiency expected if *Am* forms the same products as *Sl* from a lower energy initial state. (2) The efficiency in *Am* at the trap wavelengths (32 % at 723 nm [PSII], 43 % at 740 nm [PSI]) also exceeds that in *Sl* (30 % at 671 nm [PSII], 38 % at 695 nm [PSI]). These values confirm previously reported high efficiencies of primary reactions in both photosystems, with that of PSI exceeding that of PSII [37, 38]. The fitted values of both trap wavelengths in *Am* are >40 nm longer than those in *Sl*; the values in both species agree with previous spectroscopy-derived values within the error [45, 52, 53]. (3) The result $\lambda_{t,II} = 723$ nm in *Am* supports evidence that the primary electron donor is a Chl *d* monomer at the active-branch accessory site (Chl_{D1}) [53–55]. Additionally, one finds that the contribution of phycobilins to overall energy storage by PSI in *Am* is <10 % of the contribution to PSII. By contrast, the corresponding data indicate that in *Sl* these pigments contribute approximately equally to storage in both photosystems, consistent with previous results [56].

Figure 6.3 shows the spectral efficiencies ($\varepsilon_{max}(\lambda)$) of *A. marina* and *S. leopoliensis* reported in [9] (filled circles and open squares, respectively). The *Am* dataset includes revised efficiencies between 722.5 and 735 nm (gray filled circles), and a revised fit (thick solid curve). Figure 6.3 also shows absorbance (Abs) spectra of *Am* and *Sl* whole-cell samples used in the efficiency measurements (filled circles and open squares). The revised fit to the *Am* efficiencies incorporates a revised fit of the underlying PSI and PSII absorption bands to the observed absorbance spectrum (open triangles). The revised efficiency fit yields the same values of $\lambda_{t,II}$ and $\varepsilon_{t,II}$ obtained from the fit reported in [9] (dashed curved in Fig. 6.3)—i.e., $\lambda_{t,II}$ = 723 nm, $\varepsilon_{t,II}$ = 0.32—and the slightly revised values $\lambda_{t,I}$ = 737 nm, and $\varepsilon_{t,I}$ = 0.46, with comparable uncertainties (<∼ 5 %) and a slightly smaller overall root-mean-square error— 1.0 % vs. 1.3 %. For a detailed description of the efficiency model and fitting procedure, see the appendix in [9].

In addition to illustrating the utility of PPA, these results establish that energy storage via water-utilizing photosynthesis in *A. marina* is not thermodynamically limited by its use of far-red (to ≈750 nm) photons to initiate the primary reactions, indicating that oxygenic phototrophy is likely viable in even redder light environments. The significance of this is far reaching. For example, in the context of renewable energy research, it means that *A. marina* has adapted photochemistry in a way that has allowed it to significantly increase the solar-energy conversion efficiency [3] (Sect. 6.1) and simultaneously preserve the energy-storage efficiency [38]. Further study will therefore potentially inform efforts leading to optimally efficient, water-utilizing solar fuel technologies.

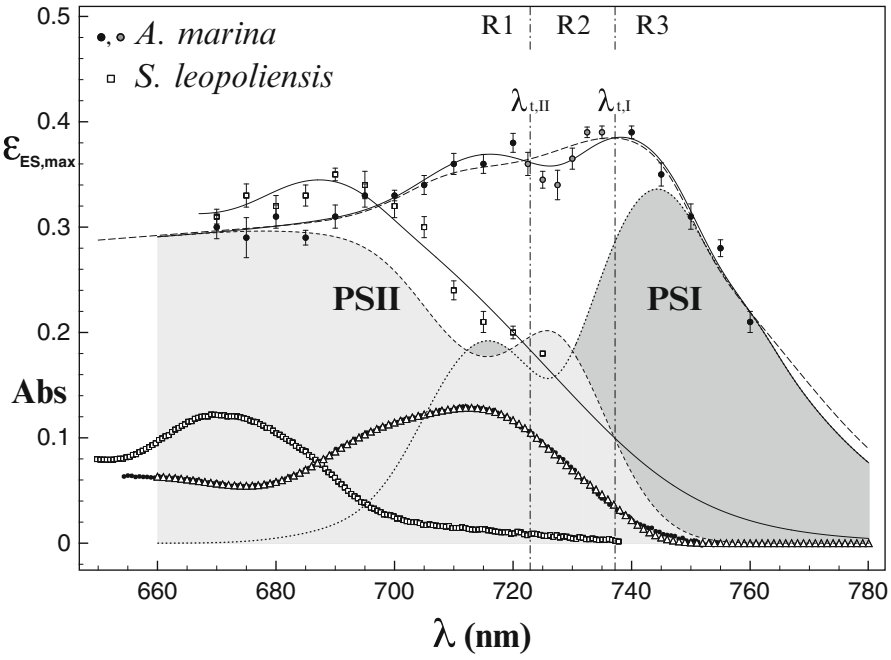

Fig. 6.3 Spectral dependence of the maximum energy-storage efficiency, $\varepsilon_{ES,max}(\lambda)$, in *A. marina* (black and gray filled circles) and *S. leopoliensis* (open squares) (see Sect. 6.3.2.1). Gray circles update the *Am* data reported in [9]. The error bar at each experimental wavelength, λ, is the rms deviation of a linear fit of ε_{ES} measurements versus pulse energy E to obtain $\varepsilon_{ES,max}$ (Sect. 6.3.2; the result shown in Fig. 2 corresponds to one point in the ε_{ES} vs. E dataset at $\lambda = 700$ nm). Thick and thin solid curves are fits to the ε_{max} data using the model described in Sect. 6.3.2.1 and [9], which assumes the PSI and PSII traps, $\lambda_{t;I,II}$, define three spectral regimes of the observed efficiency, R1, R2, and R3 (indicated for *A. marina* at top of figure), providing the photosystem-specific trap energies and efficiencies of the two cyanobacteria. The revised *A. marina* fit (RMS error = 1.0 %, 95 % confidence interval) improves on the best previously obtained fit (dashed curve; RMSE = 1.3 %) [9]. Also shown (reproduced from Ref. [9]) are absorbance (Abs) spectra of *A. marina* and *S. leopoliensis* intact-cell PPA samples; the *A. marina* absorbance fit (open triangles) corresponding to the revised efficiency fit; and the specific, λ-dependent contributions of PSI and PSII to the modeled total efficiency (labeled dashed and dotted curves with bounded areas shaded for clarity)

6.4 Conclusions

Pulsed photoacoustics is the ideal experimental method for probing the thermodynamics of photosynthesis over an extended time scale. It is one of only a few related methods able to directly measure energy changes in electron-transport processes, and is arguably the most elegant, accurately resolving photochemical enthalpy and volume changes simply by detecting the resulting acoustic wave using a microphone.

Likewise, photosynthetic systems are an ideal subject for PPA. Their large and efficient antennae allow for easy saturation of the sample with negligible change in absorption, providing an internal reference and thereby a high degree of accuracy. Samples can consist either of whole cells, providing information on in vivo photosynthesis, or of isolated thylakoid membranes or photosystem complexes, providing more specific information.

Because the temporal resolution of PPA is determined by the speed of sound in the sample medium and the dimensions of the PA cell, reactions on time scales spanning many orders of magnitude—from early photochemistry (nanoseconds) to almost complete photosynthesis (~100 ms)—can be studied. The list of information available is long; examples we have emphasized here include the following:

1. Details of thermodynamics to complement the much more extensive existing knowledge of kinetics and structure: In particular, the enthalpy and volume changes both of overall photosynthesis and of individual reaction steps in the electron-transport chain can be determined. In the latter case, time constants can be used to assign the measured changes to a specific, spectrally identified reaction. Where the free energy is known, one can also obtain entropy changes, which are of great interest because they provide insight into important but often overlooked structural contributions to energy storage.
2. With knowledge of the enthalpy, and taking advantage of the self-calibration possible with photosynthetic samples, the thermal (energy-storage) efficiency at chosen pulse energy and wavelength can be determined to an accuracy of 1 %. Linear fitting to efficiency measurements over a range of low-pulse energies provides the maximal energy-storage efficiency of the system. Experiments employing intact cells provide the overall efficiency in vivo. In oxygenic systems, the differing intrinsic efficiencies of the PSI and PSII traps allow in vivo measurements over a range of well-resolved pulse wavelengths to provide the specific contributions of the photosystems to the observed efficiency. This eliminates the need for difficult isolation and purification procedures; captures the separate efficiencies of the photosystems in their natural, interactive context; and further illustrates the incredible suitability of photosynthetic systems for investigation by PPA.
3. Importantly, obtaining the in vivo efficiency as a function of pulse wavelength also provides the unique trap energies of the photosystems *directly from energy measurements*. These are in contrast to conventional approximations of the trap energy obtained from absorption difference spectroscopy. The spectral dependence of the efficiency additionally provides information on energy-transfer processes for absorbed photon energies higher or lower than those of the traps, such as the thermodynamically limited uphill transfer of lower energy excitations.
4. Extensive additional information available to PPA includes system turnover times, quantum yields, optical cross sections, and, in the case of oxygenic photosynthesis in leaves, rates and yields of O_2 formation.

Thus, pulsed photoacoustics is a unique, simple, and powerful tool for investigating the thermodynamics of electron transport in photosynthetic systems.

Acknowledgements We gratefully acknowledge our collaborators, Dr. N. Y. Kiang and Prof. R. E. Blankenship, for their invaluable contributions to the work described in Sect. 6.3.2.1, as well as the technical expertise of Irena Zielinski-Large. We also acknowledge the NASA Astrobiology Institute (NAI), Prof. V. S. Meadows (Univ. of Washington, PI of the Virtual Planetary Laboratory Lead Team, NAI), and Dr. Carl Pilcher (Former Director, NAI) for support under Cooperative Agreement No. NNA08CN87A and the Director's Discretionary Fund program. SPM additionally acknowledges the NASA Postdoctoral Program (NPP) and NAI for support by an NAI NPP fellowship.

References

1. Dau H, Zaharieva I. Principles, efficiency, and blueprint character of solar-energy conversion in photosynthetic water oxidation. Acc Chem Res. 2009;42:1861–70.
2. Blankenship RE, Tiede DM, Barber J, Brudvig GW, Fleming G, Ghirardi M, Gunner MR, Junge W, Kramer DM, Melis A, Moore TA, Moser CC, Nocera DG, Nozik AJ, Ort DR, Parson WW, Prince RC, Sayre RT. Comparing photosynthetic and photovoltaic efficiencies and recognizing the potential for improvement. Science. 2011;332:805–9.
3. Chen M, Blankenship RE. Expanding the solar spectrum used by photosynthesis. Trends Plant Sci. 2011;16:427–31.
4. Barber J. Photosynthetic energy conversion: natural and artificial. Chem Soc Rev. 2009;38:185–96.
5. Boichenko VA, Hou JM, Mauzerall D. Thermodynamics of electron transfer in oxygenic photosynthetic reaction centers: volume change, enthalpy, and entropy of electron-transfer reactions in the intact cells of the cyanobacterium Synechocystis PCC 6803. Biochemistry. 2001;40:7126–32.
6. Hou JM, Boichenko VA, Diner BA, Mauzerall D. Thermodynamics of electron transfer in oxygenic photosynthetic reaction centers: volume change, enthalpy, and entropy of electron-transfer reactions in manganese-depleted photosystem II core complexes. Biochemistry. 2001;40:7117–25.
7. Hou JM, Boichenko VA, Wang YC, Chitnis PR, Mauzerall D. Thermodynamics of electron transfer in oxygenic photosynthetic reaction centers: a pulsed photoacoustic study of electron transfer in photosystem I reveals a similarity to bacterial reaction centers in both volume change and entropy. Biochemistry. 2001;40:7109–16.
8. Charlebois D, Mauzerall D. Energy storage and optical cross-section of PS I in the cyanobacterium Synechococcus PCC 7002 and a psaE− mutant. Photosynth Res. 1999;59:27–38.
9. Mielke SP, Kiang NY, Blankenship RE, Mauzerall D. Photosystem trap energies and spectrally-dependent energy-storage efficiencies in the Chl *d*-utilizing cyanobacterium, *Acaryochloris marina*, Biochim Biophys Acta. 2013;1827:255–265.
10. Mauzerall D. Thermodynamics of photosystem I. In: Golbeck JH, editor. Photosystem I: the light-driven plastocyanin: ferredoxin oxidoreductase. Dordrecht, The Netherlands: Springer; 2006. p. 571–81.
11. Mauzerall D, Feitelson J, Prince RC. Wide-band time-resolved photoacoustic study of electron-transfer reactions: difference between measured enthalpies and redox free energies. J Phys Chem. 1995;99:1090–3.
12. Parson WW. Thermodynamics of the primary reactions of photosynthesis. Photochem Photobiol. 1978;28:389–93.

13. Woodbury NW, Allen JP. The pathway, kinetics and thermodynamics of electron transfer in wild type and mutant reaction centers of purple nonsulfur bacteria. In: Blankenship RE, Madigan MT, Bauer CE, editors. Anoxygenic photosynthetic bacteria. The Netherlands: Kluwer Academic; 1995. p. 527–57.
14. Parson WW. Photosynthetic bacterial reaction centers: interactions among the bacteriochlorophylls and bacteriopheophytins. Annu Rev Biophys Bioeng. 1982;11:57–80.
15. Xu Q, Gunner MR. Temperature dependence of the free energy, enthalpy and entropy of P+QA- charge recombination in Rhodobacter sphaeroides R-26 reaction centers. J Phys Chem. 2000;104:8035–43.
16. de Winter A, Boxer SG. Energetics of primary charge separation in bacterial photosynthetic reaction center mutants: triplet decay in large magnetic fields. J Phys Chem A. 2003;107:3341–50.
17. Arata H, Parson WW. Enthalpy and volume changes accompanying electron transfer from P-870 to quinones in Rhodopseudomonas sphaeroides reaction centers. Biochim Biophys Acta. 1981;636:70–81.
18. Brettel K. Electron transfer and arrangement of the redox cofactors in photosystem I. Biochim Biophys Acta. 1997;1318:1869–77.
19. McMahon BH, Muller JD, Wraight CA, Nienhaus GU. Electron transfer and protein dynamics in the photosynthetic reaction center. Biophys J. 1998;74:2567–87.
20. Havaux M, Lorrain L, Leblanc RM. Photothermal beam deflection: a new method for in vivo measurements of thermal energy dissipation and photochemical energy conversion in intact leaves. Photosynth Res. 1990;24:63–73.
21. Terazima M. Enthalpy change and reaction volume of photochemical reactions measured by the transient grating method. Trends Photochem Photobiol. 1997;4:1–11.
22. Malkin S, Cahen D. Photoacoustic spectroscopy and radiant energy conversion: theory of the effect with special emphasis on photosynthesis. Photochem Photobiol. 1979;29:803–13.
23. Havaux M, Canaani O, Malkin S. Photosynthetic responses of leaves to water stress, expressed by photoacoustics and related methods: I. Probing the photoacoustic method as an indicator for water stress in vivo. Plant Physiol. 1986;82:827–33.
24. Braslavsky SE, Heibel GE. Time-resolved photothermal and photoacoustic methods applied to photoinduced processes in solution. Chem Rev. 1992;92:1381–410.
25. Feitelson J, Mauzerall D. Photoacoustic evaluation of volume and entropy changes in energy and electron transfer. Triplet state porphyrin with oxygen and naphthoquinone-2-sulfonate. J Phys Chem. 1996;100:7698–703.
26. Delosme R. On some aspects of photosynthesis revealed by photoacoustic studies: a critical evaluation. Photosynth Res. 2003;76:289–301.
27. Mesquita RC, Mansanares AM, Silva ECD, Barja PR, Miranda LCM, Vargas H. Open photoacoustic cell: applications in plant photosynthesis studies. Instr Sci Technol. 2006;34:33–58.
28. Hou HJ, Mauzerall D. Listening to PS II: enthalpy, entropy, and volume changes. J Photochem Photobiol Biol B. 2011;104:357–65.
29. Hou HJ, Mauzerall D. The A-Fx to F(A/B) step in synechocystis 6803 photosystem I is entropy driven. J Am Chem Soc. 2006;128:1580–6.
30. Feitelson J, Mauzerall D. Wide-band, time-resolved photoacoustic study of electron-transfer reactions: photoexcited magnesium porphyrin and quinones. J Phys Chem. 1993;97:8410–3.
31. Arnaut LG, Caldwell RA, Elbert JE, Melton LS. Recent advances in photoacoustic calorimetry: theoretical basis and improvements in experimental design. Rev Sci Instrum. 1992;63:5381–9.
32. Feitelson J, Mauzerall D. Enthalpy and electrostriction in the electron-transfer reaction between triplet zinc uroporphyrin and ferricyanide. J Phys Chem B. 2002;106:9674–8.
33. Edens GJ, Gunner MR, Xu Q, Mauzerall D. The enthalpy and entropy of reaction for formation of P+QA- from excited reaction centers of *Rhodobacter sphaeroides*. J Am Chem Soc. 2000;122:1479–85.

34. Mauzerall D, Hou JM, Boichenko VA. Volume changes and electrostriction in the primary photoreactions of various photosynthetic systems: estimation of dielectric coefficient in bacterial reaction centers and of the observed volume changes with the Drude-Nernst equation. Photosynth Res. 2002;74:173–80.
35. Liu Y, Edens GJ, Grzymski J, Mauzerall D. Volume and enthalpy changes of proton transfers in the bacteriorhodopsin photocycle studied by millisecond time-resolved photopressure measurements. Biochemistry. 2008;47:7752–61.
36. Mauzerall DC. Determination of oxygen emission and uptake in leaves by pulsed, time resolved photoacoustics. Plant Physiol. 1990;94:278–83.
37. Cha Y, Mauzerall DC. Energy storage of linear and cyclic electron flows in photosynthesis. Plant Physiol. 1992;100:1869–77.
38. Mielke SP, Kiang NY, Blankenship RE, Gunner MR, Mauzerall D. Efficiency of photosynthesis in a Chl d-utilizing cyanobacterium is comparable to or higher than that in Chl a-utilizing oxygenic species. Biochim Biophys Acta. 2011;1807:1231–6.
39. Edens GJ, Liu Y, Grzymski J, Mauzerall D. Pressure cell for time-resolved calorimetric measurements of photoinitiated reactions on the fractional millisecond and longer time scale. Rev Sci Instrum. 2003;74:2523–9.
40. Mauzerall D, Liu Y, Edens GJ, Grzymski J. Measurement of enthalpy and volume changes in photoinitiated reactions on the ms timescale with a novel pressure cell. Photochem Photobiol Sci. 2003;2:788–90.
41. Nickelsen K, Govindjee. The maximum quantum yield controversy: Otto Warburg and the "Midwest-Gang". Bern: Institut F R Philosophie; 2011.
42. Dutton PL, Leigh JS, Wraight CA. Direct measurement of the midpoint potential of the primary electron acceptor in Rhodopseudomonas spheroides in situ and in the isolated state: some relationships with pH and o-phenanthroline. FEBS Lett. 1973;36:169–73.
43. Popovic ZD, Kovacs GJ, Vincett PS, Alegria G, Dutton PL. Electric-field dependence of the quantum yield in reaction centers of photosynthetic bacteria. Biochim Biophys Acta. 1986;851:38–48.
44. Cho HM, Mancino LJ, Blankenship RE. Light saturation curves and quantum yields in reaction centers from photosynthetic bacteria. Biophys J. 1984;45:455–61.
45. Blankenship RE. Molecular mechanisms of photosynthesis. Oxford: Blackwell; 2002.
46. Miyashita H, Ikemoto H, Kurano N, Adachi K, Chihara M, Miyachi S. Chlorophyll d as a major pigment. Nature. 1996;383:402.
47. Swingley WD, Chen M, Cheung PC, Conrad AL, Dejesa LC, Hao J, Honchak BM, Karbach LE, Kurdoglu A, Lahiri S, Mastrian SD, Miyashita H, Page L, Ramakrishna P, Satoh S, Sattley WM, Shimada Y, Taylor HL, Tomo T, Tsuchiya T, Wang ZT, Raymond J, Mimuro M, Blankenship RE, Touchman JW. Niche adaptation and genome expansion in the chlorophyll d-producing cyanobacterium Acarylochloris marina. Proc Natl Acad Sci U S A. 2008;105:2005–10.
48. Miller SR, Augustine S, Le Olson T, Blankenship RE, Selker J, Wood AM. Discovery of a free-living chlorophyll d-producing cyanobacterium with a hybrid proteobacterial/cyanobacterial small-subunit rRNA gene. Proc Natl Acad Sci U S A. 2005;102:850–5.
49. Tomo T, Allakhverdiev SI, Mimuro M. Constitution and energetics of photosystem I and photosystem II in the chlorophyll d-dominated cyanobacterium Acaryochloris marina. J Photochem Photobiol B. 2011;104:333–40.
50. Pettai H, Oja V, Freiberg A, Laisk A. The long-wavelength limit of plant photosynthesis. FEBS Lett. 2005;579:4017–9.
51. Cassan N, Lagoutte B, Setif P. Ferredoxin-NADP + reductase. Kinetics of electron transfer, transient intermediates, and catalytic activities studied by flash-absorption spectroscopy with isolated photosystem I and ferredoxin. J Biol Chem. 2005;280:25960–72.
52. Hu Q, Miyashita H, Iwasaki I, Kurano N, Miyachi S, Iwaki M, Itoh S. A photosystem I reaction center driven by chlorophyll d in oxygenic photosynthesis. Proc Natl Acad Sci U S A. 1998;95:13319–23.

53. Schlodder E, Cetin M, Eckert HJ, Schmitt FJ, Barber J, Telfer A. Both chlorophylls a and d are essential for the photochemistry in photosystem II of the cyanobacteria, Acaryochloris marina. Biochim Biophys Acta. 2007;1767:589–95.
54. Cser K, Deak Z, Telfer A, Barber J, Vass I. Energetics of photosystem II charge recombination in Acaryochloris marina studied by thermoluminescence and flash-induced chlorophyll fluorescence measurements. Photosynth Res. 2008;98:131–40.
55. Renger T, Schlodder E. The primary electron donor of photosystem II of the cyanobacterium Acaryochloris marina is a chlorophyll d and the water oxidation is driven by a chlorophyll a/chlorophyll d heterodimer. J Phys Chem B. 2008;112:7351–4.
56. Kondo K, Ochiai Y, Katayama M, Ikeuchi M. The membrane-associated CpcG2-phycobilisome in synechocystis: a new photosystem I antenna. Plant Physiol. 2007;144:1200–10.

Part III
Separation and Stabilization of Charge

Chapter 7
Mechanism of Primary Charge Separation in Photosynthetic Reaction Centers

Sergei Savikhin and Ryszard Jankowiak

Abstract This chapter presents a review of primary charge separation processes in various photosynthetic reaction centers. Common motif of the known reaction centers is briefly discussed, followed by a comprehensive overview of the charge separation mechanisms in three major reaction center complexes for which crystal structures have been determined: bacterial reaction center, photosystem II, and photosystem I.

Keywords Charge separation • Electron transfer • Reaction center • Photosynthesis • Photosystem I • Photosystem II • Bacterial reaction center

Abbreviations

2D-ES	Two-dimensional electronic spectroscopy
BChl	Bacteriochlorophyll
BPheo	Bacteriopheophytin
BRC	Bacterial reaction center
Chl	Chlorophyll
CS	Charge separation
CT	Charge transfer

S. Savikhin, Ph.D. (✉)
Department of Physics, Purdue University, 525 Northwestern Avenue, West Lafayette, IN 47907, USA
e-mail: sergei@purdue.edu

R. Jankowiak, M.S., Ph.D.
Department of Chemistry, Kansas State University, 213 CBC Building, Manhattan, KS 66506, USA
e-mail: ryszard@ksu.edu

J. Golbeck and A. van der Est (eds.), *The Biophysics of Photosynthesis*, Biophysics for the Life Sciences 11, DOI 10.1007/978-1-4939-1148-6_7,

DADS	Decay-associated difference spectra
DAS	Decay-associated spectra
EET	Excitation energy transfer
ET	Electron transfer
FC	Franck-Condon
FRET	Förster resonance energy transfer
FWHM	Full width at half maximum
HB	Hole burning
PHB	Photochemical hole burning
Pheo	Pheophytin
PS I	Photosystem I
PS II	Photosystem II
RC	Reaction center
SHB	Spectral hole burning
WT	Wild type
ZPH	Zero-phonon hole

Photosynthesis is a dynamic research area directed towards detailed understanding of the electronic structure of photosynthetic light-harvesting antennas and reaction centers (RCs) including mechanisms of excitation energy transfer (EET) and charge separation (CS) processes. In photosynthetic systems sunlight is captured by antenna pigments and its energy is initially stored in the form of singlet electronic excitations. Light-absorbing pigments in photosynthetic RCs initiate a complex series of photo-initiated processes briefly discussed below. Due to the close proximity of antenna pigments to each other this electronic excitation can be transferred over long distances (tens of nanometers) by hopping from one pigment to another via the Förster resonance energy transfer (FRET) mechanism (see, for example, [1]), or, in the case of strongly coupled pigments, as the motion of excitons—which are excitations delocalized over several pigments [2]. Over the years the concept of excitons proved extremely useful in describing the spectroscopic properties and the processes occurring in light-harvesting antenna complexes and various RCs.

The natural lifetime of the singlet excited states for typical pigments, such as bacteriochlorophylls (BChls) or chlorophylls (Chls), is on the order of a few nanoseconds [3]. Since chemical reactions in living cells occur on a much longer time scale, the electronic energy of an excited state must be rapidly converted into a more durable form. In the case of all photosynthetic organisms, this is accomplished in the RCs where electronic excitation energy initiates charge transfer along several cofactors leading to a long-living charge-separated state. Various methods of optical spectroscopy, such as pump-probe techniques [4], spectral hole burning (SHB) [5–7], and 2-dimensional electronic spectroscopy (2D-ES) [8], are used in the study of the primary CS processes in RCs. These techniques can provide information on the CS rates and mechanisms of EET processes. In this book chapter particular attention will be devoted to the pump-probe and spectral hole burning (SHB) methodologies. Although CS is relatively well understood in photosystem I

(PS I) and bacterial RCs (BRCs), it is not yet clear at present whether a single mechanism is realized in the photosystem II (PS II) RC or two electron transfer (ET) pathways are present in isolated PS II RCs (*vide infra*).

7.1 Introduction

The reaction centers (RCs) are classified into two categories based on the nature of the electron acceptors [9, 10]. The first class is Fe-S-type RCs, which utilize iron sulfur complexes as terminal electron acceptors, and they are found in green sulfur bacteria, heliobacteria, and the photosystem I (PS I) complex of oxygenic photosynthetic organisms. The second class is Q-type RCs, which use quinone type of terminal electron acceptors and are found in purple bacteria, green filamentous bacteria, and the photosystem II (PS II) complex of all oxygenic photosynthetic organisms. The Fe-S-type RCs are often referred to as type I RC, while Q-type RCs are called type II RC [11]. Note that oxygenic photosynthetic organisms—cyanobacteria, algae, and plants—contain PS I and PS II, i.e., both types of RCs.

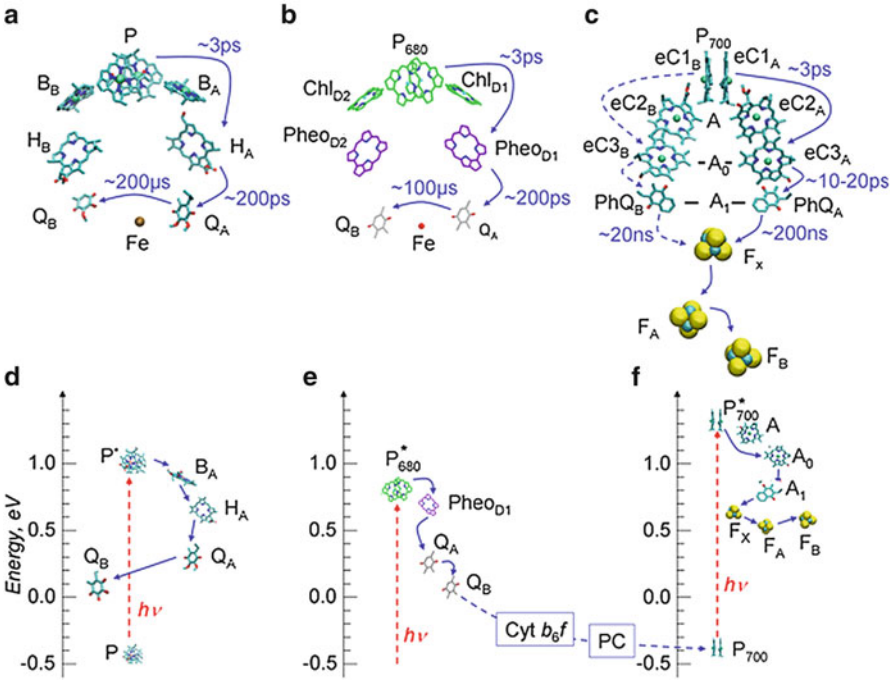

Fig. 7.1 The X-ray structures of reaction center complexes from (**a**) purple bacteria [27], (**b**) photosystem II [130], and (**c**) photosystem I [148]. Electron transfer energy diagrams for these three RCs are shown in panels **d**–**e**, respectively. Note that the first electron transfer step that is ~3 ps long involves also the intermediate pigment (B_A, Chl_{D1}, or A) as is discussed in the text

While antenna complexes found in nature vary significantly in size and organization, the RC structure is remarkably similar for all photosynthetic organisms including bacteria, algae, and plants (Fig. 7.1). A common feature of all known RCs is the presence of two branches of cofactors related via (pseudo)twofold symmetry. This structural motif appears to be essential for the function of the RC, though the functional importance of this arrangement is still debated. In all RCs the primary electron donor is identified as a *special pair* of closely spaced (bacterio)chlorophylls ((B)Chls), denoted with a letter P that is often followed by the wavelength corresponding to its characteristic red-most (Q_y) optical absorption band. Electronic excitation energy transferred from the light-harvesting antenna or direct excitation of the special pair by sunlight initiates the charge separation (CS) process. As a result an electron is rapidly (<1–5 ps) transferred to the primary electron acceptor forming a primary charge-separated state. In the case of PS I electron transfer can occur along both branches, though in all studied species branch A dominates in electron transfer [12, 13]. In the case of the purple bacterial RC (BRC) and (most likely) PS II only one branch of the RC is active [14–19], though it has been shown that in the BRC electron transfer can be redirected along an inactive branch if certain mutations are introduced into the RC protein [20, 21]. In the PS I RC the primary charge separation is followed by electron transfer to the secondary electron acceptor (A_1), and then through the iron sulfur complexes F_x and F_A to the terminal electron acceptor F_B. The large distance between the electron and the hole in the $P^+F_B^-$ radical state makes its lifetime sufficiently long (recombination ~50 ms [22]) so that the electron can be picked by a small mobile protein ferredoxin. The electrons to the oxidized special pair are provided by another mobile protein such as plastocyanin. In the case of Q-type RC the electron from the primary electron acceptor is consequently transferred to the quinone Q_A on the active side of the RC, and then further to the other quinone Q_B located on the inactive side. The latter quinone can accept two electrons generated consequently by two charge separation processes along with two protons from the surrounding water, forming a quinol (QH_2), which is released into intermembrane quinol pool acting as an electron and proton carrier.

The X-ray structures have been determined for these three major reaction center complexes (BRC, PS II and PS I) and in the following sections we consider the charge separation processes in these complexes in more detail.

7.2 Purple Bacterial Reaction Centers

The BRC is the simplest and most thoroughly studied complex among all RC complexes [23–25]. Photosynthetic purple bacteria were the first organisms for which the X-ray structure of the reaction center complex was determined [26]. The reaction center from purple bacteria consists of four BChls, two

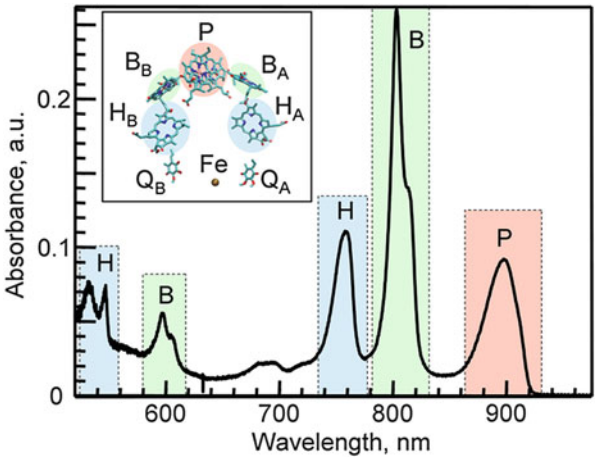

Fig. 7.2 Absorption spectrum of the reaction center complex isolated from *Rb. sphaeroides* measured at 4 K. Different bands correspond to absorption of different cofactors within the BRC as labeled. For reference, the structure of BRC is shown in the *insert*. Note that while all absorption bands are broader at room temperature, they remain well separated spectrally [24]

bacteriopheophytins (BPheo), and two quinones (Q_A and Q_B) with an iron atom positioned between them [27]. These are arranged into two branches related through pseudo-C_2 symmetry. The two branches are coordinated by two principal protein subunits, L and M, and cofactors in respective branches are denoted either with subscripts L and M or, alternatively, with subscripts A and B. In the following discussion we will use the A/B notation, with the A (L) branch being the functional branch along which electron transfer proceeds. The two closely spaced BChls form a special pair that serves as a primary electron donor. Once it is excited, a primary charge separation occurs within ~2–5 ps resulting in the formation of the radical $P^+H_A^-$. The physical concepts behind light-harvesting and primary CS, and their optical spectroscopic manifestations, have been addressed in numerous books and reviews (see, for example, [4, 6, 23, 28–30]).

All principal electron transfer cofactors in the BRC have absorption bands that are separated spectrally (Fig. 7.2), with the red-most absorption band in these complexes stemming from the special pair (P in Fig. 7.1a). In the case of organisms containing BChl *a* molecules, such as *Rhodobacter* (*Rb.*) *sphaeroides*, the special pair Q_y absorption band is between 860 and 890 nm and depends strongly on temperature (see, for example, [24, 31]). The significant red shift of this band with respect to monomeric BChl *a* is caused by strong excitonic interaction between the two closely spaced molecules that form the special pair. The BChl *a* cofactors denoted as B_A and B_B absorb at around 800 nm, and the BPheo molecules (H_A and H_B) yield an absorption band at ~760 nm. The BChl and BPheo molecules also have

significant absorption bands at ~600 nm and ~540 nm, respectively, due to the Q_x transitions. In organisms containing BChl *b*, such as *Blastochloris* (*Bl.*) *viridis*, all absorption bands are shifted to the red with the special pair absorption maximizing at about 960 nm [32].

7.2.1 The Sequence and Dynamics of Primary Charge Separation in BRCs

The spectral separation between the absorption bands of different cofactors in the BRCs greatly facilitates optical studies of charge transfer processes, since the individual chromophores can be excited and probed selectively by appropriate choice of the light wavelength. Moreover, in contrast to PS I complexes, which contain a significant number of antenna pigments, the isolated RC complexes from purple bacteria (and PS II) contain only electron transfer cofactors, which further simplifies their optical studies. The (sub)picosecond time resolution necessary to resolve the first electron transfer steps makes ultrafast spectroscopy the most suitable technique to monitor these processes in real time. However, hole-burning (HB) spectroscopy can also provide lifetimes of the zero-point level of the $S_1(Q_y)$ states due to EET and/or electron transfer, as determined by the widths of zero-phonon holes (ZPH) [5, 6]. The width of the ZPH in resonant photochemical hole-burned (PHB) spectra depends on the lifetime of the excited state, and "pure" dephasing and/or electron transfer (ET) time. ZPHs can be fitted with a Lorentzian profile, as they reflect the homogeneous line width (i.e., $\Gamma_{hom} = 1/2$ ZPH width [6, 33]).

The ET time is obtained from Γ_{hom} using Eq. (7.1):

$$\Gamma_{\mathrm{hom}}\left(cm^{-1}\right) = \frac{1}{2\pi c}\left(\frac{1}{T_1} + \frac{1}{\tau_{ET}} + \frac{2}{T_2^*}\right) \approx \frac{1}{2\pi c \tau_{ET}} \tag{7.1}$$

where T_1 is the fluorescence lifetime; T_2* is the "pure" dephasing time, which (at T = 5 K) is very large in comparison to T_1; *c* is the velocity of light in (cm s^{-1}); and τ_{ET} is the ET time [5, 6, 34–36]. Equation (7.1) provides τ_{ET} since the latter is $<<T_1$.

As an example of the use of SHB technique for CS time measurements, in Fig. 7.3 we present the experimental data obtained for the Zn-β-RC mutant of BRC from *Rb. sphaeroides* [5, 7]. In this mutant, the native BPheo in the H_A-binding site is replaced with Zn-BChl molecule that makes this cofactor *penta*- and not tetra-coordinated [31]. This mutation does not prevent the formation of the $P^+Q_A^-$ state, although under identical experimental conditions a significantly larger excitonic splitting of the dimeric P band was revealed in the Zn-RC than in the wild-type BRC. Frame a of Fig. 7.3 shows a schematic view of Zn-BChls in the Zn-β-RC mutant, and Frame b shows the low-temperature absorption spectrum of this mutant in the Q_y

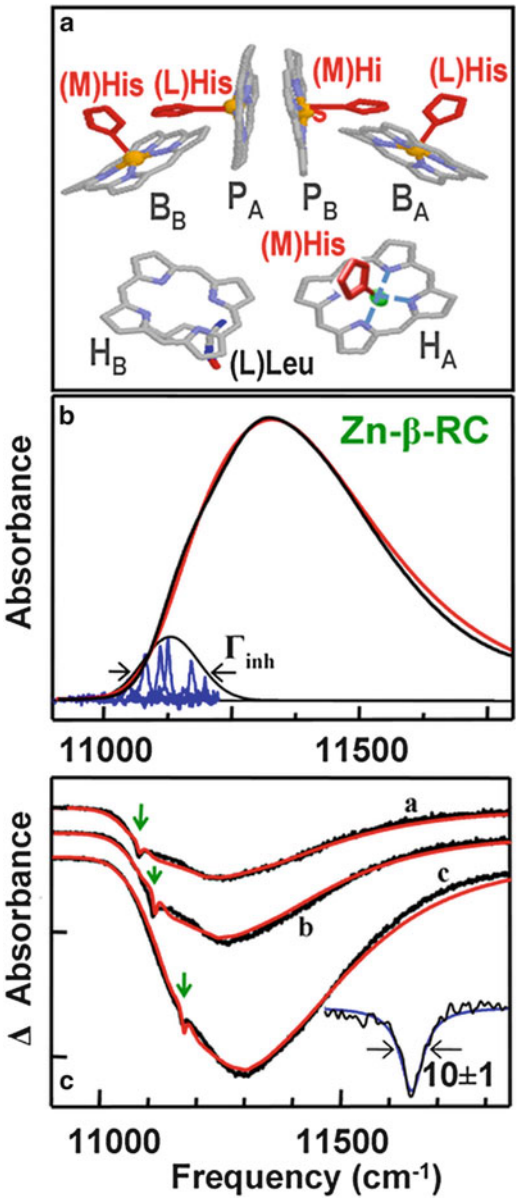

Fig. 7.3 (**a**) Schematic view of Zn-BChls with five histidine (His) residues that ligate the BChl Mg^{2+} in the Zn-β-RC, and one leucine (Leu) residue that is close to H_B. The letters L and M refer to the protein chains that residue belongs to. (**b**) *Black* and *red curves* show experimental and calculated absorption spectra of P870 for Zn-β-RC, respectively. (**c**) Calculated (*red*) and experimental (*black*) curves show the $P^+Q_A^-$ transient spectra of Zn-β-RC. *Solid arrows* refer to laser burn frequencies (ω_B). The *inset* shows a magnified view of the experimental (*black*) ZPH obtained with $\omega_B = 11\ 127\ cm^{-1}$ ($\lambda_B = 898.7$ nm) for Zn-β-RC and its Lorentzian fit (*blue*). T = 5 K. Reprinted with permission from [5]. Copyright (2012) American Chemical Society

region (black curve) with the peak of the Q_y band of the special pair appearing at 884 nm (at T = 5 K). The red curve shows the calculated absorption spectrum. The narrow blue spikes in Frame b correspond to the extracted/inverted ZPHs (corresponding to the ZPH-action spectrum), while its fit (the thin black Gaussian curve) describes the site-distribution function whose full width at half maximum (FWHM) reflects inhomogeneous broadening Γ_{inh} [31]. Measured ZPH-action spectra indicated Γ_{inh} of ~110 cm^{-1} and ~130 cm^{-1} for Zn-RC and Zn-β-RC, respectively. These experimentally determined Γ_{inh} decreased the number of variables in theoretical fits of the absorption and frequency-dependent shapes of resonant HB spectra, leading to more reliable Huang-Rhys factors for both low-frequency phonons and a pseudolocalized phonon, ω_{SP}, often referred to as the special pair marker mode [7].

Frame c of Fig. 7.3 shows an example of transient HB spectra representing $P^+Q_A^-$ radical pair, which were obtained for the same mutant at three different burning wavelengths indicated by arrows. The sharp peaks correspond to the ZPHs, which can be fitted with a Lorentzian profile reflecting a homogeneous linewidth. The primary ET times were obtained using Eq. (7.1) and all transient spectra revealed ET times of ~1 ps, which is similar to the rate previously measured in the WT *Rb. sphaeroides* RC [37]. For details regarding theoretical description of transient HB spectra and parameters, e.g., the HR factors (S), as well as ω_{SP} (often referred to as the special pair marker mode in BRCs), see [5, 6]. Here we just note that for situations in which excitonic effects are not of interest, it is sufficient to use a simple time-dependent expression for the hole-burned spectra that can be obtained by assuming a single (static) line shape for an isolated state. Finally, we note that in the BRC, the primary donor is P_A and the primary ET step is from P_A to an accessory BChl *a* (B_A). While SHB probes this primary step, it does not probe the second step which involves BPheo (H_A), or whatever is residing in the H_A site.

Using (sub)picosecond optical pump-probe spectroscopy, the special pair can be excited directly and the dynamics of electron transfer can be revealed by monitoring the bleaching of the characteristic BPheo Q_y absorption band at ~760 nm upon formation of H_A^-, or by monitoring the rise of the broad absorption band at ~660 nm that arises from the reduced H_A^-. Alternatively, one can follow the kinetics of the stimulated emission of the P* that also mirrors the primary electron transfer process. As an example, Fig. 7.4 shows the absorption difference profiles measured at different times after directly exciting the special pair of the RC from *Rb. sphaeroides* at 860 nm [38]. At 1 ps the major bleaching band is observed at 960 nm indicating the depletion of the ground state of the special pair. This band is accompanied by the broad red shoulder that arises from the stimulated emission of P*. The shoulder disappears within the first few picoseconds reflecting the formation of the charge-separated state (10 ps spectrum). This is accompanied by significant changes in the region 700–820 nm arising from the consequent reduction of BChl and then BPheo. Using the above techniques, it has been shown that the primary charge separation $P^*H_A \rightarrow P^+H_A^-$ occurs within ~3–5 ps for RCs from *Rb. sphaeroides* [14–18] and *Rb. capsulatus* [39] and within ~2 ps in RCs from *Bl. viridis* [40, 41].

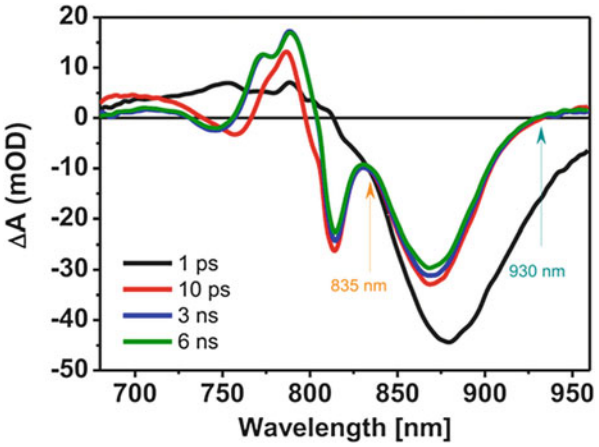

Fig. 7.4 Transient absorbance difference spectra of reaction centers from *Rb. sphaeroides* measured at 1 ps, 10 ps, 3 ns, and 6 ns after excitation with ~150 fs pulse into the special pair absorption band at 860 nm. Reprinted with permission from [38]. Copyright (2012) American Chemical Society

The distance between the special pair P and the electron acceptor H_A is, however, too large for such a rapid direct electron transfer between these cofactors. While X-ray structures showed the presence of the BChl chromophore between P and H_A, early experiments failed to reveal convincing evidence for the involvement of this cofactor in the electron transfer process suggesting that the $P^+B_A^-$ intermediate must have a very short lifetime, if it is involved at all. The optical signature of this intermediate state was finally observed as an additional transient absorption band at ~1020 nm that was assigned to the formation of B_A^- [42, 43]. Combining this observation with the stimulated emission kinetics of the P*, Arlt et al. [42] suggested the following kinetic sequence for the primary charge separation:

$$P^*B_AH_A \xrightarrow{2.3\ ps} P^+B_A^-H_A \xrightarrow{0.9\ ps} P^+B_AH_A^- \tag{7.2}$$

where respective electron transfer times are shown above the arrows. Holzwarth et al. [44] used more elaborate target analysis of decay-associated difference spectra (DADS) and obtained slightly longer lifetimes of 3.1 ps and 1.5 ps, respectively, for these two sequential electron transfer steps in a model that considered only forward electron transfer. However, it was found [44] that a better agreement with the experimental data is obtained if electron transfer is assumed to be reversible and forward electron transfer times for both steps are ~2.5 ps:

$$P^{*}B_AH_A \underset{12\ ps}{\overset{2.5\ ps}{\rightleftarrows}} P^{+}B_A^{-}H_A \underset{18\ ps}{\overset{2.5\ ps}{\rightleftarrows}} P^{+}B_AH_A^{-} \tag{7.3}$$

where the numbers above and below the arrows denote forward and backward electron transfer times, respectively.

The involvement of B_A in electron transfer was convincingly confirmed by the studies on mutated BRCs where the second step in Eq. (7.2) was slowed down. Shkuratov et al. [45, 46] replaced BPheo *a* (H_A) in the RC from *Rb. sphaeroides* with the plant pheophytin *a* (Pheo *a*). Since the latter has a more negative reduction potential, this substitution created a barrier for the second electron transfer step in Eq. (7.2) and lifetime of the $P^{+}B_A^{-}$ state was found to increase to 540–620 ps, which enabled its clear identification. Similar effect on the $P^{+}B_A^{-}$ lifetime was achieved in the work of Kirmaier et al. [47, 48] by replacing BPheo *a* with BChl *a*, whose reduction potential is also lower than that of the native BPheo *a* in the H_A site. Alternatively, protein sequence mutations in the local environments of B_A and H_A were used to modify the reduction potentials of these cofactors and increase the lifetime of the $P^{+}B_A^{-}$ state without replacing the native cofactors [49, 50], allowing direct detection of this intermediate. The presence of $P^{+}B_A^{-}$ was later confirmed in the wild-type RC from *Rb. sphaeroides* by Pawlowicz et al. [51], who applied ultrafast mid-infrared spectroscopy to visualize the dynamics of the $P^{+}B_A^{-}$ intermediate by probing the absorption changes associated with the 9-keto carbonyl (C=O) stretch vibrational mode of B_A (1670–1680 cm^{-1}), and found similar lifetimes of 3.7 and 1 ps for the two consequent electron transfer steps in Eq. (7.2). Based on the mid-IR data these authors also reported that upon formation the radical pair $P^{+}H_A^{-}$ undergoes further relaxation within ~20 ps that was tentatively ascribed to the localization of the hole on the P_A BChl *a* of the special pair.

The presence of the intermediate $P^{+}B_A^{-}$ state means that the B_A pigment is a true primary electron acceptor in the BRC. However, due to its short-lived transient character in the native BRC, the $P^{+}B_A^{-}$ state never accumulates in significant quantities and the $P^{+}H_A^{-}$ state is the first stable charge-separated state that forms within ~2–5 ps after excitation of the BRC. The electron transfer from H_A^{-} to the next electron acceptor, Q_A, is much slower and takes about 200 ps [24, 25].

A recent study using femtosecond absorption spectroscopy with excitation/probe pulses as short as 20 fs has led to the conclusion that the primary charge separation sequence (Eq. (7.2)) may involve an additional rapid charge separation step within the special pair itself. By observing transient absorption changes between 1060 and 1130 nm in RCs from *Rb. sphaeroides*, Khatypov et al. [52] inferred the initially excited P* transforms within 120–180 fs into a mixed state with a charge transfer character $P^{*}/P_A^{+}P_B^{-}$, where the $P_A^{+}P_B^{-}$ represents the special pair with separated charges. An indication of a similar ultrafast intramolecular CS within the special pair of the BRC was reported in an earlier work by Hamm and Zinth [53], and was recently supported by molecular dynamics and density functional modeling [54, 55].

Several studies have revealed that excitation of the special pair using ultrashort laser pulses leads to coherent oscillations in the optical signatures of both the P* and

B_A^- populations that last for about a picosecond, indicating that electron transfer from P* to B_A is coupled to coherent nuclear motion [52, 56–62]. According to the latest work by Shuvalov and co-workers the vibrational energy of the wave packet promotes reversible overcoming of an energy barrier between the potential energy surfaces of P* and $P^*/P_A^{\delta+}P_B^{\delta-}$ giving rise to the observed optical oscillations [52]. Alternatively, Parson and Warshel proposed that the oscillating signals can be associated with stepwise formation of $P^+B_A^-$ in concert with the nuclear motion followed by a rapid conversion into $P^+H_A^-$ [63, 64]. Fourier analysis of the oscillating signals revealed a series of frequency components between 30 and 250 cm^{-1}, but their assignments to particular nuclear vibrations are not yet clear.

In addition to the major ~3–5 ps component assigned to the primary charge separation in the BRC, the kinetics of the P* has a minor decay component with ~7 times smaller amplitude and lifetime of 10–20 ps [17, 31, 44, 60, 65–67]. Due to low amplitude this component is often ignored in the ET analysis (see, for example, [44]) and its nature is still debated. Several groups have proposed that the presence of two components indicates heterogeneity in the energy of the ET reaction within the pool of RC complexes [68–70]. However, SHB experiments demonstrated that the zero-phonon hole burned within the special pair absorption band corresponds to a single homogeneous lifetime of ~1 ps for the P* state [71], which argues against heterogeneity. Alternatively, the presence of an additional 10–20 ps component was explained by dynamic solvation of the charge-separated state, protein relaxation, and reversible electron transfer to cofactors B_B and H_B in the inactive branch of BRC [15, 65–67, 72].

The primary CS rate and the formation of $P^+H_A^-$ in the BRC were found to speed up with decreasing temperature from 3 to 5 ps at room temperature to ~1 ps at temperatures below ~30 K [73, 74]. Similarly, the rate of the consequent electron transfer $P^+H_A^- \rightarrow P^+Q_A^-$ was also found to increase from ~200 ps at RT to ~100 ps at temperatures below 100 K [75]. The increase in the electron transfer rate at low temperatures puts strict constraints on the theoretical description of the process, since opposite dependence on temperature is expected for such reactions in general.

The experimental studies of RCs are typically conducted on complexes either diluted in liquid buffer or incorporated into a solid matrix (frozen buffer). At the same time the structures of the RCs are obtained using crystals of the complexes. The crystallographic contacts in tight crystal packing may disturb the native structure of the complex and the use of X-ray structure to model the experimental data may be questionable, since the rate of electron transfer depends exponentially on the distance between electron donor and acceptor molecules. It was shown, for example, that the radiative lifetime of the singlet excited state of the monomeric Chl *a* pigment in the cytochrome b_6f complex increased four- to sixfold in crystalline phases of different symmetries, when compared to the same complex in liquid or frozen matrix [76]. However, Huang et al. [77] recently used polarization selective ultrafast spectroscopy in single crystals of the RC from *Rb. sphaeroides* and found that crystal packing did not alter the dynamics of primary CS, reporting the lifetimes

of 0.9 and 2 ps for the two consecutive steps in Eq. (7.2), though the order of these lifetimes in the above reaction could not be inferred from the measured optical kinetics. In addition to the reaction in Eq. (7.2), these authors concluded that upon excitation directly into B_A chromophore about 50 % of excitations lead directly to rapid formation of $B_A^+H_A^-$ radical, which is further converted into $P^+H_A^-$ with a ~2 ps lifetime, while in the other half of RCs the initial excitation energy is first transferred to the special pair and then reaction Eq. (7.2) takes place.

7.2.2 *Energetics of Primary Charge Separation in BRCs*

The commonly accepted energy diagram of electron transfer in the BRC is shown in Fig. 7.1d [78]. The excitation of the special pair changes its redox potential by approximately the energy of the absorbed photon bringing it to −1 V, which corresponds to the energy of an electron +1 eV. The free energy difference between P* and $P^+H_A^-$ has been estimated by many groups using the equilibrium between these two states when electron transfer to Q_A is blocked due to its prereduction or its removal from the structure [79–86]. The analysis of the delayed fluorescence in these conditions revealed the respective free energy difference of about ~0.16–0.26 eV, with most studies converging in the energy range to about of 0.21–0.26 eV [79, 80, 82, 85, 86]. A similar value of 0.25 eV was also obtained by molecular dynamic calculations [87].

Estimation of the free energy of the intermediate state $P^+B_A^-$ is a more challenging task due to its transient character and is primarily based on model calculations (see [23] and references therein). Most estimates put the energy of $P^+B_A^-$ slightly below that of P*. In Fig. 7.1d we used the result obtained by Warshel and Parson [88] by using molecular dynamics simulations that yielded $\Delta G_0 \approx -2$ kcal/mol (−0.086 eV) for the free energy of $P^+B_A^-$ in respect to P*, with an estimated uncertainty of ±2 kcal/mol. A similar calculation of the $P^+B_B^-$ radical pair energy level predicts that its free energy is higher than the energy of P* by ~4 kcal/mol (~0.17 eV) [23], which readily explains the observed inactivity of the B-branch of the BRC in electron transfer process. Qualitatively similar results were obtained in the molecular dynamics simulations by LeBard et al. [87, 89].

It is interesting to note that rather large differences in the energy levels of the two BRC branches are observed in spite of the BRC being highly symmetric. Steffen et al. [90] using Stark shifts of chromophore absorption bands in the field of the oxidized $P^+Q_A^-$ also showed that effective dielectric constants ε_{eff} around cofactors B and H in the active A-branch of BRC are higher ($\varepsilon_{eff} = 4.5$–4.7) than effective dielectric constants around respective cofactors in B-branch ($\varepsilon_{eff} = 1.5$–1.6). High value of $\varepsilon_{eff} \sim 7$ was also reported around the electron transfer cofactors in PS I RC [91], which suggests that high dielectric constant may be a common property of efficient electron transfer chains.

7.2.3 Controlling Pathways of Electron Transfer in BRCs

Under normal conditions the electron transfer in the BRC proceeds exclusively along the A-branch, and radical pairs $P^+B_B^-$ and $P^+H_B^-$ are not observed in experiment. The directionality of electron transfer is generally understood in terms of the free energy scheme (Fig. 7.1d) that places the energy of the $P^+B_B^-$ radical pair ~0.26 eV above the energy of $P^+B_A^-$ and ~0.17 eV above P* [23]. The amount of thermal energy available even at room temperature ($kT = 0.025$ eV) is insufficient to populate any measurable amount of $P^+B_B^-$. However, it has been shown that the electron transfer could be driven along the B-branch using site-specific mutations or exciting the wild-type RC complexes under special conditions as described below [74, 92–99].

For example, Lin et al. [92, 93] subjected the wild-type RC from *Rb. sphaeroides* to blue light at 390 nm exciting the RCs into the Soret band; as a result, the authors observed a rapid charge separation with the formation of H_B^-. The observed spectral features suggested that this charge-separated state did not involve the special pair and was associated with the $B_B^+H_B^-$ radical pair. Its lifetime was measured to be ~15 ps at room temperature, which increased to ~1 ns upon cooling the sample to 10 K. Interestingly, specific mutations that lowered the P/P^+ midpoint potential by up to 147 mV were also found to increase the lifetime of the $B_B^+H_B^-$ radical even at room temperature [93]. This process, however, did not provide a CS pathway along the B-branch, i.e., the electron transfer directly to Q_B. Instead, the $B_B^+H_B^-$ state was found to decay to the mainstream $P^+H_A^-$ state, possibly via recombination reforming the excited state P*. Formation of H_B^- was also detected in wild-type RCs under intense excitation at 595 nm, which presumably led to two-photon excitation of the Soret band [94]. The physiological significance of that path is unclear. It was speculated that one possible role of this rapid B-side CS could be associated with photoprotection, since it rapidly quenches higher excited states of the BRC [92].

The RC complexes from purple photosynthetic bacteria are remarkably tolerant to genetic mutations and pigment substitutions. For example, substitution of ~30 residues that coordinate RC cofactors or replacement of BChl molecules with Zn-BChl can still result in a functioning complex [7, 31, 96]. It was also shown that the coordination state of H_A in the Zn-RC did not tune the electron transfer rate [7].

The remarkable robustness of the BRC opens a way to manipulate the properties of individual cofactors via extensive site-specific mutagenesis to control electron transfer pathways. One way to force electron transfer via the B-branch is to swap the energies of radical pairs $P^+B_A^-$ and $P^+B_B^-$ (Fig. 7.1d). According to electrostatic calculations and molecular dynamic simulations the low energy of the $P^+B_A^-$ radical pair stems partly from the Tyr M210 residue [100] (in *Rb. sphaeroides* structure). It is located between the special pair and B_A and its phenolic –OH dipole is oriented in a way that favors the formation of $P^+B_A^-$ ion pair. The homologous residue on the B side of the BRC, Phe L181, does not have a similar effect on the $P^+B_B^-$ pair. Indeed, the replacement of Tyr residue in M210 position with Trp was found to slow down the primary charge separation in the RC from ~3 ps in the wild-type complex to

~50 ps in the YM210W mutant [101–108]. The first step in Eq. (7.2), $P^*B_A \rightarrow P^+B_A^-$, was found to be two-exponential with lifetimes of 29 and 63.5 ps, while the second electron transfer step, i.e., $P^+B_A^- \rightarrow P^+H_A^-$, was also found to slow down from ~0.9 ps to ~7 ps [101]. Unlike in wild-type RCs, where the primary CS rate increases at lower temperatures, CS rate in the YM210W mutant slowed down by an order of magnitude upon cooling from ~300 to 77 K [102, 105, 108], suggesting that the energy of the $P^+B_A^-$ radical pair is slightly higher than P* [101]. Note that structure of the mutated RC complex was determined in [109] and can be directly compared with the WT RC structure [101, 109].

The single YM210W mutation in the RC from *Rb. sphaeroides* is insufficient to redirect electron transfer along the B-branch. Kirmaier et al. [95] showed that a double mutation of *Rb. capsulatus* where the Tyr in the A side is swapped with the homologous residue Phe on the B side breaks the directionality of electron transfer leading to the formation of $P^+H_B^-$ with ~15 % quantum yield. Chuang et al. [96] went further and performed large-scale symmetrization of the *Rb. capsulatus* RC by substituting the entire D helix of the M subunit, that coordinates the B-branch of the RC, with that from the L subunit that coordinates the A-branch. When accompanied with three additional point mutations that affect the P^+/P oxidation potential and the energy of $P^+H_B^-$ pair, the quantum yield of the $P^+H_B^-$ formation increased to 70 %. Other mutations targeting the properties of native electron transfer cofactor have also been shown to result in partial electron transfer along the B-branch [74, 97–99]. Alternatively, the electron transfer along the A-branch can be blocked by either the removal or the substitution of the electron acceptor(s) in the A-branch of the RC [20, 110–114]. For example, Carter et al. [111] achieved up to 40 % quantum yield of electron transfer along the B-branch by introducing mutations that result in the RC with a missing B_A cofactor.

7.2.4 *Theoretical Description of the Primary Charge Separation in BRCs*

Electron transfer processes in proteins at room temperature are well described by the theory developed by Marcus [115, 116]. Consider the energy diagram of electronic states on donor (D) and acceptor (A) molecules before (DA, reactant) and after charge transfer (D^+A^-, product) as a function of a suitable reaction coordinate (Fig. 7.5a). According to the Franck-Condon principle, electron transfer occurs only when a system is in the transition state at the intersection of the potential energy surfaces, which is, in general, elevated with respect to the ground state of a reactant by activation energy $\Delta G^{\ddagger}$. In a conventional nonadiabatic approach electron transfer is much slower than the time scale of nuclear motions, and the rate of electron transfer is proportional to the average thermal population of the transition state given by the Boltzmann factor, $\exp(-\Delta G^{\ddagger}/kT)$, where k is the

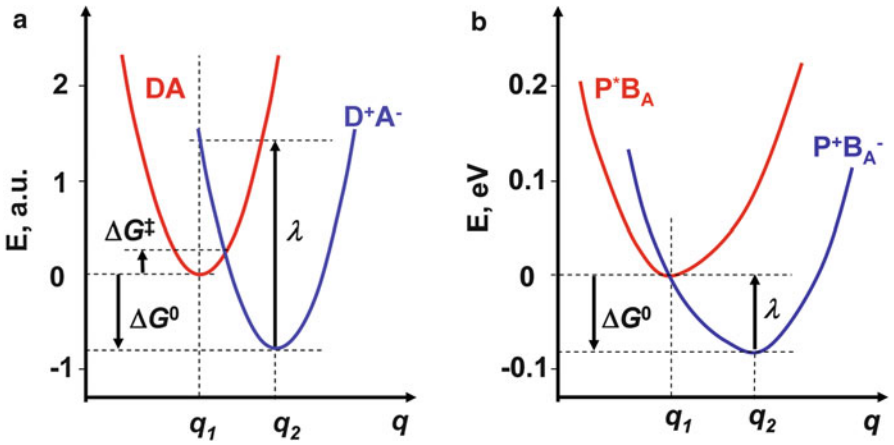

Fig. 7.5 Free energy diagram of arbitrary electron donor and acceptor molecules as a function of the reaction coordinate q (**a**). Free energies of P^*B_A and $P^+B_A^-$ calculated using molecular dynamics (**b**) [88]

Boltzmann constant and T is the temperature. For parabolic potential surfaces of the same curvature the activation energy can be expressed as

$$\Delta G^{\ddagger} = \left(\Delta G^0 + \lambda\right)^2 / 4\lambda \tag{7.4}$$

where ΔG^0 represents the standard free energy of reaction and λ is the reorganizational energy (Fig. 7.5a). The latter is defined as

$$\lambda = \hbar \int_0^{\infty} \omega J(\omega) d\omega \tag{7.5}$$

where $J(\omega)$ is the phonon spectral density (in units of angular frequency), which is sometimes referred to as the one-phonon profile and defines the total Huang-Rhys factor [117], and $\hbar$ is the Planck's constant divided by 2π ($\hbar = h/2\pi$).

The electron transfer rate is also dependent on the electronic coupling factor V that defines the probability to make a transition from DA to D^+A^- when the system passes through the transition state. Combining these factors together, the rate of electron transfer k_{ET}, described by the Fermi's golden rule rate expression, is given by [24, 115, 116, 118]

$$k_{ET} = \frac{2\pi}{\hbar} V^2 FC \tag{7.6}$$

$$FC = \frac{1}{\sqrt{4\pi\lambda kT}} \exp\left[-\frac{\left(\Delta G^0 + \lambda\right)^2}{4\lambda}\right] \tag{7.7}$$

where FC is the thermally averaged Franck-Condon factor (i.e., the FC-weighted density of states, ρ(E)) that accounts for the Franck-Condon principle. According to this equation, a maximum electron transfer rate is achieved when $\Delta G^0 = -\lambda$, which corresponds to the case when there is no activation barrier, i.e., $\Delta G^{\ddagger} = 0$. In this case the exponential term in the Franck-Condon factor vanishes and the electron transfer rate is expected to increase at lower temperatures as $\sim 1/\sqrt{T}$. The calculated energies of the P^*B_A and $P^+B_A^-$ states are in agreement with that scenario (Fig. 7.5b), and qualitatively explain the increase of the electron transfer rate of the first step in Eq. (7.2) at low temperatures, which was observed experimentally in wild-type RCs [73, 74]. Similar temperature dependence of the second electron transfer step in Eq. (7.2) indicates that this step is also non-activated, i.e., $\Delta G^{\ddagger} = 0$ [16, 73, 105]. The electronic coupling terms, V, for these two consecutive electron transfer steps were estimated to be $V_1 \approx 25\ \mathrm{cm}^{-1}$ and $V_2 \approx 50\ \mathrm{cm}^{-1}$, respectively [40, 73, 87]. Note that in the case where $\Delta G^0 \neq -\lambda$, i.e., in the presence of an activation barrier, electron transfer is expected to slow down exponentially towards lower temperatures. Qualitatively this situation has been observed in experiments on mutated RCs, where the energies of P^*B_A and/or $P^+B_A^-$ states were altered [101, 102, 105, 108]. However, Eqs. (7.6) and (7.7) fail to explain why in these mutants electron transfer can still proceed at a measurable rate even at the cryogenic temperatures. Equation (7.3) also fails to predict quantitatively the temperature dependence of the electron transfer in the WT RC at cryogenic temperatures.

The energies ΔG^0 and $\Delta G^{\ddagger}$ are thermodynamic averages and Eqs. (7.6) and (7.7) assume that there is a thermodynamic equilibrium between different vibrational states of the reactant. On a microscopic level, however, both these quantities fluctuate in time in individual RCs due to nuclear vibrations. Molecular dynamics simulations of an individual RC at room temperature show that the energy gap between the P^*B_A and $P^+B_A^-$ states fluctuates at a rate of $2 \times 10^{13}\ \mathrm{s}^{-1}$ about zero in a range of ±0.1 eV, which is comparable with the thermodynamic average value of ΔG^0 [23, 88, 89]. Wang et al. [65] provided strong experimental evidence that the energies of these states also evolve on a longer time scale comparable with the electron transfer rate due to the protein relaxation in response to the formation of P*. By introducing an additional reorganization energy into Eq. (7.7) to account for that slower process, these authors were able to reproduce the nonexponential kinetics of CS in wild-type RCs and 14 mutants with different energy gaps between the radical pairs. The presence of slow picosecond dynamics in the energy gap evolution leading to nonexponential electron transfer kinetics in RCs is supported by more detailed molecular dynamic simulations [23, 63, 64, 87, 89].

The classical treatment of electron transfer ignores the effects of quantum tunneling and zero-point vibrations that become important at the cryogenic temperatures. In quantum mechanical formalism, the classical expression for the Franck-Condon factor in Eq. (7.7) is replaced with the overlap integral of the

reactant and product wave functions coupled to quantized vibrations, allowing for electron transfer to occur via tunneling even at low temperatures when thermal energy is insufficient to overcome the activation barrier classically [23, 88]. The information about the vibrational modes and relevant Franck-Condon factors can be obtained from molecular dynamic simulations and used in quantum mechanical expression for electron transfer directly [119, 120]. Alternatively, molecular dynamics simulations can be combined with the quantum mechanical density-matrix formalism to model the electron transfer process in the BRC [23, 63, 64, 88]. Using the latter approach with five vibrational modes ranging from 30 to 235 cm^{-1} and an electronic coupling factor $V_1 \sim 20$ cm^{-1}, Parson and Warshel [64] were able to reproduce the dynamics of the first step in Eq. (7.2) from room temperature down to cryogenic temperatures.

The P^*B_A state created as the result of excitation energy transfer or directly by absorption of a photon is initially in a thermally elevated or hot vibrational state, which is not in equilibrium with the surrounding. This facilitates electron transfer even at cryogenic temperatures provided that V is sufficiently large and electron transfer occurs faster or concurrently with the vibrational relaxation of the excited special pair. It was shown that hot vibrational states can increase the primary charge separation rates in the BRC by a factor of 2–3 at temperatures below ~50 K [64]. Moreover, since the energy gap fluctuates with time in concert with nuclear vibrations, coherent excitation of an ensemble of RCs leads to oscillations in the modeled electron transfer kinetics [23, 64, 121], in agreement with the experimental observations [52, 56–62].

7.3 Photosystem II Reaction Center

As discussed in Sect. 7.2, a clear picture of CS processes and factors affecting rates of the primary electron transfer steps has been achieved for the BRC. However, the primary CS processes in the RC of PS II are not so well understood. Moreover, it is not yet clear if the structure and pigment–pigment and pigment–protein interactions in the RC are preserved after its isolation from the PS II core complex [5, 122, 123]. Functional implications regarding the primary photophysical processes in PS II, including discussion of various hypotheses regarding CS, have been recently published in [5, 124, 125]. Below we present a brief discussion of data obtained by SHB and time-resolved spectroscopies for isolated RCs of PS II. Section 7.3.1 briefly describes the structure of the PS II core and the isolated RC. In Sect. 7.3.2, we illustrate how transient HB spectra can provide CS rates in isolated PS II RCs. Section 7.3.3 discusses some of the recently obtained data on CS using time-domain spectroscopies, i.e., pump-probe and 2D-ES. In Sect. 7.3.4 the distribution of CS rates is briefly addressed, while in Sect. 7.3.5 we focus on the nature of the primary electron donor(s), and the possibility of multiple charge separation pathways in the PS II RC.

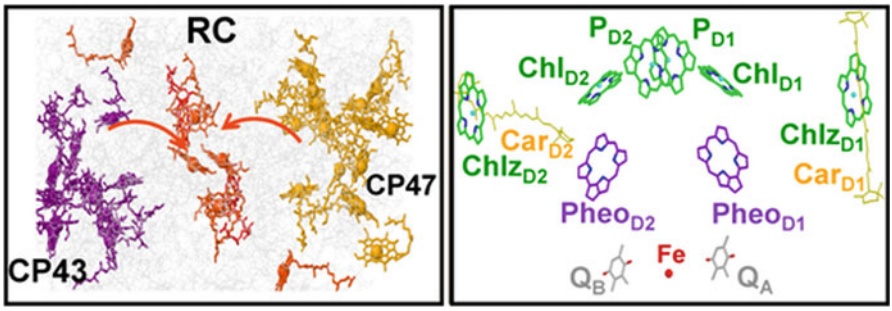

Fig. 7.6 *Left frame*: PS II core structure (top view). *Right frame*: Arrangement and labeling of pigments in the active (D1) and inactive (D2) branches of the PS II RC (side view). Notation: Chls, *green*; carotenes, *yellow*; pheophytins, *purple*; plastoquinones, *gray*; non-heme iron, *red*; and nitrogen, *blue*. Based on the structure of *T. vulcanus* (PDB file: 3ARC)

7.3.1 Structure of the PS II Core and Its Isolated RC

The PS II core is a dimeric protein complex, with each monomer consisting of the core antenna complexes CP43 and CP47 and the RC (see Fig. 7.6, left frame). This is the smallest isolated complex capable of oxygen evolution. In the membrane, the PS II core is surrounded by peripheral antenna complexes LHC II, CP24, CP26, and CP29 [126], which are not shown in Fig. 7.6 for simplicity. The arrangement of electron transfer cofactors in the PS II RC is structurally similar to the BRC, with D1 and D2 branches of the PS II RC corresponding to the A- and B-branches of the BRC (Fig. 7.1). Excitonic couplings between most pigments in the PS II RC are comparable, though the coupling between P_{D1} and P_{D2} Chls in PS II RC (Fig. 7.6) is somewhat weaker than that in the special pair of BRC. This led to multimer models for PS II RC [127, 128] and to the proposal that the exact nature of the primary electron donor may vary from RC to RC due to particular realizations of disorder in a given RC [125, 129].

Figure 7.6 shows a schematic arrangement of the CP43 and CP47 antenna complexes and the RC within the PS II core complex (left frame) and the six chlorophylls (Chls) and two pheophytins (Pheos) in the RC based on the structure of *T. vulcanus* (PDB ID 3ARC, right frame) [130]. The P_{D1} and P_{D2} Chls are analogous to the P_A and P_B BChls of the BRC special pair, respectively, while the $Chl_{D1,D2}$ and $Pheo_{D1,D2}$ molecules correspond to the monomeric $BChl_{A,B}$ and the $BPheo_{A,B}$ molecules of the BRCs (see Sect. 7.2 and Fig. 7.1). By analogy with the BRCs, it is believed that the P_{D1}/P_{D2}, Chl_{D1}, and $Pheo_{D1}$ molecules participate in primary CS in the PS II RC, although the nature of the primary electron donor in isolated PS II RCs is still a matter of debate [5, 122, 125, 129]. An obvious difference between the PS II RC and BRC is that the former contains two additional peripheral Chls (i.e., $Chlz_{D1}$ and $Chlz_{D2}$, both weakly coupled to the remaining pigments). Spectral congestion of pigments in PS II RC, and lack of crystal

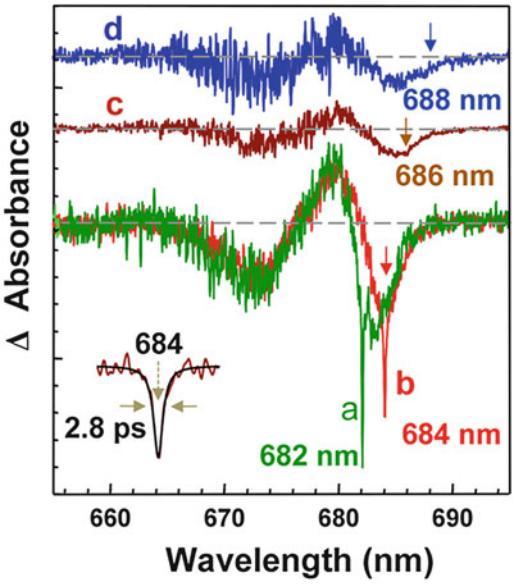

Fig. 7.7 Resonant transient HB spectra for *C. reinhardtii*; spectra *a*, *b*, *c*, and *d* were obtained with λ_B of 682.0 nm, 684.0 nm, 686.0 nm, and 688.0 nm, respectively. The *inset* corresponds to the Lorentzian fit (*black curve*) of ZPH of curve *b*. Adapted with permission from [5]. Copyright (2012) American Chemical Society

structures of the isolated RC (i.e., D1/D2/Cytb$_{559}$) preparations, makes the description of the excitonic structure, EET dynamics, and CS processes in *isolated* RCs difficult.

7.3.2 *Probing Electron Transfer Kinetics in PS II RCs by SHB*

Generation of transient HB spectra requires the presence of a third, relatively long-lived state [5, 6]. That is, the excited state evolves into a triplet state or is converted photochemically to another long-lived (μs-to-ms range) product (e.g., a CS state), leaving a transient hole in the absorption spectrum with a ZPH at the frequency of the original excitation (resonant HB) and with a shape defined by the strength of electron–phonon (el-ph) coupling. In this case, the pigment's ground state is depopulated for the lifetime of the long-lived state and a hole in absorption spectrum can be observed during that time. The transient holes shown below were acquired as the difference between the absorption spectra measured while the excitation was on and off (post-burn absorption, i.e., after saturation of a persistent hole). An example of resonant (transient) HB spectra (0.5 cm^{-1} resolution) obtained for *C. reinhardtii* is shown in Fig. 7.7 [122, 131]. These transient holes were obtained with $\lambda_B = 682.0$ nm (curve *a*),

684.0 nm (curve *b*), 686.0 nm (curve *c*), and 688.0 nm (curve *d*). Curve *c* shows an extremely weak ZPH, as indicated by the brown arrow at 686.0 nm. Note that all spectra exhibit bleaching near 673 nm and in the 684–686 nm spectral region. The ZPH widths, which varied from 2.4 to 7.6 cm^{-1} at 682 nm, depending on illumination dose, are believed to reflect a distribution of CS times (τ_{CS}). The ZPH widths of the HB spectra shown in Fig. 7.7 correspond to τ_{CS} in the range of 1.4–4.4 ps, in agreement with the previous data obtained for primary CS in spinach RCs [8, 132]. The distribution of τ_{CS} is consistent with the data obtained by 2D-ES for spinach RCs at 77 K [8] and with the earlier photon echo data [133] (see Sect. 7.3.3 for more details). Note that the ZPHs in Fig. 7.7 are nearly absent at $\lambda_B = 686.0$ nm and entirely absent at 688.0 nm and longer wavelengths, suggesting that the excited states of cofactors are strongly coupled with charge-transfer (CT) state(s) lying in the long-wavelength region (*vide infra*).

7.3.3 *Probing Electron Transfer Times in PS II RCs by Time-Domain Spectroscopies*

In this subsection we briefly discuss CS and its complexity in isolated RCs of PS II, as obtained recently by time-resolved spectroscopies. As stated above, CS is an essential step in the conversion of solar energy into chemical energy in photosynthesis. Often used time-domain spectroscopies include (1) pump-probe spectroscopy [134], (2) photon echo [133], and 2D-ES [8]. These techniques are complementary to the SHB (i.e., a high-resolution frequency-domain spectroscopy) briefly discussed in Sect. 7.3.2.

Fast processes in time-domain pump-probe spectroscopy can be investigated via transient absorption experiments using various excitation conditions on the isolated PS II RCs. Subsequently the results are analyzed by global and target analysis (see, for example, [4, 135]). Photon echo measures directly the decay of the coherence of the excited state(s) created by the coherent laser pulse [136]. In 2D-ES experiments the generated data are decomposed into two-dimensional decay-associated spectra (2D DAS) to reveal the excitation- and detection-wavelength-dependent spectral signatures associated with energy and charge transfer within the PS II RC, as well as quantum beats between different excited states due to excitonic coupling [137, 138]. Since such data are always interpreted within the context of a more or less advanced exciton model, the choice of a particular model may influence the outcome and the nature of the resulting pathways for CS, and the interpretation of experimental data may be somewhat ambiguous. Therefore, despite countless studies many controversies still exist as to the nature of the CS process in the PS II RC.

Nevertheless, it has been suggested recently that a consistent modeling of the data obtained for isolated RCs of PS II is only possible with a scheme where CS is initiated by electron transfer from both the accessory chlorophyll (Chl_{D1}) and from the special pair (the so-called P680, i.e., P_{D1}/P_{D2}), giving rise to fast and slow components of the pheophytin anion formation, respectively. It was suggested [125] that the disorder produced by slow protein motions may also cause energetic differentiation among RCs, leading to different charge separation pathways (see Sect. 7.3.5 for more detail).

The measured and simulated photon echo kinetics also suggested that the accessory chlorophyll (Chl_{D1}) in the active D1 branch of the RC core is the primary electron donor. The measured primary CS step in those samples occurred with an intrinsic time constant of about 1.5 ps, in good agreement with previously published transient absorbance data [139] and transient HB results [140, 141]. The question, however, remains how intact were the samples studied. Regarding the HB data it was reported that the data obtained for spinach RCs in [140, 141] were obtained for destabilized RC680.

The mixing of charge-transfer (CT) states with an exciton state(s) observed in recent HB data (see Sect. 7.3.2) [5, 122] is consistent with [129]. Namely, transient HB spectra showed that CT state(s) in RC684 (in the 686–695 nm range) must be present as indicated by the absence of ZPHs at $\lambda_B > 685$ nm. It was suggested that the latter could likely stem from the CT pathway initiated on P_{D1}, for which CS could be $\leq$1 ps. This assignment is in agreement with Krausz et al. [142] who showed that excitation wavelengths as long as 695.0 nm ($T = 1.7$ K) can induce CS in PS II and thus lead to Q_A^- formation. However, these authors argued that the CT state signature in the PS II RC extends far beyond 700 nm (700–730 nm), a notion that requires further confirmation, since the red absorption tail in PS II includes significant contribution of the PS II antenna pigments and no such absorption was revealed in the intact isolated RC684 complexes [122]. Novoderezhkin et al. [125] argued that in a fraction of RCs the low-temperature primary CS times are slow for both P_{D1} and Chl_{D1} CS paths. The slow CS is most effectively probed by persistent HB. In fact, Riley et al. [123] suggested that resonant persistent and transient hole-burned spectra probe slow and fast times of the broad CS time distribution, respectively. The transient holes in this work were in reasonable agreement with the fast (i.e., a few ps) CS times reported in [133]. Herascu et al. [143] have also explored the slow CS time distribution in the PS II RC from spinach (hundreds of picosecond) and obtained very good fits to the experimental data. However, the SHB results were incompatible with significant contribution of the intermediate, tens of picosecond, times to the distribution. The intermediate times, however, are not well understood and require further studies. In summary, as discussed in Sects. 7.3.2–7.3.4, it appears that the coexistence of two electron transfer paths (i.e., initiated from P_{D1} and Chl_{D1}) in PS II RCs is highly feasible, though the identity of various states involved in CS in the PS II RC is not well established.

7.3.4 Distribution of Charge Separation Rates in the PS II RC and Sample Quality

It was shown recently [5, 122] that the particular path taken by CS depends on the composition (or intactness) of the excited state of the special pair P680*. Namely, in intact PS II RCs (i.e., RC684, the subset of RCs more intact than RC680) from *C. reinhardtii* two different excited states may be formed within the RC, which can give rise to two different pathways for fast electron transfer. One of these states involves an excitonic excitation delocalized among four pigments $(P_{D1}P_{D2}Chl_{D1}Pheo_{D1})^*$, while the other one involves only two pigments $(Chl_{D1}Pheo_{D1})^*$. The latter is in agreement with the recent suggestion of two different CS pathways in spinach [144], although in this work no clear oxidation of P_{D1} was observed, suggesting that in isolated spinach RCs (possessing mostly RC680 type, i.e., the less intact RC complexes) the primary electron transfer is initiated from Chl_{D1}. HB studies [5] revealed for the first time that the shape of transient HB spectra in *C. reinhardtii* in RC684 is similar to $P^+Q_A^- - PQ_A$ spectra measured in intact PS II core complexes [145, 146], providing evidence that RC684 most likely represents the *intact* isolated RCs that possess the secondary electron acceptor, Q_A. However, more work is needed on *intact* isolated RCs (i.e., RC684), which are not easy to obtain. Therefore, it is difficult to compare the data from different laboratories, as the sample intactness may vary between different preparations. For example, our recent data on the PS II RC from *C. reinhardtii* obtained by femtosecond pump-probe spectroscopy revealed that RC684 during the concentration procedure (pump-probe experiments require high OD samples) converted to the widely studied RC680 with a typical transient hole near 680 nm, characteristic for the so-called RC680 complexes (unpublished).

A very broad rate distribution of the effective primary charge separation kinetics ranging from 1.5 ps up to a few nanoseconds was also observed in time-resolved optical studies of PS II RCs [133] in agreement with the hole-burning data [123] that also revealed large dispersion in CS times in the spinach PS II RC. Again, it is not clear if such a large distribution will be present in intact RCs, since a narrower distribution of CS time (τ_{CS}) was observed recently in resonant hole-burned spectra obtained for the isolated RC684 from *C. reinhardtii* [5, 122] (*vide supra*). A narrower distribution of CS rates is only in part consistent with the earlier data obtained by 2D-ES [8], and with the photon echo data obtained for spinach RC [133]. However, the 2D-ES experiments did not explore the long time range of CS times, as their analysis included only a single 2 ns exponent, which could as well be assigned to the fluorescence lifetime. Nevertheless, a heterogeneous distribution of time scales associated with charge transfer, ranging from ~1 to ~3 ps, was also observed in the spinach PS II RC via 2D-ES experiments [8].

7.3.5 Charge Separation Pathways in PS II RCs

The nature of the primary electron donor(s), and the possibility of multiple CS pathways in the isolated PS II RC, is still debated. Efforts continue to shed more light on CS pathways in this important biological complex. As mentioned above, both SHB and time-domain data suggested that two CS pathways are active in PS II RCs, namely the P_{D1} CS path and/or the Chl_{D1} CS path, distinguished by the nature of the primary electron donor [5, 125, 129]. Based on SHB obtained recently for *C. reinhardtii* it is feasible that the P_{D1} path is dominant for longer excitation wavelengths and is characterized by sub-picosecond CS times, while the Chl_{D1} CS path likely corresponds to shorter excitation wavelengths and longer CS times [122]. The HB spectra shown in Fig. 7.7 are in agreement with this suggestion. The ZPHs were nearly absent at $\lambda_B = 686.0$ nm and entirely absent at 688.0 nm and longer wavelengths, suggesting that the excited states of cofactors are strongly coupled with the CT state(s) lying in the long-wavelength region, as suggested by Novoderezhkin at al. [129]. However, resonant (transient) HB spectra alone [131] cannot distinguish if CS times correspond to the P_{D1} and/or Chl_{D1} CS path. Nevertheless, Acharya et al. [122] suggested that the ZPHs observed in the 680–685 nm region, corresponding to CS times of about 1.4–4.4 ps, characterize the Chl_{D1} pathway, while the observation of CT state(s) in RC684 (in the 686–695 nm range) and the absence of ZPHs at $\lambda_B > 685$ nm could be considered as evidence of the P_{D1} pathway, for which CS could be ≤ 1 ps.

Two different charge separation pathways have also been identified via time-resolved spectroscopy in the PS II RC from higher plants [144]. The authors argued that depending on protein configuration, the charge separation events follow the Chl_{D1} path, i.e., $(Chl_{D1}P_{D1}P_{D2})^* \rightarrow Chl_{D1}^{+}Pheo_{D1}^{-} \rightarrow P_{D1}^{+}Pheo_{D1}^{-}$, or the P_{D1} path, i.e., $(P_{D1}Chl_{D1})^* \rightarrow P_{D1}^{+}Chl_{D1}^{-} \rightarrow P_{D1}^{+}Pheo_{D1}^{-}$ [144]. Therefore, it was suggested that $Pheo_{D1}$ is an electron acceptor (a widely accepted view), P_{D1} is an electron donor, and Chl_{D1} can act both as an electron donor and as an acceptor. The proposed schematic is shown in Fig. 7.8. In that work, it was also suggested that the capacity of the protein to fine-tune the energy of the excited states could be advantageous under stress conditions, in which a modification of the CS kinetics might be required. If present, such functional flexibility could increase the performance of the PS II RC. It remains to be seen if the CS scenario depicted in Fig. 7.8 could be confirmed by experiments performed by different experimental techniques on samples from the *same* batch. This is necessary as isolated RCs are not very stable and may destabilize rapidly, forming RC680 [5, 122].

Very recent pump-probe data, modeled in terms of global and target analysis, also suggested that at least two different excited states must exist, $(Chl_{D1}Pheo_{D1})^*$ and $(P_{D1}P_{D2}Chl_{D1})^*$, which can give rise to two different pathways for ultrafast CS processes. For example, Romero et al. [134] applied Stark spectroscopy to study a series of site-directed PS II RC mutants from the cyanobacterium *Synechocystis* sp. PCC 6803 and argued that two different exciton states are mixed with CT states, labeled as $(P_{D2}^{\delta+}P_{D1}^{\delta-}Chl_{D1})^*_{673nm}$ and $(Chl_{D1}^{\delta+}Pheo_{D1}^{\delta-})^*_{681nm}$, where the

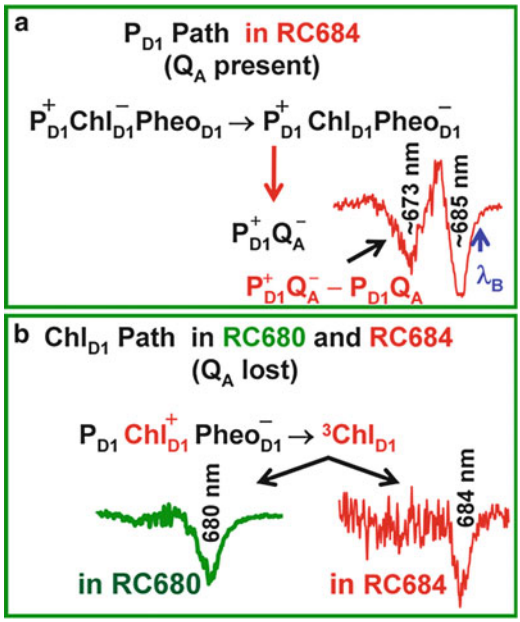

Fig. 7.8 Summary of CS events in the isolated RCs from *C. reinhardtii*, as revealed via HB spectroscopy. Frames **a** and **b** illustrate possible P_{D1} and Chl_{D1} paths of CS (with possible CT states formed) in isolated RC684 (intact) and RC680 (destabilized) complexes. Characteristic transient spectra (with labeled band minima) observed in *C. reinhardtii* for both types of RCs (i.e., RC680 and RC684) are shown for clarity; see text for details. Adapted with permission from [5]. Copyright (2012) American Chemical Society

subscripts indicate the wavelengths of the respective electronic transitions. The authors proposed that the CT state $P_{D2}^{+}P_{D1}^{-}$ acquires excited-state character due to its mixing with an exciton state, resulting in $(P_{D2}^{+}P_{D1}^{-})^{\delta}*_{684nm}$. Thus it is realistic that the states that initiate CS are mixed exciton-CT states, and that the degree of mixing between exciton and CT states determines the efficiency of charge separation. This mixing could ultimately control the selection and efficiency of a specific CS pathway, and highlights the ability of the protein environment to control the functionality of the PS II RC complex [134].

Various assignments of the site energies of P_{D1}, P_{D2}, Chl_{D1}, and Chl_{D2}, in the absence of disorder, have been proposed; for references see the SI in [131]. No consensus exists in the assignment of site energies, though accurate site energies as well as coupling constants, the strength of el-ph coupling, and contribution from CT states are critical for description of RC excitonic structure and CS mechanism(s). As mentioned above, it has been suggested that both P_{D1} and Chl_{D1} can serve as primary electron donors [122, 144]. In contrast, Raszewski et al. [147] argued that Chl_{D1} is the major electron donor, both in isolated RCs and in the PS II RC core. In none of these cases has a distinction between destabilized and intact RC complexes been made. The latter seems to be critical to provide a new insight into PS II

RC dynamics, as it was suggested that the spinach RC studied over the years was destabilized, i.e., contained mostly RC680 and not RC684 [122]. This could be the reason why in theoretical modeling of isolated RC spectra (in comparison to data obtained for the PS II core) it was necessary to arbitrarily shift the site energy of Chl_{D1} by ~4 nm [122, 131]. Our unpublished modeling data suggests that both $Pheo_{D1}$ and Chl_{D1} strongly contribute to the lowest energy exciton state, and not only Chl_{D1} as suggested in [147]. Figure 7.8 summarizes the most likely CS pathways in both RC680 and RC684 samples, revealed via HB spectroscopy, with characteristic transient spectra. To support the proposed scheme, more research is needed on samples from the same batch using various complementary techniques.

7.4 Photosystem I Reaction Center

The X-ray structures for PS I complexes isolated from cyanobacteria and from plants reveal that their electron transfer cofactors are identically positioned in the center of the complex [148–150]. The RC of PS I comprises six Chl *a* cofactors (Fig. 7.1c): the special pair P_{700} (a heterodimer of Chl *a*′ and Chl *a* denoted as $eC1_A$ and $eC1_B$, respectively), two accessory Chl *a* ($eC2_A$ and $eC2_B$), and two Chl *a* molecules denoted as $eC3_A$ and $eC3_B$, which serve as primary electron acceptors and are commonly labeled as A_0. According to the conventional model of electron transfer in the PS I RC, primary CS leads to the reduction of A_0, creating the radical ion pair $P_{700}{}^{+}A_0{}^{-}$. The unpaired electron migrates first to the phylloquinone secondary acceptor A_1 (PhQ_A and/or PhQ_B), then proceeds to the 4Fe-4S center F_x, and finally reaches the terminal iron-sulfur electron acceptors F_A and F_B before being harvested by a small mobile protein ferredoxin [4, 151, 152]. The RC of PS I is coordinated by two major protein subunits, PsaA and PsaB, that also coordinate the majority of the 90 additional Chl *a* molecules that serve as a light-harvesting antenna in the PS I complex and surround the RC.

Unlike the bacterial RC that can be isolated without its light-harvesting antenna, the PS I RC cannot be isolated from the surrounding antenna without harsh chemical treatment that inevitably damages the overall structure of the complex. Optical transition energies of the 96 Chl *a* pigments found in PS I strongly overlap—the Q_y absorption band of the PS I complex is ~30 nm wide (Fig. 7.9), while an individual Chl *a* molecule yields an absorption band that is only three times narrower at room temperature. Such spectral congestion, combined with uncertainties in optical transition energies, complicates detailed analysis of experimental data and modeling of the energy and electron transfer process in PS I.

The exact transition energies have only been measured for the special pair P700 and the primary electron acceptor A_0. The insert of Fig. 7.9 depicts the absorption difference spectra for the oxidized special pair ($P700^+ - P700$) and the reduced primary electron acceptor ($A_0{}^- - A_0$). The empirical absorption of each of these cofactors is also shown on top of the PS I absorption in Fig. 7.9. The P700 absorption is characterized by a broad (~30 nm fwhm) absorption band centered

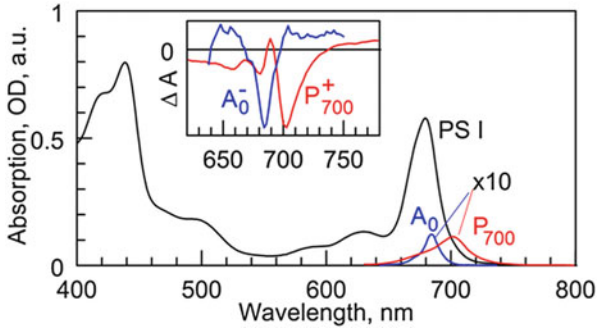

Fig. 7.9 Absorption spectrum of PS I complex (*black line*) with empirical absorption spectra of the special pair P_{700} (*red line*) and A_0 (*blue line*) derived from the respective absorption difference spectra shown in the *insert*. Note that both A_0 and P_{700} spectra are magnified about ten times and thus are generally overwhelmed with the absorption of the ~100 antenna Chl *a* pigments present in the PS I complex. *Insert*: Characteristic absorption difference band arising from oxidation of special pair ($P_{700}^{+} - P_{700}$) (*red line*) and absorption difference band due to reduction of the A_0 ($A_0^{-} - A_0$) (*red line*) [155]

at ~700 nm, and the A_0 absorption band is at ~684–686 nm and has a bandwidth of ~10 nm [153–155]. Their absorption contributes very little to the total absorption of PS I. Based on experimental data and electrochromic shift modeling it was suggested that the accessory Chl *a* (A) absorbs at ~682 nm [155], but this conclusion has not been verified in independent experiments. The spectral positions of all Chls in PS I have been derived using structure-based theoretical calculations [156, 157], though these predictions could not be experimentally verified.

Since the absorption bands of electron transfer cofactors overlap with the absorption of other pigments in the complex, direct optical excitation and optical probing of electron transfer cofactors of the PS I RC are precluded. Upon light excitation, most of the photons are absorbed by antenna pigments and thus additional time is required before excitation can be transferred to the RC to initiate charge separation. The overall lifetime of electronic excitation in the antenna, i.e., time in which the excitation is trapped by the RC with the formation of a charge-separated radical pair, has been shown to be ~20–60 ps depending on the species [158–162]. This is significantly slower than the intrinsic rate of primary charge separation, which further complicates the studies of electron transfer in the PS I complex.

We will focus below on data obtained using time-domain spectroscopy, since spectral hole-burning [163–165] and single photosynthetic complex [166] studies of PS I have so far focused on the so-called red-antenna states, or states absorbing lower in energy than P_{700}. At physiological temperatures, these low-energy pigments are capable of the uphill EET to the P_{700}, and the organism benefits from extending the photosystem absorption to a wider wavelength range. While in cyanobacteria the respective pigments are part of the core antenna, in the plant PS I they belong to the Lhca peripheral antenna complexes. (For recent review on structure and inter-subunit EET in plant and cyanobacterial PS I see [167].)

7.4.1 The Sequence and Dynamics of Primary Charge Separation (CS) in the PS I RC

When discussing the dynamics of CS and consequent electron transfer processes in a photosynthetic system, it is important to differentiate between the "effective" transfer rates and the "intrinsic" rate constants. To avoid possible ambiguity, we will adhere to the terminology defined in [168, 169]. The term "intrinsic rate constant for electron transfer" will be used exclusively to denote the kinetic rate of an individual electron transfer step from a particular electron donor molecule to a particular acceptor molecule in the assumption that all other transfer processes are blocked. The "effective rate constant" (sometimes referred to as "apparent rate constant") is defined as the rate at which a certain redox state is populated (or depopulated). Thus, the energy-trapping time of 20–65 ps observed in experiments as the decay of antenna excitation is equivalent to the *effective* CS time (time = 1/rate), since excitation trapping leads to the creation of the first radical pair and is a consequence of many individual energy transfer steps followed by a single electron transfer step. In contrast, the *intrinsic* CS time in PS I represents the kinetics in the case when the excitation is created directly on P_{700} and back-transfer from P_{700} to the antenna and charge recombination processes are blocked. Since for the PS I complex the described conditions cannot be achieved, the intrinsic rate constants cannot be directly observed in experiment and are usually obtained via model simulations.

There is unanimous agreement that the intrinsic CS rate in the PS I RC is much faster than the observed effective excitation trapping rate. Most of the studies put the intrinsic CS step lifetime in the PS I RC in the 0.5–3 ps range, and the consequent electron transfer from the primary electron acceptor A_0 to the secondary electron acceptor A_1 is believed to occur in the 10–50 ps range [4, 152]. However, the precise measurement of these important kinetic parameters presents a challenging problem. Isolation of the RC from PS I is impossible as the two main protein subunits PsaA and PsaB that coordinate the RC cofactors also bind most of the antenna Chls. The spectral congestion among RC cofactors and antenna pigments precludes selective excitation of P_{700} and complicates the isolation of the optical signals arising from the electron transfer process from the signals stemming from the EET.

As an example, Fig. 7.10 shows the typical absorption difference dynamics measured for PS I complexes after excitation at 660 nm [170]. Due to the presence of large number of antenna pigments the observed dynamics, to large extent, are determined by EET processes between the numerous antenna pigments. A global analysis of the time-dependent spectra (see Fig. 7.10a) results in DADS shown in Fig. 7.10b, where the amplitude of each exponential decay component of the fit is represented as a function of the probe wavelength. The 0.53 and 2.3 ps have a bimodal character that is typical for energy or electron transfer processes. Since the special pair is not directly excited, these components correspond primarily to the excited energy transfer towards the lowest energy pigments, i.e., energy

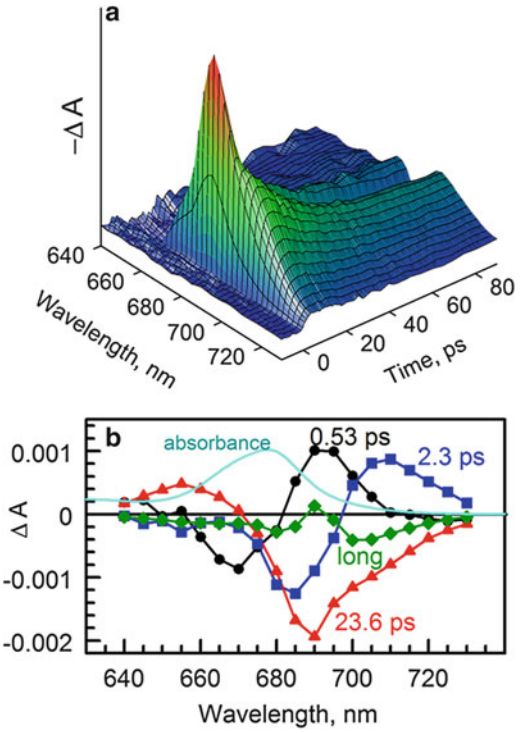

Fig. 7.10 The absorption difference as a function of probe wavelength and delay time measured after exciting PS I complexes from *Synechocystis* sp. PC 6803 at 660 nm (**a**). For better perception of the 3D surface, the ΔA axis is inverted with photobleaching in the upside direction. Plane **b** is the decay-associated difference spectrum (DADS) obtained as a resultof global fit of the data shown in plane **b**. This data is described in more detail in [170]

equilibration. The 0.53 ps is negative at ~660 nm, which corresponds to the photobleaching decay, and is positive at ~690 nm, which corresponds to photobleaching rise. It is thus consistent with the EET from the initially excited pigments to the lower energy pigments. Similarly, the 2.3 ps component reflects energy transfer to the few pigments absorbing at ~710–720 nm. The 23.6 ps component is the decay of excited states within the antenna and thus represents the *effective* excitation trapping time and the formation of the CS state. The "long" component in Fig. 7.10b is the signature of the long-living P_{700}^+ state and has the same shape as ($P_{700}^+ - P_{700}$) difference spectrum shown in the inset of Fig. 7.9. The data shown above illustrates that extracting intrinsic rates for the fast initial electron transfer steps in the PS I RC is a challenging task.

Kumazaki et al. [171–173] tried to minimize the contribution of antenna processes to the measured transient absorption and fluorescence signals by chemical treatment of the PS I complexes from spinach that removed most of the antenna Chls from the complexes, leaving only 12–14 Chls per P_{700}. Due to the small amount of antenna Chls, preferential excitation of P_{700} became possible. The authors found that the effective primary charge separation kinetics in these complexes could be described by two components of equal amplitudes with time constants of 0.8 ± 0.1 and 9 ± 1 ps [173]. The short 0.8 ps component was ascribed to the formation of the charge-separated state generated directly from the

initially excited P_{700}*, and the relatively slow 9 ps component was assumed to stem from excitations which escaped from P_{700}* to the surrounding pigments and were recaptured at later times. A kinetic model revealed that the observed data could be reproduced with an intrinsic charge separation time of 0.5–0.8 ps.

Several groups [153, 154, 172, 174–177] proposed a strategy for isolating the RC kinetics by obtaining time-resolved absorption difference profiles for PS I core complexes with open and closed RCs, where the term "open" refers to a complex with P_{700} in neutral state, and term "closed" refers to a complex where charge separation has taken place and special pair is in the oxidized state P_{700}^{+}. Since extensive experimental evidence suggests that the antenna kinetics are unaffected by the P_{700} oxidation state, the difference $\Delta\Delta A$ between absorption difference profiles for open and closed RCs ($\Delta\Delta A = \Delta A_{\text{openRC}} - \Delta A_{\text{closedRC}}$) should isolate the electron transfer processes, since they occur only in complexes with open RCs. Hastings et al. [153] applied this method to study PS I complexes from *Synechocystis* sp. *PCC 6803*. The experimental $\Delta\Delta A$ profiles probed at 686 nm exhibited an initial photobleaching rise feature of ~4 ps followed by a ~21-ps photobleaching decay. This probe wavelength corresponds to the maximum position of the A_0 absorption band, and the observed kinetics were attributed to the formation and decay of the A_0^{-} state. The authors concluded that the ~4 ps rise represented the effective energy-trapping time, which was significantly shortened as a result of annihilation caused by the use of high excitation pulse intensities, and thus 4 ps represents an upper limit for the intrinsic primary charge separation time. The 21 ps component was ascribed to the intrinsic rate of the next electron transfer step $A_0 \rightarrow A_1$. Savikhin et al. [154] have further extended this method and studied annihilation-free $\Delta\Delta A$ profiles probed in a wide spectral range with significantly lowered noise levels. Assuming that all of the antenna kinetics were cancelled by the (open-closed) subtraction procedure, the $\Delta\Delta A$ profiles should reflect the formation and decay dynamics of only three states: $P_{700}{}^{*}A_0A_1$, $P_{700}{}^{+}A_0{}^{-}A_1$, and $P_{700}{}^{+}A_0A_1{}^{-}$. Using a simple sequential model of electron transfer, $\Delta\Delta A$ profiles in a wide wavelength range were fitted globally with only two free parameters, resulting in the intrinsic times for primary CS and the following $A_0 \rightarrow A_1$ electron transfer step of 1.3 ps and 13 ps, respectively. White et al. [177] applied a similar approach to study the dynamics of the electron transfer process in PS I complexes from spinach. Using simple models of energy migration, the intrinsic rates of CS and the primary electron transfer step were estimated to be 1.4 ps and 20 ps, respectively. It was also found that even when the femtosecond pulses were tuned to preferentially excite P_{700}, only a small fraction of the initially excited P_{700}* led to the charge-separated state while the rest of the excitations escaped to the antenna.

Since the lifetime of the reduced primary electron acceptor A_0^{-} is comparable or shorter than the overall energy trapping by the RC, the knowledge of that kinetic parameter is important in modeling the electron transfer and extracting the intrinsic kinetic parameters associated with the primary charge separation and formation of $P_{700}^{+}A_0^{-}$. While the optical signature of A_0 is hard to distinguish from the signals

arising from energy/electron transfers between other Chl *a* molecules, the kinetics of the $P_{700}^{+}A_0^{-}A_1 \rightarrow P_{700}^{+}A_0A_1^{-}$ electron transfer step can be monitored via the formation of A_1^{-} (phylloquinone), which is associated with a broad near-UV absorption band around 380–390 nm [178–181]. At this probe wavelength, Brettel et al. [180] observed ΔA transient for *Synechocystis* sp. PCC 6803, which could be described by two exponentials with time constants of 7 and 28 ps. The shorter component was attributed to the antenna processes presumably accelerated due to high excitation levels, where multiple excitations were created by a laser pulse within the same complex leading to mutual quenching of singlet excited states (annihilation artifact). The longer component was interpreted as the intrinsic time of $A_0 \rightarrow A_1$ electron transfer step. However, the observed buildup of the A_1^{-} state was probably delayed by the preceding antenna equilibration and charge separation steps and the reported 28 ps time is likely to be an overestimate. Indeed, similar experiments at low excitations in the annihilation-free regime revealed a single lifetime of 30 ± 3 ps for the formation of the A_1^{-} [4]. In the absence of annihilation, the (effective) charge trapping that precedes $A_0 \rightarrow A_1$ electron transfer step occurs in 23 ps, which implies that the intrinsic $A_0 \rightarrow A_1$ transfer step is significantly faster than the measured 30-ps time constant. A good fit to the experimental data was obtained with the intrinsic lifetime of the $P_{700}^{+}A_0^{-}A_1 \rightarrow P_{700}^{+}A_0A_1^{-}$ step between 8 and 15 ps.

A different ET scenario was proposed recently by Müller et al. [169] based on optical pump-probe data obtained after exciting PS I complexes from *C. reinhardtii* at 670 and 700 nm. In these species the 700 nm pump pulses were found to predominantly excite the P_{700} dimer directly, while the 670 nm excitation represents the contrasting case when all of the electronic excitations are initially created in the antenna. By comparing pump-probe data measured in these different excitation regimes and analyzing the data in terms of species-associated difference spectra (SADS), the authors found that the experimental results could be explained if one additional radical pair was introduced to the conventional scheme of electron transfer. According to the most probable scenario proposed in the paper, the intrinsic charge separation $P_{700}^{*}A_0 \rightarrow P_{700}^{+}A_0^{-}$ time is 2.9 ps, which is combined with the backward recombination process with an intrinsic time of ~40 ps. Charge separation is followed by two fast electron transfer steps with intrinsic times of 13 ps and 35 ps, respectively, which lead to the formation of $P700^{+}A_1^{-}$. Note that P_{700} and A_0 are too far apart for direct electron transfer between them to occur within just a few picoseconds, and there is no doubt that the accessory pigment, sandwiched between these two cofactors, plays an important role in the primary charge separation, just like it does in the case of the BRC and PS II RC. This was recognized by Müller et al. [169], who proposed a possibility that the additional radical pair involves the accessory pigment, and that the true primary charge-separated state may be not $P_{700}^{+}\ A_0^{-}$, but $P_{700}^{+}\ A^{-}$ or $A^{+}A_0^{-}$. In support of this hypothesis, Holzwarth et al. [182] found that mutations near P_{700} did not affect the intrinsic primary CS rate, which is reported to be <1 ps^{-1}, arguing that the special pair is not involved in the first electron transfer step and thus cannot be

labeled as a primary electron donor. The nature of the primary CS state was further investigated by Müller et al. [183] who introduced mutations targeting properties of the two A_0 cofactors independently ($eC3_A$ and $eC3_B$ in Fig. 7.1c) in *C. reinhardtii*. Global analysis of the ΔA time-dependent profiles probed in the range of 640–760 nm combined with the modeling suggested the following minimal compartmental kinetic scheme for energy and electron transfer processes in PS I complexes:

$$\boxed{\mathrm{ANT}^*} \underset{2.7}{\overset{4.8}{\rightleftarrows}} \boxed{\mathrm{RC}^*} \begin{cases} \underset{12.5}{\overset{4.5}{\rightleftarrows}} \boxed{eC2_A^+eC3_A^-} \overset{14.5}{\rightarrow} \boxed{P_{700}^+eC3_A^-} \overset{31.3}{\rightarrow} \boxed{P_{700}^+PhQ_A^-} \rightarrow \\ \underset{63}{\overset{7.1}{\rightleftarrows}} \boxed{eC2_B^+eC3_B^-} \overset{11.2}{\rightarrow} \boxed{P_{700}^+eC3_B^-} \overset{63}{\rightarrow} \boxed{P_{700}^+PhQ_B^-} \rightarrow \end{cases} \boxed{P_{700}^+F_X^-} \tag{7.8}$$

To ease the discussion, the kinetic rates in the scheme above were converted into respective lifetimes in ps, with $rate = (lifetime)^{-1}$. The model assumes that electron transfer proceeds along both branches of the PS I RC, as it will be discussed in a later section. Following excitation, the energy equilibrates between the RC and antenna (ANT) compartment within about a picosecond, which is reflected in bidirectional kinetics in the above scheme with 1.8 ps and 2.7 ps lifetimes for forward and backward transfers, respectively. The primary CS proceeds concurrently along both branches of the RC, with the forward electron transfer rate along the A-branch (4.5 ps) being somewhat faster than electron transfer along the B-branch (7.1 ps). The model suggests that 61 % of electron transfer proceeds along the A-branch, which is similar to other estimates [184, 185]. Note that the respective *intrinsic* primary charge separation rates are faster, ~ $(0.7\ \mathrm{ps})^{-1}$ for the A-branch and ~$(1.3\ \mathrm{ps})^{-1}$ for the B-branch. The difference stems from the degeneracy of compartments in the model since RC* contains six excitonically coupled Chl *a* molecules. These intrinsic primary CS rates are on par with the rates of electron transfer between the homologous cofactors B_A and H_A of the BRC (see Eq. (7.2)). The conclusion that primary CS in the PS I RC is not initiated by P_{700} but involves the formation of $A^+A_0^-$ is supported by the studies of wild-type and mutated complexes from *C. reinhardtii* by means of time-resolved fluorescence [186] and by subpicosecond infrared spectroscopy [187]. The latter work by Donato et al. [187] was focused on the dynamics of the absorption difference signals probed in the mid-IR spectral region between 1450 and 1750 cm^{-1}, which were modeled using global and target analysis, and suggested the following energy/electron transfer scheme for PS I for the first few picoseconds following excitation:

$$\boxed{\mathrm{RED}^*} \underset{4.0}{\overset{2.5}{\rightleftarrows}} \boxed{\mathrm{ANT}^*} \underset{0.8}{\overset{1.3}{\rightleftarrows}} \boxed{\mathrm{RC}^*} \overset{0.3}{\rightarrow} \boxed{A^+A_0^-} \underset{25}{\overset{10}{\rightleftarrows}} \boxed{P_{700}^+A_1^-} \rightarrow \ldots \tag{7.9}$$

where the rate constants are converted to lifetimes and are given in ps. While this model does not distinguish between the two branches of the RC, it explicitly separates a small pool of antenna Chls that absorb on the red edge of the cumulative

antenna absorption band into a separate compartment denoted as RED*. The model did not resolve the formation of P_{700}^{+} and A_1^{-} from the primary charge-separated state $A^{+}A_0^{-}$ as two separate kinetics; instead the authors concluded that equilibrium between this state and $P_{700}^{+}A_1^{-}$ is obtained in ~6 ps, which is considerably faster than the respective electron transfer step in Eq. (7.8), and the full population of $P_{700}^{+}A_1^{-}$ is reached in ~40 ps for both branches (i.e., $P_{700}^{+}PhQ_A^{-}$ and $P_{700}^{+}PhQ_B^{-}$). Note that the intrinsic primary CS rate of $(0.3\ ps)^{-1}$ in Eq. (7.9) is also significantly faster than that in Eq. (7.8). Both groups, however, converge on the conclusion that the accessory pigment, not special pair, serves as a primary electron donor.

A different primary CS scenario was proposed by Shelaev et al. [188] based on pump-probe experiments performed with 20 fs laser pulses on the PS I complexes from *Synechocystis* sp. PCC 6803. Upon excitation a new broad band centered at around 660 nm was observed to emerge within the first 100 fs and ascribed to the formation of Chl anion radical. The authors thus concluded that the primary charge-separated state, identified as the conventional $P_{700}^{+}A_0^{-}$, is formed with the intrinsic lifetime of <100 fs. Their model did not include the accessory pigment being transiently oxidized or reduced at any time, and to explain such a fast charge separation over such a long distance the authors invoked a quantum mechanical model where quantum beats occur between several excitonic levels delocalized over all Chl pigments in the RC, including P_{700} and A_0. Due to excitonic coupling, the superposition of the excited states P_{700}^{*} and A_0^{*} is expected to oscillate with the frequency defined by the energetic gap between these two states (~240 cm^{-1}), leading to rapidly oscillating electron density and efficient formation of the $P_{700}^{+}A_0^{-}$ radical pair.

As it was demonstrated above, there is still no general agreement between various groups on the fine details of the primary charge separation and the conclusions reached in such complex data analyses are clearly model dependent.

7.4.2 The Bidirectional Electron Transfer in the PS I RC

There is a general consensus today that the electron transfer in PS I proceeds concurrently along both branches of the RC [12, 13]. The ratio of electron transfer along the branches varies between different species, though in all reports the A-branch is more efficient than the B-branch. This is quite different from the BRC and the PS II RC, where electron transfer proceeds exclusively along one branch.

The first evidence for bidirectional ET was obtained for PS I of eukaryotes such as the alga *Chlorella sorokiniana* [189] and *C. reinhardtii* [184]. Joliot and Joliot [189] used nanosecond pump-probe technique to monitor the kinetics of absorption changes in the 371–545 nm spectral range. The two components with somewhat different spectra and lifetimes of 160 and 18 ns were assigned to electron transfer to F_X from the two phylloquinones (PhQ_A and PhQ_B) and suggested that electron transfer occurs

along both branches with about equal yield. This conclusion was further confirmed in studies involving site-specific mutations around the respective phylloquinone A_1-binding sites on the PsaA and PsaB polypeptides. Guergova-Kuras et al. [184] were able to demonstrate that the lifetimes of the two decay components associated earlier with electron transfer from PhQ_A and PhQ_B to F_x could be independently manipulated by point mutations near the respective phylloquinones. The data was consistent with the 55–66 % of electron transfer proceeding along the A-branch. The bidirectional energy transfer in PS I from *C. reinhardtii* is also supported by later EPR and optical measurements [185, 190–193].

It was demonstrated that mutations in the PhQ_A and PhQ_B pocket can affect the ratio of the $[PhQ_A^-]/[PhQ_B^-]$ concentrations arising from optical excitation of PS I [185]. This ratio was 65/35 for wild-type RCs, but could be decreased to 80/20 in mutants that target the PhQ_A pocket, and decreased to 50/50 when a similar mutation was introduced in the PhQ_B pocket. Since these mutations are not expected to affect the electron transfer branching ratio, it was inferred that mutations affected the reversibility of electron transfer from the phylloquinones to F_x and the asymmetry in the driving forces for these electron transfer reactions, which in turn leads to an F_x-mediated inter-quinone electron transfer.

Cohen et al. [194] constructed identical mutations in both the PsaA and PsaB sides at the corresponding A_0 sites modifying the properties of this electron acceptor in the PS I complexes from *Synechocystis* sp. PCC 6803. In particular, the methionines in $M688_{PsaA}$ or $M668_{PsaB}$ positions were replaced by leucine or asparagine. These methionines are proposed to provide the axial ligands to the respective Mg^{2+} ions of the two A_0 chlorophylls and are expected to alter the midpoint potential of the A_0^-/A_0 redox pair, causing changes in electron transfer dynamics. Nanosecond optical and EPR experiments revealed significant differences between the PsaA-branch and the PsaB-branch mutants, which were consistent with the assumption that ET occurs primarily along the A-branch of the RC. These measurements, however, did not have the time resolution sufficient to detect changes in the first two electron transfer steps, which directly involve A_0 and would naturally be affected by such point mutations. Dashdorj et al. [195] performed a series of ultrafast pump-probe experiments where A_1^- formation was monitored via its characteristic absorption band at 390 nm. The presented data supported this conclusion and estimated that at least 80 % of electron transfer in this species proceeds along the A-branch of the RC in *Synechocystis* sp. PCC 6803. On the other hand, the evidence of the B-branch being involved in electron transfer in these species was provided by EPR spectroscopy [191, 196–198]. Careful analysis of pulsed EPR data suggested that the electron transfer in these species may be less asymmetric with 60–80 % of electrons proceeding along the A-branch [198].

The relative involvement of the two branches of the PS I RC in electron transfer has been found to be temperature dependent [199, 200]. Using optical pump-probe spectroscopy to monitor the kinetics of PhQ_A^- and PhQ_B^- decay in the PS I RC from *Synechocystis* sp. PCC 6803, Agalarov and Brettel [199] observed that the longer component ascribes to PhQ_A^- kinetics slowed down upon cooling, while the faster

phase that is associated with PhQ_B^- was not affected, though its amplitude was too low to distinguish below 223 K. Mula et al. [200] used EPR spectroscopy on samples where the phylloquinones in the A_1-binding sites were replaced by naphtaquinone molecules. Since the reduction midpoint potential of naphtaquinone is about 400 mV more positive than that of the native phylloquinone, the electron transfer from A_1 to F_x becomes blocked, while the primary charge separation rate in these samples is not affected [195]. As the samples are excited, the charge separation essentially stops upon the electron reaching one of the naphtaquinones in the A_1 sites. Experiments at low temperature ($T = 15$ K) detected the formation of PhQ_A^-, as expected, but no evidence of PhQ_B^- was found. In contrast, similar experiments on PS I RCs with native phylloquinones in the A_1 sites, where forward electron transfer was blocked by prereduction of the F_x complex, did show an evidence of PhQ_B^- formation at low temperatures [190, 191, 193, 197, 198, 201]. The nature of this discrepancy is not yet clear.

7.4.3 The Energetics of the PS I RC

The energy diagram of electron transfer in the PS I RC is shown in Fig. 7.1f [13, 202, 203]. The midpoint potential E_m of the special pair, P_{700}/P_{700}^+, was measured by electrochemical means to be between +430 and +470 mV vs. the standard hydrogen electrode (SHE) for most species including spinach, *C. reinhardtii*, and *Synechocystis* sp. PCC 6803 [203–208]. A higher value of +470 mV was reported for PS I isolated from *Thermosynechococcus elongatus* [205], indicating that the respective midpoint potential is somewhat species dependent. Upon excitation the redox potential changes by the energy roughly equal to the energy of the Q_y absorption transition of P_{700}, i.e., by 1.77 eV, bringing the P_{700}^*/P_{700}^+ midpoint potential to about -1.3 V [206].

The midpoint potential of the electron acceptor A_0/A_0^- has been estimated using delayed fluorescence to be 0.25 V less than that of P_{700}^*/P_{700}^+, resulting in -1.05 V in respect to SHE [209]. A slightly higher value of -1.01 V was obtained by means of electroluminescence [210]. Values for A_1 were estimated by several groups using electroluminescence and recombination kinetics to be between -0.7 and -0.8 V [151, 211, 212]. Note that these experiments cannot distinguish between the homologous cofactors in the two branches of the PS I RC. The redox midpoint values for the iron sulfur complexes are also marked in Fig. 7.1f and are discussed in details elsewhere [13, 202].

Since it has been suggested that the accessory pigment participates in electron transfer and may actually serve the role of a primary electron donor (or acceptor), it would be useful to identify the free energy of such an intermediate. Holzwarth et al. [213], who proposed the presence of such an intermediate, modeled femtosecond absorption difference kinetics using a simple compartmental kinetic model similar to Eq. (7.9) and found that the ratio of forward and backward transfer rates

between the excited state of the RC* and the first radical pair is consistent with the energy difference of 580–800 cm^{-1} between these states (i.e., 70–100 meV). This value is clearly smaller than the difference of 250 meV reported for P* and A_0, suggesting that the energy of $A^+A_0^-$ state (or $P_{700}^+A^-$ depending on the model), if present, lays between P_{700}^* and $P_{700}^+A_0^-$.

The PS I complexes from the cyanobacterium *Acaryochloris marina* contain mostly Chl *d* molecules instead of Chl *a*, and the Q_y absorption of the special pair in this organism is shifted to 740 nm (P_{740}). This spectral shift is accompanied by the change in the midpoint potential of P_{740}/P_{740}^+, which is lower (+335 mV) than the midpoint potential of P_{700}/P_{700}^+ [214]. However, when these two shifts are combined, the midpoint potential of the electron donor P_{740}^*/P_{740}^+ remains the same as that of P_{700}^*/P_{700}^+.

Several groups have attempted to calculate the redox potential of electron transfer cofactors using the known X-ray structure of PS I. Ishikita et al. [215] approached the problem by solving the linearized Poisson–Boltzmann equation for all atoms in the crystal structure and were able to qualitatively reproduce the observed differences for the midpoint potentials of the special pairs in the BRC, PS II, and PS I. However, the calculated midpoint potential of P_{700}/P_{700}^+ was about 100 mV higher than experimentally measured. This method also resulted in somewhat higher redox potentials for the phylloquinones: −531 mV for PhQ_A and −686 mV for PhQ_B [216, 217]. Extensive semi-continuum electrostatic calculations of all redox cofactors were performed by Ptushenko at al. [218]. The authors were able to reproduce the experimental value for the special pair, and obtained reasonable agreement with the measured values for PhQ_A and PhQ_B (−671 mV and −0.844 mV, respectively). However, the redox potentials for eC_{3A} and eC_{3B} (A_0) evaluated to −1.271 V and −1.314 V, respectively, which are significantly lower than the measured value of −1.05 V and are not much different from the midpoint potential of P_{700}^*/P_{700}^+. This discrepancy could be partially lessened in calculations where the interaction between nearby pigments is taken into account. Considering that the charge could be delocalized over dimers eC_{2A}/eC_{3A} and eC_{2B}/eC_{3B}, the respective midpoint potentials became −1.228 and −1.268 V. It is interesting to note that the calculated redox potentials of the accessory pigments eC_{2A} and eC_{2B} were −1.416 and −1.445 V, which puts them >100 mV below P_{700}^*. This is not consistent with the proposed involvement of the accessory pigment as one of the charge transfer intermediates.

7.4.4 *Theoretical Modeling of Electron Transfer in the PS I RC*

Electron transfer in the PS I RC is typically treated in terms of Marcus theory; see for example [185, 199, 202, 219]. Moser and Dutton [202] presented a calculation of electron transfer rates in the RC based on the known structure and measured

energies of the redox cofactors (Fig. 7.1c, f). To account for electron tunneling phenomenon, the electron coupling interaction factor V^2 in Eq. (7.6) can be expressed as $V^2 \cong V_0^2 e^{-\beta R}$, where the exponential term accounts for the electron density overlap with R being the edge-to-edge distance between electron donor and acceptor molecules. The factor V_0^2 represents the maximal value when the two molecules are in contact; β is the tunneling barrier and generally depends on the molecular contents of the space between the molecules. Combining that with the expression for the FC factor (Eq. (7.7)), Moser and Dutton derived the following empirical expression that can be used to estimate the downhill ET rate k at room temperature [220, 221]:

$$\log_{10} k = 13 - 0.6(R - 3.6) - 3.1\frac{\left(\Delta G^0 + \lambda\right)^2}{\lambda} \tag{7.10}$$

In this equation k is measured in s^{-1}, R is in Å, ΔG^0, and λ are in eV. While the distances R can be found from the structure and ΔG^0 have been measured or estimated for all electron transfer cofactors in the PS I RC, it is more difficult to obtain independent information about the reorganizational energies λ associated with each electron transfer step. One way to estimate λ is to manipulate the driving force of the reaction ΔG^0 and compare the observed electron transfer rates with the model predictions. Ramesh et al. [222] measured the kinetics of reduction of P_{700}^+ in several mutants of *C. reinhardtii* where the P_{700}^+/P_{700} midpoint potential was varied over a range of 136 mV. The observed up to five times difference in the rate of electron transfer for these mutants could be fit with Eqs. (7.6) and (7.7) with $\lambda = 545$ meV. The driving force for the $A_0 \rightarrow A_1$ electron transfer step was manipulated in a range of 1.2 eV by a series of A_1 substitutions by several groups [223–226]. These experiments revealed that $\lambda \approx 300$ meV, and that in the wild-type PS I RC this reaction is near its optimum where $\lambda \approx \Delta G^0$.

Using Eq. (7.10) and the above data Moser and Dutton [202] were able to reproduce well the experimentally measured picosecond kinetics of primary electron transfer steps in the model, where the two branches of the RC were assumed to be completely symmetric. Due to the symmetry, however, the electron transfer from A_1 to F_x occurred in ~10-ns time frame in both branches, which contradicts experimental measurements that show ten times difference between the respective electron transfer rates along the A- and B-branches of the RC. Since the edge-to-edge distances R between each of the phylloquinones and F_x are almost identical, the authors found that the most likely cause for such ET heterogeneity lays in different redox midpoint potentials of the two phylloquinones. A good fit of the measured kinetics is achieved when the midpoint potential of the A-branch quinone is equal to that of F_x, while the B-side quinone has a 40 mV more negative midpoint potential.

Acknowledgments The authors thank Dan Hartzler, Su Lin, and Valter Zazubovich for useful discussions. The authors acknowledge the Division of Chemical Sciences, Geosciences, and Biosciences, Office of Basic Energy Sciences of the US Department of Energy, through Grant DE-FG02-09ER16084 (to S.S.) and DE-FG02-11ER16281 (to R.J.) for support.

References

1. Şener M, Strümpfer J, Hsin J, Chandler D, Scheuring S, Hunter CN, et al. Förster energy transfer theory as reflected in the structures of photosynthetic light-harvesting systems. Chemphyschem. 2011;12(3):518–31.
2. van Amerongen H, Valkunas L, van Grondelle R. Photosynthetic excitons. Singapore: World Scientific; 2000.
3. Seely GR, Connolly JS. Fluorescence of photosynthetic pigments in vitro. In: Govindjee J, Amesz J, Fork DC, editors. Light emission by plants and bacteria. New York: Academic; 1986. p. 99–133.
4. Savikhin S. Ultrafast optical spectroscopy of photosystem I. In: Golbeck J, editor. Photosystem I, the light-driven plastocyanin:ferredoxin oxidoreductase. Advances in photosynthesis and respiration. Dordrecht: Springer; 2006. p. 155–75.
5. Jankowiak R. Probing electron-transfer times in photosynthetic reaction centers by hole-burning spectroscopy. J Phys Chem Lett. 2012;3(12):1684–94.
6. Jankowiak R, Reppert M, Zazubovich V, Pieper J, Reinot T. Site selective and single complex laser-based spectroscopies: a window on excited state electronic structure, excitation energy transfer, and electron-phonon coupling of selected photosynthetic complexes. Chem Rev. 2011;111(8):4546–98.
7. Neupane B, Jaschke P, Saer R, Beatty JT, Reppert M, Jankowiak R. Electron transfer in *Rhodobacter sphaeroides* reaction centers containing Zn-bacteriochlorophylls: a hole-burning study. J Phys Chem B. 2012;116(10):3457–66.
8. Myers JA, Lewis KLM, Fuller FD, Tekavec PF, Yocum CF, Ogilvie JP. Two-dimensional electronic spectroscopy of the D1-D2-cyt b559 photosystem II reaction center complex. J Phys Chem Lett. 2010;1(19):2774–80.
9. Hohmann-Marriott MF, Blankenship RE. Evolution of photosynthesis. Annu Rev Plant Biol. 2011;62:515–48.
10. Allen JP, Williams JC. Photosynthetic reaction centers. FEBS Lett. 1998;438:5–9.
11. Cardona T, Sedoud A, Cox N, Rutherford AW. Charge separation in Photosystem II: a comparative and evolutionary overview. Biochim Biophys Acta. 1817;2012:26–43.
12. Redding K, van der Est A. The directionality of electron transport in photosystem I. In: Golbeck J, editor. Photosystem I. Advances in photosynthesis and respiration, vol. 24. Dordrecht: Springer; 2006. p. 413–37.
13. Setif P, Leibl W. Functional pattern of photosystem I in oxygen evolving organisms. Primary processes of photosynthesis, Part 2: Principles and apparatus, vol. 9. Cambridge: The Royal Society of Chemistry; 2008. p. 147–91.
14. Holzwarth AR, Müller MG. Energetics and kinetics of radical pairs in reaction centers from *Rhodobacter sphaeroides*. A femtosecond transient absorption study. Biochemistry. 1997;36:281–7.
15. Peloquin JM, Williams JC, Lin X, Alden RG, Taguchi AKW, Allen JP, et al. Time-dependent thermodynamics during early electron transfer in reaction centers from *Rhodobacter sphaeroides*. Biochemistry. 1994;33:8089–100.
16. Lauterwasser C, Finkele U, Scheer H, Zinth W. Temperature dependence of the primary electron transfer in photosynthetic reaction centers from *Rhodobacter sphaeroides*. Chem Phys Lett. 1991;183:471–7.
17. Holzapfel W, Finkele U, Kaiser W, Oesterhelt D, Scheer H, Stilz HU, et al. Observation of a bacteriochlorophyll anion radical during the primary charge separation in a reaction center. Chem Phys Lett. 1989;160(1):1–7.
18. Martin JL, Breton J, Hoff AJ, Migus A, Antonetti A. Femtosecond spectroscopy of electron transfer in the reaction center of the photosynthetic bacterium *Rhodopseudomonas sphaeroides* R-26: direct electron transfer from the dimeric bacteriochlorophyll primary donor to the bacteriopheophytin acceptor with a time constant of 2.8 ± 0.2 psec. Proc Natl Acad Sci U S A. 1986;83(4):957–61.

19. Diner BA, Rappaport F. Structure, dynamics, and energetics of the primary photochemistry of photosystem II of oxygenic photosynthesis. Annu Rev Plant Biol. 2002;53:551–80.
20. Marchanka A, Savitsky A, Lubitz W, Möbius K, van Gastel M. B-branch electron transfer in the photosynthetic reaction center of a *Rhodobacter sphaeroides* quadruple mutant. Q- and W-band electron paramagnetic resonance studies of triplet and radical-pair cofactor states. J Phys Chem B. 2010;114(45):14364–72.
21. Haffa ALM, Lin S, Williams JC, Bowen BP, Taguchi AKW, Allen JP, et al. Controlling the pathway of photosynthetic charge separation in bacterial reaction centers. J Phys Chem. 2004;108:4–7.
22. Hiyama T, Ke B. A further study of P430: a possible primary electron acceptor of Photosystem I. Arch Biochem Biophys. 1971;147:99–108.
23. Parson WW. Mechanism of charge separation in purple bacterial reaction centers. In: Hunter CN, Daldal F, Thurnauer MC, Beatty JT, editors. The purple phototrophic bacteria. New York: Springer Science + Business Media B.V.; 2009. p. 355–77.
24. Zinth W, Wachtveitl J. The first picoseconds in bacterial photosynthesis—ultrafast electron transfer for the efficient conversion of light energy. Chemphyschem. 2005;6(5):871–80.
25. Hoff AJ, Deisenhofer J. Photophysics of photosynthesis. Structure and spectroscopy of reaction centers of purple bacteria. Phys Rep. 1997;287(1–2):1–247.
26. Deisenhofer J, Epp O, Miki K, Huber R, Michel H. X-ray structure analysis of a membrane protein complex: electron density map at 3 Å resolution and a model of the chromophores of the photosynthetic reaction center from *Rhodopseudomonas viridis*. J Mol Biol. 1984;180 (2):385–98.
27. Camara-Artigas A, Brune D, Allen JP. Interactions between lipids and bacterial reaction centers determined by protein crystallography. Proc Natl Acad Sci U S A. 2002;99:11055–60.
28. Renger T, Trostmann I, Theiss C, Madjet ME, Richter M, Paulsen H, et al. Refinement of a structural model of a pigment–protein complex by accurate optical line shape theory and experiments. J Phys Chem B. 2007;111(35):10487–501.
29. Zhang WM, Meier T, Chernyak V, Mukamel S. Exciton-migration and three-pulse femtosecond optical spectroscopies of photosynthetic antenna complexes. J Chem Phys. 1998;108 (18):7763–74.
30. Ishizaki A, Fleming GR. On the adequacy of the Redfield equation and related approaches to the study of quantum dynamics in electronic energy transfer. J Phys Chem. 2009;130 (23):234110–8.
31. Lin S, Jaschke PR, Wang H, Paddock M, Tufts A, Allen JP, et al. Electron transfer in the *Rhodobacter sphaeroides* reaction center assembled with zinc bacteriochlorophyll. Proc Natl Acad Sci U S A. 2009;106(21):8537–42.
32. Mikhailyuk IK, Knox PP, Paschenko VZ, Razjivin AP, Lokstein H. Analysis of absorption spectra of purple bacterial reaction centers in the near infrared region by higher order derivative spectroscopy. Biophys Chem. 2006;122(1):16–26.
33. Jankowiak R, Hayes JM, Small GJ. Spectral hole-burning spectroscopy in amorphous molecular solids and proteins. Chem Rev. 1993;93(4):1471–502.
34. Rebane KK. Impurity spectra of solids. New York: Plenum; 1970.
35. Völker S. Structured hole-burning in crystalline and amorphous organic solids. In: Fünfschilling J, editor. Molecular excited states, optical relaxation processes at low temperatures. Dordrecht: Kluwer; 1989. p. 113–242.
36. Moerner WE, editor. Topics in current physics, persistent spectral hole burning: science and application. New York: Springer; 1987.
37. Johnson SG, Tang D, Jankowiak R, Hayes JM, Small GJ, Tiede DM. Structure and marker mode of the primary electron donor state absorption of photosynthetic bacteria: hole-burned spectra. J Phys Chem. 1989;93(16):5953–7.
38. Guo Z, Woodbury Neal W, Pan J, Lin S. Protein dielectric environment modulates the electron-transfer pathway in photosynthetic reaction centers. Biophys J. 2012;103(9):1979–88.

39. Kirmaier C, Holten D. Subpicosecond characterization of the optical properties of the primary electron donor and the mechanism of the initial electron transfer in *Rhodobacter capsulatus* reaction centers. FEBS Lett. 1988;239(2):211–8.
40. Huppman P, Arlt T, Penzkofer H, Schmidt S, Bibikova M, Dohse B, et al. Kinetics, energetics, and electronic coupling of the primary electron transfer reactions in mutated reaction centers of *Blastochloris viridis*. Biophys J. 2002;82(6):3186–97.
41. Wasielewski MR, Tiede DM. Sub-picosecond measurements of primary electron transfer in *Rhodopseudomonas viridis* reaction centers using near-infrared excitation. FEBS Lett. 1986;204(2):368–72.
42. Arlt T, Schmidt S, Kaiser W, Lauterwasser C, Meyer M, Scheer H, et al. The accessory bacteriochlorophyll: a real electron carrier in primary photosynthesis. Proc Natl Acad Sci U S A. 1993;90(24):11757–61.
43. van Stokkum IHM, Beekman LMP, Jones MR, van Brederode ME, van Grondelle R. Primary electron transfer kinetics in membrane-bound Rhodobacter sphaeroides reaction centers: a global and target analysis. Biochemistry. 1997;36(38):11360–8.
44. Holzwarth AR, Müller MG. Energetics and kinetics of radical pairs in reaction centers from *Rhodobacter sphaeroides*. A femtosecond transient absorption study. Biochemistry. 1996;35(36):11820–31.
45. Shkuropatov AY, Shuvalov VA. Electron transfer in pheophytin a-modified reaction centers from *Rhodobacter sphaeroides* (R-26). FEBS Lett. 1993;322(2):168–72.
46. Kennis JTM, Shkuropatov AY, van Stokkum IHM, Gast P, Hoff AJ, Shuvalov VA, et al. Formation of a long-lived $P^{+}BA^{-}$ state in plant pheophytin-exchanged reaction centers of *Rhodobacter sphaeroides* R26 at low temperature. Biochemistry. 1997;36(51):16231–8.
47. Kirmaier C, Laporte L, Schenck CC, Holten D. The nature and dynamics of the charge-separated intermediate in reaction centers in which bacteriochlorophyll replaces the photoactive bacteriopheophytin. 1. Spectral characterization of the transient state. J Phys Chem. 1995;99(21):8903–9.
48. Kirmaier C, Laporte L, Schenck CC, Holten D. The nature and dynamics of the charge-separated intermediate in reaction centers in which bacteriochlorophyll replaces the photoactive bacteriopheophytin. 2. The rates and yields of charge separation and recombination. J Phys Chem. 1995;99(21):8910–7.
49. Roberts JA, Holten D, Kirmaier C. Primary events in photosynthetic reaction centers with multiple mutations near the photoactive electron carriers. J Phys Chem B. 2001;105(23):5575–84.
50. Heller BA, Holten D, Kirmaier C. Effects of Asp residues near the L-side pigments in bacterial reaction centers. Biochemistry. 1996;35(48):15418–27.
51. Pawlowicz NP, van Grondelle R, van Stokkum IHM, Breton J, Jones MR, Groot ML. Identification of the first steps in charge separation in bacterial photosynthetic reaction centers of *Rhodobacter sphaeroides* by ultrafast mid-infrared spectroscopy: electron transfer and protein dynamics. Biophys J. 2008;95(3):1268–84.
52. Khatypov RA, Khmelnitskiy AY, Khristin AM, Fufina TY, Vasilieva LG, Shuvalov VA. Primary charge separation within P_{870}^{*} in wild type and heterodimer mutants in femtosecond time domain. Biochim Biophys Acta. 2012;1817(8):1392–8.
53. Hamm P, Zinth W. Ultrafast initial reaction in bacterial photosynthesis revealed by femtosecond infrared spectroscopy. J Phys Chem. 1995;99(36):13537–44.
54. Eisenmayer TJ, de Groot HJM, van de Wetering E, Neugebauer J, Buda F. Mechanism and reaction coordinate of directional charge separation in bacterial reaction centers. J Phys Chem Lett. 2012;3(6):694–7.
55. Eisenmayer TJ, Lasave JA, Monti A, de Groot HJM, Buda F. Proton displacements coupled to primary electron transfer in the *Rhodobacter sphaeroides* reaction center. J Phys Chem B. 2013;117(38):11162–8.
56. Shuvalov VA, Yakovlev AG. Coupling of nuclear wavepacket motion and charge separation in bacterial reaction centers. FEBS Lett. 2003;540(1–3):26–34.

57. Yakovlev AG, Shkuropatov AY, Shuvalov VA. Nuclear wave packet motion between P* and $P^+B_A^-$ potential surfaces with a subsequent electron transfer to H_A in bacterial reaction centers at 90 K. Electron transfer pathway. Biochemistry. 2002;41(47):14019–27.
58. Vos MH, Rappaport F, Lambry J-C, Breton J, Martin J-L. Visualization of coherent nuclear motion in a membrane protein by femtosecond spectroscopy. Nature. 1993;363(6427):320–5.
59. Vos MH, Rischel C, Jones MR, Martin J-L. Electrochromic detection of a coherent component in the formation of the charge pair $P^+H_L^-$ in bacterial reaction centers. Biochemistry. 2000;39(29):8353–61.
60. Stanley RJ, Boxer SG. Oscillations in the spontaneous fluorescence from photosynthetic reaction centers. J Phys Chem. 1995;99(3):859–63.
61. Rischel C, Spiedel D, Ridge JP, Jones MR, Breton J, Lambry J-C, et al. Low frequency vibrational modes in proteins: changes induced by point-mutations in the protein-cofactor matrix of bacterial reaction centers. Proc Natl Acad Sci U S A. 1998;95(21):12306–11.
62. Spörlein S, Zinth W, Wachtveitl J. Vibrational coherence in photosynthetic reaction centers observed in the bacteriochlorophyll anion band. J Phys Chem B. 1998;102(38):7492–6.
63. Parson WW, Warshel A. A density-matrix model of photosynthetic electron transfer with microscopically estimated vibrational relaxation times. Chem Phys. 2004;296(2–3):201–16.
64. Parson WW, Warshel A. Dependence of photosynthetic electron-transfer kinetics on temperature and energy in a density-matrix model. J Phys Chem B. 2004;108(29):10474–83.
65. Wang H, Lin S, Allen JP, Williams JC, Blankert S, Laser C, et al. Protein dynamics control the kinetics of initial electron transfer in photosynthesis. Science. 2007;316(5825):747–50.
66. Ogrodnik A, Hartwich G, Lossau H, Michel-Beyerle ME. Dispersive charge separation and conformational cooling of $P^+H_A^-$ in reaction centers of *Rb. sphaeroides* R26: a spontaneous emission study. Chem Phys. 1999;244(2–3):461–78.
67. Hamm P, Gray KA, Oesterhelt D, Feick R, Scheer H, Zinth W. Subpicosecond emission studies of bacterial reaction centers. Biochim Biophys Acta. 1993;1142(1–2):99–105.
68. Kirmaier C, Holten D. Evidence that a distribution of bacterial reaction centers underlies the temperature and detection-wavelength dependence of the rates of the primary electron-transfer reactions. Proc Natl Acad Sci U S A. 1990;87(9):3552–6.
69. Hartwich G, Lossau H, Michel-Beyerle ME, Ogrodnik A. Nonexponential fluorescence decay in reaction centers of *Rhodobacter sphaeroides* reflecting dispersive charge separation up to 1 ns. J Phys Chem B. 1998;102(19):3815–20.
70. Wang Z, Pearlstein RM, Jia Y, Fleming GR, Norris JR. Inhomogeneous electron transfer kinetics in reaction centers of bacterial photosynthesis. Chem Phys. 1993;176(2–3):421–5.
71. Small GJ. On the validity of the standard model for primary charge separation in the bacterial reaction center. Chem Phys. 1995;197(3):239–57.
72. Woodbury NW, Peloquin JM, Alden RG, Lin X, Lin S, Taguchi AKW, et al. Relationship between thermodynamics and mechanism during photoinduced charge separation in reaction centers from *Rhodobacter sphaeroides*. Biochemistry. 1994;33(26):8101–12.
73. Huppmann P, Spörlein S, Bibikova M, Oesterhelt D, Wachtveitl J, Zinth W. Electron transfer in reaction centers of Blastochloris viridis: photosynthetic reactions approximating the adiabatic regime. J Phys Chem A. 2003;107(40):8302–9.
74. Haffa ALM, Lin S, Katilius E, Williams JC, Taguchi AKW, Allen JP, et al. The dependence of the initial electron-transfer rate on driving force in *Rhodobacter sphaeroides* reaction centers. J Phys Chem B. 2002;106(29):7376–84.
75. Kirmaier C, Holten D, Parson WW. Temperature and detection-wavelength dependence of the picosecond electron-transfer kinetics measured in *Rhodopseudomonas sphaeroides* reaction centers. Resolution of new spectral and kinetic components in the primary charge-separation process. Biochim Biophys Acta. 1985;810(1):33–48.
76. Dashdorj N, Yamashita E, Schaibley J, Cramer WA, Savikhin S. Ultrafast optical studies of the cytochrome b_6f complex in solution and in crystalline states. J Phys Chem B. 2007;111:14405–10.

77. Huang L, Ponomarenko N, Wiederrecht GP, Tiede DM. Cofactor-specific photochemical function resolved by ultrafast spectroscopy in photosynthetic reaction center crystals. Proc Natl Acad Sci U S A. 2012;109(13):4851–6.
78. Blankenship R. Origin and early evolution of photosynthesis. Photosynth Res. 1992;33 (2):91–111.
79. Ogrodnik A, Keupp W, Volk M, Aumeier G, Michel-Beyerle ME. Inhomogeneity of radical pair energies in photosynthetic reaction centers revealed by differences in recombination dynamics of P^+HA^- when detected in delayed emission and in absorption. J Phys Chem. 1994;98(13):3432–9.
80. Goldstein RA, Takiff L, Steven GB. Energetics of initial charge separation in bacterial photosynthesis: the triplet decay rate in very high magnetic fields. Biochim Biophys Acta. 1988;934(2):253–63.
81. Woodbury NW, Parson WW, Gunner MR, Prince RC, Dutton PL. Radical-pair energetics and decay mechanisms in reaction centers containing anthraquinones, naphthoquinones or benzoquinones in place of ubiquinone. Biochim Biophys Acta. 1986;851(1):6–22.
82. Hörber JKH, Göbel W, Ogrodnik A, Michel-Beyerle ME, Cogdell RJ. Time-resolved measurements of fluorescence from reaction centres of *Rhodopseudomonas sphaeroides* R26.1. FEBS Lett. 1986;198(2):273–8.
83. Woodbury NWT, Parson WW. Nanosecond fluorescence from isolated photosynthetic reaction centers of *Rhodopseudomonas sphaeroides*. Biochim Biophys Acta. 1984;767 (2):345–61.
84. Godik VI, Kotova EA, Borisov A. Nanosecond recombination luminescence of purple bacteria. The lifetime temperature dependence in Rhodospirillum rubrum chromatophores. Photobiochem Photobiophys. 1982;4(4):219–26.
85. Boxer SG, Goldstein RA, Lockhart DJ, Middendorf TR, Takiff L. Excited states, electron-transfer reactions, and intermediates in bacterial photosynthetic reaction centers. J Phys Chem. 1989;93(26):8280–94.
86. Volk M, Aumeier G, Langenbacher T, Feick R, Ogrodnik A, Michel-Beyerle M-E. Energetics and mechanism of primary charge separation in bacterial photosynthesis. A comparative study on reaction centers of Rhodobacter sphaeroides and Chloroflexus aurantiacus. J Phys Chem B. 1998;102(4):735–51.
87. LeBard DN, Matyushov DV. Energetics of bacterial photosynthesis. J Phys Chem B. 2009;113(36):12424–37.
88. Warshel A, Parson WW. Dynamics of biochemical and biophysical reactions: insight from computer simulations. Q Rev Biophys. 2001;34(04):563–679.
89. LeBard DN, Kapko V, Matyushov DV. Energetics and kinetics of primary charge separation in bacterial photosynthesis. J Phys Chem B. 2008;112(33):10322–42.
90. Steffen MA, Lao K, Boxer SG. Dielectric asymmetry in the photosynthetic reaction center. Science. 1994;264:810–6.
91. Dashdorj N, Xu W, Martinsson P, Chitnis PR, Savikhin S. Electrochromic shift of chlorophyll absorption in photosystem I from *Synechocystis sp*. PCC 6803: a probe of optical and dielectric properties around the secondary electron acceptor. Biophys J. 2004;86:3121–30.
92. Lin S, Katilius E, Haffa ALM, Taguchi AKW, Woodbury NW. Blue light drives B-side electron transfer in bacterial photosynthetic reaction centers. Biochemistry. 2001;40 (46):13767–73.
93. Haffa ALM, Lin S, Williams JC, Taguchi AKW, Allen JP, Woodbury NW. High yield of long-lived B-side charge separation at room temperature in mutant bacterial reaction centers. J Phys Chem B. 2003;107(45):12503–10.
94. Lin S, Jackson JA, Taguchi AKW, Woodbury NW. B-side electron transfer promoted by absorbance of multiple photons in *Rhodobacter sphaeroides* R-26 reaction centers. J Phys Chem B. 1999;103(22):4757–63.
95. Kirmaier C, Laible PD, Hanson DK, Holten D. B-side electron transfer to form $P^+H_B^-$ in reaction centers from the F(L181)Y/Y(M208)F mutant of *Rhodobacter capsulatus*. J Phys Chem B. 2004;108(31):11827–32.

96. Chuang JI, Boxer SG, Holten D, Kirmaier C. High yield of M-side electron transfer in mutants of *Rhodobacter capsulatus* reaction centers lacking the L-side bacteriopheophytin. Biochemistry. 2006;45(12):3845–51.
97. Katilius E, Babendure J, Lin S, Woodbury N. Electron transfer dynamics in *Rhodobacter sphaeroides* reaction center mutants with a modified ligand for the monomer bacteriochlorophyll on the active side. Photosynth Res. 2004;81(2):165–80.
98. Lin S, Xiao W, Eastman JE, Taguchi AKW, Woodbury NW. Low-temperature femtosecond-resolution transient absorption spectroscopy of large-scale symmetry mutants of bacterial reaction centers. Biochemistry. 1996;35(10):3187–96.
99. Kirmaier C, Laible PD, Czarnecki K, Hata AN, Hanson DK, Bocian DF, et al. Comparison of M-side electron transfer in Rb. sphaeroides and Rb. capsulatus reaction centers. J Phys Chem B. 2002;106(7):1799–808.
100. Alden RG, Parson WW, Chu ZT, Warshel A. Orientation of the OH dipole of tyrosine (M)210 and its effect on electrostatic energies in photosynthetic bacterial reaction centers. J Phys Chem. 1996;100(41):16761–70.
101. Pawlowicz NP, van Stokkum IHM, Breton J, van Grondelle R, Jones MR. An investigation of slow charge separation in a tyrosine M210 to tryptophan mutant of the *Rhodobacter sphaeroides* reaction center by femtosecond mid-infrared spectroscopy. Phys Chem Chem Phys. 2010;12(11):2693–705.
102. van Brederode ME, van Mourik F, van Stokkum IHM, Jones MR, van Grondelle R. Multiple pathways for ultrafast transduction of light energy in the photosynthetic reaction center of *Rhodobacter sphaeroides*. Proc Natl Acad Sci U S A. 1999;96(5):2054–9.
103. van der Vos R, Franken EM, Sexton SJ, Shochat S, Gast P, Hore PJ, et al. Optically detected magnetic field effects on reaction centers of *Rhodobacter sphaeroides* 2.4.1 and its Tyr M210 Trp mutant. Biochim Biophys Acta. 1995;1230(1–2):51–61.
104. Shochat S, Arlt T, Francke C, Gast P, Noort P, Otte SM, et al. Spectroscopic characterization of reaction centers of the (M)Y210W mutant of the photosynthetic bacterium *Rhodobacter sphaeroides*. Photosynth Res. 1994;40(1):55–66.
105. Nagarajan V, Parson WW, Davis D, Schenck CC. Kinetics and free energy gaps of electron-transfer reactions in *Rhodobacter sphaeroides* reaction centers. Biochemistry. 1993;32 (46):12324–36.
106. Jia Y, DiMagno TJ, Chan CK, Wang Z, Popov MS, Du M, et al. Primary charge separation in mutant reaction centers of *Rhodobacter capsulatus*. J Phys Chem. 1993;97(50):13180–91.
107. Finkele U, Lauterwasser C, Zinth W, Gray KA, Oesterhelt D. Role of tyrosine M210 in the initial charge separation of reaction centers of *Rhodobacter sphaeroides*. Biochemistry. 1990;29(37):8517–21.
108. Nagarajan V, Parson WW, Gaul D, Schenck C. Effect of specific mutations of tyrosine-(M) 210 on the primary photosynthetic electron-transfer process in *Rhodobacter sphaeroides*. Proc Natl Acad Sci U S A. 1990;87(20):7888–92.
109. McAuley KE, Fyfe PK, Cogdell RJ, Isaacs NW, Jones MR. X-ray crystal structure of the YM210W mutant reaction centre from *Rhodobacter sphaeroides*. FEBS Lett. 2000;467 (2–3):285–90.
110. Wakeham MC, Jones MR. Rewiring photosynthesis: engineering wrong-way electron transfer in the purple bacterial reaction centre. Biochem Soc Trans. 2005;33(Pt 4):851–7.
111. Carter B, Boxer SG, Holten D, Kirmaier C. Photochemistry of a bacterial photosynthetic reaction center missing the initial bacteriochlorophyll electron acceptor. J Phys Chem B. 2012;116(33):9971–82.
112. de Boer AL, Neerken S, de Wijn R, Permentier HP, Gast P, Vijgenboom E, et al. High yield of B-branch electron transfer in a quadruple reaction center mutant of the photosynthetic bacterium *Rhodobacter sphaeroides*. Biochemistry. 2002;41(9):3081–8.
113. de Boer A, Neerken S, de Wijn R, Permentier H, Gast P, Vijgenboom E, et al. B-branch electron transfer in reaction centers of *Rhodobacter sphaeroides* assessed with site-directed mutagenesis. Photosynth Res. 2002;71(3):221–39.

114. Czarnecki K, Kirmaier C, Holten D, Bocian DF. Vibrational and photochemical consequences of an Asp residue near the photoactive accessory bacteriochlorophyll in the photosynthetic reaction center. J Phys Chem A. 1999;103(14):2235–46.
115. Marcus RA. On the energy of oxidation-reduction reactions involving electron transfer. I. J Chem Phys. 1956;24:966–78.
116. Marcus RA, Sutin N. Electron transfers in chemistry and biology. Biochim Biophys Acta. 1985;811:265–322.
117. May V, Kühn O. Charge and energy transfer dynamics in molecular systems. Berlin: Wiley-VCH; 2000.
118. Marcus RA. Chemical and electrochemical electron-transfer theory. Annu Rev Phys Chem. 1964;15:155–96.
119. McMahon BH, Müller JD, Wraight CA, Nienhaus GU. Electron transfer and protein dynamics in the photosynthetic reaction center. Biophys J. 1998;74(5):2567–87.
120. Schulten K, Tesch M. Coupling of protein motion to electron transfer: molecular dynamics and stochastic quantum mechanics study of photosynthetic reaction centers. Chem Phys. 1991;158(2–3):421–46.
121. Ando K, Sumi H. Nonequilibrium oscillatory electron transfer in bacterial photosynthesis. J Phys Chem B. 1998;102(52):10991–1000.
122. Acharya K, Zazubovich V, Reppert M, Jankowiak R. Primary electron donor(s) in isolated reaction center of photosystem II from *Chlamydomonas reinhardtii*. J Phys Chem B. 2012;116(16):4860–70.
123. Riley K, Jankowiak R, Rätsep M, Small GJ, Zazubovich V. Evidence for highly dispersive primary charge separation kinetics and gross heterogeneity in the isolated PS II reaction center of green plants. J Phys Chem B. 2004;108(29):10346–56.
124. Renger T, Schlodder E. Primary photophysical processes in photosystem II: bridging the gap between crystal structure and optical spectra. Chemphyschem. 2010;11(6):1141–53.
125. Novoderezhkin VI, Romero E, Dekker JP, van Grondelle R. Multiple charge-separation pathways in photosystem II: modeling of transient absorption kinetics. Chemphyschem. 2011;12(3):681–8.
126. Caffarri S, Kouril R, Kereiche S, Boekema EJ, Croce R. Functional architecture of higher plant photosystem II supercomplexes. EMBO J. 2009;28(19):3052–63.
127. Durrant JR, Klug DR, Kwa SL, van Grondelle R, Porter G, Dekker JP. A multimer model for P_{680}, the primary electron donor of photosystem II. Proc Natl Acad Sci U S A. 1995;92(11):4798–802.
128. Jankowiak R, Hayes JM, Small GJ. An excitonic pentamer model for the core Q_y states of the isolated photosystem II reaction center. J Phys Chem B. 2002;106(34):8803–14.
129. Novoderezhkin VI, Dekker JP, van Grondelle R. Mixing of exciton and charge-transfer states in photosystem II reaction centers: modeling of Stark spectra with modified Redfield theory. Biophys J. 2007;93(4):1293–311.
130. Umena Y, Kawakami K, Shen J-R, Kamiya N. Crystal structure of oxygen-evolving photosystem II at a resolution of 1.9 Å. Nature. 2011;473(7345):55–60.
131. Acharya K, Neupane B, Zazubovich V, Sayre RT, Picorel R, Seibert M, et al. Site energies of active and inactive pheophytins in the reaction center of photosystem II from *Chlamydomonas reinhardtii*. J Phys Chem B. 2012;116(12):3890–9.
132. Jankowiak R, Rätsep M, Hayes J, Zazubovich V, Picorel R, Seibert M, et al. Primary charge-separation rate at 5 K in isolated photosystem II reaction centers containing five and six chlorophyll *a* molecules. J Phys Chem B. 2003;107(9):2068–74.
133. Prokhorenko VI, Holzwarth AR. Primary processes and structure of the photosystem II reaction center: a photon echo study. J Phys Chem B. 2000;104(48):11563–78.
134. Romero E, Diner Bruce A, Nixon Peter J, Coleman Wiliam J, Dekker Jan P, van Grondelle R. Mixed exciton–charge-transfer states in photosystem II: Stark spectroscopy on site-directed mutants. Biophys J. 2012;103(2):185–94.

135. van Stokkum IHM, Larsen DS, van Grondelle R. Global and target analysis of time-resolved spectra. Biochim Biophys Acta. 2004;1657(2–3):82–104.
136. Mukamel S. Principles of nonlinear optical spectroscopy. New York: Oxford University Press; 1995.
137. Savikhin S, Buck DR, Struve WS. Oscillating anisotropies in a bacteriochlorophyll protein: evidence for quantum beating between exciton levels. Chem Phys. 1997;223:303–12.
138. Brixner T, Stenger J, Vaswani HM, Cho M, Blankenship RE, Fleming GR. Two-dimensional spectroscopy of electronic couplings in photosynthesis. Nature. 2005;434(7033):625–8.
139. Wasielewski MR, Johnson DG, Seibert M, Govindjee. Determination of the primary charge separation rate in isolated photosystem II reaction centers with 500-fs time resolution. Proc Natl Acad Sci U S A. 1989;86(2):524–8.
140. Jankowiak R, Tang D, Small GJ, Seibert M. Transient and persistent hole burning of the reaction center of photosystem II. J Phys Chem. 1989;93(4):1649–54.
141. Tang D, Jankowiak R, Seibert M, Small G. Effects of detergent on the excited state structure and relaxation dynamics of the photosystem II reaction center: a high resolution hole burning study. Photosynth Res. 1991;27(1):19–29.
142. Krausz E, Hughes JL, Smith P, Pace R, Peterson Arsköld S. Oxygen-evolving photosystem II core complexes: a new paradigm based on the spectral identification of the charge-separating state, the primary acceptor and assignment of low-temperature fluorescence. Photochem Photobiol Sci. 2005;4(9):744–53.
143. Herascu N, Ahmouda S, Picorel R, Seibert M, Jankowiak R, Zazubovich V. Effects of the distributions of energy or charge transfer rates on spectral hole burning in pigment–protein complexes at low temperatures. J Phys Chem B. 2011;115(50):15098–109.
144. Romero E, van Stokkum IHM, Novoderezhkin VI, Dekker JP, van Grondelle R. Two different charge separation pathways in photosystem II. Biochemistry. 2010;49(20):4300–7.
145. Schlodder E, Coleman WJ, Nixon PJ, Cohen RO, Renger T, Diner BA. Site-directed mutations at D1-His198 and D1-Thr179 of photosystem II in *Synechocystis* sp. PCC 6803: deciphering the spectral properties of the PSII reaction centre. Philos Trans R Soc Lond B Biol Sci. 2008;363(1494):1197–202.
146. Hillmann B, Brettel K, van Mieghem F, Kamlowski A, Rutherford AW, Schlodder E. Charge recombination reactions in photosystem II. 2. Transient absorbance difference spectra and their temperature dependence. Biochemistry. 1995;34(14):4814–27.
147. Raszewski G, Saenger W, Renger T. Theory of optical spectra of photosystem II reaction centers: location of the triplet state and the identity of the primary electron donor. Biophys J. 2005;88(2):986–98.
148. Jordan P, Fromme P, Witt HT, Klukas O, Saenger W, Krauss N. Three-dimensional structure of cyanobacterial photosystem I at 2.5 Å resolution. Nature. 2001;411:909–17.
149. Amunts A, Toporik H, Borovikova A, Nelson N. Structure determination and improved model of plant photosystem I. J Biol Chem. 2010;285(5):3478–86.
150. Amunts A, Drory O, Nelson N. The structure of a plant photosystem I supercomplex at 3.4 Å resolution. Nature. 2007;447(7140):58–63.
151. Brettel K. Electron transfer and arrangement of the redox cofactors in photosystem I. Biochim Biophys Acta. 1997;1318:322–73.
152. Brettel K, Leibl W. Electron transfer in photosystem I. Biochim Biophys Acta. 2001;1507:100–14.
153. Hastings G, Kleinherenbrink FAM, Lin S, McHugh TJ, Blankenship RE. Observation of the reduction and reoxidation of the primary electron acceptor in photosystem I. Biochemistry. 1994;33(11):3193–200.
154. Savikhin S, Xu W, Martinsson P, Chitnis PR, Struve WS. Kinetics of charge separation and A0–A1 electron transfer in photosystem I reaction centers. Biochemistry. 2001;40:9282–90.
155. Chauvet A, Dashdorj N, Golbeck JH, Johnson WT, Savikhin S. Spectral resolution of the primary electron acceptor A_0 in photosystem I. J Phys Chem B. 2012;116:3380–6.

156. Byrdin M, Jordan P, Krauss N, Fromme P, Stehlik D, Schlodder E. Light harvesting in photosystem I: modeling based on the 2.5-Å structure of photosystem I from *Synechococcus elongatus*. Biophys J. 2002;83:433–57.
157. Damjanovic A, Vaswani HM, Fromme P, Fleming GR. Chlorophyll excitations in photosystem I of *Synechococcus elongatus*. J Phys Chem B. 2002;106:10251–62.
158. Dorra D, Fromme P, Karapetyan NV, Holzwarth AR. Fluorescence kinetics of photosystem I: multiple fluorescence components. In: Garab G, editor. Photosynthesis: mechanisms and effects. Dordrecht: Kluwer; 1998. p. 587–90.
159. Karapetyan NV, Holzwarth AR, Rögner M. The photosystem I trimer of cyanobacteria: molecular organization, excitation dynamics and physiological significance. FEBS Lett. 1999;460:395–400.
160. Gobets B, van Grondelle R. Energy transfer and trapping in photosystem I. Biochim Biophys Acta. 2001;1507:80–99.
161. Melkozernov AN. Excitation energy transfer in photosystem I from oxygenic organisms. Photosynth Res. 2001;70:129–53.
162. Savikhin S, Xu W, Soukoulis V, Chitnis PR, Struve WS. Ultrafast primary processes in photosystem I of the cyanobacterium *Synechocystis* sp. PCC 6803. Biophys J. 1999;76:3278–88.
163. Hayes JM, Matsuzaki S, Rätsep M, Small GJ. Red chlorophyll a antenna states of photosystem I of the cyanobacterium *Synechocystis* sp. PCC 6803. J Phys Chem B. 2000;104:5625–33.
164. Zazubovich V, Matsuzaki S, Johnson TW, Hayes JM, Chitnis PR, Small GJ. Red antenna states of photosystem I from cyanobacterium *Synechococcus elongatus*: a spectral hole burning study. Chem Phys. 2002;275:47–59.
165. Rätsep M, Johnson TW, Chitnis PR, Small GJ. The red-absorbing chlorophyll a antenna states of photosystem I: a hole-burning study of *Synechocystis* sp. PCC 6803 and its mutants. J Phys Chem B. 2000;104:836–47.
166. Jelezko F, Tietz C, Gerken U, Wrachtrup J, Bittl R. Single-molecule spectroscopy on photosystem I pigment–protein complexes. J Phys Chem B. 2000;104(34):8093–6.
167. Şener MK, Jolley C, Ben-Shem A, Fromme P, Nelson N, Croce R, et al. Comparison of the light-harvesting networks of plant and cyanobacterial photosystem I. Biophys J. 2005;89 (3):1630–42.
168. Gatzen G, Müller MG, Griebenow K, Holzwarth AR. Primary processes and structure of the photosystem II reaction center. 3. Kinetic analysis of picosecond energy transfer and charge separation processes in the D1-D2-cyt-b559 complex measured by time resolved fluorescence. J Phys Chem. 1996;100:7269–78.
169. Müller MG, Niklas J, Lubitz W, Holzwarth AR. Ultrafast transient absorption studies on photosystem I reaction centers from *Chlamydomonas reinhardtii*. 1. A new interpretation of the energy trapping and early electron transfer steps in photosystem I. Biophys J. 2003;85:3899–922.
170. Savikhin S, Xu W, Chitnis PR, Struve WS. Ultrafast primary processes in PS I from *Synechocystis* sp. PCC 6803: roles of P_{700} and A_0. Biophys J. 2000;79:1573–86.
171. Kumazaki S, Iwaki M, Ikegami I, Kandori H, Yoshihara K, Itoh S. Rates of primary electron transfer reactions in the photosystem I reaction center reconstituted with different quinones as the secondary acceptor. J Phys Chem. 1994;98:11220–5.
172. Kumazaki S, Kandori H, Petek H, Yoshihara I, Ikegami I. Primary photochemical processes in P700-enriched photosystem I particles—trap-limited excitation decay and primary charge separation. J Phys Chem. 1994;98:10335–42.
173. Kumazaki S, Ikegami I, Furusawa H, Yasuda S, Yoshihara K. Observation of the excited state of the primary electron donor chlorophyll (P700) and the ultrafast charge separation in the spinach photosystem I reaction center. J Phys Chem B. 2001;105:1093–9.

174. Nuijs AM, Shuvalov VA, van Gorkom HJ, Plijter JJ, Duysens LNM. Picosecond absorbance difference spectroscopy on the primary reactions and the antenna-excited states in photosystem I particles. Biochim Biophys Acta. 1986;850:310–8.
175. Shuvalov VA, Nuijs AM, van Gorkom HJ, Smit HWJ, Duysens LNM. Picosecond absorbance changes upon selective excitation of the primary electron donor P_{700} in photosystem I. Biochim Biophys Acta. 1986;850:319–23.
176. Wasielewski MR, Fenton JM, Govindjee. The rate of formation of P_{700}^{+}-A_0^{-} in photosystem I particles from spinach as measured by picosecond transient absorption spectroscopy. Photosynth Res. 1987;12:181–90.
177. White NTH, Beddard GS, Thorne JRG, Feehan TM, Keyes TE, Heathcote P. Primary charge separation and energy transfer in the photosystem I reaction center of higher plants. J Phys Chem. 1996;100:12086–99.
178. Brettel K, Setif P, Mathis P. Flash-induced absorption changes in photosystem I at low temperature: evidence that the electron acceptor A1 is vitamin K1. FEBS Lett. 1986;203:220–4.
179. Brettel K. Electron transfer from A_1- to an iron-sulfur center with $t_{1/2} = 200$ ns at room temperature in photosystem I. Characterization by absorption spectroscopy. FEBS Lett. 1988;239:93–8.
180. Brettel K, Vos MH. Spectroscopic resolution of the picosecond reduction kinetics of the secondary electron acceptor A_1 in photosystem I. FEBS Lett. 1999;447:315–7.
181. Lüneberg J, Fromme P, Jekow P, Schlodder E. Spectroscopic characterization of PS I core complexes from thermophilic *Synechococcus* sp.: identical reoxidation kinetics of A_1^{-} before and after removal of the iron-sulfur-clusters F_A and F_B. FEBS Lett. 1994;338:197–202.
182. Holzwarth AR, Müller MG, Niklas J, Lubitz W. Ultrafast transient absorption studies on photosystem I reaction centers from *Chlamydomonas reinhardtii*. 2: mutations near the P_{700} reaction center chlorophylls provide new insight into the nature of the primary electron donor. Biophys J. 2006;90(2):552–65.
183. Müller MG, Slavov C, Luthra R, Redding KE, Holzwarth AR. Independent initiation of primary electron transfer in the two branches of the photosystem I reaction center. Proc Natl Acad Sci U S A. 2010;107(9):4123–8.
184. Guergova-Kuras M, Boudreaux B, Joliot A, Joliot P, Redding K. Evidence for two active branches for electron transfer in photosystem I. Proc Natl Acad Sci U S A. 2001;98:4437–42.
185. Santabarbara S, Reifschneider K, Jasaitis A, Gu F, Agostini G, Carbonera D, et al. Interquinone electron transfer in photosystem I as evidenced by altering the hydrogen bond strength to the phylloquinone(s). J Phys Chem B. 2010;114(28):9300–12.
186. Giera W, Ramesh VM, Webber AN, van Stokkum I, van Grondelle R, Gibasiewicz K. Effect of the P_{700} pre-oxidation and point mutations near A_0 on the reversibility of the primary charge separation in photosystem I from *Chlamydomonas reinhardtii*. Biochim Biophys Acta. 2010;1797(1):106–12.
187. Di Donato M, Stahl AD, van Stokkum IHM, van Grondelle R, Groot M-L. Cofactors involved in light-driven charge separation in photosystem I identified by subpicosecond infrared spectroscopy. Biochemistry. 2010;50(4):480–90.
188. Shelaev IV, Gostev FE, Mamedov MD, Sarkisov OM, Nadtochenko VA, Shuvalov VA, et al. Femtosecond primary charge separation in *Synechocystis* sp. PCC 6803 photosystem I. Biochim Biophys Acta. 2010;1797(8):1410–20.
189. Joliot P, Joliot A. In vivo analysis of the electron transfer within photosystem I: are the two phylloquinones involved? Biochemistry. 1999;38(34):11130–6.
190. Santabarbara S, Kuprov I, Fairclough WV, Purton S, Hore PJ, Heathcote P, et al. Bidirectional electron transfer in photosystem I: determination of two distances between P700+ and A1- in spin-correlated radical pairs. Biochemistry. 2005;44(6):2119–28.
191. Santabarbara S, Kuprov I, Hore PJ, Casal A, Heathcote P, Evans MCW. Analysis of the spin-polarized electron spin echo of the $[P_{700}^{+}A_1^{-}]$ radical pair of photosystem I indicates

that both reaction center subunits are competent in electron transfer in cyanobacteria, green algae, and higher plants. Biochemistry. 2006;45(23):7389–403.
192. Santabarbara S, Jasaitis A, Byrdin M, Gu F, Rappaport F, Redding K. Additive effect of mutations affecting the rate of phylloquinone reoxidation and directionality of electron transfer within photosystem I. Photochem Photobiol. 2008;84(6):1381–7.
193. Poluektov OG, Paschenko SV, Utschig LM, Lakshmi KV, Thurnauer MC. Bidirectional electron transfer in photosystem I: direct evidence from high-frequency time-resolved EPR spectroscopy. J Am Chem Soc. 2005;127(34):11910–1.
194. Cohen RO, Shen G, Golbeck JH, Xu W, Chitnis PR, Valieva A, et al. Evidence for asymmetric electron transfer in cyanobacterial photosystem I: analysis of a methionine to leucine mutation of the ligand to the primary electron acceptor A_0. Biochemistry. 2004;43:4741–54.
195. Dashdorj N, Xu W, Cohen RO, Golbeck JH, Savikhin S. Asymmetric electron transfer in cyanobacterial photosystem I: charge separation and secondary electron transfer dynamics of mutations near the primary electron acceptor A_0. Biophys J. 2005;88:1238–49.
196. Bautista JA, Rappaport F, Guergova-Kuras M, Cohen RO, Golbeck JH, Wang JY, et al. Biochemical and biophysical characterization of photosystem I from phytoene desaturase and ζ-carotene desaturase deletion mutants of *Synechocystis* Sp. PCC 6803: evidence for PsaA- and PsaB-side electron transport in cyanobacteria. J Biol Chem. 2005;280(20):20030–41.
197. Srinivasan N, Karyagina I, Bittl R, van der Est A, Golbeck JH. Role of the hydrogen bond from Leu722 to the A_{1A} phylloquinone in photosystem I. Biochemistry. 2009;48 (15):3315–24.
198. Santabarbara S, Kuprov I, Poluektov O, Casal A, Russell CA, Purton S, et al. Directionality of electron-transfer reactions in photosystem I of prokaryotes: universality of the bidirectional electron-transfer model. J Phys Chem B. 2010;114(46):15158–71.
199. Agalarov R, Brettel K. Temperature dependence of biphasic forward electron transfer from the phylloquinone(s) A_1 in photosystem I: only the slower phase is activated. Biochim Biophys Acta. 2003;1604(1):7–12.
200. Mula S, Savitsky A, Mobius K, Lubitz W, Golbeck JH, Mamedov MD, et al. Incorporation of a high potential quinone reveals that electron transfer in photosystem I becomes highly asymmetric at low temperature. Photochem Photobiol Sci. 2012;11(6):946–56.
201. Fairclough WV, Forsyth A, Evans MCW, Rigby SEJ, Purton S, Heathcote P. Bidirectional electron transfer in photosystem I: electron transfer on the PsaA side is not essential for phototrophic growth in Chlamydomonas. Biochim Biophys Acta. 2003;1606:43–55.
202. Moser C, Dutton PL. Application of Marcus theory to photosystem I electron transfer. In: Golbeck J, editor. Photosystem I. Advances in photosynthesis and respiration, vol. 24. Dordrecht: Springer; 2006. p. 583–94.
203. Nakamura A, Suzawa T, Kato Y, Watanabe T. Species dependence of the redox potential of the primary electron donor P700 in photosystem I of oxygenic photosynthetic organisms revealed by spectroelectrochemistry. Plant Cell Physiol. 2011;52(5):815–23.
204. Mamedov MD, Gadzhieva RM, Gourovskaya KN, Drachev LA, Semenov AY. Electrogenicity at the donor/acceptor sides of cyanobacterial photosystem I. J Bioenerg Biomembr. 1996;28(6):517–22.
205. Nakamura A, Suzawa T, Kato Y, Watanabe T. Significant species-dependence of P_{700} redox potential as verified by spectroelectrochemistry: comparison of spinach and *Theromosynechococcus elongatus*. FEBS Lett. 2005;579(11):2273–6.
206. Krabben L, Schlodder E, Jordan R, Carbonera D, Giacometti G, Lee H, et al. Influence of the axial ligands on the spectral properties of P700 of photosystem I: a study of site-directed mutants. Biochemistry. 2000;39(42):13012–25.
207. Witt H, Schlodder E, Teutloff C, Niklas J, Bordignon E, Carbonera D, et al. Hydrogen bonding to P700: site-directed mutagenesis of threonine A739 of photosystem I in Chlamydomonas reinhardtii. Biochemistry. 2002;41(27):8557–69.

208. Hamacher E, Kruip J, Rögner M, Mäntele W. Characterization of the primary electron donor of photosystem I, P700, by electrochemistry and Fourier transform infrared (FTIR) difference spectroscopy. Spectrochim Acta A Mol Biomol Spectrosc. 1996;52(1):107–21.
209. Kleinherenbrink FAM, Hastings G, Wittmershaus BP, Blankenship RE. Delayed fluorescence from Fe-S type photosynthetic reaction centers at low redox potential. Biochemistry. 1994;33:3096–105.
210. Vos MH, van Gorkom HJ. Thermodynamics of electron transport in photosystem I studied by electric field-stimulated charge recombination. Biochim Biophys Acta. 1988;934 (3):293–302.
211. Setif P, Bottin H. Identification of electron-transfer reactions involving the acceptor A_1 of photosystem I at room temperature. Biochemistry. 1989;28(6):2689–97.
212. Vos MH, van Gorkom HJ. Thermodynamical and structural information on photosynthetic systems obtained from electroluminescence kinetics. Biophys J. 1990;58(6):1547–55.
213. Holzwarth AR, Müller MG, Niklas J, Lubitz W. Charge recombination fluorescence in photosystem I reaction centers from *Chlamydomonas reinhardtii*. J Phys Chem B. 2005;109(12):5903–11.
214. Hu Q, Miyashita H, Iwasaki I, Kurano N, Miyachi S, Iwaki M, et al. A photosystem I reaction center driven by chlorophyll *d* in oxygenic photosynthesis. Proc Natl Acad Sci U S A. 1998;95(22):13319–23.
215. Ishikita H, Saenger W, Biesiadka J, Loll B, Knapp E-W. How photosynthetic reaction centers control oxidation power in chlorophyll pairs P_{680}, P_{700}, and P_{870}. Proc Natl Acad Sci U S A. 2006;103(26):9855–60.
216. Ishikita H, Stehlik D, Golbeck JH, Knapp E-W. Electrostatic influence of PsaC protein binding to the PsaA/PsaB heterodimer in photosystem I. Biophys J. 2006;90(3):1081–9.
217. Ishikita H, Knapp EW. Redox potential of quinones in both electron transfer branches of photosystem I. J Biol Chem. 2003;278(52):52002–11.
218. Ptushenko V, Cherepanov D, Krishtalik L, Semenov A. Semi-continuum electrostatic calculations of redox potentials in photosystem I. Photosynth Res. 2008;97(1):55–74.
219. Srinivasan N, Santabarbara S, Rappaport F, Carbonera D, Redding K, van der Est A, et al. Alteration of the H-bond to the A_{1A} phylloquinone in photosystem I: influence on the kinetics and energetics of electron transfer. J Phys Chem B. 2011;115(8):1751–9.
220. Moser CC, Dutton PL. Engineering protein structure for electron transfer function in photosynthetic reaction centers. Biochim Biophys Acta. 1992;1101:171–6.
221. Moser CC, Keske JM, Warncke K, Farid RS, Dutton PL. Nature of biological electron transfer. Nature. 1992;355:796–802.
222. Ramesh VM, Guergova-Kuras M, Joliot P, Webber AN. Electron transfer from plastocyanin to the photosystem I reaction center in mutants with increased potential of the primary donor in *Chlamydomonas reinhardtii*. Biochemistry. 2002;41(50):14652–8.
223. Zybailov B, van der Est A, Zech SG, Teutloff C, Johnson TW, Shen G, et al. Recruitment of a foreign quinone into the A_1 site of Photosystem I: II. Structural and functional characterization of phylloquinone biosynthetic pathway mutants by electron paramagnetic resonance and electron-nuclear double resonance spectroscopy. J Biol Chem. 2000;275(12):8531–9.
224. Sakuragi Y, Zybailov B, Shen G, Jones AD, Chitnis PR, van der Est A, et al. Insertional inactivation of the menG gene, encoding 2-phytyl-1,4-naphthoquinone methyltransferase of *Synechocystis sp*. PCC 6803, results in the incorporation of 2-phytyl-1,4-naphthoquinone into the A_1 site and alteration of the equilibrium constant between A_1 and F_X in Photosystem I. Biochemistry. 2002;41:394–405.
225. Iwaki M, Itoh S. Electron transfer in spinach photosystem I reaction center containing benzo-, naphtho- and anthraquinones in place of phylloquinone. FEBS Lett. 1989;256(1–2):11–6.
226. Itoh S, Iwaki M, Ikegami I. Modification of photosystem I reaction center by the extraction and exchange of chlorophylls and quinones. Biochim Biophys Acta. 2001;1507(1–3):115–38.

Chapter 8
Effects of Quasi-Equilibrium States on the Kinetics of Electron Transfer and Radical Pair Stabilisation in Photosystem I

Stefano Santabarbara, Robert Jennings, and Giuseppe Zucchelli

Abstract Reaction centres are the sites of primary energy conversion in photosynthesis. The energy of the absorbed photon is trapped photochemically, with high quantum yields, in the form of electrochemical potential in a radical pair, which is then stabilised by a cascade of electron transfer (ET) reactions. These occur through a chain of redox-active cofactors that are coordinated by the reaction centre protein subunits. It is commonly considered that each of the electron transfer steps in the redox chain is associated with a significant driving force and, hence, a relatively large, negative, standard free energy difference ($\Delta G^0 \leq -100$ meV). In this scenario, the rate of the reverse reaction which describes the repopulation of the precursor is several orders of magnitude smaller than that of forward electron transfer. Hence, the actual electron transfer rate between each given pair of donor and acceptor molecules is determined almost exclusively by the molecular rate constant of the forward reaction.

S. Santabarbara (✉)
Consiglio Nazionale delle Ricerche, Istituto di Biofisica, Sede di Milano, via Giovanni Celoria 26, 20133 Milano, Italy

Dipartimento di Biologia, Universitá degli Studi di Milano, via Celoria 26, 20133 Milano, Italy
e-mail: stefano.santabarbara@cnr.it

R. Jennings
Dipartimento di Biologia, Universitá degli Studi di Milano, via Celoria 26, 20133 Milano, Italy
e-mail: robert.Jennings@unimi.it

G. Zucchelli
Consiglio Nazionale delle Ricerche, Istituto di Biofisica, Sede di Milano, via Giovanni Celoria 26, 20133 Milano, Italy
e-mail: giuseppe.zucchelli@unimi.it

J. Golbeck and A. van der Est (eds.), *The Biophysics of Photosynthesis*, Biophysics for the Life Sciences 11, DOI 10.1007/978-1-4939-1148-6_8,

However, at least for a few steps in the redox chains of both photosystem I and photosystem II, the driving force is not large and often comparable to or lower than the thermal energy at physiological temperatures. In this case, the rate constant of the backward reaction, which is determined by the equilibrium constant, is of the same order of magnitude as that of the forward electron step and hence cannot be neglected. This, in turn, has a profound impact in determining the effective electron transfer rate that can be significantly slower than that of the molecular rate for forward ET.

In this chapter we discuss some aspects of electron transfer reactions in photosystem I, in particular the steps in which reversibility determines the effective ET rate.

Keywords Electron transfer • Reversible reaction • Photosystem I • Photochemical reactions • Phyllo(semi)quinone oxidation • Kinetic modelling

8.1 Overview of Photosystem I Structure and Function and the Electron Transfer Chain

Photosystems are large macromolecular cofactor-protein complexes where primary photochemical energy conversion takes place. The overall catalytic activity of photosystems can be summarised as that of light-dependent oxido-reductases. In oxygenic photosynthesis two such complexes, called photosystem II (PS II), catalysing water oxidation-plastoquinone reduction and photosystem I (PS I), that catalyses plastocyanin oxidation and ferredoxin reduction, operate in series. In eukaryotic organisms, such as higher plants and green algae, the photosystems are localised in the thylakoid membrane of the chloroplast together with the other complexes active in photosynthetic electron transfer reactions.

Both photosystems share a common functional and structural organisation. They are organised in two units: the *core* and the *external antenna*. The core serves the function of light harvesting and it is the site of the photochemical reaction as well as of the successive electron transfer reactions. The external antenna instead has light-harvesting function only. Whereas the cores of both photosystems (PS II and PS I) appear to be substantially conserved through evolution, the external antenna shows great variability, which reflects the adaptation to different environmental niches.

The core of PS I is composed of 12–13 different polypeptides, the specific number varying from species to species [1–3]. The subunits which have higher molecular weights, the gene products of *PsaA* and *PsaB*, form a heterodimer which binds a host of cofactors including approximately 100 molecules of chlorophyll (Chl) *a*, 30 of ß-carotene, 2 phylloquinones and a [4Fe-4S] iron-sulphur cluster [4, 5]. Two other [4Fe-4S] clusters are bound to the PsaC subunit which is evolutionarily related to the class of bacterial ferredoxins [6]. The majority of the pigments bound to the core have light-harvesting function, and are referred to as *core antenna* or *inner antenna*.

A cluster of six Chl *a* molecules functions as the photochemical catalytic centre, and comprises the primary electron donor and the electron acceptor(s). Crystallographic models of the PS I cores have been presented both for a cyanobacterial [4] and a higher plant [5] model based on X-ray diffraction data. Comparison of the two crystallographic models does not highlight differences in the organisation and specific binding sites of the putative electron transfer cofactors. Thus, the structural organisation of the redox-active species is not influenced by species-specific differences in the so-called minor subunits composition. Nevertheless, there is a major structural difference between higher plants and cyanobacterial PS I: while PS I is monomeric [1, 2], i.e. composed of a single core unit, in eukaryotes, in prokaryotes, the most abundant form is that of a trimer [3, 7, 8]. The presence of PS I monomers in cyanobacteria has also been suggested [7] and it is possible that, in vivo, a functional equilibrium between the two types of superstructures exists, depending on environmental factors [7]. While the structural organisation of the redox centres is virtually identical in the structures obtained from *Pisum sativum* [5] and *Synechococcus elongatus* [4], differences emerge when comparing the positions of inner antenna pigments. This has been discussed in terms of the spectroscopic properties of the isolated complexes, which are markedly different, especially in relation to the absorption and fluorescence emission spectra [9–11].

At odds with the high degree of conservation of structural motifs and most of the cofactor-binding sites observed in the core, the *external* antenna displays great variability. In higher plants and green algae the distal antenna is composed of transmembrane Chl *a*/*b*-binding proteins that are collectively known as LHC I (see [12–14] and reference therein). The crystallographic model obtained in pea PS I indicates the binding of four LHC I monomers per core [5, 15, 16]. However, biochemical data suggest the presence of up to eight LHC I monomers per photosystem [17]. LHC I complexes are organised as two heterodimers, composed of the Lhca 1-Lhca 4 and Lhca 2-Lhca 3 monomers, respectively. Those are observed both in the X-ray structure [5, 15, 16] and biochemical studies [12–14, 18]. Cyanobacteria posses a water-soluble antenna, the phycobilisome, in place of the transmembrane LHC as the external antenna (see, e.g. [19] and references therein).

8.1.1 Overview of Photosystem I Electron Transfer Chain

The electron transfer cofactors are, from a structural point of view, organised in two parallel redox chains related by a C_2 symmetry axis which is perpendicular to the plane of the membrane (Fig. 8.1) and falls, with good approximation, at the interface of the PsaA:PsaB protein heterodimer. We will refer to electron transfer chains A (ETC_A) and B (ETC_B) to identify the cofactors which are coordinated preferentially by the PsaA and the PsaB subunits, respectively. The cluster of pigments assigned to the reaction centre is relatively separated from the other

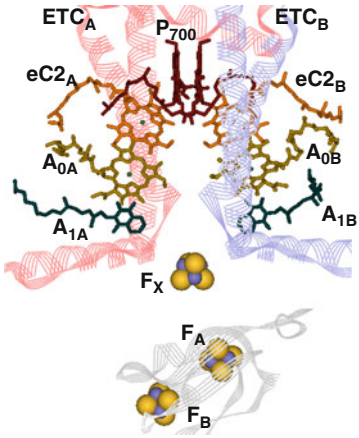

Fig. 8.1 Schematic representation of the electron transfer chains (ETC_A and ETC_B) in the reaction centre of photosystem I, based on the structural model of Jordan et al. [4]. Also indicated are portion of the reaction centre subunits, PsaA (*pink*); PsaB (*light blue*) and PsaC (*grey*)

antenna Chls (average distance with the nearest neighbours which are part of $ETC_{A/B}$ is ~18 Å). The photochemical reaction centre appears to be composed of three Chl *a* pseudo-dimers. One is located at the interface of PsaA:PsaB, each subunit binding one-half of the dimer. This dimer is generally assigned to the pigments on which the (meta)-stable radical cation produced by charge separation, P_{700}^+, is located [20, 21]. The Chl *a* comprising P_{700}, that in structural studies are called eC_{1A} and eC_{1B}, are positioned with their porphyrin rings almost parallel to the symmetry axis [4, 5] (Fig. 8.1). The other two dimers are composed of chlorophylls $eC2_A/eC3_A$ and $eC2_B/eC3_B$, where the subscripts indicate their positions in ETC_A and ETC_B. Chl (s) eC2 are often referred to as "*accessory*" chlorophylls, while eC3 corresponds to A_0, which was the first electron acceptor identified by spectroscopic methods. Photochemical charge separation occurs from the lowest excited singlet state of the Chls composing the reaction centre. The kinetics of primary charge separation are most commonly considered to occur in a few tens of picoseconds (reviewed extensively in [9, 22, 23]), although lower limits in the range of 0.5–1 ps have also been discussed in the literature [24]. Recent studies [25–28] have suggested that photochemical charge separation might initiate at the level of the accessory chlorophyll, rather than P_{700}, as is usually thought. Moreover, it has also been suggested that, analogous to the case of PS II, primary charge separation is associated with a small driving force, so that the rate constant of repopulation of the reaction centre excited state by the back reaction is comparable with that of primary charge separation [29, 30]. Hence, the rate of reversibility of primary photochemistry is an important factor in determining the *effective* photochemical trapping rate. These aspects are discussed in further detail in this chapter. Irrespective of the model for the primary ET reactions, there is a general agreement in considering that A_0 acts as the primary electron acceptor and that the *overall* population time of the radical pair $[P_{700}^+A_0^-]$, which is determined both by rate constant of electron transfer events and by excited state migration in the photosystem antenna, is in the range of 10–40 ps [9, 25–28, 31].

The $A_{0(A/B)}$ ($eC_{3(A/B)}$) chlorophylls are adjacent to the phylloquinone molecules ($A_{1(A/B)}$) which act as the next electron transfer intermediate [22, 23, 32]. The phylloquinones are reduced to the semi-quinone radical form, A_1^- in about 40–80 ps (e.g. [33, 34]). Oxidation of A_1^- by the next electron acceptor, the [4Fe-4S] cluster F_X, which is, as P_{700}, bound at the interface of PsaA:PsaB, displays polyphasic kinetics with the best characterised components having lifetimes of about ~20 and ~200 ns (reviewed extensively in [23, 32, 35–37]). It is generally accepted that the fast rate is associated with the oxidation of the A_{1B}^- (the phylloquinone bound by the PsaB subunit) while the slow phase is associated to the oxidation of A_{1A}^- (bound to the PsaA subunit). This hypothesis, which is referred to as "*bidirectional*" electron transfer model, was initially proposed by Joliot and Joliot [38] and successively substantiated by a host of spectroscopic studies using site-directed mutants of both A_1- and A_0-binding sites [23, 32, 35–37]. Bidirectional ET has been, so far, only observed in PS I, but it might represent a general property of "type I" RC of which PS I is part. Instead, both in PS II and in the reaction centre of purple bacteria that are part of the "type II" RC family, only one of the symmetrically arranged putative redox chains is known to be functionally active in primary photochemical reactions. The necessity of performing asymmetric electron transfer is probably linked to the two-electron reduction of the terminal electron acceptors of type II RC (PS II and purple bacterial RC). The quinone (Q_B) is reduced to quinole in a sequential reaction involving two photochemical events, each leading to the single reduction of Q_A which is the electron donor to Q_B. Moreover, whereas a quinone (Q_B) acts as the terminal acceptor bound to PS II (and this is a characteristic of "type II" reaction centres), the iron-sulphur clusters F_A and F_B, which operate in series and are not bound by the PsaA:PsaB heterodimer but by the PsaC subunit, are the terminal acceptors in PS I [4–6]. The use of Fe-S clusters as terminal acceptors is a general characteristic of "type I" reaction centres.

In general terms, electrons transfer in photosynthetic RC involves a series of coupled redox reactions that are most commonly described as a sequence of thermodynamically favourable steps. In this framework, each single reaction is expected to be associated with a standard free energy difference $\Delta G^0 \ll 0$ meV. Considering, as a reasonable approximation, values of ΔG^0 of the order of -100 meV, it turns out that the rate of the reverse reaction for an electron transfer step is significantly slower (often exceeding two orders of magnitudes) than that of the forward reaction. In the case of a "closed" donor-acceptor pair system, the redox pair will reach its equilibrium population, irrespectively of the actual rate constants and timescale considered. However, in a redox chain, involving sequential electron transfer steps, as is encountered in the photosynthetic RC, each ET step is coupled to another, generally thermodynamically favourable, reaction. Then, the population of the ET intermediates is far from the equilibrium value provided that the precursor redox pair is depopulated faster by the formation of the next redox pair in the chain than its reversal to the state it derived from. These are the conditions, which are not uncommon in photosynthetic RC, under which the *effective* rate of the electron transfer step in the redox chain is determined almost exclusively by the rate of the

forward electron transfer reaction. In these cases, as we discuss further in Sect. 8.3, the lifetimes, which are measured by any appropriate technique which enables one to follow the electron transfer events, closely match the inverse of the actual molecular rate constant.

However this is not always the case. For instance, in PS I, which we use as a model system to introduces this issue, it has been suggested that both primary charge separation [25–28] and A_1^- oxidation are coupled to small driving forces [23, 39], to the limit of being slightly energetically uphill [23, 31, 37]. In these cases, the rates of the back reactions differ only by about one order of magnitude (or less) compared to those of forward ET transfer and are comparable to the rate of depopulation of these ET intermediates by the next redox pair in the ET chain. Thus, the backward rates cannot be neglected in these circumstances and, as it will be shown, they have a pronounced effect in determining the *effective* ET kinetics. As a consequence, the lifetimes measured experimentally are not related directly to the actual molecular rate constant.

The focus of this chapter is the discussion of the effect of small driving forces on the ET kinetics. In particular, we will describe relevant examples occurring in the PS I reaction centre, although similar situations are encountered also in other relevant biological systems. In the following sessions we present a brief overview of description of the ET transfer rate according to Marcus formalism (Sect. 8.2), a mathematical description of a general system of coupled ET reactions (Sect. 8.3), and derive the general expression of an "open" simple two-level system. The final two sections discuss the impact of backward rates, and hence of reversibility on the time scale of the event under consideration, in determining the *effective* ET transfer time for the case of primary charge separation (Sect. 8.4) and A_1^- oxidation (Sect. 8.5).

8.2 Rate of Electron Transfer Between a Donor and an Acceptor Molecule

In order to discuss the effect of electron transfer reversibility in particular steps of the transfer chain of PS I, we will make use of kinetic modelling, which consists in the solution of a system of linear differential equations that is described in detail in the subsequent section (Sect. 8.3) of this chapter. The kinetic constants will be computed according to the nuclear mediated tunnelling of electron transfer theory, which is often referred as the Marcus theory [40, 41]. We will present here only a brief overview which is useful to understand the parameters used in the kinetic modelling. More in-depth discussion of the Marcus theory is presented in several reviews (e.g. [40, 41], as well as Chap. 4 by Moser et al. of this book).

The rate of tunnelling-mediated electron transfer ($k_{D\rightarrow A}$) between a donor (D) and an acceptor (A) molecule can be described by the application of the so-called Fermi's golden rule [40, 41]:

$$k_{D\to A} = \frac{2\pi}{\hbar}|H_{DA}|^2 \cdot f(T) \tag{8.1}$$

where $\hbar$ is the Dirac constant, $|H_{DA}|$ is the electronic element of the system Hamiltonian and $f(T)$ is a function describing the temperature-dependent Franck-Condon factors, which are common to both the electron donor and the electron acceptor. Considering the coupling of electron transfer with nuclear tunnelling described by a single, mean, oscillator of angular frequency $\overline{\omega}$, it is possible to describe the Franck-Condon factors in terms of a Gaussian density function [41, 42],

$$f(T) = \frac{1}{\sqrt{2\pi}\sigma(T)} e^{-\frac{\left(\Delta G^0+\lambda_t\right)^2}{2\sigma(T)^2}} \tag{8.2}$$

that, with respect to the standard Gibbs free energy difference (ΔG^0), has a maximum when $\Delta G^0 = -\lambda_t$, where λ_t is the total reorganisation energy. The potential energies of the (initial) D^-A and the (final) DA^- redox pair, including the surrounding medium, are described, in this framework, by parabolic functions with respect to the nuclear coordinates displacement. The minimum of each parabola represent the equilibrium state of each pair. The reorganisation energy described the reconfiguration of the medium surrounding the (final) DA^- redox state. From an energetic point of view, it is equivalent to the displacement of the DA^- pair from its energy minimum to a position on its parabolic potential curve which allows a vertical transition from the energy minimum of the (initial) state DA^-. Such "vertical" transition is required by the Frank-Condon approximation The variance, σ^2, of $f(T)$ is described by

$$\sigma^2(T) = \lambda_t \hbar\overline{\omega} \cdot \coth\frac{\hbar\overline{\omega}}{2k_B T}, \tag{8.3}$$

where k_B is the Boltzmann constant. Under the condition $k_B T \gg \hbar\overline{\omega}$, Eq. (8.3) reduces to $\sigma^2(T) = 2\lambda_t k_B T$ that, substituted into Eqs. (8.1) and (8.2), gives

$$k_{D\to A} = \frac{\pi}{\hbar}\frac{|H_{DA}|^2}{\sqrt{\pi\lambda_t k_B T}} e^{-\frac{\left(\Delta G^0+\lambda_t\right)^2}{4\lambda_t k_B T}}. \tag{8.4}$$

This is the formula derived by Marcus [40, 41]. Since Eq. (8.4) is valid when the temperature is sufficiently high (or the coupled mode is of very low frequency), it is said to hold true in the high-temperature limit, which is generally the case for physiological temperatures. It is worth mentioning that, in the original work of Hopfield [42], two nuclear modes, one specifically coupled to the donor and the other to the acceptors, were considered and that Jortner [43] derived an expression that allows considering more than just a single (mean) nuclear frequency coupled to electron transfer. The latter expression [43] is more general than that obtained by Hopfield [42]. However, in the high-temperature limit it also converges to Eq. (8.4).

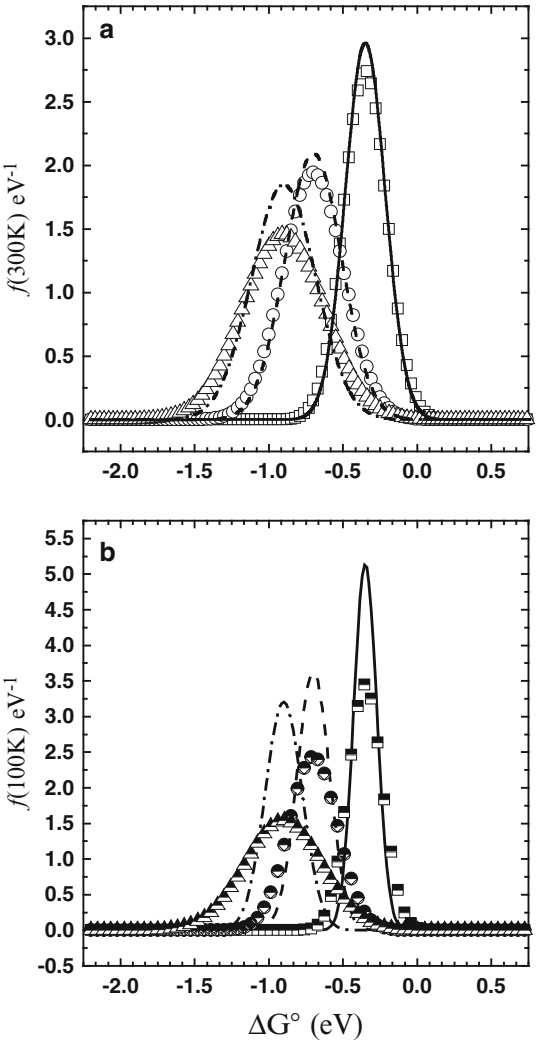

Fig. 8.2 Dependence of the function describing the Franck-Condon factor ($f(T)$) at 300 K (Panel (**a**)) and 100 K (Panel (**b**)) as a function of ΔG^0. The functions were calculated for different values of the reorganisation energy λ_t, and assuming either the high-temperature limit (*solid lines*) or considering explicitly the coupling with a nuclear mode of 300 cm^{-1} (*symbols*). The calculations were performed for $\lambda_t = 0.35$ eV (*solid lines*, *squares*), $\lambda_t = 0.7$ eV (*dashed lines*, *circles*) and $\lambda_t = 0.9$ eV (*dash-dotted lines*, *triangles*)

To exemplify this, Fig. 8.2 presents the calculated values of $f(T)$ as a function of ΔG^0 using the high-temperature limit (Eq. (8.4), solid lines) and considering explicitly the coupling with a mean nuclear mode (symbols, Eqs. (8.1–8.3)) of 300 cm^{-1}, i.e. a mode of "intermediate" strength, for different values of λ_t ranging from 0.35 to 0.9 eV. The calculations were performed at 300 K, i.e. close to room temperature, and 100 K that is often encountered in spectroscopic investigation. It can be easily appreciated that at 300 K there is no significant difference between the two models, whereas at 100 K the coupling with nuclear modes induces a broadening of $f(T)$ that will determine higher rates of ET when ΔG^0 is significantly different from $-\lambda_t$.

Reverse reaction. The rates describing the reverse reaction $k_{A\to D}$, i.e. the transfer of an electron back from the acceptor to the donor, and which is often referred to as the "back reactions", is obtained by substituting ΔG^0 with $-\Delta G^0$ in Eq. (8.4) (in the high-temperature limit) or in Eqs. (8.1–8.3) when considering explicitly the coupling with a nuclear mode. Yet, at least for the high-temperature limit, the ratio of "forward" and "back" rates is simply described by the classic Boltzmann distribution:

$$\frac{k_{D\to A}}{k_{A\to D}} = e^{-\frac{\Delta G^0}{k_B T}} \tag{8.5}$$

and it is therefore equivalent to the equilibrium constant, K_{eq}.

Temperature dependence of the reaction. From the inspection of Eqs. (8.1–8.4) it emerges that the temperature dependence of the reaction rate constant is determined uniquely by the Franck-Condon factors. Moreover, the Marcus Eq. (8.4) in which nuclear modes are not considered explicitly can be readily compared with the Arrhenius formula $k = k_{\max} \cdot e^{-\frac{E^{\ddagger}}{k_B T}}$, where $k_{\max}$ is the maximal rate which, in this case, is an empirical parameter, and $E^{\ddagger}$ is the activation energy. It is useful to introduce the parameter $\Delta G^{\ddagger}$, which represents the standard free activation energy, that, by comparison of the Arrhenius formula with Eq. (8.4), is equivalent to

$$\Delta G^{\ddagger} = \frac{\left(\Delta G^0 + \lambda_t\right)^2}{4\lambda_t} \tag{8.6}$$

Thus, if the value of ΔG^0 is known by independent measurements, the analysis of the temperature dependence of the process allows, in principle, for an experimental estimation of λ_t. Still, it should be noticed that Eq. (8.6) is valid for the high-temperature limit (Eq. (8.4)), and hence in rather narrow temperature ranges, and it is not strictly valid when coupling with nuclear modes is strong. This renders the experimental evaluation of λ_t often difficult, unless the other factors determining the reaction rate are known already.

Moreover, under the conditions $\Delta G^0 = -\lambda_t$ not only the reaction rate attains its maximal value, but also, since $\Delta G^{\ddagger} = 0$, the temperature dependence associated with the exponential term in Eqs. (8.2) and (8.4) vanishes. Yet, a weak temperature dependence of the reaction remains due to the term under square root in the pre-exponential term of Eqs. (8.3) and (8.4).

8.2.1 Parameters Determining the Values of the Rate Constant

The rate of electron transfer (Eq. (8.4)) is determined by four quantities: the standard free energy ΔG^0, the reorganisation energy λ_t, the value of the electronic coupling element of the Hamiltonian $|H_{DA}|$ and, when necessary to consider it explicitly, by the mean nuclear frequency coupled to transfer, $\overline{\omega}$.

Standard free energy difference (ΔG^0). Estimates for the value of ΔG^0 can be obtained from independent measurements, for instance from the redox titration of the electron donors and acceptors. However, depending on the distance between the electron donor and acceptors, the values obtained from equilibrium titration might represent an overestimation, due to the presence of Coulombic interactions between the charged species composing the radical pair. This effect is expected to be more prominent for primary and secondary radical pair due to the inverse third power dependence on the charges distance. However, as donor and acceptor become progressively separated in space, after each ET event in the redox chain, Coulombic terms will tend to become progressively smaller.

Moreover, the redox titrations are often not straightforward or possible in biological samples, especially when the cofactors operate at high reducing or oxidising potentials. For instance, in PS I, only the potential of the terminal donor P_{700}^{+} and acceptors $F_{A/B/X}$ were determined directly [44–50] (with some spread in the determined values, particularly for F_X [22]). The titration of phylloquinone A_1 (probably A_{1A}) has also been reported [51], yet the value of $E^0 = -530$ mV appears excessively oxidising to be reliable. Values of E^0 for the cofactors not directly accessible by redox titration have been estimated by different computational techniques [52–54] based on semi-empirical or ab initio methods; even in this case there is not a general agreement between the different approaches and some of the values reported seem inconsistent with the observed ET reaction rates (see discussion in [23]).

Reorganisation energy (λ_t). Experimental estimates of the reorganisation energy can be obtained, as already mentioned, from the analysis of the reaction rate temperature dependence when ΔG^0 for the process is known and coupling with nuclear modes is negligible (or explicitly considered, provided that the mode frequency is known). Nevertheless, the estimation of its values, especially for ET in biological samples, has proven to be relatively difficult and often dependent on the simplification employed during the data analysis. Still, in a survey of several reactions occurring in an extended sample of redox-active protein, Moser et al. [55, 56] reported a broad distribution of values for λ_t, with the most frequent falling between 0.5 and 1 eV and a mean close to 0.7 eV. Alternative approaches which can lead to the estimation of the value of λ_t relies on either ab initio or semi-empirical electrostatic calculations (e.g. [57–60]); however also these values depend on the quality of the structural model and on the level of approximation as well as the assumptions (for instance partial charges on residues, dielectric constant and refractive index of the bulk protein) employed in the calculations.

Electronic element of the Hamiltonian ($|H_{DA}|$). Direct experimental evaluation of the value of the electronic element is, in general, cumbersome and most of the values reported in the literature are derived from the analysis (fit) of the reaction temperature dependences, which is possible when all other relevant parameters are known, or just a few of them are fit simultaneously with $|H_{DA}|^2$. It can be shown [41, 42] that the value of $|H_{DA}|$ is dependent on the shape and the height of the tunnelling barrier that the electron needs to transit during the transfer. Computational approaches,

based on ab initio or semi-empirical methods, can be employed to estimated the value of $|H_{DA}|^2$ when a structural model with sufficient resolution is available [59, 61, 62]. However, for large molecular complexes the calculations are computationally expensive and generally yield different results depending on the level of approximation (and the portion of protein-cofactor volume) employed. On the other hand, considering a simple square tunnelling barrier it is possible to describe the electronic elements to a first approximation as [41, 42]

$$\left|H_{DA}\right|^2 = \left|H_{DA}\right|_0^2 \cdot e^{-\beta r_{DA}} \tag{8.7}$$

where $|H_{DA}|_0^2$ is the maximal value under conditions of "contact". This maximal of value is damped exponentially as a function of the donor-acceptor separation, r_{DA} (which is an approximation for the "length" of the tunnelling barrier) modulated by the attenuation constant, β, that depends on the medium surrounding the redox-active moieties.

From the extensive survey of proteins active in electron transfer reactions [55–57] an average value of β in the range of 1.2–1.5 Å^{-1} has been proposed (an average value $\overline{\beta} = 1.35\ \text{Å}^{-1}$ will be used in our calculations) and the value of r_{DA} is the edge-to-edge distance of cofactors involved in the reaction, corrected by the van der Waals radii (~3.6 Å). A good approximation for the value of $|H_{DA}|_0^2$ is obtained by considering crossing a potential barrier height of ~2 eV which yields a value of about $\sim 1 \times 10^{-3}$ eV^2. It should be borne in mind that such values are only approximate and, in turn, the description of the electron transfer rate has to be considered only as a first-order approximation, reliable within an order of magnitude.

8.3 Description of the Kinetic of a System of Coupled First-Order ET Reactions

In this section we present a description of a kinetic model suitable to represent the cascade of *intra-complex* electron transfer reactions, all of which are characterised by first-order order rate constants, as those occurring in a photosynthetic RC. Such a kinetic model describes the temporal evolution of each component in the system, following a brief (instantaneous) excitation, such as a single turnover flash excitation for the case of an RC. This problem has a general connotation, as it is applicable to any form of coupled reactions. We start by discussing the general description of a system of coupled first-order reactions composed of an arbitrary number, N, of states (S_i). We explicitly consider an "open" system, i.e. in which there is at least an output from the system that is described by the constant k_{out} associated with the state S_N. This scenario relates more closely to photosynthetic RCs in which the initial excitation, after conversion into a radical pair species, leads to the transfer of electrons outside the RC, a process mediated by diffusible redox carriers (e.g. plastoquinone, plastocyanin, ferredoxin). These processes are not

meant to be described in detail and are simply accounted for by macroscopic rate constants which accounts for the exit from the system.

In the most general situation it is necessary to consider communication between *all* the different states present in the system; this is described by pairwise first-order rate constants, $k_{i,n}/k_{n,i}$, that represent the actual *forward* and *backward* constants for each given process. The temporal evolution of the system is described by a system of linear differential equation (with respect to time) having the general form:

$$\begin{cases} \dot{S}_1 = -\sum\limits_{\substack{i=1 \\ i \neq 1}}^{N} k_{1i} S_1(t) + k_{21} S_2(t) + k_{31} S_3(t) + \ldots + k_{N1} S_N(t) \\ \dot{S}_2 = k_{12} S_1(t) - \sum\limits_{\substack{i=1 \\ i \neq 2}}^{N} k_{2i} S_2(t) + k_{32} S_3(t) + \ldots + k_{N2} S_N(t) \\ \vdots \\ \dot{S}_N = k_{1N} S_1(t) + k_{2N} S_2(t) + k_{3N} S_3(t) + \ldots - \sum\limits_{\substack{i=1 \\ i \neq N}}^{N} k_{Ni} S_N(t) - k_{out} S_N(t) \end{cases} \tag{8.8}$$

where the negative sum comprises all the rate constants describing depopulation events from the given state S_i and $\dot{S}_i$ is the first derivative with respect to time. Any further output from the system occurring from any of the S_i level other than that already considered from the "final" state S_N is easily factored in by including the relevant rate constants in the summations. Although the system of differential equations presented in Eq. (8.8) represents a general situation, in practice, when considering a linear cascade of electron transfer reactions such as that occurring in a photosynthetic RC, it is generally necessary to consider only the rate constants relating to depopulation and population of two successive states, so that the system significantly simplifies. Still, for redox chains involving more than two, coupled, ET steps (or any system comprising more than two states, independently on their nature) analytical solutions can only be found for particular cases. In order to provide a simple example for which general and analytical solution can be retrieved, we will discuss the case of a two-level system in the Appendix. Yet, for more complex scenarios it is necessary to rely on numerical methods to find the solutions of the system of linear differential equations. Those are generally based on linear algebra methods because those are general and are therefore more straightforwardly implemented in numerical approaches. Hence, those will be discussed briefly.

The system of equations (Eq. (8.8)) can be expressed in compact matrix notation as

$$\dot{\mathbf{S}}(t) = \mathbf{R}_N \cdot \mathbf{S}(t) \tag{8.9}$$

where $\mathbf{S}(t)$ is the vector describing the temporal evolution of the redox intermediate populations and $\dot{\mathbf{S}}(t)$ is its first derivative with respect to time. Both vectors have the

dimension of the number of ET steps in the redox chain. $\mathbf{R}_N$ is a square matrix containing the molecular rate constants between couples of donor-acceptors as its elements and is therefore referred to as the *rate matrix*. Equation (8.9) has the form of common linear differential equation; just the terms are vectors and a matrix rather than functions and scalar values. For the simulations which are presented in this chapter, the elements of $\mathbf{R}_N$ will be computed using the tunnelling-mediated ET theory as a starting point, with the approximations already described in the previous section. However, alternative methods, known as "target" analysis, that consider the rate constants as free fit/adjustable parameters are also commonly used.

If the matrix $\mathbf{R}_N$ can be diagonalised, which is often the case, the systems of linear differential equations have general solutions with the form of a weighted sum of exponential functions:

$$\mathbf{S}(t) = \sum_{i=1}^{N} c_i \mathbf{V}_i e^{\gamma_i t} \tag{8.10}$$

where γ_i and $\mathbf{V}_i$ are, respectively, the eigenvalues and the eigenvectors verifying the diagonalisation conditions $\mathbf{R}_N \cdot \mathbf{V}_i = \gamma_i \cdot \mathbf{V}_i$. The eigenvalues are univocally determined by finding the root of the characteristic polynomial of the matrix $(\mathbf{R}_N - \gamma \mathbf{I}_N)$, where $\mathbf{I}_N$ is the identity matrix of the same order as $\mathbf{R}_N$, and are related to the experimentally observed lifetimes ($\tau_{i,obs}$) by the simple relation $\tau_{i,obs} = \gamma_i^{-1}$.

A very common approximation, often encountered in the literature, is that of considering the inverse of the experimentally determined lifetimes ($\tau_{i,obs}^{-1}$) as a good approximation for the rate constant describing a given ET reaction. Yet, since the values of γ_i (or $\tau_{i,obs}^{-1}$) are the roots of the characteristic polynomial of $\mathbf{R}_N$, which represent a combination of all the different rate constants composing the rate matrix, such approximation is not accurate (and in certain cases it is incorrect), if not under special circumstances.

The eigenvectors constitute a basis of the matrix $\mathbf{R}_N$; hence the solutions of the system of equations are defined except for scaling constants (c_i), which are determined by the boundary or the initial conditions, most commonly the concentration of the states at $t \to 0$, or any known state that can be controlled by the experimental conditions. Thus, by the determination of the eigenvalues, which describes the (inverse) measured lifetimes and the eigenvectors for a particular initial conditions, which described the (population) amplitude associated with each eigenvalue/lifetime, the temporal evolution of the system is fully described.

It should be noted though that the eigenvalues describe the population evolution (i.e. the concentrations or better, the molar fractions, of the states involved in the system), whereas in an experiment the measured signal will depend also on the spectroscopic characteristics of the cofactors (i.e. absorption, fluorescence, magnetisation and so on, depending on the methodology adopted to monitor the reactions). For instance, when cofactors of different chemical nature act as donors/acceptors, they will have distinct absorption spectra (ε) and distinct difference extinction coefficients ($\Delta\varepsilon$). These "spectroscopic" properties act as scaling factors

which bias the amplitudes of the "*net*" population evolution and constitute a complication in the data analysis. On the other hand, if the chemical nature of the cofactors is unknown, the "spectroscopic" characteristics are a key tool to reveal their properties.

In the remaining part of this chapter we discuss two particular cases: primary charge separation and oxidation of semi-phylloquinone acceptors A_1^- in the reaction centre of PS I as in both cases it has been suggested that the *effective* ET dynamics are strongly influenced by the rapid reaction reversibility.

8.4 Reversibility of Primary Charge Separation in Photosystem I

Primary photochemistry in PS I takes place from the singlet excited state of a pigment cluster that can be considered to have a minimal size of six chlorophyll *a* molecules, one of which is a 13′ epimer and is part of a hetero-dimer constituting the terminal electron donor (P_{700}) which is positioned at the interface of the PsaA and PsaB core subunits. The other four Chl *a* are organised in two pseudo-dimers, each composed, according to structural model nomenclature, of chls $eC2_{A/B}$, (the so-called accessory chls), and $eC3_{A/B}$ (also known as $A_{0A/B}$) that is the first electron acceptor(s) that has (have) been identified spectroscopically. Each of these "eC_2–eC_3" dimers forms an angle of about 30° with respect to the C_2 symmetry axis that is instead parallel to P_{700} (Fig. 8.3a for a schematic representation). This structural arrangement determines significant excitonic interactions amongst the pigments in the cluster. Within the point dipole approximation, an interaction energy of 320 cm^{-1} can be estimated for the chl *a*–chl *a*′ dimer composing P_{700}, and ~255 cm^{-1} for the eC2–eC3 couples, whereas the coupling between eC_2 and the components of P_{700} is ~80 cm^{-1}, e.g. [23, 61, 63]. However, as the distances between these chromophores are close to space occupancy as determined by the van der Waals radii, the assumption of point dipole should lead to an overestimate of the couplings. Renger and Schlodder [63] determined, using the extended dipole approximation, couplings of 157 cm^{-1} for the P_{700} dimer and of 136 cm^{-1} between A_0 and the eC2. These are about one-half of those determined by the point-dipole approximation, but still significant, and are larger than those estimated for the eC2–eC1 pairs. Still, couplings of this order of magnitude lead to exciton interactions, so that the lowest singlet excited state from which charge separation takes place should be considered that of the six Chl *a* composing the reaction centre that will be referred to as RC*. The core of PS I also binds a large number of chlorophyll *a* (~100) molecules which function as a proximal antenna together with the photochemical reaction centre. In the case of cyanobacteria; some of the core antenna chlorophylls absorb at wavelengths longer than the lower excited state of the reaction centre itself, and are often referred as the "red spectral forms" (see [9] for a review). Such spectral forms are also present in PS I from higher plants, but in

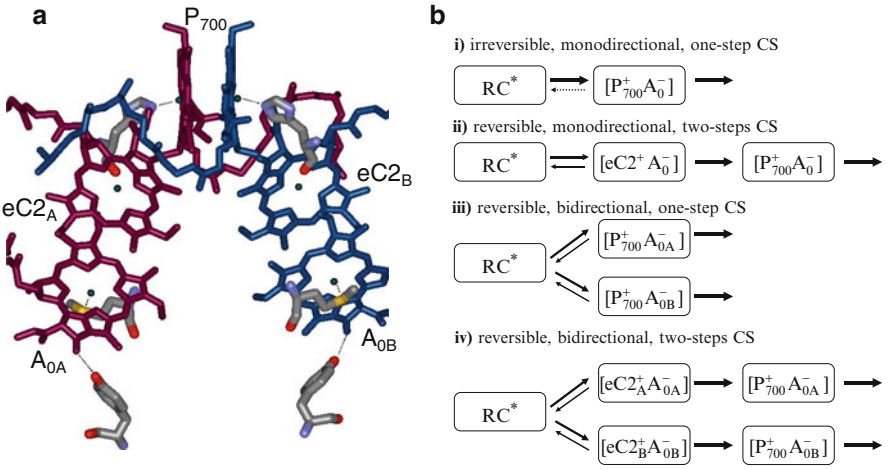

Fig. 8.3 Panel (**a**): Schematic representation of the arrangement of the cofactors involved in primary photochemical reactions and charge stabilisation. ETC_A: *purple*; ETC_B: *dark blue*. Also shown are the principal interactions with the residue involved in the coordination of P_{700} and $A_{0A/B}$. Panel (**b**): Different kinetic models describing primary charge separation reactions, as discussed in the text

this case are bound to the LHC I external antenna [13, 14]. The red forms play an important role in light harvesting under leaf shading conditions, since far-red light penetrated more deeply through canopy being less absorbed [64]. At the same time, the presence of these low-energy states in the antenna was demonstrated to have a pronounced effect on the overall photochemical kinetics, which can be interpreted in terms of reversible excited state transfer to and from the red forms and the bulk antenna [9, 16, 65–69]. Since the details of excited state equilibration are outside the main topic of this chapter, this issue will not be further discussed. However, it is worth mentioning that interpretation of experimental data acquired by the spectroscopic techniques of choice to monitor primary photochemistry, such as ultrafast optical transient spectroscopy or fluorescence lifetimes, needs to take into consideration energy transfer events in the antenna because they occur on timescales which overlap with both the primary radical pair population and the successive radical pair stabilisation events.

The sequence of primary charge separation and successive electron transfer events in PS I has received considerable attention in the last decade. Primary photochemistry has been generally described as starting from the P_{700} dimer that acts as the primary electron donor and directly reduces the primary acceptor A_0 [9, 22, 23, 68], hence leading to formation of the $[P^+_{700}A^-_0]$ radical pair in a single-step, rapid and substantially irreversible reaction (Fig. 8.3b). The timescale for this process is most commonly reported in the 10–40 ps range [9, 22, 23, 64–68, 70], even though more rapid kinetics have also been suggested [9, 24]. This would yield, to a first approximation, photochemical rate constant. In the order of 50–150 ns^{-1}. However, in more recent investigations, initially in the isolated PS I purified from

C. reinhardtii [25, 27] and successively in a higher plant preparation [26], it has been suggested that the stabilisation of the charge-separated state takes place via a two-step reaction mechanism. The first step, that represents the actual photochemical reaction, was suggested to be rapidly reversible and hence associated with a small driving force. The second step, which again leads to the population of $[P^{+}_{700}A^{-}_{0}]$, was instead considered to be substantially irreversible, at least on the timescale of these ET events (Fig. 8.3b). The photochemical rate constants reported in these studies [25–27] are in the range of 350–400 ns^{-1}, which are significantly faster than the values proposed for a single-step mechanism associated with a large driving force. In the two-step photochemical charge separation/stabilisation mechanism, the rates for the reverse reaction, that is the repopulation of *RC**, were estimated in the 25–43 ns^{-1} interval, yielding equilibrium constants of $9 < K^{eq}_{fc} < 14$. From these values, the free energy difference for charge separation is $-67 < \Delta G^{0}_{fc} < -57$ meV, i.e. ~2.5 k_BT at 300 K. The successive reaction, which leads to the population of $[P^{+}_{700}A^{-}_{0}]$, was described by rate constants in the 75–90 ns^{-1} range [25–27], which is within the spread of values reported for a single-step irreversible charge separation, albeit in the upper range of values [9, 68]. The values of the rate constants for the back reaction leading to the repopulation of the primary radical pair were not reported, and hence assumed to be small enough to be neglected on the timescale considered. In other terms, the second step in the proposed reaction mechanism is assumed to be (substantially) irreversible on the timescale of the investigation.

A two-step reaction scheme involves necessarily a role of the accessory chl (eC2) as an electron transfer intermediate, being either the primary electron acceptor or the primary electron donor. Müller and co-workers [25, 27] favoured the hypothesis that the eC2 acted as the primary donor, based on the interpretation of transient optical spectra. This suggestion was successively confirmed by the same group based on the study of site-directed mutants of the A_0-binding site [28] and also by others, who performed experiments under conditions where P_{700} was either in neutral form or oxidised at the time photochemistry is initiated [71]. A similar mechanism involving reversible radical pairs was also proposed for PS II by Holzwarth and co-workers based on the analysis of fluorescence decay [29, 30, 72] and more recently on ultrafast transient absorption measurements [73]. Also for the case of PS II, it was suggested, based on the effect of site-directed mutants involved in the coordination of electron P_{680} [74] and successively by complementary approaches [72], that the primary electron donor of PS II is one of the accessory chlorophylls (reviewed in [75, 76]) that are arranged in a functionally equivalent position within the reaction centre to those of PS I [77].

Based on the emerging evidence for the functionality of two parallel ET branches in PS I [23, 31, 32, 35–37] it has been suggested that the kinetics retrieved from ultrafast transient optical spectroscopy by Müller et al. [25] could also be interpreted in terms of two primary radical pairs, each populated on one of the active braches of PS I [23, 31], rather than by a two-step (mono-directional) charge separation mechanism (Fig. 8.3b). This model of primary photochemistry also considered

rapid reversibility of primary charge separation and assumed, for simplicity, equal rates for the two parallel electron transfer branches [23] (Fig. 8.3b). Within this framework, i.e. a one-step, rapidly reversible, charge separation involving two functional electron transfer chains, and accounting for excited state equilibration processes in the antenna [23, 31], a value of about 100–200 ns^{-1} for the photochemical rate was proposed, which corresponds to an overall photochemical de-excitation of the reaction centre excited state (RC*) of ~300 ns^{-1} that is in line with the estimates of Müller et al. [25] and Slavov et al. [26]. Based on the analysis of single point mutants (PsaA-Tyr696 and PsaB-Tyr676) affecting H-bond donation to the peripheral rings of both A_{0A} and A_{0B} a further update of the model describing primary photochemical events has been presented [28]. The most complex kinetic model considers a two-step charge separation as well as the two functional ET chains of PS I (ETC_A and ETC_B), in which the first reaction is rapidly reversible in both branches [28]. The combined analysis of the experimental results obtained with wild type and mutants of the $A_{0A/B}$-binding sites allowed estimation of the photochemical rate, as well as the back reaction, on both ETC_A and ETC_B, which were suggested to be unequal [28]. Moreover, the experimental results provided further evidence for the $eC2_{A/B}$ chlorophylls acting as the primary electron donor on both ET branches [28]. A molecular rate of 220 ns^{-1} was reported for the photochemical population of the $[eC2_A^+A_{0A}^-]$ radical pair and of 140 ns^{-1} for the population of $[eC2_B^+A_{0B}^-]$. From these values an overall photochemical de-excitation of the RC* of ~350 ns^{-1} is obtained, which is similar to the value of 350–400 ns^{-1} proposed for the mono-directional scenario [25–27]. The rates for reversible reactions were estimated as 8 and 16 ns^{-1} for primary charge separation occurring on the ETC_A and ETC_B, respectively, yielding the equilibrium constants $K_{fc,A}^{eq} \simeq 25$ and $K_{fc,B}^{eq} \simeq 9$, equivalent to standard free energy differences $\Delta G_{fc,A}^0 = -83$ meV and $\Delta G_{fc,B}^0 = -56$ meV. Considering the *overall* photochemical de-excitation of RC* (i.e. the sum of photochemical charge separation of each branch) and its overall repopulation (i.e. the sum of the backward rates), a *mean* equilibrium constant $\overline{K}_{fc}^{eq} = 14$ is obtained. This corresponds to a *mean* value of Gibbs free energy difference $\Delta\overline{G}_{fc}^0 = -68$ meV. Hence, in general terms the value of $|\Delta G_{fc}^0|$ is 2–3 k_BT at RT. Accepting the suggestion that charge separation is initiated from the accessory chlorophylls [25, 28], from the free energy difference reported above, and considering that the edge-to-edge distance is 3.6 Å between $eC2_A$ and A_{0A} and 3.7 Å between $eC2_B$ and A_{0B} (note that these are on the contact limit when the molecular radii are accounted for) it is possible to estimate the values of the total reorganisation energy using Eqs. (8.1–8.4) and the approximation discussed in Sect. 8.2 of this chapter. From the parameters just discussed values in the range of 0.51–0.54 eV for $\lambda_{t,fc}$ are computed. They represent reasonable figures considering that similar estimates were obtained for reduction of P_{700}^+ by plastocyanin [78, 79]. From the values of $\lambda_{t,fc}$ and $\Delta G_{fc,A/B}^0$ it is possible to estimate the activation energy $\Delta G_{fc}^{\ddagger}$ in the (90–100) meV interval, i.e. ~5 k_BT at room temperature. Thus, in the presence of a relatively constant value of $\lambda_{t,fc}$ and $\Delta G_{fc}^{\ddagger}$, it is mainly the larger absolute value of

$\Delta G^0_{fc,\mathrm{A}}$ with respect to $\Delta G^0_{fc,\mathrm{B}}$ which determines both a faster rate of charge separation on $\mathrm{ETC_A}$ and a lower value of the rate constant associated with the reversal of the primary charge-separated states on this electron transfer chain. Within this framework, this would lead to a preferential statistical utilisation of $\mathrm{ETC_A}$ with respect to $\mathrm{ETC_B}$ at the level of photochemical events, which can be quantified as a ratio of about 0.6:0.4 [23, 32, 35–37].

The charge-separated state is substantially stabilised by the next ET steps, which lead to the formation of the $[\mathrm{P}^+_{700}\mathrm{A}^-_{0\mathrm{A}}]$ and the $[\mathrm{P}^+_{700}\mathrm{A}^-_{0\mathrm{B}}]$ radical pairs. These reactions are described as being irreversible [25–28]. Müller et al. [28] estimated values of 69 and 89 ns^{-1} for the population of these two radical pairs from the $[\mathrm{eC2}^+_{\mathrm{A}}\mathrm{A}^-_{0\mathrm{A}}]$ and the $[\mathrm{eC2}^+_{\mathrm{B}}\mathrm{A}^-_{0\mathrm{B}}]$ precursors, respectively. Considering a value for the reorganisation energy of the order of 0.5 eV, similar to that obtained for primary change separation, and based on the edge-to-edge distance between $\mathrm{eC2}_{\mathrm{A/B}}$ and P_{700} of 4.7–4.8 Å, it is possible to estimate the values for $\Delta G^0_{fc,\mathrm{RP2A}} = -170$ meV and $\Delta G^0_{fc,\mathrm{RP2B}} = -185$ meV, and activation energies $51 < \Delta G^{\ddagger}_{RP2} < 58$ meV. From these values, the equilibrium constants for the population of $[\mathrm{P}^+_{700}\mathrm{A}^-_{0\mathrm{A/B}}]$ from $[\mathrm{eC2}^+_{\mathrm{A/B}}\mathrm{A}^-_{0\mathrm{A/B}}]$ are in the $0.7–1.3 \times 10^3$ range, so that the assumption of a substantially irreversible reaction within the time window of ET reactions considered is reasonable. From the *mean* value of $\Delta\overline{G}^0_{fc,\mathrm{RP2}}$ estimated the total energy drop from RC* to the "stabilised" radical pairs $[\mathrm{P}^+_{700}\mathrm{A}^-_{0\mathrm{A/B}}]$ exceeds 240 meV. This value is consistent with the estimated activation energy of $[\mathrm{P}^+_{700}\mathrm{A}^-_{0\mathrm{A/B}}]$ charge recombination, at least at low temperatures, which is in the range of 175–250 meV [22, 80–82]. For the values of $\lambda_t = 0.5$ eV and $\Delta G^0_{P^+_{700}A^-_0} = 250\,\mathrm{meV}$ discussed above and considering an edge-to-edge distance between P_{700} and A_0 of 9.7 Å it is possible to calculate, using Eqs. (8.1–8.4), a recombination time of ~45 ns that, considering the simplification employed in obtaining these values, is in reasonable agreement with the experimental value of about 25 ns [22].

To summarise the description of the kinetics of primary charge separation and radical pair stabilisation, we present in Fig. 8.4 the population evolution of the radical pairs involved. These are calculated on the basis of the results reported by Müller et al. [28], for a bidirectional model, and also including the weak reversibility of the secondary radical pairs, whereas the population of the next, ternary, radical pairs $[\mathrm{P}^+_{700}\mathrm{A}^-_{1\mathrm{A/B}}]$ is not treated explicitly as it is considered to be an irreversible "output" from the system. In the absence of an output that macroscopically describes the successive electron transfer reactions, the populations of the redox pairs that are explicitly considered will not decay to zero, but tend to their Boltzmann populations.

The simulations are performed using the kinetic model described in Sect. 8.3 of this chapter, hence solving a system of linear differential equations of the kind of Eq. (8.9). In the model of Fig. 8.4 excited state equilibration is described only in terms of a "bulk" antenna coupled to RC*, whereas the contribution of the red spectral forms to the overall trapping dynamics, which was proven to be significant

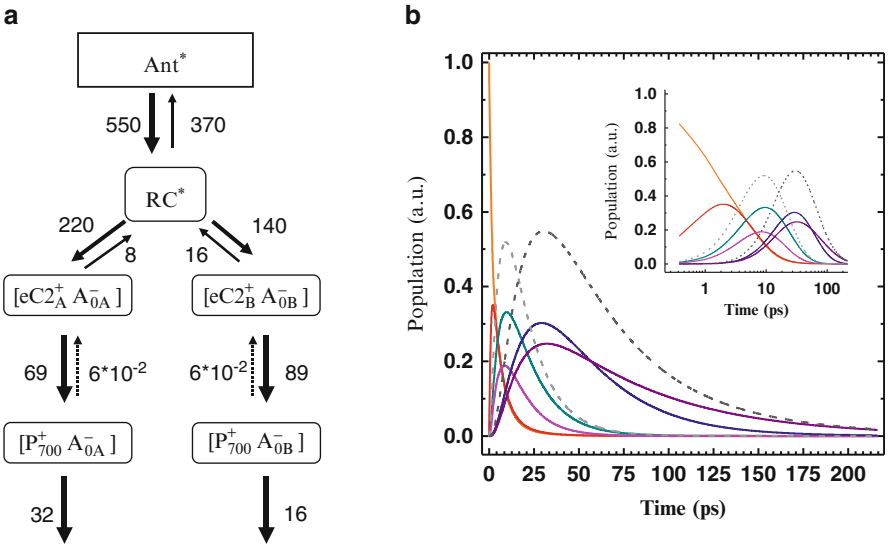

Fig. 8.4 Panel (**a**): Kinetic model, rearranged from that originally presented by Müller et al. [28] used to calculate the temporal evolution of primary photochemistry and successive charge-stabilisation events. The values of the rate constants are ns^{-1}. Initial populations Ant*(0) = 0.9; RC*(0) = 0.1; all others are zero. Panel (**b**): Calculated population evolution of Ant*(*t*): *orange line*; RC*(*t*): *red line*; $[eC2^{+}_{A}A^{-}_{0A}](t)$: *green line* $[eC2^{+}_{B}A^{-}_{0B}](t)$: *magenta*; $[P^{+}_{700}A^{-}_{0A}](t)$: *blue line* and $[P^{+}_{700}A^{-}_{0B}](t)$: *purple line*. Also shown are the *overall* evolutions of $[eC2^{+}_{(A+B)}A^{-}_{0(A+B)}](t)$ (*dashed line*, *light grey*) and $[P^{+}_{700}A^{-}_{0(A+B)}](t)$ (*dashed line*, *dark grey*). The *insert* shows the same kinetic traces on logarithmic timescale. Global lifetimes: 908 fs, 5.1 ps, 10.5 ps, 14.8 ps, 31.5 ps, 62.5 ps

(e.g. [9, 17, 65–70]), is not taken into account. Although this represents a simplified description of the system, it allows one to focus on the ET reactions. From this kinetic modelling (Fig. 8.4) the following lifetimes are determined: 0.9, 5, 10, 14, 31 and 62 ps. It is worth noting that these lifetimes are very closely spaced, especially those in the 5–14 ps range, and that it has been possible to distinguish them only through the analysis of mutants altered at the level of $A_{0A/B}$ coordination [28]. In the case of the wild type, the reported lifetimes fall into a rather broad distribution, from which they cannot be simply disentangled. Within this framework, the faster components are essentially associated with the decay of the excited state in the bulk antenna (~1 and 5 ps) and the population (~1 ps) and the depopulation (5 ps) of RC*. This yields an average lifetime for antenna de-excitation of ~3 ps, which is significantly faster than the values of the order of 10–20 ps typically obtained by monitoring the fluorescence decay [9, 65–70]. This discrepancy originates from neglecting the detailed excited state equilibration, which is the subject of other reviews [9, 68], in the kinetic model of Fig. 8.4a. In the simulation presented here, the $[eC2^{+}_{A}A^{-}_{0A}]$ and $[eC2^{+}_{B}A^{-}_{0B}]$ radical pairs are populated with average lifetimes of 6.4 ps and 5 ps respectively, and are

depopulated with lifetimes of 13.5 ps and 10.5 ps, respectively, that matches the rise times of the successive radical pair couples $[P^{+}_{700}A^{-}_{0A}]$ and $[P^{+}_{700}A^{-}_{0B}]$. Those, in turn, decay with lifetimes of 23.5 ps and 37 ps, respectively. The maximal population of $[eC2^{+}_{A}A^{-}_{0A}]$ and $[eC2^{+}_{B}A^{-}_{0B}]$ is 0.33 and 0.19, corresponding to a ratio of 0.64:0.36, in favour of ETC_A, whereas the maximal populations of $[P^{+}_{700}A^{-}_{0A}]$ and $[P^{+}_{700}A^{-}_{0B}]$ are 0.30 and 0.25 corresponding to a ratio of 0.55:0.45. These ratios represent the statistical utilisation of the two parallel electron transfer branches and are within the range reported in the literature for higher plants [23, 31, 32, 35–37], even though somewhat more asymmetric ratios have been often reported for PS I of cyanobacteria [23, 31, 32, 35–37]. Thus, irrespective of the details, the statistical utilisation of the two electron transfer chains is determined both by the actual charge separation rate on each ET branch, the charge stabilisation rates and, significantly, also by the equilibrium constant for the rapidly reversible primary radical pair.

8.5 Reversibility of Electron Transfer from $A^{-}_{1A/B}$ and F_X

The oxidation of the next electron acceptor A_1^{-} is characterised by complex kinetics that are described by a minimum of two exponential components [22, 23, 32, 35–37]. In the wild type reaction centres, are characterised by lifetimes in the range of 5–25 ns and 200–350 ns, with the slower component possessing, in general, a larger fractional amplitude. A so-called "*intermediate*" phase, with an associated lifetime in the range of 160–180 ns, is also resolved in the wild type, in studies where the temperature dependence of the reaction has been investigated [79, 83, 84]. There is now a general consensus in considering that the "fast" 5–25 ns component reflects principally the oxidation of A^{-}_{1B} and the "slow" 200–350 ns phase the oxidation of A^{-}_{1A}, according to the bidirectional ET model [23, 32, 35–37]. Most of the initial evidence in favour of bidirectional ET came from the analysis of PS I reaction centre mutants involved directly in the coordination or located in the proximity to the binding site of the phylloquinones A_{1A} and A_{1B} (reviewed in [23, 32, 35–37]). The naphthol ring of both phylloquinones interacts with the indole ring of a tryptophan residue (PsaA-Trp697, PsaB-Trp677 according to *S. elongatus* numbering), leading to a π-stacking interaction between the aromatic moieties. The substitution of the PsaA-Trp697 residue with different side chains leads to the lengthening of A_1^{-} oxidation kinetics. This was due to a selective change in the value of the ~250 ns lifetimes observed in the wild type to 450–1,200 ns, in mutants, the precise value depending on the substitution (e.g. [85–88]). On the other hand, the lifetime associated with the faster oxidation phase (~20 ns) remained substantially unaltered, and so did the amplitudes associated with both components. The opposite effect was observed for mutations of the PsaB-Trp677 residue, which led to shifts of the ~20 ns lifetime to 40–80 ns, whereas the value of the ~250 ns component remained unchanged [85–88]. Similar effects were also monitored for substitutions of other residue side chains located in the

proximity to the phylloquinone, particularly A_{1A}^- which is somewhat better characterised [32, 35–37]. Interestingly, in mutants where the lifetime of the slow component exceeded approximately 800 ns, it was also possible to resolve the intermediate 160–180 ns component at room temperature [87, 88].

From inspection of the structural models other interesting coordination features emerge: both phylloquinones appear to be asymmetric hydrogen bonded. Only the keto-carbonyl group at the C_4 position interacts with the RC subunits, whereas that at C_1 appears to be too far from any suitable donor to allow direct H-bond formation. Moreover, the H-bond donor is not an amino acid side chain but the peptide bond involving the residues PsaA-Leu722 and PsaB-Leu706. Hence, in principle, it is not possible to completely suppress this interaction. Yet, in mutants in which the leucine side chain has been substituted, the oxidation of A_1^- became faster, with a lifetime of ~180 ns instead of 250 ns for PsaA-Leu722 mutants [88–91] and ~15 ns instead of 25 ns in PsaB-Leu706 mutants [89]. This effect was initially interpreted as a weakening of H-bond donation, due to steric hindrance of the substituted side chains (Tyr and Thr) compared to Leu [89]. More recently it was suggested that it might instead be associated with changing of the nuclear frequencies coupled to specific ET reactions [91]. These experimental results provide solid evidence in favour of the functionality of two ET branches in PS I. Further evidence in favour of the bidirectional electron transfer model came also from studies in which mutants of residues involved in the coordination of both A_1 and A_0 have been analysed by either optical transient spectroscopy with sub-picosecond resolution [28, 92–94] or time-resolved electron spin resonance measurements [32, 37, 95–102].

The most significant asymmetry in the primary sequence of the PS I RC subunits is the presence of a tryptophan in PsaB (PsaB-Trp673) where a glycine (Gly693) is found in the homologous position of PsaA. These residues are close to the phylloquinone-binding sites, yet does not appear to directly interact with A_{1B}. When substituted, in an attempt to attain greater symmetry of the protein environment (PsaB-W673G mutant referred as PsaB-W669G in the original publication [101], the actual *Chlamydomonas reinhardtii* numbering), the oxidation kinetics were significantly slower than in the wild type and dominated by an 885 ns decay component. Since the crystallographic models [3–5] suggest that the binding of A_{1A} and A_{1B} by the respective protein subunits, PsaA and PsaB, is remarkably similar except for the exchange of PsaB-Trp673 with Gly in PsaA. Because F_X is coordinated at the interface of PsaA:PsaB heterodimer, it is a common electron acceptor to both the electron transfer chains. Moreover, the edge-to-edge distances between the two phylloquinones and this cofactor are the same (within fractions of Å). Hence, there is not a clear explanation, from structural perspectives, for the about one order of magnitude differences in the lifetimes associated primarily with A_{1B}^- and A_{1A}^- oxidation. This suggests that the distinct kinetics arise from energetic factors, such as the reorganisation energy, the standard free energy difference or the nuclear modes coupled to these reactions. The value of λ_t should be relatively constant in a restricted portion of the protein complex, so that it is unlikely that the one order of magnitude difference in the measured lifetime for the phylloquinones,

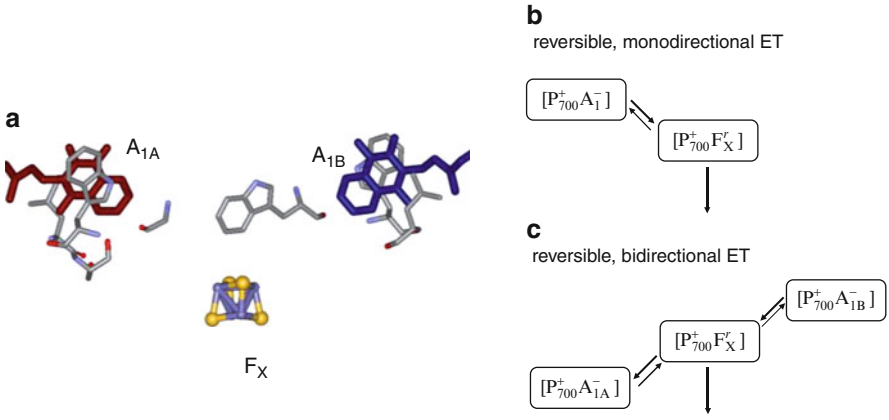

Fig. 8.5 Panel (**a**): Schematic representation of the arrangement of the cofactors involved in secondary electron transfer reactions in PS I. Also shown is the principal residue involved in the coordination of A_{1A} and A_{1B}. Panel (**b**): Kinetic model considering a partially reversible oxidation of A_1^- by F_X for mono-directional ET, after Brettel ([22] and reference therein). Panel (**c**): Kinetic model considering a partially reversible oxidation of $A^-_{1(A/B)}$ by F_X for the bidirectional ET, after Santabarbara et al. ([23] and reference therein)

which are less than 15 Å apart, can be explained in this terms. Moreover, the main coupled frequency is generally less than 600 cm^{-1}; at room temperature this should not be particularly influential, although it might affect more significantly the temperature dependence (see Sect. 8.2). Thus, the most likely candidate to explain the difference between the ~20 and ~250 ns lifetimes is an asymmetry in the Gibbs free energy differences $\Delta G^0_{A^-_{1A/B}\rightarrow F_X}$.

Based on these considerations, a model was proposed [23] that describes, in a semi-quantitative manner, the kinetics of A_1^- oxidation considering reversibility (on the timescale of the ET event) of electron transfer between $A^-_{1A/B}$ and F_X (presented in Fig. 8.5). The suggestion that A_1^- oxidation by F_X is associated with a small driving force and, hence, that the effect of the backward reactions in determining the *effective* ET rate should not be neglected was initially put forward by Brettel and co-workers [22, 39] within the mono-directional ET framework. At that time there was a lack of experimental evidence in favour of the functionality of two electron transfer branches. The kinetic scheme proposed by Brettel was referred as the "shallow equilibrium" model, and is also presented in Fig. 8.5 for completeness.

The model later proposed by Santabarbara et al. [23] considered an important contribution of rapidly reversible ET for both A^-_{1A} and A^-_{1B} oxidation, whereas the successive electron transfer events, the reduction of F_A from F^r_X (the superscript *r* indicates the reduced form of the 4Fe-4S clusters), were considered to be substantially irreversible on the timescale of ET event and hence associated with a large, negative, value of $\Delta G^0_{F^r_X\rightarrow F_A}$ [23]. This was based on the evidence from direct redox titration of the iron-sulphur clusters in PS I: the standard potential for F^r_A/F_A

couple was estimated as −(520–550) mV [22, 44, 46–50], whereas that of F_X^r/F_X as −(650–730) mV [22, 45, 49], so that the value of $\Delta G^0_{F_X^r \rightarrow F_A}$ is less than −100 meV.

In order to model A_1^- oxidation, according to the kinetic scheme reported in Fig. 8.5, it is necessary to adjust the values of the reorganisation energy, which is considered homogeneous for all these ET reactions, and that of $\Delta G^0_{A^-_{1A/B} \rightarrow F_X}$, as all the other parameters are either fixed (as discussed in Sect. 8.2) or derived from the structural model, such as the edge-to-edge distances that are 9 Å between $A_{1A/B}$ and F_X and 11.6 Å between F_X and F_A. Considering reorganisation energies, λ_t, in the order of 0.5–0.75 eV, as commonly reported for electron transfer proteins [55–57], the values of $\Delta G^0_{A^-_{1A} \rightarrow F_X}$ and $\Delta G^0_{A^-_{1B} \rightarrow F_X}$ required to model the experimental kinetics fall in the (− 5)−(+ 40) meV and the −(10–60) meV intervals, respectively. Thus, in general, $\Delta G^0_{A^-_{1A} \rightarrow F_X}$ was $\pm 1 - 2.5 k_B T$ at room temperature. Moreover, from these values, the difference in standard potential between the two phylloquinones is in the 20–120 mV interval. Such relatively small energy gaps can be rationalised on the basis of differences in the strengths of H-bond donation from residues of the PsaB and PsaA subunits to the A_{1A} and A_{1B} quinones, respectively. In this respect, recent evidence indicates that the naphtone plane of A^-_{1B} is slightly rotated with respect to the molecular axis [102]; this will render H-bond donation from PsaB-L706 residue less favourable than for the A^-_{1A}. This is qualitatively in agreement with predicted differences in the redox potentials. In Fig. 8.6b are shown the calculated population evolutions of the $[P^+_{700}A^-_{1A}]$, $[P^+_{700}A^-_{1B}]$ and $[P^+_{700}F^r_X]$ radical pairs considering an average value of 0.7 eV for λ_{t,A_1F_X}. In this case the value of $\Delta G^0_{A^-_{1A} \rightarrow F_X}$ is +10 meV, that of $\Delta G^0_{A^-_{1B} \rightarrow F_X}$ is −25 meV and that of $\Delta G^0_{F_X^r \rightarrow F_A}$ is −150 meV (Fig. 8.6a). The most significant features of this description of A_1^- oxidation can be summarised as follows:

1. A^-_{1A} oxidation is coupled to a smaller driving force with respect to A^-_{1B} oxidation. Whereas A^-_{1B} oxidation appears to be always favourable from a thermodynamic point of view, A^-_{1A} appears to be slightly endergonic or only weakly exergonic. Hence, the oxidation of A_1^- is driven, principally, by the coupling to the largely thermodynamic favourable reduction of F_A by F^r_X.
2. The actual *forward* rate constant for oxidation of both phylloquinones, $k_{A^-_{1A} \rightarrow F_X}$ and $k_{A^-_{1B} \rightarrow F_X}$, only differ by about a factor of 2. For the example reported above the values are 55 μs^{-1} and 30 μs^{-1}. Note that a ten-fold difference in the modelled lifetimes (the kinetic system eigenvalues) is modelled instead, in accordance to the experimental data. This is due to the difference in the *reverse* reaction rate determined by the larger equilibrium constant for A^-_{1B} compared to A^-_{1A} oxidation. Since the latter ET step is predicted to be slightly endergonic, it follows that $k_{F^r_X \rightarrow A_{1A}} \geq k_{A^-_{1A} \rightarrow F_X}$.
3. In such an energetic scheme the commonly adopted approximation $\tau^{-1}_{obs} \simeq k_{ET}$, where τ_{obs} is the measured lifetime and k_{ET} the actual rate constant, is far from being accurate, and this is evident for the $A^-_{1A} \rightarrow F_X$ reaction.

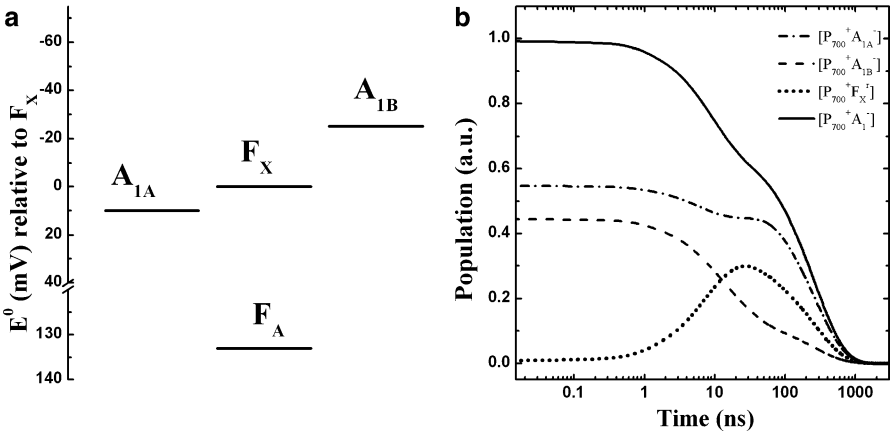

Fig. 8.6 Panel (**a**): Energetic scheme used to model the secondary electron transfer reactions in PS I; shown is the reduction-oxidation potential on a scale relative to F_X. Panel (**b**): Simulation of population evolution of $[P^+_{700}A^-_{1A}](t)$: *dashed-dotted line*; $[P^+_{700}A^-_{1B}](t)$: *dashed lines*; $[P^+_{700}F^r_X](t)$: *dotted line*. Also shown is the *overall* quinone oxidation, $[P^+_{700}A^-_{1(A+B)}]$, as a *solid black line*. The same value of $\lambda_t = 0.7$ eV was used in the simulations, initial populations: ($[P^+_{700}A^-_{1A}](0) = 0.55$, $[P^+_{700}A^-_{1B}](0) = 0.45$, $[P^+_{700}F^r_X](0) = 0$). All other relevant parameters are discussed in the text. Global lifetimes: 8.8, 21.9, 259 ns

4. Since three intermediates are considered, the model yields three lifetimes, i.e. more than those usually resolved experimentally. For energetic schemes, similar to those reported in Figs. 8.5 and 8.6, two of these lifetimes fall in the 5–40 ns range. Typically, one of these lifetimes is associated with a very small fractional amplitude when the total evolution of $[P^+_{700}A^-_1]$ is considered (i.e. $[P^+_{700}A^-_1] = [P^+_{700}A^-_{1A}] + [P^+_{700}A^-_{1B}]$). The two lifetimes in the tens of nanosecond time window can be considered to describe collectively the fast phase of A^-_1 oxidation. It is likely that the two lifetimes predicted by the kinetic model are too closely spaced to be resolved in the measurements, and it is their weighted average which is extracted from the analysis of experimental data. The hundreds of nanosecond lifetime obtained by the kinetic model corresponds, to a good approximation, to the "*slow*" phase of $[P^+_{700}A^-_1]$ reduction observed in the measurements.
5. Both the $[P^+_{700}A^-_{1A}]$ and $[P^+_{700}A^-_{1B}]$ radical pairs decay with multi-exponential kinetics. Still the ~250 ns lifetime dominates the relaxation of the $[P^+_{700}A^-_{1A}]$ radical pair whereas the 8 and 21 ns lifetimes dominate the decay of $[P^+_{700}A^-_{1B}]$, so that the average depopulation of these radical pairs is 257 ns and 88 ns, respectively, whereas the *overall* average depopulation of $[P^+_{700}A^-_1]$ is 181 ns.
6. The small amplitude of the second lifetimes in the tens of ns (~21 ns), when considering the total $[P^+_{700}A^-_{1A}]$ evolution, is due to the opposite sign of the amplitudes (the kinetic model system eigenvector associated with this

eigenvalue) which is positive, i.e. a decay for $[P_{700}^{+}A_{1B}^{-}]$, and negative, i.e. a rise, for $[P_{700}^{+}A_{1A}^{-}]$. This effectively constitutes a net population transfer from A_{1B}^{-} to A_{1A}^{-}, mediated by F_X [89], that is driven by A_{1A}^{-} being the most oxidising species of these three ET intermediates.

7. The radical pair $[P_{700}^{+}F_X^{r}]$ is populated with an average time of 8 ns and decays in 213 ns, which is similar to the overall depopulation of $[P_{700}^{+}A_1^{-}]$ so that both radical pairs depopulate on very close timescales.

The model just discussed is a semi-quantitative description that provides a simple explanation for a number of experimental data in terms of a single microscopic variable, the standard free energy difference for the reactions. It also highlights that kinetic modelling represents a useful analytical tool to uncover, when possible, some microscopic parameters which are otherwise hidden in the experimental data. Some of the information retrieved is, for instance, the asymmetry in the standard potential of the two phylloquinone molecules, especially the indication of a slightly uphill energy transfer from A_{1A}^{-} to F_X (whereas the transfer from A_{1B}^{-} to F_X is a favourable, downhill, process). This energetic scenario describes, qualitatively, the heterogeneity of ET at cryogenic temperatures [22, 84], under a simple framework: the fraction of centres populating the stable redox pair $[P_{700}^{+}F_{A/B}^{r}]$ at low temperatures utilise the thermodynamically favourable ETC_B chain, whereas the centres in which $[P_{700}^{+}A_1^{-}]$ recombination is observed represent the fraction of PS I in which electrons are transferred through the strongly thermally activated chain ETC_A chain. Actually there is solid evidence, particularly from the time-resolved EPR experiments, that the phylloquinone observed at cryogenic temperature by monitoring radical pair recombination is A_{1A} [95–102]. To observe signal arising from the $[P_{700}^{+}A_{1B}^{-}]$ radical pair it is usually necessary to reduce F_X [95–102] prior to the experiments, so that transfer to $F_{A/B}$ is blocked.

Moreover, the model just discussed allows description of the effect of mutations at the phylloquinone-binding site simply in terms of a shift of the standard midpoint potential, and hence the free energy difference [23, 37, 89, 101]. Commonly shifts in the order of ± 50 meV account for the experimentally determined changes in the lifetimes [23, 37, 89, 101], at room temperature. Obviously, this is an assumption and might represent, in certain cases, an oversimplification. For instance, it has been suggested that different nuclear modes coupled to the ET, as a result of modified H-bond donation to A_{1A}, are responsible for increasing the overall electron transfer velocity in the PsaA-L722T mutant at room temperature and, especially, for differences in the temperature dependence of the kinetics [91]. Obviously, further refinement of both the experiments and the analysis is required to extract the exact values of the microscopic and thermodynamic parameters determining the ET in PS I. Yet, for a qualitative to a semi-quantitative level of approximation the $A_{1A} \leftrightarrow F_X$ "equilibration" model appears to be sufficiently robust.

Finally, we briefly mention another interesting case of reversible ET that can be very informative and has been extensively utilised to characterise the intermediate

in photosynthetic RCs, including PS I, which is that of the so-called charge recombination reactions (reviewed in [22]). Those are typically, albeit not exclusively, observed under experimental conditions or sample modifications, by either biochemical or molecular genetic approaches, that "block" the ET reaction at a given point of the chain. This can be achieved, for instance by the removal of one or more ET cofactors or their reduction previous to the initiation of photochemistry. In this case, the system is not "open" anymore: in the absence of rapid reduction/oxidation of the "inactivated" ET intermediate, the probability of recombination reactions leading to the repopulation of either the ground or the excited state of the species involved in upstream ET events becomes significant.

However, charge recombination reactions take place on timescales which are typically much extended compared to those of functional operation of the photosystem. For instance, the recombination of $[P_{700}^{+}A_{0}^{-}]$ is characterised by a lifetime of ~20–40 ns [80–82], whereas the oxidation of the same radical pair by forward ET occurs with an average lifetime of ~30 ps, i.e. almost a three orders of magnitude difference. Similarly, the recombination of the $[P_{700}^{+}A_{1}^{-}]$ pair is characterised by lifetimes in the range of 10–100 μs [22, 84], whereas the oxidation of A_{1}^{-} by F_X is described by an average lifetime of ~150 ns. Recombination of $[P_{700}^{+}F_{X/A/B}^{-}]$ occurs on even longer timescale, which is in the 3–100 ms [22, 84] window and largely exceeds the overall turnover time of the whole PS I complex under physiological conditions.

8.6 Conclusion

In this chapter we have discussed some examples of ET reactions whose *effective* velocities appear to be limited by rapid reaction reversibility due to the coupling with small driving forces eliminated as redundant and a repetition. In particular, we have considered photochemical charge separation and the oxidation of the phyllosemiquinones A_{1A}^{-} and A_{1B}^{-} by F_X within the reaction centre of PS I. Another example within the PS I reaction centre is electron transfer between the terminal acceptors, F_A^r and F_B, that is also coupled to a small driving force of about $-40 < \Delta G^{0}_{F_A^r \rightarrow F_B} < 40$ meV based on the titrated redox potentials [22, 23, 44–50]. Moreover, rapidly reversible photochemical charge separation has also been discussed for the case of PS II reaction centre, and reactions coupled to weak driving forces are not uncommon in nature.

For the particular examples considered, the presence of steps in the redox chain of PS I which are associated with small driving forces, and hence for which the rate of back reaction is comparable with that of forward reaction, provides reasonable descriptions for the difference in the statistical utilisation of the two functional redox chains ETC_A and ETC_B as determined by $RC^* \rightleftarrows [eC_{2A/B}^{+}A_{0A/B}^{-}] \rightarrow [P_{700}^{+}A_{0A/B}^{-}]$ reactions scheme and explains, qualitatively, the one order of magnitude difference in the measured lifetimes describing the oxidation of A_{1}^{-}. A general

overview on the whole PS I energetics seems to indicate that the only reactions associated with large driving forces are the reduction of $A_{1A/B}$ from $A^{-}_{0A/B}$ and the reduction of F_A from F^{r}_{X}. Since these reactions are kinetically coupled to those which are rapidly reversible, the large energy drop associated with them effectively drives the system and allows for an efficient and stable charge separation.

Acknowledgements S.S. wishes to thank Drs. Saul Purton (University College London), Fabrice Rappaport (Institut de Biologie Physico-Chimique, Paris) and Kevin Redding (Arizona State University) for useful and constructive discussion on some of the issues discussed here in the course of collaborative studies. We also wish to thank Dr. Anna Paola Casazza (IBBA, CNR, Milan) for discussion and useful suggestion on editing this chapter.

Appendix

Two-state model. We start by considering the simplest possible kinetic scheme for an open system, which is represented by a couple of acceptor–donor molecule with an output from just one of the two states of the system. This is described by the reaction scheme $A \underset{k-1}{\overset{k_1}{\rightleftarrows}} B \overset{k_2}{\rightarrow}$, for which it is possible to write the following system of differential equations:

$$\begin{cases} \dfrac{dA(t)}{dt} \equiv \dot{A} = -k_1 A(t) + k_{-1} B\big(t\big) \\ \dfrac{dB(t)}{dt} \equiv \dot{B} = -(k_{-1} + k_2) B\big(t\big) + k_1 A\big(t\big) \end{cases} \tag{8.11}$$

that can be written, in matrix form, as

$$\begin{bmatrix} \dot{A}(t) \\ \dot{B}(t) \end{bmatrix} = \begin{bmatrix} -k_1 & k_{-1} \\ k_1 & -(k_{-1} + k_2) \end{bmatrix} \begin{bmatrix} A(t) \\ B(t) \end{bmatrix} \tag{8.12}$$

where the rate matrix $\mathbf{R}$ is

$$\mathbf{R}_2 = \begin{bmatrix} -k_1 & k_{-1} \\ k_1 & -(k_{-1} + k_2) \end{bmatrix} \tag{8.13}$$

From $\mathbf{R}_2$ it is possible to calculate both the two eigenvalues, $\gamma_{1,2}$:

$$\gamma_{1,2} = -\frac{1}{2}(k_1 + k_{-1} + k_2 \pm \Delta); \quad \text{with} \quad \Delta = \Big(4k_{-1}k_1 + (-k_1 + k_{-1} + k_2)^2\Big)^{\frac{1}{2}} \tag{8.14}$$

and the two eigenvectors:

$$\begin{bmatrix} \gamma_1 + k_{-1} + k_2 \\ k_1 \end{bmatrix}; \quad \begin{bmatrix} \gamma_2 + k_{-1} + k_2 \\ k_1 \end{bmatrix}. \tag{8.15}$$

Note that, in this case, Δ is always real, and so are the eigenvalues.

The knowledge of the eigenvalues and eigenvectors permits to write the general solution for the system of differential Eq. (8.11):

$$\begin{bmatrix} A(t) \\ B(t) \end{bmatrix} = c_1 e^{\gamma_1 t} \begin{bmatrix} \gamma_1 + k_{-1} + k_2 \\ k_1 \end{bmatrix} + c_2 e^{\gamma_2 t} \begin{bmatrix} \gamma_2 + k_{-1} + k_2 \\ k_1 \end{bmatrix}, \tag{8.16}$$

where c_1 and c_2 are two constants that can be determined when the initial conditions A(0) and B(0) are defined.

We can do now some observations that have general value. The first one concerns the often encountered "approximation" $\tau_{i,obs}^{-1}(\simeq\gamma_i) \simeq k_i$. From this example it is evident that, in general, the values of $\gamma_{1,2}$ Eq. (8.14) are different from those of the rate constants describing the *forward* electron transfer reactions (i.e. k_1 and k_2). Instead $\gamma_{1,2}$ represents a combination of all the rate constants involved in the processes, including the back reactions (in this example k_{-1}). The values of $\gamma_{1,2}$ approach those of $k_{1,2}$ only when $k_{-1} \to 0$ or, more realistically, when $k_{-1} \ll k_1$. For the concrete case of a relevant physical process, considering that $k_{-1} = k_1 \cdot e^{\frac{\Delta G^0}{k_B T}}$ this condition is verified when $\Delta G^0 < 0$ and $|\Delta G^0| \gg k_B T$, i.e. when the reaction is largely exergonic. In this case, the sequence of reactions can be considered as "decoupled" and treated as being almost independent.

It is also interesting to discuss the eigenvectors (Eq. (8.15)), which contain values that are directly proportional to the amplitudes retrieved from the analysis of the experimental kinetics (Eq. (8.16)), when described as a linear sum of exponentials. For instance, we consider the case in which the initial conditions are defined as $i.c = [A(0) = 1; B(0) = 0]$ (i.e. the population is initially all in one of the two states of the systems). In this case the values of the two constants c_1 and c_2 are obtained solving the equations

$$\begin{bmatrix} 1 \\ 0 \end{bmatrix} = c_1 \begin{bmatrix} \gamma_1 + k_{-1} + k_2 \\ k_1 \end{bmatrix} + c_2 \begin{bmatrix} \gamma_2 + k_{-1} + k_2 \\ k_1 \end{bmatrix}. \tag{8.17}$$

This gives

$$c_1 = \frac{1}{\gamma_1 - \gamma_2} = \frac{1}{\Delta}; \quad c_2 = \frac{1}{\gamma_2 - \gamma_1} = -\frac{1}{\Delta} \tag{8.18}$$

and the temporal evolution of the states A(t) and B(t) results in

$$\begin{bmatrix} A(t) \\ B(t) \end{bmatrix} = \frac{1}{\Delta}\begin{bmatrix} \gamma_1 + k_{-1} + k_2 \\ k_1 \end{bmatrix} e^{\gamma_1 t} - \frac{1}{\Delta}\begin{bmatrix} \gamma_2 + k_{-1} + k_2 \\ k_1 \end{bmatrix} e^{\gamma_2 t} \tag{8.19}$$

so that by knowing the values of the eigenvalues (and therefore of the lifetimes) the dynamics of the system are fully determined. From this simple example it is also evident that the amplitudes are also dependent on *all* the reaction rate constants that compose the matrix $\mathbf{R}_2$. Therefore, the analysis of the amplitudes, in parallel with that of the lifetimes, does also provide information about the molecular rate constants that are often the parameters of interest. Moreover, since the rate constants k_i will display temperature dependence so will the amplitudes. Thus, when possible, both experimental observables (amplitudes and lifetimes) should be analysed simultaneously and cross-checked for consistency.

References

1. Scheller HV, Jensen PE, Haldrup A, Lunde C, Knoetzel J. Role of subunits in eukaryotic photosystem I. Biochim Biophys Acta. 2001;1507:41–60.
2. Jensen PE, Haldrup A, Rosgaard L, Scheller HV. Molecular dissection of photosystem I in higher plants: topology structure and function. Physiol Plant. 2003;119:313–21.
3. Fromme P, Jordan P, Krauss N. Structure of photosystem I. Biochim Biophys Acta. 2001;1507:5–31.
4. Jordan P, Fromme P, Witt HT, Klukas O, Saenger W, Krauss N. Three dimensional structure of cyanobacterial Photosystem I at 2.5 Å resolution. Nature. 2001;411:909–17.
5. Ben-Shem A, Frolow F, Nelson N. Crystal structure of plant photosystem I. Nature. 2003;426:630–5.
6. Vassiliev IR, Antonkine ML, Golbeck JH. Iron-sulfur clusters in type I reaction centers. Biochim Biophys Acta. 2001;1507:139–60.
7. Kruip J, Bald D, Boekema E, Rögner M. Evidence for the existence of trimeric and monomeric Photosystem I complexes in thylakoid membranes from cyanobacteria. Photosynth Res. 1994;40:279–86.
8. Karapetyan NV, Dorra D, Schweitzer G, Bezsmertnaya IN, Holzwarth AR. Fluorescence spectroscopy of the longwave chlorophylls in trimeric and monomeric photosystem I core complexes from the cyanobacterium Spirulina platensis. Biochemistry. 1999;36:13830–7.
9. Gobets B, van Grondelle R. Energy transfer and trapping in Photosystem I. Biochim Biophys Acta. 2001;1507:80–99.
10. Sener MK, Park S, Lu D, Damjanovic A, Ritz T, Fromme P, Schulten K. Excitation migration in trimeric cyanobacterial photosystem I. J Chem Phys. 2004;120:11183–95.
11. Sener MK, Jolley C, Ben-Shem A, Fromme P, Nelson N, Croce R, Schulten K. Comparison of the light-harvesting networks of plant and cyanobacterial photosystem I. Biophys J. 2005;89:1630–42.
12. Jansson S. The light harvesting Chlorophyll *a*/*b* binding proteins. Biochim Biophys Acta. 1994;1184:1–19.
13. Jennings RC, Bassi R, Zucchelli G. Antenna structure and energy transfer in higher plant photosystems. In: Mattay J, editor. Topics in current chemistry. Berlin: Spinger-Verlag; 1996. p. 147–81.
14. Croce R, Morosinotto T, Castelletti S, Breton J, Bassi R. The Lhca antenna complexes of higher plants photosystem I. Biochim Biophys Acta. 2002;1556:29–40.

15. Dekker JP, Boekema EJ. Supramolecular organization of thylakoid membrane proteins in green plants. Biochim Biophys Acta. 2005;1706:12–39.
16. Galka P, Santabarbara S, Khuong TT, Degand H, Morsomme P, Jennings RC, Boekema EJ, Caffarri S. Functional analyses of the plant photosystem I-light-harvesting complex II supercomplex reveal that light-harvesting complex II loosely bound to photosystem II is a very efficient antenna for photosystem I in state II. Plant Cell. 2012;24:2963–78.
17. Croce R, Zucchelli G, Garlaschi FM, Bassi R, Jennings RC. Excited state equilibration in the photosystem I light harvesting I complex: P_{700} is almost isoenergetic with its antenna. Biochemistry. 1996;35:8572–9.
18. Jansson S, Andersen B, Sheller HV. Nearest-neighbor analysis of higher-plant photosystem I holocomplex. Plant Physiol. 1996;112:409–20.
19. Glazer AN. Light harvesting by phycobilisomes. Annu Rev Biophys Biophys Chem. 1985;14:47–77.
20. Kok B. On the reversible absorption change at 705 nm in photosynthetic organisms. Biochim Biophys Acta. 1956;22:394–401.
21. Döring G, Bailey JR, Kreutz W, Weikard J, Witt HT. Some new results in photosynthesis. Naturwissenschaften. 1968;55:219–24.
22. Brettel K. Electron transfer and arrangement of the redox cofactor in photosystem I. Biochim Biophys Acta. 1997;1318:322–73.
23. Santabarbara S, Heathcote P, Evans MCW. Modelling of the electron transfer reactions in Photosystem I by electron tunnelling theory: the phylloquinones bound to the PsaA and the PsaB reaction centre subunits of PS I are almost isoenergetic to the iron–sulfur cluster F_X. Biochim Biophys Acta. 2005;1708:283–310.
24. Beddard GS. Exciton coupling in the Photosystem I reaction center. J Phys Chem B. 1998;102:10966–73.
25. Müller MG, Niklas J, Lubitz W, Holzwarth AR. Ultrafast transient absorption studies on Photosystem I reaction centers from *Chlamydomonas reinhardtii*. 1. A new interpretation of the energy trapping and early electron transfer steps in Photosystem I. Biophys J. 2003;85:3899–922.
26. Slavov C, Ballottari M, Morosinotto T, Bassi R, Holzwarth AR. Trap-limited charge separation kinetics in higher plant photosystem I complexes. Biophys J. 2008;94:3601–12.
27. Holzwarth AR, Müller MG, Niklas J, Lubitz W. Ultrafast transient absorption studies on photosystem I reaction centers from *Chlamydomonas reinhardtii*. 2: mutations near the P700 reaction center chlorophylls provide new insight into the nature of the primary electron donor. Biophys J. 2006;90:552–65.
28. Müller MG, Slavov C, Luthra R, Redding KE, Holzwarth AR. Independent initiation of primary electron transfer in the two branches of the photosystem I reaction center. Proc Natl Acad Sci U S A. 2010;107:4123–8.
29. Schatz GH, Brock H, Holzwarth AR. Kinetic and energetic model for the primary processes in photosystem II. Biophys J. 1998;54:397–405.
30. Schatz GH, Brock H, Holzwarth AR. Picosecond kinetics of fluorescence and absorbance changes in photosystem II particles excited at low photon density. Proc Natl Acad Sci U S A. 1987;84:8414–8.
31. Santabarbara S, Galuppini L. Electron and energy transfer in the photosystem I of cyanobacteria: insight from compartmental kinetic modelling. In: Gaul PM, Marler HJ, editors. Handbook on cyanobacteria: biochemistry, biotechnology and application. Hauppauge, NY: Nova Science Publisher; 2009. p. 1–50.
32. Srinivasan N, Golbeck JH. Protein-cofactor interactions in bioenergetic complexes: the role of the A_{1A} and A_{1B} phylloquinones in Photosystem I. Biochim Biophys Acta. 2009;1787:1057–88.
33. Brettel K, Vos MH. Spectroscopic resolution of the picosecond reduction kinetics of the secondary electron acceptor A_1 in photosystem I. FEBS Lett. 1999;447:315–7.

34. Hecks B, Wulf K, Breton J, Leibl W, Trissl HW. Primary charge separation in photosystem I: a two-step electrogenic charge separation connected with $P_{700}^{+}A_0^{-}$ and $P_{700}^{+}A_1^{-}$ formation. Biochemistry. 1994;33:8619–24.
35. Rappaport F, Diner BA, Redding K. Optical measurements of secondary electron transfer in photosystem I. In: Golbeck JH, editor. Photosystem I: the light-driven plastocyanin:ferredoxin oxidoreductase. Dordrecht: Kluwer Academic Publishers; 2006. p. 223–44.
36. Redding K, van der Est A. The directionality of electron transport in photosystem I. In: Golbeck JH, editor. Photosystem I: the light-driven plastocyanin:ferredoxin oxidoreductase. Dordrecht: Kluwer Academic Publishers; 2006. p. 413–37.
37. Santabarbara S, Galuppini L, Casazza AP. Bidirectional electron transfer in the reaction centre of photosystem I. J Integr Plant Biol. 2010;52:735–49.
38. Joliot P, Joliot A. In vivo analysis of the electron transfer within photosystem I: are the two phylloquinones involved? Biochemistry. 1999;38:11130–6.
39. Brettel K. Electron transfer from acceptor A_1 to the iron-sulfur cluster in photosystem I measured with a time resolution of 2 ns. In: Garab G, editor. Photosynthesis: mechanisms and effects, vol 1. Dordrecht, The Netherlands: Kluwer Academic Publishing; 1998. p. 611–5.
40. Marcus RA, Sutin N. Electron transfer in chemistry and biology. Biochim Biophys Acta. 1985;811:265–322.
41. Devault D. Quantum mechanical tunnelling in biological systems. Cambridge: Cambridge University Press; 1980.
42. Hopfield JJ. Electron transfer between biological molecules by thermally activated tunnelling. Proc Natl Acad Sci U S A. 1974;71:3640–4.
43. Jortner J. Temperature dependent activation energy for electron transfer between biological molecules. J Chem Phys. 1976;64:4860–8.
44. Evans MCW, Reeves SG, Cammack R. Determination of the oxidation-reduction potential of the bound iron–sulphur proteins of the primary electron acceptor complex of photosystem I in spinach chloroplasts. FEBS Lett. 1974;49:111–4.
45. Chamorowsky SK, Cammack R. Direct determination of the midpoint potential of the acceptor X in chloroplast Photosystem I by electrochemical reduction and electron spin resonance. Photochem Photobiophys. 1982;4:195–200.
46. Ke B, Bulen WA, Shaw ER, Breeze RH. Determination of oxidation-reduction potentials by spectropolarimetric titration: application to several iron-sulfur proteins. Arch Biochem Biophys. 1974;162:301–9.
47. Nugent JH, Moller BL, Evans MCW. Comparison of the EPR properties of photosystem I iron-sulphur centres A and B in spinach and barley. Biochim Biophys Acta. 1981;634:249–55.
48. Jordan R, Nessau U, Schlodder E. Charge recombination between the reduced iron-sulphur centres and P700+. In: Garab G, editor. Photosynthesis: mechanism and effects. Dordrecht, The Netherlands: Kluwer Academic Publisher; 1998. p. 663–7.
49. Ke B. The primary electron acceptor of photosystem I. Biochim Biophys Acta. 1973;301:1–33.
50. Golbeck JH, Parrett KG, McDermott AE. Photosystem I charge separation in the absence of center A and B. III. Biochemical characterization of a reaction center particle containing P-700 and F_X. Biochim Biophys Acta. 1987;893:149–60.
51. Munge B, Das SK, Llagan R, Pendon Z, Yang J, Frank HA, Rusling JF. Electron transfer reactions of redox cofactors in spinach Photosystem I reaction centre proteins in lipid films on electrodes. J Am Chem Soc. 2003;125:12457–63.
52. Ishikita H, Knapp EW. Redox potential of quinones in both electron transfer branches of photosystem I. J Biol Chem. 2003;278:52002–11.
53. Karyagina I, Pushkar Y, Stehlik D, van der Est A, Ishikita H, Knapp EW, Jagannathan B, Agalarov R, Golbeck JH. Contributions of the protein environment to the midpoint potentials of the A1 phylloquinones and the Fx iron-sulfur cluster in photosystem I. Biochemistry. 2007;46:10804–16.

54. Ptushenko VV, Cherepanov DA, Krishtalik LI, Semenov AY. Semi-continuum electrostatic calculations of redox potentials in photosystem I. Photosynth Res. 2008;97:55–74.
55. Moser CC, Dutton PL. Engineering protein structure for electron transfer function in photosynthetic reaction centers. Biochim Biophys Acta. 1992;1101:171–6.
56. Moser CC, Keske JM, Warncke K, Farid RS, Dutton PL. Nature of biological electron transfer. Nature. 1992;355:796–802.
57. Page CC, Moser CC, Chen X, Dutton PL. Natural engineering principles of electron tunnelling in biological oxidation-reduction. Nature. 1999;402:47–52.
58. Warshel A, Russel ST. Calculations of electrostatic interactions in biological systems and in solutions. Q Rev Biophys. 1984;17:283–422.
59. Warshel A, Parson WW. Computer simulations of electron transfer reactions in solution and in photosynthetic reaction centers. Annu Rev Phys Chem. 1991;42:279–309.
60. Sharp KA. Calculation of electron transfer reorganisation energy using the finite difference Poisson–Boltzmann model. Biophys J. 1988;73:1241–50.
61. Ivashin N, Larsson S. Electron transfer pathways in Photosystem I reaction centers. Chem Phys Lett. 2003;375:383–7.
62. Petrenko A, Redding K. Intermolecular electron transfer and exchange integrals in photosystem I. Chem Phys Lett. 2004;400:98–103.
63. Renger T, Schlodder E. Modeling the optical spectra and light harvesting in photosystem I. In: Golbeck JH, editor. Photosystem I: the light-driven plastocyanin:ferredoxin oxidoreductase. Dordrecht, The Netherlands.: Kluwer Academic Publishers; 2006. p. 595–610.
64. Rivadossi A, Zucchelli G, Garlaschi FM, Jennings RC. The importance of PS I chlorophyll red forms in light-harvesting by leaves. Photosynth Res. 1999;60:209–15.
65. Engelmann E, Zucchelli G, Casazza AP, Brogioli D, Garlaschi FM, Jennings RC. Influence of the photosystem I-light harvesting complex I antenna domains on fluorescence decay. Biochemistry. 2006;45:6947–55.
66. Jennings RC, Zucchelli G, Croce R, Garlaschi FM. The photochemical trapping rate from red spectral states in PSI–LHCI is determined by thermal activation of energy transfer to bulk chlorophylls. Biochim Biophys Acta. 2003;1557:91–8.
67. Ihalainen JA, van Stokkum IH, Gibasiewicz K, Germano M, van Grondelle R, Dekker JP. Kinetics of excitation trapping in intact Photosystem I of *Chlamydomonas reinhardtii* and *Arabidopsis thaliana*. Biochim Biophys Acta. 2005;1706:267–75.
68. Melkozernov AN. Excitation energy transfer in Photosystem I from oxygenic organisms. Photosynth Res. 2001;70:129–53.
69. Croce R, Dorra D, Holzwarth AR, Jennings RC. Fluorescence decay and spectral evolution in intact photosystem I of higher plants. Biochemistry. 2000;39:6341–8.
70. Jennings RC, Zucchelli G, Santabarbara S. Photochemical trapping heterogeneity as a function of wavelength, in plant photosystem I (PSI-LHCI). Biochim Biophys Acta. 1827;2013:779–85.
71. Di Donato M, Stahl AD, van Stokkum IH, van Grondelle R, Groot ML. Cofactors involved in light-driven charge separation in photosystem I identified by subpicosecond infrared spectroscopy. Biochemistry. 2011;50:480–90.
72. Miloslavina Y, Szczepaniak M, Müller MG, Sander J, Nowaczyk M, Rögner M, Holzwarth AR. Charge separation kinetics in intact photosystem II core particles is trap-limited. A picosecond fluorescence study. Biochemistry. 2006;45:2436–42.
73. Holzwarth AR, Müller MG, Reus M, Nowaczyk M, Sander J, Rögner M. Kinetics and mechanism of electron transfer in intact photosystem II and in the isolated reaction center: pheophytin is the primary electron acceptor. Proc Natl Acad Sci U S A. 2006;103:6895–8900.
74. Diner BA, Schlodder E, Nixon PJ, Coleman WJ, Rappaport F, Lavergne J, Vermaas WF, Chisholm DA. Site-directed mutations at D1-His198 and D2-His197 of photosystem II in Synechocystis PCC 6803: sites of primary charge separation and cation and triplet stabilization. Biochemistry. 2001;40:9265–81.

75. Diner BA, Rappaport F. Structure, dynamics, and energetics of the primary photochemistry of photosystem II of oxygenic photosynthesis. Annu Rev Plant Biol. 2002;53:551–80.
76. van Brederode ME, van Grondelle R. New and unexpected routes for ultrafast electron transfer in photosynthetic reaction centers. FEBS Lett. 1999;455:1–7.
77. Umena Y, Kawakami K, Shen JR, Kamiya N. Crystal structure of oxygen-evolving photosystem II at a resolution of 1.9 Å. Nature. 2011;473:55–60.
78. Ramesh VM, Guergova-Kuras M, Joliot P, Webber AN. Electron transfer from plastocyanin to the photosystem I reaction center in mutants with increased potential of the primary donor in *Chlamydomonas reinhardtii*. Biochemistry. 2002;41:14652–8.
79. Santabarbara S, Redding KE, Rappaport F. Temperature dependence of the reduction of P_{700}^{+} by tightly bound plastocyanin *in vivo*. Biochemistry. 2009;48:10457–66.
80. Vos MH, van Gorkom HJ. Thermodynamics of electron transfer in Photosystem I studied by electric field-stimulated charge recombination. Biochim Biophys Acta. 1988;934:293–302.
81. Kleinherenbrink FA, Hastings G, Wittmerhaus BP, Blankenship RE. Delayed fluorescence from Fe-S type photosynthetic reaction centers at low redox potential. Biochemistry. 1994;33:3096–105.
82. Shibata Y, Akai S, Kasahara T, Ikegami I, Itoh S. Temperature-dependent energy gap of the primary charge separation in photosystem I: study of delayed fluorescence at 77–268 K. J Phys Chem B. 2008;112:6695–702.
83. Agalarov R, Brettel K. Temperature dependence of biphasic forward electron transfer from the phylloquinone(s) A_1 in photosystem I: only the slower phase is activated. Biochim Biophys Acta. 2003;1604:7–12.
84. Schlodder E, Falkenberg K, Gergeleit M, Brettel K. Temperature dependence of forward and reverse electron transfer from A_1^{-}, the reduced secondary electron acceptor in photosystem I. Biochemistry. 1998;37:9466–76.
85. Guergova-Kuras M, Boudreaux B, Joliot A, Joliot P, Redding K. Evidence for two active branches for electron transfer in photosystem I. Proc Natl Acad Sci U S A. 2001;98:4437–42.
86. Xu W, Chitnis PR, Valieva A, van der Est A, Brettel K, Guergova-Kuras M, Pushkar YN, Zech SG, Stehlik D, Shen G, Zybailov B, Golbeck JH. Electron transfer in cyanobacterial photosystem I: II. Determination of forward electron transfer rates of site-directed mutants in a putative electron transfer pathway from A_0 through A_1 to F_X. J Biol Chem. 2003;278:27876–87.
87. Byrdin M, Santabarbara S, Gu F, Fairclough WV, Heathcote P, Redding K, Rappaport F. Assignment of a kinetic component to electron transfer between iron-sulfur clusters F_X and $F_{A/B}$ of Photosystem I. Biochim Biophys Acta. 2006;1757:1529–38.
88. Santabarbara S, Jasaitis A, Byrdin M, Gu F, Rappaport F, Redding KE. Additive effect of mutations affecting the rate of phylloquinone reoxidation and directionality of electron transfer within photosystem I. Photochem Photobiol. 2008;84:1381–7.
89. Santabarbara S, Reifschneider K, Jasaitis A, Gu F, Agostini G, Carbonera D, Rappaport F, Redding KE. Interquinone electron transfer in photosystem I as evidenced by altering the hydrogen bond strength to the phylloquinone(s). J Phys Chem B. 2010;114:9300–12.
90. Srinivasan N, Santabarbara S, Rappaport F, Carbonera D, Redding K, van der Est A, Golbeck JH. Alteration of the H-bond to the A_{1A} phylloquinone in Photosystem I: influence on the kinetics and energetics of electron transfer. J Phys Chem B. 2011;115:1751–9.
91. Mula S, McConnell MD, Ching A, Zhao N, Gordon HL, Hastings G, Redding KE, van der Est A. Introduction of a hydrogen bond between phylloquinone PhQ_A and a threonine side-chain OH group in photosystem I. J Phys Chem B. 2012;116:14008–16.
92. Ramesh VM, Gibasiewicz K, Lin S, Bingham SE, Webber AN. Replacement of the methionine axial ligand to the primary electron acceptor A_0 slows the A_0^{-} reoxidation dynamics in photosystem I. Biochim Biophys Acta. 2007;1767:151–60.
93. Giera W, Gibasiewicz K, Ramesh VM, Lin S, Webber A. Electron transfer from A to A_1 in Photosystem I from *Chlamydomonas reinhardtii* occurs in both the A and B branch with 25-30 ps lifetime. Phys Chem Chem Phys. 2009;11:5186–91.

94. Gibasiewicz K, Ramesh VM, Lin S, Redding K, Woodbury NW, Webber AN. Excitonic interactions in wild-type and mutant PSI reaction centers. Biophys J. 2003;85:2547–59.
95. Xu W, Chitnis P, Valieva A, van der Est A, Pushkar YN, Krzystyniak M, Teutloff C, Zech SG, Bittl R, Stehlik D, Zybailov B, Shen G, Golbeck JH. Electron transfer in cyanobacterial photosystem I: I. Physiological and spectroscopic characterization of site-directed mutants in a putative electron transfer pathway from A_0 through A_1 to F_X. J Biol Chem. 2003;278:27864–75.
96. Cohen RO, Shen G, Golbeck JH, Xu W, Chitnis PR, Valieva AI, van der Est A, Pushkar Y, Stehlik D. Evidence for asymmetric electron transfer in cyanobacterial photosystem I: analysis of a methionine-to-leucine mutation of the ligand to the primary electron acceptor A_0. Biochemistry. 2004;43:4741–54.
97. Santabarbara S, Kuprov I, Fairclough WV, Purton S, Hore PJ, Heathcote P, Evans MCW. Bidirectional electron transfer in photosystem I: determination of two distances between P_{700}^+ and A_1^- in spin-correlated radical pairs. Biochemistry. 2005;44:2119–28.
98. Santabarbara S, Kuprov I, Hore PJ, Casal A, Heathcote P, Evans MCW. Analysis of the spin-polarized electron spin echo of the [P_{700}^+ A_1^-] radical pair of photosystem I indicates that both reaction center subunits are competent in electron transfer in cyanobacteria, green algae, and higher plants. Biochemistry. 2006;45:7389–403.
99. Poluektov OG, Paschenko SV, Utschig LM, Lakshmi KV, Thurnauer MC. Bidirectional electron transfer in photosystem I: direct evidence from high-frequency time-resolved EPR spectroscopy. J Am Chem Soc. 2005;127:11910–1.
100. Santabarbara S, Kuprov I, Poluektov O, Casal A, Russell CA, Purton S, Evans MCW. Directionality of electron-transfer reactions in photosystem I of prokaryotes: universality of the bidirectional electron-transfer model. J Phys Chem B. 2010;114:15158–71.
101. Ali K, Santabarbara S, Heathcote P, Evans MCW, Purton S. Bidirectional electron transfer in photosystem I: replacement of the symmetry-breaking tryptophan close to the PsaB-bound phylloquinone A_{1B} with a glycine residue alters the redox properties of A_{1B} and blocks forward electron transfer at cryogenic temperatures. Biochim Biophys Acta. 2006;1757:1623–33.
102. Berthold T, von Gromoff ED, Santabarbara S, Stehle P, Link G, Poluektov OG, Heathcote P, Beck CF, Thurnauer MC, Kothe G. Exploring the electron transfer pathways in photosystem I by high-time-resolution electron paramagnetic resonance: observation of the B-side radical pair $P_{700}^+A_{1B}^-$ in whole cells of the deuterated green alga *Chlamydomonas reinhardtii* at cryogenic temperatures. J Am Chem Soc. 2012;134:5563–76.

Chapter 9
Energetics of Cofactors in Photosynthetic Complexes: Relationship Between Protein–Cofactor Interactions and Midpoint Potentials

James P. Allen and JoAnn C. Williams

Abstract In photosynthetic organisms, solar energy drives electron and proton transfer reactions across cell membranes in order to create energy-rich compounds. These reactions are performed by pigment–protein complexes, including bacterial reaction centers and photosystem II. In this chapter we discuss how electron transfer is determined by the transition energies and oxidation–reduction midpoint potentials of the cofactors and how protein environments can alter the energetics of these cofactors, in particular the primary electron donors, the bacteriochlorophyll dimer of reaction centers and P680 of photosystem II. A Hückel model is presented that provides an accurate description of the electronic structure of the bacteriochlorophyll dimer, including why specific protein interactions, namely, electrostatic and hydrogen bonding interactions, alter not only the oxidation–reduction midpoint potentials but also the electron spin distribution. A special focus is placed on how protein environments can create strong oxidants, including the ability of photosystem II to perform the highly oxidizing reactions needed to oxidize water and the involvement of the Mn_4Ca cluster in this process.

Keywords Oxidation–reduction potential • Electron transfer • Bacteriochlorophyll • Bacteriopheophytin • Chlorophyll • Bacteriochlorophyll dimer • Manganese cluster • Reaction centers • Photosystem II

J.P. Allen, Ph.D. (✉) • J.C. Williams, Ph.D.
Department of Chemistry and Biochemistry, Arizona State University, Tempe, AZ 85287-1604, USA
e-mail: jallen@asu.edu; jwilliams@asu.edu

J. Golbeck and A. van der Est (eds.), *The Biophysics of Photosynthesis*, Biophysics for the Life Sciences 11, DOI 10.1007/978-1-4939-1148-6_9,

9.1 Introduction

In anoxygenic and oxygenic photosynthesis, the absorption of light results in the conversion of the light energy into chemical energy through a series of electron and proton transfer reactions in pigment–protein complexes. In anoxygenic photosynthetic bacteria, light energy is initially absorbed by antenna complexes and the energy is transferred to the reaction center, where the primary photochemistry occurs, namely, the creation of a charge-separated state [1, 2]. In purple bacteria, absorption of light by the reaction center results in excitation of a bacteriochlorophyll (BChl) dimer followed by the transfer of an electron through a series of electron acceptors, a BChl monomer, a bacteriopheophytin (BPhe) monomer, and the primary quinone, until the secondary quinone is reduced. After reduction of the oxidized BChl dimer by an exogenous cytochrome c_2 or a bound tetraheme cytochrome, light can be absorbed again, leading to the transfer of a second electron to the secondary quinone in a process that is coupled to the uptake of two protons. After the second electron transfer, the quinol carries the electrons and protons to the cytochrome bc_1 complex in a cycle that generates the proton gradients needed for the creation of energy-rich compounds.

In oxygenic photosynthesis, two pigment–protein complexes, photosystem I and II, absorb light energy and perform electron transfer reactions [3]. Unlike the cyclic pathway found in purple bacteria, cyanobacteria, algae, and plants make use of the Z scheme, which has terminal electron donors and acceptors. In this scheme, light excitation of photosystem II results in oxidation of the primary electron donor, P680, which is reduced by a redox active tyrosine, Y_Z, followed by reduction of $Y_Z^{\bullet+}$ by the site of water oxidation, namely, the Mn_4Ca cluster. As described by the S cycle, after four photons of light have been absorbed and four electrons have been transferred, two water molecules bound to the Mn_4Ca cluster are converted into molecular oxygen. The use of water as an electron donor in this four-electron, four-proton process places special constraints on the energetics of the manganese cluster. In this review, the energetics of both the bacterial reaction center and photosystem II are discussed, with an emphasis on the differences and similarities of the primary electron donors. Also discussed are efforts to modify the bacterial reaction center such that it gains functional cofactors corresponding to Y_Z and the Mn_4Ca cluster.

In photosynthetic complexes, the light-driven reactions are able to proceed with essentially every photon producing useful reactions, corresponding to a quantum efficiency of near unity. In addition to efficiently performing these light-induced forward reactions, unfavorable side reactions and undesired back reactions are minimized [4]. This balance is achieved by fine-tuning the properties of the cofactors through interactions with the protein in which they are embedded. Theoretical treatments have identified the aspects of electron transfer that the protein surrounding the cofactors of the reaction center can modulate: the energetics, the coupling, and the protein dynamics [5]. This chapter reviews how interactions with the protein can alter the energetics of the cofactors, in particular the oxidation–reduction

midpoint potential. For this analysis, the focus is on how interactions with the protein can alter the energetics of the tetrapyrroles of reaction centers and photosystem II, including how these interactions influence the energetics of cofactors to make them highly oxidizing and capable of performing water oxidation.

9.2 The Structures of Bacterial Reaction Centers and Photosystem II

In the purple bacterium *Rhodobacter* (*Rb.*) *sphaeroides*, the reaction center consists of three protein subunits, termed the L, M, and H subunits, and ten cofactors: four BChl *a* molecules, two BPhe *a* molecules, two quinones, a non-heme iron, and a carotenoid. The structures of the bacterial reaction centers from *Rb. sphaeroides* and *Blastochloris* (*Bl.*) *viridis* have been determined by X-ray diffraction [6–12]. These structures have shown that the reaction center consists of a core domain that is formed by the L and M subunits, which each have five transmembrane helices related to each other by a twofold symmetry axis (Fig. 9.1). The H subunit consists largely of a cytoplasmic domain with only one transmembrane helix. The core domain contains the cofactors that are divided into two branches also related by a twofold symmetry axis, with only one branch being active in performing electron transfer in wild-type reaction centers. The core domain can be biochemically isolated and is active, although the presence of the H subunit is required for stability of the complex [13].

Photosystem II is a much larger complex as it contains over 20 protein subunits and approximately 80 cofactors, most of which are chlorophylls (Chls) [3]. The large size reflects the dual function of photosystem II in harvesting light and performing electron transfer reactions. The three-dimensional structures of photosystem II from the cyanobacteria *Thermosynechococcus elongatus* and *Thermosynechococcus vulcanus* [14–18] show that the complex can be thought to have an outer domain that harvests light and surrounds a core domain that performs the primary electron transfer reactions and contains the cofactors involved in the primary photochemistry. The core domain is formed by two protein subunits, D1 and D2, that are evolutionarily related to the L and M subunits of the reaction center and exhibit the same pattern of five transmembrane helices arranged about a twofold symmetry axis (Fig. 9.1). These two subunits encase four Chls, two pheophytins (Phes), two quinones, and a non-heme iron whose positions show a remarkable structural similarity with the corresponding cofactors of bacterial reaction centers. In addition, the core contains some cofactors not present in reaction centers, two Chls, Y_Z, and the Mn_4Ca cluster. The core domain of photosystem II can be biochemically isolated although full activity requires the presence of the additional subunits [19].

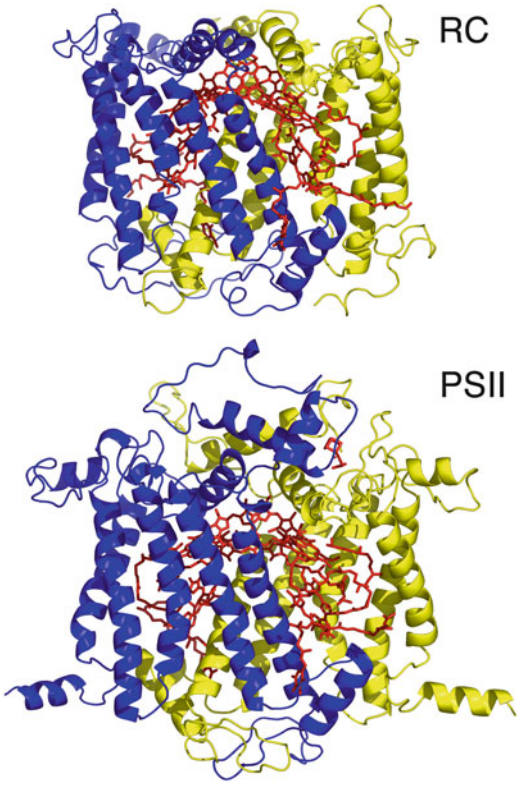

Fig. 9.1 Three-dimensional structures of the core domain of the bacterial reaction center (RC) and photosystem II (PSII) showing the cofactors involved in the electron transfer. The view is perpendicular to the twofold symmetry axis that relates the two branches of cofactors (*red*) and transmembrane helices of the core subunits (L (*yellow*) and M (*blue*) subunits of the reaction center, and D1 (*yellow*) and D2 (*blue*) subunits of photosystem II). The coordinates are from Allen and coworkers [8] (PDB file 4RCR) and Ferreira and coworkers [15] (PDB file 1S5L)

In reaction centers from *Rb. sphaeroides*, the primary electron donor, P865, is a BChl dimer with the two tetrapyrroles overlapping at the ring A position with a separation of ~3 Å (Fig. 9.2). Photosystem II has two Chls at the equivalent position that presumably represent the primary electron donor, P680 (Fig. 9.2), at least in the final oxidized state [20, 21]. For both P865 and P680, the central magnesium atoms are coordinated by histidine residues, L173 and M202 in reaction centers and D1-198 and D2-197 in photosystem II, that are found at similar locations in the structures. While the general orientations of the two Chls are similar to the corresponding BChls in reaction centers, the relative angles between the tetrapyrroles are slightly different, resulting in a longer separation distance of 3.3 Å in photosystem II [18].

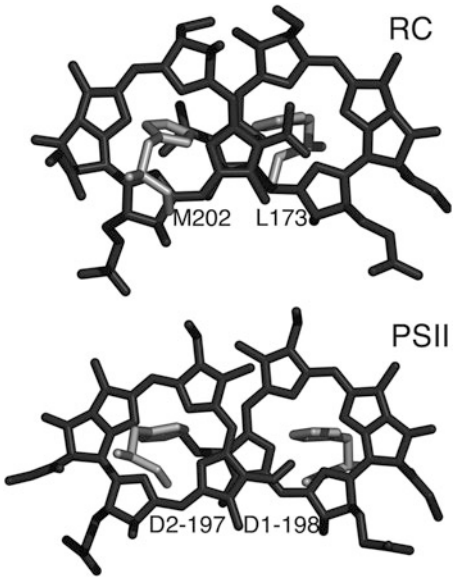

Fig. 9.2 Three-dimensional structures of P865 from the bacterial reaction center (RC) and P680 from photosystem II (PSII). For the reaction center, the coordinating ligands of the BChls, His L173 and His M202, are shown. For photosystem II, the coordinating ligands of the Chls, His D1-198 and His D2-197, are shown. The view is the same as shown in Fig. 9.1. The coordinates are from Allen and coworkers [8] (PDB file 4RCR) and Ferreira and coworkers [20] (PDB file 1S5L)

9.3 Transition Energies of Tetrapyrroles

In photosynthesis, energy and electron transfer is initiated by the absorption of light that results in the excitation of an electron from the ground state to an excited state. The energetics of these transitions are primarily determined by the chemical composition of the pigments. The tetrapyrroles of reaction centers from *Rb. sphaeroides* are BChl *a* and BPhe *a* with the corresponding cofactors of photosystem II being Chl *a* and Phe *a*. The chemical composition of Chl *a* compared to BChl *a* differs with a vinyl group rather than an acetyl group at the ring A position as well as a difference in the hydration at the ring B position [22]. The presence of the central magnesium in BChl *a* and Chl *a* distinguishes these tetrapyrroles from BPhe *a* and Phe *a*, respectively. When in monodisperse solutions, BChl *a* and BPhe *a* have optical spectra with a Q_y band at 772 nm and 749 nm, respectively, while Chl *a* and Phe *a* have transitions at the shorter wavelengths of 662 nm and 667 nm, respectively. In addition to the Q_y bands, the optical spectra have absorption bands due to the Q_x and Soret transitions at shorter wavelengths. In some organisms the optical absorption bands are significantly shifted because of incorporation of cofactors with alternate substituents; for example *Bl. viridis* makes use of BChl *b* that has a Q_y transition at 794 nm.

One of the major effects of the incorporation of tetrapyrroles into the photosynthetic complexes is an alteration of their transition energies compared to those measured for the isolated tetrapyrroles. For reaction centers from *Rb. sphaeroides*, the optical spectrum has Q_y bands at 760, 802, and 865 nm. The peaks at 760 nm and 802 nm are associated with the Bphe and BChl monomers, respectively, while the 865 nm peak is assigned to P865. In photosystem II, the optical absorption band associated with P680 is not resolved from the contributions of the other Chls as the Q_y peaks are all centered near 680 nm.

The observed spectral shifts of the pigments in the proteins compared to the isolated pigments arise from a combination of protein interactions and pigment–pigment interactions. In certain instances, shifts in the optical spectrum can be attributed to changing interactions between a tetrapyrrole and a specific residue. For example, the position of the Q_x transition of the BPhe monomer on the active branch can be shifted from 546 to 534 nm by removing a hydrogen bond from Glu L104 to the keto group [23, 24]. However, changing the hydrogen bonds to the conjugated system of a tetrapyrrole is not generally correlated with a shift in the absorption peak. In general, theoretical modeling of the excited states of tetrapyrroles has proven to be difficult because of uncertainties in key parameters such as accounting for the contribution of electron–vibrational coupling [25, 26].

New techniques are being developed to experimentally determine these key parameters needed to describe the excited states. These methodologies make use of the general approach of two-dimensional transient optical spectroscopy, where the couplings between pigments are found by analysis of the off-diagonal peaks, similar to procedures used in two-dimensional nuclear magnetic resonance spectroscopy [27, 28]. One of the best-characterized systems using this technique is the BChl-*a* containing FMO protein, or Fenna-Matthews-Olson protein, which is a light-harvesting protein in green bacteria. The three-dimensional structures of this protein from *Prosthecochloris aestuarii*, *Chlorobaculum tepidum*, and *Pelodictyon phaeum* have been determined, showing a conserved arrangement of eight BChls within two β-sheets, with one BChl being largely disordered in the structures [29–34] (Fig. 9.3). The optical spectrum of the BChl cofactors of the FMO protein shows a broad peak centered near 810 nm associated with the unresolved Q_y transitions of the BChl cofactors. Measurements of the FMO protein using this optical technique identified not only the contributions of the individual BChls to the optical spectrum but also specific energy transfer pathways among the BChl cofactors (Fig. 9.3).

9.4 Oxidation–Reduction Midpoint Potentials of Tetrapyrroles

After light excitation, an electron is transferred, resulting in oxidation of the electron donor and reduction of the electron acceptor. The ability of a cofactor to serve as either an electron donor or acceptor is determined by the oxidation–reduction midpoint potential of the cofactor. The potential is sensitive to the chemical nature of the cofactor, for example the potential for BChl *a* typically is 0.1–0.2 V lower in

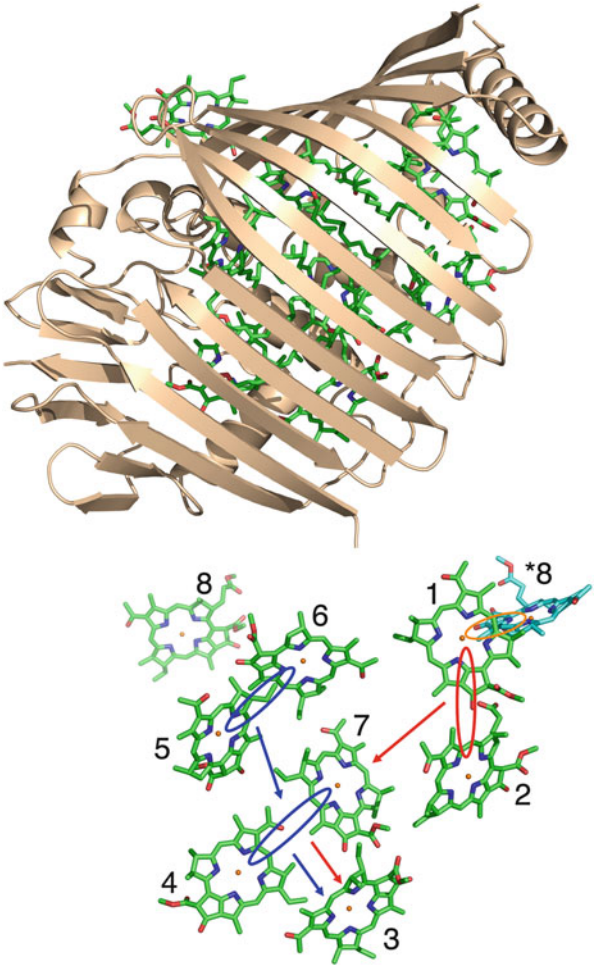

Fig. 9.3 The three-dimensional structure of the FMO protein from *Pelodictyon phaeum* and model for energy couplings. Shown is one subunit of the FMO protein (wheat) that is a trimer in the cell. Each protein subunit is composed of two β sheets that enclose seven BChls, with an eighth BChl being located at the protein–protein interface of the trimer (atom type). The couplings between the BChls are illustrated by *ellipses* with the direction of energy flow shown by *arrows*. Figure adapted from Brixner and coworkers [27] and Larson and coworkers [34] using coordinates from the PDB file 3OEG

value than the potential of Chl *a*, while Chl *d* typically has a slightly higher potential by ~0.1 V compared to the Chl *a* potential [35]. The oxidation–reduction midpoint potentials of isolated tetrapyrroles are also sensitive to the particular solvent, with typical values being +0.81 V and 1.14 V for Chl *a* and Phe *a* in acetonitrile [36].

The oxidation–reduction midpoint potentials of most of the tetrapyrroles bound to the bacterial reaction center and photosystem II are largely unknown. Experimental measurements using chemical or electrochemical titrations have not

been successful because of the lack of equilibrium between the cofactors and the potential of the solution, a problem that is often found for cofactors buried within proteins. The oxidation–reduction midpoint potentials are sometimes inferred based upon electron transfer measurements. For example, the lack of electron transfer along the inactive branch of the cofactors in bacterial reaction centers has been interpreted as arising from those cofactors having unfavorable energetics for electron transfer due to higher potentials compared to the corresponding cofactors on the active branch [37]. In contrast, a wealth of experimental data exists concerning the oxidation–reduction midpoint potential of primary electron donors; therefore, we focus on the effect of protein interactions on those pigments in detail below.

9.5 Oxidation–Reduction Midpoint Potential of P865

In anoxygenic bacteria, the primary electron donor must efficiently transfer an electron from the excited state of the BChl dimer to the nearby electron acceptors as well as be reduced by secondary electron donors, all of which part of the overall electron transfer pathway. In *Rb. sphaeroides*, the excited donor P865* transfers an electron through a BChl monomer to the BPhe monomer on the A branch. The difference in energy between the P865*$BPhe_A$ excited state and the $P865^{\bullet+}$ $BPhe_A^{\bullet-}$ charge-separated state has been estimated to be 0.20–0.26 eV using transient optical spectroscopy [37]. Although estimates of energy differences between transient states are made difficult by the complex nature of the kinetic decays, the energetics can be modeled as arising from a time-dependence of the relative energies due to dynamical motion of the protein [38].

The P865/$P865^{\bullet+}$ midpoint potential of wild-type reaction centers from *Rb. sphaeroides* is 0.50 V [39–42]. The oxidized donor $P865^{\bullet+}$ is reduced by an exogenous cytochrome c_2 having an oxidation–reduction midpoint potential of 0.35 V [43]. With this difference in the oxidation–reduction midpoint potentials, the energy differences are favorable for both secondary electron transfer from cytochrome c_2 and forward electron transfer [44]. For reaction centers from *Bl. viridis* that have a bound tetraheme cytochrome, the midpoint potentials of the BChl dimer and the heme closest to the BChl dimer have been measured to be 0.50 V and 0.38 V, respectively [45, 46]. Thus, the energetics for the primary and secondary electron donors are very comparable despite the structural differences between a small cytochrome that binds transiently compared to a large bound cytochrome.

9.6 Electrostatic Interactions of P865 with Ionizable Amino Acid Residues

The energy of $P865^{\bullet+}$ is sensitive to electrostatic interactions with charged amino acid residues with a dependence that is determined by the distance and effective dielectric constant. The dielectric constant provides a measure of the screening of

the medium between two charges with values ranging from 4 for hydrophobic protein environments to 80 for charges on the protein surface and exposed to water. The effect of electrostatic interactions between P865 and the protein on the properties of P865 was investigated by alterations that either inserted or removed ionizable residues at several different positions located approximately 10–15 Å from P865 (L135, L155, L170, L247, M164, and M199) [47–49]. Several of these mutants exhibited a pronounced pH dependence of the P865/$P865^{\bullet+}$ midpoint potential compared to wild type, demonstrating the effect of an electrostatic interaction between the altered amino acid residue and $P865^{\bullet+}$. The P865/$P865^{\bullet+}$ midpoint potential was generally found to decrease up to 60 mV due to the introduction of a negative charge located approximately 10 Å from the donor or increase up to 50 mV due to the introduction of a positive charge. These changes in the midpoint potential show that the introduced charges are screened with a bulk dielectric constant having a value of ~20 that can be more explicitly modeled using an exponential dependence for the dielectric constant. In general, the changes of the midpoint potential of P865 measured for these mutants are in agreement with electrostatic models, provided that the charges due to the altered amino acid residues are largely screened [48–50].

9.7 Hydrogen Bonding to the Conjugated Macrocycles of P865

BChl *a* has two positions, at the acetyl group of ring A and the keto carbonyl of ring E, that are part of the conjugated macrocycle and can serve as proton acceptors. To investigate how hydrogen bonds influence the electronic structure of the dimer, mutants were constructed in which the number of hydrogen bonds to these positions was altered (Fig. 9.4). Wild-type reaction centers have one

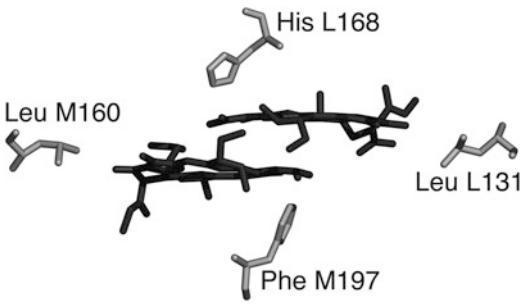

Fig. 9.4 Three-dimensional structure of P865 and nearby amino acid resides Leu L131, His L168, Leu M160, and Phe M197. In wild type, there is one hydrogen bond to His L168. Hydrogen bonds were introduced by substitutions of His at L131, M160, and M197 in different combinations. Substitution of Phe to His at 168 results in loss of the existing hydrogen bond. The coordinates are from Allen and coworkers [8] (PDB file 4RCR)

hydrogen bond between His L168 and the acetyl group of the A side of P865, and this hydrogen bond can be removed by a His to Phe mutation, while the complementary mutation, Phe to His at M197 at the symmetry-related residue, introduces a hydrogen bond to the acetyl group of the B side of P865 [51–54]. Histidine residues introduced at Leu L131 and Leu M160 form hydrogen bonds with the keto carbonyl groups of the A side and B side of P865, respectively [40]. By constructing mutants with different combinations of these alterations, the number of bonds was decreased to zero or increased to four [42]. The gain or loss of a hydrogen bond at each position was measured by use of Fourier transform infrared (FTIR) spectroscopy. For the mutants that were designed to introduce new hydrogen bonds to the keto carbonyls of P865 by the substitutions Leu to His at L131 and Leu to His at M160, large frequency downshifts of the vibrational bands assigned to the keto carbonyl groups were observed [55]. The gain of a hydrogen bond to the acetyl substituent of the B side of P865 in the Phe to His at M197 mutant and the loss of the hydrogen bond to the acetyl substituent of the A side of P865 in the His to Phe at L168 mutant were clearly evident in the infrared spectra of the primary donor obtained using Fourier transform Raman spectroscopy [56] and X-ray diffraction [57].

When the single hydrogen bond between His L168 and the acetyl group of the A side of P865 in wild type is removed by replacement of His with Phe, the optical absorption band at 865 nm shifts slightly to shorter wavelengths, and the midpoint potential of P865 decreases [52–54]. Structural studies show that the substitution of His L168 with Phe does not alter the overall structure of the protein, and the only significant changes other than the mutation are a 20°–27° rotation of the acetyl group and a small displacement of the A side of P865 [53, 58]. When several different amino acid residues were substituted at L168, systematic shifts were observed in the decrease in the P865/$P865^{\bullet+}$ midpoint potential and the shift of the 865 nm band, with His forming the strongest bond [53].

The most striking effect that the alteration of the hydrogen bonds has on P865 is the pronounced change in the midpoint potential with the number of hydrogen bonds. Wild-type reaction centers have one hydrogen bond and a P865/$P865^{\bullet+}$ midpoint potential of 505 mV (Table 9.1). Removal of this hydrogen bond with the His to Phe mutation at L168 results in P865 having no hydrogen bonds and a 95 mV decrease in the midpoint potential. The addition of a single hydrogen bond, resulting in a total of two hydrogen bonds from His to P865, increases the P865/$P865^{\bullet+}$ midpoint potential by 60–125 mV. When P865 has three or four hydrogen bonds, the P865/$P865^{\bullet+}$ midpoint potential increases even further, to a maximum of 765 mV for a mutant that has a total of four hydrogen bonds. The mechanism by which the number of hydrogen bonds controls the P865/$P865^{\bullet+}$ midpoint potential can be understood in terms of a Hückel molecular orbital model as described in the following section.

Table 9.1 Effect of changing hydrogen bonds on the P865/P865$^{\bullet+}$ midpoint potential and unpaired spin density ratio of P865$^{\bullet+}$

			Residues[c]									
			Hydrogen bonded to keto carbonyl		Hydrogen bonded to acetyl		Change compared to no hydrogen bonds		Change compared to wild type (hydrogen bond at L168)		Change compared to hydrogen bonds at L168 and M197	
Number of hydrogen bonds	E_m (mV)[a]	ρ_A/ρ_B[b]	L131	M160	L168	M197	ΔE_m (mV)[d]	$\Delta\rho_A/\rho_B$[e]	ΔE_m (mV)[d]	$\Delta\rho_A/\rho_B$[e]	ΔE_m (mV)[d]	$\Delta\rho_A/\rho_B$[e]
0	410	0.75					0	1.0				
1	485	2.34		His			75	+3.1				
1	485	0.28	His				75	−2.7				
1	505	2.09			His[f]		95	+2.8	0	1.0		
1	545	0.68				His	135	−1.1				
2	565	4.94		His	His				60	+2.4		
2	585	0.89	His		His				80	−2.3		
2	630	1.83			His	His			125	−1.1	0	1.0
3	635	2.21	His	His	His				130	+1.1		
3	700	4.87		His	His	His					70	+2.7
3	710	nd	His		His	His					80	
4	765	nd	His	His	His	His					135	

[a]P865/P865$^{\bullet+}$ oxidation–reduction midpoint potential [42]
[b]P865$^{\bullet+}$ unpaired spin density ratio [62]
[c]Wild-type residues: Leu L131, Leu M160, His L168, and Phe M197; substitution of Phe for His at L168 removes the single hydrogen bond found in wild type
[d]Change in P865/P865$^{\bullet+}$ oxidation–reduction midpoint potential ($E_m(2) - E_m(1)$)
[e]Relative change in unpaired spin density ratio $((\rho_A/\rho_B(2))/(\rho_A/\rho_B(1))$ for $\rho_A/\rho_B(2) > \rho_A/\rho_B(1)$, $-(\rho_A/\rho_B(1))/(\rho_A/\rho_B(2))$ for $\rho_A/\rho_B(2) > \rho_A/\rho_B(1))$
[f]Wild-type hydrogen-bonding configuration

9.8 Modeling the Electronic Structure of P865

Many of the properties of P865 can be characterized in terms of a Hückel molecular orbital model. In this model, P865 is represented by two BChl molecules, A and B, corresponding to the L and M sides, that are coupled together as described by the parameter β (Fig. 9.5). The energies of the molecular orbitals of each BChl are considered to be energetically inequivalent because of different interactions with the surrounding protein. This inequivalence is modeled by poising the two molecules at energies ε_A and ε_B that differ by $\Delta\alpha$. The energy difference between the two molecular orbitals of the coupled system, ΔE, is then given by:

$$\Delta E = \sqrt{\Delta\alpha^2 + 4\beta^2} \tag{9.1}$$

The model predicts that the electron spin densities, ρ_A and ρ_B, of the two BChls of P865 will be inequivalent according to the ratio:

$$\rho_A / \rho_B = \left[(\Delta\alpha + \Delta E) / 2\beta \right]^2 \tag{9.2}$$

The P865/P865$^{\bullet+}$ midpoint potential is determined by the energy of the highest occupied molecular orbital, and the model predicts that the midpoint potential E_m (P865/P865$^{\bullet+}$) is directly related to the value of the spin density ratio ρ_A/ρ_B according to:

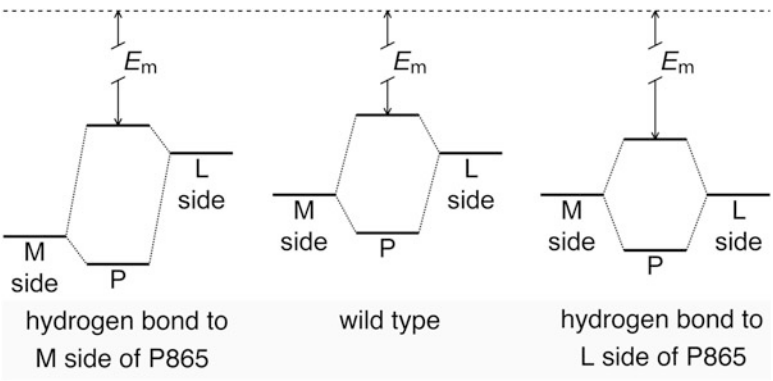

Fig. 9.5 Hückel model of P865. In wild type, the molecular orbitals are split by the inequivalence in the energies of the BChls on the L side (or equivalently the A side) and M side (or equivalently the B side) and their coupling according to Eq. (9.1). The E_m value of P865/P865$^{\bullet+}$ corresponds to the energy difference between the highest molecular orbital and the continuum. The introduction of a hydrogen bond to the M side of P865 stabilizes the energy of that BChl resulting in a larger E_m value and a more asymmetric dimer. The introduction of a hydrogen bond to the L side of the dimer also results in a larger E_m value but a more symmetric dimer. Modified from Williams and Allen [5]

$$E_m(P865/P865^{\bullet+}) = -\epsilon_B - \beta\sqrt{\rho_A/\rho_B} \tag{9.3}$$

The Hückel model provides a platform to understand a number of features of the electronic structure of P865 that can be measured experimentally and related to the ΔE, β, and Δα parameters [49, 59–61]. For example, the FTIR spectrum of wild-type reaction centers has a broad band centered at 2,600 cm^{-1} that has been assigned as an intervalence charge-transfer band, yielding a value of 320 meV for ΔE [60]. Similarly, the asymmetry of the unpaired electron spin density over $P865^{\bullet+}$, which has a spin density ratio for ρ_A/ρ_B of 2.09 for wild-type reaction centers as determined by electron nuclear double resonance spectroscopy, yields an estimate of 0.37 for the Δα/β ratio [59].

The Hückel model can be used qualitatively to explain the trends evident in the spin density ratios of the hydrogen-bonding mutants, which have a range of values from 0.28 to 4.94 (Table 9.1) [62]. In this model, the energy of the BChl near M160 in wild type is lower compared to the energy of the BChl near L131 (Fig. 9.5). Hydrogen bonds to M160 stabilize the nearby BChl of P865, making the energies of the two halves more asymmetric, whereas hydrogen bonds to L131 make the dimer more symmetric. Because the spin density reflects this asymmetry, the M160 mutants have an increase in the ρ_A/ρ_B ratio, while the L131 mutants show a decrease in this ratio. In both cases stabilization results in a higher E_m ($P865/P865^{\bullet+}$), that is, a larger amount of energy is required to remove an electron from P865 to the continuum. The effects on the ρ_A/ρ_B ratio are additive, for example in the mutant with hydrogen bonds introduced to the keto groups of both BChls of P865 by changes at both L131 and M160, the energies of both BChls change. Because the change in energy on both sides is similar, the relative asymmetry is unchanged, resulting in essentially the same spin density ratio as measured in wild type. Another set of mutants was tested in which a series of amino acid residues was substituted at L131 and M160 [63, 64]. For each mutant, electrochemical titrations and electron nuclear double resonance measurements were performed, and the resulting set of data demonstrates a well-defined correlation between ρ_A/ρ_B and E_m ($P865/P865^{\bullet+}$) [64, 65].

The mutations at L168 or M197 change the hydrogen bonding to the acetyl groups of P865, in a different position than L131 and M160, which are near the keto group of ring E of the BChls (Fig. 9.4). The introduction of a hydrogen bond at M197 does not alter the spin density ratio significantly, while an increase in the spin density ratio is observed when a hydrogen bond is added at L168. Mutations at these two positions are more difficult to interpret, since the changes may result in rotation of the acetyl groups in the mutants relative to wild type, with a consequent change in the conjugation of the macrocycle. Structural rearrangements may contribute to the observed effects in addition to the contributions from the change in energy due to the hydrogen bond.

The model provides estimates of energies for the heterodimer mutants, which have changes at His L173 or His M202, the two ligands to P865. Substitution with Leu results in incorporation of a BChl-BPhe dimer in place of P865 [66–71]. The heterodimer mutants have many spectral and electron-transfer changes

although the directionality of transfer along the active branch is maintained. Notably, the oxidation–reduction midpoint potential of the heterodimer is 0.64 V compared to 0.50 V for wild type [72]. This increase can be understood using the Hückel model, as the energy associated with the BPhe side of the heterodimer is increased compared to the corresponding BChl of P865 because of the higher midpoint potential of BPhe compared to BChl. The increase in the difference in energies of the two macrocycles causes the spin density distribution to become more localized on the BChl side. In addition, the optical bands associated with the heterodimer have a significant increase in their broadness compared to P865 because of the contribution of charge-transfer states [73].

While the model provides a simple qualitative description of the effects of different mutations on the properties of P865, more complete descriptions of the electronic states are required in order to accurately describe the effects of protein interactions. For example, the reorganization energy associated with charge transfer, λ, is the energy change needed to move a charge from one side of the dimer to the other [64, 65]. Incorporating this term into the model generates a modified relationship between the midpoint potential and spin density in which large values of this term compared to ΔE would significantly alter the localization of charge and asymmetry of $P865^{\bullet+}$. For the reaction center mutants with alterations at residues L131 and M160, resulting in changes in the hydrogen bonds to P865 at the two keto positions, the revised model provides estimates that the energy associated with the introduction of a hydrogen bond to stabilize a BChl is approximately 100 meV, the coupling, β, is 120–160 meV, and the reorganization energy, λ, is 100–200 meV [64]. To model the broadness of the optical bands in the near infrared region, it is necessary to include the contribution of vibrational states [48]. Also contributing to the IR band at 2,600 cm^{-1} is a second electronic transition between the second highest occupied molecular orbital and the highest occupied molecular orbital, which is only partially filled in the $P865^{\bullet+}$ state [65]. Combining the contributions of the two transitions with the use of several vibrational modes results in a greatly improved correspondence between the calculated and experimental optical spectra [65] including the $P865^{\bullet+}$ Stark spectrum [74]. The resulting values of the coupling, β, and reorganization energy, λ, are 126 meV and 139 meV, respectively, with a value of 69 meV for Δα in wild type. Thus, the Hückel model can be extended with the additional parameters to provide an accurate, quantitative description of the electronic structure of P865.

9.9 Achieving High Oxidation–Reduction Midpoint Potentials for Water Oxidation

In order to oxidize water, P680 must have a high oxidation–reduction midpoint potential of at least +0.82 V at pH 7 and +0.93 V at pH 5, which is the pH range of the thylakoid lumen. Because of its high value, the $P680/P680^{\bullet+}$ midpoint potential

cannot be directly measured, but it has been estimated to be approximately 1.1–1.3 V based upon electron transfer measurements, making P680 the strongest known biological oxidant [3, 20, 75]. The effect of the interactions with the surrounding protein environment on the P680/P680$^{\bullet+}$ midpoint potential has been calculated for photosystem II [76, 77]. Based upon these computational calculations of the electrostatic contributions, the dipolar and charged amino acid residues result in a significant increase in the P680/P680$^{\bullet+}$ midpoint potential, with residues D1-176 to D1-195 and D2-176 to D2-194 having the largest influence. The presence of the positive charges from the Mn_4Ca cluster on the P680/P680$^{\bullet+}$ midpoint potential has been estimated to increase the P680/P680$^{\bullet+}$ midpoint potential by 0.1–0.2 V, although experimental measurements of electron transfer rates suggest that the potential is higher when the Mn_4Ca cluster is removed [20].

A number of factors contribute to the increase in potential of ~0.7 V for P680 compared to P865, including the difference of ~0.2 V due to the presence of Chl *a* instead of BChl *a*. As discussed above, the P865/P865$^{\bullet+}$ midpoint potential can be increased by the addition of hydrogen bonds to the macrocycle, raising the potential to above 0.75 V. However, the presence of the vinyl group on Chl *a* rather than the acetyl group found in BChl *a* limits the possible hydrogen bonds to P680 to those involving the two keto groups. Such hydrogen bonds are weak according to FTIR measurements [20] and their influence on the high midpoint potential of P680 has not been established. Another factor is the weaker coupling of P680 compared to P865 due to their structural differences. A preferential localization of the unpaired electron of P680$^{\bullet+}$ is observed that is attributed to an asymmetry in the energies of the two Chls of P680 [77, 78]. This asymmetry is calculated to be partially due to differences in the electrostatic interactions with the surrounding protein with residues Asp D1-61, Asn D1-181, Asn D1-298, His D2-61, Arg D2-180, and Arg D2-294 having critical contributions. The Hückel model predicts that the P680/P680$^{\bullet+}$ midpoint potential is correlated to the electron spin distribution and that the weaker coupling of P680 should increase the potential by ~0.1 V.

The high P680/P680$^{\bullet+}$ midpoint potential is required to oxidize water, which occurs through the sequential transfer of four electrons from the Mn_4Ca cluster, which becomes systematically oxidized during the S cycle. A key property of the Mn_4Ca cluster is that as it becomes more oxidized the oxidation–reduction midpoint potentials associated with the Mn_4Ca cluster remain relatively constant, achieved by coupling electron transfer with proton transfer. This coupling maintains a sufficient driving force for electron transfer to P680 through Y_Z while minimizing unfavorable reactions that would be driven by the presence of highly oxidizing states [79]. None of the oxidation–reduction midpoint potentials associated with the different oxidation states of the Mn_4Ca cluster have been experimentally established although electron transfer considerations suggest values near 1 V [20, 79].

The ability to manipulate the bacterial reaction center such that it becomes highly oxidizing has provided the opportunity to redesign the protein to have a new Mn cofactor that is capable of performing oxidation–reduction reactions. A binding site for Mn was created in the highly oxidizing reaction centers at a location analogous to that of the Mn_4Ca cluster of photosystem II (Fig. 9.6). As an initial step, the

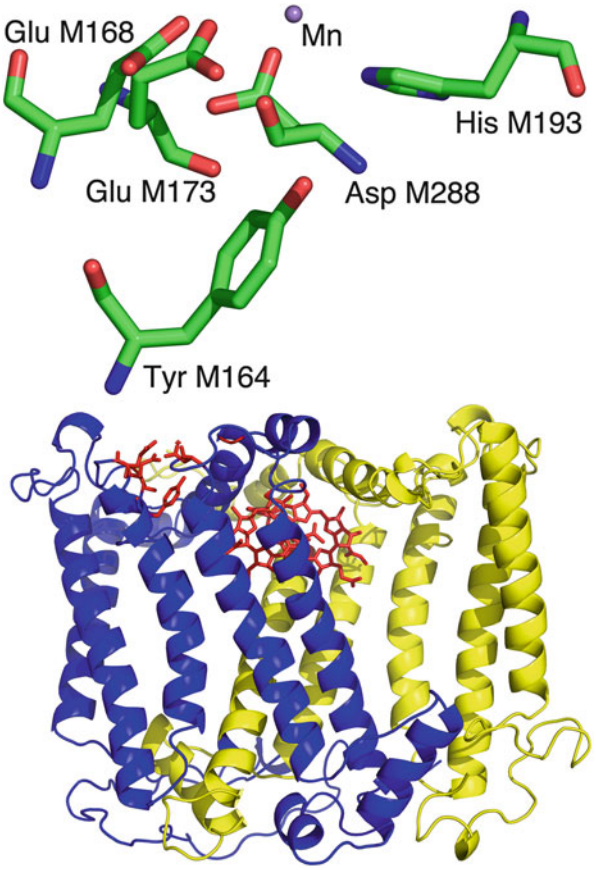

Fig. 9.6 Three-dimensional structure of the Mn-binding bacterial reaction centers. (*Top*) The mononuclear Mn cofactor (*purple sphere*) and several surrounding amino acid residues, Tyr M164, Glu M168, Glu M173, His M193, and Asp M288 (atom type). (*Bottom*) The Mn-binding site is located approximately 10 Å from P865 at a location analogous to the position of the Mn_4Ca cluster of photosystem II. Shown are the L (*yellow*) and M (*blue*) subunits, P865 (*red*), and the amino acid residues forming the Mn-binding site (*red*). Several residues near the binding site in the reaction center, Glu M173, His M193, and Tyr M164, have counterparts in photosystem II, namely, Asp D1-170, His D1-190, and Tyr D1-161, respectively. The three-dimensional structure of the mutant with the bound Mn was determined by X-ray diffraction [57] (PDB file 1Z9J)

introduction of two carboxylates, at M168 and M288, with a tyrosine at M164, produced a site capable of binding a mononuclear Mn cofactor [57, 80]. Several residues near the binding site in the reaction center are conserved including Glu M173, His M193, and Tyr M164 that correspond to Asp D1-170, His D1-190, and Tyr D1-161, respectively, in photosystem II. Electron transfer measurements demonstrate that the Mn cofactor serves as a rapid secondary electron donor to P865. The Mn^{2+}/Mn^{3+} midpoint potential was experimentally determined to be 0.63 V by measuring the equilibrium between the Mn cofactor and $P865^{\bullet+}$ for a series of mutants with different $P865/P865^{\bullet+}$ midpoint potentials [81].

The ability of the Mn cofactor incorporated in bacterial reaction centers to participate in oxidation–reduction reactions was shown by its ability to catalyze oxygen production from superoxide [82]. Light excitation of the Mn-binding reaction centers leads to the Mn^{2+} $P865^{\bullet+}$ Q^{-} charge-separated state that quickly converts to Mn^{3+} P865 Q^{-}. In the presence of superoxide, the Mn^{3+} is reduced to Mn^{2+} and the superoxide is converted into molecular oxygen following the equivalent reactions of Mn-superoxide dismutase. However, Mn-binding reaction centers are not capable of the metal-oxidizing reaction of converting superoxide into hydrogen peroxide, as found in Mn-superoxide dismutase, despite favorable energetics for this process, presumably because of the necessity of coupling this reaction with the transfer of two protons. The continuing investigation of properties of the Mn-binding mutants coupled with intensive studies of the Mn_4Ca cluster should provide an insight into how the midpoint potentials of Mn-cofactors are influenced by protein interactions, in particular how the protein environment poises the Mn_4Ca cluster at the potentials needed to efficiently oxidize water.

References

1. Blankenship RE, Madigan MT, Bauer CE, editors. Anoxygenic photosynthetic bacteria. Dordrecht: Kluwer; 1995.
2. Hunter CN, Daldal F, Thurnauer MC, Beatty JT, editors. The purple phototrophic bacteria. Dordrecht: Springer; 2009.
3. Wydrzynski TJ, Satoh K, editors. Photosystem II: the light-driven water:plastoquinone oxidoreductase. Dordrecht: Springer; 2005.
4. Rutherford AW, Osyczka A, Rappaport F. Back-reactions, short-circuits, leaks and other energy wasteful reactions in biological electron transfer: redox tuning to survive life in O_2. FEBS Lett. 2012;586(5):603–16.
5. Williams JC, Allen JP. Directed modification of reaction centers from purple bacteria. In: Hunter CN, Daldal F, Thurnauer MC, Beatty JT, editors. The purple phototrophic bacteria. Dordrecht: Kluwer; 2009.
6. Deisenhofer J, Epp O, Miki K, Huber R, Michel H. Structure of the protein subunits in the photosynthetic reaction centre of *Rhodopseudomonas viridis* at 3 Å resolution. Nature. 1985;318(6047):618–24.
7. Deisenhofer J, Epp O, Sinning I, Michel H. Crystallographic refinement at 2.3 Å resolution and refined model of the photosynthetic reaction centre from *Rhodopseudomonas viridis*. J Mol Biol. 1995;246(3):429–57.
8. Allen JP, Feher G, Yeates TO, Komiya H, Rees DC. Structure of the reaction center from *Rhodobacter sphaeroides* R-26: the cofactors. Proc Natl Acad Sci U S A. 1987;84(16):5730–4.
9. Chang CH, El-Kabbani O, Tiede D, Norris J, Schiffer M. Structure of the membrane-bound protein photosynthetic reaction center from *Rhodobacter sphaeroides*. Biochemistry. 1991;30 (22):5352–60.
10. Ermler U, Fritzsch G, Buchanan SK, Michel H. Structure of the photosynthetic reaction centre from *Rhodobacter sphaeroides* at 2.65 Å resolution: cofactors and protein-cofactor interactions. Structure. 1994;2(10):925–36.
11. McAuley KE, Fyfe PK, Ridge JP, Isaacs NW, Cogdell RJ, Jones MR. Structural details of an interaction between cardiolipin and an integral membrane protein. Proc Natl Acad Sci U S A. 1999;96(26):14706–11.

12. Camara-Artigas A, Brune D, Allen JP. Interactions between lipids and bacterial reaction centers determined by protein crystallography. Proc Natl Acad Sci U S A. 2002;99 (17):11055–60.
13. Debus RJ, Feher G, Okamura MY. LM complex of reaction centers from *Rhodopseudomonas sphaeroides* R-26: characterization and reconstitution with the H subunit. Biochemistry. 1985;24(10):2488–500.
14. Zouni A, Witt HT, Kern J, Fromme P, Krauss N, Saenger W, Orth P. Crystal structure of photosystem II from *Synechococcus elongatus* at 3.8 Å resolution. Nature. 2001;409 (6821):739–43.
15. Ferreira KN, Iverson TM, Maghlaoui K, Barber J, Iwata S. Architecture of the photosynthetic oxygen-evolving center. Science. 2004;303(5665):1831–8.
16. Loll B, Kern J, Saenger W, Zouni A, Biesiadka J. Towards complete cofactor arrangement in the 3.0 Å resolution structure of photosystem II. Nature. 2005;438(7070):1040–4.
17. Yano J, Kern J, Sauer K, Latimer MJ, Pushkar Y, Biesiadka J, Loll B, Saenger W, Messinger J, Zouni A, Yachandra VK. Where water is oxidized to dioxygen: structure of the photosynthetic Mn_4Ca cluster. Science. 2006;314(5800):821–5.
18. Umena Y, Kawakami K, Shen JR, Kamiya N. Crystal structure of oxygen-evolving photosystem II at a resolution of 1.9 Å. Nature. 2011;473(7345):55–60.
19. Nanba O, Satoh K. Isolation of a photosystem II reaction center consisting of D-1 and D-2 polypeptides and cytochrome *b*-559. Proc Natl Acad Sci U S A. 1987;84(1):109–12.
20. Rappaport F, Diner BA. Primary photochemistry and energetics leading to the oxidation of the $(Mn)_4Ca$ cluster and to the evolution of molecular oxygen in photosystem II. Coord Chem Rev. 2008;252(3–4):259–72.
21. Renger G, Renger T. Photosystem II: the machinery of photosynthetic water splitting. Photosynth Res. 2008;98(1–3):53–80.
22. Grimm B, Porra RJ, Rüdiger W, Scheer H, editors. Chlorophylls and bacteriochlorophylls. Dordrecht: Springer; 2006.
23. Bylina EJ, Kirmaier C, McDowell L, Holten D, Youvan DC. Influence of an amino-acid residue on the optical properties and electron transfer dynamics of a photosynthetic reaction centre complex. Nature. 1988;336(6195):182–4.
24. Breton J, Nabedryk E, Allen JP, Williams JC. Electrostatic influence of Q_A reduction on the IR vibrational mode of the 10a-ester C = O of H_A demonstrated by mutations at residues Glu L104 and Trp L100 in reaction centers from *Rhodobacter sphaeroides*. Biochemistry. 1997;36 (15):4515–25.
25. Dahlbom MG, Reimers JR. Successes and failures of time-dependent density functional theory for the low-lying excited states of chlorophylls. Mol Phys. 2005;103(6–8):1057–65.
26. Rätsep M, Cai ZL, Reimers JR, Freiberg A. Demonstration and interpretation of significant asymmetry in the low-resolution and high-resolution Q_y fluorescence and absorption spectra of bacteriochlorophyll *a*. J Chem Phys. 2011;134(2):024506.
27. Brixner T, Stenger J, Vaswani HM, Cho M, Blankenship RE, Fleming GR. Two-dimensional spectroscopy of electronic couplings in photosynthesis. Nature. 2005;434(7033):625–8.
28. Read EL, Engel GS, Calhoun TR, Mančal T, Ahn TK, Blankenship RE, Fleming GR. Cross-peak-specific two-dimensional electronic spectroscopy. Proc Natl Acad Sci U S A. 2007;104 (36):14203–8.
29. Matthews BW, Fenna RE, Bolognesi MC, Schmid MF, Olson JM. Structure of a bacteriochlorophyll *a*-protein from the green photosynthetic bacterium *Prosthecochloris aestuarii*. J Mol Biol. 1979;131(2):259–85.
30. Tronrud DE, Schmid MF, Matthews BW. Structure and X-ray amino acid sequence of a bacteriochlorophyll *a* protein from *Prosthecochloris aestuarii* refined at 1.9 Å resolution. J Mol Biol. 1986;188(3):443–54.
31. Li YF, Zhou W, Blankenship RE, Allen JP. Crystal structure of the bacteriochlorophyll *a* protein from *Chlorobium tepidum*. J Mol Biol. 1997;271(3):456–71.

32. Ben-Shem A, Frolow F, Nelson N. Evolution of photosystem I-from symmetry through pseudosymmetry to asymmetry. FEBS Lett. 2004;564(3):274–80.
33. Tronrud DE, Wen J, Gay L, Blankenship RE. The structural basis for the difference in absorbance spectra for the FMO antenna protein from various green sulfur bacteria. Photosynth Res. 2009;100(2):79–87.
34. Larson CR, Seng CO, Lauman L, Matthies HJ, Wen J, Blankenship RE, Allen JP. The three-dimensional structure of the FMO protein from *Pelodictyon phaeum* and the implications for energy transfer. Photosynth Res. 2011;107(2):139–50.
35. Watanabe T, Kobayashi M. Electrochemistry of chlorophylls. In: Scheer H, editor. Chlorophylls. Boca Raton, FL: CRC Press; 1991.
36. Kobayashi M, Ohashi S, Iwamoto K, Shiraiwa Y, Kato Y, Watanabe T. Redox potential of chlorophyll *d in vitro*. Biochim Biophys Acta. 2007;1767(6):596–602.
37. Woodbury NW, Allen JP. The pathway, kinetics and thermodynamics of electron transfer in wild type and mutant reaction centers of purple nonsulfur bacteria. In: Blankenship RE, Madigan MT, Bauer CE, editors. Anoxygenic photosynthetic bacteria. Dordrecht: Kluwer; 1995.
38. Wang H, Lin S, Allen JP, Williams JC, Blankert S, Laser C, Woodbury NW. Protein dynamics control the kinetics of initial electron transfer in photosynthesis. Science. 2007;316 (5825):747–50.
39. Moss DA, Leonhard M, Bauscher M, Mäntele W. Electrochemical redox titration of cofactors in the reaction center from *Rhodobacter sphaeroides*. FEBS Lett. 1991;283(1):33–6.
40. Williams JC, Alden RG, Murchison HA, Peloquin JM, Woodbury NW, Allen JP. Effects of mutations near the bacteriochlorophylls in reaction centers from *Rhodobacter sphaeroides*. Biochemistry. 1992;31(45):11029–37.
41. Nagarajan V, Parson WW, Davis D, Schenck CC. Kinetics and free energy gaps of electron-transfer reactions in *Rhodobacter sphaeroides* reaction centers. Biochemistry. 1993;32 (46):12324–36.
42. Lin X, Murchison HA, Nagarajan V, Parson WW, Allen JP, Williams JC. Specific alteration of the oxidation potential of the electron donor in reaction centers from *Rhodobacter sphaeroides*. Proc Natl Acad Sci U S A. 1994;91(22):10265–9.
43. Dutton PL, Petty KM, Bonner HS, Morse SD. Cytochrome c_2 and reaction center of *Rhodopseudomonas sphaeroides* Ga. membranes. Extinction coefficients, content, half-reduction potentials, kinetics, and electric field alterations. Biochim Biophys Acta. 1975;387 (3):536–56.
44. Lin X, Williams JC, Allen JP, Mathis P. Relationship between rate and free energy difference for electron transfer from cytochrome c_2 to the reaction center in *Rhodobacter sphaeroides*. Biochemistry. 1994;33(46):13517–23.
45. Nitschke W, Dracheva SM. Reaction center associated cytochromes. In: Blankenship RE, Madigan MT, Bauer CE, editors. Anoxygenic photosynthetic bacteria. Dordrecht: Kluwer; 1995.
46. Alric J, Cuni A, Maki H, Nagashima KVP, Verméglio A, Rappaport F. Electrostatic interaction between redox cofactors in photosynthetic reaction centers. J Biol Chem. 2004;279 (46):47849–55.
47. Williams JC, Haffa ALM, McCulley JL, Woodbury NW, Allen JP. Electrostatic interactions between charged amino acid residues and the bacteriochlorophyll dimer in reaction centers from *Rhodobacter sphaeroides*. Biochemistry. 2001;40(50):15403–7.
48. Johnson ET, Parson WW. Electrostatic interactions in an integral membrane protein. Biochemistry. 2002;41(20):6483–94.
49. Johnson ET, Müh F, Nabedryk E, Williams JC, Allen JP, Lubitz W, Breton J, Parson WW. Electronic and vibronic coupling of the special pair of bacteriochlorophylls in photosynthetic reaction centers from wild-type and mutant strains of *Rhodobacter sphaeroides*. J Phys Chem B. 2002;106(45):11859–69.
50. Muegge I, Apostolakis J, Ermler U, Fritzsch G, Lubitz W, Knapp EW. Shift of the special pair redox potential: electrostatic energy computations of mutants of the reaction center from *Rhodobacter sphaeroides*. Biochemistry. 1996;35(25):8359–70.

51. Stocker JW, Taguchi AKW, Murchison HA, Woodbury NW, Boxer SG. Spectroscopic and redox properties of sym1 and (M)F195H: *Rhodobacter capsulatus* reaction center symmetry mutants which affect the initial electron donor. Biochemistry. 1992;31(42):10356–62.
52. Murchison HA, Alden RG, Allen JP, Peloquin JM, Taguchi AKW, Woodbury NW, Williams JC. Mutations designed to modify the environment of the primary electron donor of the reaction center from *Rhodobacter sphaeroides*: phenylalanine to leucine at L167 and histidine to phenylalanine at L168. Biochemistry. 1993;32(13):3498–505.
53. Spiedel D, Roszak AW, McKendrick K, McAuley KE, Fyfe PK, Nabedryk E, Breton J, Robert B, Cogdell RJ, Isaacs NW, Jones MR. Tuning of the optical and electrochemical properties of the primary donor bacteriochlorophylls in the reaction centre from *Rhodobacter sphaeroides*: spectroscopy and structure. Biochim Biophys Acta. 2002;1554(1–2):75–93.
54. Arlt T, Bibikova M, Penzkofer H, Oesterhelt D, Zinth W. Strong acceleration of primary photosynthetic electron transfer in a mutated reaction center of *Rhodopseudomonas viridis*. J Phys Chem. 1996;100(29):12060–5.
55. Nabedryk E, Allen JP, Taguchi AKW, Williams JC, Woodbury NW, Breton J. Fourier transform infrared study of the primary electron donor in chromatophores of *Rhodobacter sphaeroides* with reaction centers genetically modified at residues M160 and L131. Biochemistry. 1993;32(50):13879–85.
56. Mattioli TA, Williams JC, Allen JP, Robert B. Changes in primary donor hydrogen-bonding interactions in mutant reaction centers from *Rhodobacter sphaeroides*: identification of the vibrational frequencies of all the conjugated carbonyl groups. Biochemistry. 1994;33(7):1636–43.
57. Thielges M, Uyeda G, Cámara-Artigas A, Kálmán L, Williams JC, Allen JP. Design of a redox-linked active metal site: manganese bound to bacterial reaction centers at a site resembling that of photosystem II. Biochemistry. 2005;44(20):7389–94.
58. Lancaster CRD, Bibikova MV, Sabatino P, Oesterhelt D, Michel H. Structural basis of the drastically increased initial electron transfer rate in the reaction center from a *Rhodopseudomonas viridis* mutant described at 2.00-Å resolution. J Biol Chem. 2000;275 (50):39364–8.
59. Plato M, Lendzian F, Lubitz W, Möbius K. Molecular orbital study of electronic asymmetry in primary donors of bacterial reaction centers. In: Breton J, Verméglio A, editors. The photosynthetic bacterial reaction center II: structure, spectroscopy, and dynamics. New York: Plenum; 1992.
60. Breton J, Nabedryk E, Parson WW. A new infrared electronic transition of the oxidized primary electron donor in bacterial reaction centers: a way to assess resonance interactions between the bacteriochlorophylls. Biochemistry. 1992;31(33):7503–10.
61. Huber M. On the electronic structure of the primary electron donor in bacterial photosynthesis—the bacteriochlorophyll dimer as viewed by EPR/ENDOR methods. Photosynth Res. 1997;52(1):1–26.
62. Rautter J, Lendzian F, Schulz C, Fetsch A, Kuhn M, Lin X, Williams JC, Allen JP, Lubitz W. ENDOR studies of the primary donor cation radical in mutant reaction centers of *Rhodobacter sphaeroides* with altered hydrogen-bond interactions. Biochemistry. 1995;34 (25):8130–43.
63. Artz K, Williams JC, Allen JP, Lendzian F, Rautter J, Lubitz W. Relationship between the oxidation potential and electron spin density of the primary electron donor in reaction centers from *Rhodobacter sphaeroides*. Proc Natl Acad Sci U S A. 1997;94(25):13582–7.
64. Müh F, Lendzian F, Roy M, Williams JC, Allen JP, Lubitz W. Pigment-protein interactions in bacterial reaction centers and their influence on oxidation potential and spin density distribution of the primary donor. J Phys Chem B. 2002;106(12):3226–36.
65. Reimers JR, Hush NS. A unified description of the electrochemical, charge distribution, and spectroscopic properties of the special-pair radical cation in bacterial photosynthesis. J Am Chem Soc. 2004;126(13):4132–44.
66. Bylina EJ, Youvan DC. Directed mutations affecting spectroscopic and electron transfer properties of the primary donor in the photosynthetic reaction center. Proc Natl Acad Sci U S A. 1988;85 (19):7226–30.

67. Kirmaier C, Holten D, Bylina EJ, Youvan DC. Electron transfer in a genetically modified bacterial reaction center containing a heterodimer. Proc Natl Acad Sci U S A. 1988;85 (20):7562–6.
68. McDowell LM, Gaul D, Kirmaier C, Holten D, Schenck CC. Investigation into the source of electron transfer asymmetry in bacterial reaction centers. Biochemistry. 1991;30(34):8315–22.
69. van Brederode ME, van Stokkum IHM, Katilius E, van Mourik F, Jones MR, van Grondelle R. Primary charge separation routes in the BChl:BPhe heterodimer reaction centers of *Rhodobacter sphaeroides*. Biochemistry. 1999;38(23):7545–55.
70. King BA, de Winter A, McAnaney TB, Boxer SG. Excited state energy transfer pathways in photosynthetic reaction centers. 4. Asymmetric energy transfer in the heterodimer mutant. J Phys Chem B. 2001;105(9):1856–62.
71. Camara-Artigas A, Magee C, Goetsch A, Allen JP. The structure of the heterodimer reaction center from *Rhodobacter sphaeroides* at 2.55 Å resolution. Photosynth Res. 2002;74(1):87–93.
72. Allen JP, Artz K, Lin X, Williams JC, Ivancich A, Albouy D, Mattioli TA, Fetsch A, Kuhn M, Lubitz W. Effects of hydrogen bonding to a bacteriochlorophyll-bacteriopheophytin dimer in reaction centers from *Rhodobacter sphaeroides*. Biochemistry. 1996;35(21):6612–9.
73. Zhou H, Boxer SG. Charge resonance effects on electronic absorption line shapes: application to the heterodimer absorption of bacterial photosynthetic reaction centers. J Phys Chem B. 1997;101(29):5759–66.
74. Treynor TP, Andrews SS, Boxer SG. Intervalence band Stark effect of the special pair radical cation in bacterial photosynthetic reaction centers. J Phys Chem B. 2003;107(40):11230–9.
75. Klimov VV, Allakhverdiev SI, Demeter S, Krasnovskii AA. Photoreduction of pheophytin in photosystem 2 of chloroplasts with respect to redox potential of the medium. Dokl Akad Nauk SSSR. 1979;249(1):227–30.
76. Ishikita H, Saenger W, Biesiadka J, Loll B, Knapp EW. How photosynthetic reaction centers control oxidation power in chlorophyll pairs P680, P700, and P870. Proc Natl Acad Sci U S A. 2006;103(26):9855–60.
77. Saito K, Ishida T, Sugiura M, Kawakami K, Umena Y, Kamiya N, Shen JR, Ishikita H. Distribution of the cationic state over the chlorophyll pair of the photosystem II reaction center. J Am Chem Soc. 2011;133(36):14379–88.
78. Takahashi R, Hasegawa K, Noguchi T. Effect of charge distribution over a chlorophyll dimer on the redox potential of P680 in photosystem II as studied by density functional theory calculations. Biochemistry. 2008;47(24):6289–91.
79. Tommos C, Babcock GT. Proton and hydrogen currents in photosynthetic water oxidation. Biochim Biophys Acta. 2000;1458(1):199–219.
80. Kálmán L, Thielges MC, Williams JC, Allen JP. Proton release due to manganese binding and oxidation in modified bacterial reaction centers. Biochemistry. 2005;44(40):13266–73.
81. Kálmán L, Williams JC, Allen JP. Energetics for oxidation of a bound manganese cofactor in modified bacterial reaction centers. Biochemistry. 2011;50(16):3310–20.
82. Allen JP, Olson TL, Oyala P, Lee WJ, Tufts A, Williams JC. Light-driven oxygen production from superoxide by Mn-binding bacterial reaction centers. Proc Natl Acad Sci U S A. 2012;109(7):2314–8.

Part IV
Donor Side Intermediates and Water Splitting

Chapter 10
The Radical Intermediates of Photosystem II

K.V. Lakshmi, Christopher S. Coates, Stuart Smith, and Ruchira Chatterjee

Abstract The solar water-splitting protein complex, photosystem II (PSII), catalyzes one of the most energetically demanding reactions in nature by using light energy to drive the catalytic oxidation of water to dioxygen. Light-driven electron and proton-coupled electron transfer (PCET) reactions, which are exquisitely tuned by smart protein matrix effects, are central to this water-splitting chemistry. PSII contains a series of charge-transfer cofactors, such as the special chlorophylls, pheophytin, primary and secondary plastoquinones, tetranuclear manganese-calcium-oxo cluster, and two symmetrically placed redox-active tyrosine residues, Y_D and Y_Z, that participate in the charge-transfer reactions. These cofactors are functionally very distinct and the versatility is provided by their distinct local environments in PSII. This chapter

This study is supported by the Photosynthetic Systems Program, Office of Basic Energy Sciences, the United States Department of Energy (DE-FG02-07ER15903).

K.V. Lakshmi (✉) • C.S. Coates
Department of Chemistry and Chemical Biology, Rensselaer Polytechnic Institute, 110 8th Street, 12180 Troy, NY, USA

The Baruch '60 Center for Biochemical Solar Energy Research, Rensselaer Polytechnic Institute, 110 8th Street, 12180 Troy, NY, USA
e-mail: lakshk@rpi.edu

S. Smith
Department of Physics, Rensselaer Polytechnic Institute, 12180 Troy, NY, USA

The Baruch '60 Center for Biochemical Solar Energy Research, Rensselaer Polytechnic Institute, 110 8th Street, 12180 Troy, NY, USA

R. Chatterjee
Department of Chemistry and Chemical Biology, Rensselaer Polytechnic Institute, 110 8th Street, 12180 Troy, NY, USA

The Baruch '60 Center for Biochemical Solar Energy Research, Rensselaer Polytechnic Institute, 110 8th Street, 12180 Troy, NY, USA

Physical Biosciences Division, Lawrence Berkeley National Laboratory, 94720 Berkeley, CA, USA

J. Golbeck and A. van der Est (eds.), *The Biophysics of Photosynthesis*, Biophysics for the Life Sciences 11, DOI 10.1007/978-1-4939-1148-6_10,

focuses on providing the reader with an outline of the primary electron transfer reactions of PSII and a description of the structure and function of the charge-transfer cofactors that participate in the primary electron transfer pathway.

Keywords Type II reaction centers • Bacterial reaction center • Photosystem II • Electron transfer • Proton-coupled electron transfer • D1 polypeptide • D2 polypeptide • Primary electron transfer pathway • Oxygen-evolving complex • Mn_4Ca-oxo cluster • Water oxidation • Special chlorophylls • P_{680} • Pheophytin • Plastoquinone • Primary quinone • Secondary quinone • Redox-active tyrosine • EPR spectroscopy • NMR spectroscopy • EXAFS • XANES • FTIR spectroscopy • Optical spectroscopy • Resonance Raman spectroscopy • Mutagenesis

10.1 Introduction

Nature converts solar energy to chemical energy using photosynthesis. In photosynthesis, two photoreactions take place in type II and type I reaction centers prior to carbon fixation in higher plants and cyanobacteria [1–4]. The first photoreaction takes place in the type II photosynthetic reaction center, photosystem II (PSII), where water is oxidized to dioxygen. The second photoreaction occurs in the type I reaction center, photosystem I (PSI), where the reducing equivalents required for the carbon fixation reactions are generated and stored as NADPH or "biohydrogen." The overall equation of oxygenic photosynthesis, where carbon dioxide and water are converted to carbohydrates and dioxygen in the presence of light, is as follows:

$$CO_2 + H_2O + h\nu \rightarrow (CH_2O) + O_2 \tag{10.1}$$

where (CH_2O) represents carbohydrates.

Photosystem II catalyzes one of the most energetically demanding reactions in nature by using light energy to drive the catalytic oxidation of water to dioxygen. PSII is a membrane protein complex that consists of a heterodimer of core polypeptides (D1/D2), an assortment of intrinsic and extrinsic polypeptides, antenna peptides, several redox cofactors, and a catalytic tetranuclear manganese calcium-oxo (Mn_4Ca-oxo) cluster in the oxygen-evolving complex (OEC) (Fig. 10.1) [2, 5, 6]. The photoexcitation of the PSII reaction center results in a series of charge-separation reactions that culminate in the formation of reducing equivalents for further use in photosynthesis [5, 7, 8]. The key components in the transfer of charge equivalents in the primary electron transfer pathway of PSII are the special chlorophyll molecules, P_{680}; pheophytin electron acceptor on the D1 polypeptide, $Pheo_{D1}$; primary and secondary quinones, Q_A and Q_B; catalytic tetranuclear manganese calcium-oxo (Mn_4Ca-oxo) cluster; and the redox-active tyrosine residues, Y_D and Y_Z (Fig. 10.2). These cofactors are assembled to facilitate highly efficient light-driven electron and proton transfer across the thylakoid membrane.

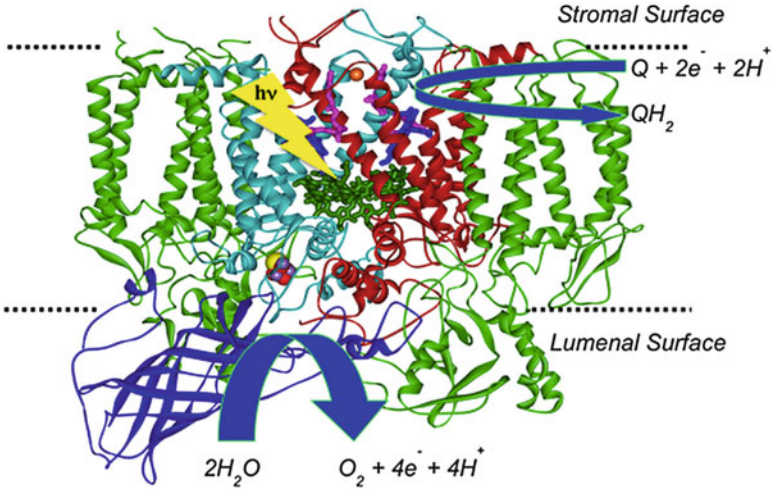

Fig. 10.1 The X-ray crystal structure of PSII from the cyanobacterium, *Thermosynechococcus vulcanus* [28]. The heterodimeric core polypeptide subunits, D1 and D2, are shown in *red* and *cyan*, respectively, the CP43 and CP47 polypeptides are in *green*, and the manganese-stabilizing protein is in *royal blue*. The special chlorophyll cofactors are shown in *green*, the pheophytin molecules are in *blue*, the non-heme Fe(II) center is in *orange*, and the primary and secondary plastoquinones, Q_A and Q_B, are in *pink*. The manganese ions, oxygen atoms, and the calcium ion in the catalytic Mn_4Ca-oxo cluster are shown in *purple*, *red*, and *yellow*, respectively. PDB ID: 3ARC [28]

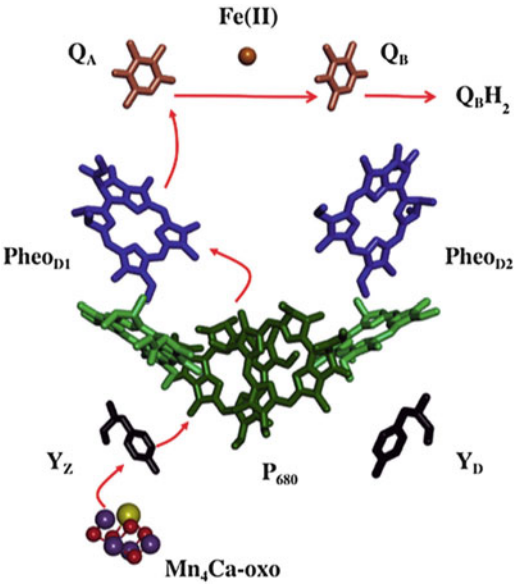

Fig. 10.2 The cofactors that participate in the primary and secondary electron transfer pathway of PSII. The special chlorophyll molecules, P_{680}, are shown in *green*, the pheophytins are in *blue*, the non-heme Fe(II) center is in *orange*, and the primary and secondary plastoquinone acceptors, Q_A and Q_B, are in *brown*. The manganese ions, oxygen atoms, and the calcium ion in the catalytic Mn_4Ca-oxo cluster are shown in *purple*, *red*, and *yellow*, respectively. Please note that the phytyl chains of the Chl a, pheophytin, and quinone cofactors have been omitted for clarity. PDB ID: 3ARC [28]

The primary electron transfer pathway of PSII provides a unique opportunity to investigate the factors that influence in vivo light-induced charge-transfer reactions in a protein matrix. The primary electron transfer pathway (depicted as red arrows in Fig. 10.2) involves the photoexcitation of special chlorophyll molecules, P_{680}, that leads to the formation of the P_{680}^{+}-$Pheo_{D1}^{-}$ charge-separated state. The initial charge separation is rapidly stabilized by forward electron transfer from $Pheo_{D1}^{-}$ to the primary and secondary plastoquinone electron acceptors, Q_A and Q_B, respectively. In turn, the highly oxidizing cationic state of the special chlorophylls, P_{680}^{+}, is reduced by the Mn_4Ca-oxo cluster in the oxygen-evolving complex (OEC) via proton-coupled electron transfer at the redox-active tyrosine residue, Y_Z. Reiteration of these reactions results in the oxidation of water to dioxygen at the Mn_4Ca-oxo cluster in the OEC and the release of reducing equivalents in the form of labile plastoquinols [2, 5, 6, 9].

The structure of PSII, until a decade ago, had been inferred from spectroscopic data that was obtained in conjunction with biochemical and mutagenesis studies. Crucial to the functional organization of the OEC as well as the tuning and control of the redox properties of the charge-transfer cofactors is the role of the surrounding protein environment. Over the years, a wealth of information on the structure and function of the charge-transfer cofactors has been provided by X-ray spectroscopy [10], electron paramagnetic resonance (EPR) spectroscopy [11], optical spectroscopy [12–16], vibrational spectroscopy [17], and quantum mechanical calculations [18]. For example, X-ray absorption near-edge structure (XANES) has been used to address the oxidation state and symmetry of the manganese ions in the Mn_4Ca-oxo cluster in the different S state intermediates of the OEC and X-ray absorption fine structure (EXAFS) has provided information on the number, type, and distances of the amino acid ligands and neighboring manganese atoms in the Mn_4Ca-oxo cluster in the OEC of PSII [19].

In parallel, magnetic resonance spectroscopy methods, such as continuous-wave (*cw*) and pulsed electron paramagnetic resonance (EPR) and nuclear magnetic resonance (NMR) spectroscopy methods, have been widely used to investigate the radical intermediates that are formed in the primary and secondary electron transfer pathways of PSII. It is notable that in the pre-X-ray crystallography era of PSII, the most important information on the location, structure, and function of the charge-transfer cofactors of PSII was provided by *cw* and pulsed EPR spectroscopy. The key EPR spectroscopy measurements of PSII included saturation recovery EPR on the location of the redox-active tyrosine and β-carotene cofactors, Y_Z, Y_D, and β-Car; *cw* and pulsed EPR spectroscopy of the S states of the OEC; pulsed EPR spectroscopy of spin-correlated radical pairs; and *cw* and pulsed EPR spectroscopy of the charge-transfer cofactors, such as Y_Z, Y_D, $Pheo_{D1}$, Q_A, and Q_B [20–23]. In addition, proton NMR relaxation enhancement (NMR-PRE) spectroscopy was used to study the change in the oxidation state of the manganese ions in the Mn_4Ca-oxo cluster during the S state turnover of the OEC [24].

Vibrational spectroscopy methods, such as Fourier transform infrared (FTIR) spectroscopy, have also been extensively used to probe the properties of key amino acid residues and cofactors of PSII [17]. FTIR spectroscopy has provided structural information on the hydrogen-bonding and protonation states of the redox-active tyrosine residues, Y_D and Y_Z, and the S states of the OEC of PSII [17]. It has also provided direct information on the coordination sphere of the Mn_4Ca-oxo cluster [25].

In the past decade, X-ray crystal structures of PSII at 1.9–3.8 Å resolution have begun to play an important role in understanding structure and function of the charge-transfer cofactors of PSII [26–30]. The first X-ray crystal structure of PSII at 3.8 Å resolution was published by Zouni and co-workers in 2001 [26]. Subsequent improvements in the quality of crystals and methodology has allowed for significant enhancement of the resolution of the structures. The recent X-ray crystal structure of PSII at 1.9 Å resolution is a remarkable breakthrough that has allowed for the determination of the geometry of the Mn_4Ca-oxo cluster and the amino acid and water ligands that are coordinated to the catalytic cluster in the dark S_1 state of the OEC [28].

In this chapter, we review the biophysics of the charge-transfer cofactors that participate in the primary electron transfer pathway of PSII which results in light-driven water oxidation and the release of charge equivalents. Our aim is to introduce the reader to the primary electron transfer pathway and describe the unique structural and functional properties of the charge-transfer cofactors.

10.2 The Special Chlorophylls, P_{680}

The special chlorophyll molecules, P_{680}, are located on the lumenal side of the thylakoid membrane and serve as the primary electron donor of PSII [5]. P_{680} was used to be considered a "special pair" of chlorophylls; however, in the past decade a combination of molecular genetics, spectroscopy, and high-resolution X-ray crystallography has demonstrated that P_{680} is a tetrameric pigment complex and the organization of the pigments leads to the unique properties that facilitate the primary photochemistry of PSII [31]. The pigment complex comprises four chlorophyll a (Chl a) molecules (Fig. 10.3) that are ligated to the protein through histidine ligands. The central Chl a molecules, P_{D1} and P_{D2}, have parallel ring planes with a center-to-center distance of 10 Å [28–30]. The 10 Å separation between P_{D1} and P_{D2} weakens the excitonic coupling of the special chlorophylls [32–34]. The accessory Chl a molecules, Chl_{D1} and Chl_{D2}, are located at center-to-center distances of 9.8 Å and 10 Å from P_{D1} and P_{D2}, respectively, and the ring planes are inclined at a 30° angle with respect to the plane of the thylakoid membrane.

The primary photochemistry of PSII is initiated when the reaction center receives a photon with a wavelength of 680 nm (as denoted by the subscript in

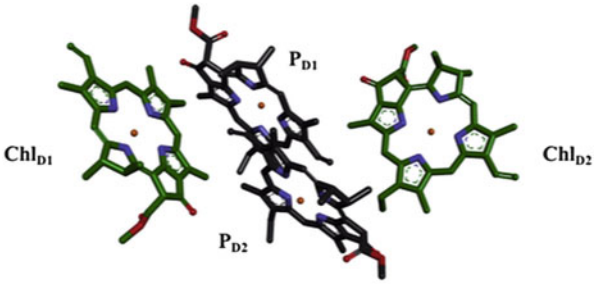

Fig. 10.3 The special chlorophyll molecules that comprise the primary electron donor, P_{680}, of PSII. P_{680} comprises four Chl a molecules, namely the central chlorophylls, P_{D1} and P_{D2}, and the accessory chlorophylls, Chl_{D1} and Chl_{D2} (shown in *green*). Please note that the phytyl chains of the Chl a molecules have been omitted for clarity. PDB ID: 3ARC [28]

"P_{680}") with 1.82 eV energy and P_{680} is photoexcited to P_{680}*. The photoexcited state, P_{680}*, rapidly transfers an electron to a pheophytin acceptor in the D1 polypeptide (Fig. 10.2), $Pheo_{D1}$, which results in the formation of the P_{680}^{+}-$Pheo_{D1}^{-}$ charge-separated pair:

$$P_{680} + h\nu \rightarrow P_{680}^{*} \rightarrow P_{680}^{+}\text{-}Pheo_{D1}^{-} \tag{10.2}$$

In PSII, the oxidation of water to dioxygen is catalyzed by the strong oxidizing power of P_{680}^{+}. In fact, P_{680}^{+} is the most oxidizing species that is known in biology with an oxidation potential of ~1.25 V. It exceeds the oxidizing power of all of the other natural photosynthetic reaction centers by at least 0.5 V and fulfills the energetic prerequisite for the oxidation of water to dioxygen in PSII.

Although the basic principles of photosynthetic reaction centers are very similar and have been highly conserved during evolution, the pigment complex, P_{680}, is unique in its oxidizing power. There are several features that are thought to affect the high oxidation potential of P_{680}^{+}. It has been suggested that the high oxidation potential could be inherent to the pigment molecule, Chl a, that constitutes P_{680}. While it is true that the potential of Chl a is 0.1–0.2 V higher than bacteriochlorophyll a, this is not enough to explain the difference in the oxidation potential of the special chlorophyll and bacteriochlorophyll molecules, P_{680} and P_{870}, of PSII and the bacterial reaction center, respectively [35, 36]. In other studies, the weak electronic coupling between the Chl a molecules of P_{680} has been suggested as the reason for the high oxidation potential of P_{680}^{+} [32–34]. Charge delocalization over the entire pigment complex would reduce the oxidation potential; hence, it is thought that a weak coupling between the Chl a molecules increases the oxidation potential of P_{680} of PSII. It has also been suggested that the surrounding protein environment could lead to the unusually high oxidation potential of P_{680} [31]. The reasons for the unusually high oxidation potential of P_{680}^{+} are yet to be understood and remain a challenge for current and future research.

The key questions on the photochemistry of the special chlorophylls are (1) where is the primary charge separation initiated and (2) is the oxidized cationic state of the primary donor and the triplet state located on the same chlorophyll molecule(s). Initially, differential absorption spectroscopy was used to identify the primary donor (and acceptor) species of PSII [37]. However, it was difficult to characterize the triplet and primary cationic state of P_{680} due to the spectral congestion of the absorbance spectra. Recently, the application of FTIR difference spectroscopy by Noguchi, Breton, and co-workers has demonstrated that the Chl a molecule on which the excited triplet state, $^3P_{680}$, is localized is different from the Chl a molecule(s) on which the primary cationic state, P_{680}^+, is localized [38, 39]. Based on this observation, it has been suggested that the excited and cationic state of P_{680} is the accessory chlorophyll molecule, Chl_{D1}, rather than the central chlorophyll molecules, P_{D1} or P_{D2} (Fig. 10.3) [40]. It is proposed that during photoexcitation of P_{680}, the electronic excitation energy is funneled to the accessory chlorophyll, Chl_{D1}, which is then followed by electron transfer that leads to the formation of the charge-separated state, $Chl_{D1}^+Pheo_{D1}^-$. Subsequently, the hole is transferred from Chl_{D1}^+ to a central chlorophyll molecule, P_{D1}, for charge stabilization. It has been confirmed by biochemical and biophysical studies using mutagenesis [41], FTIR spectroscopy [42, 43], *cw* [44]/pulsed EPR [45] spectroscopy, and density functional theory (DFT) calculations [46] that the excited triplet state is thermally distributed between P_{D1} and Chl_{D1} at room temperature and the electron hole is stabilized on P_{D1}.

10.3 The Primary Pheophytin Acceptor, $Pheo_{D1}$

The primary electron acceptor in PSII is a pheophytin molecule in the D1 polypeptide, $Pheo_{D1}$. The photoexcitation of the special chlorophylls, P_{680}, leads to the formation of the charge-separated pair P_{680}^+-$Pheo_{D1}^-$:

$$P_{680}\text{-}Pheo_{D1} + h\nu \rightarrow P_{680}^*\text{-}Pheo_{D1} \rightarrow P_{680}^+\text{-}Pheo_{D1}^- \qquad (10.3)$$

As can be seen in Fig. 10.4, the structure of the pheophytin acceptor is similar to Chl a except that it is lacking the central Mg^{2+} ion. The pheophytin cofactors, $Pheo_{D1}$ and $Pheo_{D2}$, are located at a center-to-center distance of 10.7 Å and 10.6 Å from Chl_{D1} and Chl_{D2}, respectively, with their head groups perpendicular to the plane of the thylakoid membrane [28–30]. Since the electron-deficient $Pheo_{D1}$ molecule is within van der Waals distance of the photoexcited special chlorophylls, P_{680}^*, this leads to rapid electron transfer from P_{680}^* to $Pheo_{D1}$ (~2 ps) that results in the formation of the reductant, $Pheo_{D1}^-$. Although there are two symmetry-related pheophytin cofactors, $Pheo_{D1}$ and $Pheo_{D2}$, in the D1 and D2 polypeptides of PSII (Fig. 10.2), respectively, it has been demonstrated that the pheophytin

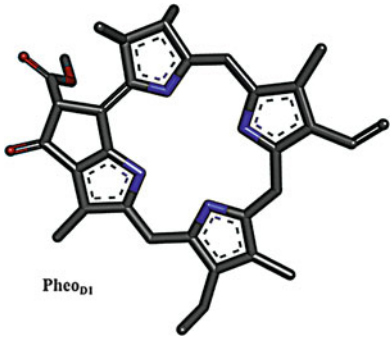

Fig. 10.4 The pheophytin electron acceptor, Pheo$_{D1}$, of PSII. The chemical structure of the pheophytin molecule is similar to Chl a; however, it lacks the central Mg^{2+} ion. Please note that the phytyl chain of the pheophytin cofactor has been omitted for clarity. PDB ID: 3ARC [28]

molecule in the D1 polypeptide, Pheo$_{D1}$, is active in the primary electron transfer pathway of PSII while the corresponding pheophytin in the D2 polypeptide, Pheo$_{D2}$, is inactive in electron transfer [47]. Initial studies had proposed that the difference between the pheophytin cofactor of the active and inactive branch of PSII was that the pheophytin in the active branch, Pheo$_{D1}$, contains a hydrogen bond [37]. However, recent chemical reduction [48] and molecular replacement [49–51] studies demonstrate that both Pheo$_{D1}$ and Pheo$_{D2}$ display Qy absorption maxima at 676–680 nm and Qx transitions at 543 nm. The identical Qx transitions of Pheo$_{D1}$ and Pheo$_{D2}$ suggest the presence of similar hydrogen bonds. This has been confirmed by mutagenesis [37, 52], high-frequency EPR spectroscopy [53] and resonance Raman spectroscopy [54] making this one of the key open questions regarding the pheophytin electron acceptors, Pheo$_{D1}$ and Pheo$_{D2}$, of PSII.

10.4 The Primary and Secondary Quinones, Q_A and Q_B

In the previous sections, we have described the photoexcitation of P_{680} and the formation of the charge-separated state, P_{680}^{+}-Pheo$_{D1}^{-}$. P_{680}^{+} and Pheo$_{D1}^{-}$ are within van der Waals distance of each other which makes Pheo$_{D1}^{-}$ a favorable reductant of P_{680}^{+}. Unfortunately, this could lead to rapid charge recombination that would decrease the efficiency of primary electron transfer in PSII. However, in type II reaction centers, namely, PSII (in higher plants and cyanobacteria) and the bacterial reaction center, the charge recombination problem is solved by the introduction of closely spaced primary and secondary quinone electron acceptors, Q_A and Q_B, respectively. As described in the previous sections, the photoexcitation of P_{680} leads to the rapid formation of the charge-separated state, P_{680}^{+}-Pheo$_{D1}^{-}$. This results in forward electron transfer to the primary and secondary quinone, Q_A and Q_B, respectively. As depicted in Eq. (10.4), this leads to the formation of the P_{680}^{+}-Q_A^{-} and P_{680}^{+}-Q_B^{-} states:

$$\begin{aligned} P_{680}\text{-}Pheo_{D1}\text{-}Q_A\text{-}Q_B + h\nu &\rightarrow P_{680}{}^{*}\text{-}Pheo_{D1}\text{-}Q_A\text{-}Q_B \\ &\rightarrow P_{680}{}^{+}\text{-}Pheo_{D1}{}^{-}\text{-}Q_A\text{-}Q_B \\ &\rightarrow P_{680}{}^{+}\text{-}Pheo_{D1}\text{-}Q_A{}^{-}\text{-}Q_B \\ &\rightarrow P_{680}{}^{+}\text{-}Pheo_{D1}\text{-}Q_A\text{-}Q_B{}^{-} \end{aligned} \quad (10.4)$$

Quinone molecules are commonly utilized as charge-transfer cofactors in a wide variety of reactions that are crucial for photosynthesis and respiration [26, 27, 29, 30, 55–60]. In photosynthetic protein complexes, both type I and type II oxygenic and anoxygenic reaction centers contain quinone cofactors that are known to participate in electron- and proton-transfer reactions. The bacterial reaction center and PSII utilize benzoquinone molecules to facilitate electron transfer and proton-coupled electron transfer (PCET) reactions [26–30, 32, 55–58]. In contrast, PSI uses naphthoquinone molecules for electron transfer reactions [59, 60]. There are significant differences in the function of the quinone cofactors in the different reaction centers. It has been observed that similar quinones can operate at up to 800 mV lower reduction potential when present in type I reaction centers [61–65].

The versatility of the quinone cofactors and the diversity of their biological function are controlled by both intra- and intermolecular interactions. The differences in the functional specificity of quinones are suggested to arise from the structure and location of the quinone cofactor, the geometry of its binding site, and the "smart" matrix effects from the surrounding protein environment that greatly influence the charge-transfer properties [63]. It has been suggested that the features that tune and control the charge-transfer properties of the Q_A and Q_B cofactors of PSII are (1) π stacking and hydrophobic interactions with amino acid side chains or lipid molecules [30, 66, 67], (2) hydrogen (H–) bonds with neighboring amino acid residues [68], (3) the presence of the non-heme Fe(II) center in close proximity [66], and (4) the orientation of the isoprenoid tail of the plastoquinone molecule [69]. Therefore, knowledge of the electronic structure and its correlation with the chemical structure of the quinones as well as the interaction with the local protein environment is important to understand the versatility of quinone function in photosynthesis.

PSII contains identical plastoquinone molecules in the primary, Q_A, and secondary, Q_B, site that are symmetrically located on either side of the non-heme iron (Fig. 10.5) [28–30]. The quinone cofactors of PSII exhibit very different charge-transfer properties; Q_A is a single-electron acceptor while Q_B is a two-electron, two-proton acceptor that undergoes PCET reactions [29, 67, 70]. Q_A is fixed and non-exchangeable in a relatively hydrophobic environment and is unable to undergo protonation. However, Q_B is labile and is located in a hydrophilic environment comprising ionizable amino acids and water molecules that are able to deliver protons.

The symmetrical quinones, Q_A and Q_B, are each pinned in position by H-bonds to both of the carbonyl groups of each quinone ring. Further, there are additional (multiple) H-bonds to the distal carbonyl group of Q_B [28, 71]. These additional H-bonds presumably stabilize the $Q_B{}^{-}$ semiquinone relative to $Q_A{}^{-}$ and thus contribute to the driving force required for forward electron transfer. The additional

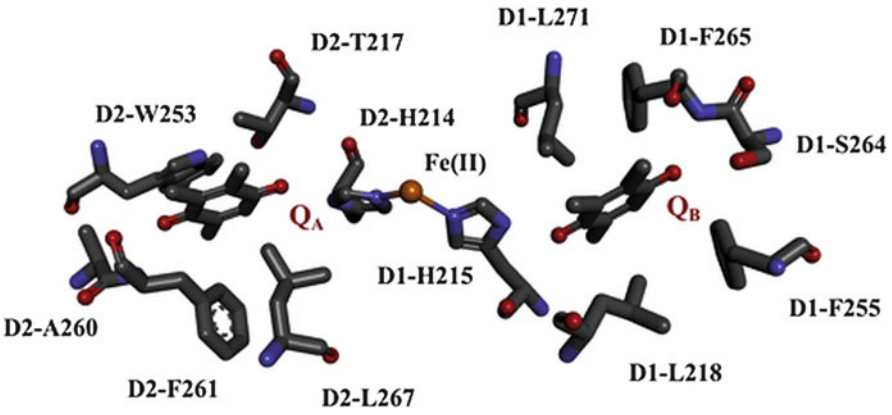

Fig. 10.5 The binding site of Q_A and Q_B electron acceptors of PSII with the neighboring amino acid residues that participate in π stacking, hydrophobic and hydrogen bond interactions with the quinones, Q_A and Q_B. Please note that the isoprenoid chains of the quinone molecules have been omitted for clarity. PDB ID: 3ARC [28]

H-bonds may help in regulating electron transfer and stabilizing Q_B^- without allowing protonation. The proximal carbonyl group of the two quinones is involved in H-bonds with the histidine residues that are ligated to the non-heme iron (Fig. 10.5) [28–30]. The Q_A–D2-H214–Fe(II)–D1-H215–Q_B pattern appears to be a good structure for electron transfer, with the two quinones held at an edge-to-edge distance of 13 Å. However, it is important to note that the non-heme Fe(II) center does not participate in electron transfer between the primary and secondary quinones, Q_A and Q_B. The actual rates of electron transfer (400 μs–1 ms) are much slower than the theoretical rates of ~0.4 μs based on the distance between the quinone electron acceptors [72]. This is thought to be due to possible conformational rearrangement of the quinone, the protein environment, and proton-transfer reactions. Once Q_A is reduced to Q_A^-, the electrons are transferred to Q_B in 400 μs but in the presence of reduced Q_B^-, Q_A^- transfers an electron more slowly, at 0.6–0.8 ms [73]. The Q_A^--to-Q_B electron transfer is likely limited by rearrangements in the Q_B-binding site, the formation of H bonds, protonation of protein groups close to Q_B^-, and conformational changes in the protein. The reasons for the slower rate of electron transfer from Q_A^- to Q_B/Q_B^- still remain an open question.

10.5 The Redox-Active Tyrosine Residues, Tyrosine Z and Tyrosine D

Photosystem II contains two symmetrically placed redox-active tyrosine residues, Y_D and Y_Z, one on each subunit of the heterodimeric polypeptide core (Figs. 10.2 and 10.8a, b). Both tyrosine residues, Y_Z and Y_D, undergo light-driven PCET reactions

and site-directed mutagenesis has implicated the histidine residues, D1-H190 and D2-H189, as the immediate proton acceptors for Y_Z and Y_D, respectively. The Y_Z residue is in close proximity with the Mn_4Ca-oxo cluster, while the symmetrically placed Y_D residue is distant from the OEC. The function of the symmetry-related tyrosine residues is quite distinct as the smart matrix effects from the surrounding protein environment are thought to greatly influence tyrosine function in PSII. The Y_Z residue is kinetically competent and is directly involved in the PCET reactions of the light-driven water oxidation reaction of PSII [74, 75]. In contrast, it is proposed that the PCET redox at Y_D poises the catalytic Mn_4Ca-oxo cluster [76] and may electrostatically tune the adjacent monomeric redox-active chlorophyll and β-carotene in the secondary electron transfer pathway of PSII [31, 77]. The Y_D residue is also considered to be a generator of a positive charge in a hydrophobic environment that could be potentially important for accelerating the kinetics of Y_Z oxidation [32].

Although both Y_Z and Y_D undergo light-driven PCET reactions in PSII, the recent 1.9 Å X-ray crystal structure of PSII highlights differences in the surrounding protein environment of these residues (Fig. 10.6a, b) [28]. The PCET reactions at the Y_Z residue are thought to involve electron transfer to P_{680}^+ and proton transfer to D1-H190. The results of the recent X-ray crystal structure clearly support the existence of a H-bond between Y_Z and D1-H190 (Fig. 10.6b) [28]. It is important to note that the p*K*a values of the reduced and oxidized forms of tyrosine are very different, 10 and −2, respectively [78], so it is likely that the Y_Z residue will both gain a proton upon reduction and lose a proton upon oxidation. The presence of PCET at the Y_Z residue has been confirmed by isotope effect and pH-dependent studies [79–83]. Babcock and co-workers had previously proposed a hydrogen-abstraction hypothesis for PCET at Y_Z [75]. A concerted electron/proton-transfer mechanism has also been proposed from thermodynamic analysis in manganese-depleted PSII. In contrast, Nugent and co-workers have suggested that Y_Z exists as a tyrosinate [84]. The nanosecond H/D kinetic isotope effect of Y_Z oxidation in the intact OEC is almost unity [80, 85, 86]. This observation is in agreement with the presence of a hydrogen-bonding network that is stabilized by the Mn_4Ca-oxo cluster that further facilitates proton movement around Y_Z (Fig. 10.6b) [87–91]. Since Y_Z may be photooxidized at very low temperatures, at least in the lower S states of the OEC, it has been suggested that the Y_Z side chain accepts and releases its proton via a hydrogen bond [28, 92, 93]. This is similar to the Y_D residue [94–97]; however, it is not known whether Y_Z^- is really protonated or not. It may be that the proton, both in the oxidized and in the reduced states of the Y_Z residue, is located somewhere between the phenolic oxygen and its hydrogen-bonding partner. There exists another hypothesis where during the S-state transition the same proton might remain near Y_Z, moving only the small distance between Y_Z and D1-H190 according to the redox state of Y_Z. This mechanism has been supported by optical spectroscopy and proton release measurements [86, 98–102]. Currently, there is a vast body of research that is being conducted to elucidate the mechanism of PCET at the Y_Z and Y_D residues of PSII.

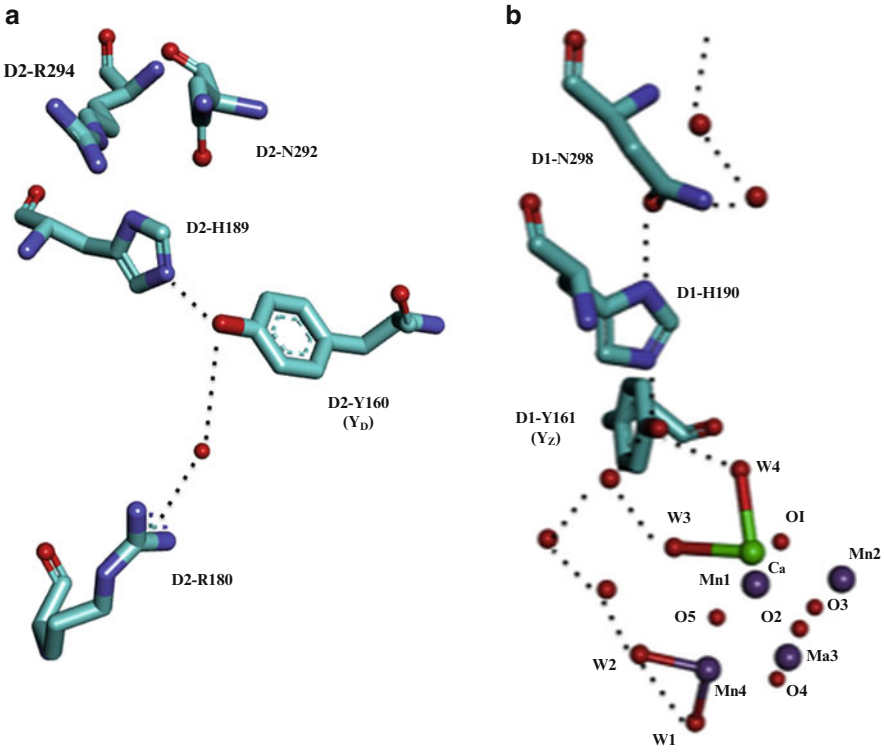

Fig. 10.6 The structure and environment of the redox-active tyrosine residues (**a**) Y_D and (**b**) Y_Z of PSII. Also shown are the water molecules that are present in proximity of the Y_D and Y_Z residues. PDB ID: 3ARC [28]

10.6 The Tetranuclear Manganese-Calcium-Oxo (Mn_4Ca-Oxo) Cluster

The photoexcitation of P_{680} results in the rapid formation of the charge-separated state, P_{680}^{+}-$Pheo_{D1}^{-}$, that is stabilized by forward electron transfer that results in the P_{680}^{+}-$Pheo_{D1}$-Q_A^{-}-Q_B and P_{680}^{+}-$Pheo_{D1}$-Q_A-Q_B^{-} states. As we have discussed previously, P_{680}^{+} is a strong oxidant that renders it competent for water oxidation. The hole on P_{680}^{+} is rapidly re-reduced by electron transfer from the Mn_4Ca-oxo cluster (Fig. 10.7) via the redox-active tyrosine residue, Y_Z, in the oxygen-evolving complex (OEC) of PSII (Fig. 10.2) [28–30].

During the light-driven water oxidation reaction of PSII, the catalytic Mn_4Ca-oxo cluster cycles through five intermediate S (or charge-storage) states, S_0–S_4, in the Kok cycle that result in the oxidation of two substrate water molecules to dioxygen (Fig. 10.8) [103]. The S_1 state is the dark-stable ground state of the OEC of PSII. Each S-state transition (with the exception of the S_4-to-S_0 transition)

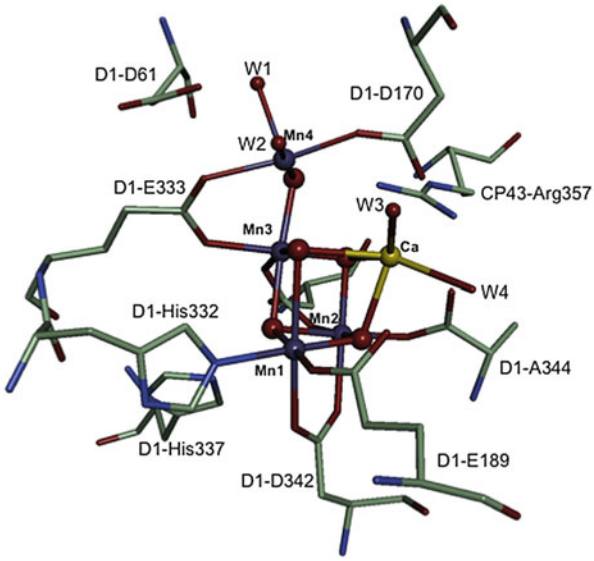

Fig. 10.7 The structure of the Mn_4Ca-oxo cluster and its ligand environment in the OEC of PSII. The manganese ions are shown in *purple*, calcium in *yellow*, and oxygen in *red*. PDB ID: 3ARC [28]

is induced by the photochemical oxidation of the special chlorophylls, P_{680}, and involves electron- or proton-coupled electron transfer (PCET) reaction(s).

There has been immense interest in elucidating the molecular and electronic structure of the OEC of PSII and, in particular, the fate of the substrate water molecules and the Mn_4Ca-oxo cluster in each of the S-state intermediates to understand the requirements for minimizing the energetic penalty for solar water oxidation. The OEC of PSII has been studied extensively by structural, spectroscopic, biochemical, and computational methods [10, 18, 25–30, 104–111]. While single-crystal X-ray diffraction has provided important insight into the molecular geometry of the OEC in the stable S_1 state [26, 27, 29, 30, 67], a high-resolution structure of the S_1 state was obtained recently after dramatic improvements in sample preparation and methodology [28].

Based on the recent 1.9 Å resolution X-ray crystal structure of PSII [28], the Mn_4Ca-oxo cluster consists of three manganese ions and a calcium ion that form a distorted cubane with μ-oxo bridges and a fourth manganese ion that is a dangler that is also linked to the distorted cubane through a μ-oxo bridge (Fig. 10.7) [28]. The major breakthrough of the 1.9 Å resolution X-ray crystal structure was the identification of some of the ligands of the Mn_4Ca-oxo cluster including the μ-oxo oxygen atoms that are coordinated to the metal ions. Most importantly, four water molecules were identified among the ligands: two water molecules that are ligated to the dangler manganese ion and the other two water molecules that are ligated to the Ca^{2+} ion in the S_1 state of the OEC [28]. The X-ray crystal structure has been further refined using advanced density functional theory (DFT) calculations [112].

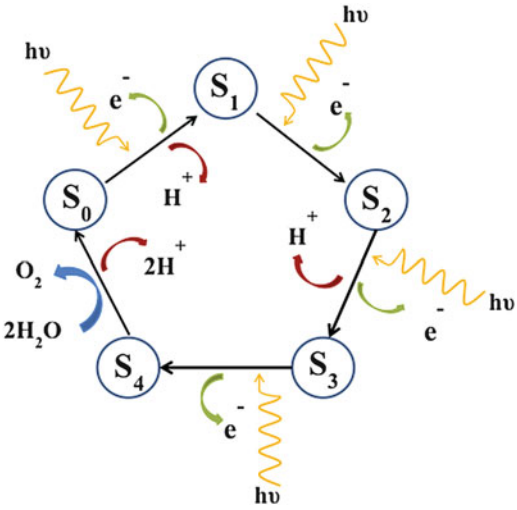

Fig. 10.8 The catalytic S- (or charge-storage) state cycle of the OEC of PSII [103]. Each S-state transition involves the absorption of a photon and the transfer of an electron and/or proton. The final S_4-to-S_0 state transition results in O–O bond formation and the release of dioxygen

The structure of the S-state intermediates of the OEC has also been investigated by electron paramagnetic resonance (EPR), electron nuclear double resonance (ENDOR), electron spin echo envelope modulation (ESEEM), X-ray absorption, and Fourier transform infrared (FTIR) spectroscopy [25, 108, 109, 111, 113–119]. X-ray spectroscopy has provided measurements of the metal-to-metal distances in the Mn_4Ca-oxo cluster. In conjunction with X-ray diffraction, EPR, and X-ray spectroscopy, recent DFT and quantum mechanical/molecular modeling (QM/MM) studies have proposed several mechanisms for substrate activation and water oxidation in the OEC of PSII [18, 110, 120–122]. Although there have been detailed proposals for the mechanism of solar water oxidation in PSII, there is little experimental data available on the structure and activation of the bound water molecules in the OEC of PSII. Further, there is also a lack of structural data on the bound water molecules in the higher S-state photochemical intermediates of the catalytic Mn_4Ca-oxo cluster. This is especially difficult as the higher S states are transient and have limited stability. While X-ray absorption spectroscopy is highly sensitive to the location of the metal ions, it is not suited to probe the location of the water molecules in the OEC of PSII. Other techniques, such as FTIR and conventional EPR spectroscopy, have also yielded limited structural information.

In an exciting development, recent two-dimensional (2D) hyperfine sublevel correlation (HYSCORE) spectroscopy studies by Lakshmi and co-workers have detected weak magnetic interactions between the paramagnetic Mn_4Ca-oxo cluster of the S_2 state of the OEC (Fig. 10.8) and the surrounding proton and nitrogen atoms [123, 124]. These studies have unambiguously identified the structure and location of the bound substrate water in the S_2 state of the OEC that interact with the Mn_4Ca-oxo cluster. In addition, these studies also identify the nitrogen atoms of amino acids that are in close proximity of the Mn_4Ca-oxo cluster in the S_2 state of the OEC. This makes for an interesting comparison of the structure of the OEC in the S_1 and S_2 intermediates that are obtained from the 1.9 A X-ray crystal structure [28] and 2D HYSCORE spectroscopy [123, 124], respectively.

10.7 Conclusions

In this chapter, we describe the role of the charge-transfer cofactors that are involved in the primary electron transfer pathway that results in the water oxidation reaction of PSII. Water oxidation is one of the most energetically demanding reactions, and as such it has a set of very stringent requirements. First, the oxidation of water requires a dauntingly large potential of ~1.25 V. Second, the oxidation of two molecules of water to dioxygen is a four-electron reaction, Eq. (10.5), which requires multi-step, multi-electron transfers and the storage of oxidizing equivalents. This is particularly difficult to accomplish, as each redox reaction must alter the potential of the respective cofactors so as to minimize reverse transport of the electron or hole that could lead to recombination. Third, in order to keep the OEC from accumulating positive charge during the Kok S-state cycle [103], there is a need for efficient redox leveling during the water oxidation reaction:

$$2H_2O + h\nu \rightarrow O_2 + 4e^- + 4H^+ \tag{10.5}$$

All of these requirements are most elegantly fulfilled by the charge-transfer cofactors of PSII (Fig. 10.2). The primary photochemistry of PSII leads to the generation of a highly oxidizing hole, P_{680}^+, which is the only naturally occurring chemical species that is capable of initiating the water oxidation reaction. Next, the multi-step, multi-electron reactions of PSII are conducted through a series of cofactors (the special chlorophyll molecules, P_{680}; pheophytin electron acceptor on the D1 polypeptide, $Pheo_{D1}$; primary and secondary quinones, Q_A and Q_B; redox-active tyrosine residues, Y_Z; and the catalytic Mn_4Ca-oxo cluster that are described in this chapter). These cofactors (a) are optimally tuned for downhill electron transfer and (b) minimize recombination of the initial charge-separated state, P_{680}^+-$Pheo_{D1}^-$, through rapid forward electron transfer. This is possible as the time scales of the primary charge separation and subsequent forward electron transfer reactions are estimated to be in the picosecond and microsecond range, respectively. In contrast, charge recombination between Q_A^- or Q_B^- and P_{680}^+ is thought to be on the order of milliseconds, which is at least 10^3 times slower than the individual forward electron transfer reactions. The multi-electron ($4e^-$) transfers in Eq. (10.5) are facilitated by the storage of oxidizing equivalents on the manganese ions in the Mn_4Ca-oxo cluster where the manganese ion(s) advances (advance) through several oxidation states. Thus, the storage of charge equivalents on the Mn_4Ca-oxo cluster efficiently couples the one-electron photochemistry of the primary charge separation with the four-electron redox chemistry that is absolutely vital for water oxidation in the OEC of PSII. Last but not least, the redox leveling that minimizes the energetic penalty for multi-electron transfers from the OEC is achieved by the highly efficient PCET reactions that are conducted at the redox-active tyrosine residue, Y_Z, and the Mn_4Ca-oxo cluster of PSII. Every part of this complex sequence of events has a vital niche in the

water oxidation reaction. Even if the cofactors themselves are unaltered, miniscule changes in the environment could bring the entire reaction to a halt.

In order to describe the role of the charge-transfer cofactors in the water oxidation reaction, we present recent studies that were conducted on P_{680}, $Pheo_{D1}$, Q_A, Q_B, Y_D, Y_Z, and the Mn_4Ca-oxo cluster of PSII. In the past decade, we recognized that the charge-transfer cofactors of PSII are exquisitely tuned by smart matrix effects of the surrounding protein environment. This has led to progress in understanding the functional tuning of these cofactors, which is an ongoing effort. As mentioned in the preceding sections, there are several open questions regarding the highly oxidizing nature of P_{680}, $Pheo_{D1}$ in the active branch, the difference in the redox properties of Q_A and Q_B, the mechanism of PCET at Y_Z, and the structure and activation of the substrate water molecules in the OEC of PSII. In the future, a combination of the high-resolution X-ray crystal structures of PSII and advances in spectroscopic techniques are promising for the study of the higher oxidation state intermediates of the OEC. This is important for the elucidation of the mechanism of water oxidation in PSII.

References

1. Blankenship RE. Molecular mechanisms of photosynthesis. Oxford: Blackwell; 2002.
2. McEvoy JP, Brudvig GW. Water-splitting chemistry of photosystem II. Chem Rev. 2006;106:4455–83.
3. Nicholls DG, Ferguson SJ. Bioenergetics 3. New York: Academic Press; 2002.
4. Blankenship RE. Origin and early evolution of photosynthesis. Photosynth Res. 1992;33:91–111.
5. Debus RJ. The manganese and calcium-ions of photosynthetic oxygen evolution. Biochim Biophys Acta. 1992;1102:269–352.
6. Tommos C, Babcock GT. Oxygen production in nature: a light-driven metalloradical enzyme process. Acc Chem Res. 1998;31:18–25.
7. Iverson TM. Evolution and unique bioenergetic mechanisms in oxygenic photosynthesis. Curr Opin Chem Biol. 2006;10:91–100.
8. Barber J, Anderson JM. Photosystem II: molecular structure and function—introduction. Philos Trans R Soc Lond B Biol Sci. 2002;357:1325–8.
9. Hansson O, Wydrzynski T. Current perceptions of photosystem-II. Photosynth Res. 1990;23:131–62.
10. Yachandra VK, Sauer K, Klein MP. Manganese cluster in photosynthesis: where plants oxidize water to dioxygen. Chem Rev. 1996;96:2927–50.
11. Miller AF, Brudvig GW. A guide to electron-paramagnetic resonance spectroscopy of photosystem II membranes. Biochim Biophys Acta. 1991;1056:1–18.
12. Schlodder E. Introduction to optical methods in photosynthesis. Photosynth Res. 2009;101:93–104.
13. Novoderezhkin V, Romero E, Dekker J, van Grondelle R. Multiple charge-separation pathways in photosystem II: modeling of transient absorption kinetics. Chemphyschem. 2011;12:681–8.
14. van Mieghem F, Brettel K, Hillmann B, Kamlowski A, Rutherford A, Schlodder E. Charge recombination reactions in photosystem II. 1. Yields, recombination pathways, and kinetics of the primary pair. Biochemistry. 1995;34:4798–813.

15. Hillmann B, Brettel K, Van Mieghem F, Kamlowski A, Rutherford A, Schlodder E. Charge recombination reactions in photosystem-II. 2. Transient absorbency difference spectra and their temperature dependence. Biochemistry. 1995;34:4814–27.
16. Lewis K, Oglivie J. Probing photosynthetic energy and charge transfer with two dimensional electronic spectroscopy. J Phys Chem Lett. 2012;3:503–10.
17. Berthomieu C, Hienerwadel R. Fourier transform infrared (FTIR) spectroscopy. Photosynth Res. 2009;101:157–70.
18. Sproviero EM, Gascon JA, McEvoy JP, Brudvig GW, Batista VS. Computational studies of the O_2-evolving complex of photosystem II and biomimetic oxomanganese complexes. Coord Chem Rev. 2008;252:395–415.
19. Yano J, Yachandra VK. X-ray absorption spectroscopy. Photosynth Res. 2009;102:241–54.
20. Lakshmi KV, Brudvig GW. Pulsed electron paramagnetic resonance methods for macromolecular structure determination. Curr Opin Struct Biol. 2001;11:523–31.
21. Lakshmi KV, Brudvig GW. Electron paramagnetic resonance distance measurements in photosynthetic reaction centers. In: Berliner LJ, Eaton SS, Eaton GR, editors. Biological magnetic resonance: distance measurements in biological systems by EPR. New York: Kluwer Academic/Plenum Publishers; 2000. p. 513–67.
22. Stehlik D, Mobius K. New EPR methods for investigating photoprocesses with paramagnetic intermediates. Annu Rev Phys Chem. 1997;48:745–84.
23. Prisner T, Rohrer M, MacMillan F. Pulsed EPR spectroscopy: biological applications. Annu Rev Phys Chem. 2001;52:279–313.
24. Bovet JM, Park EJ, Sharp RR. NMR paramagnetic relaxation enhancements due to manganese in the S_0 and S_2 states of photosystem II-enriched membrane-fragments and in the detergent-solubilized photosystem II complex. Photosynth Res. 1993;38:347–54.
25. Chu HA, Hillier W, Law NA, Babcock GT. Vibrational spectroscopy of the oxygenevolving complex and of manganese model compounds. Biochim Biophys Acta. 2001;1503:69–82.
26. Zouni A, Witt HT, Kern J, Fromme P, Krauss N, Saenger W, Orth P. Crystal structure of photosystem II from Synechococcus elongatus at 3.8 angstrom resolution. Nature. 2001;409:739–43.
27. Kamiya N, Shen JR. Crystal structure of oxygen-evolving photosystem II from Thermosynechococcus vulcanus at 3.7 angstrom resolution. Proc Natl Acad Sci U S A. 2003;100:98–103.
28. Umena Y, Kawakami K, Shen JR, Kamiya N. Crystal structure of oxygen-evolving photosystem II at a resolution of 1.9 angstrom. Nature. 2011;473:55–60.
29. Ferreira KN, Iverson TM, Maghlaoui K, Barber J, Iwata S. Architecture of the photosynthetic oxygen-evolving center. Science. 2004;303:1831–8.
30. Loll B, Kern J, Saenger W, Zouni A, Biesiadka J. Towards complete cofactor arrangement in the 3.0 angstrom resolution structure of photosystem II. Nature. 2005;438:1040–4.
31. Diner BA, Rappaport F. Structure, dynamics, and energetics of the primary photochemistry of photosystem II of oxygenic photosynthesis. Annu Rev Plant Biol. 2002;53:551–80.
32. Rutherford AW, Faller P. Photosystem II: evolutionary perspectives. Philos Trans R Soc Lond B Biol Sci. 2003;358:245–53.
33. Lubitz W, Lendzian F, Bittl R. Radicals, radical pairs and triplet states in photosynthesis. Acc Chem Res. 2002;35:313–20.
34. Renger G, Holzwarth AR. Primary electron transfer. In: Wydrzynski TJ, Satoh K, editors. The light-driven water/plastoquinone oxidoreductase. Dordrecht, The Netherlands: Kluwer; 2005. p. 139–75.
35. Seely GR. Energetics of electron-transfer reactions of chlorophyll and other compounds. Photochem Photobiol. 1978;27:639–54.
36. Watanabe T, Kobayashi M. Electrochemistry of chlorophylls. In: Scheer H, editor. Chlorophylls. Boca Raton, FL: CRC Press; 1991. p. 287–315.
37. Moenneloccoz P, Robert B, Lutz M. A resonance Raman characterization of the primary electron-acceptor in photosystem II. Biochemistry. 1989;28:3641–5.

38. Noguchi T, Tomo T, Inoue Y. Fourier transform infrared study of the cation radical of P_{680} in the photosystem II reaction center: evidence for charge delocalization on the chlorophyll dimer. Biochemistry. 1998;37:13614–25.
39. Sarcina M, Breton J, Nabedryk E, Diner BA, Nixon PJ. FTIR studies on the P_{680} cation and triplet states in WT and mutant PSII reaction centres of Synechocystis 6803. In: Garab G, editor. XIth international congress on photosynthesis—mechanisms and effects. Budapest, Hungary, Vol I–V. 1998;1053–56.
40. Raszewski G, Saenger W, Renger T. Theory of optical spectra of photosystem II reaction centers: location of the triplet state and the identity of the primary electron donor. Biophys J. 2005;88:986–98.
41. Diner BA, Schlodder E, Nixon PJ, Coleman WJ, Rappaport F, Lavergne J, Vermaas WFJ, Chisholm DA. Site-directed mutations at D1-His198 and D2-His97 of photosystem II in Synechocystis PCC 6803: sites of primary charge separation and cation and triplet stabilization. Biochemistry. 2001;40:9265–81.
42. Noguchi T, Inoue Y, Satoh K. FT-IR studies on the triplet-state of P_{680} in the photosystem II reaction center: triplet equilibrium within a chlorophyll dimer. Biochemistry. 1993;32:7186–95.
43. Okubo T, Tomo T, Sugiura M, Noguchi T. Perturbation of the structure of P_{680} and the charge distribution on its radical cation in isolated reaction center complexes of photosystem II as revealed by Fourier transform infrared spectroscopy. Biochemistry. 2007;46:4390–7.
44. Kamlowski A, Frankemoller L, van der Est A, Stehlik D, Holzwarth L. Evidence for delocalization of the triplet state $^3P_{680}$ in the D1-D2-Cyt b_{559} complex of photosystem II. Phys Chem Chem Phys. 1996;100:2045–51.
45. Zech SG, Kurreck J, Eckert HJ, Renger G, Lubitz W, Bittl R. Pulsed EPR measurement of the distance between P_{680}^+.and Q_A^-.in photosystem II. FEBS Lett. 1997;414:454–6.
46. Takahashi R, Hasegawa K, Noguchi T. Effect of charge distribution over a chlorophyll dimer on the redox potential of P_{680} in photosystem II as studied by density functional theory calculations. Biochemistry. 2008;47:6289–91.
47. Mimuro M, Tomo T, Nishimura Y, Yamazaki I, Satoh K. Identification of a photochemically inactive pheophytin molecule in the spinach D1-D2-Cyt b_{559} complex. Biochim Biophys Acta. 1995;1232:81–8.
48. Shkuropatov AY, Khatypov RA, Volshchukova TS, Shkuropatova VA, Owens TG, Shuvalov VA. Spectral and photochemical properties of borohydride-treated D1-D2-Cyt b_{559} complex of photosystem II. FEBS Lett. 1997;420:171–4.
49. Germano M, Shkuropatov AY, Permentier H, de Wijn R, Hoff AJ, Shuvalov VA, van Gorkom HJ. Pigment organization and their interactions in reaction centers of photosystem II: optical spectroscopy at 6 K of reaction centers with modified pheophytin composition. Biochemistry. 2001;40:11472–82.
50. Germano M, Shkuropatov AY, Permentier H, Khatypov RA, Shuvalov VA, Hoff AJ, Van Gorkom HJ. Selective replacement of the active and inactive pheophytin in reaction centres of Photosystem II by 131-deoxo-131-hydroxy-pheophytin a and comparison of their 6 K absorption spectra. Photosynth Res. 2000;64:189–98.
51. Shkuropatov AY, Khatypov RA, Shkuropatova VA, Zvereva MG, Owens TG, Shuvalov VA. Reaction centers of photosystem II with a chemically-modified pigment composition: exchange of pheophytins with 131-deoxo-131-hydroxy-pheophytin a. FEBS Lett. 1999;450:163–7.
52. Giorgi LB, Nixon PJ, Merry SAP, Joseph DM, Durrant JR, Rivas JD, Barber J, Porter G, Klug DR. Comparison of primary charge separation in the photosystem II reaction center complex isolated from wild-type and D1-E130 mutants of the cyanobacterium Synechocystis PCC 6803. J Biol Chem. 1996;271:2093–101.
53. Dorlet P, Xiong L, Sayre RT, Un S. High field EPR study of the pheophytin anion radical in wild type and D1-E130 mutants of photosystem II in Chlamydomonas reinhardtii. J Biol Chem. 2001;276:22313–6.

54. Germano M, Pascal A, Shkuropatov AY, Robert B, Hoff AJ, van Gorkom HJ. Pheophytin-protein interactions in photosystem II studied by resonance Raman spectroscopy of modified reaction centers. Biochemistry. 2002;41:11449–55.
55. Lancaster CRD, Michel H. Refined crystal structures of reaction centres from Rhodopseudomonas viridis in complexes with the herbicide atrazine and two chiral atrazine derivatives also lead to a new model of the bound carotenoid. J Mol Biol. 1999;286:883–98.
56. Allen JP, Feher G, Yeates TO, Rees DC, Deisenhofer J, Michel H, Huber R. Structural homology of reaction centers from Rhodopseudomonas sphaeroides and Rhodopseudomonas viridis as determined by X-ray diffraction. Proc Natl Acad Sci U S A. 1986;83:8589–93.
57. Feher G, Allen JP, Okamura MY, Rees DC. Structure and function of bacterial photosynthetic reaction centers. Nature. 1989;339:111–6.
58. Deisenhofer J, Epp O, Miki K, Huber R, Michel H. Structure of the protein subunits in the photosynthetic reaction center of Rhodopseudomonas viridis at 3 angstrom resolution. Nature. 1985;318:618–24.
59. Krauss N, Schubert WD, Klukas O, Fromme P, Witt HT, Saenger W. Photosystem I at 4 angstrom resolution represents the first structural model of a joint photosynthetic reaction centre and core antenna system. Nat Struct Biol. 1996;3:965–73.
60. Jordan P, Fromme P, Witt HT, Klukas O, Saenger W, Krauss N. Three-dimensional structure of cyanobacterial photosystem I at 2.5 angstrom resolution. Nature. 2001;411:909–17.
61. Brettel K, Leibl W. Electron transfer in photosystem I. Biochim Biophys Acta. 2001;1507:100–14.
62. Ptushenko VV, Cherepanov DA, Krishtalik LI, Semenov AY. Semi-continuum electrostatic calculations of redox potentials in photosystem I. Photosynth Res. 2008;97:55–74.
63. Srinivasan N, Golbeck JH. Protein-cofactor interactions in bioenergetic complexes: the role of the A_{1A} and A_{1B} phylloquinones in Photosystem I. Biochim Biophys Acta. 2009;1787:1057–88.
64. Ishikita H, Knapp EW. Oxidation of the non-heme iron complex in photosystem II. Biochemistry. 2005;44:14772–83.
65. Ishikita H, Knapp EW. Redox potential of quinones in both electron transfer branches of photosystem I. J Biol Chem. 2003;278:52002–11.
66. Kern J, Renger G. Photosystem II: structure and mechanism of the water:plastoquinone oxidoreductase. Photosynth Res. 2007;94:183–202.
67. Guskov A, Kern J, Gabdulkhakov A, Broser M, Zouni A, Saenger W. Cyanobacterial photosystem II at 2.9 angstrom resolution and the role of quinones, lipids, channels and chloride. Nat Struct Mol Biol. 2009;16:334–42.
68. Deligiannakis Y, Hanley J, Rutherford AW. 1D- and 2D ESEEM study of the semiquinone radical Q_A^- of photosystem II. J Am Chem Soc. 1999;121:7653–64.
69. Zheng M, Dismukes GC. The conformation of the isoprenyl chain relative to the semiquinone head in the primary electron acceptor Q_A of higher plant PSII (plastosemiquinone) differs from that in bacterial reaction centers (ubisemiquinone or menasemiquinone) by ca 90 degrees. Biochemistry. 1996;35:8955–63.
70. Debus RJ, Feher G, Okamura MY. Iron-depleted reaction centers from Rhodopseudomonas sphaeroides r-26.1—characterization and reconstitution with Fe^{2+}, Mn^{2+}, Co^{2+}, Ni^{2+}, Cu^{2+} and Zn^{2+}. Biochemistry. 1986;25:2276–87.
71. Chatterjee R, Milikisiyants S, Coates CS, Lakshmi KV. High-resolution two-dimensional ^{1}H and ^{14}N hyperfine sublevel correlation spectroscopy of the primary quinone of photosystem II. Biochemistry. 2011;50:491–501.
72. Moser CC, Page CC, Dutton PL. Tunneling in PSII. Photochem Photobiol Sci. 2005;4:933–9.
73. de Wijn R, van Gorkom HJ. Kinetics of electron transfer from Q_A to Q_B in photosystem II. Biochemistry. 2001;40:11912–22.
74. Vrettos JS, Limburg J, Brudvig GW. Mechanism of photosynthetic water oxidation: combining biophysical studies of photosystem II with inorganic model chemistry. Biochim Biophys Acta. 2001;1503:229–45.
75. Hoganson CW, Babcock GT. A metalloradical mechanism for the generation of oxygen from water in photosynthesis. Science. 1997;277:1953–6.

76. Styring S, Rutherford AW. In the oxygen-evolving complex of photosystem II the S_0 state is oxidized to the S_1 state by D_+ signal-II slow. Biochemistry. 1987;26:2401–5.
77. Tracewell CA, Brudvig GW. Two redox-active β carotene molecules in Photosystem II. Biochemistry. 2003;42:9127–36.
78. Tommos C, Babcock GT. Proton and hydrogen currents in photosynthetic water oxidation. Biochim Biophys Acta. 2000;1458:199–219.
79. Ahlbrink R, Haumann M, Cherepanov D, Bogershausen O, Mulkidjanian A, Junge W. Function of tyrosine-Z in water oxidation by photosystem II: electrostatical promotor instead of hydrogen abstractor. Biochemistry. 1998;37:1131–42.
80. Diner BA, Force DA, Randall DW, Britt RD. Hydrogen bonding, solvent exchange, and coupled proton and electron transfer in the oxidation and reduction of redox-active tyrosine Y_Z in Mn-depleted core complexes of Photosystem II. Biochemistry. 1998;37:17931–43.
81. Mamedov F, Sayre RT, Styring S. Involvement of histidine 190 on the D1 protein in electron/proton transfer reactions on the donor side of photosystem II. Biochemistry. 1998;37:14245–56.
82. Hays AMA, Vassiliev IR, Golbeck JH, Debus RJ. Role of D1-His190 in proton-coupled electron transfer reactions in photosystem II: a chemical complementation study. Biochemistry. 1998;37:11352–65.
83. Kuhne H, Brudvig GW. Proton-coupled electron transfer involving Tyrosine-Z in photosystem II. J Phys Chem B. 2002;106:8189–96.
84. Nugent JHA, Rich AM, Evans MCW. Photosynthetic water oxidation: towards a mechanism. Biochim Biophys Acta. 2001;1503:138–46.
85. Haumann M, Bogershausen O, Cherepanov D, Ahlbrink R, Junge W. Photosynthetic oxygen evolution: H/D isotope effects and the coupling between electron and proton transfer during the redox reactions at the oxidizing side of Photosystem II. Photosynth Res. 1997;51:193–208.
86. Christen G, Seeliger A, Renger G. P_{680}^+ reduction kinetics and redox transition probability of the water-oxidizing complex as a function of pH and H/D isotope exchange in spinach thylakoids. Biochemistry. 1999;38:6082–92.
87. Haumann M, Mulkidjanian A, Junge W. Tyrosine-Z in oxygen-evolving photosystem II: a hydrogen-bonded tyrosinate. Biochemistry. 1999;38:1258–67.
88. Berthomieu C, Hienerwadel R, Boussac A, Breton J, Diner BA. Hydrogen bonding of redox-active tyrosine Z of photosystem II probed by FTIR difference spectroscopy. Biochemistry. 1998;37:10547–54.
89. Jeans C, Schilstra MJ, Ray N, Husain S, Minagawa J, Nugent JHA, Klug DR. Replacement of tyrosine D with phenylalanine affects the normal proton transfer pathways for the reduction of P_{680}^+ in oxygen-evolving Photosystem II particles from Chlamydomonas. Biochemistry. 2002;41:15754–61.
90. Noguchi T, Inoue Y, Tang XS. Structural coupling between the oxygen-evolving Mn cluster and a tyrosine residue in photosystem II as revealed by Fourier transform infrared spectroscopy. Biochemistry. 1997;36:14705–11.
91. Berthomieu C, Hienerwadel R. Vibrational spectroscopy to study the properties of redoxactive tyrosines in photosystem II and other proteins. Biochim Biophys Acta. 2005;1707:51–66.
92. Zhang CX, Boussac A, Rutherford AW. Low-temperature electron transfer in photosystem II: a tyrosyl radical and semiquinone charge pair. Biochemistry. 2004;43:13787–95.
93. Zhang CX, Styring S. Formation of split electron paramagnetic resonance signals in photosystem II suggests that Tyrosine-Z can be photooxidized at 5 K in the S_0 and S_1 states of the oxygen-evolving complex. Biochemistry. 2003;42:8066–76.
94. Faller P, Goussias C, Rutherford AW, Un S. Resolving intermediates in biological proton-coupled electron transfer: a tyrosyl radical prior to proton movement. Proc Natl Acad Sci U S A. 2003;100:8732–5.

95. Faller P, Rutherford AW, Debus RJ. Tyrosine D oxidation at cryogenic temperature in photosystem II. Biochemistry. 2002;41:12914–20.
96. Babcock GT, Barry BA, Debus RJ, Hoganson CW, Atamian M, McIntosh L, Sithole I, Yocum CF. Water oxidation in photosystem II from radical chemistry to multi-electron chemistry. Biochemistry. 1989;28:9557–65.
97. Tang XS, Chisholm DA, Dismukes GC, Brudvig GW, Diner BA. Spectroscopic evidence from site-directed mutants of Synechocystis PCC 6803 in favor of a close interaction between histidine-189 and redox-active tyrosine-160 both of polypeptide D2 of the photosystem II reaction center. Biochemistry. 1993;32:13742–8.
98. Junge W, Haumann M, Ahlbrink R, Mulkidjanian A, Clausen J. Electrostatics and proton transfer in photosynthetic water oxidation. Philos Trans R Soc Lond B Biol Sci. 2002;357:1407–17.
99. Rappaport F, Lavergne J. Charge recombination and proton transfer in manganesedepleted photosystem II. Biochemistry. 1997;36:15294–302.
100. Rappaport F, Blancharddesce M, Lavergne J. Kinetics of electron transfer and electrochromic change during the redox transitions of the photosynthetic oxygenevolving complex. Biochim Biophys Acta. 1994;1184:178–92.
101. Eckert HJ, Renger G. Temperature-dependence of P_{680}^{+} reduction in O_2-evolving PSII membrane fragments at different redox states S_i of the water oxidizing system. FEBS Lett. 1988;236:425–31.
102. Renger G. Coupling of electron and proton transfer in oxidative water cleavage in photosynthesis. Biochim Biophys Acta. 2004;1655:195–204.
103. Kok B, Forbush B, McGloin M. Cooperation of charges in photosynthetic O_2 evolution 1. A linear 4-step mechanism. Photochem Photobiol. 1970;11:457.
104. Peloquin JM, Britt RD. EPR/ENDOR characterization of the physical and electronic structure of the OEC Mn cluster. Biochim Biophys Acta. 2001;1503:96–111.
105. Messinger J, Nugent JHA, Evans MCW. Detection of an EPR multiline signal for the S_0 state in photosystem II. Biochemistry. 1997;36:11055–60.
106. Ahrling KA, Peterson S, Styring S. The S_0 state EPR signal from the Mn cluster in photosystem II arises from an isolated S = 1/2 ground state. Biochemistry. 1998;37:8115–20.
107. Kulik LV, Epel B, Lubitz W, Messinger J. ^{55}Mn pulse ENDOR at 34 GHz of the S_0 and S_2 states of the oxygen-evolving complex in photosystem II. J Am Chem Soc. 2005;127:2392–3.
108. Debus RJ. Protein ligation of the photosynthetic oxygen-evolving center. Coord Chem Rev. 2008;252:244–58.
109. Yano J, Pushkar Y, Glatzel P, Lewis A, Sauer K, Messinger J, Bergmann U, Yachandra V. High-resolution Mn EXAFS of the oxygen-evolving complex in photosystem II: structural implications for the Mn_4Ca cluster. J Am Chem Soc. 2005;127:14974–5.
110. Sproviero EM, Gascon JA, McEvoy JP, Brudvig GW, Batista VS. Quantum mechanics/molecular mechanics structural models of the oxygen-evolving complex of photosystem II. Curr Opin Struct Biol. 2007;17:173–80.
111. Yano J, Kern J, Sauer K, Latimer MJ, Pushkar Y, Biesiadka J, Loll B, Saenger W, Messinger J, Zouni A, Yachandra VK. Where water is oxidized to dioxygen: structure of the photosynthetic Mn_4Ca cluster. Science. 2006;314:821–5.
112. Luber S, Rivalta I, Umena Y, Kawakami K, Shen J-R, Kamiya N, Brudvig GW, Batista VS. S_1-state model of the O_2-evolving complex of photosystem II. Biochemistry. 2011;50:6308–11.
113. Pushkar YL, Yano J, Sauer K, Boussac A, Yachandra VK. Structural changes in the Mn_4Ca cluster and the mechanism of photosynthetic water splitting. Proc Natl Acad Sci U S A. 2008;105:1879–84.
114. Chu HA, Hillier W, Debus RJ. Evidence that the C-terminus of the D1 polypeptide of photosystem II is ligated to the manganese ion that undergoes oxidation during the S_1 to S_2 transition: an isotope-edited FTIR study. Biochemistry. 2004;43:3152–66.

115. Noguchi T, Ono T, Inoue Y. Detection of structural-changes upon S_1-to-S_2 transition in the oxygen-evolving manganese cluster in photosystem II by light-induced Fourier transform infrared difference spectroscopy. Biochemistry. 1992;31:5953–6.
116. Noguchi T, Sugiura M. Flash-induced Fourier transform infrared detection of the structural changes during the S-state cycle of the oxygen-evolving complex in photosystem II. Biochemistry. 2001;40:1497–502.
117. Yamada H, Mino H, Itoh S. Protons bound to the Mn cluster in photosystem II oxygenevolving complex detected by proton matrix ENDOR. Biochim Biophys Acta. 2007;1767:197–203.
118. Britt RD, Campbell KA, Peloquin JM, Gilchrist ML, Aznar CP, Dicus MM, Robblee J, Messinger J. Recent pulsed EPR studies of the Photosystem II oxygen-evolving complex: implications as to water oxidation mechanisms. Biochim Biophys Acta. 2004;1655:158–71.
119. Su JH, Messinger J. Is Mn-bound substrate water protonated in the S_2 state of photosystem II? Appl Magn Reson. 2010;37:123–36.
120. Sproviero EM, Gascon JA, McEvoy JP, Brudvig GW, Batista VS. Quantum mechanics/molecular mechanics study of the catalytic cycle of water splitting in photosystem II. J Am Chem Soc. 2008;130:3428–42.
121. Siegbahn PEM. Quantum chemical studies of manganese centers in biology. Curr Opin Chem Biol. 2002;6:227–35.
122. Siegbahn PEM. Structures and energetics for O_2 formation in photosystem II. Acc Chem Res. 2009;42:1871–80.
123. Chatterjee R, Milikisiyants S, Lakshmi KV. Two-dimensional ^{14}N HYSCORE spectroscopy of the coordination geometry of ligands in dimanganese di-μ-oxo mimics of the oxygen-evolving complex of photosystem II. Phys Chem Chem Phys. 2012;14:7090–7.
124. Milikisiyants S, Chatterjee R, Coates CS, Koua FHM, Shen JR, Lakshmi KV. The structure and activation of substrate water molecules in the S_2 state of photosystem II studied by hyperfine sublevel correlation spectroscopy. Energy Environ Sci. 2012;5:7747–56.

Chapter 11
Structure-Function Relationships in the Mn_4CaO_5 Water-Splitting Cluster

Jian-Ren Shen

Abstract Mn_4CaO_5 cluster is the catalytic center for photosynthetic water-splitting harbored in photosystem II (PSII), a huge, multi-subunit membrane–protein complex located in the thylakoid membranes from cyanobacteria to higher plants. The structure of PSII has been analyzed at 1.9 Å resolution by X-ray crystallography, revealing a clear picture of the Mn_4CaO_5 cluster. In this chapter, principles of crystallization and crystal structure analysis are briefly introduced, followed by descriptions of the structure of the Mn_4CaO_5 cluster and its implications in the mechanism of water-splitting. Based on the geometric organization of the Mn_4CaO_5 cluster, the location of four terminal water ligands, the possible oxidation states of the four Mn ions reported so far, as well as the structural changes revealed by replacing the Ca ion with Sr, a mechanism for water-splitting was proposed and discussed.

Keywords Photosystem II • Oxygen evolution • Crystal structure • Photosynthesis • Membrane proteins • Crystallization • S-state

Abbreviations

DFT	Density functional theory
EM	Electron microscopy
EPR	Electron paramagnetic resonance
EXAFS	Extended X-ray absorption fine structure
FTIR	Fourier transform infrared spectroscopy

J.-R. Shen, Ph.D. (✉)
Photosynthesis Research Center, Graduate School of Natural Science and Technology, Okayama University, Tsushima Naka 3-1-1, Kita-ku, Okayama 700-8530, Japan
e-mail: shen@cc.okayama-u.ac.jp

J. Golbeck and A. van der Est (eds.), *The Biophysics of Photosynthesis*, Biophysics for the Life Sciences 11, DOI 10.1007/978-1-4939-1148-6_11,

NMR Nuclear magnetic resonance
OEC Oxygen-evolving complex
PSII Photosystem II

11.1 Introduction

Photosynthetic water-splitting is catalyzed by a Mn_4CaO_5 cluster, which is harbored in photosystem II (PSII), a large, multi-subunit membrane protein complex located in the thylakoid membranes of all oxygenic photosynthetic organisms [1]. The splitting of water using the energy from the sunlight produces electrons, protons, and molecular oxygen. While the former two products are the sources of energy required for the synthesis of ATP by the ATP synthase and reducing power, both are necessary for the fixation of carbon dioxide into carbohydrates, the latter product is indispensable for sustaining the oxygenic life on the earth. Thus, the photosynthetic water-splitting is one of the most important biochemical reactions occurring on the earth.

In order to understand the mechanism of water-splitting, it is essential to elucidate the structure of the Mn_4CaO_5 cluster and its surrounding protein environment. The main methods for solving the structure of biomacromolecules are X-ray crystallography, nuclear magnetic resonance (NMR), and electron microscopy (EM). X-ray crystallography is the most powerful method for structure determination of biomacromolecules, while the NMR method is subjected to limitations in molecular masses that can be treated, and the structures of very few proteins have been solved at an atomic resolution by the EM method. Since PSII is a large membrane–protein complex, (for example, the typical PSII core complex with a full oxygen-evolving activity from cyanobacteria contains 20 different subunits with a total molecular mass of 350 kDa, see Chapters 1–3 in [1, 2]), the only way available to analyze the structure of this type of huge protein complexes at an atomic detail is X-ray crystallography.

The basic procedure for X-ray crystallography is protein sample preparation, crystallization, diffraction data collection, phase determination, electron density analysis, model building, and refinement. The most important and also the most difficult step in X-ray crystallography is obtaining a single crystal with a good quality and reasonably high resolution. Owing to remarkable technical and methodological advances in recent years, it has become rather easy to obtain crystals of soluble proteins. However, getting well-diffracted single crystals of membrane proteins still remains a major obstacle and a rate-limiting step in solving their structures by X-ray crystallography. This is especially true for large, multi-subunit membrane–protein complexes such as PSII. Once a well-diffracted single crystal is obtained, obtaining phase information necessary for calculation of the electron density map can sometimes be a time-consuming task; however, there are several alternative methods to solving this problem now, so that in most cases this will not present a major obstacle.

In the following, the principles of protein crystallization and X-ray structure analysis are briefly described, followed by introduction and discussions on the structure and function of the oxygen-evolving complex (OEC) of PSII that have been revealed from the structural and functional analyses of PSII.

11.2 Crystallization of Soluble and Membrane Proteins

11.2.1 Principles of Protein Crystallization

Protein crystals are ordered arrays of a single, homogeneous protein, or a complex of multiple proteins. Because the quality and resolution of a crystal depend on the degree of ordering of the protein molecules within the crystal, a highly purified, homogeneous protein or protein complex preparation is a prerequisite for getting a high quality crystal. The homogeneity of a protein or a protein complex is evaluated from a number of different properties of the protein in question, among them, the main ones include the absence of contaminating components, a homogeneous net total charge, and a homogeneous size distribution of the protein particles in solution. While the former one is easily evaluated from electrophoresis, the latter two are more difficult to be determined. To determine whether the protein of interest is homogeneous in charge distribution, one can usually use ion-exchange column chromatography, isoelectric point electrophoresis, etc. To determine the homogeneity of size distribution, conventional size-exclusion chromatography can be used along with dynamic light-scattering measurement, various native polyacrylamide electrophoresis, etc.

Various factors can influence the purity and homogeneity of a protein solution, since even a single protein may adopt slightly different, multiple conformations in solution due to influences of various factors such as salts and/or other chemicals, redox reagents, detergents, temperature, pH, etc. Thus, not only exclusion of other protein components is important for getting a good start for crystallization, keeping the protein conformation as uniform as possible is also extremely important. Another factor to be considered is the stability of the protein in solution, since in most cases the process of crystallization takes several days to several weeks at 4 °C to room temperature; in many cases, purified protein cannot sustain such a long time without losing its active conformation. This is especially important for membrane proteins and their complexes, since membrane proteins are crystallized in the presence of detergents (see below), the stability of most membrane proteins will be reduced in the presence of detergents.

In principle, crystallization is achieved by bringing a protein solution into a supersaturated state, so that the protein molecules exceeding the saturation concentration can no more be dissolved and will be partitioned into an aggregated phase. The supersaturated state can be divided into three phases [3, 4]: one is a metastable phase where proteins can still exist in the solubilized form despite that

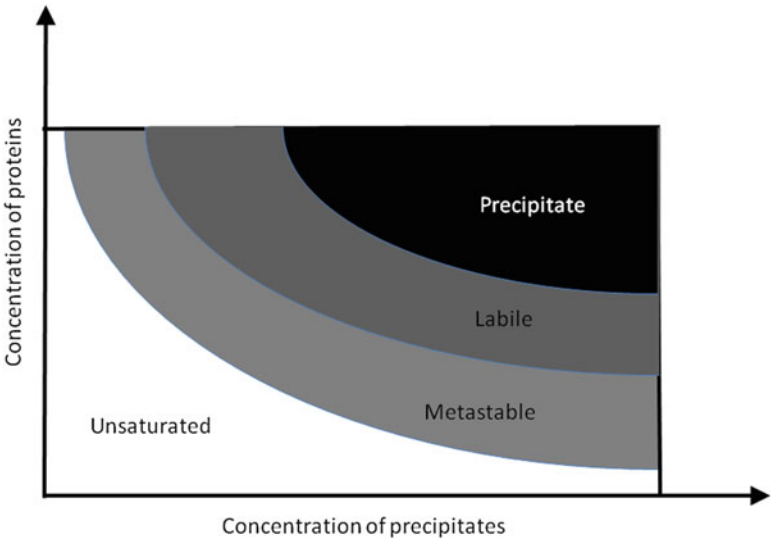

Fig. 11.1 Phase diagram. The concentration of proteins is plotted against increased concentrations of precipitates, but it can be other factors such as temperature, pH, etc. Saturation level increases as the color goes from *white* to *black*. The *white* region represents unsaturated solutions where crystals will dissolve. The supersaturated region can be divided further into three regions, namely the metastable phase where only crystal growth will occur, the labile phase where nucleation and growth compete, and the precipitate region which has the highest supersaturation and precipitation of amorphous protein will occur in this region

its concentration already exceeds (slightly) the saturation concentration; the second one is a labile phase which has a higher degree of saturation where the crystal nuclei can be formed; and the third one is a precipitation phase where the supersaturation reaches a high level that enables the solutes (proteins) to precipitate immediately (Fig. 11.1). The nuclei of crystals formed in the labile phase can grow in either the labile phase or metastable phase. The labile phase will give a faster growth of the crystals, whereas the metastable phase results in a slower growth due to lower degree of supersaturation. In general, slower growth of crystals is preferred to ensure the quality and resolution of the crystals to be obtained, since faster growth of the crystals will bring more chances of occurrence of disorders in the crystal packing due to increases in the occurrence of errors caused by the fast attachment of new protein molecules into the already existed small crystals, resulting in imperfect arrangement of the protein molecules in the crystal. This means that a lower degree of supersaturation such as in the metastable state will facilitate the growth of high quality crystals. In practice, however, the degree of supersaturation is not easy to control, and it is determined by experience in most cases. A slower growth rate means that a longer time is needed to obtain the crystals, which will require enough stability of the protein under the conditions employed, a requirement to be found often difficult to be met by certain proteins. Thus, the choice of growth rate for

crystals depends on the balance between the stability of the protein in question and the quality of the crystal to be obtained.

In order to bring a protein solution into a supersaturated state, various "precipitants" are used; these include various salts, polymers (the typical one is polyethylene glycols (PGEs)), and even organic solvents. For the success of crystallization, not only the type and concentration of the precipitants but also a number of other factors need to be considered; these include the pH of the solution (type of buffer used), salts and redox reagents co-existed, temperature, additives etc., in addition to the purity and homogeneity of the protein samples used. The process of crystallization is therefore to find an appropriate condition that enables the separation of protein molecules into an ordered array from a supersaturated solution while preventing the formation of precipitants and random aggregation [5–7]. It is noticed, however, that the crystallization often occurs in the interface between solution and aggregation, so that appearance of some aggregation is inevitable in some cases. High quality crystals, on the other hand, are usually obtained in the best growth conditions where no aggregation will be observed.

11.2.2 Methods of Protein Crystallization

A number of methods have been developed to bring a protein solution into a supersaturated state [5–7]. The most widely used ones are batch crystallization, vapor diffusion, and dialysis methods. In the batch (or micro-batch) method, a protein solution is mixed with a precipitant solution to bring it to a supersaturated state, which is then covered with a layer of oil to prevent evaporation. The mixed solution is allowed to stay for a few hours to a few days during which the crystals are formed. In the micro-batch method used recently, the mixed protein solution layer is covered by a layer of paraffin oil which allows water molecules to pass through very slowly, enabling a slow evaporation to occur to enhance the degree of supersaturation. The batch method is easy to use and set up, so can be used for screening a large number of different conditions. Due to the constancy or small change in the degree of supersaturation during the entire process of crystallization, however, the batch method is used for the formation of crystals only in a narrow range of precipitant concentration as well as other conditions.

Vapor diffusion is the most widely used method for crystallization in which a protein solution is mixed with typically an equal volume of a precipitant solution. The mixed protein solution is still unsaturated, which is then spotted into a sealed chamber where a large excess volume of the precipitant solution is included. The water will evaporate from the protein solution toward the precipitant solution, bringing the protein solution to the supersaturated state during the course of evaporation. Depending on the setup of the protein and precipitant solutions, the vapor diffusion method can be divided into hanging drop, sitting drop, and sandwich drop methods. Evaporation of water molecules enables relatively a large change in the concentration of both protein and other components; thus, vapor

diffusion allows screening of relatively a large range of conditions among which crystals may be formed. Vapor diffusion is also easy to use and set up, and is thus suitable for screening a large number of conditions.

The dialysis method uses a dialysis membrane to separate the protein solution and the precipitant solution. During the crystallization process, the precipitant can enter into the protein solution, and the water molecules can also go out from the protein solution to the precipitant solution, reaching equilibrium between the two solutions. This method allows the control of the final composition of the protein solution by controlling the composition of the precipitant solution; however, the setup of this method is often time-consuming so that it is often not suitable for screening a large number of conditions which are required for the initial screening of crystallization for a novel protein.

11.2.3 Crystallization of Membrane Proteins

Crystallization of membrane proteins and their complexes resembles that of soluble proteins, but membrane proteins have large areas of hydrophobic surfaces, which make them insoluble in water. Thus, membrane proteins need proper detergents for their solubilization, purification, and stabilization, which make the purification and crystallization of membrane proteins more difficult than soluble proteins. The most commonly used detergents for membrane proteins are those of nonionic detergents, as they appear to be most mild in solubilizing membrane proteins. Detergents form micelles in solution, which will surround the membrane proteins to ensure their solubilization in aqueous solutions. The concentrations needed to form micelles (critical micelle concentration, CMC) are largely different among different types of detergents. The choice of a proper detergent for the success of crystallization of a particular membrane protein or membrane protein complex, however, appears not easy, as the detergent needs to be in proper interaction not only with the membrane protein but also with the other components in the crystallization solution [8, 9]. Another issue is that, a detergent suitable for the solubilization and purification of a membrane protein may not be suitable for formation of a high quality crystal; thus, the detergent needs to be changed for crystallization after purification. The addition of detergents to the crystallization conditions dramatically increases the number of conditions that need to be screened; this is one of the major reasons why membrane proteins are more difficult to be crystallized in addition to the hydrophobic nature of them that hinders crystallization.

In the practice of membrane protein crystallization, addition of small, amphiphilic molecules was often found to improve the crystals, which are assumed to fill in the spaces in the crystal packing that are not occupied by detergents and protein amino acid residues [8, 9]. In addition, a unique approach to utilize the hydrophobic nature of membrane proteins for crystallization was also developed, which is the lipid cubic phase method. In this method, a cubic phase is formed by a high concentration of lipids (usually monoolein) which enables the membrane proteins

to be incorporated to form an ordered array [10–12]. Another approach that has been used successfully in crystallization of some membrane proteins is to reduce the hydrophobic surface of a membrane protein and increase its hydrophilic surface by binding of monoclonal antibody fragments [13], or by fusion with a soluble protein such as T4 lysozyme [14, 15], so that the membrane protein can be crystallized in a way more like a soluble protein.

11.3 X-ray Structure Analysis

In the conventional optical microscopy, visible light is used to visualize small objects not directly visible by eyes. In order to do so, light reflected from the small objects is collected and magnified by suitable lenses at a proper distance from the objects. The resolution, or the smallest distance of two points that can be identified, by this method, is limited by the wavelength of the light used, since the resolution cannot be significantly higher than the wavelength of the light used, which is in the range of 400–700 nm for the visible light. To reveal the atomic structure of molecules, X-ray at wavelengths of around 1 Å has to be used, since a typical distance for a C–C bond is around 1.5 Å. Due to the high energy of X-rays, however, no suitable lenses are available to collect and magnify the X-rays; thus, an alternative method employing calculations must be used.

A crystal is made up of identical, basic units arranged equally in all directions in the space (Fig. 11.2a). The repeated unit of a crystal is called "unit cell," and its properties are defined by three lengths *a*, *b, c*, along the x, y, z directions, as well as three angles α, β, γ, between each pair of the axes (Fig. 11.2b). These values constitute the unit cell parameters, which are different among different types of

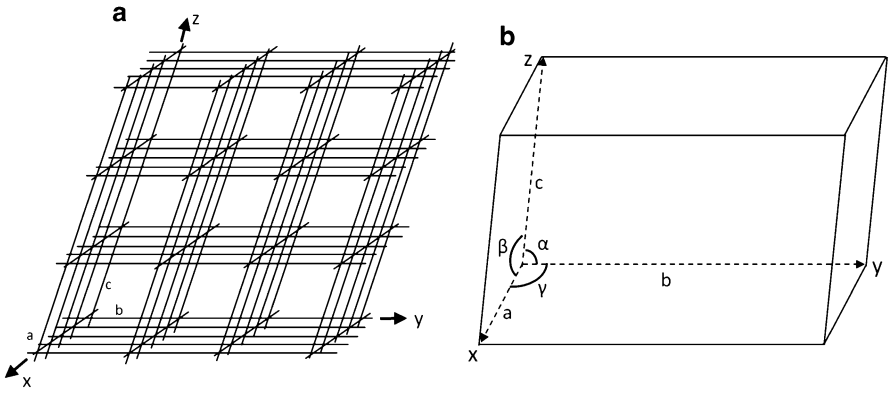

Fig. 11.2 Schematic representation of crystal packing and a unit cell of a crystal. (**a**) Schematic representation of a region of a crystal, where identical units are arranged in exactly the same way. (**b**) A unit cell from a crystal, showing the definition of six parameters that define the symmetry and properties of the crystal

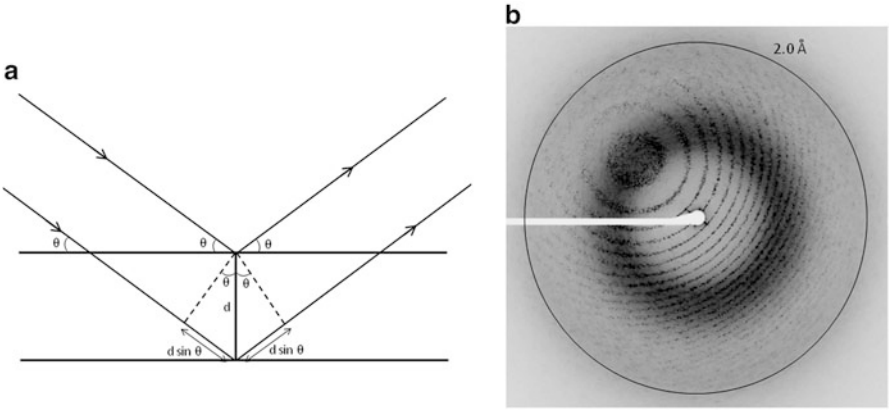

Fig. 11.3 Occurrence of diffraction from crystallographic planes and an example of diffraction pattern. (**a**) The crystal can be considered to consist of a series of planes, each of which scatter the incident wave. Two such crystal planes were shown here. The difference between the scattered waves from these two planes is the difference in the pathlength between these planes, which equals 2d sinθ. When this path difference equals a multiple of the wavelength, the waves add constructively and a diffraction peak is observed. (**b**) An example of diffraction pattern, taken from a crystal of oxygen-evolving photosystem II core complex. The *circle* represents the resolution point of 2.0 Å

crystals, and their relationship is related with the symmetry of the crystal. The arrangement of the unit cells constitutes the lattice of the crystal, and there are 14 lattices (Bravais lattices) that are allowed for protein crystals [16–18].

When an incident X-ray hits an object, the electrons of atoms in the object were forced to oscillate, generating a second X-ray having the same energy (wavelength) as that of the incident X-ray (Thomson Scattering). This second X-ray is scattered from every atom constituting the object, and can be captured at a distance much longer than the inter-atom distances behind the object. If the object is a crystal, that is, an ordered array of identical units, then the "diffracted" X-rays are summed up in some places but canceled out in other places, giving rise to visible (detectable) "diffraction spots." This is the phenomenon of interference of multiple waves with the same wavelength. To illustrate this, we consider that the incident wave (X-ray) hits two planes of atoms in a crystal with an angle of θ (Fig. 11.3a). The path difference between the two waves scattered from the two planes at the same angle θ is "2d sinθ," where *d* is the distance between the two planes. Diffraction spot is observed only when the path difference is equal to a multiple of the wavelength according to:

$$2d\ \sin\theta = n\lambda$$

where *n* is an integer. This is the Bragg's law that determines whether a diffraction spot can be observed or not from a crystal. From this relationship, one can easily deduce that the maximum value of *d*, that is, the largest distance between two adjacent layers in the crystal that can yield diffraction, is given by:

$$d = \lambda/2$$

This is the theoretical limit of resolution with a given wavelength λ. In practice, this limit of resolution is rarely achieved with protein crystals due to various imperfections existed within the crystals.

The diffraction pattern (see Fig. 11.3b for an example) is determined by the arrangement of atoms in the repeated units within the crystal; in other words, the amplitude and position of every diffraction spot in the diffraction pattern contain information regarding the arrangement of atoms (species and position of the atoms) within the crystal. Thus, the diffraction patterns can be used to determine the molecular structure of the crystal. The relationship between the diffraction pattern and molecular structure, however, is reciprocal, and the diffraction pattern can be considered to represent the molecular structure in a reciprocal space relative to the molecular structure in the real space [16–18]. This relationship is related by a mathematical treatment Fourier transform; thus, the molecular structure in the crystal can be deduced from the diffraction pattern by the method of Fourier transform, and vice versa. During this treatment, however, the phase information of the X-ray wave that yielded the diffraction pattern is lost, so that it has to be determined separately by another method [16–18]. This is the phase problem in protein crystallography.

Several methods have been developed to solve the phase problem, among which the most traditional one is the multiple isomorphous replacement (MIR) method. In this method, crystals are soaked with metal (heavy atom) compounds, and the diffraction pattern is measured and compared with native crystals without metals bound. This gives rise to the position of the metals bound to the protein crystal, which is then used to calculate the phase information. The second method utilizes multiple anomalous dispersion (MAD) from a single metal, in which diffraction pattern is measured with several wavelengths around the transition energy of the metal bound to the protein. Since each metal has a characteristic absorption wavelength in the X-ray region, the differences in the diffraction measured around this specific wavelength are primarily contributed by the electrons of that metal, which is thus used for locating the position of the metal and for generating the initial phase information. The third method is the molecular replacement (MR) method, which utilizes a known structure of a homologous protein as the initial search model. All of the above methods have been widely used, with the latter two becoming increasingly popular owing to the availability of intense, tunable X-rays from synchrotron radiation facilities and a number of atoms with anomalous scattering capability, as well as the increasing number of solved structures.

Because the diffraction of X-rays is caused by electrons of atoms, the results calculated from the diffraction pattern are distributions of electrons in a three-dimensional space, or an electron density map. The molecular structure is then built by fitting amino acid residues and ligands into the electron density map, which is the process of model building. In order to obtain the model that best fits with the experimentally obtained electron density map, the model initially obtained is refined against the experimental data through many cycles of refinement until reaching a state that gives a minimum difference between the experimentally obtained electron density map and model. During this refinement process,

knowledge of stereochemistry such as constraints in the configuration of amino acids and their spatial conflicts in the three-dimensional structure of the protein is incorporated to minimize the model errors.

The quality of the structures obtained from the X-ray crystallography is determined by a number of factors, among which the most important one is the resolution which in turn depends on the degree of order of molecules in the crystal. A higher resolution represents a more accurate, reliable structure than a lower resolution. A higher resolution will also give a lower value of R factor, a parameter related to the reliability of the structure, as well as a lower average temperature factor (*B*-factor).

11.4 Crystal Structure Analysis of PSII

PSII is an integral membrane protein complex found in the thylakoid membranes from prokaryotic cyanobacteria to higher plants. The composition of PSII core capable of oxygen evolution varies slightly from cyanobacteria to higher plants. In the cyanobacterial PSII whose structure has been solved at an atomic resolution, there are 17 transmembrane subunits and 3 peripheral, hydrophilic subunits, which gives rise to a total molecular mass of 350 kDa [1, 2]. The purified PSII, especially those from thermophilic cyanobacteria, exists predominately in a dimeric form [19–21], which is thought to be also the functional form dominant in vivo.

Since PSII is an extremely large membrane–protein complex, its structure has to be solved by X-ray crystallography. The large, membranous nature of the complex also presented a major challenge to obtain high resolution crystals of PSII. The first crystal structure of PSII was reported by Zouni and colleagues in 2001 at a resolution of 3.8 Å, from a thermophilic cyanobacterium *Thermosynechococcus elongatus* [21]. The use of the thermophilic cyanobacterium enabled them to obtain a highly stable, active PSII core dimer preparation as was already shown previously [22, 23]. In this structure, the position of major PSII subunits was assigned in a Cα model, together with the position of the Mn_4Ca cluster that catalyzes the water-splitting reaction. The side chain structures of amino acids and positions of some small subunits were not given due to the limited resolution. Subsequently, Kamiya and Shen reported a 3.7 Å structure of PSII dimer from a closely related thermophilic cyanobacterium *Thermosynechococcus vulcanus*, in which a few more subunits were assigned, together with some residues with their side chains assigned [24]. However, the structure of the Mn_4Ca cluster was still not clear, since each of the metal atoms and the presumed oxo-bridges connecting the metal atoms were not separated in the electron density map, making the electron density of the metal cluster like a ball packed with all of the five metal ions and possible oxo-bridges. The resolution of the PSII structure was raised to 3.5 Å [25], 3.0 Å [26], and 2.9 Å resolutions [27] gradually, which continuously improved the structure of the whole complex in terms of the side chain orientations of amino acid residues, a number of

cofactors such as chlorophylls, carotenoids, lipids, a bicarbonate ion, etc. The presence of Ca^{2+} as an integral part of the water-oxidizing catalyst was demonstrated by a number of biochemical and biophysical studies including EPR and EXAFS measurements, and its global position in the Mn_4Ca cluster was first identified in the 3.5 Å structure from anomalous scattering at a wavelength near the Ca absorption edge [25], which was confirmed subsequently by the higher resolution structures [26, 27]. However, the detailed structure of the Mn_4Ca cluster, as well as its exact ligand environment, the position of water molecules, etc., remained obscure even in the 2.9 Å structure. In fact, the electron density for the Mn_4Ca cluster was still a ball encapsulating all of the metal ions and oxo-bridges, and the electron densities for each of the atoms were not separated, so that the position of the individual atoms cannot be clearly determined from the experimentally obtained electron density, and the structural model has to incorporate constraints from previous results mainly from extended X-ray absorption fine structure (EXAFS) measurements and electron paramagnetic resonance (EPR) studies.

The atomic structure of the PSII dimer complex was reported in 2011 by Shen and his colleagues at a resolution of 1.9 Å [28]. At this resolution, the electron densities for the individual atoms in the Mn_4Ca cluster were clearly separated, allowing determination of the structure of the metal cluster unambiguously. In addition, the structure revealed the coordination environment of the metal cluster in much more detail than the previously obtained structure, as well as the presence of a huge number of water molecules associated with various residues in the PSII dimer. In the following, we describe the structure of PSII at the atomic resolution, with the focus on the detailed structure of the Mn_4Ca cluster, and its functional implications in the mechanism of water-splitting.

11.4.1 Overall Structure of the PSII Dimer

The overall structure of PSII dimer analyzed at the 1.9 Å resolution is shown in Fig. 11.4a, which contains 19 subunits per monomer, among which 16 are transmembrane subunits and 3 are membrane peripheral subunits required for oxygen evolution. Among the transmembrane subunits of PSII, D1 and D2 subunits have five transmembrane helices each and form the reaction center of PSII to which most of the electron transfer cofactors are bound. Two other large transmembrane subunits are CP47 and CP43 (CP stands for chlorophyll protein), which have six transmembrane helices each and are located in the two sides of the D1/D2 core. These two subunits bind a large number of chlorophylls (17 for CP47 and 12 for CP43) which function as light-absorbing antenna chlorophylls to transfer the light energy to the reaction center chlorophylls. In addition to these large transmembrane subunits, 12 small subunits (with molecular mass less than 10 kDa) were found, most of them have one transmembrane helix and only PsbZ has two transmembrane helices. These give rise to a total of 35 transmembrane helices for a PSII monomer.

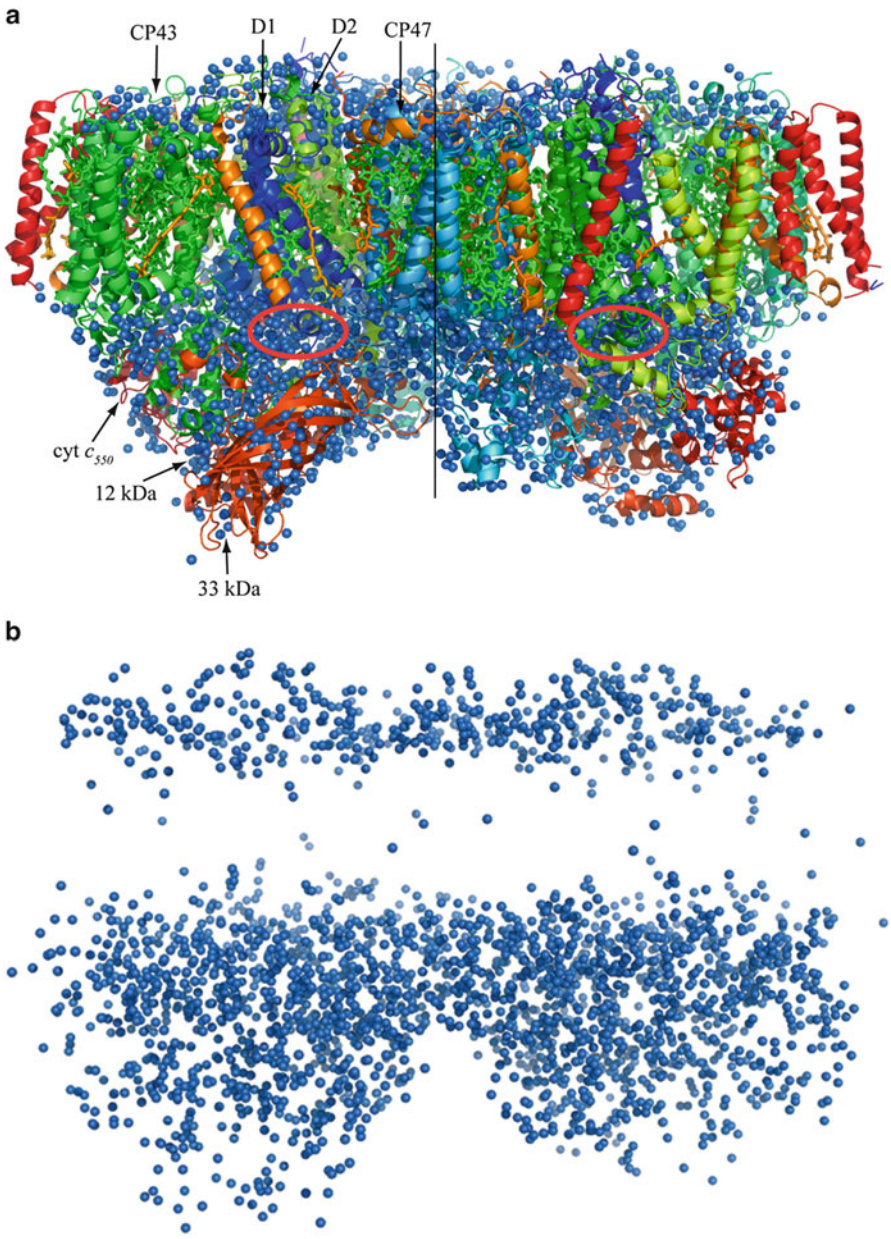

Fig. 11.4 Overall structure of PSII dimer. (**a**) Overall structure of a PSII dimer analyzed at 1.9 Å resolution. View from a direction perpendicular to the membrane normal. The *line* in the middle represents the non-crystallographic twofold axis dividing the two monomers, and the two *red circles* indicate the region where the water-splitting catalytic center, the Mn_4CaO_5 cluster, binds. (**b**) Distribution of the water molecules. All of the protein and cofactors except water were removed from panel (**a**), showing the distribution of water molecules in the PSII dimer

PsbY, one of the low molecular mass of PSII with one single transmembrane helix located in the peripheral region close to PsbE and PsbF (the α- and β-subunits of cytochrome b559), was not present in the crystal structure, indicating that it is lost during crystallization due to its weak association with the PSII core complex.

The three peripheral, hydrophilic subunits are PsbO (33 kDa), PsbV (cytochrome *c550*), and PsbU (12 kDa), located in the lumenal side of the thylakoid membrane. They form a cap for the site of oxygen evolution (the Mn_4CaO_5 cluster), shielding it from the bulk solution with a large area of hydrophilic protein region. These extrinsic proteins have been shown to be important for maintaining the activity and stability of the oxygen-evolving complex (OEC).

In addition to the protein subunits, 35 chlorophylls, 2 pheophytins, 11 β-carotenes, 2 plastoquinones, 1 bicarbonate, 1 *b*-type and 1 *c*-type cytochromes, 1 non-heme iron, more than 20 lipid molecules, at least 2 chlorides, a Mn_4CaO_5 cluster, etc., are present in a PSII monomer.

One of the most significant features of the high resolution structure of PSII was the presence of a huge number of water molecules within it. In total, nearly 2,800 water molecules were found in a PSII dimer; these water molecules were distributed in two layers, one in the surface of the cytoplasmic (stromal) side and the other one in the surface of the lumenal side, of the thylakoid membrane (Fig. 11.4b). Very few water molecules were found in the transmembrane region. These distribution of the water molecules demonstrates a typical feature for a membrane protein complex. The few water molecules present in the transmembrane region were found to serve as ligands or hydrogen-bonding partners of chlorophylls that are not ligated by an amino acid residue. Typically, the Mg ion of the chlorin ring of chlorophylls is ligated by an amino acid residue; in most cases it is a His residue. Among the 35 chlorophylls in a PSII monomer, however, 7 chlorophylls do not have an amino acid residue as a ligand for its Mg ion. Instead, it is ligated by a water molecule [28]. For such chlorophylls that are ligated by water, there are usually two additional water molecules existing in the vicinity of the chlorin ring and form hydrogen bonds to the carbonyl groups of the chlorin ring as well as the direct water ligand, which are probably required to stabilize the chlorin ring not directly ligated to an amino acid residue.

11.4.2 Structure of the Mn_4CaO_5 Cluster

The Mn_4CaO_5 cluster is bound in a pocket formed by residues of D1 and CP43 in the lumenal surface of the thylakoid membrane (cycled regions in Fig. 11.4a). Because the interatomic distances within the cluster is in the range of 1.7–2.6 Å, it is not possible to separate each of the atoms in the crystal structures up to 2.9 Å resolution. At these low resolutions, the electron density for the whole cluster is connected, making it look like a pear-shaped ball (or a soccer ball), so that the placement of individual atoms within the ball was not possible based on the experimentally

obtained electron density map only [21, 24–27]. Early models of the metal cluster was thus built with the constrains obtained from other approaches, notably from EXAFS experiments. The results of EXAFS experiments have suggested that there should be 2–3 Mn–Mn distances of 2.7–2.8 Å, as well as some longer distances in the range of 3.0–3.3 for Mn–Mn and Mn–Ca [29–34]. These distances were used to place the Mn and Ca atoms within the electron density of the pear-shaped ball albeit with no clear separation of the electron density for the individual atoms. An even worse situation was seen for oxo-bridges, which must be present in order to connect the Mn–Mn and Mn–Ca pairs and have been suggested also from EXAFS experiments. Since Mn and Ca have much more electrons than those of oxygen atoms, the diffracted X-rays by these metal ions are much stronger than that diffracted by oxygens. Thus, the electron density forming the pear-shaped ball at lower resolutions is largely contributed by the Mn and Ca ions, and the densities contributed by oxygen atoms are very weak, making the assignment of oxo-bridges essentially impossible at low resolutions.

In the 1.9 Å resolution structure of PSII [28], the electron densities for each of the metal ions, together with the oxo-bridged oxygens, were clearly separated, allowing the assignment of each atom unambiguously (Fig. 11.5a). As a result, the catalytic center for water oxidation was found to contain five oxygen atoms in addition to four Mn and one Ca ions, forming a Mn_4CaO_5 cluster (Fig. 11.5b). Since the number of electrons of Mn (with a valence of III or IV) is three or four larger than that of Ca (II), the electron density of the Ca ion is slightly lower than those of the Mn ions (Fig. 11.5a). This is also an illustration for the quality of the electron density obtained at the atomic resolution, as the slight differences in the intensity of the electron density between Mn and Ca ions are not easy to be distinguished at a lower resolution. The core of the cluster is a distorted cubane made up by three Mn ions (Mn1–Mn3), four oxygen atoms (O1–O3, and O5), and one Ca ion. The fourth Mn (Mn4) is located outside of the cubane and connected to the cubane core by two oxo-bridges via O4 and O5. The shape of the whole cluster resembles that of a distorted chair, with the cubane serving as the chair base and the outside Mn (Mn4) serving as the back of the chair (Fig. 11.5c).

The distorted shape represents one of the most significant features of the Mn_4CaO_5 cluster structure, that is, the instable or flexible nature of the metal complex (see below for further discussions). The distortion is mainly caused by two reasons. One is the differences in the Mn–O distances. Among the five oxygen atoms, O1–O4 have bond distances to their nearby Mn ions in the range of 1.8–2.2 Å, which is similar to those typically found in Mn oxide compounds. The distances between O5 and its nearby Mn ions, however, were found to be extremely longer in the crystal structure, namely 2.4, 2.5, 2.6 Å for O5–Mn3, O5–Mn4, and O5–Mn1, respectively. These distances, in particular the O5–Mn4, O5–Mn1 distances, are much longer than those expected for normal Mn oxides, suggesting a weak binding of the O5 atom to the nearby Mn ions (see below for more detailed discussions). The other reason that contributed to the distortion in the structure of the Mn_4CaO_5 cluster is the differences between typical Mn–O and Ca–O distances.

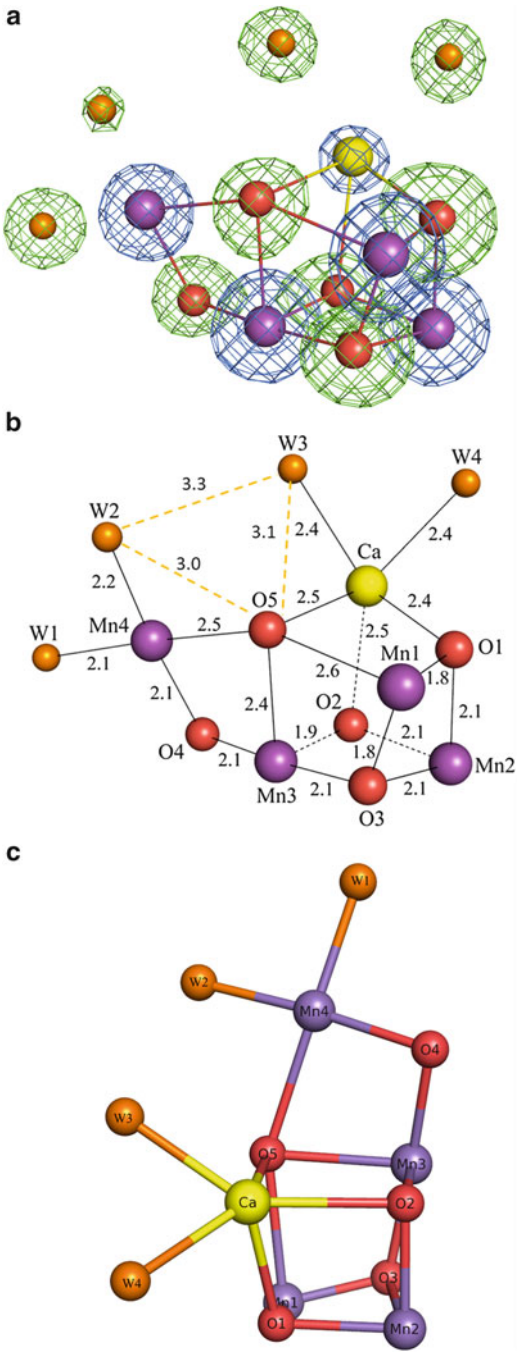

Fig. 11.5 Structure of the Mn_4CaO_5 cluster. (**a**) Individual atoms of the Mn_4CaO_5 cluster, superimposed with the 2Fo-Fc map (*blue*) contoured at 5σ for manganese and calcium atoms, and with the omit map (*green*) contoured at 7σ for oxygen atoms and water molecules. (**b**) Bond distances (in Å) between metal ions and oxo-bridges or water molecules within the Mn_4CaO_5 cluster. (**c**) Distorted chair form of the Mn_4CaO_5 cluster. The structure of the cluster was rotated relative to that shown in (**b**), to show the chair form more clearly

As described above, while the typical Mn–O distances are in the range of 1.8–2.2 Å, the typical distances of Ca–O are in the range of 2.4–2.6 Å due to a lower positive charge of the Ca ion compared with that of Mn ions. The incorporation of the only Ca ion in the metal cluster therefore contributed to the distorted shape of the structure, which may be important for the flexibility or catalytic activity of the catalytic core.

In addition to the oxo-bridged oxygens, four water molecules are associated with the Mn_4CaO_5 cluster as terminal ligands [28]. These water ligands are designated W1–W4, among which two (W1 and W2) are associated with Mn4, whereas the other two (W3, W4) are associated with the Ca ion (Fig. 11.5). Interestingly, no other direct water ligands were found to associate with the remaining three Mn ions, indicating that the region formed by Mn4, Ca, and the four water molecules is highly hydrophilic, and may play an important role in water-splitting. Among these four water molecules, W2 bound to Mn4, and W3 bound to Ca, are in hydrogen-bonding distances to O5. Furthermore, W2 and W3 are also within a hydrogen-bond distance with each other. These suggested that the area formed by W2, W3, and O5 may constitute the site of O–O bond formation during the water-splitting reaction (see below for further discussions).

The distances of the two water ligands to Mn4 are 2.1–2.2 Å, whereas those between W3 and W4 to Ca are 2.4 Å. The slightly shorter distances between water and Mn4 reflect a higher valence of Mn4 than that of the Ca ion, and thus a slightly stronger binding of the water ligands to Mn4 than those to the Ca ion.

11.4.3 Comparison of Mn–Mn and Mn–O Distances Between the Crystal Structure and EXAFS Studies and Theoretical Calculations

The shortest distances between Mn ion pairs are 2.8 Å for Mn1–Mn2, 2.9 Å for Mn2–Mn3, and 3.0 Å for Mn3–Mn4 in the 1.9 Å resolution crystal structure. These distances are slightly longer than the distances reported from EXAFS experiments, where it was suggested that there are at least two Mn–Mn distances of 2.7–2.8 Å [29, 30, 35], and a third one at 2.8 Å may also be present [31, 33, 34, 36]. While these differences may fall within the experimental errors, as the results of crystal structure analysis at 1.9 Å resolution bear an average error of 0.16 Å for the interatomic distances [28], theoretical calculations using the coordinates of the crystal structure have been performed to examine the Mn–Mn as well as Mn–O distances. Extensive quantum mechanical/molecular mechanical (QM/MM) calculations using the coordinates of the crystal structure have resulted in model structures for the Mn_4CaO_5 cluster where the shortest Mn–Mn distances resemble those of EXAFS results but slightly shorter (0.1–0.2 Å) than those of the crystal structure [37–45]. This has been taken as evidence to indicate that the crystal structure is in a reduced

state than that of the S_1-state presumed in the X-ray structural analysis. While this possibility cannot be excluded at present due to possible X-ray radiation damage, there is another source of difference that needs to be considered. Since in the X-ray structure analysis at 1.9 Å resolution, the hydrogen atom cannot be assigned, so that the four terminal water ligands have been assumed as H_2O, and the five oxo-bridged oxygens have been assigned as O^{2-}. It is possible that the protonation states of some of the water molecules and/or oxo-bridges are different from those assumed in the crystal structure, and the exact combination of the protonation states is not known at present. A combination of the protonation states different from the real structure may affect the results of theoretical calculations.

More profound differences were found in the distances of Mn1–O5 and Mn4–O5 between the crystal structure and theoretical calculations. As described above, both of the distances between Mn1 and O5, and between Mn4 and O5, are unusually long, which were never obtained in theoretical calculations if the O5 atom is in an O^{2-} form. Assuming that O5 is in a deprotonated state (O^{2-}), theoretical calculations yielded a result showing that the distance between Mn4 and O5 is in the range of 1.8–2.3 Å, whereas that between Mn1 and O5 is in the range of 2.8–3.3 Å [37–45]. This suggests that the O5 atom is bonded to Mn4 but not to Mn1; therefore Mn4 is 6-coordinated whereas Mn1 is 5-coordinated in the S_1-state (see below for more detailed discussions). This is remarkably different from that of the crystal structure, where O5 sits in nearly the middle between Mn4 and Mn1, and suggested that it is weakly bonded to both Mn4 and Mn1, resulting in a quasi-five-coordinated structure for both Mn4 and Mn1 in the S_1-state. The term "quasi-five-coordinated" is used to indicate that the sixth ligand is at a distance apparently longer than the usual Mn–O distance. The unusually longer distances between O5–Mn4 and O5–Mn1 may again caused by the possible radiation damage during X-ray data collection. However, when O5 is assumed to be in a protonated state, namely, an OH^- form, a DFT calculation yielded Mn4–O5 and Mn1–O5 distances that are rather close to the crystal structure [39]. This suggests that O5 may be in a protonated state. Alternatively, theoretical calculations performed so far may have not incorporated the protein environment surrounding the Mn_4CaO_5 cluster in an area large enough to account the precise structure of the cluster. In any cases, the unusual position of O5 is consistent with the above discussions that the area around O5 may form the reaction site for water-splitting and O–O bond formation.

11.4.4 Ligand Environment of the Mn_4CaO_5 Cluster

The Mn_4CaO_5 cluster is coordinated by seven amino acids, among which six are carboxylate residues and one is a His residue (Fig. 11.6a) [28]. The six carboxylate residues are D1-D170, D1-E189, D1-E333, D1-D342, D1-A344, and CP43-E354,

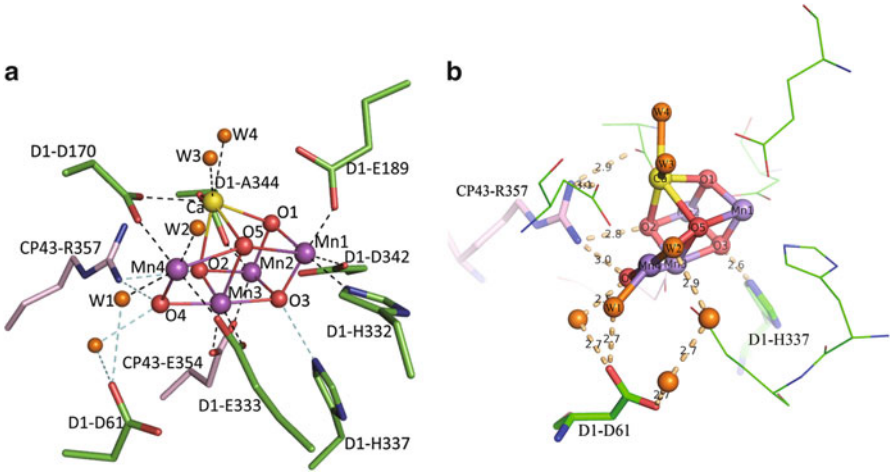

Fig. 11.6 Ligand environment of the Mn_4CaO_5 cluster. (**a**) Direct ligands to the Mn_4CaO_5 cluster. (**b**) Three residues, namely D1-D61, D1-H337, and CP43-R357, that form hydrogen bonds to the oxo-bridged oxygens in the Mn_4CaO_5 cluster

Table 11.1 Ligands for each of the metal ions in the Mn_4CaO_5 cluster of PSII

Atom	Ligands	Atom	Ligands	Atom	Ligands	Atom	Ligands	Atom	Ligands
Mn1	O1	Mn2	O1	Mn3	O2	Mn4	O4	Ca	O1
	O3		O2		O3		O5		O2
	O5		O3		O4		D170A		O5
	E189A		D342A		O5		E333A		D170A
	H332A		A344A		E333A		W1		A344A
	D342A		E354C		E354C		W2		W3
									W4

among which five are bi-dentate ligands and only D1-E189 is a mono-dentate ligand to Mn1. D1-A344 is the C-terminal residue of the D1 subunit, and two additional residues D1-E333 and D1-D342 are located in the C-terminal of the D1 subunit, illustrating that the C-terminal region of the D1 subunit is heavily involved in maintaining the structure of the Mn_4CaO_5 cluster. The only His residue is D1-H332, which is ligated to Mn1. These ligands, together with the oxo-bridges and terminal water ligands, constitute the saturated ligand environment for the Mn_4CaO_5 cluster. As a result, all of the four Mn ions are 6-coordinated (see above discussions for Mn4 and Mn1), and the Ca ion is 7-coordinated (Table 11.1).

In addition to the direct ligands to the Mn_4CaO_5 cluster, most of which are negatively charged; three residues are located close to the cluster and form hydrogen bonds with one or more of the oxo-bridged oxygens. These three residues are CP43-R357, D1-H337, and D1-D61 (Fig. 11.6b), and they are either positively charged, neutral or negatively charged. Among these three residues, CP43-R357 forms hydrogen bonds to both O2 and O4, D1-H337 forms a hydrogen bond to O3,

whereas D1-D61 is connected to O4 by hydrogen bond via a water molecule. These hydrogen bonds may be important to maintain the distorted, flexible structure of the Mn_4CaO_5 cluster. If we assume that no hydrogen bonds are present for the oxygen atoms, the O–Mn bonds in the cluster would have distances similar to those found in typical Mn oxides, which are in the range of 1.8–2.2 Å. These short distances will yield a rigid, un-distorted structure of the cluster difficult to undergo structural changes accompanying the S-state transitions. In other words, the "flexibility" expected from the distorted structure of the metal cluster will be lost, which would yield a compound with little or no catalytic activity for water-splitting. It is thus the distorted chair form, or the flexibility, of the Mn_4CaO_5 cluster that is most important for the water-splitting activity. Photosynthetic organisms have gained this "instable" structure through a long time of evolution, and have maintained this structure for even a longer time from the advent of prokaryotic cyanobacteria some 2.7 billion years ago to higher plants we see today.

11.4.5 Effects of Sr^{2+} Substitution for Ca^{2+} on the Structure of the Mn_4CaO_4 Cluster

Since the only Ca ion in the Mn_4CaO_5 cluster can be easily removed without destroying the overall structure of the cluster, and its removal completely diminishes oxygen evolution, its role in oxygen evolution has been studied extensively [46–50]. From the structural features of the Mn_4CaO_5 cluster revealed at the atomic resolution [28], one of the roles of the Ca ion appears to introduce the distortion into the structure as mentioned above. We can easily imagine that if the cluster is made up with Mn and O atoms only, its structure would become symmetric and hardly be distorted, and the resulted compound will become a rigid, stable one unable to undergo structural changes. This happens to most artificially synthesized Mn–O compounds, which are rigid, stable, and with no or low catalytic activity. Introduction of a Ca ion into Mn–O compounds has been successful in some cases; however, the position of the Ca ion is not exactly the same as that found in the native Mn_4CaO_5 cluster, so that no artificially synthesized Mn–Ca–O compounds have been obtained that match the catalytic activity of the native cluster.

Another important role that might be expected for the Ca ion, and that was implied from the crystal structure, is the binding of substrate water molecule. In the crystal structure, two water molecules were found to associate with the Ca ion; one of these two water molecules may thus function as one of the substrate water for O–O bond formation. In order to explore this possibility, the Ca was replaced with Sr, and the resulted Sr-substituted PSII was used for crystallization and crystal structural analysis [51]. Sr^{2+} is the only divalent ion capable of supporting water-splitting with an activity half of Ca-containing PSII. Thus, slight structural changes are expected by replacing Ca^{2+} with Sr^{2+}, which may be responsible for the decrease in oxygen evolution. The structure of Sr-substituted PSII was analyzed

at a resolution of 2.1 Å, which showed several small differences in the Mn–O and Sr–O distances compared with that of the Mn_4CaO_5 cluster [51]. The most significant difference, however, was found in the bond distance between Sr and one of the water ligands, W3, which became 2.6 Å, a distance 0.2 Å longer than the corresponding distance in the Mn_4CaO_5 cluster. On the other hand, the distance between W4 and Sr became 2.3 Å, which is largely similar with the corresponding distance (2.4 Å) in the Mn_4CaO_5 cluster. These results suggest that W3 binds to Ca^{2+} more weakly than W4, and is thus more mobile than W4. In fact, the position of W3 was found to be moved by 0.5 Å in the Sr^{2+}-substituted PSII relative to that in the native PSII [51]. This implies that W3 may have a higher reactivity than W4, which further implies that W3 may be involved in the water-splitting and O–O bond formation.

11.4.6 Possible Mechanisms of O–O Bond Formation

Water oxidation proceeds through the S-state cycle [52–54], where four photons are absorbed to drive sequential removal of four electrons from the Mn_4CaO_5 cluster, leading to the successive accumulation of four oxidizing equivalents in the metal cluster. The removal of electrons is accompanied by release of protons, which typically has a pattern of 1, 0, 1, 2 for the S_0–S_1, S_1–S_2, S_2–S_3, and S_3–(S_4)–S_0 transitions [55, 56]. The S_0, S_1-states are dark stable, whereas S_2, S_3-states are unstable at room temperature, and the S_4-state is highly unstable that has not been trapped stably under normal (room temperature and normal oxygen pressure) conditions. The O–O bond formation occurs during the S_3–(S_4)–S_0 transition.

The oxidation states of the four Mn ions in the S_1-state are believed to be in a combination of (III, III, IV, IV) based on EPR (ENDOR) studies on the mulitline signal characteristic of the S_2-state [57–61], as well as FXAFS studies [33, 35], although a lower oxidation state has been proposed that can also explain the experimental data [40, 62]. The oxidation states of the individual Mn ions in the S_1 and S_2-states, however, have not been assigned unambiguously. It has been reported that Mn1, the only Mn ion to which an amino acid ligand other than a carboxylate group (D1-His332) is associated, is 5-coordinated in the S_2-state, suggesting that it is in a valance of III (3+) in the S_2-state [63]. If this is the case, this Mn ion must be III also in the S_1-state. The other Mn that has a valence of III in the S_1-state is not clear; no experimental evidence relating to this Mn has been obtained. As described above, the specific O5 is sitting in the middle between Mn1 and Mn4 in the crystal structure, and both distances of O5 to Mn1 and Mn4 are exceptionally longer compared to typical Mn–O distances found in Mn oxide. This suggests that both Mn1 and Mn4 have a weak sixth ligand, implying that they are not fully 6-coordinated. The long bonding distances between Mn1 and Mn4 to O5 can be explained by a large Jan-Teller distortion that Mn(III) possesses, which is in support of the notion that Mn1 is III in the S_1-state. This in turn implies that Mn4 is also III in the S_1-state.

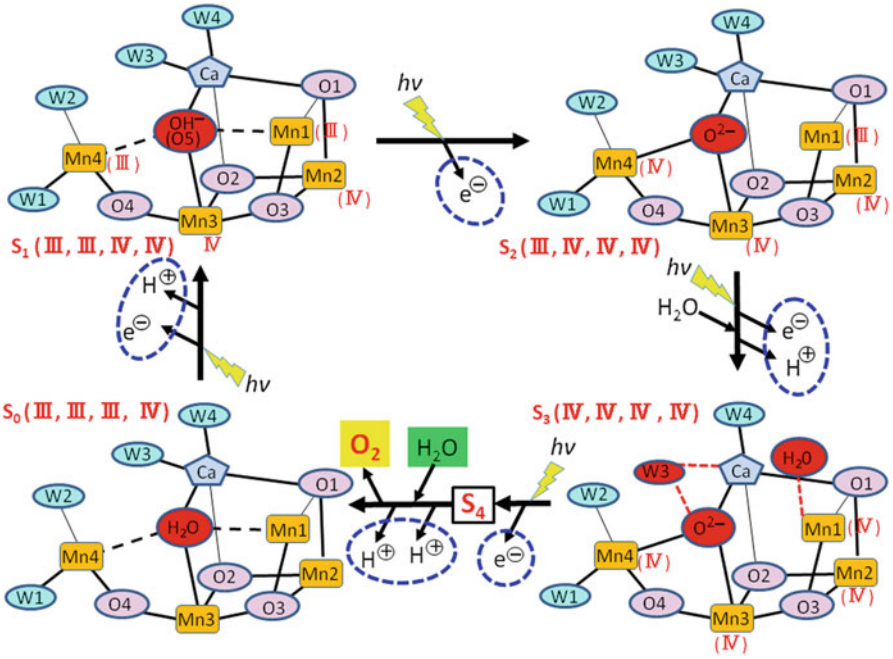

Fig. 11.7 A possible mechanism of water-splitting and O–O bond formation based on the atomic structure of the Mn_4CaO_5 cluster. See text for detailed discussions

Based on these considerations, as well as the discussions described above that the O–O bond formation may occur in the area formed by W2, W3, and O5, we may propose a mechanism for the formation of water-splitting and O–O bond formation, which is illustrated in Fig. 11.7. In this proposed mechanism, the Mn_4CaO_5 cluster has a (III, III, IV, IV) valence combination in the S_1-state, with the Mn4 and Mn1 in the III form, and Mn2 and Mn3 in the IV form. In this state, the O5 is assumed to be an OH^- species based on its long distances and thus weak binding to Mn1 and Mn4. Upon transition from S_1 to S_2 by absorption of one photon, one electron is removed from Mn4, leading to a IV state of Mn4. Due to this change, the binding of O5 to Mn4 becomes stronger than that to Mn1, resulting in a movement of O5 toward Mn4. This results in a "full" 6-coordinates for Mn4, whereas breaks the bond between O5 and Mn1, yielding a 5-coordinated Mn1 in the S_2-state, as has been suggested previously. No protons are released during this transition, and the possible structural changes may be small due to the removal of only one electron from S_1-to-S_2 transition.

In the subsequent transition from S_2 to S_3, one electron and one proton are removed. The electron may be removed from the only 3+ Mn ion remained, which is Mn1, resulting in a Mn(IV) species in the Mn1 site. This Mn1 will require to be 6-coordinated, which may be fulfilled by insertion of a new water ligand during this transition. Indeed, the insertion of a water molecule has been suggested from Fourier

transform infrared (FTIR) spectroscopic experiments [64, 65]. On the other hand, the proton may be released from the O5 site (which was assumed to be an OH^- species in the S_2-state), resulting in an O^{2-} species in this state. These changes may result in a large structural rearrangement of the whole cluster, which has been suggested from previous FTIR, EXAFS, and EPR experiments [35, 47, 49, 57, 59, 66]. One presumed consequence of this structural rearrangement may be a move of the position of W3 toward O5, resulting in a closer distance between these two species, or even already a formation of the "pseudo-double bond" of O–O between these two species.

In the S_3–(S_4)–S_0 transition, one electron and two protons are removed, accompanied by an insertion of a new water molecule. The two protons may be removed from W3, or one from W3 and one from another species, which may reinforce the O–O bond formed between W3 and O5. These changes finally force the breakage of bonds between W3 and Ca, as well as those between O5 and nearby metals, thereby release one O_2 molecule. The O_5 position may be occupied by the newly inserted water molecule in the S_0-state, from which one proton is removed during the transition from S_0 to S_1. This completes one cycle of the water oxidation reaction.

It should be pointed out that the above proposed mechanism is one of the possible mechanisms for water oxidation, and there are other possibilities that cannot be excluded at present. For example, the O–O bond formation may occur between W2 and W3 without the involvement of O5, or even between O5 and a newly inserted water molecule bound to Mn1 as proposed by Siegbahn [67, 68], since Mn1 has a 5-coordinated structure and may be actively involved in the structural rearrangements during the S-state transitions. Answers to the real mechanism for water oxidation may not be obtained until the structural rearrangements occurred during the S-state transitions are elucidated.

11.4.7 Hydrogen-Bond Networks and Proton Channels

During the S-state transitions, four protons must be removed. Since the Mn_4CaO_5 cluster is embedded deeply in the PSII protein matrix covered by a large area formed by thee hydrophilic, extrinsic subunits, as well as the membrane-extrinsic loops of large transmembrane subunits CP47, CP43, D1, and D2 [28], there must be channels for the exit of protons outside of the catalytic site to the lumenal bulk solution as well as channels for the inlet of substrate water molecules. In the atomic structure of PSII, there are indeed a number of well-defined hydrogen-bond networks connecting the Mn_4CaO_5 cluster to the lumenal surface of the PSII protein complex, which may function as proton exit channels or water inlet channels [27, 28, 69–71].

One example of such channels is mediated by Y_Z, an electron mediator between the Mn_4CaO_5 cluster and the PSII reaction center chlorophylls. Y_Z has been identified to be Tyr161 of the D1 subunit, and a well-defined hydrogen-bond network was found between D1-Tyr161 and the Mn_4CaO_5 cluster [28]. This network

extends further from D1-Tyr161 to the lumenal bulk phase. First, D1-Tyr161 is hydrogen-bonded to the two water molecules coordinated to Ca either directly (W4) or indirectly (W3) through another water (Fig. 11.8a). The hydrogen bond between the additional water and D1-Tyr161 that mediates the link from W3 to Tyr161 has a length of 2.6 Å, suggesting that this is a strong (low barrier) hydrogen bond [28, 72]. This additional water also mediates the hydrogen bond between the two water molecules bound to Mn4 and D1-Tyr161. On the other hand, another strong hydrogen bond was found between D1-Tyr161 and the ε-nitrogen of D1-His190, which has a distance of 2.5 Å and is in the opposite side of the Mn_4CaO_5 cluster. D1-His190 was further hydrogen-bonded to D1-Asn298 and to several water molecules and amino acid residues including CP43-Ala411, D1-Asn322, and PsbV-Tyr137, leading to an exit pathway to the lumenal bulk solution (PsbV-Tyr137 is the C-terminal residue of the PsbV subunit) (Fig. 11.8a) [28]. This hydrogen-bond network is located in the interfaces between D1, CP43, and PsbV subunits, and may function as an exit channel for protons that arise from proton-coupled electron transfer (PCET) via Y_Z. This is in support of the existence of a PCET pathway involving D1-Tyr161 and D1-His190 as suggested previously [73–75]. PsbV-Tyr137 at the exit of this channel is surrounded by several charged residues including D1-Arg323, D1-His304, and PsbV-Lys129; these residues may therefore function to regulate the proton excretion through the PCET pathway.

Another example of the hydrogen-bond network starts from one of the ligands to the Mn_4CaO_5 cluster, D1-E333, and mediated by D1-D61 and Cl-1 [28]. Cl-1 is one of the two chloride binding sites found in PSII, which are located in two sides of the Mn_4CaO_5 cluster and have distances of 6–7 Å to the Mn_4CaO_5 cluster [76, 77]. Cl-1 is surrounded by D1-K317, D1-E333, and two water molecules. The hydrogen-bond network extends from D1-D61 and Cl-1 through several amino acid residues and water molecules formed by the interfaces of D2, PsbO, and CP47, to the surface of the protein complex in the lumenal bulk solution (Fig. 11.8b). This hydrogen-bond network may function for the exit of protons or inlet of water molecules. In fact, both D1-D61 and Cl-1 have been suggested to be important for the activity of oxygen evolution from either mutagenesis [78] or Cl-depletion studies [79, 80].

11.5 Concluding Remarks and Future Perspectives

The geometric structure of the Mn_4CaO_5 cluster has been revealed from the structural analysis of PSII at an atomic level, which made PSII the largest membrane protein whose structure was solved beyond 2.0 Å resolution. Although there are still some debates regarding the bond distances of Mn–Mn and Mn–O in the crystal structure probably due to possible radiation damages, the mechanism of water oxidation and O–O bond formation could be considered based on the current structure where a huge number of water molecules are revealed. The exact reaction mechanism and the structural rearrangements possibly occurring during the S-state

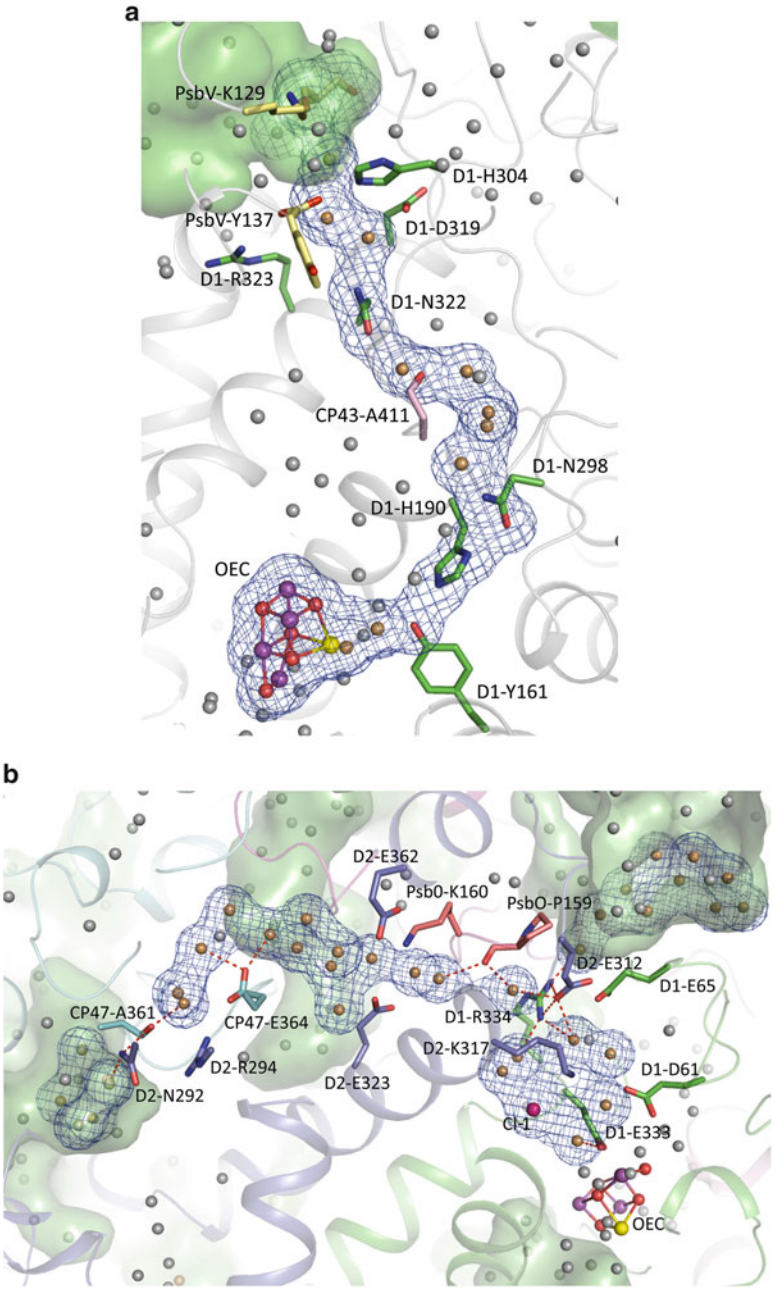

Fig. 11.8 Examples of hydrogen-bond networks found in the atomic resolution structure of PSII. (**a**) A hydrogen-bond network mediated by Y_Z, D1-Tyr161. The network starts from the water molecules hydrogen-bonded to Ca, through D1-Tyr161, several water molecules and amino acid residues, and finally exits to the lumenal bulk solution through PsbV-K129. The *green* area in the *upper left* side represents lumenal solution phase. (**b**) Hydrogen-bond network mediated by Cl-1. The network starts from one of the ligand to the Mn_4CaO_5 cluster D1-E333, through Cl-1, D1-D61, several water molecules and amino acid residues, and exits to the lumenal solution. The *green* regions represent lumenal solution phase

transitions, however, have to be determined until some, or all, of the structures of the intermediate S-states can be obtained. This will be greatly benefited by the use of the high resolution crystals already obtained, as well as a combination of various advanced biophysical techniques such as X-ray absorption spectroscopy, advanced EPR techniques, and FTIR. These spectroscopic techniques may yield unique information regarding the structures, dynamics, and oxidation states of the catalytic site. In addition, the availability of X-ray free electron lasers (XFEL) is worth to be mentioned in particularly, since it provides ultra-short pulses (fs) of intense X-rays which may allow diffraction data to be collected free of radiation damage (a principle so-called diffraction before explosion), as well as data collection from shortly lived intermediate states. Elucidation of the water-splitting mechanism will be important for the designing of artificial catalyst capable of splitting water using the energy from the sun, a source of ultimate clean energy for powering life on the earth.

Acknowledgements Structural analysis of PSII at the atomic resolution described in this chapter was performed in collaboration with Drs. Nobuo Kamiya, Yasufumi Umena, and Keisuke Kawakami, and analysis of the Sr-PSII was performed in collaboration with Dr. Faisal H.M. Koua in addition to the above colleagues. I thank these colleagues for their continuous contributions. The work performed in the author's laboratory is supported by a Grant-in-Aid for Specially Promoted Research from MEXT/JSPS of Japan.

References

1. Wydrzynski TJ, Satoh K, editors. Photosystem II, The light-driven water:plastoquinone oxidoreductase. Dordrecht, The Netherlands: Springer; 2005.
2. Shen JR, Henmi T, Kamiya N. Structure and function of photosystem II. In: Fromme P, editor. Photosynthetic protein complexes. A structural approach. Weinheim: Wiley-VCH Verlag GmbH & Co. KGaA; 2008. p. 83–106.
3. Li M, Chang WR. Protein crystallization. Photosynth Res. 2009;102:223–9.
4. Weber PC. Overview of protein crystallization methods. Macromol Crystallogr A. 1997;276:13–22.
5. Bergfors TM, editor. Protein crystallization: techniques, strategies, and tips. San Diego, CA: International University Line (IUL); 1999.
6. Chayen NE, Saridakis E. Protein crystallization: from purified protein to diffraction-quality crystal. Nat Methods. 2008;5:147–53.
7. McPherson A. Crystallization of biological macromolecules. New York, NY: Cold Spring Harbor Laboratory Press; 1999.
8. Michel H, editor. Crystallization of membrane proteins. Boca Raton, FL: CRS press; 1990.
9. Iwata S, editor. Methods and results in crystallization of membrane proteins. San Diego, CA: International University Line (IUL); 2003.
10. Caffrey M, Cherezov V. Crystallizing membrane proteins using lipidic mesophases. Nat Protoc. 2009;4:706–31.
11. Katona G, Andréasson U, Landau EM, et al. Lipidic cubic phase crystal structure of the photosynthetic reaction centre from *Rhodobacter sphaeroides* at 2.35 Å resolution. J Mol Biol. 2003;331:681–92.
12. Landau EM, Rosenbusch JP. Lipidic cubic phases: a novel concept for the crystallization of membrane proteins. Proc Natl Acad Sci U S A. 1996;93(25):14532–5.

13. Hunte C, Michel H. Crystallization of membrane proteins mediated by antibody fragments. Curr Opin Struct Biol. 2002;12:503–8.
14. Cherezov V, Rosenbaum DM, Hanson MA, Rasmussen SG, Thian FS, Kobilka TS, Choi HJ, Kuhn P, Weis WI, Kobilka BK, Stevens RC. High-resolution crystal structure of an engineered human β2-adrenergic G protein-coupled receptor. Science. 2007;318:1258–65.
15. Rosenbaum DM, Cherezov V, Hanson MA, Rasmussen SG, Thian FS, Kobilka TS, Choi HJ, Yao XJ, Weis WI, Stevens RC, Kobilka BK. GPCR engineering yields high-resolution structural insights into β2-adrenergic receptor function. Science. 2007;318:1266–73.
16. Allen JP, Seng C, Larson C. Structures of proteins and cofactors: X-ray crystallography. Photosynth Res. 2009;102:231–40.
17. Drenth J. Principles of protein X-ray crystallography. New York, NY: Springer; 1999.
18. Chayen NE, Helliwell JR, Snell EH. Macromolecular crystallization and crystal perfection. Oxford: Oxford University Press; 2010.
19. Kuhl H, Kruip J, Seidler A, Krieger-Liszkay A, Bunker M, Bald D, Scheidig AJ, Rogner M. Towards structural determination of the water-splitting enzyme. Purification, crystallization, and preliminary crystallographic studies of photosystem II from a thermophilic cyanobacterium. J Biol Chem. 2000;275:20652–9.
20. Shen JR, Kamiya N. Crystallization and the crystal properties of the oxygen-evolving photosystem II from *Synechococcus vulcanus*. Biochemistry. 2000;39:14739–44.
21. Zouni A, Witt HT, Kern J, Fromme P, Krauß N, Saenger W, Orth P. Crystal structure of photosystem II from *Synechococcus elongatus* at 3.8 Å resolution. Nature. 2001;409:739–43.
22. Shen JR, Inoue Y. Binding and functional properties of two new extrinsic components, cytochrome *c*550 and a 12 kDa protein, in cyanobacterial photosystem II. Biochemistry. 1993;32:1825–32.
23. Sugiura M, Inoue Y. Highly purified thermo-stable oxygen-evolving photosystem II core complex from the thermophilic cyanobacterium *Synechococcus elongatus* having His-tagged CP43. Plant Cell Physiol. 1999;40:1219–31.
24. Kamiya N, Shen JR. Crystal structure of oxygen-evolving photosystem II from *Thermosynechococcus vulcanus* at 3.7-Å resolution. Proc Natl Acad Sci U S A. 2003;100:98–103.
25. Ferreira KN, Iverson TM, Maghlaoui K, Barber J, Iwata S. Architecture of the photosynthetic oxygen-evolving center. Science. 2004;303:1831–8.
26. Loll B, Kern J, Saenger W, Zouni A, Biesiadka J. Towards complete cofactor arrangement in the 3.0 Å resolution structure of photosystem II. Nature. 2005;438:1040–4.
27. Guskov A, Kern J, Gabdulkhakov A, Broser M, Zouni A, Saenger W. Cyanobacterial photosystem II at 2.9 Å resolution and role of quinones, lipids, channels and chloride. Nat Struct Mol Biol. 2009;16:334–42.
28. Umena Y, Kawakami K, Shen JR, Kamiya N. Crystal structure of oxygen-evolving photosystem II at a resolution of 1.9 Å. Nature. 2011;473:55–60.
29. Dau H, Liebisch P, Haumann M. The structure of the manganese complex of photosystem II in its dark-stable S_1-state: EXAFS results in relation to recent crystallographic data. Phys Chem Chem Phys. 2004;6:4781–92.
30. Dau H, Grundmeier A, Loja P, Haumann M. On the structure of the manganese complex of photosystem II: extended-range EXAFS data and specific atomic resolution models for four S-states. Philos Trans R Soc Lond B. 2008;363:1237–44.
31. Pushkar Y, Yano J, Glatzel P, Messinger J, Lewis A, Sauer K, Bergmann U, Yachandra V. Structure and orientation of the Mn_4Ca cluster in plant photosystem II membranes studied by polarized range-extended X-ray absorption spectroscopy. J Biol Chem. 2007;282:7198–208.
32. Sauer K, Yano J, Yachandra VK. X-ray spectroscopy of the photosynthetic oxygen-evolving complex. Coord Chem Rev. 2008;252:318–35.
33. Yano J, Kern J, Sauer K, Latimer MJ, Pushkar Y, Biesiadka J, Loll B, Saenger W, Messinger J, Zouni A, Yachandra VK. Where water is oxidized to dioxygen: structure of the photosynthetic Mn_4Ca cluster. Science. 2006;314:821–5.

34. Zein S, Kulik LV, Yano J, Kern J, Pushkar Y, Zouni A, Yachandra VK, Lubitz W, Neese F, Messinger J. Focusing the view on nature's water-splitting catalyst. Philos Trans R Soc Lond B. 2008;363:1167–77.
35. Haumann M, Müller C, Liebisch P, Iuzzolino L, Dittmer J, Grabolle M, Neisius T. Meyer-KlauckeW, Dau H. Structural and oxidation state changes of the photosystem II manganese complex in four transitions of the water oxidation cycle (S_0/S_1, S_1/S_2, S_2/S_3, and S_3, S_4/S_0) characterized by X-ray absorption spectroscopy at 20 K and room temperature. Biochemistry. 2005;44:1894–908.
36. Yano J, Pushkar Y, Glatzel P, Lewis A, Sauer K, Messinger J, Bergmann U, Yachandra VK. High-resolution Mn EXAFS of the oxygen-evolving complex in photosystem II: structural implications for the Mn_4Ca cluster. J Am Chem Soc. 2005;127:14974–5.
37. Ames W, Pantazis DA, Krewald V, Cox N, Messinger J, Lubitz W, Neese F. Theoretical evaluation of structural models of the S_2 state in the oxygen evolving complex of photosystem II: protonation states and magnetic interactions. J Am Chem Soc. 2011;133:19743–57.
38. Grundmeier A, Dau H. Structural models of the manganese complex of photosystem II and mechanistic implications. Biochim Biophys Acta. 2012;1817:88–105.
39. Isobe H, Shoji M, Yamanaka S, Umena Y, Kawakami K, Kamiya N, Shen JR, Yamaguchi K. Theoretical illumination of water-inserted structures of the $CaMn_4O_5$ cluster in the S_2 and S_3 states of oxygen-evolving complex of photosystem II: full geometry optimizations by B3LYP hybrid density functional. Dalton Trans. 2012;41:13727–40.
40. Petrie S, Gatt P, Stranger R, Pace RJ. Modelling the metal atom positions of the photosystem II water oxidising complex: a density functional theory appraisal of the 1.9 angstrom resolution crystal structure. Phys Chem Chem Phys. 2012;14:11333–43.
41. Siegbahn PEM. The effect of backbone constraints—the case of water oxidation by the oxygen evolving complex in photosystem II. ChemPhysChem. 2011;12:3274–80.
42. Siegbahn PE. Water oxidation mechanism in photosystem II, including oxidations, proton release pathways, O–O bond formation and O_2 release. Biochim Biophys Acta. 2013;1827 (8–9):1003–19. doi:10.1016/j.bbabio.2012.10.006.
43. Yamaguchi K, Isobe H, Yamanaka S, Saito T, Kanda K, Shoji M, Umena Y, Kawakami K, Shen JR, Kamiya N, Okumura M. Full geometry optimizations of the mixed-valence $CaMn_4O_4X(H_2O)_4$ (X = OH or O) cluster in OEC of PS II: degree of symmetry breaking of the labile Mn-X-Mn bond revealed by several hybrid DFT calculations. Int J Quan Chem. 2013;113:525–41.
44. Yamaguchi K, Yamanaka S, Isobe H, Saito T, Kanda K, Umena Y, Kawakami K, Shen JR, Kamiya N, Okumura M, Nakamura H, Shoji M, Yoshioka Y. The nature of chemical bonds of the $CaMn_4O_5$ cluster in oxygen evolving complex of photosystem II: Jahn-Teller distortion and its suppression by Ca doping in cubane structures. Int J Quan Chem. 2013;113:453–73.
45. Luber S, Rivalta I, Umena Y, Kawakami K, Shen JR, Kamiya N, Brudvig GW, Batista VS. S_1-state model of the O_2-evolving complex of photosystem II. Biochemistry. 2011;50:6308–11.
46. Boussac A, et al. Biosynthetic Ca^{2+}/Sr^{2+} exchange in the photosystem II oxygen-evolving enzyme of *Thermosynechococcus elongatus*. J Biol Chem. 2004;279:22809–19.
47. Cox N, et al. Effect of Ca^{2+}/Sr^{2+} substitution on the electronic structure of the oxygen-evolving complex of photosystem II: a combined multifrequency EPR, ^{55}Mn-ENDOR, and DFT study of the S_2 state. J Am Chem Soc. 2011;133:3635–48.
48. Ishida N, et al. Biosynthetic exchange of bromide for chloride and strontium for calcium in the photosystem II oxygen-evolving enzymes. J Biol Chem. 2008;283:13330–40.
49. Pushkar Y, Yano J, Sauer K, Boussac A, Yachandra VK. Structural changes in the Mn_4Ca cluster and the mechanism of photosynthetic water splitting. Proc Natl Acad Sci U S A. 2008;105:1879–84.
50. Suzuki H, Taguchi Y, Sugiura M, Boussac A, Noguchi T. Structural perturbation of the carboxylate ligands to the manganese cluster upon Ca^{2+}/Sr^{2+} exchange in the S-state cycle of photosynthetic oxygen evolution as studied by flash-induced FTIR difference spectroscopy. Biochemistry. 2006;45:13454–64.

51. Koua FHM, Umena Y, Kawakami K, Shen JR. Structure of Sr-substituted photosystem II at 2.1 Å resolution and its implications in the mechanism of water oxidation. Proc Natl Acad Sci U S A. 2013;110:3889–94.
52. Dau H, Haumann M. The manganese complex of photosystem II in its reaction cycle—basic framework and possible realization at the atomic level. Coord Chem Rev. 2008;252:273–95.
53. Joliot P. Period-four oscillations of the flash-induced oxygen formation in photosynthesis. Photosynth Res. 2003;76:65–72.
54. Kok B, Forbush B, McGloin M. Cooperation of charges in photosynthetic oxygen evolution. I. A linear four step mechanism. Photochem Photobiol. 1970;11:457–75.
55. Junge W, Haumann M, Ahlbrink R, Mulkidjanian A, Clausen J. Electrostatics and proton transfer in photosynthetic water oxidation. Philos Trans R Soc Lond B. 2002;357:1407–18.
56. Suzuki H, Sugiura M, Noguchi T. Monitoring proton release during photosynthetic water oxidation in photosystem II by means of isotope-edited infrared spectroscopy. J Am Chem Soc. 2009;131:7849–57.
57. Britt RD, Campbell KA, Peloquin JM, Gilchrist ML, Aznar CP, Dicus MM, Robblee J, Messinger J. Recent pulsed EPR studies of the photosystem II oxygen-evolving complex: implications as to water oxidation mechanisms. Biochim Biophys Acta. 2004;1655:158–71.
58. Kulik LV, Epel B, Lubitz W, Messinger J. ^{55}Mn pulse ENDOR at 34 GHz of the S_0 and S_2 states of the oxygen-evolving complex in photosystem II. J Am Chem Soc. 2005;127:2392–3.
59. Kulik LV, Epel B, Lubitz W, Messinger J. Electronic structure of the Mn_4OxCa cluster in the S_0 and S_2 states of the oxygen-evolving complex of photosystem II based on pulse ^{55}Mn-ENDOR and EPR spectroscopy. J Am Chem Soc. 2007;129:13421–35.
60. McEvoy JP, Gascon JA, Batista VS, Brudvig GW. The mechanism of photosynthetic water splitting. Photochem Photobiol Sci. 2005;4:940–9.
61. Peloquin JM, Campbell KA, Randall DW, Evanchik MA, Pecoraro VL, Armstrong WH, Britt RD. ^{55}Mn ENDOR of the S_2-state multiline EPR signal of photosystem II: implications on the structure of the tetranuclear Mn cluster. J Am Chem Soc. 2000;122:10926–42.
62. Kolling DR, Cox N, Ananyev GM, Pace RJ, Dismukes GC. What are the oxidation states of manganese required to catalyze photosynthetic water oxidation? Biophys J. 2012;103:313–22.
63. Stich TA, Yeagle GJ, Service RJ, Debus RJ, Britt RD. Ligation of D1-His332 and D1-Asp170 to the manganese cluster of photosystem II from *Synechocystis* assessed by multifrequency pulse EPR spectroscopy. Biochemistry. 2011;50:7390–404.
64. Noguchi T. FTIR detection of water reactions in the oxygen-evolving centre of photosystem II. Philos Trans R Soc Lond B Biol Sci. 2008;363:1189–94.
65. Suzuki H, Sugiura M, Noguchi T. Monitoring water reactions during the S-state cycle of the photosynthetic water-oxidizing center: detection of the DOD bending vibrations by means of Fourier transform infrared spectroscopy. Biochemistry. 2008;47:11024–30.
66. Noguchi T. Fourier transform infrared analysis of the photosynthetic oxygen-evolving center. Coord Chem Rev. 2008;252:336–46.
67. Siegbahn PE. A structure-consistent mechanism for dioxygen formation in photosystem II. Chem Eur J. 2008;14:8290–302.
68. Siegbahn PE. Structures and energetics for O_2 formation in photosystem II. Acc Chem Res. 2009;42:1871–80.
69. Gabdulkhakov A, Guskov A, Broser M, Kern J, Müh F, Saenger W, Zouni A. Probing the accessibility of the Mn_4Ca cluster in photosystem II: channels calculation, noble gas derivatization, and cocrystallization with DMSO. Structure. 2009;17:1223–34.
70. Ho FM, Styring S. Access channels and methanol binding site to the $CaMn_4$ cluster in Photosystem II based on solvent accessibility simulations, with implications for substrate water access. Biochim Biophys Acta. 2008;1777:140–53.
71. Murray JW, Barber J. Structural characteristics of channels and pathways in photosystem II including the identification of an oxygen channel. J Struct Biol. 2007;159:228–37.
72. Saito K, Shen JR, Ishida T, Ishikita H. Short hydrogen bond between redox-active Tyrosine Y_Z and D1-His190 in the photosystem II crystal structure. Biochemistry. 2011;50:9836–44.

73. Hays AMA, Vassiliev IR, Golbeck JH, Debus RJ. Role of D1-His190 in the proton-coupled oxidation of tyrosine Y_Z in manganese-depleted Photosystem II. Biochemistry. 1999;38:11851–65.
74. Hoganson CW, Babcock GT. A metalloradical mechanism for the generation of oxygen from water in photosynthesis. Science. 1997;277:1953–6.
75. Tommos C, Babcock GT. Proton and hydrogen currents in photosynthetic water oxidation. Biochim Biophys Acta. 2000;1458:199–219.
76. Kawakami K, Umena Y, Kamiya N, Shen JR. Location of chloride and its possible functions in oxygen-evolving photosystem II revealed by X-ray crystallography. Proc Natl Acad Sci U S A. 2009;106:8567–72.
77. Murray JW, Maghlaoui K, Kargul J, Ishida N, Lai TL, Rutherford AW, Sugiura M, Boussac A, Barber J. X-ray crystallography identifies two chloride binding sites in the oxygen evolving centre of Photosystem II. Energ Environ Sci. 2008;1:161–6.
78. Debus RJ. Protein ligation of the photosynthetic oxygen-evolving center. Coord Chem Rev. 2008;252:244–58.
79. Popelková H, Yocum CF. Current status of the role of Cl^- ion in the oxygen-evolving complex. Photosynth Res. 2007;93:111–21.
80. Wincencjusz H, van Gorkom HJ, Yocum CF. The photosynthetic oxygen evolving complex requires chloride for its redox state $S_2 \rightarrow S_3$ and $S_3 \rightarrow S_0$ transitions but not for $S_0 \rightarrow S_1$ or $S_1 \rightarrow S_2$ transitions. Biochemistry. 1997;36:3663–70.

Chapter 12
Water and Oxygen Diffusion Pathways Within Photosystem II. Computational Studies of Controlled Substrate Access and Product Release

Serguei Vassiliev and Doug Bruce

Abstract The problem of finding and characterizing channels responsible for controlling the movement of small molecules within protein complexes is addressed, using photosystem II (PSII) of photosynthesis as an example. The shortcomings of traditional methods of searching for channels in static crystallographic structures are discussed. Basic concepts and advantages of molecular dynamics (MD) simulations and existing computational approaches based on MD structures to finding water channels are introduced. The use of MD to observe water diffusion within proteins, visualize water flow, and localize water channels is described. This is followed by more detailed characterization and analysis of the found channels, with respect to their permitivity for water. The second part of the chapter focuses on oxygen channels within PSII. The experimental and computational techniques for characterization of oxygen channels in proteins are reviewed. A powerful computational technique, based on analysis of 3D energy maps, is introduced. The construction of oxygen 3D free energy maps for PSII and their analysis using a wavefront propagation technique is described to find oxygen diffusion pathways and characterize the rate of oxygen diffusion within PSII.

Keywords Water channels • Oxygen channels • Molecular dynamics • Permeation barriers

S. Vassiliev, Ph.D. (✉) • D. Bruce, Ph.D.
Department of Biology, Brock University, 500 Glenridge Ave.,
St. Catharines, ON, Canada L2S 3A1
e-mail: svassiliev@brocku.ca; dbruce@brocku.ca

J. Golbeck and A. van der Est (eds.), *The Biophysics of Photosynthesis*,
Biophysics for the Life Sciences 11, DOI 10.1007/978-1-4939-1148-6_12,

12.1 Water Oxidation in PSII, Early Ideas for Substrate Access and Product Release

Photosystem II (PSII) is a pigment–protein complex embedded in the thylakoid membranes of plant and algal chloroplasts and cyanobacteria that catalyses the light induced oxidation of water and reduction of plastoquinone in oxygenic photosynthesis [1, 2]. This catalytic function is performed by light driven electron transfer reactions through redox cofactors of the PSII reaction center. By coupling water oxidation to photochemistry, PSII taps into an abundant energy supply that ultimately powers most forms of life. The heart of PSII's unique ability is the oxygen-evolving complex (OEC), consisting of a cluster of four high-valence manganese ions and a calcium ion. Water cleavage requires accumulation of four oxidation equivalents in the Mn_4CaO_5 cluster according to the S-cycle proposed by Joliot and Kok [3, 4].

The oxidation of water to O_2 requires a very strong oxidant and is thus prone to side reactions resulting in the formation of reactive oxygen species. The OEC is surrounded by a hydrophobic pocket and buried deep within the protein to prevent excessive water and solute access to the catalytic site [5]. The restricted access of large competitive water analogs to the water splitting reaction first led to the proposal that the site of water oxidation was protected by the protein [6]. Subsequent studies confirmed this idea by showing that perturbation of the protein, via release of extrinsic PSII polypeptides, resulted in H_2O_2 formation at the expense of O_2 evolution, a condition reversed by the addition of kosmotropic solutes that promote protein aggregation [5]. Access to the OEC was probed in an ESEEM study that showed binding of alcohols to the Mn_4CaO_5 cluster decreasing with increasing molecular weight, leading the authors to suggest the presence of a water channel [7]. As O_2 and protons are released from the same catalytic site, channels for the exit of both have also been suggested [8, 9]. With requirements for three potentially independent channels, the "plumbing" of PSII could be complex.

12.2 Introduction to the Problem of Finding Channels Within Molecular Labyrinths

Finding small molecule pathways inside proteins is not simple even when the atomic structure of the protein is known. Small molecules may enter the protein through multiple channels that are not apparent from examination of static X-ray structures. The underlying physical phenomenon is the 3D motion of a probe molecule within a molecular labyrinth. The probe experiences continuously varying forces arising from interactions with all protein and internal solvent atoms. This problem can be described by a system of partial differential equations, the Eikonal equation. We will describe this equation in detail in Sect. 12.6.

Most of the proposed approximation methods to estimate the possibility of a small molecule migrating through a protein consider only geometrical factors and treat the protein atoms as static hard spheres. However, even within such simplified models, the problem is challenging. Current solutions can study paths of a small molecule as approximated by a spherical probe inside a protein. A program "Caver" for solving the shortest path problem in this context was presented by Petrek et al. [10]. The algorithm approximated a protein volume with a 3D grid where a cost function was assigned for each grid point related to the distance from the closest protein atom. The graph-searching Dijkstra's algorithm was then used to find the lowest cost path from the single source (active site) to the external environment. One of the drawbacks of Dijkstra's algorithm is that it operates on a graph constructed from a discrete set of grid points and cannot converge to the solution of a continuous Eikonal problem. Regardless of how fine the grid is, it always produces a stairstep path. The use of fast marching methods to solve the Eikonal equation addresses this limitation of Dijkstra's method. A more advanced fast marching method capable of exploring geometric configurations of a more complex nature than a spherical ligand molecule has been presented recently [11].

A significant limitation of both of these models is that only one particular static conformation of the protein is considered. In reality small molecule migration in proteins occurs not along permanently open channels, but rather along transient channel connections arising from formation of protein dynamics cavities [12]. In certain cases, the small molecule energy may be sufficient to induce local protein structure reorganization that would lead to widening of narrow gorges. For example, a CO molecule in myoglobin can reside in several internal cavities. It has been observed that the migration of the CO molecule into each cavity induced structural changes of the protein, leading to an expansion of the cavity within the protein [13].

Computational models of small molecule pathways inside proteins can be extended to account for dynamical effects of the protein. In these methods the ligands interact with dynamical structures [11]. Two basic types of computational strategies have been developed to study the interaction of small molecules within a dynamical protein matrix and to compute the free energy of placement of small molecules inside a protein: (1) methods in which the probe molecule is included explicitly in the dynamic simulations, and the free energy profile of the diffusion process is computed; and (2) methods that use molecular dynamics simulations in the absence of the probe molecule, and incorporate it implicitly afterwards. For a good review of recent approaches see [14]. Explicit methods provide accurate and detailed free energy profile descriptions of small molecule pathways, but are computationally expensive [14, 15]. Implicit ligand sampling (ILS) techniques are much faster [16, 17].

12.3 Channels in Static X-ray Diffraction Structures of PSII

A search for the expected channels within PSII became possible after publication of X-ray crystal structures of the PSII core complex [18, 19] The "Caver" program was used initially to search for connecting cavities forming channels within the 1S5L.pdb structure of PSII [20]. Three channels were found, the widest and the least hydrophillic (1) was suggested to carry oxygen, a more polar channel (2) was assigned to water and protons, and the most polar channel (3) was designated for protons alone. The Caver algorithm searches for the shortest pathways of a chosen minimal diameter from a particular point inside the protein to the surface. The program thus biases the search for channels toward a set of round "pipelines." A more comprehensive identification of cavities near the OEC in the 2AXT.pdb structure of PSII, regardless of connection to the surface, revealed a complex system of potential channels [21]. The approach taken in that work was a large step forward in understanding how water is carried to the active site and revealed a complex interconnected network of water pores and cavities within PSII. A higher resolution structure of PSII, 3BZ1, was subsequently analyzed by the "Caver" program [10, 22, 23] which generated a system of eight channels originating at the OEC that merged into six exits on the lumenal side of PSII. The largest channels were in positions similar to the "water channels" found in earlier studies. A number of "new" channels with smaller minimum diameters were also identified and based on their size and the placement of hydrophilic residues they were assigned as proton channels.

All of the initial efforts to identify water channels within PSII were based on the identification and analysis of cavities found within X-ray structures. There are two main problems with this approach.

1. The existence of a cavity in a crystallographic structure does not necessarily mean that it is occupied by water. To test whether or not such a cavity could "hold" water one could place explicit water molecules within the structure and then determine their potential energy. This approach was used successfully in a DFT-QM/MM study of OEC which identified a chain of hydrogen-bonded water molecules approaching the Mn_4CaO_5 cluster along two distinct pathways [24, 25]. This study, however, was computationally limited and included only a small protein region adjacent to the active site of water splitting.
2. Channels observed within static structures have fixed boundaries and a rigid lining [20, 21]. This is an unrealistic picture as proteins and the channels within them are dynamic at physiological temperatures. Thermal motions of protein will continuously modify channel parameters and may lead to the transient opening and closing of connections between cavities and openings to the surface [12]. These dynamic processes may be involved in controlling the movement of water with the protein. As proposed in [26], dynamic simulations of water diffusion are essential to the understanding of water channels and water movement in PSII.

12.4 How to Apply Molecular Dynamics to PSII

12.4.1 Molecular Dynamics Basics

Molecular dynamics (MD) is a computer simulation of the time dependent behavior of atoms and molecules in a molecular system. Within MD simulations the atoms and molecules interact for a period of time, producing a trajectory of the motion of the atoms. To achieve this goal MD solves Newton's equations of motion for N interacting atoms. Each atom in a MD system experiences forces from all other atoms in the simulation system. These forces accelerate atoms, and change with time as the positions of atoms are changing. To solve equations of motion the system is propagated in very small time steps, updating forces at every step. The system is followed for some time, and care is taken that the temperature and pressure remain at the desired values. To evaluate interactions between atoms simulation programs requires a "force field." A "force field" contains a mathematical formula and parameters that describe properties and interactions between all atoms in the system. There are two types of interactions in MD: (1) interactions between nonbonded atoms (electrostatic and van der Waals), and (2) interactions between bonded atoms (stretching, bending, and torsion). For MD simulations all individual molecules in a simulation system must be identified and matched to a database of molecular parameters in the force field. This processing is done by comparing residue names and atom names in an initial PDB structure file to a loaded force field database. While peptide bonds between amino acids in a single chain can be automatically assigned based on chain specification in PDB file, there is no mechanism within the PDB standard to specify disulphide bonds or bonds between protein and cofactors. Such additional bonds are specified during preparation of molecular parameter files for the system. The most frequently used force fields for macromolecules are CHARMM, AMBER, GROMACS, and OPLS.

12.4.2 Setting Up Molecular Dynamics Simulations for PSII

To prepare MD simulations the X-ray structure file must be thoroughly checked. Standard force fields include libraries of molecular parameter files describing bonded interactions and partial atomic charges of amino acids and nucleic acids. Additional molecular mechanics parameter files must be prepared for all cofactors. Disulphide bonds must be made manually. If up to five terminal amino acids are missing, they can be added if they are expected to be functionally important. Adding more than five amino acids is generally not recommended, as finding the optimal folding pattern in this case may be computationally expensive and not reliable. Protonation patterns of the protein must be assigned. Histidines require close attention. This amino acid has a pKa of 6.5. This means that, at physiologically relevant pH values, relatively small changes in its environment will change

its average charge. In addition a neutral form of His can have a proton at epsilon or delta positions. Proper assigning of a His form is very important for PSII as some histidines are axial ligands to chlorophyll. Glutamic and aspartic acids can sometimes be neutral, e.g., in hydrophobic environments, or when negatively charged cofactors or other acidic amino acids are nearby. For simulations of integral membrane systems a protein must be inserted into a lipid membrane. An initial membrane patch can be built and equilibrated separately from the protein. MD simulation requires the membrane to be oriented in the XY plane. After equilibration of the membrane patch, the PSII core complex is embedded into the lipid bilayer by rotating/translating it to be centered in the membrane patch and properly oriented with respect to the membrane normal. All lipid molecules overlapping with the protein are then removed. This approach works well for small proteins with simple shapes. In the case of PSII, however, after this procedure quite large gaps were found between the lipid and protein. Due to the large size of the simulation system a very long simulation time would be required to wait until these gaps will be filled spontaneously during equilibration. Therefore these gaps were filled manually using the interactive molecular dynamics (IMD) feature of VMD/NAMD [27, 28]. Lipid molecules were placed above the membrane and then interactively guided into the empty gaps. After the protein/membrane system is built the whole system, including internal protein cavities, must be neutralized and solvated. Sodium ions were added to neutralize the system. To neutralize the system its electrostatic potential is computed and ions are placed at the most energetically favorable locations. Even the latest 1.9 Å X-ray diffraction structure [29] does not reveal all the water molecules associated with PSII, especially the more mobile water molecules. To fill internal protein cavities, water molecules can be placed using the DOWSER program [30]. The DOWSER program finds cavities, places water molecules in internal cavities, and adjusts their position and orientation to minimize interaction energy with the protein. After energy minimization only water molecules with energies <-12 kcal/mol are retained. The threshold water–protein interaction energy was set to this value which had previously been found to be optimal for distinguishing hydrated cavities from empty cavities [31]. In [32] more than 900 buried water molecules were added to each of the PSII simulations (Fig. 12.1a reproduced from [32]). Most of the internal water molecules were located in the area of the "large channel system" as described in [21]. The whole simulation system including internal water molecules is then solvated by overlapping it with a pre-equilibrated box of water.

After "filling" PSII with water and successful building of the molecular topology for the whole simulation system the MD system is equilibrated. Equilibration is a multistage process involving (1) energy minimization of all hydrogen atoms, (2) energy minimization of water and lipids, (3) MD simulation of only water for 500 ps at 300 K, (4) MD simulation of only water and lipids for 500 ps at 300 K. (5) After the solvent and membrane reach initial equilibrium the protein part can be gradually released by successive weakening of the harmonic constraint potential. (6) Equilibration of the full system. Equilibration can be monitored by following

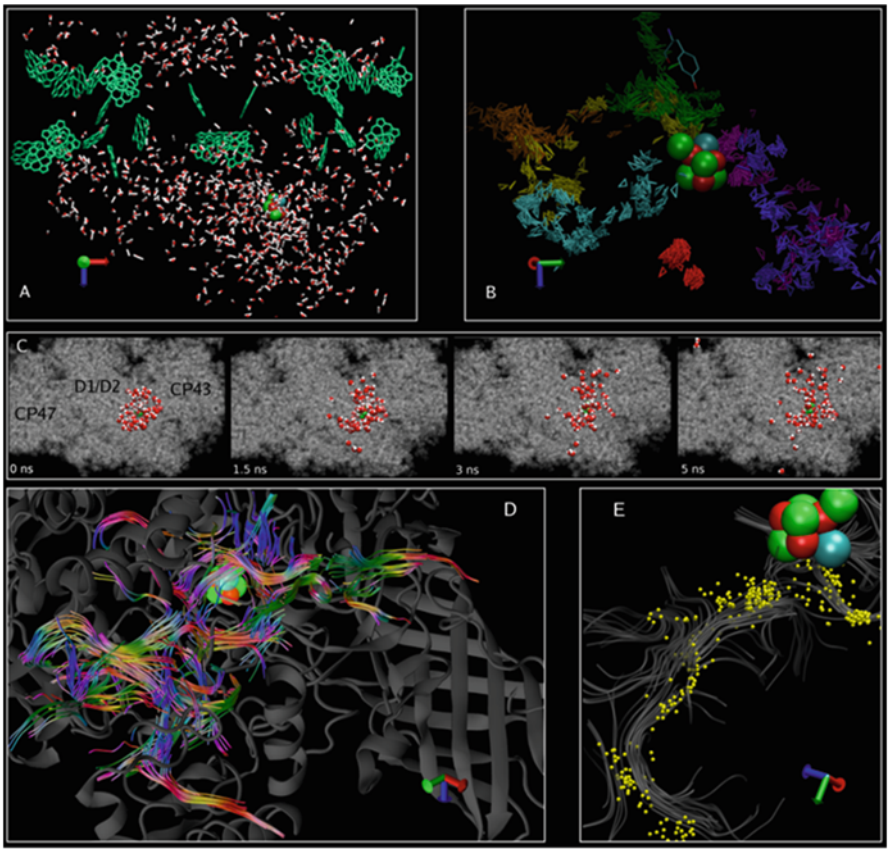

Fig. 12.1 Structure and dynamics of water in the MD simulation of PSII in the presence of the OEC. The thylakoid membrane is in XY plane. (**a**) Water molecules in PSII. (**b**) Trajectories of motion of several representative water molecules. (**c**) Snapshots from the dynamics simulation showing diffusion of water molecules inside the protein. Water molecules within 10 Å of the OEC were selected (time 0 ns) and viewed again at later time intervals (1.5, 3, and 5 ns). View is along the Z axis looking from the lumen. (**d**) Water streamlines in the interior of PSII obtained from analysis of 10 ns MD simulation. Streamlines are color coded by direction: *red* streamlines propagate along the X-direction, *green*—Y, *blue*—Z. The protein is shown as *grey ribbon*. (**e**) Streamlines (*grey*) overlapped with the trajectory of one representative water molecule from the MD run (*yellow*)

the RMSD deviation of the simulation from the original X-ray coordinates. In [32] the structure was found to stabilize after about 2 ns. After equilibration the MD system can be left to run for further analysis of water movement, in [32] the MD systems were run for 10 ns.

12.5 Approaches to Finding Water Channels and Determining Water Pathways Within Molecular Dynamic Simulations

12.5.1 Observing Water Diffusion Within Proteins

The first dynamic simulations of water diffusion pathways were limited to smaller proteins in which well-defined channels with relatively simple geometry had been identified, such as aquaporins [33–36] and lysozyme crystals [37, 38]. In cases like these, standard simulation analysis methods, including radial distribution functions, mean square displacement, and calculation of solvent density along the direction of the channel, were sufficient to characterize and understand water channels. However, larger protein systems may have multiple channels and cavities with complex shapes and different sizes. In addition these channels often exhibit multiple interconnections and branch points and the dynamics of water may be further complicated by transient opening of some channels [12].

In the initial MD simulations of PSII water was observed to move across the protein/water interface at multiple points as well as moving within the protein. This is shown in Fig. 12.1b, c reproduced from [32]. The variety of motions exhibited by different water molecules during the course of the simulation can be exposed by comparing their trajectories of motion, several of which are shown in Fig. 12.1b. The individual trajectories illustrate the different mobilities of water molecules in different regions of PSII. The complexity of the system makes it difficult to identify and characterize all of the possible pathways for water motion through the protein.

A complete description of "channels" in the dynamic system would require some kind of determination of time-averaged structures for all of the nanopores within a full trajectory of PSII structures in the MD simulation. However, such an analysis would still not characterize the actual movement of water through PSII. Specialized data analysis techniques, designed to track the direction of water flow, would be required to visualize which nanopores and channel systems were used to move water through PSII.

12.5.2 Visualization of Equilibrium Water Flow Using Streamline Tracking

MD simulations of water solvated PSII include hundreds of water molecules moving in complex patterns in many different areas of the protein with no obvious "channels" dominating the overall picture. To make sense of this, a rigorous analysis of water movement within the MD simulation is essential. To help map water movement within PSII a tool was developed, based on a "fiber tracking" streamlining technique originating from fluid dynamics, to locate areas characterized by highly

anisotropic motions of water, "streams" [32]. This technique is used in MRI imaging to measure the location, orientation, and anisotropy of water tracts in soft fibrous tissues [39–43].

The idea behind the application of such a strategy to PSII was to characterize the diffusion of water molecules within this complex molecular labyrinth. The movement of water molecules in tissue or in a nanoscale molecular labyrinth proceeds along multiple different directions simultaneously. Any anisotropic organization of the molecular system that constrains water motion will be reflected in the pattern of diffusion. Directionality of diffusion can be represented by a tensor which is described with nine components, each one associated with a pair of axes xx, yy, zz, xy, yx, xz, zx, yz. Diffusion tensors can be extracted from the dynamics simulation. To calculate the 3D tensor field covering the region of interest, the simulation system volume is divided into n small cubic elements (voxels) with a volume of about 1 $Å^3$ each. For all voxels containing a water molecule at time t the position of this water molecule at time $(t+\Delta t)$ is determined and the tensor elements are calculated according to the Einstein relation:

$$T^{\alpha\beta} = \frac{\left\langle \left[\alpha(t+\Delta t) - \alpha(t)\right]\right\rangle \cdot \left\langle \left[\beta(t+\Delta t) - \beta(t)\right]\right\rangle}{2\Delta t} \qquad \alpha,\beta = \{x,y,z\}$$

To obtain all nine tensor elements α and β are sequentially substituted with x, y, and z. Δt is time interval that was used to save the molecular trajectory. Tensor elements are averaged over the time window of the MD run and the diffusion tensor is diagonalized to find the direction of fastest motion:

$$\mathbf{T} = \{\mathbf{v_1}, \mathbf{v_2}, \mathbf{v_3}\} \begin{pmatrix} \lambda_1 & 0 & 0 \\ 0 & \lambda_2 & 0 \\ 0 & 0 & \lambda_3 \end{pmatrix} \{\mathbf{v_1}, \mathbf{v_2}, \mathbf{v_3}\}^T$$

Eigenvalue λ_i of the diffusion tensor describes the diffusion rate along the direction of the corresponding eigenvector $\boldsymbol{\nu}_i$. Channels (fibers) are characterized by anisotropic linear diffusion ($\lambda_1 > \lambda_2 \cong \lambda_3$). The eigenvector associated with the largest eigenvalue of the diffusion tensor is parallel to the local channel direction [40]. Therefore, the vector tangent to the trajectory at point s is equal to the eigenvector calculated at this point, and the channel trajectory is described by a system of three differential equations:

$$\frac{d\mathbf{r}}{ds} = \boldsymbol{\nu}_1(\mathbf{r}(s))$$

In this equation $\mathbf{r}$ is a three-dimensional vector defining position in space, $\mathbf{v_1}$ is the principal eigenvector, obtained as described in the previous paragraph, and s is a parameter of the parametric curve that has values s(x,y,z). To track a channel the system is solved numerically for an initial condition, which specifies a starting point: $\mathbf{r}(0) = \mathbf{r_0}$. Solution of this system of differential equations requires a

continuous and smooth direction field. Due to a limited time frame in molecular dynamics simulations, the diffusion tensor data is discrete, noisy, and coarsely sampled.

To perform reliable and robust fiber tracking a continuous smooth representation of the direction field is generated using a trilinear interpolation on the tensor matrix elements [40]. To find all channels originating in a region of interest first voxels with high linear anisotropy "seed points" are identified. Then the streamline is integrated from each of the seed point in both directions. To find an end of the streamline several conditions are checked: (1) acute turns ($>80°$) are not allowed; (2) the length of the streamline is not allowed to exceed the maximum dimension of the tensor field; (3) either the anisotropy or diffusion rate below threshold values is not allowed. Typical values for these thresholds in [32], respectively, were anisotropy >0.2 (meaning that fastest motion is at least 1.5 times faster than motion in any other directions) and diffusion rate >0.01 Å^2/ps. For comparison, the experimental diffusion rate of water is 0.25 Å^2/ps.

Streamline analysis differs from following the motion of individual water molecules in several important aspects. Individual water molecules in microscopic systems undergo stochastic Brownian motion as illustrated in Fig. 12.1b, c, and e. In contrast, individual fibers in a streamline analysis are calculated from the overall diffusional motion of all water molecules found in each volume element (voxel) of the simulated system over the entire time course of the MD simulation. This analysis can be performed if time and ensemble averaged dynamics of the water molecules are time independent, as is the case when a molecular dynamics system reaches a stationary equilibrated state. Fiber tracks are started in voxels which exhibit the highest anisotropy of water diffusion. Neighboring voxels with a high diffusion rate favoring a particular direction are then connected by tracking algorithm to give streamlines. Streamlines thus represent areas where water molecules have moved the most in a directional manner during the course of the MD simulation. The time and ensemble averaging implemented in streamline tracing makes the technique exceptionally robust and capable of detecting streams connecting locations even if none of the individual water molecules have actually travelled the whole path during the simulation time window.

When applied to PSII MD simulations the fiber tracking technique found streamlines forming a complex network leading from the surface of the protein to the buried Mn_4CaO_5 cluster. Water streamlines were found in spaces free of protein backbone atoms and in most cases free of all protein heavy atoms. Some streams were found in areas transiently occupied by protein side chains. The streamline systems were mainly found in the same regions as the cavities previously described in analyses of static X-ray structures [20–22]. In general, the motions of individual water molecules within the MD simulation matched the streamline directions, but as expected, showed random deviations (Fig. 12.1e), due to the stochastic nature of diffusion. The advantage of the streamline analysis was apparent when water was found to be moving not only in previously identified water channels, but also in so-called proton channels and in regions that had not previously been identified as channels.

The streamline tracking approach revealed a system of branching pathways of water movement within PSII connecting the OEC to multiple distinct entrance points on the lumenal surface of the protein. Transient changes in connections between channels and entrance points that potentially serve to moderate both the flow of water near the OEC and the exchange of water inside and outside of the protein were observed [32], supporting the concept that regulatory mechanisms may control water flow and access to the Mn_4CaO_5 cluster.

The movement of water within PSII appears different from water conduction observed within smaller proteins. Dynamic simulations of water movement within aquaporin-1 and aquaglyceroporin have shown water molecules moving in single file in a correlated manner within well-defined channels [33, 44]. In PSII, water was observed in complex hydrogen bond networks within highly branched channels of variable size. Water entered PSII through multiple openings, many transitory in nature (Figs. 12.2 and 12.3 reproduced from [32]) and for the most part water pathways followed interfaces between polypeptide subunits. In terms of function, the redundancy offered by a manifold of interconnected water transport pathways through a "sponge-like" region of lumenally exposed polypeptides would be a robust way to ensure adequate water supply to the OEC. The interconnected network of channels running through PSII protein may also function as a filter. The OEC is susceptible to reactions with small molecules which could be carried in with water. Incoming ions and cellular reductants are potentially harmful as they may impair water splitting by over-reducing the OEC or competing for binding sites.

Areas restricting water movement were clearly observed in MD simulations. Restrictions were caused by transiently open pores both at the surface of the protein and in regions connecting different channel systems. This pattern of water flow is consistent with the idea of a kinetic barrier, required to slow movement of water near the Mn_4CaO_5 cluster and facilitate the ordered binding of substrate water and the formation of the O–O bond [5]. Regulation of substrate delivery to the active site by the transient opening of passages in protein has been observed previously in acetylcholine esterase [45]. Even with the action of transient barriers in PSII, water molecules were observed to move between the OEC and bulk water in the lumen within 10 ns, much faster than the 1.6 ms turnover time of the water splitting reaction [46].

Streamline tracing has been very useful in the identification of transiently formed channels in a complex system of nanopores. This approach to the study of water movement in PSII introduced a novel perspective to the question of how water reaches the OEC.

12.5.3 Continuous Water Injection Near the Active Site

Although several water molecules had been observed to permeate through some channels in PSII within the time window of MD simulations, the limited time window of equilibrium MD simulation may be insufficient for the observation of

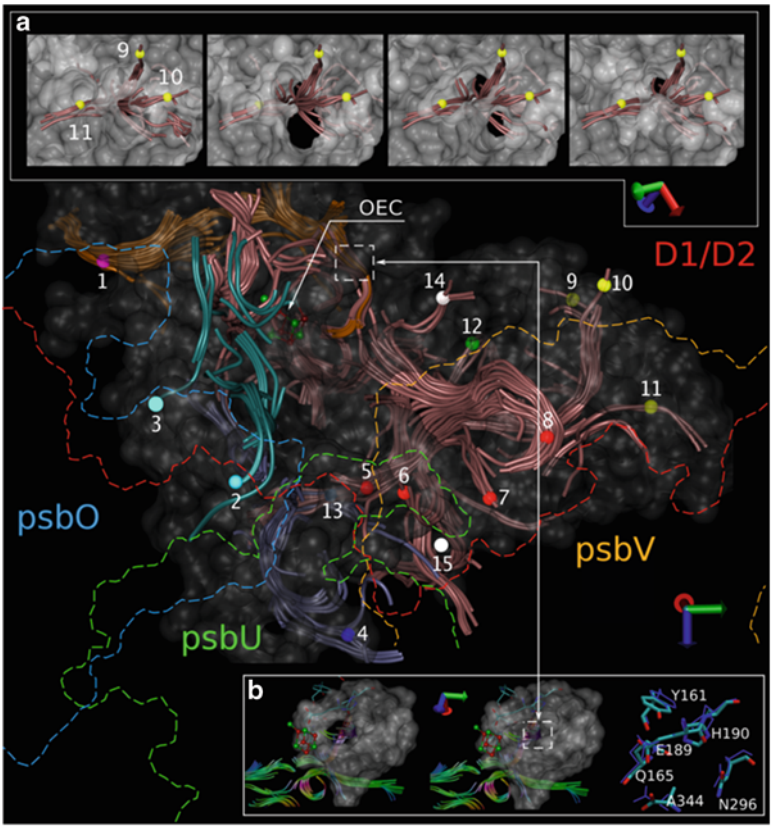

Fig. 12.2 Water streamlines in PSII in the presence of the OEC. The surface of the protein immediately surrounding the previously described "broad," "narrow," and "back" channels and the "large" channel system [21] is shown in *grey*. *Numbered circles* show points where streamlines exit the protein and enter the lumen. These exit points are compared to the exits reported previously in Fig. 4 of [21] which were denoted as "dashed arrow" exit, two "dotted arrow" exits, and "solid arrow" exit. Streamlines in the area of the "back" channel are shown in *orange* with a *purple* exit point (point 1). Streamlines and exit points in the area of the "broad" channel are shown in *cyan* (points 2, 3). Streamlines and exit points in the area of the "narrow" channel are shown in *blue* (point 4). Streamlines in the area of the "large" channel system and near OEC are shown in *pink*. *Red spheres*—exits near the "dashed arrow" exit (points 5–8). *Yellow spheres*—exits near the two "dotted arrow" exits (points 9–11). *Green sphere*—exit near the "solid arrow" exit (point 12). *Blue sphere*—exit from the "large" channel system leading into the "narrow" channel (point 13). *Upper white sphere*—new exit near CP43-Thr412 (point 14). *Lower white sphere*—new exit near PsbV-Asp79 (point 15). *Inserts* A and B show snapshots at different times of the protein solvent-accessible surface and streamlines in two areas of PSII. *Insert A*—area near the two "dotted arrow" exits. Transient opening permits water access into the "large" channel system. *Insert B* shows the proximal end of the "back" channel. The streamline in the "back" channel continues all the way to the Mn_4CaO_5 cluster due to transient opening of the proximal end of the channel, see text for details. The protein has been clipped close to this region to facilitate visualization of the opening. Residues previously proposed to act as a "control gate" in [21] are found in this region and are shown by licorice

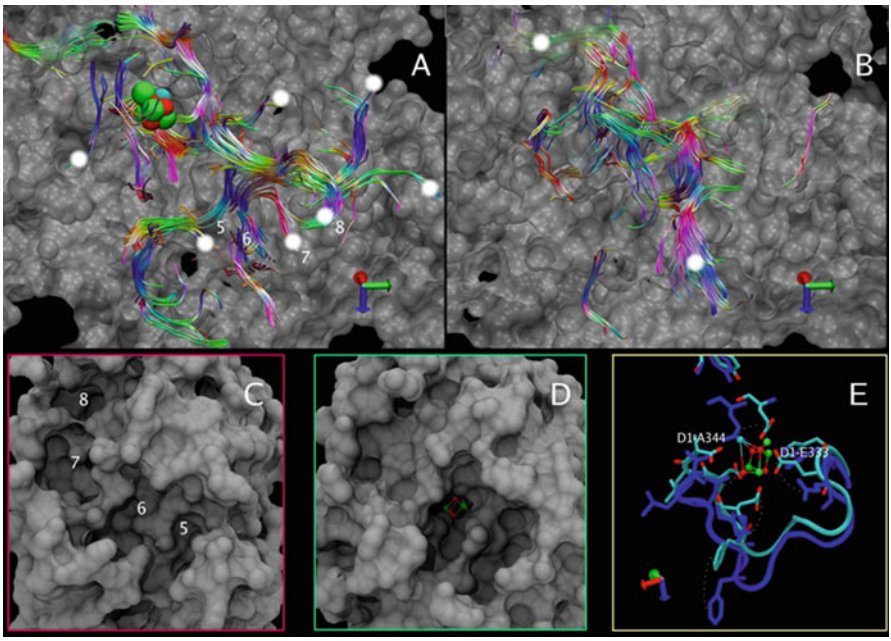

Fig. 12.3 Comparison of the simulation with and without OEC. (**a**) (with OEC) and (**b**) (without OEC) show the streamlines; protein is in *gray* and has been clipped below the streamlines for clarity. *White circles* show the most probable entrance points; in the simulations at least one water molecule entered the protein via each of these points and ultimately reached the OEC sphere. In the simulation with OEC the water path is curved and branched with multiple water entrance points; without OEC, the pathway is relatively straight with only two open entrances. Panels **c** (with OEC) and **d** (without OEC) show the surface of the protein in the region of the entrance point represented by the *lower white circle* in panel **b**. The view is along a line from that entrance point straight back to the OEC site. In panel **c** (with OEC) although a number of channel openings are seen, the OEC is covered by protein and is not visible; in panel **d** (without OEC) a "ghost" OEC has been placed at the OEC site to allow visualization of the straight and wide channel that goes from the lumenal surface all the way in to the active site. Panel **e** shows the change in conformation of the protein in the region of the OEC site between the simulation in the presence of OEC (grey licorice) and the absence of the OEC (blue licorice)

water molecules propagating through all potential diffusion pathways. In silico it is possible to accelerate the diffusion process and further characterize water pathways within PSII. Water flow can be accelerated by controlled injection of water molecules into the protein. This approach was used in [47] where water molecules were injected near the Ca^{2+} or near the "dangling" Mn(4), two sites at the OEC that have been suggested as binding sites for the two substrate water molecules, w_1* and w_2*, respectively, of the water splitting reaction [24]. Water molecule were injected every 50 ps over a total simulation time span of 20 ns, which created a small overpressure driving water flow (Fig 12.4, reproduced from [47]). The injection of a full sized water molecule into the simulation would break the energetic continuity of the MD trajectory. To minimize perturbation of the system energy, it was

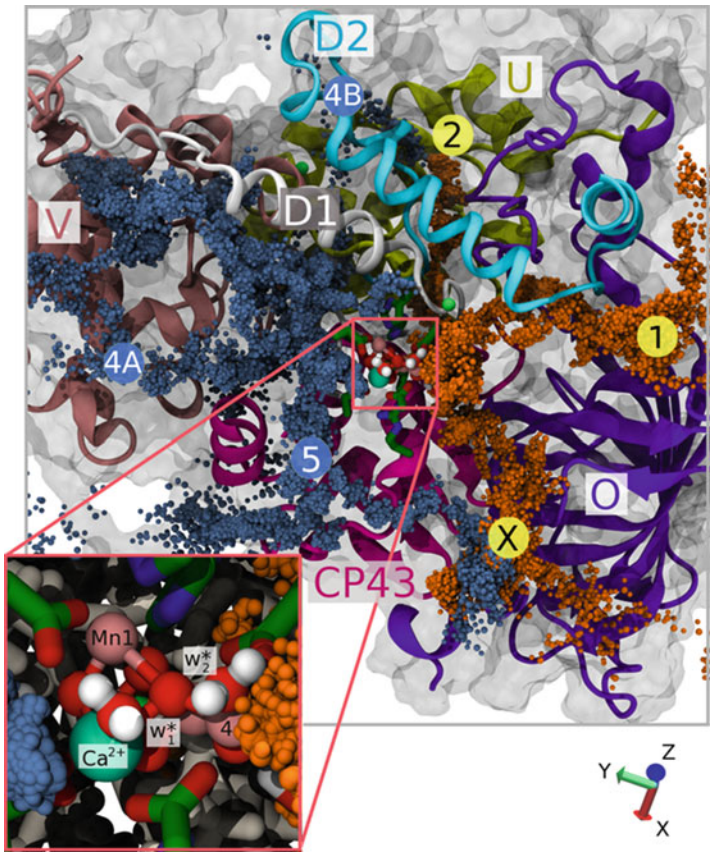

Fig. 12.4 Trajectories of injected water molecules within PSII MD simulations. Water molecules injected in PSII at one side of the OEC (near water binding site w_1^*) are shown by *blue spheres* and water molecules injected at another side of the OEC (near water binding site w_2^*) are shown by *orange spheres*. View is from the stromal side approximately along the normal to the membrane (Z-axis). Membrane is in the XY plane. Protein above the OEC is clipped for clarity. In the zoomed window the locations of the binding sites w_1^* and w_2^* as well as the OEC atoms, Mn(1), Mn(4), and Ca^{2+}, are shown. Mn numbering as in PDB ID: 3ARC. Segments of PSII polypeptides O, U, V, D1, D2, and CP43 are shown in colored *cartoon* format. The locations of water channels 1, 2, 4A, 4B, 5, and X (see text and Table 1 of [47] for details) are shown

necessary to scale down the Lennard-Jones and electrostatic parameters of the injected water molecule and minimize the energy of the inserted water molecule while the rest of the system was kept frozen. The energetic parameters of the injected water molecule were then grown stepwise to full scale to allow uninterrupted continuation of the MD trajectory. The injection procedure increased the water content of PSII which ultimately stabilized at a 35 % increase after approximately 7 ns. The water injection technique revealed localized changes in protein structure involving only the side chains of specific residues, but

showed no evidence of large scale structural changes affecting the entire PSII core complex.

Following streamlines and injecting water into the MD simulations revealed a number of possible water channels within PSII. The routes taken by water molecules injected at one side of the OEC (near Mn(4)) were different from the routes of the water injected near Ca^{2+} supporting the existence of two separate channel systems. The overall picture arising for the movement of water within PSII was one of multiple channels with multiple entrance points many of which exhibited dynamic changes in structure which would influence their relative permeability. But which channels carry the most water? The next step in understanding how water finds its way through this dynamic protein labyrinth is calculating the energetic costs of water movement through the individual channels.

12.6 Characterization of Channel Permittivity, Permeation Barriers for Substrate and Product

12.6.1 How to Calculate the Energetic Cost of Water Movement Through Channels

Multiple steered molecular dynamics can be used (MSMD) to calculate the free energy of water permeating through a channel. In MSMD simulations, water permeation is accelerated by the application of an external force. One of the water molecules is pulled by one end of a spring while the other end of the spring moves with constant velocity. Integration of the external force required to do this work along a path allows the construction of free energy profiles a. k. a potentials of mean force (PMF) for an individual water molecule as it moves through a channel. This approach has been shown to be as efficient as traditional umbrella sampling; however, it has the advantage of uniform sampling of a reaction coordinate which is particularly beneficial when a PMF contains narrow barrier regions [48].

This technique requires knowledge of the channel topology. Each channel to be studied is divided into several straight segments. The pulling force is applied to a water molecule in the direction of the segment. To prevent lateral displacement in wide or branched channels or entering dead ends, the water molecule should be constrained to move within a cylinder along the segment axis. The spring constant should be adjusted so that the position of the pulled water closely follows the constraint center. In most cases a constraint force of 10 kcal/(mol $Å^2$) is sufficient.

If channel system topology is not precisely known, an initial screening set of fast simulations (velocity of 0.1 Å/ps) may help to obtain first impressions about the energy barriers.

Once channels are accurately identified, production simulations are performed where a water molecule is pulled with a velocity of 0.01 Å/ps. The process should be

repeated several times for each channel. Statistical errors can then be calculated using bootstrap analysis. Complete PMFs of each channel are constructed N times by randomly selecting segments from all available simulations from which the average and standard deviations were calculated. The final equilibrium free energy profile across the channel is calculated from an ensemble of independent irreversible simulations, employing the Jarzynski identity [49], according to which the effective PMF $G_{eff}(r)$ was calculated as:

$$\exp\left(-\frac{G_{eff}(r)}{k_B T}\right) = \frac{1}{N}\sum_{i=1}^{N}\exp\left(\frac{-G_i(r)}{k_B T}\right)$$

where r is distance along the channel, k_B is the Boltzmann constant, T is the simulation temperature (300 K), and N is the number of simulations.

12.6.2 Determination of Permeation Barriers for Water Within PSII

A new 1.9 Å structure of PSII [29] revealing more detail than ever before of the area immediately surrounding the OEC was used to create an updated MD simulation of PSII to use for this purpose. The 1.9 Å structure suggested a cuboidal structure of the Mn_4CaO_5 cluster similar to previous models, although with a different ligation scheme in which Ca^{2+} is bridged to Mn centers by the carboxylate moieties of D1-D170 and D1-A344 [29, 50]. In addition, binding sites for two Cl^- ions were found in the vicinity of the Mn_4CaO_5 cluster. The goal of the MD study based on the new structure was to determine potentials of mean force (PMFs) for water permeating through PSII by using the technique of multiple steered molecular dynamics (MSMD).

The calculation of free energy profiles for water permeating along individual channels can reveal which channels would supply the bulk of water to the OEC and identify the major constriction sites. These energetic barriers to water flow may serve critical roles as selectivity filters restricting both the access of solutes detrimental to the water oxidation reaction and the loss of Ca^{2+} and Cl^- from the OEC. MSMD was used to identify channels with the lowest energy barriers and the amino acids responsible for establishing those barriers. To address the physiological relevance of water permeation through PSII the energetic barriers determined for the PSII channels were compared to the barriers for water flow previously calculated for aquaporins. Aquaporins can permeate ~$3 \cdot 10^9$ water molecules per second [51, 52]. Calculations based on MD simulations have shown that water permeation through the water pores of aquaporins requires crossing energy barriers of ~3 kcal/mol [53]. If it is assumed that permeability is proportional to exp ($-\Delta G^*_{max}/k_B T$), a channel with an activation energy of 14 kcal/mol at 300 K would permeate ~100 molecules/s, and a channel with an activation energy of

20 kcal/mol would permeate only ~10^{-3} molecules/s, which would certainly become limiting for water oxidation. MSMD confirmed water permeation through three of the water channels found in earlier studies, the "narrow" channel, the "large channel system" and the "broad" channel [20, 21, 32]. The energetic barrier for water permeating through the previously identified "back" channel was >20 kcal/mol, too high to allow transport of water, supporting the prior observation of a break in water "streamlines" in the hydrophobic area of this channel [32]. In addition water permeation was observed through a channel that was not previously assigned to water, but had been suggested to be a putative proton exit channel [54]. MSMD found that all channels in PSII had an activation energy of at least 9–10 kcal/mol. For comparison, this barrier is higher than the ~7 kcal/mol barrier of a comparable patch of POPC lipid bilayer [53]. However, the permeability of a channel with an activation energy of about 10 kcal/mol is still ~5,000 molecules/s, more than sufficient to satisfy the substrate delivery requirement in PSII. None of the channels permitted free and unrestricted access of water to the OEC, supporting the idea that regulatory mechanisms exist to control water flow and access to the Mn_4CaO_5 cluster.

12.7 Oxygen Channels

12.7.1 Overview of Experimental and Computational Techniques for Characterization of Oxygen Channels in Proteins

Molecular oxygen participates in numerous cellular processes and interacts with a variety of reaction sites within many different proteins. Formerly, the idea of unconstrained oxygen diffusion through proteins was generally accepted [55]. However, this point of view is changing as a number of studies (hydrogenase [12], myoglobin [16], aquaporin [56], copper amine oxidases [57], flavoenzymes [58], cytochrome oxidase [59], fluorescent proteins [60, 61], and lipoxygenases [62, 63]) have described specific oxygen diffusion channels. Experimental localization of molecular oxygen within proteins is difficult. It is highly mobile and usually is not resolved in X-ray crystal structures. In some cases mimicking oxygen with xenon or krypton, which have higher electron densities, has allowed the detection of potential oxygen binding sites [64]. However, the validity of this approach to characterize oxygen channels has been challenged [65, 66]. Other techniques, like tryptophan fluorescence quenching, suffer from relatively low spatial resolution. The application of computational methods is an alternative and promising approach to determine the localization of oxygen in a protein as shown in [67] in which a new strategy for the investigation of oxygen pathways was applied to PSII.

12.7.2 How Does Oxygen Leave PSII?

In contrast to water access, which was shown in MSMD studies to be controlled/restricted, likely to stabilize the OEC during its turnover cycle, oxygen exhaust is presumed to be as fast as possible to prevent unwanted oxidative damage. Channels have often been assumed to be selective and early studies of static structures assigned individual channels to water, oxygen, or protons based solely on their composition (proportion of hydrophobic/polar residues along the channel) and/or width (it has been speculated that the wide "large" channel system was particularly suitable for fast removal of oxygen from the vicinity of OEC) [21, 23].

Channel discovery and characterization in PSII by MD techniques has focused on water. Studies have quantified the permittivity of water and reinforced the idea of control of water access to the OEC. However, these studies say nothing about the movement of molecular oxygen within PSII. Early computational cavity searches of X-ray structures assigned the more hydrophobic static channels to oxygen. The only experimental result related to molecular oxygen diffusion within PSII was an X-ray structural study which revealed two krypton binding sites [23]. How does oxygen move through PSII and how does this relate to the movement of water?

While water is relatively abundant in the interior of PSII, oxygen is not. Computational approaches to follow water movement in PSII described above depend on the relatively large numbers of water molecules and cannot be simplistically applied to identify oxygen pathways. To study oxygen migration in PSII 3D free energy maps were constructed using an implicit ligand sampling method.

12.7.3 Using 3D Free Energy Maps to Study Channel Topology

12.7.3.1 Constructing 3D Free Energy Maps

The implicit ligand sampling (ILS) method relies on the assumption that small and hydrophobic gas ligands interact weakly with the protein matrix and thus protein dynamics calculations are independent of the presence of the gas molecule [12]. ILS computes the potential of mean force (PMF) corresponding to the placement of a small probe molecule everywhere inside a protein. This allows for the generation of a 3D map of the energetic cost function for the ligand within the protein. Migration pathways or channels through the protein can be found by following the lowest energy pathways through this map. It has been shown that ILS provides a good description of channel topology and a reasonable approximation to the free energy landscape [15].

12.7.3.2 Overview of Approaches for Analysis of 3D Free Energy Maps

To date the ILS method has been applied only to relatively small proteins. In most cases channel topology was apparent from a visual inspection of iso-energy surfaces of the three-dimensional free energy map. However, in more complex proteins calculation of the free energy profiles requires the use of an algorithm searching for the minimal energy path. Previously this has been achieved by identification of all saddle points in the free energy map, and then connecting them to the local minima using a steepest descent algorithm [63]. This algorithm was successfully applied to single chain lipoxygenases [62, 63]. However, the algorithm is incomplete as it only identifies fragments of the minimal energy path. Afterward a search for the optimal combination of all fragments into a complete path from the active site to the surface still has to be performed. In addition it is not robust in the case of highly branched protein channels. These limitations became apparent when this algorithm was applied to PSII. The free energy landscape of oxygen within PSII is extremely complex with a large number of oxygen binding cavities. Finding channel systems that can be accessed by gas in this case is a difficult question to answer even when the free energy landscape is known.

In [67] a more advanced approach for identification and energetic characterization of channel systems in complex molecular labyrinths has been presented. It explicitly accounts for protein dynamics and protein–ligand interaction. First the three-dimensional cost function for the ligand entering each grid point was constructed by computing the free energy maps. The free energy maps were calculated using molecular dynamics and ILS. Then, to find minimal energy paths the Eikonal equation for wavefront propagation through heterogeneous media (where slowness of the media is proportional to the cost function) was solved using the finite-differences method. Overall the algorithm for finding dynamic ligand pathways included four steps:

1. Perform molecular dynamics simulation to obtain molecular trajectory of motion.
2. Use trajectory to compute the 3D free energy map for O_2 in the region of interest.
3. Choose a starting point and compute wavefront propagation using the 3D slowness field obtained from the 3D free energy map.
4. Examine isosurfaces of wavefront arrival times and locate points where the wavefront exits the protein. Starting from each of the exit points backtrace the wavefront to its origin.

12.7.3.3 Application of Wave Dynamics to Describe Oxygen Permeation

Consider a molecule that is constrained to move in a subset of the whole volume occupied by a protein. The molecule starts at an initial point $\mathbf{r_0}$ and moves within a

protein. At an unspecified time T it reaches the boundary of a protein and incurs a terminal cost associated with permeation through all energetic barriers encountered on its way. In addition to the terminal cost there is a traveling cost related to the total length of the trajectory. We are interested in a numerical method for finding a trajectory that minimizes the sum of the traveling and the terminal cost. The solution to the problem can be obtained, in principle, by solving the Hamilton–Jacobi (HJ) equation. However, since an exact solution of the HJ equation is usually impossible, the problem has to be solved using an approximative method. The Eikonal equation, which is a special case of a stationary HJ with certain constraints, is widely used for solving similar problems in the fields of path planning [68], medical imaging [69], seismic wave modeling [70], and computer vision [71]. The Eikonal approximation can be used to solve the problem of finding optimal oxygen trajectories. Since the closest physical process described by the Eikonal equation is the propagation of a wave through heterogeneous media, the terms "wave" and "wavefront" are used to describe its solution. Of course individual oxygen molecules do not move as waves; however wave dynamics is appropriate for the description of ensemble averaged movement.

The Eikonal equation has the form:

$$(\nabla t(x,y,z))^2 = \left(\frac{\partial t}{\partial x}\right)^2 + \left(\frac{\partial t}{\partial y}\right)^2 + \left(\frac{\partial t}{\partial z}\right)^2 = s^2(x,y,z)$$

where $s(x,y,z)$ is an inverse velocity field (usually called slowness) of the medium and $t(x,y,z)$ is the travel time from some reference point $\mathbf{r_0}$ to point $\mathbf{r}$. Solution of the Eikonal equation requires knowledge of "slowness" at any point $\mathbf{r}$ within the volume. This quantity can be obtained from a 3D free energy map computed using the ILS method. To accomplish this the velocity of the probe at point $\mathbf{r}$ is assumed to be proportional to $\exp(-\Delta G(\mathbf{r})/k_B T)$, where $\Delta G(\mathbf{r})$ is the free energy of placing an oxygen probe molecule at point $\mathbf{r}$, and k_B is the Boltzmann constant.

The Eikonal equation was solved numerically in [67] using the finite differences method implemented in the time_3d subroutine from FDTIMES package [72]. The time_3d subroutine requires a rectangular set of cubic cells, each cell having uniform "slowness." The value in each cell is a product of slowness and grid spacing. This product has the dimension of time, and computed time values are expressed with the same time unit. The second input is the coordinates of a point source $\mathbf{r_0}$ at time = 0.0. The result of this calculation is a 3D field of the travel times from a reference point $\mathbf{r_0}$ to all points on the grid. Location of the wavefront at a certain time is represented by the isosurface of this data.

12.7.3.4 Finding Minimal Resistance Paths

The minimal cost paths from any point of the grid (the only interesting points are where oxygen exits the protein) to its initial position $\boldsymbol{r_0}$ can be easily backtraced

with the use of the time field obtained by finite differences. Starting from the exit point the path is iteratively traced by moving toward smaller values in the 3D time field (moving down the gradient by the method of steepest descent). This path is described by a system of three differential equations:

$$\frac{d\mathbf{r}}{ds} = -\nabla t(\mathbf{r}(s))$$

In this equation **r** is a three-dimensional vector defining position in space, *t* is the 3D map of arrival times, obtained as described in the previous paragraph, and s is a parameter of the parametric curve that has values s(x,y,z). To track a channel the system was solved numerically for an initial condition which specifies a starting point: $\mathbf{r}(0) = \mathbf{r_0}$. This was implemented in [73] by integrating the steepest descent using the standard fourth order Runge–Kutta method. This method requires calculation of the gradient at any point inside the 3D travel time map. The gradients were calculated using the intermediate differences approach [74], which introduced less smoothing than conventional central differences method and produced better results.

12.7.4 Finding Oxygen Exit Pathways in PSII

12.7.4.1 3D Free Energy Map of Oxygen in the Interior of PS II Complex

In [67] free energy maps for oxygen were computed using 10 ns long MD simulations. A total of 10,000 snapshots were included in the analysis. The grid spacing was 0.5 Å and at each point 12 oxygen orientations were considered. Lennard-Jones parameters and O–O bond length for oxygen molecules were taken from [75]: $\sigma = 1.507$, $\varepsilon = -0.097$, O–O bond length = 1.22 Å. The ILS calculations were performed with VMD v.1.9 program [27]. The 3D free energy map of PSII computed using the ILS method is shown in Fig. 12.5. It shows areas within the protein where oxygen has a high probability of residing. As seen from this figure, the free energy map is very complex and does not show distinct channels upon visual examination. Instead it revealed many small low energy cavities isolated from each other by energetic barriers. Thus, visual inspection of this volumetric map was insufficient to localize low energy pathways. Several small areas with high binding affinity to oxygen were found near the catalytic site of PSII. Two areas were suitable for the initial localization of oxygen; these are shown as *s1* and *s2* in Fig. 12.5. Oxygen binding site *s1* is in direct contact with water molecule w_2* near the so-called "dangling" Mn(4) which has previously been suggested to be a binding site for one of the two substrate water molecules of the water splitting reaction [24]. Site *s2* is separated from both putative substrate water binding sites w_1* and w_2* by D1-V185 and D1-E189. Sites *s1* and *s2* are separated from

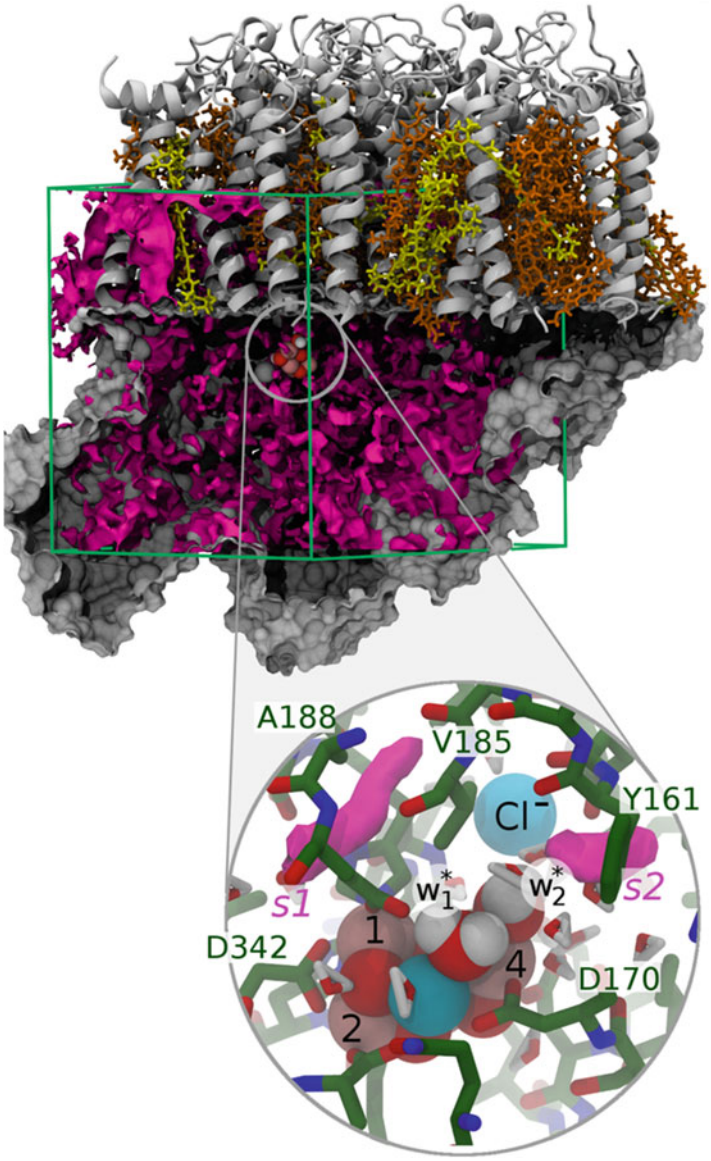

Fig. 12.5 Free energy map of oxygen (shown in *purple*) obtained using ILS and overlapped with PSII. The enlarged zoom-in area shows the neighborhood of OEC. Two proposed substrate water molecules and chloride ion are shown as *spheres*. Two areas with high oxygen binding affinity (*s1* and *s2*)

each other by water molecule w_2* and D1-V185. After water oxidation, w_1* and w_2* are converted into protons and molecular oxygen and thus both sites could be accessible to the oxygen product. The oxygen product is expected to migrate to one of these areas rapidly. To find oxygen channels leading from

OEC to the bulk solvent centers of each of these binding sites were used as starting points in the wavefront propagation analysis aimed to find the path of the least resistance.

12.7.4.2 Search for Oxygen Diffusion Pathways in PSII

The free energy map indicated that the hydrophobic transmembrane regions of PSII did not exhibit a higher probability for oxygen occupancy than the extrinsic parts of the protein complex [73]. All waves initiated at various sites around the OEC propagated much faster through the extrinsic solvent exposed protein than through hydrophobic transmembrane domains. Isosurfaces generated for several representative travel times are shown in Fig. 12.6 reproduced from [67].

No evidence was found supporting the hypothesis that oxygen gas can diffuse through hydrophobic transmembrane areas of PSII. The only exception was one branch of the wavefront which was slowly moving toward the special pigment P680, the photochemically active reaction center [73]. This finding was consistent with the high susceptibility of the reaction center of PSII for oxidative damage.

The wave originating from one of the starting sites *s1* reached the bulk solvent faster than the waves originating from any other location. This wave split into two branches and exited the protein at two sites. Oxygen exit sites are depicted as sites *e1* and *e2* in Figs. 12.6 and 12.7. Two minimal resistance paths were obtained by tracing wavefronts back from exit sites *e1* and *e2* to the source of the wave at *s1*, and are shown in Fig. 12.7. They merge into a single pathway at a distance about 10 Å from the OEC. The wave initiated in *s1* site did not overlap with the wave initiated at the *s2* site indicating the presence of an energetic barrier between these two sites. The wave originating at the *s2* site revealed a slightly slower pathway, which exited the protein at *e3*. The third major channel *e3-s2* connecting the protein surface with the active site was identified with the help of this wave, Fig. 12.7.

The combined "MD + ILS + wavefront propagation" approach, introduced in [73], was successful in the search for oxygen migration pathways within the large PSII protein complex. Application of this approach revealed three distinct oxygen channels in PSII. Both channels *s1-e1* and *s1-e2* were consistent with the two experimentally observed krypton binding sites (Kr9 and Kr10) [23] which were found to be located within channel *s1-e1* and channel *s1-e2*, respectively.

Channel *s1-e1* was similar to a previously suggested (based on Dijkstra's search on the static structure) oxygen channel B1 [23] and water channel 4a identified by molecular dynamics in [47]. Channel branch B2 matching channel *s1-e2* was also previously described. However, in the static structure B2 was blocked for passage of oxygen at one location [23]. The dynamic approach implemented in [73] revealed that the free energy cost for oxygen permeation through this channel is only 2.5 kcal/mol higher than the cost of permeation through the common part of

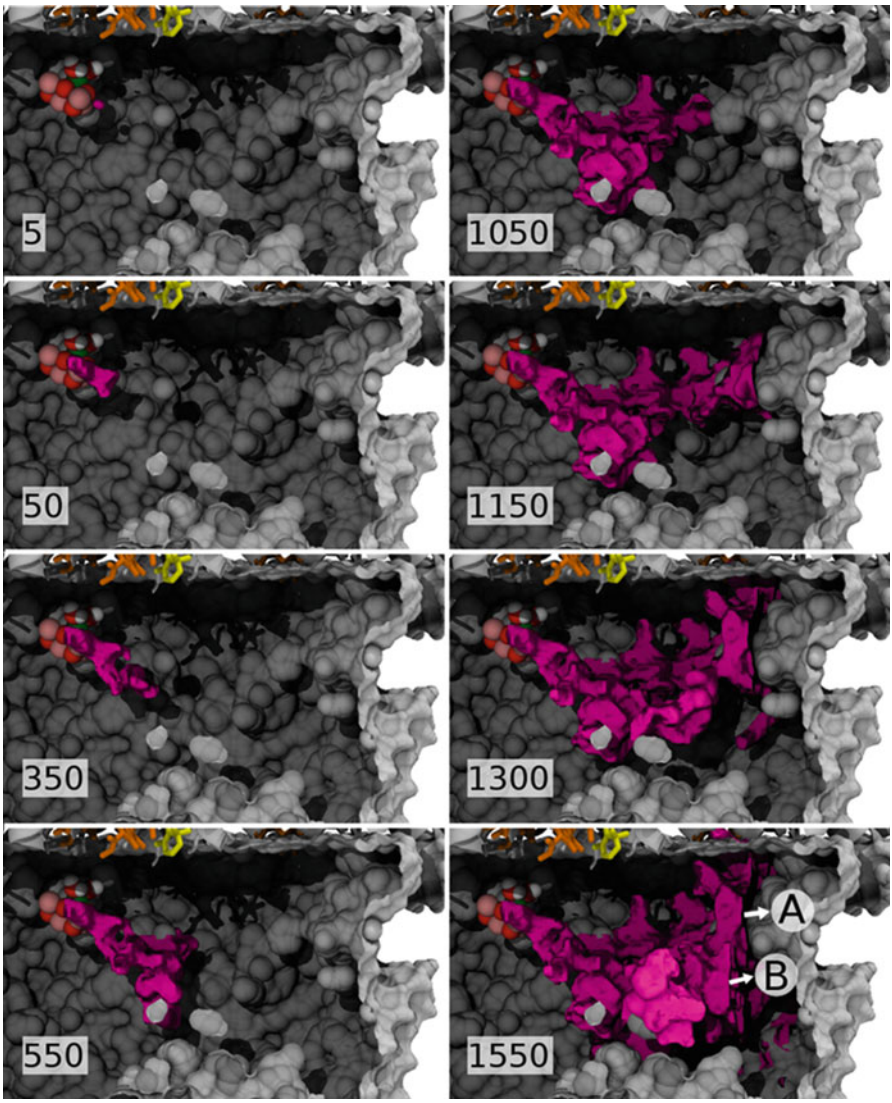

Fig. 12.6 Wavefront propagation in PSII (*magenta* color) for the source located at one of the low energy sites near OEC marked by a *yellow star* in the *upper left panel*. The location of the OEC cluster within PSII (*grey* color) is shown using *red* (oxygen atoms) and *pink* (manganese atoms) *spheres*. Numbers in each panel indicate the time in arbitrary units elapsed from initiation of the wave. Time 0 corresponds to start of the wavefront propagation at the source point; time 1.0 is time of exit from the protein along the fastest path A

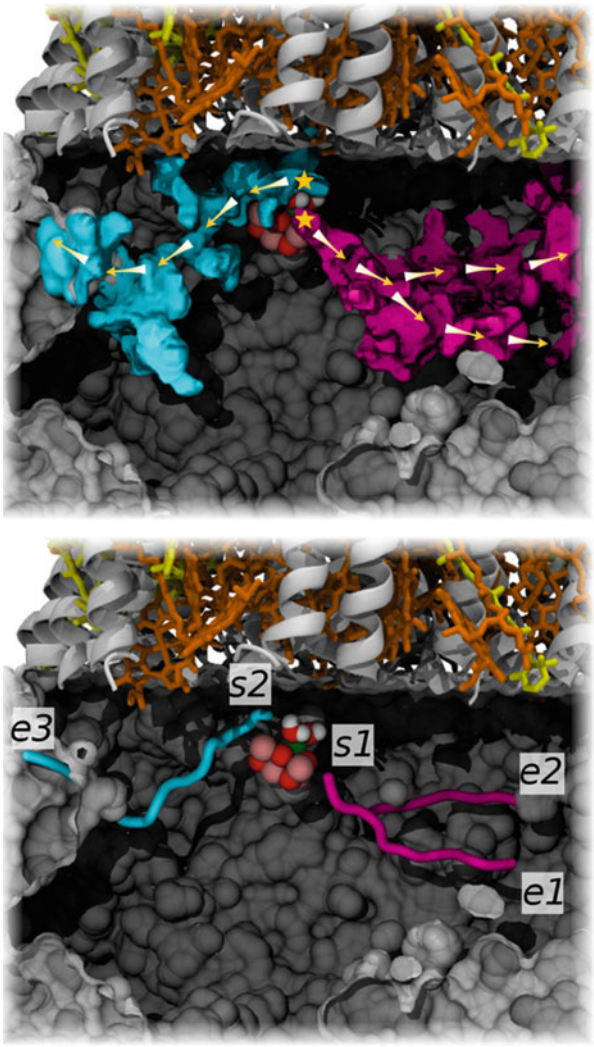

Fig. 12.7 Snapshot of wavefront propagations through the free energy map of PSII showing the fastest pathways of oxygen diffusion away from *s1* (*purple* isosurface) and *s2* (*cyan* isosurface). The locations of the wave sources are marked by *yellow stars*. (*lower panel*) The minimal energy paths obtained by backtracing the wavefronts from their exit points to their respective starting point

channels *s1-e1* and *s2-e2*. Channels B1 and B2, described in [23], correspond to two branches in the large channel system. See Table 1 of [47] for details of comparative channel nomenclature.

12.7.4.3 How Fast Is Oxygen Leaving PSII?

To answer this question, free energy profiles of oxygen and water along channels should be compared. For meaningful comparisons an accurate free energy profile for oxygen should be obtained preferably with the same method as used for water.

While ILS provides a reasonable qualitative picture of free energy landscapes and a fast and good general description of the channel system it has been recently shown to be inaccurate in predictions of permeation barriers [15]. The ILS method relies on the assumption that a small neutral ligand interacts weakly with the protein matrix and that its presence would not affect the dynamics of the system. This assumption, however, may not always be accurate. Therefore, for more accurate and quantitative free energy profile descriptions of each channel, explicit ligand simulations should be performed. We are working at present on determinations of accurate free energy profiles for both oxygen and water using umbrella sampling simulations.

12.7.4.4 Comparison to Oxygen Channels in Other Enzymes

Cytochrome oxidase is an integral membrane protein complex that shares a number of features with PSII. Like PSII it requires permeation of water, protons, and oxygen to an active site buried within the protein. However, in contrast to PSII, cytochrome oxidase needs protons to reduce molecular oxygen to water. Oxygen is delivered to the active site via a channel that has been well characterized by extensive Xe gas pressurization crystallography [59]. The oxygen channel is a large hydrophobic Y-shaped channel that connects the a_3–Cu_B center in the active site of the complex to two hydrophobic regions on the surface of the protein buried within the lipid bilayer. The cytochrome oxidase oxygen channel does not contain water. Although PSII and cytochrome oxidase both require efficient transport of oxygen, the former benefits by minimizing the concentration and the latter by maximizing the concentration at the active site. This functional difference translates into very different structural organizations. In cytochrome oxidase a selective hydrophobic channel connecting the active site of cytochrome oxidase with the oxygen rich membrane ensures maximal substrate density. In PSII the oxygen release channels avoid contact with the membrane and direct oxygen toward multiple aqueous exit sites characterized by much lower effective oxygen concentrations than the membrane. This organization maximizes the removal of oxygen from the active site and minimizes its potentially dangerous contact with PSII chromophores.

In both PSII and cytochrome ba_3 oxidase significant rearrangements within the protein are not necessary for oxygen permeation likely because both systems benefit from fast permeation for activity. In contrast, gas diffusion in heme nitric oxide/oxygen binding (H-NOX) domains from the family of gas-sensing proteins does not occur through discrete, continuous channels. In these systems, protein dynamics controls O_2 and NO diffusion through transiently formed pathways [76]. This restricted diffusion would facilitate the trapping of O_2 at the heme iron [77], a strategy which may be important for anaerobic organisms to sense low amounts of O_2.

12.8 Conclusions and Future Directions

Diffusion of water and oxygen in PSII has been characterized using a variety of computational approaches based on equilibrium and accelerated molecular dynamics. Areas of PSII complex permeable for substrate and product have been localized. The current analysis, however, is limited to the PSII core complex with OEC in an over reduced state, as found in the X-ray structure. While permeation of substrate and product far from the OEC is not likely to be affected by conformational changes occurring between the four S-states of water oxidation, it is not clear at present what pathways are functionally important in the vicinity of the OEC. Until more is known concerning the structural changes of the OEC associated with progression of the S-states and formation of molecular oxygen the details of water and oxygen oxygen exchange between the active site and channel systems will remain obscure to computational studies. Accounting for structural changes accompanying the catalytic cycle in future will help to elucidate such mechanistic details of water/oxygen binding and exchange in the immediate neighborhood of the OEC. Another interesting aspect that can be addressed computationally in the future is the permeation of oxygen evolution inhibitors such as hydroxylamine and ammonia. Computational studies of water and oxygen diffusion in PSII have opened the possibility of experimentally testing the potential roles of individual water/oxygen channels in modulating substrate/product migration by designing mutations targeting regions in each branch of the tunnel network at sites relatively distant from the OEC.

References

1. Barber J. Photosystem II: the engine of life. Q Rev Biophys. 2003;36:71–89.
2. Govindjee. Photosystem II: the light-driven water: plastoquinone oxidoreductase, edited by Thomas J. Wydrzynski and Kimiyuki Satoh, Volume 22, Advances in Photosynthesis and Respiration, Springer, Dordrecht, The Netherlands. Photosynth Res. 2006;87:331–5.
3. Joliot P, Barbieri G, Chabaud R. A new model of photochemical centers in system-2. Photochem Photobiol. 1969;10:309.
4. Kok B, Forbush B, McGloin M. Cooperation of charges in photosynthetic O2 evolution. 1. A linear four step mechanism. Photochem Photobiol. 1970;11:457–75.
5. Wydrzynski T, Hillier W, Messinger J. On the functional significance of substrate accessibility in the photosynthetic water oxidation mechanism. Physiol Plant. 1996;96:342–50.
6. Radmer R, Ollinger O. Topography of the O-2-evolving site determined with water analogs. FEBS Lett. 1983;152:39–43.
7. Force DA, Randall DW, Lorigan GA, Clemens KL, Britt RD. ESEEM studies of alcohol binding to the manganese cluster of the oxygen evolving complex of Photosystem II. J Am Chem Soc. 1998;120:13321–33.
8. Anderson JM, Chow WS. Structural and functional dynamics of plant photosystem II. Phil Trans Roy Soc Lond B. 2002;357:1421–30.
9. Wraight CA. Chance and design - proton transfer in water, channels and bioenergetic proteins. Biochim Biophys Acta Bioenerg. 2006;1757:886–912.
10. Petrek M, Otyepka M, Banas P, Kosinova P, Koca J, Damborsky J. CAVER: a new tool to explore routes from protein clefts, pockets and cavities. BMC Bioinform. 2006;7:316.

11. Haranczyk M, Sethian JA. Navigating molecular worms inside chemical labyrinths. Proc Natl Acad Sci U S A. 2009;106:21472–7.
12. Cohen J, Kim K, King P, Seibert M, Schulten K. Finding gas diffusion pathways in proteins: application to O-2 and H-2 transport in Cpl [FeFe]-hydrogenase and the role of packing defects. Structure. 2005;13:1321–9.
13. Tomita A, Sato T, Ichiyanagi K, Nozawa S, Ichikawa H, Chollet M, Kawai F, Park SY, Tsuduki T, Yamato T, Koshihara S, Adachi S. Visualizing breathing motion of internal cavities in concert with ligand migration in myoglobin. Proc Natl Acad Sci U S A. 2009;106:2612–6.
14. Arroyo-Manez P, Bikiel DE, Boechi L, Capece L, Di Lelia S, Estrin DA, Marti MA, Moreno DM, Nadra AD, Petruk AA. Protein dynamics and ligand migration interplay as studied by computer simulation. Biochimica Biophys Acta Protein Proteom. 2011;1814:1054–64.
15. Forti F, Boechi L, Estrin DA, Marti MA. Comparing and combining implicit ligand sampling with multiple steered molecular dynamics to study ligand migration processes in heme proteins. J Comput Chem. 2011;32:2219–31.
16. Cohen J, Arkhipov A, Braun R, Schulten K. Imaging the migration pathways for O-2, CO, NO, and Xe inside myoglobin. Biophys J. 2006;91:1844–57.
17. Cohen J, Olsen KW, Schulten K. Finding gas migration pathways in proteins using implicit ligand sampling. Globins Nitric Oxide React Protein B. 2008;437:439–57.
18. Ferreira KN, Iverson TM, Maghlaoui K, Barber J, Iwata S. Architecture of the photosynthetic oxygen-evolving center. Science. 2004;303:1831–8.
19. Loll B, Kern J, Saenger W, Zouni A, Biesiadka J. Towards complete cofactor arrangement in the 3.0 angstrom resolution structure of photosystem II. Nature. 2005;438:1040–4.
20. Murray JW, Barber J. Structural characteristics of channels and pathways in photosystem II including the identification of an oxygen channel. J Struct Biol. 2007;159:228–37.
21. Ho FM, Styring S. Access channels and methanol binding site to the CaMn4 cluster in Photosystem II based on solvent accessibility simulations, with implications for substrate water access. Biochim Biophys Acta Bioenerg. 2008;1777:140–53.
22. Guskov A, Kern J, Gabdulkhakov A, Broser M, Zouni A, Saenger W. Cyanobacterial photosystem II at 2.9-angstrom resolution and the role of quinones, lipids, channels and chloride. Nat Struct Mol Biol. 2009;16:334–42.
23. Gabdulkhakov A, Guskov A, Broser M, Kern J, Muh F, Saenger W, Zouni A. Probing the accessibility of the Mn4Ca cluster in photosystem II: channels calculation. Noble gas derivatization, and cocrystallization with DMSO. Structure. 2009;17:1223–34.
24. Sproviero EM, McEvoy JP, Gascon JA, Brudvig GW, Batista VS. Computational insights into the O-2-evolving complex of photosystem II. Photosynth Res. 2008;97:91–114.
25. Sproviero EM, Gascon JA, McEvoy JP, Brudvig GW, Batista VS. Computational studies of the O-2-evolving complex of photosystem II and biomimetic oxomanganese complexes. Coord Chem Rev. 2008;252:395–415.
26. Ho FM. Uncovering channels in photosystem II by computer modelling: current progress, future prospects, and lessons from analogous systems. Photosynth Res. 2008;98:503–22.
27. Humphrey W, Dalke A, Schulten K. VMD - visual molecular dynamics. J Mol Graphics. 1996;14:33–8.
28. Kale L, Skeel R, Bhandarkar M, Brunner R, Gursoy A, Krawetz N, Phillips J, Shinozaki A, Varadarajan K, Schulten K. NAMD2: greater scalability for parallel molecular dynamics. J Comput Phys. 1999;151:283–312.
29. Kawakami K, Umena Y, Kamiya N, Shen JR. Structure of the catalytic, inorganic core of oxygen-evolving photosystem II at 1.9 angstrom resolution. J Photochem Photobiol B Biol. 2011;104:9–18.
30. Hermans A, Xia X, Cavanaugh D. DOWSER. Department of Biochemistry and Biophysics, School of Medicine, University of North Carolina, Chapel Hill, NC 27599-7260. 1998. http://hekto.med.unc.edu/HERMANS/software/DOWSER/

31. Zhang L, Hermans J. Hydrophilicity of cavities in proteins. Protein Struct Funct Genet. 1996;24:433–8.
32. Vassiliev S, Comte P, Mahboob A, Bruce D. Tracking the flow of water through photosystem II using molecular dynamics and streamline tracing. Biochemistry. 2010;49:1873–81.
33. Zhu FQ, Tajkhorshid E, Schulten K. Molecular dynamics study of aquaporin-1 water channel in a lipid bilayer. FEBS Lett. 2001;504:212–8.
34. de Groot BL, Grubmuller H. Water permeation across biological membranes: mechanism and dynamics of aquaporin-1 and GlpF. Science. 2001;294:2353–7.
35. Chakrabarti N, Roux B, Pomes R. Structural determinants of proton blockage in aquaporins. J Mol Biol. 2004;343:493–510.
36. de Groot BL, Frigato T, Helms V, Grubmuller H. The mechanism of proton exclusion in the aquaporin-1 water channel. J Mol Biol. 2003;333:279–93.
37. Hu Z, Jiang J, Sandler SI. Water in hydrated orthorhombic lysozyme crystal: insight from atomistic simulations. J Chem Phys. 2008;129:075105.
38. Hu ZQ, Jiang JW. Molecular dynamics simulations for water and ions in protein crystals. Langmuir. 2008;24:4215–23.
39. Lebihan D, Breton E, Lallemand D, Grenier P, Cabanis E, Lavaljeantet M. Mr imaging of intravoxel incoherent motions - application to diffusion and perfusion in neurologic disorders. Radiology. 1986;161:401–7.
40. Basser PJ, Pajevic S, Pierpaoli C, Duda J, Aldroubi A. In vivo fiber tractography using DT-MRI data. Magn Reson Med. 2000;44:625–32.
41. Zaraiskaya T, Kumbhare D, Noseworthy MD. Diffusion tensor imaging in evaluation of human skeletal muscle injury. J Magn Reson Imag. 2006;24:402–8.
42. Basser PJ, Jones DK. Diffusion-tensor MRI: theory, experimental design and data analysis - a technical review. NMR Biomed. 2002;15:456–67.
43. Johansen-Berg H, Rushworth MFS. Using diffusion imaging to study human connectional anatomy. Annu Rev Neurosci. 2009;32:75–94.
44. Jensen MO, Park S, Tajkhorshid E, Schulten K. Energetics of glycerol conduction through aquaglyceroporin GlpF. Proc Natl Acad Sci U S A. 2002;99:6731–6.
45. Zhou HX, Wlodek ST, McCammon JA. Conformation gating as a mechanism for enzyme specificity. Proc Natl Acad Sci U S A. 1998;95:9280–3.
46. Dau H, Haumann M. The manganese complex of photosystem II in its reaction cycle - basic framework and possible realization at the atomic level. Coord Chem Rev. 2008;252:273–95.
47. Vassiliev S, Zaraiskaya T, Bruce D. Exploring the energetics of water permeation in photosystem II by multiple steered molecular dynamics simulations. Biochim Biophys Acta Bioenerg. 2013;1817:1671–8.
48. Park S, Khalili-Araghi F, Tajkhorshid E, Schulten K. Free energy calculation from steered molecular dynamics simulations using Jarzynski's equality. J Chem Phys. 2003;119:3559–66.
49. Jarzynski C. Equilibrium free-energy differences from nonequilibrium measurements: a master-equation approach. Phys Rev E. 1997;56:5018–35.
50. Umena Y, Kawakami K, Shen JR, Kamiya N. Crystal structure of oxygen-evolving photosystem II at a resolution of 1.9 angstrom. Nature. 2011;473:55–U65.
51. Zeidel ML, Ambudkar SV, Smith BL, Agre P. Reconstitution of functional water channels in liposomes containing purified red-cell Chip28 protein. Biochemistry. 1992;31:7436–40.
52. Vanhoek AN, Verkman AS. Functional reconstitution of the isolated erythrocyte water channel Chip28. J Biol Chem. 1992;267:18267–9.
53. Hub JS, de Groot BL. Mechanism of selectivity in aquaporins and aquaglyceroporins. Proc Natl Acad Sci U S A. 2008;105:1198–203.
54. Ishikita H, Saenger W, Loll B, Biesiadka J, Knapp EW. Energetics of a possible proton exit pathway for water oxidation in photosystem II. Biochemistry. 2006;45:2063–71.
55. Calhoun DB, Vanderkooi JM, Woodrow GV, Englander SW. Penetration of dioxygen into proteins studied by quenching of phosphorescence and fluorescence. Biochemistry. 1983;22:1526–32.

56. Wang Y, Cohen J, Boron WF, Schulten K, Tajkhorshid E. Exploring gas permeability of cellular membranes and membrane channels with molecular dynamics. J Struct Biol. 2007;157:534–44.
57. Johnson BJ, Cohen J, Welford RW, Pearson AR, Schulten K, Klinman JP, Wilmot CM. Exploring molecular oxygen pathways in Hansenula polymorpha copper-containing amine oxidase. J Biol Chem. 2007;282:17767–76.
58. Baron R, Riley C, Chenprakhon P, Thotsaporn K, Winter RT, Alfieri A, Forneris F, van Berkel WJH, Chaiyen P, Fraaije MW, Mattevi A, McCammon JA. Multiple pathways guide oxygen diffusion into flavoenzyme active sites. Proc Natl Acad Sci U S A. 2009;106:10603–8.
59. Luna VM, Fee JA, Deniz AA, Stout CD. Mobility of Xe atoms within the oxygen diffusion channel of cytochrome ba(3) oxidase. Biochemistry. 2012;51:4669–76.
60. Roy A, Carpentier P, Bourgeois D, Field M. Diffusion pathways of oxygen species in the phototoxic fluorescent protein KillerRed. Photochem Photobiol Sci. 2010;9:1342–50.
61. Chapagain PP, Regmi CK, Castillo W. Fluorescent protein barrel fluctuations and oxygen diffusion pathways in mCherry. J Chem Phys. 2011;135.
62. Saam J, Rosini E, Molla G, Schulten K, Pollegioni L, Ghisla S. O-2 reactivity of flavoproteins dynamic access of dioxygen to the active site and role of a H + relay system in D-amino acid oxidase. J Biol Chem. 2010;285:24439–46.
63. Saam J, Ivanov I, Walther M, Holzhutter HG, Kuhn H. Molecular dioxygen enters the active site of 12/15-lipoxygenase via dynamic oxygen access channels. Proc Natl Acad Sci U S A. 2007;104:13319–24.
64. Tilton RF, Kuntz ID, Petsko GA. Cavities in proteins - structure of a metmyoglobin-xenon complex solved to 1.9-A. Biochemistry. 1984;23:2849–57.
65. Ho FM. Structural and mechanistic investigations of photosystem II through computational methods. Biochim Biophys Acta. 2012;1817:106–20.
66. Ho FM. Wydrzynski T, Hillier W, editors. Substrate and Product Channels in Photosystem II. *Molecular solar fuels*, Cambridge: Royal Society of Chemistry; 2012, pp. 208–248.
67. Zaraiskaya T, Vassiliev S, Bruce D. Revealing molecular oxygen migration pathways in photosystem II using implicit ligand sampling and wavefront propagation. J Comput Sci 2014;5: 549–55.
68. Garrido S, Moreno L, Blanko D, Munoz ML. Sensor-based global planning for mobile robot navigation. Robotica. 2007;25:189–99.
69. Cohen LD, Deschamps T. Segmentation of 3D tubular objects with adaptive front propagation and minimal tree extraction for 3D medical imaging. Comput Meth Biomech Biomed Eng. 2007;10:289–305.
70. De Ridder S, Dellinger J. Ambient seismic noise eikonal tomography for near-surface imaging at Valhall. Lead Edge. 2011;30:506–12.
71. Alvino C, Unal G, Slabaugh G, Peny B, Fang T. Efficient segmentation based on Eikonal and diffusion equations. Int J Comput Math. 2007;84:1309–24.
72. Podvin P, Lecomte I. Finite-difference computation of traveltimes in very contrasted velocity models - a massively parallel approach and its associated tools. Geophys J Int. 1991;105:271–84.
73. Shir OM, Emmerich M, Back T. Adaptive niche radii and niche shapes approaches for niching with the CMA-ES. Evol Comput. 2010;18:97–126.
74. Bosma M, Smit J, Terwisscha J, van Scheltinga J. Super resolution volume rendering hardware. Tenth Workshop on graphics hardware. EuroGraphics Technical Report Series EG95 HW. 1995.
75. Hansen N, Agbor FAB, Keil FJ. New force fields for nitrous oxide and oxygen and their application to phase equilibria simulations. Fluid Phase Equilib. 2007;259:180–8.
76. Winter MB, Herzik MA, Kuriyan J, Marletta MA. Tunnels modulate ligand flux in a heme nitric oxide/oxygen binding (H-NOX) domain. Proc Natl Acad Sci U S A. 2011;108:E881–9.
77. Zhang YB, Lu M, Cheng YK, Li ZQ. H-NOX domains display different tunnel systems for ligand migration. J Mol Graph Model. 2010;28:814–9.

Part V
Evolution of the Photosynthetic Apparatus

Chapter 13
From Ionizing Radiation to Photosynthesis

Alexander N. Melkozernov

Abstract This chapter focuses on the driving forces of the origin and the evolution of the early anoxygenic photosynthesis before the onset of the oxygenic cyanobacterial photosynthesis 2.8–2.4 billion years ago. The early Earth conditions were sustained by the global cycling of carbon dioxide among the atmosphere, primordial crust, and the ocean. High-energy ultraviolet radiation played a decisive role in this interaction, maintaining the temperature of the ocean and promoting mildly oxidizing conditions in the atmosphere and the upper layers of the ocean. Constrained by the sterilizing effect of the UV radiation and the evaporating consequences of the Late Heavy Bombardment, chemolithotrophic life was likely to emerge at the seafloor under excess of carbon dioxide and a constant flux of reducing hydrothermal fluids. Trophic diversification had launched the expansion of the chemolithotrophic lineages to the photic zone. Alternative hypotheses of the terrestrial origin of life with implications for the origin of photosynthesis are discussed. The review reconstructs the development of the ancient photosynthetic habitats under the strong selective pressure of the UV radiation and discusses available hypotheses of the origin of photosynthesis with regard to emergence of workable photosynthetic mechanism. The evolution of the homodimeric proto-photosystem and its divergence to the homodimeric iron–sulfur-type and the homodimeric quinone-type reaction centers were probably driven by the availability of the exogenous electron donors in a series of ecological successions from the oceanic photic zone to the shallow water habitats and microbial mats. This process had eventually resulted in the advent of independence of the photosynthetic organisms from the geochemical conditions in cyanobacterial lineages that were able to oxidize water.

A.N. Melkozernov, Ph.D. (✉)
Department of Chemistry and Biochemistry, Arizona State University,
Tempe, AZ 85287-1604, USA
e-mail: alexander.melkozernov@asu.edu

J. Golbeck and A. van der Est (eds.), *The Biophysics of Photosynthesis*,
Biophysics for the Life Sciences 11, DOI 10.1007/978-1-4939-1148-6_13,

Keywords Photosynthesis • Evolution • Chemoautotrophy • Photoautotrophy • UV selective pressure • Reaction center • Photosystem I • Photosystem II

Abbreviations

BChl	Bacteriochlorophyll
BChlide	Bacteriochlorophyllide
BIFs	Banded iron formations
Chl	Chlorophyll
COR	Chlorophyllide oxidoreductase
Chlide	Chlorophyllide
Fe–S	Iron–sulfur
Ga	Giga annum
GOE	Great Oxidation Event
LUCA	Last unified common ancestor
PSI	Photosystem I
PSII	Photosystem II
POR	Protochlorophyllide oxidoreductase
PChlide	Protochlorophyllide
RC	Reaction center
rTCA	Reductive tricarboxylic acid cycle
UroIII	Uroporphyrinogen III
UV	Ultraviolet

13.1 Introduction

Photosynthesis is a fundamental biological process supplying Earth's biosphere with oxygen and energy for living. Once emerged on Earth, this process had significantly altered the geological history of our planet by converting solar energy into metabolic energy of organic compounds and by dramatically changing the atmosphere from carbon dioxide dominated to oxygen containing. This chapter focuses on the driving forces of the origin and the evolution of the early anoxygenic photosynthesis before the onset of the oxygenic photosynthesis in cyanobacteria 2.8–2.4 billion years ago. The bacteriorhodopsin-based phototrophic systems, although they are apparently ancient, diverse, and spread among several phyla of Archaea and Eubacteria, are not considered in the review as they are not photosynthetic but limited to photoheterotrophy, a light-driven assimilation of organic compounds.

Our planet Earth is located in the habitable zone of the solar system [1, 2], where the mass of the planet and the distance to the Sun largely define the $CO_2/H_2O/N_2$ atmosphere and the presence of liquid water on the surface [3]. Within half a billion years Earth had developed from the magma globe to the planet with intimately linked interior, ocean, and the atmosphere. Solar electromagnetic radiation,

specifically high-energy UV, played a decisive role in this interaction of the lithosphere, hydrosphere, and atmosphere, maintaining the temperature of the ocean, the mildly oxidizing conditions in the atmosphere and constraining the emergence of life (see Sect. 13.2).

The long-standing geological paradox implies a very short time between the end of the harsh Earth bombardment (4.1 Ga) and the evidence of the early cellular life (3.4–3.8 Ga). This could be explained by the earlier start to life in the deep sea under protection of the ocean depths from the surface destructive forces and the harsh solar radiation. Although the origin of life is not the focus of this review, the subject is important for setting up a context for the origin of photoautotrophy. Recent discoveries of astounding diversity of the autotrophic microbial life in the ocean and beneath, progress in genomics and metagenomics, and discoveries of the hydrothermal vents with conditions that are far from equilibrium contributed to the emerging consensus that the excess of carbon dioxide in the ocean and a constant flux of reducing fluids at the seafloor predetermined the origin of the chemolithoautotrophic life [4] (see Sect. 13.3). In a broader sense, photolithoautotrophy is a special case of the chemolithoautotrophy with energy of light and not chemical energy providing reducing power for fixation of carbon dioxide.

Harsh surface conditions were nevertheless conducive to a synthesis of certain amount of organic compounds due to the atmospheric UV photochemistry, electric discharges, as well as impacts of the space bodies bombarding the Earth and delivery of the organics from space [5]. The total organic carbon synthesized or delivered on Earth could amount to 3×10^{11} kg year^{-1} under reducing conditions and two orders of magnitude less if conditions are neutral [6]. Given the volume of the Hadean Ocean of 1.8×10^{21} l [7] the concentration of the organic carbon in the ocean would be in the micromolar range for reducing conditions or even less for neutral conditions. In a state close to equilibrium, the chances of the primordial soup developing into the self-sustained metabolic pathways could be rather limited. Furthermore, the Earth hydrothermal system circulates through the very hot crust a volume of the entire ocean once every 10 million years, which constrained the primordial soup evolution [8]. Section 13.4 of the review analyzes the alternative hypothesis of the terrestrial origin of life under reducing conditions of geothermal ponds and the UV-driven photochemical synthesis of the organic compounds and discusses the prospects of the early emergence of the proto-photosynthetic systems.

Within the framework of the chemolithotrophic origin of life, the emergence of the photosynthesis is a matter of the evolutionary expansion of the autotrophic ancestors from the deep sea environments to the surface of the ocean (Sect. 13.5). The review reconstructs the development of the ancient photosynthetic habitats in the upper layers of the ocean and the first shallow water habitats under strong selective pressure of the UV radiation.

Recent discoveries of new phyla of photosynthetic organisms, progress in whole-genome sequencing and genome-wide phylogenetic analyses, and breakthroughs in crystal structure determination of two types of the photosynthetic reaction centers (RC), photosystem I (PSI, iron–sulfur type) and photosystem II (PSII, quinone type) once again raised the question of when and how the ancient

proto-reaction centers had emerged and which type of the RC was ancestral. Sections 13.6–13.8 of the chapter address the available hypotheses of the origin of photosynthesis and analyze the scenario of the evolution of a homodimeric proto-RC as an ancestral PSI-like reaction center and its divergence to a heterodimeric PSI and PSII driven by availability of the electron donors in a series of ecological successions from the oceanic photic zone to the shallow water habitats. We know that this process had eventually resulted in the advent of real independence of the photosynthetic organisms from the geochemical conditions in cyanobacterial lineages that were able to oxidize water. Detailed mechanisms of what happened are unknown. As all photosynthetic RCs share similar protein folds and fundamental mechanisms of the primary charge separation and stabilization the monophyletic origin of photosynthesis is beyond question. However, single-gene phylogenetic trees for the photosynthetic organisms illustrate independent evolutionary histories for many components of the photosynthetic apparatus. Section 13.9 of the chapter discusses available genomic information and attempts of reconstruction of the early phylogenies of the photosynthetic organisms as part of the Tree of Life.

13.2 Solar Radiation and the Early Stages of the Earth Geological History

13.2.1 Formation of Atmosphere, Lithosphere, and Hydrosphere

Geological history of the planet Earth had started 4.56 billion years ago (Ga, Giga-annum) with accretion of the interplanetary dust particles, small space bodies, comets, and meteorites (see timeline in Fig. 13.1) [9–11]. Being in the gravitational field of the Sun, the primary accretion disc overheated by nuclear reactions and interactions with highly energetic cosmic γ-rays, X-rays, and extreme ultraviolet radiation had developed into a magma globe. Within 250 million years the planet reached the mass of the present state and its molten content began to differentiate into the core of denser materials (largely iron) with dissolved hydrogen and mantle containing less dense materials (silicon, oxygen, and sulfur) [11–13]. At the early stage, the less dense gases had formed a proto-atmosphere, which contained a strongly reduced mixture of H_2O, CH_4, NH_3, H_2, and He. This proto-atmosphere was largely remnants of the proto-planetary gas dominated by H_2, He, and extremely reduced gaseous species.

4.5 Ga ago the young Sun rotated faster and emitted more short-wavelength radiation (extreme UV with $\lambda < 200$ nm) [14]. Photolysis of water, methane, and ammonia in the proto-atmosphere under strong UV radiation produced hydrogen, which hydrodynamically escaped to space. Oxygen left from the photolysis of water was bound by available elements in the form of oxides (Na_2O, MgO, Al_2O_3, SiO_2, K_2O, and CaO). These processes as well as a catastrophic collision

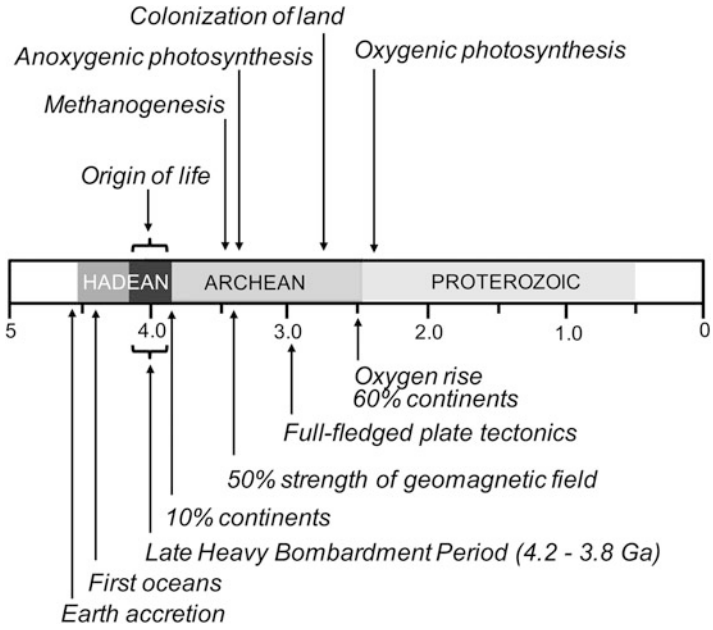

Fig. 13.1 Timeline of the history of Earth before the oxygen rise with major geological and biological events

of the Earth 4.5 Ga ago followed by formation of the Moon [15] are thought to cause a significant loss of the primordial reducing atmosphere [16].

Subsequent processes changed a geological history of the Earth as the early atmosphere was replaced by a secondary atmosphere, which originated due to degassing of the Earth's interior. Low-density melts from the mantle (largely silicates) rose to the surface and formed the crust [12, 17]. Solidification of the upper layers of magma 4.5 Ga ago induced a release of water as steam and carbon dioxide into the atmosphere. By estimates, the Earth atmosphere in the early Hadean era was a dense mixture of 550 bars of H_2O and 100 bars of CO_2 [16, 18]. As any heated object, Earth continued to lose heat into the space and the temperature of the solidifying crust reached a point when the water vapor atmosphere had collapsed to hydrosphere [11, 16, 18]. The ocean on Earth had appeared 4.4 Ga ago as evidenced by the isotopic composition of the zircons that indicates the presence of crust and liquid water [19]. Degassing of the Earth mantle upon solidification and the collapse of the steam atmosphere is not the only source of water on Earth. Carbonaceous chondrites that were falling on the Earth from space for more than 0.5 billion years could contain up to 22 % of water [20]. This suggests that space icy bodies could significantly contribute to the Earth water volume [16].

Solar radiation played an important role in setting up the atmosphere composition and the temperature in the ocean [21]. According to "Faint Young Sun paradox" hypothesis, the brightness of Sun was 30–25 % smaller 4.5 Ga ago due

to lower solar energy generation rates resulting in lower visible and infrared fluxes [3, 14]. Presence of high concentrations of the CO_2, a greenhouse gas, through Hadean period sustained high temperatures in the atmosphere and the ocean, which is evidenced by the strong carbonation of the oceanic crust [22]. However, CO_2 content in the atmosphere gradually decreased from 40 to 210 bar (early Hadean) to 5 to 25 bar (early Archean) [20]. The lower solar radiation and smaller concentration of CO_2 in the early Archean would predict temperatures on the surface of the planet below freezing point [21]. However, modeling predicts that an average temperature of ~60 °C could be maintained by 2–6 bars of CO_2 and less than 1 % of methane in the early Archean atmosphere [23]. Thus, relatively hot temperatures of the atmosphere and the ocean were maintained by the balance between two potential greenhouse gases, CO_2 and CH_4. The concentration of methane was kept low by its UV photolysis in the atmosphere [24].

Major carbon sinks, which facilitated the decrease of CO_2 in the atmosphere in early-to-mid Archean, were (1) deposition of carbonates in the ocean due to weathering of the seafloor basalt (binding of CO_3^{2-} by divalent cations), (2) ocean crust recycling in the mantle, and (3) plate tectonics [25, 26]. As the first two processes were active since the appearance of the oceanic crust, the last process had started playing in full in the middle of Archean (>3 Ga years ago, see Fig. 13.1) [26, 27]. Thick continental crust grew continuously due to magma extrusion processes during the late Hadean eon [17] reaching 10 % by 3.8 Ga years [13] and 50–60 % by the end of the Archean eon (2.5 Ga) [26, 28]. Today the oceans cover 70 % of the Earth surface meaning that in the late Hadean (~4 Ga) the continents occupied less than 3 % of the surface of the Earth and the planet was essentially a water world.

Geochemists do not share a concept of Archean reducing atmosphere, which is quite popular in the biological literature. Rather, a wealth of evidence builds up a consensus that the Hadean volcanic gases consisted largely of oxidative species such as CO_2, N_2, SO_2, and H_2O with much smaller proportion of H_2, CH_4, and NH_3, which is not very different from that emitted today [11, 29–31].

13.2.2 Emission Properties of Sun and Electromagnetic Radiation on Early Earth

During the Hadean eon the stronger solar winds in the form of highly energetic subatomic particles, X-rays, and ultraviolet emission irradiated the early Earth atmosphere causing ionization and destruction of the atmospheric gases [32]. At present, the Earth's magnetic field protects the life of the planet from destruction. However, in the Archean period the magnetic field was underdeveloped and suppressed by the stronger magnetic field of the young Sun; therefore it was inefficient [33]. 3.45 Ga ago the strength of the magnetic field was at 50 % of the

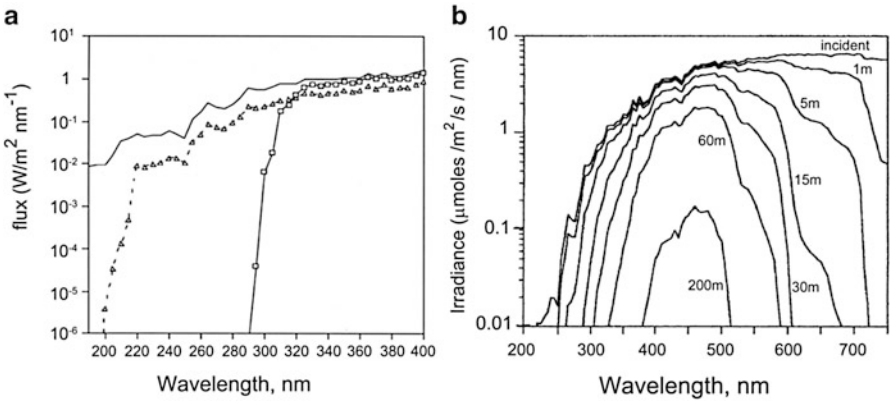

Fig. 13.2 Solar electromagnetic radiation reaching the Archean Earth. (**a**) Electromagnetic radiation in the 200–400 nm wavelength range: extraterrestrial UV flux 3.5 Ga ago (*solid line*); UV flux reaching through Archean atmosphere containing 40 mbar CO_2 (*dashed line* with *triangles*); present-day flux (*solid line* with *open squares*). Taken from Cockell and Raven [35] with permission. (**b**) Depth dependence of the spectral quality of electromagnetic radiation penetrating into the Archean oceans. Taken from Cockell [115] with permission

present-day strength, thus suggesting that earlier the surface of the Earth was susceptible to the bigger extent of cosmic ray's destruction [34].

The UV radiation was also stronger [14, 32, 35, 36]. Specifically, the high-energy UV fluxes at 3.5 Ga were six times larger than the present levels [36]. High atmospheric concentration of the CO_2 absorbed a great deal of the extreme ultraviolet below 200 nm. However, the atmosphere and the upper layers of the ocean were transparent for the UV radiation in the 200–350 nm region (Fig. 13.2). Additionally, high-energetic cosmic rays entering the Earth atmosphere generated a cascade of the secondary UV emission bombarding the Earth [32].

13.2.3 Late Heavy Bombardment

Location of the Hadean Earth in the zone of the asteroid belts had caused a severe bombardment of the surface by space objects of different sizes for nearly 700 million years [37]. The last ocean-vaporizing event was thought to be around 4.2 Ga ago [3, 15]. According to model calculations, a 500 km asteroid upon impact would vaporize the surface to the state of rock vapor mixture, which is absolutely inconsistent with life [15]. Smaller objects (i.e., bodies of 100 km) would increase the ocean temperature up to 100 °C and annihilate the photic zone and 200 m of the upper layers of the ocean [3]. This emphasizes the importance of deepwater oceans as a safe cradle of life since this period (4.1–3.8 Ga ago) is widely thought to be associated with the origin of life.

13.2.4 Water Exchange with the Crust

Hydrothermally active oceanic crust played an important role in the circulation of the reduced gases and minerals through the water. There was a substantial movement of water masses through the oceanic crust [38]. The temperature gradients induced constant percolation of the seawater through the heated hydrothermal vents. Lava from the underlying mantle and the seawater under contact produced serpentinization of minerals, a rock-weathering process releasing hydrogen, hydrogen sulfide, methane, and ammonia and washing out reduced metals such as iron, nickel, and cobalt into the water [39, 40].

Summarizing this section, the early Earth conditions were maintained through the global cycling of carbon dioxide among the atmosphere, mantle, and the ocean [41]. The ocean temperature had been controlled by the ratio of the greenhouse gases in the atmosphere, CO_2 and methane. The surface of the Earth was exposed to increased solar fluxes of the UV radiation, cosmic rays, and the severe asteroid bombardment. The UV had driven photolysis of the atmospheric gases and the upper layers of the ocean followed by escape of hydrogen into the space and entrapment of all oxygen by the crust minerals. Despite the overall slightly oxidizing atmosphere the oceanic crust was a constant source of reducing disequilibria due to hydrothermal activity and serpentinization.

13.3 Hypothesis of Chemolithotrophic Origin of Life and Spread of Autotrophy on Earth

13.3.1 Hydrothermal Vents as a Cradle of Life

The discovery of hydrothermal vents in 1977 [42] introduced a different prospect on the idea of origin of life. Hydrothermal vents were common in Hadean and Archean eons [43]. Of special interest are the seafloor alkaline hydrothermal vents that constantly generate thermodynamic geochemical disequilibrium due to a process of serpentinization, which occurs when oceanic water is hydrodynamically pulled through the crust [39, 40, 43, 44]. As a result hydrothermal fluids are enriched in H_2, H_2S, CH_4, and derivatives as well as reduced ions of transition metals (see Fig. 13.3a). At the exit of the hydrothermal vent the alkaline mineral fluids precipitate upon a contact with cooler ocean water and form insoluble chimneys. The growing hydrothermal mound is a network of porous microcompartments with semipermeable membranes. Given the alkalinity of the hydrothermal fluids and the acidity of the Archean CO_2-rich ocean, the semipermeable inorganic membranes had likely established the natural inorganic chemiosmotic systems with a proton-motive force [44, 45] (see Fig. 13.3b). Similar systems reconstructed under laboratory conditions were shown to maintain redox and pH

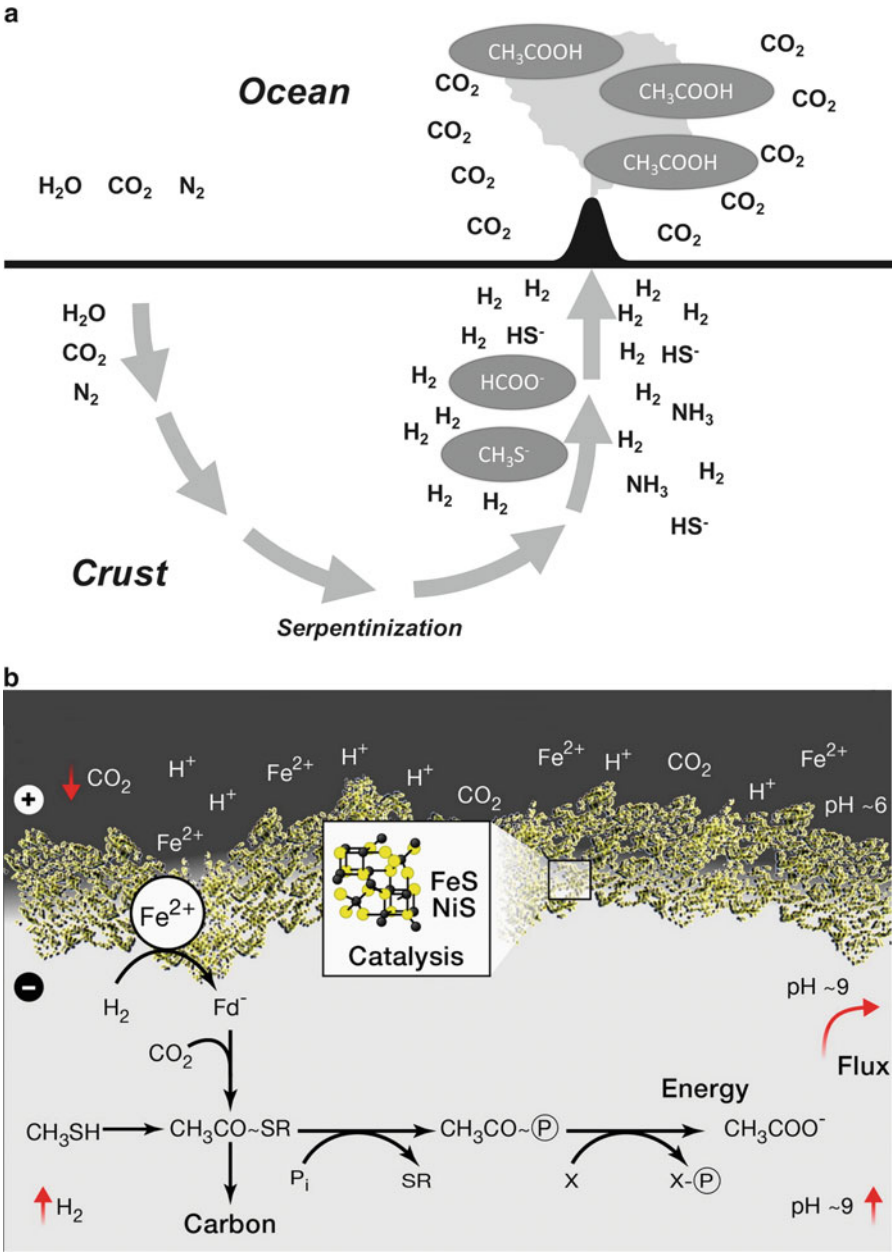

Fig. 13.3 Geochemical redox disequilibria on the interface between oceanic crust and water. (**a**) Percolation of seawater through the hot crust induces a process of serpentinization that enriches the hydrothermal fluids with H_2, H_2S, CH_4, other organic derivatives, and transition metals. Taken from Martin and Russell [49] with permission. (**b**) Microporous compartments with semipermeable inorganic membranes in the alkaline hydrothermal vents provide natural reactive environment for generation of reducing power in the form of reduced Fe–S centers (primordial ferredoxins, Fd) for reduction of CO_2 and synthesis of organic compounds such as acetyl-thioesters ($CH_3CO\sim SR$) and acetyl-phosphates ($CH_3CO\sim P$), which were supposedly involved in synthesis of energy-storing compounds (X-P). Taken from Lane and Martin [44] with permission

gradients [46, 47]. The natural geochemical disequilibrium at alkaline hydrothermal vents had likely sustained chemical reduction of carbon dioxide by abundant hydrogen enhanced by catalytic iron–sulfur minerals. By chemically generating a reducing power, such a system favored synthesis of methane and various derivative organic compounds [40, 45, 48, 49]. Microporous inorganic compartments had dramatically increased the yield of the organic compounds. Exchange of acetyl groups between thioesters and phosphates is thought to establish the primordial pathway of synthesis of energy-rich molecules [49] (Fig. 13.3b).

Under stable non-equilibrium conditions the compartmentalized carbon fixation reactions had evolved into autocatalytic metabolic networks and later had acquired self-replicating capacity through evolution of the RNA-protein catalysis [49, 50]. Experimental findings indicate that the system would be capable of natural chemical synthesis of variable organic derivatives giving rise to primitive peptides and nucleic acids [48]. Thus, a mineral-based network of semipermeable microcompartments naturally generated by alkaline hydrothermal vents is a possible hatchery for the first chemolithoautotrophic systems living off the geochemical thermodynamic disequilibria [39, 40, 44, 45]. The protocells probably stayed within these natural reactor communities until they were able to maintain their transmembrane chemiosmotic gradients and synthesis of ATP by coupling the CO_2 reduction reactions to electrogenic translocation of sodium [44].

If metabolic systems had already functioned in this community, many primordial bioenergetic enzymes should have existed before the first lineages started diversification [51, 52]. The so-called pre-LUCA phase (*L*ast *U*niversal *C*ommon *A*ncestor) is a hypothetical state where the barriers between the species were likely blurred due to sharing enzymes and the substantial exchange of genetic information [50]. The first enzymes maintained the energy-conserving pathways of anaerobic respiration that facilitated the transmembrane transfer of electrons from reduced donors (exogenous hydrogen, hydrogen sulfide, or ferrous ions) to the oxidized acceptors on the other side of the membrane (carbon dioxide, sulfur, and nitrogen compounds) [52–54].

13.3.2 Carbon Fixation Pathways

Driven by environmental and biogeochemical changes diversification of evolving organisms led to changes in the autotrophic carbon assimilation pathways. Presently, 5–6 autotrophic carbon fixation pathways are known to exist in different prokaryotes [55–59] (Table 13.1 and Fig. 13.4). More than 14 different carboxylating enzymes have evolved to fix carbon dioxide in the pathways [4, 56]. Biosynthetic pathways share five universal precursors: acetyl-CoA, pyruvate, oxaloacetate, succinyl-CoA, and α-ketoglutarate [60, 61]. The most archaic metabolic pathways are reductive acetyl-CoA pathway (the Wood-Ljungdahl pathway), reverse *t*ricarboxylic *a*cid *c*ycle (r-TCA) operating on the ancient carboxylic acids [55, 56, 62], or a primitive combination of both [60]. These pathways are widely

Table 13.1 Diversity of autotrophic carbon fixation pathways. Modified from Berg [55]. See also Fig. 13.4

CO_2 fixation pathway	ATP requirement[a]	Key CO_2-fixing enzymes	Carbon isotope fractionation (‰)[b]	Photosynthetic representatives
Calvin cycle	7–9	Rubisco and phosphorybulokinase	~−25	Plants, algae, cyanobacteria, phototrophic representatives of α- and β-proteobacteria, *Oscillochloris* from *Chloroflexi*
Reductive tricarbonic acid cycle	2	2-Oxoglutarate synthase, Isocitrate dehydrogenase, pyruvate synthase, pepcarboxylase	−2 to −12	Green sulfur bacteria
r-Acetyl-CoA pathway	1	Acetyl-CoA synthase–CO dehydrogenase and formylmethanofuran dehydrogenase (in methanogens)	<−30	None
3-Hydroxypropionate cycle	5–7	Acetyl-CoA and propionyl-CoA carboxylase	~−14	Representatives of genus *Chloroflexus*
3-Hydroxypropionate/4-hydroxybutyrate cycle	6–9	Acetyl-CoA and propionyl-CoA carboxylase	−0.2 to −3.8	None

[a]Per 1 molecule of pyruvate
[b]Calculated as $\delta^{13}C‰ = [(^{13}C/^{12}C_{sample} - {}^{13}C/^{12}C_{standard})/(^{13}C/^{12}C_{standard})] * 1{,}000$

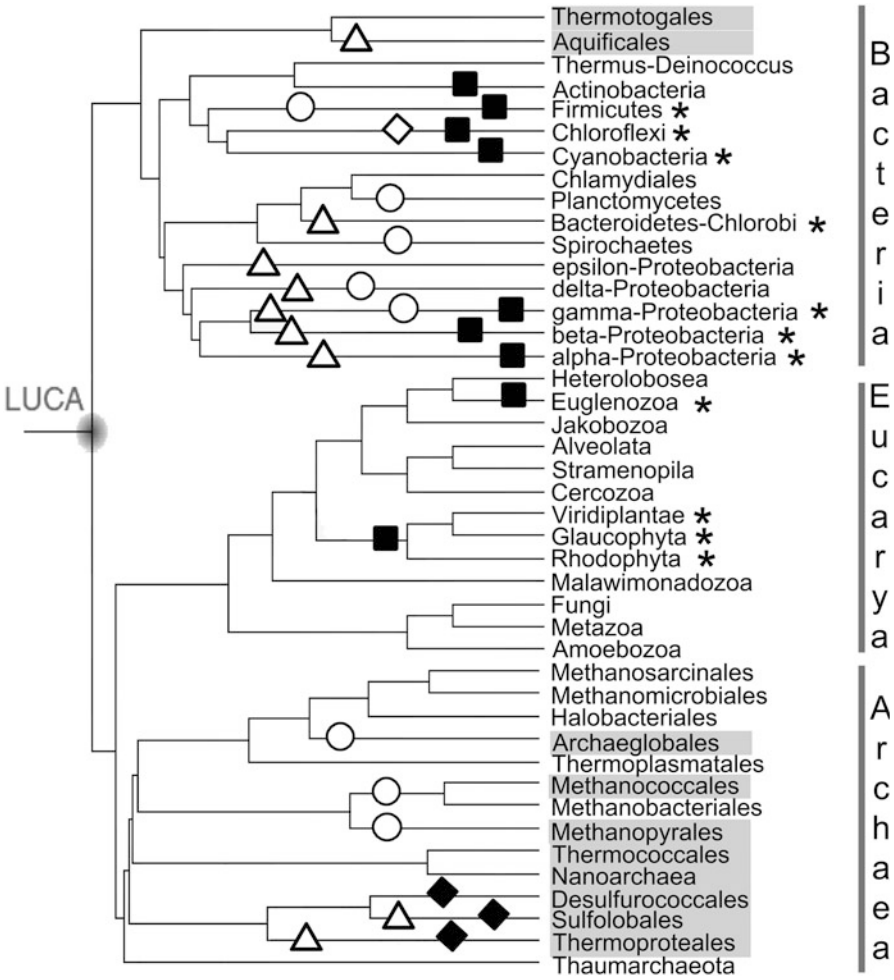

Fig. 13.4 Distribution of autotrophic CO_2 fixation pathways among different phylogenetic taxa of the Tree of Life. Modified from Boussau and Gouy [196] with permission. Based on data in [41, 56, 59, 62, 69]. Taxa with photosynthetic representatives are labeled with *asterisks*. Autotrophic pathways are labeled as follows: reduced TCA cycle (*open triangles*); reduced acetyl-CoA pathway (*open circles*); 3-hydroxypropyonate cycle (*open rhombus*); 3-hydroxypropyonate/4-hydroxybutyrate cycle (*closed rhombus*); Calvin cycle (*closed squares*). Names of hyperthermophilic lineages are *shaded*

spread among branches of the phylogenetic tree (Fig. 13.4). For example, the rTCA cycle is found in deep-branching chemolithotrophic *Aquificales* [57] and Archaea [55], in anaerobic photolithoautotrophic green sulfur bacteria [63, 64], and in clustering with them chemolithoautotrophic δ- and ε-proteobacteria living off the hydrothermal vents at the seafloor [65–67].

Development of a particular carbon fixation pathway in the microorganism depends on energy metabolism, which in turn is affected by the environment conditions. The ATP requirements for different pathways are different (Table 13.1). Life under reducing conditions at hydrothermal vents needs less ATP; therefore primordial reverse TCA and reductive acetyl CoA pathways use minimum 1–2 molecules of ATP for autotrophic synthesis of one molecule of pyruvate [68, 69]. On the contrary, the Calvin-Benson cycle found in photosynthesizing proteobacteria, cyanobacteria, and eukaryotic algae and plants (Fig. 13.4 and Table 13.1) is energy demanding as it requires at least nine molecules of ATP per synthesis of one molecule of glyceraldehyde-3-phosphate.

The Calvin-Benson cycle had not been found in deep-branching hyperthermophilic prokaryotes and it is a sole carbon fixation pathway in autotrophic oxygenic cyanobacteria and eukaryotic photosynthesizers (Fig. 13.4). It is thought to be rather late metabolic invention [55] because it became dominant in the late Archean eon with a rise of oxygen in the atmosphere. However, it likely evolved under anaerobic conditions. For example, green sulfur bacteria do not employ Calvin cycle; however, they possess the so-called Rubisco-like proteins that are not involved in carbon fixation but, based on the analysis of the genome, are somehow affiliated with sulfur metabolism [64].

Phylogenetic trees show no evidence of unified evolutionary history of the autotrophic carbon fixation pathways. All known mechanisms are rather distinct and independently evolved. Ancient gene exchange via viruses and gene transfer agents probably contributed to the spread of the pathways [70].

13.3.3 Iron–Sulfur Clusters, Quinones, and Porphyrin-Like Molecules

Phylogenetic analyses indicate that the ancient enzymes such as hydrogenases, cytochrome NO reductases, quinone NO reductases, and Rieske cytochrome *b* oxidoreductases had likely appeared before the split of archaebacteria and Eubacteria [51, 52, 71, 72]. These critical enzymes, many of which are metal containing, were needed to deal with reduced electron donors and oxidized electron acceptors present in the extracellular environment. It is not surprising that the structures of the active sites of many critical enzymes are often reminiscent of minerals in hydrothermal vents [73, 74].

Antiquity of iron–sulfur clusters, cyclic tetrapyrroles, and quinones is supported by their presence among the enzyme cofactors shared by Archaea and Eubacteria and possibly the pre-LUCA systems [71]. Iron–sulfur clusters (Fe–S) comprising the active sites of more than hundred enzymes [75] demonstrate a connection to the iron–sulfur chemistry of primordial hydrothermal vents. Fe–S clusters are able to bind a variety of inorganic ligands [76] that modify their redox properties. Low-potential Fe–S clusters and ferredoxins are important for building up a

reducing power for carbon dioxide fixation in photosynthetic proto-reaction centers (see Sect. 13.8 below).

Quinones were shared by different redox enzymes in membranes as quinone pools because of their lipophilic nature, membrane mobility, and ability to bind protons. Menaquinones are considered primordial pre-LUCA quinones [77] because they are shared by a majority of archaeal and eubacterial phyla [52, 78]. Planar cyclic tetrapyrrole molecules have been selected as enzyme cofactors due to their flexible electronic structure and a broad range of redox potential, which is largely influenced by the nature of the ligand to the central metal ion and the chemical nature of the ring substituents [79]. Evolution of cyclic tetrapyrroles is central to understanding the evolution of photosynthesis and is discussed in Sect. 13.6.

Summarizing this section, replenishing reducing conditions at late Hadean–early Archean hydrothermal vents provided thermodynamic disequilibria for versatile organic synthesis based on reduction of abundant carbon dioxide. After compartmentalization and acquisition of self-reproducing catalytic RNAs these self-sustained biochemical processes had evolved into primordial chemolithotrophic cells. Strong UV radiation, increased cosmic rays, and intermittent sterilizing bombardments of the surface of the ocean for almost 700 million years had likely kept the primordial organisms at the bottom of the sea until the end of the Late Heavy Bombardment period (~3.8 Ga, see Fig. 13.1) [3, 80]. The first lineages of chemolithotrophic Archaea and Eubacteria further diversified into organisms with different metabolisms and membrane enzyme's mediated electron transfer from available reduced electron donors (primarily hydrogen and hydrogen sulfide) to a variety of electron acceptors (CO_2, nitrate, sulfate, Fe^{3+}). The fact that chemolithoautotrophy and photolithoautotrophy have similar metabolic consequences but use different sources of energy makes the evolutionary transition from the latter towards anoxygenic photosynthesis simple and evolutionarily beneficial in the environment with depleted sources of electron donors.

13.4 Prebiotic UV-Driven Photochemistry and the Possibility of Origin of Life in Terrestrial Environments

During Hadean and early Archean period the Earth was a water world with scarce continental masses. As the crust was constantly melting it could not withstand formation of mountain ridges; therefore the landscape was largely flat and flooded with occasional protrusions of subaerial volcanoes [43]. Local terrestrial geothermal systems are hypothesized to be a potential site of the origin of life on Earth [81]. Terrestrial hot springs are fed by the hydrothermal fluids and the steam heated by underlying magma. Propagating through the crust the hot fluids and the vapour would be enriched in NH_3, H_2S, CO_2, phosphorous compounds, and transition metals.

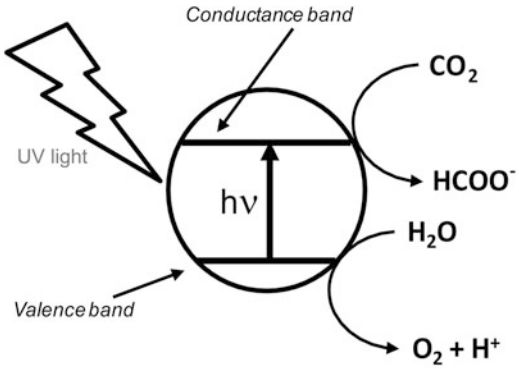

Fig. 13.5 UV-driven photochemistry catalyzed by minerals in Hadean–early Archean terrestrial environments on Earth. Absorption of light by a semiconductor such as TiO_2 or ZnO forms an electron–hole pair, which drives reaction sequences such as reduction of carbon dioxide coupled with oxidation of water. Various products of the reaction include methane, methanol, formaldehyde, or formic acid [83]

The stratified porous siliceous moiety of the terrestrial ponds is suggested to carry diverse prebiotic organic synthesis fueled by the UV radiation. Many oxides and sulfides of the transition metals are semiconductors that absorb light in the UV region. Under excess of carbon dioxide the photochemical reactions likely involved photo-driven reduction of CO_2 on mineral surfaces. Absorption of the quantum of light generates a photoelectron in the conductance band and a hole in the valence band (Fig. 13.5). There is a wealth of experimental data with observation of UV-driven reduction of CO_2 by minerals such as FeO, TiO_2, ZnO, ZnS, and WO [82]. The products of the reduction are varied from simple methane, methanol, formaldehyde, and formic acid [83] to more complex organic acids including intermediates of the biological reverse TCA cycle [84–88]. Thus, the UV-driven photochemical synthesis of diverse organic compounds in the terrestrial environments of the early Earth is plausible.

The primordial geothermal ponds of condensed vapor would contain the products of prebiotic UV-driven inorganic photosynthesis compartmentalized by porous siliceous ZnS- and MnS-containing masses. This system would favor prebiotic synthesis of the first nucleotides, selection of catalytic RNAs, and a transition to the "RNA world" [89]. The primordial ribozymes involved ions that were abundant in the geothermal pond (K^+, Zn^{2+}, Mn^{2+}). Mulkidjanian et al. [81] argue that the discharge from the geothermal springs would have a K^+/Na^+ ratio, which is similar to that in modern cells. The membranes of the hypothetical protocells were probably leaky for small molecules and the primordial K^+/Na^+ ratio would sustain the ionic environment for the protocell's enzymes. Once the protocells obtained the ion-tight membranes they were thought to invade the seawater environments.

According to the hypothesis presented above [81] the first living cells were likely heterotrophic and were living off the organic compounds largely synthesized

by the UV-driven photochemistry. However, the prospects of survival of the terrestrial protocells are compromised by the Late Heavy Bombardment period (4.1–3.8 Ga), a series of intermittent impacts that would sterilize the surface of the Earth [3]. Based on this consideration, even though the conditions for the origin of life had existed earlier in Hadean eon the survival of life at the surface would be questionable.

Prediction of the events that occurred 3–4 billion years ago is inevitably fraught with uncertainty, which always allows for the existence of alternative hypotheses. The hypothesis of the terrestrial origin of life has a direct implication for the origin of photosynthesis. Sam Granick had put forward an idea that the natural photosynthesis evolved from prebiotic pre-porphyrin systems based on the UV-driven photochemistry of the minerals available in the late Hadean–early Archean ocean [90]. These systems could have been replaced by the prebiotic porphyrin-based photosynthetic systems later evolved into the full-fledged light-driven photosynthetic systems supplying electrochemical energy for living cells (see Sect. 13.7.1).

13.5 Primordial Bioreactors of Anoxygenic Photosynthesis

13.5.1 Geological, Isotopic, and Microfossil Record of the Early Autotrophy

It is widely accepted that the first geological signatures that might be attributed to the presence of life correlate with the end of the Late Heavy Bombardment period (4.1–3.8 Ga) [3]. There are a number of pieces of evidence from carbon isotope analysis of the carbonaceous materials in the 3.85–3.8 Ga sediments from Isua Supracrustal Belt in Western Greenland that argue in favor of existence of the autotrophic life [91–93] (see Table 13.1 for carbon isotope fractionation data for extant autotrophs). The rocks older than 3.8 Ga are highly metamorphosed and damaged. Therefore, any evidence of the microfossils and stromatolite structures dated by the time around 3.8 Ga ago should be taken with caution and considered as suggestive evidence [94].

The Archean ocean was largely anoxic based on isotopic analysis of sulfur [95] and the ratio of isotopes of U and Th [96, 97]. Existence of the banded iron formations (BIFs) in the early Archean (3.8–3.5 Ga) also suggests the early microbial life. BIFs are rocks formed by layers of oxidized iron alternating with silicate-containing minerals [95, 98]. Well-preserved laminated structures in BIFs imply that Fe^{2+} ions dissolved in oceanic water had been precipitated and deposited in layers. The oldest structures are dated by 3.8–3.5 Ga [99]. The rates of the UV-driven Fe^{2+} photochemistry were shown to be insignificant as compared to the rates of the biological iron oxidation as evidenced by experiments on simulation of the UV photooxidation of the ferrous ions and the thermodynamic modeling [100]. Thus, in the early Archean ocean the iron minerals were most likely oxidized by ancestors of the marine anoxygenic chemo- or photolithotrophs [100–104].

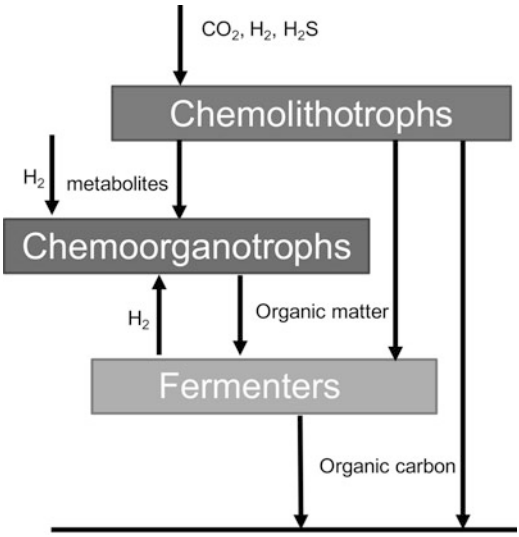

Fig. 13.6 Differentiation of metabolism in pre-photosynthetic Archean microbial communities. Chemolithotrophs autotrophically fixed CO_2 using hydrogen or hydrogen sulfide from the hydrothermal vents. Chemoorganotrophs oxidized hydrogen or metabolites released by other bacteria as a source of electrons for anaerobic respiration. Fermenters live off the oxidation of the bulk organic matter in the community. Similar differentiation likely occurred in the photic zone with the phototrophic communities occupying upper layers of the ocean and in microbial mats in shallow waters and terrestrial environments

Note that the early Archean BIFs should be distinguished from the more pronounced but significantly younger BIFs formed during the Great Oxidation Event (around 2.45 Ga).

The best preserved early Archean rocks have been discovered in several sites in Australia (Pilbara Craton) and South Africa (Barberton) [98, 105]. At the end of the Hadean period (4.0–3.8 Ga), the ocean and the underlying oceanic crust had been predominant while continental crust was local and constituted less than 10 % of modern continents (see above). The preserved ancient continental crust in Pilbara Craton is formed by extrusion of magma and modified by hydrothermal dynamics, volcanic activity, and sedimentation.

Two major habitats, hydrothermal settings and shallow waters, have brought the most interesting findings shedding light on the microbial diversity of the early life [98]. Carbon isotope record of the 3.46 Ga old Pilbara rocks supports ubiquity of the early methane-producing microorganisms, possible ancestors of extant thermophilic and strictly anaerobic methanogenic archaebacteria that couple hydrogen oxidation with carbon dioxide reduction at the hydrothermal vents [106, 107]. Sulfur isotope data from similar environments suggests that microbes with sulfur-based metabolisms existed as early as 3.5 Ga ago, providing evidence for the earliest chemoautotrophic and chemoorganotrophic marine microbial ecosystems (Fig. 13.6) [108–110].

13.5.2 Increased UV Flux as a Constraint for the Evolution of Photosynthesis

Early Archean microbial communities based on hydrothermal settings (Sect. 13.3) had most likely exhausted the sources of reduced electron donors such as hydrogen and hydrogen sulfide due to expansion of microbial community and stratification into different trophic levels (chemolithotrophs, chemoorganotrophs, fermenters) (see Fig. 13.6). Survival of the earliest branches of life was possible upon expansion into new habitats and discovering new opportunities for growth using new sources of energy (light). Apparently, the emergence of the photosynthetic prokaryotes was constrained by the sterilizing UV radiation in the upper photic zone (see Fig. 13.2). This constraint had been overcome by ancestors of the anoxygenic photosynthesizers by 3.5 Ga. Combined isotopic, geological, and microfossil record provides evidence of developed microbial communities in the early shallow water habitats from ~3.5 Ga onward with the presence of anoxygenic photosynthesizing microorganisms dated by ~3.4 Ga [96, 97, 111–114].

Proteins and nucleic acids absorbing the UV light are the primary targets of the UV-induced damage. On the basis of the radiation transfer model [115], the rates of the DNA damage for the microbial cells on the surface of the early Archean ocean are predicted to be three orders of magnitude higher than the present level. However, at the depth of 30 m the DNA damage rates would be comparable to those in modern prokaryotes (see Fig. 13.2b) [35]. The present-day UV-induced DNA damage would correspond to 500-fold reduction of the UV irradiance as compared to the levels of the Archean Earth [116].

13.5.3 Scenario 1: Emergence of Phototrophs in the Ocean Photic Zone

Communities of chemoautotrophic and photoautotrophic microorganisms have similar impacts on the environment; that is, they both autotrophically produce carbon that would have similar microfossil traces. However, they likely occupied different ecological niches and had different productivity [117–119]. Table 13.2 illustrates estimates of the productivity of the early Archean microbial communities based on metabolisms that were dependent on geochemically produced fluxes of hydrogen and availability of sulfides and ferrous ions in the seawater.

If the first photosynthesizers were dependent on hydrogen and hydrogen sulfide available at hydrothermal settings, then it is likely that the early Archean chemolithoautotrophic ancestors of photosynthesizers were picked up by the upward streams of the hydrothermal plumes ending up in the photic zone [120] (Fig. 13.7a). Living off the hydrothermal plumes, these anoxygenic Eubacteria had likely evolved the photosynthetic machinery integrated into well-developed pathways of autotrophic carbon fixation and anaerobic respiration. Harnessing the

Table 13.2 Productivity of early Archean anoxygenic microbial communities based on ecosystem modeling [117–119]

Microbial community	Primary production of carbon, mol $year^{-1}$
Archean H_2-based methanogenesis	3.4×10^{12}
H_2-based anoxygenic photosynthesis	2.9×10^{13}
Sulfur-based anoxygenic photosynthesis	2.3×10^{12}
Fe-based anoxygenic photosynthesis	$1.7–5.0 \times 10^{14}$
Present-day net primary production	$5 \times 10^{15}–9 \times 10^{15}$
Modern terrestrial photosynthesis	4.7×10^{15}
Modern oceanic photosynthesis	4.0×10^{15}

energy of light had boosted the productivity by one order of magnitude as compared to the hydrogen-based chemolithotrophs such as methanogens and sulfate-reducing bacteria [117, 119] (see Table 13.2). In the new habitats, the metabolic costs associated with the DNA repair were compensated by the advantage of photoautotrophy and the acceleration of the adaptive evolution due to increased rate of the UV-induced mutations. Experiments with evolution under the UV selective pressure showed that bacteria are able to acquire the UV tolerance during several hundreds of generations [121]. Thus, the colonization of the upper layers of the photic zone by anoxygenic phototrophs could have happened relatively fast.

The gradual growth of the continental crust, which had started in the late Hadean and has lasted ever since, contributed to formation of shallow water habitats (Fig. 13.7b). Instability of the seafloor imposed by the unfolding tectonic processes had likely restricted a steady supply of strong reductants such as H_2 and H_2S. With an exhaustion of H_2 and H_2S, the new evolutionary pressure had appeared to use new electron donors for CO_2 reduction and first of all abundant iron Fe^{2+}, which is a weaker reductant than H_2 and S^{2-}.

Switch to iron-based photosynthesis could have occurred in the same microbial population. Extant anoxygenic phototrophs demonstrate the ability to use a variety of electron donors under changing conditions. Anoxygenic iron-based photosynthesis freed the bacteria of their dependence on redox disequilibria in geological processes with three orders of magnitude boost in productivity (Table 13.2) [117]. In shallow waters the Fe^{2+} supply was limited due to UV-driven iron oxidation. At the same time, photochemically formed ferric ions were beneficial as a UV screen [122].

Despite the higher doses of the UV radiation, gradual expansion of marine anoxygenic phototrophs to shallow waters and littoral and tidal environments had brought new forms of the UV protection. In the new environments, turbidity currents and increased amounts of particulate matter would effectively screen the UV radiation [123]. Adaptive stratification of the microbial communities of shallow waters into different trophic levels (see Fig. 13.6) had translated into microbial mats with phototrophs occupying upper levels of the community. Particulate matter in

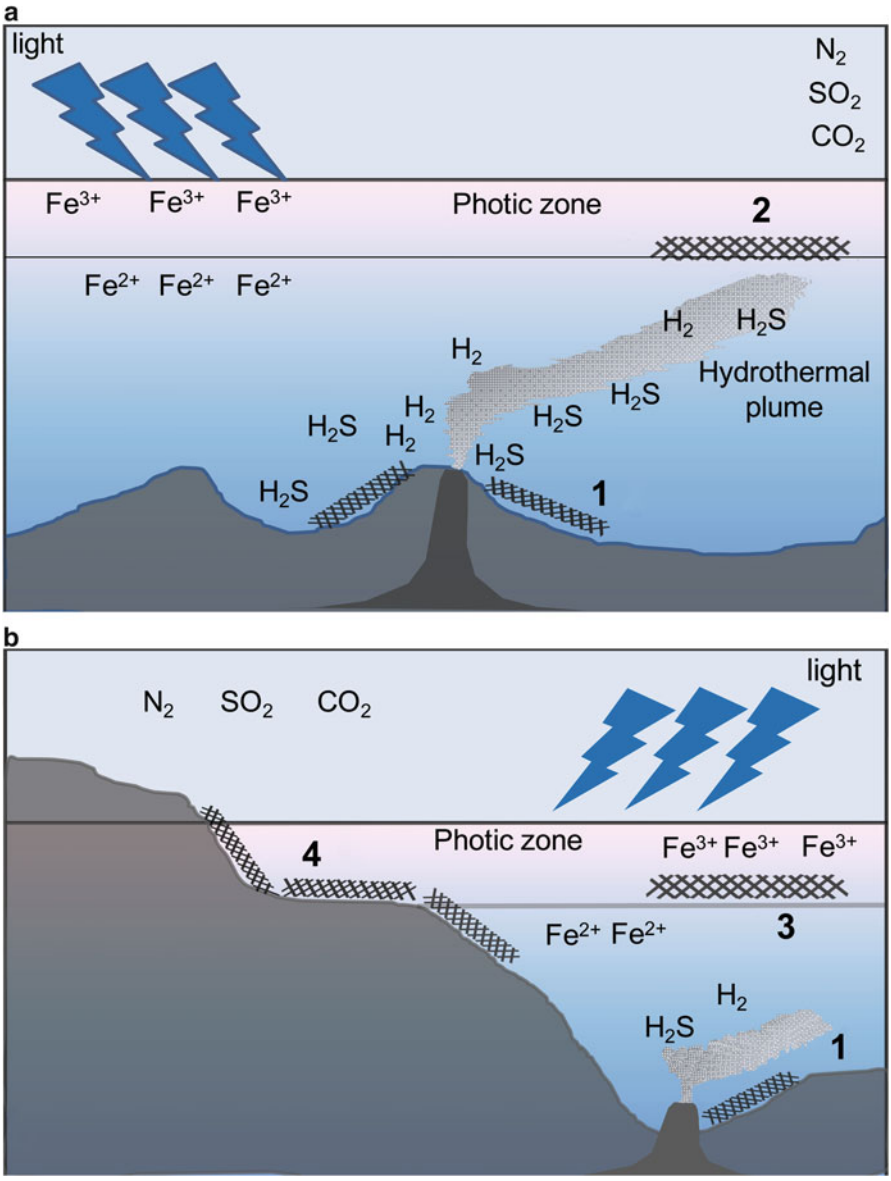

Fig. 13.7 Expansion of the chemolithotrophs to the photic zone in anoxic Archean ocean (**a**) followed by occupation of shallow waters due to growth of the continental crust (**b**). (*1*) Microbial habitats at the seafloor and hydrothermal vents; (*2*) free living anoxygenic photosynthetic autotrophs at the bottom of the photic zone living off the hydrothermal plumes; (*3*) and (*4*) diversification of the anoxygenic phototrophs for free living and mat-forming communities in the shallow waters, respectively

the water above the microbial mat, ferric ions, calcium carbonate, and white sand effectively shielded the microorganisms in the upper layers from the deleterious UV radiation. In addition to the UV screening, the pronounced mineralization of the microbial layers in mats helped in keeping the space between the microbial participants, which is a decisive factor for syntrophic associations [124].

13.5.4 Scenario 2: Emergence of Phototrophs in the Terrestrial Habitats

In contrast to a gradual emergence of the phototrophs in the photic zone (scenario 1 above), the ancestor chemotrophic communities (see Sect. 13.3) could reach the photic zone via geodynamic lifting of the slices of the oceanic crust (the so-called obduction) [125] subjecting the microorganisms to harsh UV radiation and visible light. Alternatively, the heterotrophic ancestors originated in terrestrial geothermal ponds (Sect. 13.4) could be forced to utilize light energy in competition for the organic compounds synthesized in UV-driven mineral catalysis in geothermal ponds. Despite the mechanism of subjecting the ancestors to the light the only surviving strategies for the primordial phototrophs in terrestrial habitats would be hiding from the UV light under the natural mineral screens, which however transmit enough light (visible or near IR) for photosynthesis. Mineral-encrusted lithified layered structure of the microbial mats would meet the requirements of the UV protection and the diversified ecological stratification (Fig. 13.6).

Summarizing, the geological evolution of the early Archean environments had gone through the phase of extreme volcanic or hydrothermal activity and had been succeeded by relatively normal shallow marine conditions with tidal cyclicity, which sustained microbial mats. The evolution of the structure of the microbial mats has likely paralleled the evolution of the photosynthesis as the newer anoxygenic forms were occupying more productive and more dangerous uppermost level in the mats [8, 35, 120, 126, 127]. With widespread appearance of the shallow water and terrestrial habitats new possibilities had opened for the anoxygenic phototrophs in colonizing land, which had resulted in global scale consequences [128].

13.6 Evolution of Metabolic Pathways of Biosynthesis of Chlorophyll and Bacteriochlorophyll

Photosynthetic reaction centers do not function without pigments; therefore, evolution of the (bacterio)chlorophyll (BChl) biosynthesis is principal for understanding the evolution of a workable mechanism of photosynthesis.

13.6.1 Connections Among the Branches of the Tetrapyrrole Biosynthesis Framework

Anoxygenic photoautotrophy had emerged after the split of Eubacteria and Archaea; therefore, the evolution of the (B)Chl biosynthetic pathway is rooted in the ancient tetrapyrrole biosynthetic pathways.

The first steps of the metabolic transformation of the aminolevulinic acid (ALA) up to the formation of uroporphyrinogen III (UroIII) are common for the biosynthesis of all tetrapyrroles (Fig. 13.8a) with UroIII being the last common precursor [129–131]. Methylation of UroIII leads to precorrin-2 branching to a synthesis of Co-containing cobalamins, Ni-containing F430 factors, Fe-containing sirohemes, the heme d_1, and the alternative pathway to the protoheme. Alternatively, oxidative decarboxylation of UroIII launches a series of reactions yielding the protoporphyrin IX, which is a branch point for biosynthesis of the Fe-containing protoheme and the Mg-containing (B)Chls [129].

Which tetrapyrrole pathway is primordial? A variety of tetrapyrroles (cobalamins, sirohemes, F430 factor, and protohemes) is involved in the active sites of the enzymes that catalyze simple and important reactions of primitive metabolism in deeply rooted prokaryotes, both Eubacteria and archaebacteria [131–134]. For example, sirohemes, the simplest Fe-containing derivatives of sirohydrochlorin, are involved in the active centers of anaerobic nitrite and sulfite reductases [134]. The Co-containing tetrapyrroles function in corrinoid iron–sulfur proteins (CoFeSP) that couple the ancient acetyl-CoA (Ljungdahl-Wood) pathway of the autotrophic carbon fixation to the transmembrane translocation of Na^+ in anaerobic acetogens [52] (see Sect. 13.3.2 and Fig. 13.4). The genes coding for the subunits of the sirohydrochlorin Co-chelatase are homologous to the genes coding for the siroheme Fe-chelatase and the protoporphyrin IX Fe-chelatase indicating the common ancestry [131]. Most Archaea and some primitive bacteria lack enzymes catalyzing the conversion of Uro III to the protoporphyrin IX and the protoheme. Instead, they evolved an alternative and probably archaic pathway of the protoheme biosynthesis through the UroIII–precorrin–sirohydrochlorin branch (Fig. 13.8a). Some sulfate-reducing and denitrifying bacteria use siroheme for the biosynthesis of protoheme [132]. Thus, it is likely that this branch is older than the UroIII–protoporphyrin IX branch [134] giving rise to the protohemes and the (B)Chls.

Recent phylogenetic analyses show that all photosynthetic organisms share the enzymes of the core (B)Chl biosynthesis pathway suggesting that a single pathway of the chlorophyll biosynthesis was present in the ancestral photosynthetic bacterium [129, 131, 135]. The most important step in the (B)Chl pathway is insertion of Mg^{2+} into the molecule of protoporphyrin IX catalyzed by a branching enzyme, protoporphyrin IX Mg-chelatase (Fig. 13.8b). How had this enzyme evolved is uncertain although its evolutionary connections with the cobalt-chelatase from the O_2-dependent cobalamin biosynthesis pathway [131, 136] and the Fe-chelatase from the heme biosynthesis [137] are shedding some light on possible solutions of the problem.

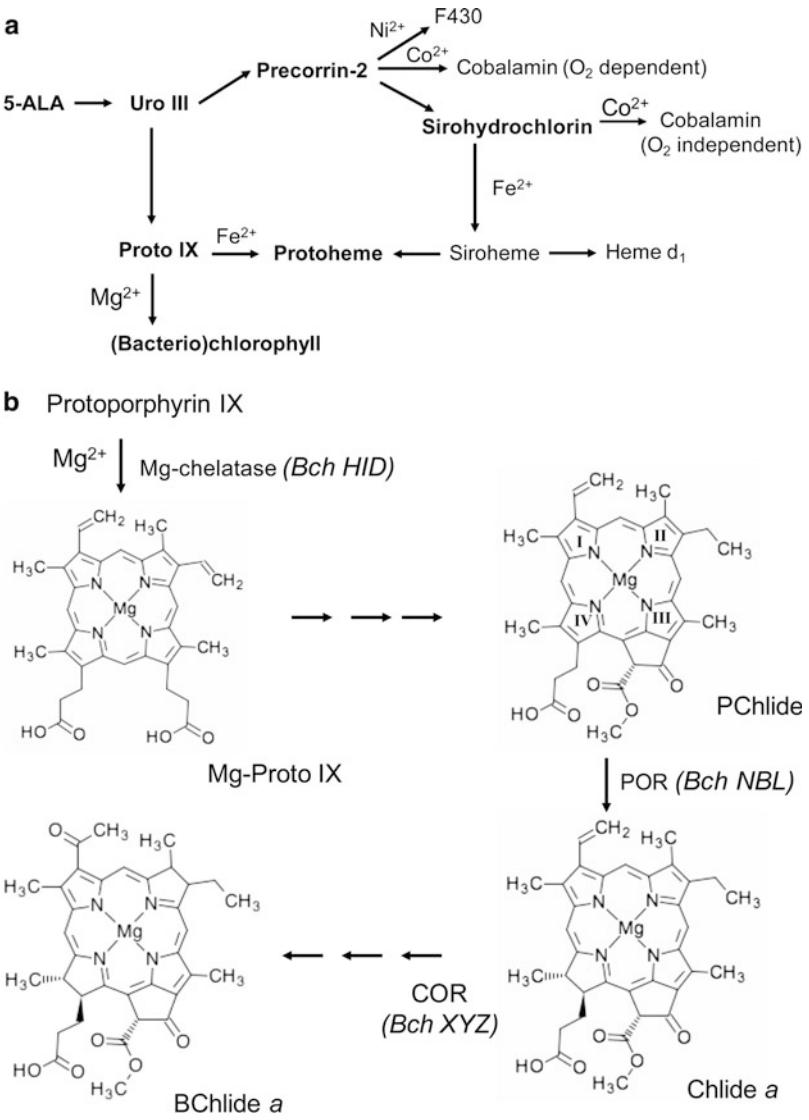

Fig. 13.8 Pathways of biosynthesis of various cyclic tetrapyrroles. (**a**) Ancient pathways of synthesis of common precursor uroporphyrinogen III (uroIII) and branch point intermediates, precorrin-2, sirohydrochlorin, and protoporphyrin IX (proto IX). Based on [129–131]. See text for details. (**b**) Schematic representation of the biosynthesis of Chlide and BChlide based on [129] and [131]. Mg-chelatase inserts Mg^{2+} ion into a molecule of proto IX followed by a series of consecutive tetrapyrrole ring's modifications and reductions yielding Chlide (reduction of C17=C18 double bond in ring IV) and BChlide (subsequent reduction of C7=C8 double bond in ring II). Bch HID, subunits of Mg-chelatase; Pchlide, protochlorophyllide; Bch NBL, subunits of protochlorophyllide reductases (POR); Bch XYZ, subunits of chlorophyllide reductases (COR). See text for details

Mg-chelatase is a multisubunit enzyme coded by three genes, BchH, BchI, and BchD. The enzyme has a sequence and structure similarity with a Co-chelatase from an O_2-dependent pathway of the cobalamin biosynthesis [136] (see Fig. 13.8a). Phylogenetic analyses of the genes indicate that both the Mg-chelatase and the Co-chelatase have evolved from one anaerobic ancestor enzyme. On the other hand, the anaerobic sirohydrochlorin Co-chelatase is homologous to the sirohydrochlorin Fe-chelatase producing siroheme and the protoporphyrin IX Fe-chelatase from the classical heme biosynthesis pathway. It is known that iron chelatases are promiscuous with regard to the central metal ion. They can catalyze insertion of Co^{2+} and Zn^{2+} into protoporphyrin IX. A mutation of the Mg-chelatase from the photosynthetic α-proteobacterium *Rhodobacter sphaeroides* is shown to launch an accumulation of a Zn-containing BChl *a* and its metabolic precursors in a pathway with indication that the Fe-chelatase is functioning using Zn^{2+} instead of Fe^{2+} [137]. As Zn and Mg are interchangeable, it is proposed that the Fe-chelatase had been likely recruited for the Zn-(B)Chl biosynthesis and had participated in the ancestral pathway that functioned prior to the evolution of the Mg-chelatase [137, 138].

Fe-chelatases and Mg-chelatases are unrelated and have different structures but catalyze similar reactions, i.e., insertion of Mg into protoporphyrin IX. It is likely that nature used this evolutionary pattern for selection of the enzymes catalyzing some downstream metabolic transformations of the Mg-protoporphyrin IX (Fig. 13.8b). For example, under anaerobic and aerobic conditions each of the three steps from conversion of the Mg-protoporphyrin IX monomethyl ester to the chlorophyllide is catalyzed by unrelated proteins having different structures but performing the same catalytic function [129]. Apparently, the genes for aerobic catalysis had appeared in the late Archean in response to oxygenation of the atmosphere.

One of the important key enzymes is the anaerobic protochlorophyllide oxidoreductase (POR) that reduces the C17=C18 double bond in the pyrrole ring IV of the protochlorophyllide to form the chlorophyllide (Fig. 13.8b). The enzyme coded by bchLNB shows a striking similarity to the nitrogenase nifHDK complex [139]. Surprisingly, this similarity extends over another enzyme, chlorophyllide oxidoreductase (COR), catalyzing a reduction of the C7=C8 double bond in the pyrrole ring II of Chlide in a key step towards the BChlide biosynthesis (Fig. 13.8b). The similarity with nitrogenases indicates that these enzymes originated from nitrogenase-like enzymes in ancestors that were capable of nitrogen fixation [140].

13.6.2 Chlorophyll vs. Bacteriochlorophyll

All extant anaerobic phototrophs use bacteriochlorophyll. Chemically, the BChl molecule is more reduced than the Chl molecule (see Fig. 13.8b), which is consistent with reducing conditions of the Achaean ocean. Simple logics would conclude that primordial photoautotrophs had used Bchl instead of Chl. However, the first

four common steps of enzymatic transformations of Mg-protoporphyrin IX converge to chlorophyllide *a*, a branch point intermediate giving rise to two distinct pathways of metabolic modifications of chlorophylls and bacteriochlorophylls [129, 131] (see Fig. 13.8b). Granick [90] had postulated that in the biosynthetic pathway each intermediate tetrapyrrole metabolite could have been the end product of the evolution; that is, it was functional; otherwise it could not be selected by evolution. According to Granick hypothesis, the primordial phototrophs had likely utilized Chl since Chlide is a metabolic precursor of BChlide (Fig. 13.8). Based on that, the BChl-containing species would have appeared later in evolution. It should be noted though that the key enzymes that reduce ring IV in the chlorophyllide precursor and ring II in the bacteriochlorophyllide precursor are related to nitrogenases, which are enzymes of broad selectivity with the ability to catalyze a reduction of a range of compounds with double and triple bonds [139]. It is hypothesized that the ancestral nitrogenase-like reductases involved in the BChl biosynthesis were nonspecific and were able to reduce both rings in one molecule, thus producing BChl-like molecule in one step [141]. It is also reasonable that the presence of these inefficient enzymes could explain having both Chls and BChls in the photosynthetic ancestors [142]. Some modern BChl-containing anoxygenic phototrophs (i.e., heliobacteria, phototrophic *Acidobacteria* and *Chlorobi*) have Chl *a*-related pigment as a redox-active electron acceptor in the reaction center. This might be a remnant of the primordial reaction center (see Sect. 13.8).

Overall, it is likely that nature utilized various mechanisms of metabolic pathway's evolution such as evolution of new metabolic steps that followed the Granick mechanism or recruitment of the preexisting metabolic building blocks into the assembly of the ancestral (B)Chl biosynthetic pathway.

13.7 Searching for Workable Mechanism of Emergence of Photosynthesis

Photosynthesis is a complex process requiring functioning of the transmembrane machinery of the charge separation and stabilization and developed metabolism of carbon fixation. Even the most primitive photosynthetic bacteria existing today possess quite a complex photosynthetic apparatus, which acquisition would definitely require time to evolve. This highlights the evolutionary possibility that some elements of the photosynthetic machinery were adapted from preexisting organisms. It very well may be that the chemo- and photoautotrophy had coevolved in pre-LUCA communities; however, only deep-branching lineages of hyper- and thermophilic chemolithoautotrophs at the deep-sea hydrothermal vents seem to survive and gave rise to a diversity of archaeal, eubacterial, and eukaryotic lineages (Fig. 13.4). Note, however, that the hypothesis presented in Sect. 13.4 puts the origin of photosynthesis significantly closer to the origin of life. This uncertainty makes the hypotheses of the origin of photosynthesis presented

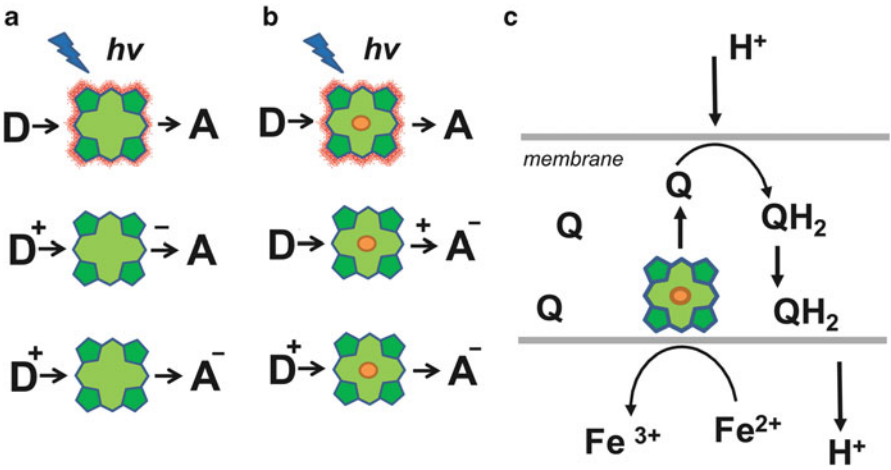

Fig. 13.9 Photochemical reactions of cyclic tetrapyrroles in solutions. (**a**) Photoexcitation of the free base porphyrin is followed by a reduction by the exogenous donor (D) and a subsequent electron transfer to the primary acceptor (A). (**b**) Photoexcited metal-containing porphyrins (for example, Mg- or Zn-binding BChls) obtain reducing power and transfer electron to the acceptor A followed by rereduction of the pigment by the donor. (**c**) Primitive membrane reaction center with Chls photosensitizing electron transfer from a donor (Fe^{2+} ions) to a quinone molecule (Q), which after double reduction and protonation (QH_2) shuttles across the membrane releasing protons and diffusing back to the other side of the membrane

in this section rather speculative. The experimental testing of the hypotheses requires development of new approaches such as directed protein evolution, which belongs to a promising field of synthetic biology.

13.7.1 Hypotheses of Abiotic Emergence of Photosynthesis

Possibility of spontaneous abiotic synthesis of a variety of the porphyrins from acyclic compounds [143, 144] suggests that they were probably involved in solution photochemistry in Hadean–early Archean ocean.

Proto-photosynthetic systems are thought to be sensitized by the porphyrins having photocatalytic properties similar to those in the inorganic photosynthetic systems [90, 145] (see Sect. 13.4). The tetrapyrrole macrocycle can be easily and reversibly oxidized or reduced by a series of inorganic and organic electron donors (D) and acceptors (A) (Fig. 13.9). Free-base precursors of chlorophyll, uroporphyrins, and protoporphyrins absorb visible light in the blue-green region of the spectrum (400–500 nm). Under excitation the pigments are being photoreduced by nearby inorganic electron donors (such as Fe^{2+}) and subsequently oxidized by available electron acceptors [79] (see Fig. 13.9a).

Metallated porphyrins are more evolutionarily advantageous as they obtain strong photoreducing properties under the excitation, and sustain numerous modifications of the tetrapyrrole ring resulting in broadening of the region of absorption in the range from near UV to near IR [79] (Fig. 13.9b). The reactions in solutions were inefficient and limited by diffusion of the substrates and thus occurred through long-lived triplet excited states. The nature of the central metal ion is critical for the yield of the photochemical reaction. If porphyrins had chelated transition metal ions with empty d-orbitals (Fe^{2+}, Co^{2+}, Ni^{2+}, etc.) then the lifetime of the excited state would be very short (picoseconds) due to self-quenching [79, 146]. On the opposite, insertion of Mg^{2+} or Zn^{2+} into the porphyrin molecule would lengthen the excited-state lifetime to nanoseconds due to singlet-triplet intersystem crossing. Compartmentalization of the tetrapyrroles in network of the natural inorganic microcompartments or in the lipid vesicles likely increased the specificity of the reactions [147, 148] (Fig. 13.9c).

In lipid membranes the porphyrins had likely sensitized a simple light-driven electron transfer from Fe^{2+} to quinones, which after double reduction and protonation probably shuttled across the membrane releasing protons and diffusing back to the other side of the membrane (Fig. 13.9c) [142]. Porphyrins are prone to aggregation and self-quenching of the excitation. Under selective pressure this would require binding of the pigments to the protein at some point of the prebiotic evolution [149] (see Sect. 13.8). Overall, the hypotheses of the prebiotic emergence of photosynthesis [79] postulate that abiotically available porphyrins and their derivatives were assembled into the first protophotosynthetic systems, compartmentalized, and integrated into the first living cells [150]. It is unknown whether binding to the protein happened in the pre-LUCA communities (see Sect. 13.4 above) or the protophotosynthetic systems were captured by the primitive protocells.

13.7.2 Proto-Reaction Centers as Ancient UV-Protective Proteins

One of the hypotheses of the origin of photosynthesis postulates the UV protection proteins as progenitors of the photosynthetic proto-RC [142, 150, 151]. Origin of the protein is uncertain. It could emerge de novo by multiple duplication events from simpler pigment-binding membrane proteins [152]. Alternatively, it can be recruited from a pool of porphyrin-binding proteins (see below). In the Archean time, the absorption of the strong UV fluxes by the protein was apparently damaging; however, weaker fluxes attenuated by seawater (Fig. 13.2b) or by minerals could promote the excitation of the aromatic amino acids, which are naturally present in the membrane proteins. If the proteins contained chromophores such as ancient metal-porphyrins then an overlap of broad absorption bands of the chromophores with the emission spectra of the excited aromatic amino acids would

ensure Förster resonance excitation energy transfer from amino acids to the porphyrins. Due to the electronic structure of Fe-, Co-, and Ni-containing porphyrins their excited state lives only for picoseconds and would dissipate very fast [146], thus protecting the protein from damage.

Further selection for Zn- or Mg-binding tetrapyrroles would be beneficial as in these molecules the excitation lives for nanoseconds allowing for transfer of the excitation towards natural excitation traps. Accidental binding of the exogenous iron–sulfur clusters or quinones from the shared membrane pools could induce charge separation between the excited porphyrins and the quinones or Fe–S centers followed by dissipative charge recombination [150]. The excitation also could be transferred to neighbors in the primitive photoprotective light-harvesting antennas. With increased number of pigments some excitation traps could form due to close location of the pigments in the protoantenna further enhancing the dissipative function of the antenna [153].

It is possible that a gene coding for the hypothetical porphyrin-binding protein would duplicate and give rise to a gene coding for the protein with a new function. The bacteria bearing this gene could survive only if the dissipator protects an important membrane process such as light-driven generation of reducing power. The function of transmembrane electron transfer could be picked up by the evolution through selection of the cofactor-binding sites that could result in changed efficiency of the charge separation in the reaction center [154] (see Sect. 13.8).

13.7.3 Hypothetical Origin of Reaction Centers from Infrared Thermotaxis Systems

At the deep-sea hydrothermal systems, the chemolithotrophic organisms living off the reducing fluids are able to thrive in millimeter layer of comfortable temperature balancing in the thermal gradient between the hot vent and the ocean water. The openings of the hydrothermal vents at the seafloor were shown to emanate the black body radiation (the so-called geothermal light) in a spectral range from 650 to 1,050 nm [155]. This light was enough to support strictly anaerobic and photolithotrophic life of the deep-sea green sulfur bacteria [156], which are known for living in extremely low-light habitats by developing gigantic light-harvesting antennas (chlorosomes) supplying energy for the photosynthetic reaction centers and autotrophic carbon fixation through primitive rTCA cycle. Sensing of the infrared light by primordial chemolithotrophs could have been a significant evolutionary trait in the early Archean. BChl molecules in anoxygenic phototrophs absorb light in the near IR (730–1,100 nm) via a Q_y transition absorption band. Nisbet et al. [157] hypothesized that primordial systems of the infrared light sensing by Bchl-like molecules could have been converted into the ancient photosynthetic systems and helped the chemolithotrophic bacteria to survive. The finding of the

green sulfur bacteria living off the geothermal light [156] should be considered as suggestive evidence as the adaptation of the green sulfur bacteria to low light and deep sea might have been acquired later in evolution.

13.7.4 Hypothetical Recruitment of Existing Membrane-Bound Oxidoreductase for the Role of Photosystem

According to this scenario the proto-RCs have been possibly built based on available membrane oxidoreductases in the anaerobic chemiosmotic electron transfer chains in ancestors of the first photosynthetic Eubacteria. Under selective pressure the genes coding for the recruited protein could have been duplicated and evolved into genes coding for the protein with a new function, a stable light-induced generation of reducing power for the metabolism [52].

Recruitment of the protein folds is widespread in evolution [138, 158]. This process is based on a broad substrate specificity of the primordial enzymes and a conservation of the protein folds. The transmembrane helix bundle is a structural motif of all transmembrane oxidoreductases [159]. Stronger packing of transmembrane helices in lipid bilayers cooperatively works towards the orientation of helix's axes along the normal to the membrane, which constrains the binding of planar chromophores such as porphyrins or Chls to the protein [160, 161]. As a result, the two proteins can almost be structurally superimposed even with a low percentage of sequence identity. Photosynthetic RCs are light-driven oxidoreductases. As such, the RCs resemble many other membrane oxidoreductases, for example, cytochrome bc_1 and b_6f complexes and NADH dehydrogenase. Some of these proteins seem to have common ancestry in Eubacteria and Archaea [71]. One of the hypotheses [162] proposes an evolutionary link between the cytochrome *b* and the reaction center polypeptides, thus exploring the possibility that the photosynthetic RCs had originated from ancient cytochrome oxidoreductases with broad substrate specificity.

13.8 Driving Forces for the Evolution of the Photosynthetic Reaction Center

The prebiotic proto-RCs may have been monomeric [142, 151], assembled in the Hadean pre-LUCA communities and integrated later as a dimer protein into the heterotrophic protocells originated in the hatcheries of the geothermal ponds (see Sect. 13.4 and Sects. 13.5.4 and 13.7.1). Alternatively, the chemotrophic ancestors originated at the deep-sea hydrothermal vents (Sect. 13.3) could have

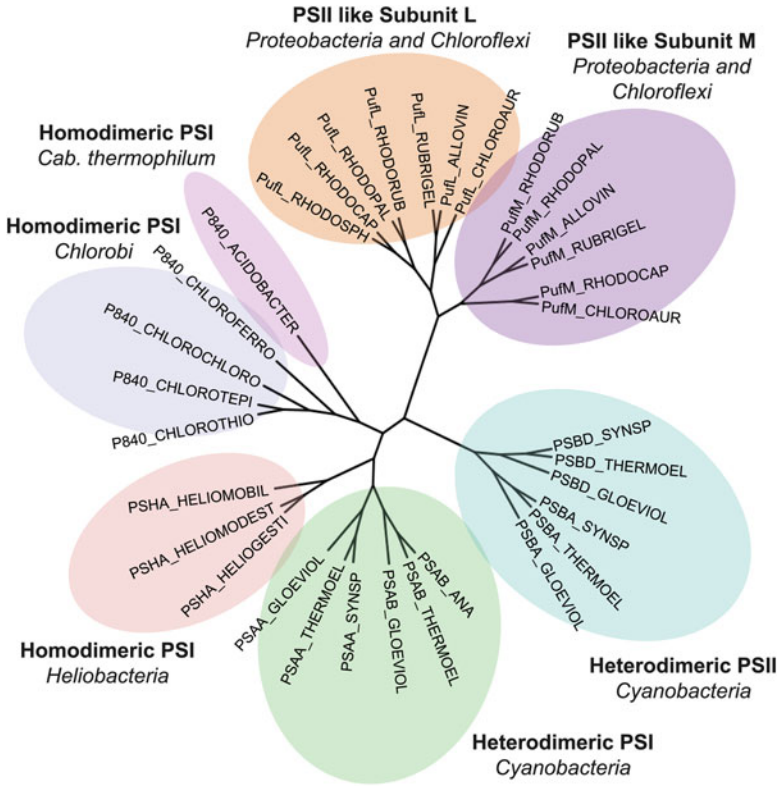

Fig. 13.10 Phylogenetic tree based on multiple sequence alignment of photosynthetic reaction center subunits in extant photosynthetic organisms. Note a significant heterogeneity between the L and M subunits of the reaction center from purple bacteria and *Chloroflexus*. The tree is generated using Archaeopteryx

recruited some proteins assembled as homodimers for the light-driven generation of reducing power (Sect. 13.7.4) after encountering light in the ocean's photic zone (Sect. 13.5.3).

Primitive homodimeric layout of the RC is found in the extant photosynthetic bacteria from three out of six phyla, i.e., in green-sulfur bacteria (*Bacteroidetes/Chlorobi*) [63, 64], *Heliobacteria* (*Firmicutes*) [163] and the only known photosynthesizer from *Acidobacteria* [164, 165] (Fig. 13.10). Despite the uncertain mechanisms of the emergence of the photosynthesis there is a consensus that all photosynthetic RCs, both PSI (Fe–S type) and PSII (Q type) have a common origin. This is supported by similarities in amino acid sequences, protein folds, pigments, and the cofactors of the electron transfer and common fundamental mechanisms of light-induced transmembrane electron transfer and charge stabilization [166–173] (Figs. 13.10 and 13.11).

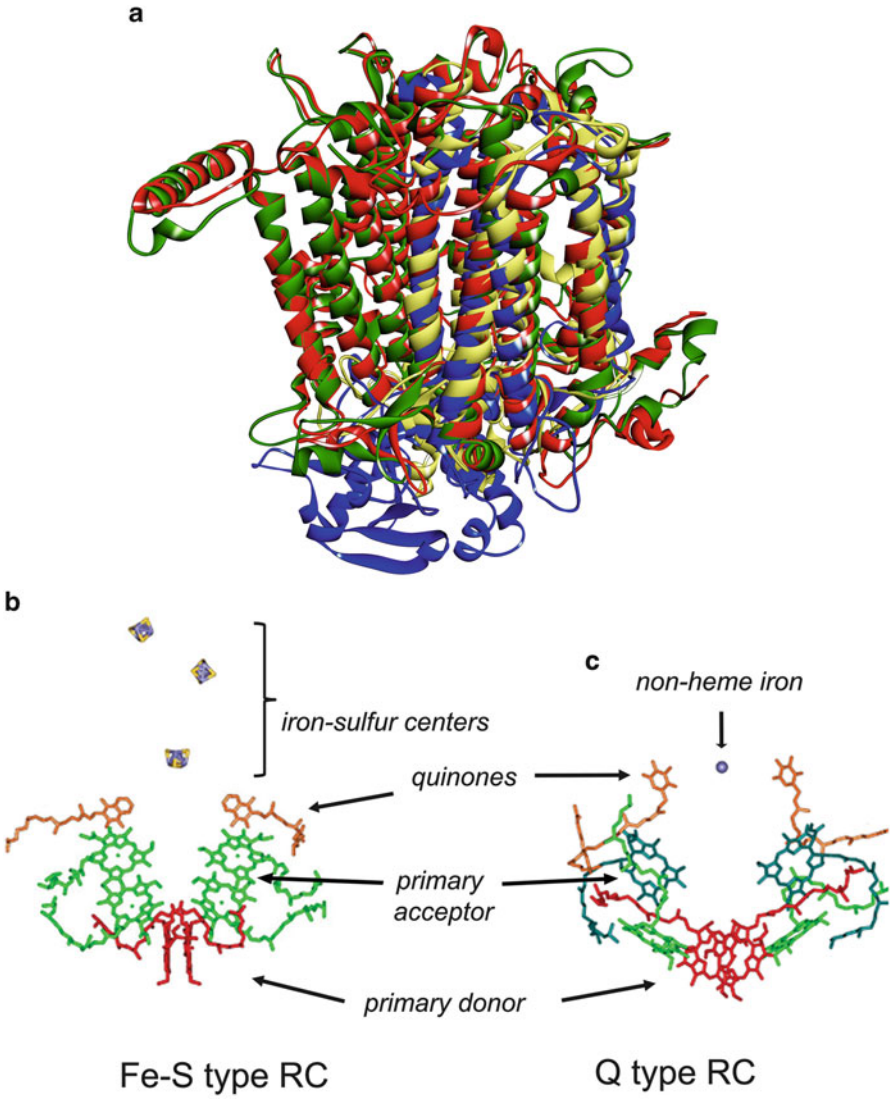

Fig. 13.11 Similar protein folds and layouts of cofactors of electron transfer in reaction centers of extant photosynthetic organisms. (**a**) Overlap of 3D protein structures of the PSI RC proteins from cyanobacteria, PsaA (*red*), PsaB (*green*) (pdb code 1JBO), and the PSII RC proteins from cyanobacteria, PsbA (*yellow*), and PsbD (*blue*) (pdb code 1S5L). (**b** and **c**) Layouts of two branches of electron cofactors in the Fe–S-type RC (**b**) and Q-type RC (**c**). Electron transfer chains start with the dimeric primary donor and are mediated by accessory chlorophylls, primary acceptors (chlorophylls (**b**) and pheophytins (**c**), respectively) and quinones (secondary acceptors). In the Fe–S-type RC (PSI), two electron transfer chains converge to iron–sulfur clusters. In the Q-type RC (PSII) only one chain is functional due to differentiation of the quinone functions. See text for details

13.8.1 Evolutionary Significance of the C2 Symmetry in Proto-Homodimeric RC

Homodimeric protein assembly is energetically advantageous, less metabolically costly, and more protected from degradation due to a reduced surface area [174]. It is likely that the C2 symmetry in arrangements of the subunits and the cofactors of the electron transfer in the photosynthetic reaction centers is an evolutionary imprint of the progenitor homodimeric RC with two identical subunits.

A principal molecule of any RC and the proto-RC in particular is the primary electron donor, which upon photoexcitation launches a transmembrane electron transfer. Dimeric arrangement of the primary donor is likely a consequence of the protein dimerization (Fig. 13.11, parts *b* and *c*). Each of the redox-active pigments in the dimer is bound to the protein and fixed on the interface between the two monomers. The protein plays a crucial role keeping the distance between the Chls in the dimer; otherwise, the excitation could be quenched as happens in Chl dimers in solution [175]. The interface between the two subunits of the proto-RC (Fig. 13.12, part *a*) had likely provided a scaffold for binding of the cofactors of the transmembrane electron transfer. Physical dimensions of the tetrapyrrole rings, the natural thickness of the membrane, and the transmembrane orientation of the protein helices had likely determined the alignment of the cofactors.

Primitive light-driven oxidoreductases were inefficient due to non-optimal distances and orientation of cofactors of the electron transfer and loosely bound secondary electron donors and acceptors (menaquinones and Fe–S clusters) (Fig. 13.12, part *a*). Under reducing conditions the Fe–S complexes and the quinones could be easily over-reduced. In this case, the doubly reduced and protonated quinones might have shuttled to the other side of the membrane where they were shared by other anaerobic oxidoreductases.

13.8.2 Driving Forces for Evolution of Homodimeric Fe–S-Type RC

The instability of charge separation had inferred a driving force towards optimization of the transmembrane electron transfer reactions and stabilization of the charge separation through binding of the secondary electron acceptors and donors (Fig. 13.12, part *b*).

Fixing the Fe–S complex as a stable terminal acceptor had several consequences for the evolution of the homodimeric PSI. Its stability was advantageous for producing more reducing equivalents for a variety of metabolic processes such as reductive TCA, sulfur assimilation, amino acid and nucleotide metabolism, and nitrogen fixation [176, 177]. Coupling to different metabolic pathways was likely mediated by a group of small and diverse ferredoxin-like Fe–S proteins including loosely bound tertiary electron acceptors, analogs of F_A and F_B in the extant PSI

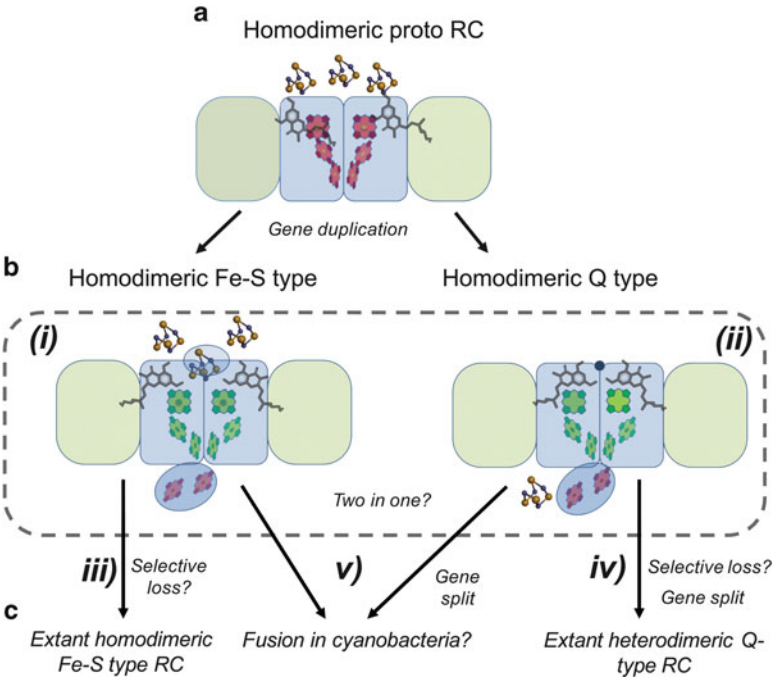

Fig. 13.12 Scheme of evolutionary development of the photosynthetic reaction centers: (**a**) Homodimeric proto-photosystem consisting of two identical monomers having RC part (*blue*) and antenna part (*green*). RC cofactors are ancestral chlorophylls, quinones (menaquinones), and Fe–S acceptors. (**b**) *i*) Homodimeric Fe–S-type RC with stabilized charge separation and bound terminal acceptors (Fe–S clusters) and secondary donors (heme-containing proteins). (*ii*) Homodimeric Q-type RC with differentially bound quinones (Q_A and Q_B), none-heme iron, and bound secondary donors (cytochromes and high-potential Fe–S centers). (**c**) Ancient homodimeric RC gave rise to extant homodimeric PSI (*iii*), extant heterodimeric RCs in photosynthetic proteobacteria and *Chloroflexi* (*iv*), and heterodimeric PSI and PSII in extant cyanobacteria (*v*). See text for details

homodimer-containing organisms. Stable binding of the terminal electron acceptor, Fe–S cluster, in the interface between two subunits on the acceptor side had confined PSI to one-electron redox chemistry in two symmetric branches of electron transfer that converge on terminal electron acceptor (Fig. 13.12, part *b*(*i*)). In cyanobacteria, the heterodimeric PSI is equipped with protein subunits on the acceptor side of the membrane that fix the position of the quaternary acceptors (F_A and F_B) and further stabilize charge separation. In the homodimeric PSI from *Heliobacteria* and photosynthesizing *Acidobacteria*, these proteins are likely not developed [178].

Stronger binding of two quinones that mediated transfer of one electron from photoreduced BChls to the Fe–S center was likely the next step in the stabilization of the charge separation in the PSI. The selective pressure was imposed on the protein to change the redox potential of the quinones bound to the symmetry-related

sites of the homodimer in such a way that the reduction of the terminal iron–sulfur center is fast enough to avoid the double reduction of the quinones, which would block the RC. Ancestors with this type of the RC gave rise to extant anoxygenic phototrophs with the homodimeric PSI (Fig. 13.12, part *c*(*iii*)).

13.8.3 Driving Forces for Evolution of Homodimeric Q-Type RC

Driving forces and consequences of the evolution of type 2 reaction centers were different. The changes might have been triggered by depletion of the reducing electron donors in the photic zone (Fig. 13.7, part *a*) followed by occupation of new ecological niches such as shallow water habitats (Fig. 13.7, part *b*) with weaker electron donors such as Fe^{2+}.

Within the RC the changes included a modification of the primary electron acceptor (pheophytinization of the primary acceptor) and the redox tuning of two quinone acceptors (Fig. 13.12, part *b*(*ii*)). Situation with two loosely bound quinones or two tightly bound quinones was not evolutionarily beneficial for the homodimeric Q-type RC as it affected the efficiency of the charge separation in the reaction center. In these RCs each quinone in the symmetry-related branches might end up in reduced semiquinol state followed by blocking of the electron transfer in both chains and destabilization of the RC due to electrostatic repulsion [179]. Nature found a solution to this problem by (1) differential binding of two quinones and (2) muting the redox properties of the iron on the acceptor side.

The differential binding of two quinones was likely achieved by random mutations of the quinone-binding sites [154] that caused a stronger affinity for the first quinone (analogous to Q_A), the change of its redox potential to ensure one electron reduction by the pheophytinized primary acceptor followed by a double reduction of the second quinone coupled with the proton transport (Fig. 13.12, part *b*(*ii*)). Thus, the double reduction and the double protonation of the second quinone (Q_B analog) had switched the electron transfer from bidirectional to unidirectional electron transfer mode [180]. Another adaptive change was muting the redox properties of the iron on the acceptor side. A double protonation of the loosely bound quinone in the homodimeric Q-type RC allowed shuttling of QH_2 to the other side of the membrane, thus achieving a twofold evolutionary benefit by preventing charge recombination in the RC and building the ΔpH gradient for the ATP synthesis.

A broader range of minerals became available through weathering of the crust in the tidal zones. Extant anoxygenic phototrophs demonstrate the use of a range of electron donors such as iron [102], manganese [181], As (III) [182], and nitrite NO_2^- [183]. Adaptations to weaker electron donors probably included recruitment of the proteins from the anaerobic respiration pathways in the ancestor membranes (mostly heme-containing cytochromes or high-potential Fe–S proteins) to adjust to

reducing potentials of new sources of electrons. The RCs in extant phototrophs from *Proteobacteria* and *Chloroflexi* lack the antenna part; therefore they likely emerged from the ancestors with the homodimeric Q-type RC via gene splitting (Fig. 13.12, part *c*(*iv*)).

The so-called fusion hypothesis [151, 169] proposes that two different types of the RCs had evolved through gene duplication of the proto-RC (Fig. 13.12, part *b*(*i*) and (*ii*)). According to this, cyanobacteria obtained two types of the RCs by LGT from ancient *Heliobacteria* (PSI type) and *Chloroflexi* (PSII type) (Fig. 13.12, part *c*(*v*)). Alternative models propose that the ancestor would have sustained possessing two reaction centers in one organism [152, 184] (Fig. 13.12 part *b*, dashed outline). The ancestors named protocyanobacteria gave rise to modern cyanobacteria and diverse lineages of anoxygenic phototrophs through differential loss of photosystems and gene splits (Fig. 13.12 part *c*) (see also Chap. 14).

In summary, the evolution of an ancestral homodimeric proto-RC and its divergence to a homodimeric PSI (Fe–S type), which functions in extant anoxygenic *Chlorobi*, *Heliobacteria*, and *Acidobacteria*, and the hypothetical homodimeric PSII (Q type) were driven by availability of the electron donors in a series of ecological successions from the oceanic photic zone to the shallow water habitats. This process had eventually resulted in the advent of real independence of the photosynthetic organisms from the geochemical conditions in cyanobacterial lineages that were able to oxidize water. The major designs of type 1 and type 2 reaction centers had been evolutionarily settled in photosynthetic lineages of six eubacterial phyla by the time of the Great Oxidation Event around 2.3–2.5 billion years ago.

13.9 Origin of Anoxygenic Photosynthesis: Support from Molecular Phylogeny and the Whole-Genome Analysis

The photosynthesizing prokaryotes are found only among Eubacteria suggesting that the photoautotrophy emerged after the split of the Eubacteria and the Archaea. Despite the evolutionary benefits, photosynthesis is limited to 6 out of 32 described taxa. Given the fact that we know merely 5 % of the microbial diversity in the ocean, one might expect that new photosynthetic taxa will be discovered. On the other hand, this patchy distribution is surprising and should have an evolutionary explanation, especially compared to a stunning microbial and phylogenetic diversity of chemolithoautotrophs living off the redox disequilibria at the ocean floor and beneath the oceanic crust [38, 67, 185].

Comparison of the phototrophs using single photosynthetic gene phylogenies shows no coherent relationships among the different photosynthetic bacteria and supports separate evolutionary histories of pigment-synthesizing enzymes, photosystems, light-harvesting complexes, and carbon metabolic pathways [151, 186, 187].

This clearly indicates that genes coding for the core proteins of the photosynthetic machinery may have been transferred through the mechanisms of lateral gene transfer (LGT) facilitated by gene transfer agents and viruses [172, 187–189].

Phylogeny inconsistencies imposed by the LGT do not contradict the monophyletic origin of life [190, 191]. This implies that at some point the distribution of the photosynthetic genes and some other critical genes in the genome had occurred through vertical inheritance, from ancestors to descendants. The question is how to detect the evolutionary signal (vertical inheritance) accounting for the processes that destroy the signal (LGT, different rates of evolution or artifacts of the phylogenetic tree building).

Recently published genome-wide analyses of the phylogenetic trees of Eubacteria based on concatenation of numerous gene families have a very-well-resolved split of the tree into two branching superclades preceded by deep-rooted lineages, which are supposedly hyperthermophiles [192–200]. Raymond et al. [201] have performed the whole-genome comparisons of species from five different photosynthetic taxa by maximum likelihood mapping and observed a consistent separate clustering of *Proteobacteria* and *Chlorobi* on the one hand and the *Heliobacteria*, *Chloroflexi*, and *Cyanobacteria* on the other hand, which is consistent with the observed split in the phylogenetic trees (see Figs. 13.4 and 13.13a, b).

Interpretations of the trees available in literature are based on two competing hypotheses, which are supported by two different topologies of the trees. The first topology (Figs. 13.4 and 13.13a) [192–196] supports deep branching of hyperthermophilic *Aquificae* and *Thermotogae* followed by a split of ancestrally marine and first emerging Eubacteria named *Hydrobacteria by* Battistuzzi et al. [193] and emerging later superclade of Eubacteria called *Terrabacteria*. *Hydrobacteria* include among others photosynthetic representatives of *Chlorobi*, *Acidobacteria*, and *Proteobacteria*, while *Terrabacteria* include among others photosynthesizing *Heliobacteria* (*Firmicutes*), *Chloroflexi*, and *Cyanobacteria*. The second topology (see Fig. 13.13b) supports deep-branching extremophiles of *Deinococcus-Thermus* group and hyperthermophilic *Thermotogae* followed by a split into similar superclades but with the opposite time of emergence [197, 200].

13.9.1 Phylogenies Favoring Deep-Sea Origin of Life

The first topology (Fig. 13.13a) would favor the hypothesis of the deep-sea origin of life at the hydrothermal vents (Sect. 13.5.3). Using molecular clock method Battistuzzi and Hedges [194, 195] mapped the evolutionary changes onto a geological timeline based on the evidence from the isotopic analysis, microfossil record, and biomarkers. According to this timeline, the divergence of deep-sea hyperthermophilic classes *Aquificae* and *Thermotogae* had possibly occurred 4.19 billion years ago, and the split of *Hydrobacteria* and *Terrabacteria* had occurred around 3.13 billion years ago with a credibility interval of 3.6–2.8 Ga. Note that the evidence of diverse anoxygenic photosynthetic communities in shallow water

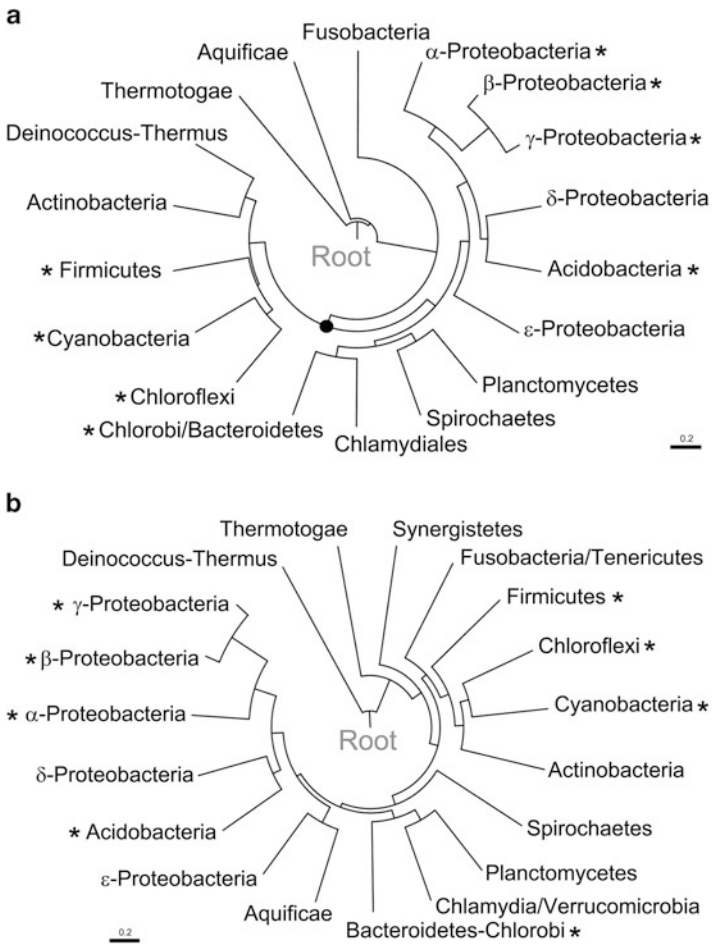

Fig. 13.13 Two major topologies of the phylogenetic trees of Eubacteria based on concatenation of numerous gene families support competing hypotheses of the evolution of Eubacteria with implications on evolution of bacterial photosynthesis. (**a**) Phylogeny from Battistuzzi et al. [195] indicates the early split of *Hydrobacteria* and *Terrabacteria* preceded by deep-rooted hyperthermophilic lineages. *Dot* at the split indicates hypothetical phototrophic ancestor. (**b**) Phylogeny from Wu et al. [200] indicates deep-rooted lineages such as *Deinococcus-Thermus* and *Thermotogae* followed by a split between two superclades with earlier emergence of *Firmicutes*. Lineages with photosynthetic representatives are labeled by *asterisks*. See text for detail. The trees are built in Archaeopteryx using data from [195] (**a**) and [200] (**b**)

habitats is dated by 3.4–3.3 Ga [96, 97] (see Sect. 13.5.3). The common ancestor of *Hydrobacteria* and *Terrabacteria* was proposed to be photosynthetic (shown as black dot in Fig. 13.13a) [193] in agreement with earlier ideas [119, 193, 202–204]. This ancestor could have emerged from the chemoautotrophic predecessors that encountered light energy in the ocean photic zone (Sect. 13.5.3).

Following this scenario the common photosynthetic ancestor had likely possessed the primitive inefficient RC with broad specificity for cofactors (see Sect. 13.8.1 and Fig. 13.12, part *a*) and the primitive (B)Chl biosynthetic pathway (see Sect. 13.6). At depths of 30–60 m (see Fig. 13.2b and Sect. 13.5.2) the ancestor would encounter light in the 350–600 nm spectral region, which would be consistent with functioning of Chl derivatives on initial steps of the pathway (Fig. 13.8b) provided that the Granick mechanism governs the (B)Chl pathway evolution (Sect. 13.6.2). If massive recruitment of the enzymes from the ancient tetrapyrrole biosynthetic pathways had occurred, the pigment composition might have been different.

Diversification of *Hydrobacteria* could have been launched by occupation of shallow and deep waters with varying composition of the electron donors for photosynthesis (Sect. 13.5.3). The descendants could have possessed homodimeric Fe–S-type RC (Fig. 13.12, part *b* (*i*)) or homodimeric Q-type RC (Fig. 13.12, part *b* (*ii*)) depending on the environmental conditions. The evolutionary diversification of *Terrabacteria* is attributed to the colonization of land by ancestors of *Firmicutes*, *Actinobacteria*, *Chloroflexi*, and *Cyanobacteria*. Many of these bacteria are able to produce spores that withstand extreme conditions, most notable of which is drying out [205]. These groups are shown to have increased susceptibility to LGT [192]. In *Firmicutes*, a significant interphylum LGT [192, 206] may explain that *Heliobacteria* obtained the homodimeric Fe–S-type RC from hydrobacterial descendants (e.g., *Chlorobi*). In a similar way, proteobacterial lineages possessing a substantial genomic flexibility in marine microbial populations due to the LGT [192, 207] could have donated the Q-type RC to *Chloroflexi* [208].

13.9.2 Phylogenies Supporting Terrestrial Origin of Life

The second topology (see Fig. 13.13b) supports the deep-branching extremophiles of *Deinococcus-Thermus* group and hyperthermophilic *Thermotogae* and location of the superclade that gave rise to *Firmicutes*, *Actinobacteria*, *Chloroflexi*, and cyanobacteria lineages at the base of the eubacterial tree [197, 198, 200]. This topology would favor the terrestrial origin of life as the deep-branching lineages include heterotrophic non-photosynthetic bacteria (see Sect. 13.4). A group of *Deinococcus-Thermus* demonstrates extreme tolerance to ionizing radiation and drying that would be consistent with the conditions of the early Archean terrestrial habitats. Group of *Firmicutes* consistently cluster with *Chloroflexi* and *Cyanobacteria* [192, 197, 200]; however, they branch off earlier followed by divergence of *Chloroflexi* and *Cyanobacteria* [208] (Fig. 13.13b). Following the scenario of the terrestrial origin of life (Sects. 13.4 and 13.5.4) the heterotrophic lineages could have incorporated prebiotically developed photosynthetic blocks (see Sect. 13.7.1) and could have given rise to the photoheterotrophs. For example, thermophilic *Heliobacteria*, the extant photosynthesizing *Firmicutes*, are primitive obligate heterotrophs with Clostridia-type metabolism that are able to

photoheterotrophically oxidize simple organic compounds using light-driven PS1 homodimeric oxidoreductases [58]. Microbial mats in the Archean terrestrial and shallow water habitats (Sect. 13.5.4) could have been natural bioreactors of the terrestrial anoxygenic photosynthesis that eventually gave rise to oxygenic cyanobacterial lineages. Diverse molecular phylogeny of cyanobacteria suggests their origin in freshwater habitats [209]. Note that the terrestrial origin of cyanobacteria is also consistent with the origin of the Terrabacteria superclade within the phylogenies of Battistuzzi et al. [195, 203] with later emergence of cyanobacteria (see above).

The existence of the common photosynthetic ancestor for *Hydrobacteria* and *Terrabacteria* (Sect. 13.9.1 above) would imply that the majority of the descendants had lost their photosynthetic traits except those retained in several phyla through vertical inheritance and LGT. Alternatively, the photosynthetic ancestor could have given rise only to lineages of photosynthetic Eubacteria while its predecessors had given rise to the rest of the non-photosynthetic lineages via selective loss and LGT. Under any scenario, a relatively short time between the origin of anoxygenic photosynthesis (3.5 Ga) and the emergence of cyanobacteria (3.0–2.8 Ga) would imply that the strong UV radiation selection pressure in the shallow water and terrestrial habitats may have accelerated the evolution due to increased mutation rates by several orders of magnitudes as suggested by the simulated condition experiments [210]. Furthermore, around 3.0 Ga full-fledged plate tectonics came into action [26, 27], which significantly increased the availability of minerals due to weathering of rocks, which resulted in ecological domination of cyanobacteria in the photic zone and the upper layers of the microbial mats.

13.10 Concluding Remarks

In conclusion, some cautionary remarks should be taken into consideration when choosing between the competing hypotheses of the origin of life and photosynthesis.

Geochemists tend to believe that the early Earth atmosphere was rather slightly oxidizing or neutral than reducing. It is likely that consensus has emerged that a start of life needed a constant generation of thermodynamic disequilibria and highly reducing conditions for the synthetic reactions. Deep-sea hydrothermal vents that were common through Hadean and Archean time had provided such thermodynamic disequilibria and those reducing conditions on the global scale. Given high concentrations of CO_2, the reactive conditions at the alkaline hydrothermal vents were conducive to the origin of chemoautotrophic life. Alternatively, the hypothesis of the terrestrial origin of life emphasizes on a local start of heterotrophic life boosted by thermodynamic disequilibria provided by terrestrial geothermal ponds or similar environments and enhanced by the UV-driven photochemical synthesis of the organic compounds that fed the heterotrophic protocells.

When life had started is fundamental question as development of the genetic code would need time. It is suggested that the components of the protocells such as metabolic blocks, compartmentalized membrane systems, or RNA-based coding and translation could have been evolved in the pre-LUCA communities, natural reactive habitats such as proposed for the deep-sea hydrothermal vents [53] or the geothermal ponds [81]. This means that the pre-LUCA development could have started earlier in the Hadean (~4.3 Ga). Unfortunately, the timing of this is compromised by uncertainty with the degree of impacts from the heavy meteorite bombardment, which is thought to be characteristic of this time. It is possible that life had emerged several times but it was intermittently sterilized on the surface.

Within the framework of the terrestrial origin of life emergence of primitive photosynthesis could have occurred not long after the origin of life. The primordial photosynthetic components that were supposedly synthesized at the pre-LUCA stage could have been integrated into the simple heterotrophic protocells. In this case the evolution of the tetrapyrrole pathways would mirror the evolution of photosynthesis, and the early start of photosynthesis would favor the Granick hypothesis. The early photoheterotrophic organisms could diverge into mixotrophs in the ocean depending on the source of electron donors for photosynthesis. Recent discoveries of non-photosynthetic heterotrophic and photoheterotrophic species in *Chlorobi* family [211] would support a scenario of the photoheterotrophic life later turned mixotrophic and strictly autotrophic.

However, widely accepted hypothesis of the Late Heavy Bombardment (4.2–3.8 Ga) would imply that only hyperthermophiles had chances to survive through the bottleneck of the bombardment. The discovery of endolithic and subsurface habitats of both terrestrial and marine microorganisms living off the rock geochemistry as deep as 3 km [212] would support this idea. This is also supported by recent modeling studies concluding that the Earth habitable zone could not have been destroyed even by the harshest impacts [80] giving preference to the seafloor and the oceanic deep crust primordial habitats and excluding the terrestrial habitats.

Thus, the deep-rooted hyperthermophilic chemoautotrophic survivors of Eubacteria could possibly give rise to the photosynthetic lineages when they encountered light in the photic zone. The photosynthesis in the photic zone could have appeared after the end of the bombardment around 3.8 Ga and could have settled in shallow water habitats by 3.4 Ga as evidenced by microfossil records of the diverse microbial life including shallow water anoxygenic photosynthesis.

We do not know what type of metabolism the photosynthetic ancestors possessed. Based on the properties of extant chemoautotrophs this could be as primitive as the reductive acetyl-CoA pathway, the reductive TCA pathway, or a combination of both. As photosynthesis is generally considered to be a complex process the recruitment of the ancestor's available systems for new light-driven generation of the reducing power for the CO_2 reduction would be evolutionarily justified. For the same reason, the BChl biosynthetic pathway could have been built based on recruitment of the available ancient pathways and the enzymes and their adjustment to the synthesis of Mg- or Zn-containing Chls, Bchls, or both.

Should we consider the connection of the PSI with metabolism primeval? Iron–sulfur centers in the PSI possibly descended from the primordial iron–sulfur clusters or primitive ferredoxins that catalytically mediated the reduction of CO_2 in the microporous compartments of the alkaline hydrothermal vents (see Fig. 13.3b). The PSI is a major producer of the light-generated reducing power for the carbon fixation and other metabolic pathways through a series of Fe–S-containing proteins, which are shared by many metabolic networks. The ancient bacteria possessing proto-reaction centers would immediately benefit from the new source of energy by outgrowing their competitors and surviving by natural selection.

Finally, current uncertainty in the origin of photosynthesis is determined by the fact that the competing hypotheses provide alternative explanations and have different levels of conclusive evidence or experimental testing. Future discoveries of new photosynthetic phyla, improved quality of genome-wide phylogenetic analysis, experiments on simulation of the primordial conditions, and directed evolution will inevitably lead to a synthesis of unified concept of the evolution of photosynthesis.

Acknowledgements The author is thankful to Professor Anthony Larkum and an anonymous reviewer for critical reading of the manuscript and insightful suggestions.

References

1. von Bloh W, Cuntz M, Schroder KP, Bounama C, Franck S. Habitability of super-earth planets around other suns: models including red giant branch evolution. Astrobiology. 2009;9(6):593–602.
2. Cockell CS, Raven JA, Kaltenegger L, Logan RC. Planetary targets in the search for extrasolar oxygenic photosynthesis. Plant Ecol Diver. 2009;2(2):207–19. doi:10.1080/17550870903329328.
3. Kasting JF. The primitive Earth. In: Wong JT-F, Lazcano A, editors. Prebiotic evolution and astrobiology. Austin, TX: Landes Biosciences; 2008. p. 1–8.
4. Rothschild LJ. The evolution of photosynthesis ... again? Phil Trans Roy Soc B Biol Sci. 2008;363(1504):2787–801.
5. Deamer DW. The first living systems: a bioenergetic perspective. Microbiol Mol Biol Rev. 1997;61(2):239–61.
6. Chyba C, Sagan C. Endogenous production, exogenous delivery and impact-shock synthesis of organic molecules: an inventory for the origins of life. Nature. 1992;355(6356):125–32. doi:10.1038/355125a0.
7. Pope EC, Bird DK, Rosing MT. Isotope composition and volume of Earth's early oceans. Proc Natl Acad Sci. 2012;109(12):4371–6.
8. Nisbet EG, Sleep NH. The habitat and nature of early life. [Review]. Nature. 2001;409(6823):1083–91.
9. McGuinness ET. Some molecular moments of the Hadean and Archaean aeons: a retrospective overview from the interfacing years of the second to third millennia. Chem Rev. 2010;110(9):5191–215. doi:10.1021/cr0500611.

10. Montmerle T. The formation of solar type stars: boundary conditions for the origin of life? In: Gargoud M, Barbier B, Martin H, Reisse J, editors. Lectures in astrobiology. Berlin: Springer; 2005. p. 29–59.
11. Wood BJ, Walter MJ, Wade J. Accretion of the Earth and segregation of its core. Nature. 2006;441(7095):825–33. doi:10.1038/nature04763.
12. Harrison TM. The Hadean crust: evidence from > 4 Ga zircons. Annual review of earth and planetary sciences. Palo Alto, CA: Annual Reviews; 2009. p. 479–505.
13. Taylor SR, McLennan SM. The geochemical evolution of the continental crust. [Review]. Rev Geophys. 1995;33(2):241–65.
14. Claire MW, Sheets J, Cohen M, Ribas I, Meadows VS, Catling DC. The Evolution of solar flux from 0.1 nm to 160 μm: quantitative estimates for planetary studies. Astrophys J. 2012;757(1):95.
15. Sleep NH, Zahnle KJ, Kasting JF, Morowitz HJ. Annihilation of ecosystems by large asteroid impacts on the early Earth. Nature. 1989;342(6246):139–42. doi:10.1038/342139a0.
16. Lammer H, Kislyakova KG, Odert P, Leitzinger M, Schwarz R, Pilat-Lohinger E, et al. Pathways to Earth-like atmospheres. Orig Life Evol Biosph. 2011;41(6):503–22.
17. Martine H. Genesis and evolution of the primitive Earth continental crust. In: Gargoud M, Barbier B, Martin H, Reisse J, editors. Lectures in astrobiology. Berlin: Springer; 2005. p. 113–63.
18. Elkins-Tanton L. Formation of early water oceans on rocky planets. Astrophys Space Sci. 2011;332(2):359–64.
19. Wilde SA, Valley JW, Peck WH, Graham CM. Evidence from detrital zircons for the existence of continental crust and oceans on the Earth 4.4 Gyr ago. Nature. 2001;409 (6817):175–8.
20. Pinti DL. The origin and evolution of the oceans. In: Gargoud M, Barbier B, Martin H, Reisse J, editors. Lectures in astrobiology. Berlin: Springer; 2005. p. 83–112.
21. Farquhar J. Atmospheric evolution, Earth. In: Gornitz V, editor. Encyclopedia of paleoclimatology and ancient environments. Dordrecht, The Netherlands: Springer; 2009. p. 61–5.
22. Shibuya T, Tahata M, Kitajima K, Ueno Y, Komiya T, Yamamoto S, et al. Depth variation of carbon and oxygen isotopes of calcites in Archean altered upper oceanic crust: Implications for the CO_2 flux from ocean to oceanic crust in the Archean. Earth Planet Sci Lett. 2012;321:64–73.
23. Kasting JF, Howard MT, Wallmann K, Veizer J, Shields G, Jaffres J. Paleoclimates, ocean depth, and the oxygen isotopic composition of seawater. Earth Planet Sci Lett. 2006;252(1–2):82–93.
24. Catling DC, Claire MW. How Earth's atmosphere evolved to an oxic state: a status report. Earth Planet Sci Lett. 2005;237(1–2):1–20. doi:10.1016/j.epsl.2005.06.013.
25. Hawkesworth CJ, Kemp AIS. Evolution of the continental crust. [Review]. Nature. 2006;443 (7113):811–7.
26. Van Kranendonk MJ. Onset of plate tectonics. Science. 2011;333(6041):413–4.
27. Dhuime B, Hawkesworth CJ, Cawood PA, Storey CD. A change in the geodynamics of continental growth 3 billion years ago. Science. 2012;335(6074):1334–6.
28. Gaillard F, Scaillet B, Arndt NT. Atmospheric oxygenation caused by a change in volcanic degassing pressure. Nature. 2011;478(7368):229–32. doi:10.1038/nature10460.
29. Mojzsis SJ. Early Earth. Leftover lithosphere. Nat Geosci. 2010;3(3):148–9.
30. Scaillet B, Gaillard F. Earth science: redox state of early magmas. Nature. 2011;480 (7375):48–9. doi:10.1038/480048a.
31. Trail D, Watson EB, Tailby ND. The oxidation state of Hadean magmas and implications for early Earth's atmosphere. Nature. 2011;480(7375):79–82. doi:10.1038/nature10655.
32. Dartnell LR. Ionizing radiation and life. [Review]. Astrobiology. 2011;11(6):551–82.
33. Jardine M. Sunscreen for the Young Earth. Science. 2010;327(5970):1206–7.
34. Tarduno JA, Cottrell RD, Watkeys MK, Hofmann A, Doubrovine PV, Mamajek EE, et al. Geodynamo, solar wind, and magnetopause 3.4 to 3.45 billion years ago. Science. 2010;327(5970):1238–40.

35. Cockell CS, Raven JA. Ozone and life on the Archaean Earth. Phil Trans Roy Soc A Math Phys Eng Sci. 2007;365(1856):1889–901.
36. Ribas I, Guinan EF, Güdel M, Audard M. Evolution of the solar activity over time and effects on planetary atmospheres. I. High-energy irradiances (1–1700 Å). Astrophys J. 2005;622 (1):680–94.
37. Gomes R, Levison HF, Tsiganis K, Morbidelli A. Origin of the cataclysmic Late Heavy Bombardment period of the terrestrial planets. Nature. 2005;435(7041):466–9. doi:10.1038/nature03676.
38. Edwards KJ, Wheat CG, Sylvan JB. Under the sea: microbial life in volcanic oceanic crust. Nat Rev Micro. 2011;9(10):703–12. doi:10.1038/nrmicro2647.
39. Russell MJ, Hall AJ, Martin W. Serpentinization as a source of energy at the origin of life. Geobiology. 2010;8(5):355–71.
40. Sleep NH, Bird DK, Pope EC. Serpentinite and the dawn of life. Phil Trans Roy Soc B Biol Sci. 2011;366(1580):2857–69.
41. Falkowski PG. 8.05 - Biogeochemistry of primary production in the sea. In: Heinrich DH, Karl KT, editors. Treatise on geochemistry. Oxford: Pergamon; 2003. p. 185–213.
42. Holden JF, Breier JA, Rogers KL, Schulte MD, Toner BM. Biogeochemical processes at hydrothermal vents: microbes and minerals, bioenergetics, and carbon fluxes. Oceanography. 2012;25(1):196–208.
43. Arndt NT, Nisbet EG. Processes on the Young Earth and the habitats of early life. Annu Rev Earth Planet Sci. 2012;40(1):521–49.
44. Lane N, Martin WF. The origin of membrane bioenergetics. Cell. 2012;151(7):1406–16.
45. Martin W, Baross J, Kelley D, Russell MJ. Hydrothermal vents and the origin of life. Nat Rev Micro. 2008;6(11):805–14. doi:10.1038/nrmicro1991.
46. Alpermann T, Rüdel K, Rüger R, Steiniger F, Nietzsche S, Filiz V, et al. Polymersomes containing iron sulfide (FeS) as primordial cell model. Orig Life Evol Biosph. 2011;41 (2):103–19.
47. Mielke RE, Robinson KJ, White LM, McGlynn SE, McEachern K, Bhartia R, Kanik I, Russell MJ. Iron-sulfide-bearing chimneys as potential catalytic energy traps at life's emergence. Astrobiology. 2011;11(10):933–50.
48. Saladino R, Crestini C, Pino S, Costanzo G, Di Mauro E. Formamide and the origin of life. Phys Life Rev. 2012;9(1):84–104.
49. Martin W, Russell MJ. On the origin of biochemistry at an alkaline hydrothermal vent. Phil Trans Roy Soc B Biol Sci. 2007;362(1486):1887–926.
50. Koonin EV, Martin W. On the origin of genomes and cells within inorganic compartments. Trends Genet. 2005;21(12):647–54. doi:10.1016/j.tig.2005.09.006.
51. Baymann F, Lebrun E, Brugna M, Schoepp–Cothenet B, Giudici–Orticoni MT, Nitschke W. The redox protein construction kit: pre-last universal common ancestor evolution of energy-conserving enzymes. Philos Trans R Soc Lond B Biol Sci. 2003;358(1429):267–74.
52. Schoepp-Cothenet B, van Lis R, Atteia A, Baymann F, Capowiez L, Ducluzeau A-L, et al. On the universal core of bioenergetics. Biochim Biophys Acta Bioenerg. 2013;1827(2):79–93.
53. Lane N, Allen JF, Martin W. How did LUCA make a living? Chemiosmosis in the origin of life. Bioessays. 2010;32(4):271–80.
54. Martin WF. Hydrogen, metals, bifurcating electrons, and proton gradients: The early evolution of biological energy conservation. FEBS Lett. 2012;586(5):485–93. doi:10.1016/j.febslet.2011.09.031.
55. Berg IA. Ecological aspects of the distribution of different autotrophic CO_2 fixation pathways. Appl Environ Microbiol. 2011;77(6):1925–36.
56. Fuchs G. Alternative pathways of carbon dioxide fixation: insights into the early evolution of life? Annu Rev Microbiol. 2011;65(1):631–58.
57. Hügler M, Huber H, Molyneaux SJ, Vetriani C, Sievert SM. Autotrophic CO_2 fixation via the reductive tricarboxylic acid cycle in different lineages within the phylum *Aquificae*: evidence for two ways of citrate cleavage. Environ Microbiol. 2007;9(1):81–92.

58. Tang K-H, Tang YJ, Blankenship RE. Carbon metabolic pathways in phototrophic bacteria and their broader evolutionary implications. [Review]. Front Microbiol. 2011;2:165.
59. Thauer RK. A fifth pathway of carbon fixation. Science. 2007;318(5857):1732–3.
60. Braakman R, Smith E. The emergence and early evolution of biological carbon-fixation. PLoS Comput Biol. 2012;8(4):e1002455. doi:10.1371/journal.pcbi.1002455.
61. Morowitz H. Beginnings of cellular life: Metabolism recaptures biochemistry. New Haven, CT: Yale University Press; 1992.
62. Hugler M, Sievert SM. Beyond the Calvin cycle: autotrophic carbon fixation in the ocean. In: Carlson CA, Giovannoni SJ, editors. Annual review of marine science, vol. 3. Palo Alto, CA: Annual Reviews; 2011. p. 261–89.
63. Davenport C, Ussery D, Tümmler B. Comparative genomics of green sulfur bacteria. Photosynth Res. 2010;104(2):137–52.
64. Eisen JA, Nelson KE, Paulsen IT, Heidelberg JF, Wu M, Dodson RJ, et al. The complete genome sequence of *Chlorobium tepidum* TLS, a photosynthetic, anaerobic, green-sulfur bacterium. Proc Natl Acad Sci. 2002;99(14):9509–14.
65. Campbell BJ, Cary SC. Abundance of reverse tricarboxylic acid cycle genes in free-living microorganisms at deep-sea hydrothermal vents. Appl Environ Microbiol. 2004;70 (10):6282–9.
66. Campbell BJ, Engel AS, Porter ML, Takai K. The versatile epsilon-proteobacteria: key players in sulphidic habitats. Nat Rev Micro. 2006;4(6):458–68. doi:10.1038/nrmicro1414.
67. Sievert SM, Vetriani C. Chemoautotrophy at deep-sea vents past, present, and future. Oceanography. 2012;25(1):218–33.
68. Bar-Even A, Flamholz A, Noor E, Milo R. Thermodynamic constraints shape the structure of carbon fixation pathways. Biochim Biophys Acta Bioenerg. 2012;1817(9):1646–59. doi:10.1016/j.bbabio.2012.05.002.
69. Berg IA, Kockelkorn D, Ramos-Vera WH, Say RF, Zarzycki J, Hügler M, et al. Autotrophic carbon fixation in archaea. Nat Rev Micro. 2010;8(6):447–60. doi:10.1038/nrmicro2365.
70. Brüssow H. The not so universal tree of life or the place of viruses in the living world. Phil Trans Roy Soc B Biol Sci. 2009;364(1527):2263–74.
71. Ducluzeau A-L, van Lis R, Duval S, Schoepp-Cothenet B, Russell MJ, Nitschke W. Was nitric oxide the first deep electron sink? Trends Biochem Sci. 2009;34(1):9–15. doi:10.1016/j.tibs.2008.10.005.
72. Giacometti G, Giacometti G. Evolution of photosynthesis and respiration: which came first? Appl Magn Reson. 2010;37(1):13–25.
73. Fontecilla-Camps JC, Amara P, Cavazza C, Nicolet Y, Volbeda A. Structure–function relationships of anaerobic gas-processing metalloenzymes. Nature. 2009;460 (7257):814–22. doi:10.1038/nature08299.
74. Rees DC, Howard JB. The interface between the biological and inorganic worlds: iron-sulfur metalloclusters. Science. 2003;300(5621):929–31.
75. Meyer J. Iron–sulfur protein folds, iron–sulfur chemistry, and evolution. J Biol Inorg Chem. 2008;13(2):157–70.
76. Rickard D, Luther GW. Chemistry of iron sulfides. Chem Rev. 2007;107(2):514–62. doi:10.1021/cr0503658.
77. Nitschke W, Russell MJ. Hydrothermal focusing of chemical and chemiosmotic energy, supported by delivery of catalytic Fe, Ni, Mo/W, Co, S and Se, forced life to emerge. [Review]. J Mol Evol. 2009;69(5):481–96.
78. Schütz M, Brugna M, Lebrun E, Baymann F, Huber R, Stetter K-O, et al. Early evolution of cytochrome *bc* complexes. J Mol Biol. 2000;300(4):663–75. doi:10.1006/jmbi.2000.3915.
79. Mauzerall D. Oceanic photochemistry and evolution of elements and cofactors in the early stages of the evolution of life. In: Falkowski PG, Knoll AH, editors. Evolution of primary producers in the sea. London: Elsevier Academic Press; 2007. p. 7–21.
80. Abramov O, Mojzsis SJ. Microbial habitability of the Hadean Earth during the late heavy bombardment. Nature. 2009;459(7245):419–22. doi:10.1038/nature08015.

81. Mulkidjanian AY, Bychkov AY, Dibrova DV, Galperin MY, Koonin EV. Origin of first cells at terrestrial, anoxic geothermal fields. Proc Natl Acad Sci. 2012;109(14):E821–30.
82. Chittenden G, Schwartz A. Prebiotic photosynthetic reactions. Biosystems. 1981;14 (1):15–32.
83. Inoue T, Fujishima A, Konishi S, Honda K. Potoelectrocatalytic reduction of carbon dioxide in aqueous suspensions of semiconductor powders. Nature. 1979;277(5698):637–8.
84. Guzman MI, Martin ST. Prebiotic metabolism: production by mineral photoelectrochemistry of alpha-ketocarboxylic acids in the reductive tricarboxylic acid cycle. Astrobiology. 2009;9 (9):833–42.
85. Saladino R, Brucato JR, Sio AD, Botta G, Pace E, Gambicorti L. Photochemical synthesis of citric acid cycle intermediates based on titanium dioxide. Astrobiology. 2011;11(8):815–24.
86. Wang W, Li Q, Yang B, Liu X, Yang Y, Su W. Photocatalytic reversible amination of alpha-keto acids on a ZnS surface: implications for the prebiotic metabolism. Chem Commun. 2012;48(15):2146–8.
87. Zhang XV, Ellery SP, Friend CM, Holland HD, Michel FM, Schoonen MAA, et al. Photodriven reduction and oxidation reactions on colloidal semiconductor particles: Implications for prebiotic synthesis. J Photochem Photobiol Chem. 2007;185(2–3):301–11.
88. Zhang XV, Martin ST. Driving parts of Krebs cycle in reverse through mineral photochemistry. J Am Chem Soc. 2006;128(50):16032–3. doi:10.1021/ja066103k.
89. Gilbert W. Origin of life: the RNA world. Nature. 1986;319(6055):618. doi:10.1038/319618a0.
90. Granick S. Speculations on the origins and evolution of photosynthesis. Ann N Y Acad Sci. 1957;69(2):292–308.
91. Mojzsis SJ, Arrhenius G, McKeegan KD, Harrison TM, Nutman AP, Friend CRL. Evidence for life on Earth before 3,800 million years ago. Nature. 1996;384(6604):55–9.
92. Rosing MT. C-13-depleted carbon microparticles in > 3700-Ma sea-floor sedimentary rocks from west Greenland. Science. 1999;283(5402):674–6.
93. Schidlowski M. A 3,800-million-year isotopic record of life from carbon in sedimentary-rocks. [Review]. Nature. 1988;333(6171):313–8.
94. Brasier M, McLoughlin N, Green O, Wacey D. A fresh look at the fossil evidence for early Archaean cellular life. Phil Trans Roy Soc B Biol Sci. 2006;361(1470):887–902.
95. Farquhar J, Zerkle A, Bekker A. Geological constraints on the origin of oxygenic photosynthesis. Photosynth Res. 2011;107(1):11–36.
96. Tice MM, Lowe DR. Photosynthetic microbial mats in the 3,416-Myr-old ocean. Nature. 2004;431(7008):549–52. doi:10.1038/nature02888.
97. Tice MM, Lowe DR. Hydrogen-based carbon fixation in the earliest known photosynthetic organisms. Geology. 2006;34(1):37–40.
98. Hickman AH. Review of the Pilbara Craton and Fortescue Basin, Western Australia: crustal evolution providing environments for early life. [Review]. Island Arc. 2012;21(1):1–31.
99. Mloszewska AM, Pecoits E, Cates NL, Mojzsis SJ, O'Neil J, Robbins LJ, et al. The composition of Earth's oldest iron formations: the Nuvvuagittuq Supracrustal Belt (Quebec, Canada). Earth Planet Sci Lett. 2012;317:331–42.
100. Konhauser KO, Amskold L, Lalonde SV, Posth NR, Kappler A, Anbar A. Decoupling photochemical Fe(II) oxidation from shallow-water BIF deposition. Earth Planet Sci Lett. 2007;258(1–2):87–100.
101. Bird LJ, Bonnefoy V, Newman DK. Bioenergetic challenges of microbial iron metabolisms. Trends Microbiol. 2011;19(7):330–40. doi:10.1016/j.tim.2011.05.001.
102. Crowe SA, Jones C, Katsev S, Magen C, O'Neill AH, Sturm A, et al. Photoferrotrophs thrive in an Archean Ocean analogue. Proc Natl Acad Sci. 2008;105(41):15938–43.
103. Emerson D, Fleming EJ, McBeth JM. Iron-oxidizing bacteria: an environmental and genomic perspective. Annu Rev Microbiol. 2010;64(1):561–83.
104. Jiao Y, Kappler A, Croal LR, Newman DK. Isolation and characterization of a genetically tractable photoautotrophic Fe(II)-oxidizing bacterium, *Rhodopseudomonas palustris* strain TIE-1. Appl Environ Microbiol. 2005;71(8):4487–96.

105. Buick R, Thornett JR, McNaughton NJ, Smith JB, Barley ME, Savage M. Record of emergent continental crust ~3.5 billion years ago in the Pilbara Craton of Australia. Nature. 1995;375(6532):574–7.
106. Bapteste E, Brochier C, Boucher Y. Higher-level classification of the Archaea: evolution of methanogenesis and methanogens. Archaea. 2005;1(5):353–63.
107. Ueno Y, Yamada K, Yoshida N, Maruyama S, Isozaki Y. Evidence from fluid inclusions for microbial methanogenesis in the early Archaean era. Nature. 2006;440(7083):516–9. doi:10.1038/nature04584.
108. Philippot P, Van Zuilen M, Lepot K, Thomazo C, Farquhar J, Van Kranendonk MJ. Early Archaean microorganisms preferred elemental sulfur, not sulfate. Science. 2007;317 (5844):1534–7.
109. Shen Y, Buick R, Canfield DE. Isotopic evidence for microbial sulphate reduction in the early Archaean era. Nature. 2001;410(6824):77–81. doi:10.1038/35065071.
110. Wacey D, Kilburn MR, Saunders M, Cliff J, Brasier MD. Microfossils of sulphur-metabolizing cells in 3.4-billion-year-old rocks of Western Australia. Nat Geosci. 2011;4(10):698–702.
111. Allwood AC, Grotzinger JP, Knoll AH, Burch IW, Anderson MS, Coleman ML, et al. Controls on development and diversity of Early Archean stromatolites. Proc Natl Acad Sci. 2009;106(24):9548–55.
112. Allwood AC, Walter MR, Kamber BS, Marshall CP, Burch IW. Stromatolite reef from the Early Archaean era of Australia. Nature. 2006;441(7094):714–8. doi:10.1038/nature04764.
113. Beukes N. Biogeochemistry: early options in photosynthesis. Nature. 2004;431(7008):522–3. doi:10.1038/431522b.
114. Westall F, Cavalazzi B, Lemelle L, Marrocchi Y, Rouzaud JN, Simionovici A, et al. Implications of in situ calcification for photosynthesis in a similar to 3.3 Ga-old microbial biofilm from the Barberton greenstone belt, South Africa. Earth Planet Sci Lett. 2011;310(3–4):468–79.
115. Cockell C. Ultraviolet radiation and the photobiology of earth's early oceans. Orig Life Evol Biosph. 2000;30(5):467–500.
116. Cockell CS. Biological effects of high ultraviolet radiation on early earth—a theoretical evaluation. J Theor Biol. 1998;193(4):717–29. doi:10.1006/jtbi.1998.0738.
117. Canfield DE, Rosing MT, Bjerrum C. Early anaerobic metabolisms. Phil Trans Roy Soc B Biol Sci. 2006;361(1474):1819–36.
118. Kharecha P, Kasting J, Siefert J. A coupled atmosphere-ecosystem model of the early Archean Earth. [Review]. Geobiology. 2005;3(2):53–76.
119. Sleep NH, Bird DK. Evolutionary ecology during the rise of dioxygen in the Earth's atmosphere. Phil Trans Roy Soc B Biol Sci. 2008;363(1504):2651–64.
120. Nisbet EG, Fowler CMR. Archaean metabolic evolution of microbial mats. Proc Roy Soc Lond Ser B Biol Sci. 1999;266(1436):2375–82.
121. Beblo K, Douki T, Schmalz G, Rachel R, Wirth R, Huber H, et al. Survival of thermophilic and hyperthermophilic microorganisms after exposure to UV-C, ionizing radiation and desiccation. Arch Microbiol. 2011;193(11):797–809.
122. Gómez F, Aguilera A, Amils R. Soluble ferric iron as an effective protective agent against UV radiation: implications for early life. Icarus. 2007;191(1):352–9. doi:10.1016/j.icarus.2007.04.008.
123. Hader DP, Kumar HD, Smith RC, Worrest RC. Effects of solar UV radiation on aquatic ecosystems and interactions with climate change. Photochem Photobiol Sci. 2007;6(3):267–85.
124. Weibel DB. Building communities one bacterium at a time. Proc Natl Acad Sci. 2008;105 (47):18075–6.
125. Russell MJ, Arndt NT. Geodynamic and metabolic cycles in the Hadean. Biogeosci Disc. 2004;1(1):591–624.
126. Westall F, de Ronde CEJ, Southam G, Grassineau N, Colas M, Cockell C, et al. Implications of a 3.472–3.333 Gyr-old subaerial microbial mat from the Barberton greenstone belt, South Africa for the UV environmental conditions on the early Earth. Phil Trans Roy Soc B Biol Sci. 2006;361(1474):1857–76.

127. Tice MM, Thornton DCO, Pope MC, Olszewski TD, Gong J. Archean microbial mat communities. In: Jeanloz R, Freeman KH, editors. Annual review of earth and planetary sciences, vol. 39. Palo Alto, CA: Annual Reviews; 2011. p. 297–319.
128. Falkowski PG, Fenchel T, Delong EF. The microbial engines that drive Earth's biogeochemical cycles. Science. 2008;320(5879):1034–9.
129. Chew AGM, Bryant DA. Chlorophyll biosynthesis in bacteria: the origins of structural and functional diversity. Annu Rev Microbiol. 2007;61(1):113–29.
130. Heinemann IU, Jahn M, Jahn D. The biochemistry of heme biosynthesis. Arch Biochem Biophys. 2008;474(2):238–51.
131. Sousa FL, Shavit-Grievink L, Allen JF, Martin WF. Chlorophyll biosynthesis gene evolution indicates photosystem gene duplication, not photosystem merger, at the origin of oxygenic photosynthesis. Genome Biol Evol. 2013;5(1):200–16.
132. Bali S, Lawrence AD, Lobo SA, Saraiva LM, Golding BT, Palmer DJ, et al. Molecular hijacking of siroheme for the synthesis of heme and d1 heme. Proc Natl Acad Sci. 2011;108 (45):18260–5.
133. Hennig SE, Jeoung JH, Goetzl S, Dobbek H. Redox-dependent complex formation by an ATP-dependent activator of the corrinoid/iron-sulfur protein. Proc Natl Acad Sci U S A. 2012;109(14):5235–40.
134. Holliday GL, Thornton JM, Marquet A, Smith AG, Rebeille F, Mendel R, et al. Evolution of enzymes and pathways for the biosynthesis of cofactors. Nat Prod Rep. 2007;24(5):972–87.
135. Masuda T, Fujita Y. Regulation and evolution of chlorophyll metabolism. Photochem Photobiol Sci. 2008;7(10):1131–49.
136. Lundqvist J, Elmlund D, Heldt D, Deery E, Söderberg CAG, Hansson M, et al. The AAA + motor complex of subunits CobS and CobT of cobaltochelatase visualized by single particle electron microscopy. J Struct Biol. 2009;167(3):227–34.
137. Jaschke PR, Hardjasa A, Digby EL, Hunter CN, Beatty JT. A bchD (magnesium chelatase) mutant of *Rhodobacter sphaeroides* synthesizes zinc bacteriochlorophyll through novel zinc-containing intermediates. J Biol Chem. 2011;286(23):20313–22.
138. Jensen RA. Enzyme recruitment in evolution of new function. Annu Rev Microbiol. 1976;30 (1):409–25.
139. Muraki N, Nomata J, Ebata K, Mizoguchi T, Shiba T, Tamiaki H, et al. X-ray crystal structure of the light-independent protochlorophyllide reductase. Nature. 2010;465(7294):110–4. doi:10.1038/nature08950.
140. Raymond J, Siefert JL, Staples CR, Blankenship RE. The natural history of nitrogen fixation. Mol Biol Evol. 2004;21(3):541–54.
141. Blankenship RE, Hartman H. The origin and evolution of oxygenic photosynthesis. Trends Biochem Sci. 1998;23(3):94–7.
142. Larkum AWD. The evolution of photosynthesis. In: Renger G, editor. Primary processes of photosynthesis, Part 2: Principles and apparatus. Cambridge: RSC Publishing; 2008. p. 491–521.
143. Lindsey J, Ptaszek M, Taniguchi M. Simple formation of an abiotic porphyrinogen in aqueous solution. Orig Life Evol Biosph. 2009;39(6):495–515.
144. Lindsey JS, Chandrashaker V, Taniguchi M, Ptaszek M. Abiotic formation of uroporphyrinogen and coproporphyrinogen from acyclic reactants. New J Chem. 2011;35 (1):65–75.
145. Mercer-Smith JA, Mauzerall DC. Photochemistry of porphyrins: a model for the origin of photosynthesis. Photochem Photobiol. 1984;39(3):397–405.
146. Scheer H. An overview of chlorophylls and bacteriochlorophylls: biochemistry, biophysics, functions and application. In: Grimm B, Porra RJ, Ruduger W, Scheer H, editors. Chlorophylls and bacteriochlorophylls: biochemistry, biophysics, functions and applications. Dordrecht, The Netherlands: Springer; 2006. p. 1–26.

147. Krasnovsky AA. Chemical evolution of photosynthesis. Orig Life Evol Biosph. 1976;7(2):133–43.
148. Soares ARM, Taniguchi M, Chandrashaker V, Lindsey JS. Self-organization of tetrapyrrole constituents to give a photoactive protocell. Chem Sci. 2012;3(6):1963–74.
149. Mauzerall DC. Evolution of porphyrins. Clin Dermatol. 1998;16(2):195–201.
150. Mulkidjanian AY, Junge W. On the origin of photosynthesis as inferred from sequence analysis - A primordial UV-protector as common ancestor of reaction centers and antenna proteins. Photosynth Res. 1997;51(1):27–42.
151. Larkum AWD. The evolution of chlorophylls and photosynthesis. In: Grimm B, Porra RJ, Ruduger W, Scheer H, editors. Chlorophylls and bacteriochlorophylls: biochemistry, biophysics, functions and applications. Dordrecht: Springer; 2006. p. 261–82.
152. Mulkidjanian AY, Koonin EV, Makarova KS, Mekhedov SL, Sorokin A, Wolf YI, et al. The cyanobacterial genome core and the origin of photosynthesis. Proc Natl Acad Sci. 2006;103 (35):13126–31.
153. Melkozernov AN, Blankenship RE. Photosynthetic functions of chlorophylls. In: Grimm B, Porra RJ, Ruduger W, Scheer H, editors. Chlorophylls and bacteriochlorophylls: biochemistry, biophysics, functions and applications. Dordrecht, The Netherlands: Springer; 2006. p. 397–412.
154. Wakeham MC, Frolov D, Fyfe PK, van Grondelle R, Jones MR. Acquisition of photosynthetic capacity by a reaction centre that lacks the QA ubiquinone; possible insights into the evolution of reaction centres? Biochim Biophys Acta Bioenerg. 2003;1607(1):53–63. doi:10.1016/j.bbabio.2003.08.008.
155. Van Dover CL, Reynolds GT, Chave AD, Tyson JA. Light at deep-sea hydrothermal vents. Geophys Res Lett. 1996;23(16):2049–52.
156. Beatty JT, Overmann J, Lince MT, Manske AK, Lang AS, Blankenship RE, et al. An obligately photosynthetic bacterial anaerobe from a deep-sea hydrothermal vent. Proc Natl Acad Sci U S A. 2005;102(26):9306–10.
157. Nisbet EG, Cann JR, Vandover CL. Origins of photosynthesis. Nature. 1995;373(6514):479–80.
158. Caetano-Anollés G, Kim HS, Mittenthal JE. The origin of modern metabolic networks inferred from phylogenomic analysis of protein architecture. Proc Natl Acad Sci. 2007;104 (22):9358–63.
159. Pohorille A, Wilson MA, Chipot C. Membrane peptides and their role in protobiological evolution. [Review]. Orig Life Evol Biosph. 2003;33(2):173–97.
160. Bowie JU. Solving the membrane protein folding problem. Nature. 2005;438(7068):581–9. doi:10.1038/nature04395.
161. Eilers M, Shekar SC, Shieh T, Smith SO, Fleming PJ. Internal packing of helical membrane proteins. Proc Natl Acad Sci. 2000;97(11):5796–801.
162. Xiong J, Bauer CE. A cytochrome *b* origin of photosynthetic reaction centers: an evolutionary link between respiration and photosynthesis. J Mol Biol. 2002;322(5):1025–37. doi:10.1016/S0022-2836(02)00822-7.
163. Sattley WM, Madigan MT, Swingley WD, Cheung PC, Clocksin KM, Conrad AL, et al. The genome of *Heliobacterium modesticaldum*, a phototrophic representative of the firmicutes containing the simplest photosynthetic apparatus. J Bacteriol. 2008;190(13):4687–96.
164. Bryant DA, Costas AMG, Maresca JA, Chew AGM, Klatt CG, Bateson MM, et al. *Candidatus Chloracidobacterium thermophilum*: an aerobic phototrophic acidobacterium. Science. 2007;317(5837):523–6.
165. Garcia Costas AM, Liu Z, Tomsho LP, Schuster SC, Ward DM, Bryant DA. Complete genome of *Candidatus Chloracidobacterium thermophilum*, a chlorophyll-based photoheterotroph belonging to the phylum *Acidobacteria*. Environ Microbiol. 2012;14(1):177–90.
166. Baymann F, Brugna M, Mühlenhoff U, Nitschke W. Daddy, where did (PS)I come from? Biochim Biophys Acta Bioenerg. 2001;1507(1–3):291–310. doi:10.1016/S0005-2728(01)00209-2.

167. Blankenship RE. Molecular mechanisms of photosynthesis. Oxford: Blakwell Science; 2002.
168. Heathcote P, Fyfe PK, Jones MR. Reaction centres: the structure and evolution of biological solar power. [Review]. Trends Biochem Sci. 2002;27(2):79–87.
169. Hohmann-Marriott MF, Blankenship RE. Evolution of photosynthesis. In: Merchant SS, Briggs WR, Ort D, editors. Annual review of plant biology, vol. 62. Palo Alto, CA: Annual Reviews; 2011. p. 515–48.
170. Nelson N. Photosystems and global effects of oxygenic photosynthesis. Biochim Biophys Acta Bioenerg. 2011;1807(8):856–63. doi:10.1016/j.bbabio.2010.10.011.
171. Nitschke W, Rutherford AW. Photosynthetic reaction centers - variations on a common structural theme. Trends Biochem Sci. 1991;16(7):241–5.
172. Sadekar S, Raymond J, Blankenship RE. Conservation of distantly related membrane proteins: photosynthetic reaction centers share a common structural core. Mol Biol Evol. 2006;23(11):2001–7.
173. Schubert W-D, Klukas O, Saenger W, Witt HT, Fromme P, Krauß N. A common ancestor for oxygenic and anoxygenic photosynthetic systems: a comparison based on the structural model of photosystem I. J Mol Biol. 1998;280(2):297–314. doi:10.1006/jmbi.1998.1824.
174. Goodsell DS, Olson AJ. Structural symmetry and protein function. Annu Rev Biophys Biomol Struct. 2000;29(1):105–53.
175. Beddard GS, Porter G. Concentration quenching in chlorophyll. Nature. 1976;260 (5549):366–7. doi:10.1038/260366a0.
176. Hosoya-Matsuda N, Inoue K, Hisabori T. Roles of thioredoxins in the obligate anaerobic green sulfur photosynthetic bacterium chlorobaculum tepidum. Mol Plant. 2009;2(2):336–43.
177. Romberger SP, Golbeck JH. The bound iron-sulfur clusters of Type-I homodimeric reaction centers. [Review]. Photosynth Res. 2010;104(2–3):333–46.
178. Romberger SP, Golbeck JH. The F-X iron-sulfur cluster serves as the terminal bound electron acceptor in heliobacterial reaction centers. Photosynth Res. 2012;111(3):285–90.
179. Rutherford AW, Faller P. Photosystem II: evolutionary perspectives. Philos Trans R Soc Lond B Biol Sci. 2003;358(1429):245–53.
180. Rutherford AW, Osyczka A, Rappaport F. Back-reactions, short-circuits, leaks and other energy wasteful reactions in biological electron transfer: Redox tuning to survive life in O-2. FEBS Lett. 2012;586(5):603–16.
181. Khorobrykh AA, Terentyev VV, Zharmukhamedov SK, Klimov VV. Redox interaction of Mn–bicarbonate complexes with reaction centres of purple bacteria. Phil Trans Roy Soc B Biol Sci. 2008;363(1494):1245–51.
182. Kulp TR, Hoeft SE, Asao M, Madigan MT, Hollibaugh JT, Fisher JC, et al. Arsenic(III) fuels anoxygenic photosynthesis in hot spring biofilms from Mono Lake, California. Science. 2008;321(5891):967–70.
183. Griffin BM, Schott J, Schink B. Nitrite, an electron donor for anoxygenic photosynthesis. Science. 2007;316(5833):1870.
184. Allen JF, Martin W. Evolutionary biology: out of thin air. Nature. 2007;445(7128):610–2. doi:10.1038/445610a.
185. Swan BK, Martinez-Garcia M, Preston CM, Sczyrba A, Woyke T, Lamy D, et al. Potential for chemolithoautotrophy among ubiquitous bacteria lineages in the dark ocean. Science. 2011;333(6047):1296–300.
186. Blankenship RE. Early evolution of photosynthesis. Plant Physiol. 2010;154(2):434–8.
187. Bryant DA, Frigaard N-U. Prokaryotic photosynthesis and phototrophy illuminated. Trends Microbiol. 2006;14(11):488–96. doi:10.1016/j.tim.2006.09.001.
188. Mix L, Haig D, Cavanaugh C. Phylogenetic analyses of the core antenna domain: investigating the origin of photosystem I. J Mol Evol. 2005;60(2):153–63.
189. Raymond J, Zhaxybayeva O, Gogarten JP, Gerdes SY, Blankenship RE. Whole-genome analysis of photosynthetic prokaryotes. Science. 2002;298(5598):1616–20.
190. Theobald DL. A formal test of the theory of universal common ancestry. Nature. 2010;465(7295):219–22. doi:10.1038/nature09014.

191. Woese C. The universal ancestor. Proc Natl Acad Sci U S A. 1998;95(12):6854–9.
192. Abby SS, Tannier E, Gouy M, Daubin V. Lateral gene transfer as a support for the tree of life. Proc Natl Acad Sci. 2012;109(13):4962–7.
193. Battistuzzi F, Feijao A, Hedges SB. A genomic timescale of prokaryote evolution: insights into the origin of methanogenesis, phototrophy, and the colonization of land. BMC Evol Biol. 2004;4(1):44.
194. Battistuzzi FU, Hedges SB. A major clade of prokaryotes with ancient adaptations to life on land. Mol Biol Evol. 2009;26(2):335–43.
195. Battistuzzi FU, Hedges SB. Eubacteria. In: Hedges SB, Kumar S, editors. The timetree of life. New York, NY: Oxford University Press; 2009. p. 106–15.
196. Boussau B, Gouy M. What genomes have to say about the evolution of the Earth. Gondwana Res. 2012;21(2–3):483–94. doi:10.1016/j.gr.2011.08.002.
197. Ciccarelli FD, Doerks T, von Mering C, Creevey CJ, Snel B, Bork P. Toward automatic reconstruction of a highly resolved tree of life. Science. 2006;311(5765):1283–7.
198. Gaucher EA, Kratzer JT, Randall RN. Deep phylogeny—how a tree can help characterize early life on earth. Cold Spring Harb Perspect Biol. 2010;2(1):a002238.
199. Pace NR. A molecular view of microbial diversity and the biosphere. Science. 1997;276 (5313):734–40.
200. Wu D, Hugenholtz P, Mavromatis K, Pukall R, Dalin E, Ivanova NN, et al. A phylogeny-driven genomic encyclopaedia of Bacteria and Archaea. Nature. 2009;462(7276):1056–60. doi:10.1038/nature08656.
201. Raymond J, Zhaxybayeva O, Gogarten JP, Blankenship RE. Evolution of photosynthetic prokaryotes: a maximum-likelihood mapping approach. Phil Trans Roy Soc Lond Ser B Biol Sci. 2003;358(1429):223–30.
202. Hartman H. Photosynthesis and the origin of life. Orig Life Evol Biosph. 1998;28(4–6):515–21.
203. Sleep NH. The Hadean-Archaean environment. Cold Spring Harb Perspect Biol. 2010;2(6): a002527.
204. Woese CR. Bacterial evolution. Microbiol Rev. 1987;51(2):221–71.
205. Rothschild LJ, Mancinelli RL. Life in extreme environments. Nature. 2001;409(6823):1092–101.
206. Zhaxybayeva O, Swithers KS, Lapierre P, Fournier GP, Bickhart DM, DeBoy RT, et al. On the chimeric nature, thermophilic origin, and phylogenetic placement of the thermotogales. Proc Natl Acad Sci. 2009;106(14):5865–70.
207. McDaniel LD, Young E, Delaney J, Ruhnau F, Ritchie KB, Paul JH. High frequency of horizontal gene transfer in the oceans. Science. 2010;330(6000):50.
208. Gupta R. Evolutionary relationships among photosynthetic bacteria. Photosynth Res. 2003;76(1–3):173–83.
209. Blank CE, Sánchez-Baracaldo P. Timing of morphological and ecological innovations in the cyanobacteria – a key to understanding the rise in atmospheric oxygen. Geobiology. 2010;8 (1):1–23.
210. Moeller R, Reitz G, Nicholson WL, Horneck G, Team P. Mutagenesis in bacterial spores exposed to space and simulated martian conditions: data from the EXPOSE-E spaceflight experiment PROTECT. Astrobiology. 2012;12(5):457–68.
211. Liu Z, Klatt CG, Ludwig M, Rusch DB, Jensen SI, Kuhl M, et al. '*Candidatus Thermochlorobacter aerophilum*' an aerobic chlorophotoheterotrophic member of the phylum *Chlorobi* defined by metagenomics and metatranscriptomics. ISME J. 2012;6(10):1869–82.
212. Edwards KJ, Becker K, Colwell F. The deep, dark energy biosphere: intraterrestrial life on earth. In: Jeanloz R, editor. Annual review of earth and planetary sciences, vol. 40. Palo Alto, CA: Annual Reviews; 2012. p. 551–68.

Chapter 14
Origin of Oxygenic Photosynthesis from Anoxygenic Type I and Type II Reaction Centers

John F. Allen

Abstract All anoxygenic photosynthetic bacteria currently known have photosynthetic reaction centers of only one type, either type I or II. In contrast, all oxygenic photosynthetic systems—of plants, algae, and cyanobacteria—have both type I and type II reaction centers. Molecular oxygen is the oxidation product of water in a type II reaction center that is connected, in series, with a type I reaction center. Around 2.4 billion years ago, the evolutionary origin of this series connection initiated biological water oxidation and began to transform our planet irrevocably. Here I consider the question of how separate type I and type II reaction centers diverged from a common ancestor. How they later became linked together, to become interdependent, is also considered, and an answer proposed. The "redox switch hypothesis" for the first cyanobacterium envisages an evolutionary precursor in which type I and type II reaction center genes are present in the genome of a single anoxygenic bacterial lineage, but never expressed at the same time, their gene products forming different reaction centers for light energy conversion under different growth conditions. I suggest that mutation disrupting redox control allowed these two reaction centers to coexist—an arrangement selected against prior to the acquisition of a catalyst of water oxidation while having a selective advantage thereafter. Predictions of this hypothesis include a modern, anoxygenic descendent of the proto-cyanobacterium whose disabled redox switch triggered the Great Oxidation Event, transforming both biology and Earth's surface geochemistry.

Keywords Electron transport • Photochemistry • Evolution • Molecular oxygen • Redox switch hypothesis • Gene expression • Biogeochemistry

J.F. Allen, Ph.D. (✉)
Research Department of Genetics, Evolution and Environment, University College London, Gower Street, London WC1E 6BT, UK
e-mail: j.f.allen@ucl.ac.uk

J. Golbeck and A. van der Est (eds.), *The Biophysics of Photosynthesis*, Biophysics for the Life Sciences 11, DOI 10.1007/978-1-4939-1148-6_14,

14.1 Two Light Reactions in Photosynthesis, Isolated or Connected

The primary process in photosynthesis is light-induced separation of electrical charge across a membrane [1]. In photochemical reaction centers this charge separation lasts long enough for its recombination to occur only after a number of secondary reactions have taken place. These secondary reactions include electron transport in a chain of coupled oxidation-reduction reactions, proton translocation to establish delocalized transmembrane gradients of pH (proton concentration) and electrical charge, and synthesis of ATP from ADP and inorganic phosphate. These reactions are together sufficient for complete photosynthesis, defined as the conversion of radiant energy into biologically useful chemical free energy. One or more assimilatory reactions, acting on environmental and inorganic substrates, are usually coupled, in turn, to the secondary reactions of photosynthesis. Thus photosynthesis is often linked to assimilation of carbon dioxide in photoautotrophy or to assimilation of molecular nitrogen in photodiazotrophy, providing essential inputs not only of energy but also of elemental carbon or nitrogen into living cells, organisms, and ecosystems. Biological, ecological, and geochemical nitrogen, carbon, and oxygen cycles can be viewed as the eventual, long-term return of electrons to a photooxidized chlorophyll that is the primary electron donor, P, in a photosynthetic reaction center. At its simplest:

$$\mathrm{DPA} + h\nu \rightarrow \mathrm{DP^*A} \rightarrow \mathrm{DP^+A^-} \rightarrow \mathrm{D^+PA^-}$$

where D is an electron donor, A stands for a chain of acceptors, P is the primary donor, and P* is its excited state. A committed reductionist might summarize ensuing reactions as follows:

$$\mathrm{D^+PA^-} \rightarrow \mathrm{DPA} + \textit{biology}$$

While all photochemical reaction centers use light to separate charge, moving an electron across a membrane, reaction centers can be divided into two distinct types according to the chemical identity of their immediate secondary electron donors and acceptors, each serving to stabilize the charge separation in a different way. The characteristics of the two types of reaction centers, and the relationship between them, are outlined in Fig. 14.1.

Type I reaction centers take an electron from a donor such as a cytochrome or the copper protein, plastocyanin, and use the energy of an absorbed quantum to pass the electron, through transient intermediates, to an iron-sulfur acceptor (a ferredoxin) on the opposing side of the membrane. Bacterial type I reaction centers (Fig. 14.1) then drive a linear electron transfer from any one of a range of inorganic donors to reduced ferredoxin, which supplies its electron, at low potential, to drive one or more of the coupled assimilatory reactions. In chloroplasts of cyanobacteria, plants, and algae, the type I reaction center is the core of photosystem I, which supplies electrons, also via ferredoxin, to $NADP^+$ and H^+, giving NADPH, which is oxidized again in the reactions of CO_2 assimilation. In photosynthetic bacteria, a hydrophilic

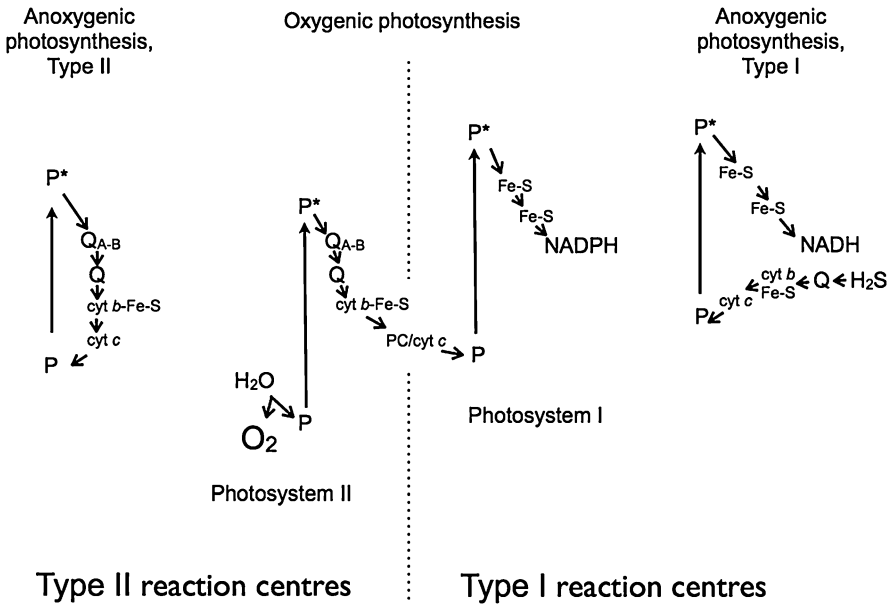

Fig. 14.1 Pathways of photosynthetic electron transport through reaction centers of type I and type II. *Arrows* indicate the direction of transfer of an electron, or liberation of oxygen. The vertical scale is one of redox potential—the tendency to donate or accept the electron. Light generates the excited state, P*, of the primary electron donor, P. P* is a strong electron donor, and loses an electron. In type II reaction centers, the electron passes to a pair of membrane-intrinsic quinones, Q_A and Q_B. In type I reaction centers, the electron passes to a chain of membrane-bound iron-sulfur centers, Fe-S, including water-soluble ferredoxin. Oxygenic photosynthesis couples the type II reaction center of photosystem II to the type I reaction center of photosystem I, allowing oxidation of water to supply electrons, and electrons pass through both reaction centers, reducing $NADP^+$ as the terminal electron acceptor. Anoxygenic photosynthesis has either a type I or a type II reaction centers, but never both. In all cases, a central cytochrome *b*-c_1 (or *b*-*f*)–Fe-S complex oxidizes a quinone pool, Q, in a proton-translocating cycle that transduces the free energy of the chemical redox reactions to a chemiosmotic, transmembrane proton-motive force, the intermediate between electron transport and ATP synthesis. *Cyt* cytochrome, *PC* plastocyanin

type I acceptor, ferredoxin, supplies electrons directly into assimilatory reactions with soluble components as intermediates in CO_2 fixation and nitrogen fixation. Type I photosynthesis is essentially a linear, or noncyclic, electron transfer, though the electron may return to re-reduce the primary donor after a few steps in a cyclic pathway in special circumstances, driving ATP synthesis without coupled net oxidation-reduction of any external substrate.

Type II reaction centers, in contrast, have lipophilic quinones as secondary electron acceptors. In anoxygenic bacterial type II reaction centers, the secondary donor is a cytochrome, which is re-reduced with electrons from the proton-translocating cytochrome *b*-c_1 complex, itself reduced by the reduced quinone (Fig. 14.1). The overall pathway of anoxygenic type II electron transfer is therefore cyclic, again with no net substrate-level oxidation or reduction. While type II

photosynthesis is cyclic in anoxygenic bacteria, the type II reaction center of cyanobacteria and of chloroplasts of plants and algae has a predominantly noncyclic pathway. In the latter, electrons are obtained from an inorganic donor—water. The oxidation product is free, molecular oxygen—photosynthesis is then *oxygenic*. The type II reaction center of oxygenic photosynthesis forms the core of photosystem II. Its eventual electron acceptor, from its reduced quinone secondary acceptor, plastoquinone, via the cytochrome *b-f* complex, is the type I reaction center of photosystem I.

Oxygenic photosynthesis takes electrons from water at a standard redox potential (H_2O/O_2) of +810 mV to $NADP^+$ at a standard redox potential ($NADPH/[NADP^+ + H^+]$) of −320 mV. The energy required to move an electron through more than 1.1 V comes from two photochemical reaction centers, one type II and the other type I. Their series connection means that they have the same electrical current, while their electrical potentials are added. Thus oxygenic photosynthesis of cyanobacteria and chloroplasts always requires two separate photosystems, photosystem II and photosystem I (Fig. 14.1). The terminology derives from the pigment systems I and II, proposed by Hill and Bendall [2] as components of electron transport in "the chloroplast reaction." The reaction center terminology of type I and type II derives from the evident biophysical and structural similarity of the reaction centers of photosystems I and II with each of the two major types of single, isolated reaction center found in anoxygenic photosynthetic bacteria. Anoxygenic photosynthesis uses just one reaction center of either type I or type II, and therefore has a quantum requirement of 1 for transfer of one electron. In contrast, oxygenic photosynthesis requires the coupling of the two distinct reaction centers of photosystem I and photosystem II, and therefore has a corresponding quantum requirement of 2. For assimilatory reactions such as CO_2 fixation, requiring four electrons, these differing quantum requirements are equivalent to 4 per CO_2 molecule for anoxygenic photosynthesis and 8 for oxygenic photosynthesis.

If anoxygenic photosynthesis requires half the number of quanta, why has the less quantum-efficient, *oxygenic* form of photosynthesis come to dominate biological energy flux and the global carbon cycle? The answer lies in the universal availability of the electron donor, water, in contrast to the potentially limiting supply of more easily oxidized electron donors such as hydrogen sulfide, hydrogen, Fe^{2+}, and reduced carbon compounds. Furthermore, inorganic electron donors other than water must have become less abundant after the advent of oxygenic photosynthesis, as oxygen began to suffuse the atmosphere [3]. Once water oxidation and oxygen evolution appeared and began to distribute oxygen as the energetically preferred terminal electron acceptor for respiration, then electron donors originally useful to single-photosystem, anoxygenic photosynthetic bacteria became restricted to special environments. Donors such as H_2S are now provided either from localized or transient geochemical efflux or as products of anaerobic respiration. Once photosynthesis had begun to produce oxygen, there was no turning back.

14.2 Anoxygenic Type I and Type II Reaction Centers: Divergence from a Common Ancestor

A wealth of spectroscopic evidence has long supported the resemblance, summarized in Fig. 14.1, between anoxygenic type I and the reaction center of photosystem I, and between anoxygenic type II and the reaction center of photosystem II [4–8]. This resemblance turned out to have a deep evolutionary foundation when it was seen that core protein subunits in the newly resolved structure of a purple bacterial, type II, reaction center exhibit functional amino acid sequence similarities with proteins of chloroplast photosystem II, as deduced from the nucleotide sequence of chloroplast DNA [9, 10]. An emerging structure of photosystem I from a cyanobacterium then indicated that the type I-type II division extends to the architecture and disposition of the central, membrane-spanning α-helices that traverse the membrane, holding the donors and acceptors in place for light-driven charge separation [11]. Today it is indisputable that the cores of photosystems I and II are examples of reaction centers of types I and II, respectively [12–16].

In evolutionary terminology, two structures are said to be homologous if they share a common ancestor. There can be no doubt that type I and type II reaction centers are homologous. What did their common ancestor look like, what were its electron donors and acceptors, and which sort of photosynthesis did it perform—cyclic or noncyclic? Figure 14.2 depicts reaction centers spanning a membrane, with divergence and specialization of type I and II reaction centers arising from a single ancestral and more versatile form that combined features of both. The prototype reaction center is depicted as having been capable of both cyclic, proton-motive electron transport and noncyclic electron transport with H_2S and ferredoxin as donor and acceptor, respectively. It should be noted that some authors favor the idea of the common ancestor having been a type I center [17] while others favor type II [18], each viewing the alternative type as a subsequent derivative of the favored precursor.

Vectorial electron transport—donor and acceptor lying on, or near, opposing sides of a membrane—is fundamental to biology, and not unique to photosynthesis. It is relevant and natural to ask how a vectorial electron carrier, predating light capture and conversion, might first have acquired a photoelectrochemical component, driving a reaction that had previously depended on an existing transmembrane redox gradient. This is an open question, and a fundamental one for understanding life on Earth and, perhaps, our prospect of our discovering life elsewhere. The answer may incidentally help to resolve the priority dispute between type I and type II reaction centers. At present it seems that a case can be made for either type I or type II coming first, while Fe-S centers, the hallmarks of type I, are likely to be more ancient electron carriers than quinones and cytochromes [19, 20]. With some exceptions, photosynthetic bacteria that are

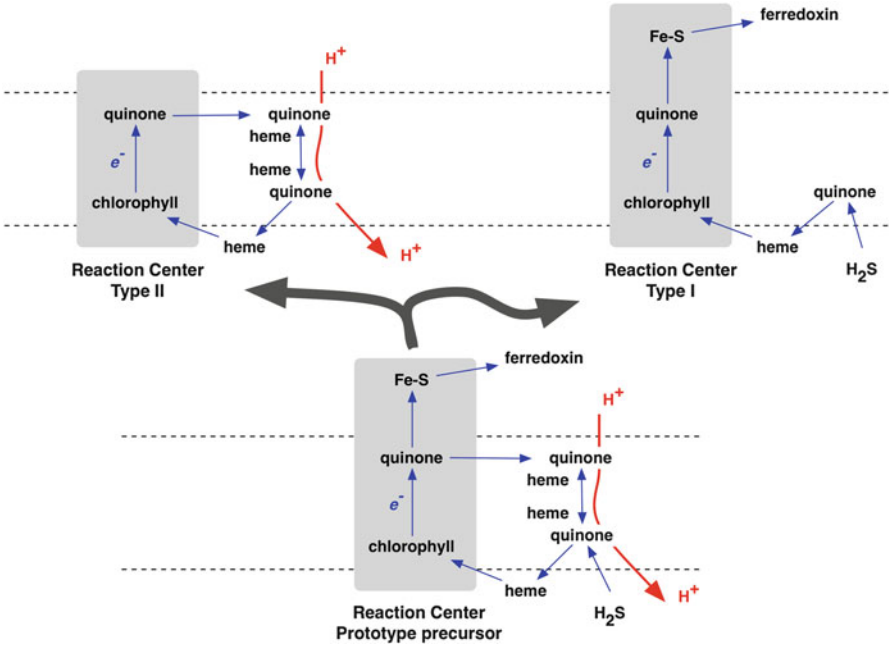

Fig. 14.2 Divergence of reaction center structure and function. A prototype photosynthetic reaction center diverges to give separate, type I and type II reaction centers, each preserving a subset of the original reaction center's functions. The primary electron donor is a chlorophyll molecule. The type I reaction center becomes adapted to noncyclic, H_2S-oxidizing electron transport with the iron-sulfur protein ferredoxin as the dominant secondary electron acceptor. The type II reaction center in turn becomes committed largely to cyclic electron transport, re-reducing the quinone. In the type II center a quinone is the predominant electron acceptor and also serves in a proton-translocating Q-cycle involving cytochrome hemes as electron carriers, eventually returning electrons to chlorophyll. Adapted from [59]

dependent on type I centers alone are also typically obligate anaerobes—still in hiding, as it were, from oxygen. Type II anoxygenic bacteria have adapted to survive aerobic environments by temporarily abandoning photosynthesis completely, becoming transiently chemotrophic. In facultatively phototrophic and anoxygenic bacteria, a redox genetic switch controls expression, on illumination and anoxia, of the apparatus of type II photosynthesis [21, 22]. This versatility may have been a later evolutionary acquisition, in which case type II came second, and modern type I anoxygenic photosynthetic bacteria more closely resemble the common ancestral form. However, there is a case for redox genetic switching being no novel innovation, being present even in the first living cells [23]. "Which came first?" remains a question for future research.

14.3 How Did the Two Divergent and Isolated Reaction Centers, Type I and Type II, Reconnect, and so Become Interdependent?

Two central electron transport pathways (Figs. 14.1 and 14.2), each with its own reaction center, must have become coupled together in series to comprise the oxygenic "Z-scheme" [24]. While photosynthetic production of oxygen from water occurs at the electron donor side of photosystem II, there is no oxygen evolution without photosystem I, which acts as the electron acceptor of photosystem II. Without exception, this series connection of a type I and a type II photochemical reaction center is necessary for sustained oxygen-evolving photosynthesis, where each photosystem depends absolutely on the other. Thus there is no single-reaction-center oxygenic photosynthesis. In fact, the resulting quantum requirement, for oxygen evolution, of 8 [25] is a minimum to which oxygenic photosynthetic systems approximate by means of both posttranslational [26] and transcriptional [27] mechanisms for optimal distribution of absorbed light energy between the two photochemical reaction centers. For maximal quantum yield of oxygen, redistribution of excitation energy and adjustment of photosystem stoichiometry occur in proportion to the varying and interrelated capacity of the two reaction centers to utilize this energy in photochemistry [28, 29]. A redox genetic switch, perhaps initiating oxygenesis itself, clearly found new applications following the onset of two-light-reaction photosynthesis.

Since type I and type II reaction centers evolved by diverging, under natural selection, from a common ancestor (Fig. 14.2), it follows that oxygenic photosynthesis, which depends on their coming together again, was a later addition to the photosynthetic repertory. The conclusion is that oxygenic photosynthesis appeared later, and evolved from anoxygenic photosynthesis. There is now abundant, diverse, and independent geochemical evidence that the Earth's atmosphere was largely anoxic from the planet's formation at 4.6 Gigayears, through a billion years or more of early life, metabolism, and ecology [30], up until the "Great Oxidation Event" at about 2.4 Gigayears (Fig. 14.3). Thus the emergence of oxygenic photosynthesis changed everything, imposing a requirement for oxygen tolerance on biochemical metabolism that is, to this day, fundamentally anaerobic. A self-renewing supply of free oxygen also meant the appearance of an abundant terminal electron sink for energetically favored aerobic respiration, eventually creating the conditions for complex, multicellular life. Molecular oxygen coincidentally allowed photo-conversion of diatomic oxygen to ozone in the upper atmosphere, creating a long-pass filter to attenuate ionizing ultraviolet radiation and making possible the colonization of the land.

A number of suggestions have been made concerning the eventual coupling of two anoxygenic reaction centers to give the oxygenic Z-scheme, with its interdependent photosystems I and II [6]. One idea with wide support is lateral gene transfer between different species and lineages, either from a type II-containing genetic donor to a type I recipient, or vice versa, from a type I genetic

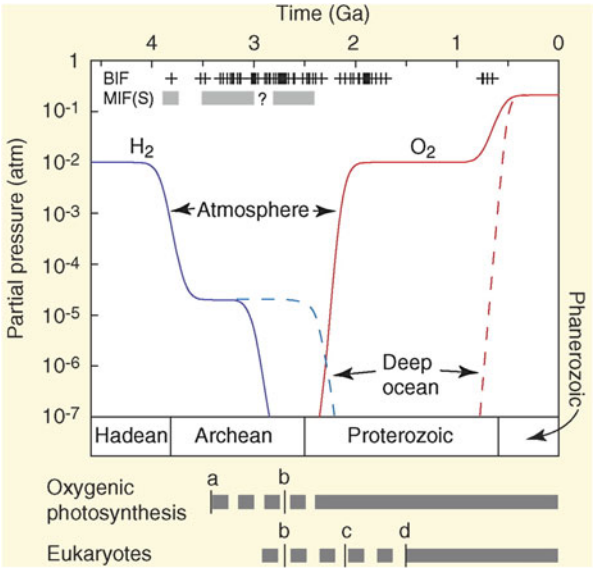

Fig. 14.3 Geochemical evolution of the atmosphere and oceans. BIF: banded iron formations. MIF(S): mass-independent fractionation of sulfur isotopes. Approximate time points: (**a**) the earliest evidence for anoxygenic photosynthesis; (**b**) the earliest known occurrence of steranes and 2-methylhopanes, taken as markers for aerobic metabolism; (**c**) the first putative eukaryotic microfossils; and (**d**) the first known assemblages of diverse eukaryotic microfossils in shallow marine sediments. Reproduced from [71]

donor to type II recipient. The complexity of a photosystem, correctly regulated and assembled by means of protein assembly factors and molecular chaperones, might make lateral gene transfer an implausible explanation for the coming together of photosystems I and II; the probability of every imported component being synthesized and fitting in place may be small. Nevertheless, it is notable that anoxygenic photosynthetic bacteria carry photosynthesis genes packaged into operons [22], so plasmid or viral [31] vectors can transfer a compatible and integrated set of photosystem genes. Concerted migration of a complete and active genetic system, coupled with its own membrane-bound metabolism, might be more likely to achieve such a result. This is a process now thought to lie, much later, at the endosymbiotic origin of chloroplasts and mitochondria in eukaryotic cells.

Another suggestion for the origin of the Z-scheme is that type I and type II reaction centers survived as functional entities within one or more distinct anoxygenic bacterial lineages [32, 33], eventually to hit upon the trick of water oxidation at the donor side of the type II center. A problem with this hypothesis is that the two separate modes of anoxygenic electron transport would have had to take place in separate membranes, or even in metabolically isolated subcellular compartments. One reason for this requirement is that if the two modes were present in the same membrane at the same time, then linear electron transport by

type I reaction centers would destroy redox poise required for sustained cyclic electron transport around the type II reaction center. Cyclic electron transport requires each electron carrier to be available as both a donor and as an acceptor. A linear electron transport pathway intersecting a cyclic one causes over-reduction (absence of acceptors) or over-oxidation (absence of donors) unless some compensatory mechanism exists to balance electron influx and efflux [34]. Such mechanisms are now found in oxygenic photosynthesis, where photosystem I on its own can cycle a proportion of electrons to drive proton pumping and ATP synthesis independently of NADPH production [35, 36]. In anoxygenic photosynthesis, however, it is difficult to see any additional benefit of controlled interaction of type I photosynthesis with type II photosynthesis, given that type I electron transport is capable, on its own, of electron cycling through the cytochrome complex in the absence of an external electron donor. The need for a mechanism achieving redox poise of type I cyclic electron transport arises primarily only after the advent of molecular oxygen, which competes with $NADP^+$ for electrons from photosystem I [37], and which results in inhibition by over-oxidation if electron input from photosystem II is restricted for any reason.

If both lateral gene transfer and simultaneous type I and type II photochemistry are unlikely, then what is left? There is a third hypothesis, an alternative to coordinated DNA transfer as well as to the proposition that anoxygenic type I and type II centers somehow functioned, and survived, in a shared membrane. This third hypothesis envisages a redox switch to select between *genes* for type I and type II reaction centers. These genes are proposed to have been continually present in a single genome but never expressed at the same time—not, at least, without disastrous consequences. One eventually favorable consequence happened to be photo-oxidation of manganese and then of water, permanently emancipating phototrophy from localized, fleeting, or irregular supplies of H_2S. The reaction product, oxygen, was difficult to live with. In due course, however, oxygen became impossible for many organisms to live without.

14.4 The Redox Switch Hypothesis for the First Cyanobacterium

Bacteria are usually highly versatile in their ability to use different energy sources, coupling them to any of a variety of sources and sinks for carbon, nitrogen, and electrons [38]. Thus the divergence, indicated in Fig. 14.2, of type I and type II reaction centers from a common ancestor need not have depended on loss of the complementary reaction center and its genes. Figure 14.4 describes a sequence of events in which the *capacity* for either type I or type II photosynthesis was retained within a single lineage of cells. Metabolic flexibility in anoxygenic photosynthesis might be particularly advantageous in environments with fluctuating supplies of H_2S, as found today in the vicinity of hydrothermal springs [39]. In the Archean

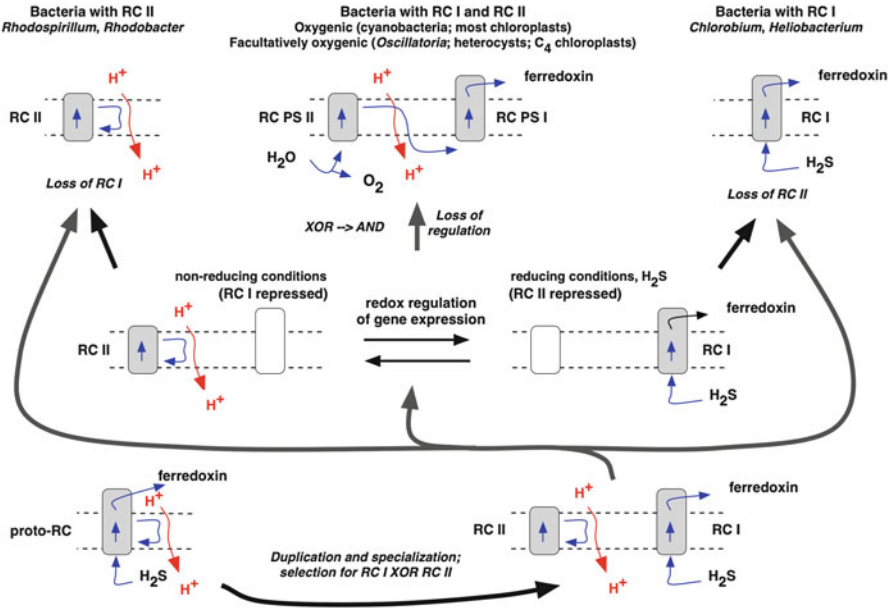

Fig. 14.4 Retention of genes for both type I and type II centers in a single genome, selection between their expression by means of redox regulation, and oxygenic photosynthesis as the accidental consequence of a broken switch. Type I (RC I) and type II (RC II) reaction centers separate, allowing specialization and eventual loss of the redundant reaction center in photoautolithotrophic (type I-containing) lineages (e.g., *Chlorobium*, *Heliobacillus* spp.) and in photoorganotrophic (type II-containing) lineages (e.g., *Rhodobacter*, *Rhodospirillum* spp.). A versatile, facultatively chemoautotrophic photosynthetic bacterium retains genes for both type I and type II reaction centers. In this proposed ancestor of cyanobacteria and chloroplasts, expression of type I center genes in the presence of H_2S is accompanied by repression of type II genes. In the absence of H_2S, type II genes are induced, and type I genes become repressed. Subsequent impairment of regulatory control allows coexistence of type I and type II reaction centers, with complementary functions. In place of H_2S, the type II center, as photosystem II (PS II), oxidizes water, liberating oxygen, and donates electrons to the type I center, as photosystem I (PS I). The proposed loss of the redox regulatory switch replaces the logical (Boolean) relation "Type I ***XOR*** Type II" (each type excluding the other) with "Type I ***OR*** Type II" (either is, and both are, allowed). This in turn leads to "Type I ***AND*** Type II" when interdependency of photosystems I and II is established in the noncyclic electron transport chain of oxygenic photosynthesis. Adapted from [59]

eon, such environments are likely to have been common, with varying H_2S concentration a normal state of affairs. Before the advent of O_2 as a respiratory electron acceptor, geochemical H_2S will have been widespread, but periodically diluted by rainfall in lakes, rivers, and streams, and additionally by rising tides in littoral rock pools [3, 40].

The scheme in Fig. 14.4 proposes that redox regulation of gene expression, all under strictly anoxic conditions, determines whether type I or type II reaction center genes are expressed in a single anoxygenic bacterial cell whose genome carries them both. Quinone-level redox control provides a suitable mechanism, given the

established redox regulatory control of gene transcription in both phototrophic [21, 41–43] and chemotrophic [44–47] bacteria. An inducible type II reaction center is retained at the core of photosystem II in the cyanobacterium *Oscillatoria limnetica*, which exhibits anaerobic type I photosynthesis in the presence of H_2S, but oxygenic, two-light reaction photosynthesis in its absence [48].

In the absence of H_2S, selection would have favored opportunistic use of weak environmental reductants, including organic substrates, to allow slow, catalytic donation of electrons into a cyclic chain that would otherwise become over-oxidized. It is possible that the inorganic catalyst of photosynthetic water oxidation [49, 50] first served such a poising role for purely anoxygenic, type II photosynthesis, and that this occurred in the inducible type II photosynthesis of the bacterium that also housed temporarily unexpressed genes for a reaction center of type I (Fig. 14.4).

The universal inorganic catalyst of photosynthetic water oxidation is Mn_4CaO_5, a well-defined cluster of five metal and five oxygen atoms [15]. The cluster seems to have no independent existence, and dissociates without its amino-acid side-chain ligands [51]. Its biological assembly suggests that environmental Mn^{2+} itself was an initial substrate and electron donor [20]. Bicarbonate enhances and stabilizes light-induced electron transfer from Mn^{2+} to P^+ in isolated type II reaction centers and may have itself been a precursor secondary electron donor [51]. An additional possibility for the initial advantage of association of a type II center with manganese lies in the latter's UV-absorbing property, providing a screen for ionizing radiation [52]. Mn^{2+} ions will donate electrons readily to a biochemically exposed P^+ in photosystem II (P_{680}) [53] and to an engineered purple bacterial type II reaction center (P_{870}) [54]. Re-reduction of higher oxidation states of manganese by the superoxide anion radical, or by H_2O itself, liberates O_2.

Geochemical data on drill cores from an early Paleoproterozoic succession at 2.415 Gigayears preserved in South Africa indicate substantial enrichment with manganese carbonate [55]. These results are interpreted as evidence that the extensive oxidation of manganese predated the rise of atmospheric oxygen, providing support for the hypothesis that the water-oxidizing complex of photosystem II evolved from a photosystem originally driving oxidation of manganese [55]. The advantage of moving to water as the initial electron donor would have been to free the bacterium from the need for substrate quantities of Mn^{2+}, provided that sufficient manganese could be assimilated to maintain the catalytic complex. Water oxidation might initially have been a minor pathway, since the reaction would have been slow, and the product, molecular oxygen, was toxic. A trickle of oxygen, produced as a by-product of useful regulatory water oxidation, would have been scrubbed from the immediate environment by dilution, or by acting as a respiratory electron sink for neighboring chemoheterotrophs. Subsequent selection, however, can be expected to have increased the redox midpoint potential of the primary chlorophyll electron donor by tuning its protein environment [54, 56, 57] while more effectively coupling the water-oxidation complex to re-reduction of the primary donor, today exemplified by the redox-active tyrosine that links the oxygen-evolving Mn_4CaO_5 cluster with P_{680}^+ [56–58].

Once a mechanism for water oxidation was in place, any mutation producing constitutive expression of both type I and type II genes would provide entirely new functions for each of the two reaction centers, previously forbidden from operating at the same time. Coupling of type II and type I centers simultaneously through a single, shared quinone pool would have allowed the two centers to function in series, and therefore in cooperation—the acceptors for the type II center, oxidizing water, became identical with the donors for the type I center, reducing ferredoxin. This coupling would have provided the first oxygenic bacteria with the advantages of both modes of photosynthesis—ATP synthesis and reduction of soluble, low-potential ferredoxin—while also releasing them from dependency on transient supplies of H_2S for photoautolithotrophic growth. It is proposed (Fig. 14.4) that the origin of the "Z-scheme" of two light reactions, connected in series, occurred by these means [20, 52, 59, 60].

14.5 What Was the Precursor?

The advent of oxygenic photosynthesis had global, irreversible impact, and can be viewed as the most far-reaching event in the history of life, second only to its origin [61]. The redox switch hypothesis for the genesis of the cyanobacteria suggests the persistence today of a two-light-reaction, phototrophic anaerobe retaining genes for both type I and type II reaction centers. This proto-cyanobacterium, a versatile anoxygenic phototroph, should be able to switch between sulfide-oxidizing, photolithotrophic, type I photosynthesis, and sulfide-independent, photoorganotrophic, type II photosynthesis. This organism can be autotrophic, assimilating carbon dioxide, in both modes of photosynthetic metabolism, since the proton-motive cytochrome b-c_1 complex acts not only to provide energy for ATP synthesis. In modern purple non-sulfur anoxygenic photosynthetic bacteria, the same proton-motive force supplies energy for reverse respiratory electron transport from succinate, reducing $NAD(P)^+$ to NAD(P)H for CO_2 and N_2 assimilation.

The green, filamentous, anaerobic phototroph *Chloroflexus aurantiacus* grows in environments with variable sulfide content [39]. *Chloroflexus aurantiacus* has genes only for type II reaction center core proteins (PufLM) and not for type I (PscA) [62] contrary to a previous suggestion [60]. It is uncertain whether this conclusion will hold for all *Chloroflexus* species. In addition, *Chloroflexus* has a major, peripheral, membrane-extrinsic light-harvesting antenna, the chlorosome, originally discovered and characterized in the type I reaction center-containing bacterium *Chlorobium* [38]. *Chloroflexus* may therefore be a close relative both of cyanobacteria and of the anoxygenic phototroph predicted by the hypothesis proposed here and depicted in Fig. 14.4. Figure 14.5 shows a scheme in which the proposed, metabolically versatile proto-cyanobacterium is the last common ancestor of *Chlorobium*, *Chloroflexus*, and cyanobacteria. Facultative type I and type II-plus-type I photosynthesis is seen in the cyanobacterium *Oscillatoria*

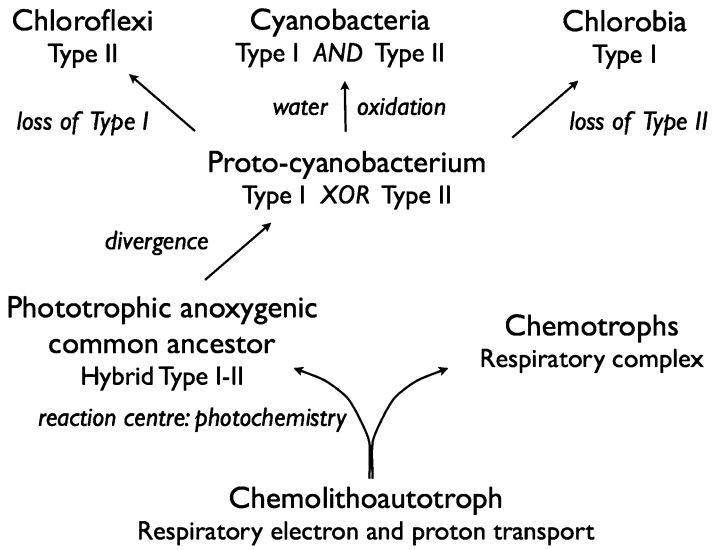

Fig. 14.5 Proposed evolutionary development of photochemical reaction centers from a respiratory chain complex. Vectorial electron transport and proton translocation originate in a respiratory complex. Photochemical charge separation is introduced to form a combined type I-type II reaction center in the common ancestor of all phototrophs, and the prototype reaction center shown in Fig. 14.2. Type I and II reaction centers themselves then diverge, being refined by natural selection operating on products of genes expressed under different growth conditions while retained within single genomes of versatile phototrophic lineages. These lineages give rise to the proposed proto-cyanobacterium, from which loss of type I reaction center genes gave Chloroflexi, loss of type II genes gave Chlorobia, and retention of both type I and type II genes gave cyanobacteria

limnetica, which has inducible photosystem II and reaction center core proteins homologous to PscA and PufLM [63].

The redox switch hypothesis (Fig. 14.4) predicts specific, sulfide-responsive redox regulatory control in an anoxygenic, phototrophic bacterium containing genes for both type I and II reaction centers. Such an organism could be expected to share some of the characteristics of *Chloroflexus* and *Oscillatoria*. Suitable habitats still exist. It is therefore to be expected that this bacterium is either an undiscovered or a known species as yet incompletely characterized. Such a bacterium will be a modern example of the species in which photosynthetic oxygen evolution originated, and from which cyanobacteria, and their eventual chloroplast descendants, evolved (Fig. 14.4). It can also be considered whether the redox switch will be found to share components in common with the quinone redox regulatory mechanisms involved in control of respiration and photosynthesis in bacteria, as well as in state transitions and control of photosystem stoichiometry in cyanobacteria [41] and chloroplasts [64].

14.6 Evidence and Evidence Required: An Anoxygenic Phototroph That Switches Between Type I and Type II

Meta-analysis of genome sequences concludes that there is no deep division between type I and type II anoxygenic bacteria with respect to enzymes of chlorophyll biosynthesis [65]. Such a division might be expected if a unique origin of cyanobacteria occurred from within a lineage represented by one or the other group of extant anoxygenic bacteria. Therefore chlorophyll synthesis seems to argue against a fusion of preexisting reaction centers to give photosystems I and II. This conclusion [65] implies that the two original reaction center types were supplied with chlorophyll by a single biosynthetic pathway, as they are today in oxygenic phototrophs. The obvious inference is that a versatile cyanobacterial progenitor retained the capacity to synthesize both type I and type II reaction centers, as depicted in Fig. 14.4.

Comparative genomics points to an origin of cyanobacteria within modern Subsection V, which contains filamentous, N_2-fixing, heterocyst-bearing, freshwater forms [66]. This finding is consistent with the proposed affinity of the proto-cyanobacterium with species of the genera *Chloroflexus* and *Oscillatoria*. This study [66] also lends weight to the assumption that the first oxygenic phototroph lived under conditions of low salinity, where further freshwater periodically diluted the H_2S in its habitat. A further implication of these results [66] is that the advantage of water oxidation might have been that it provided essentially limitless reductant, not for carbon fixation, as often supposed, but for nitrogen fixation, as shown in the inclusive scheme for type I electron transport in Fig. 14.6. The continuation of water-oxidizing diazotrophy from the Archean into the Proterozoic may also provide a new perspective on the endosymbiosis that gave rise to the chloroplasts of eukaryotic algae and plants.

The redox switch hypothesis (Fig. 14.4) predicts specific, sulfide-responsive redox regulatory control in an anaerobic, phototrophic bacterium retaining genes for both type I and II reaction centers. Anoxic lakes with a varying H_2S influx are known [67–70]. It is therefore to be expected that a recognizable descendant of the proto-cyanobacterium is either as yet undiscovered or else a known species, incompletely characterized. In the early Archean, the whole biosphere was anoxic (Fig. 14.3), and the proposed precursor of oxygenic cyanobacteria may have been a dominant primary producer, adapted to surface light intensities rather than to low-light environments to which its direct descendants may be confined today. It is likely to have contained chlorophyll rather than bacteriochlorophyll.

It is now a realistic prospect to take samples from anoxic, low-light environments for metagenomic sequencing in order to see if type I and type II genes indeed ever cohabit a single genome. Looking beyond the anticipated success of such a finding, enrichment culture conditions can easily be envisaged. These could begin by setting up a cyclical influx of H_2S at concentrations that vary at a frequency found in the bacterium's natural habitat. A wealth of information and insight would then be forthcoming concerning primary photochemistry, biophysics,

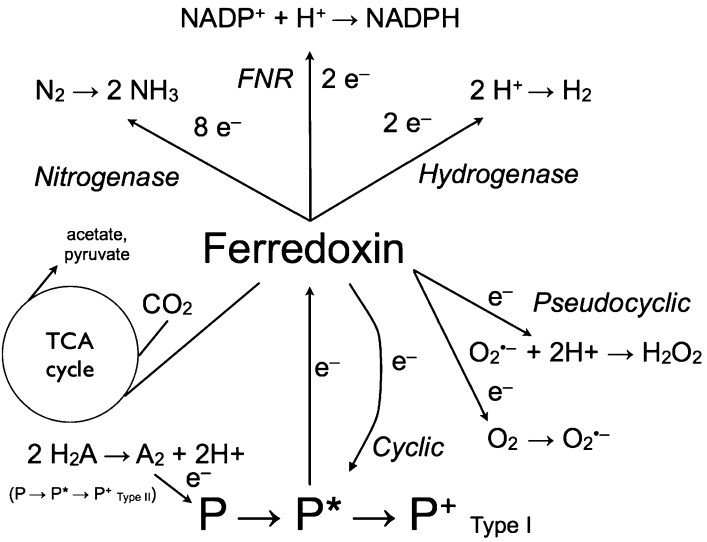

Fig. 14.6 The versatility of type I photosynthetic reaction centers. Pathways of electron transfer from the primary donor, P. Soluble ferredoxin is a major branch point in transferring electrons onwards from membrane-bound Fe-S centers to reduce substrates involved in a range of pathways, notably terminating with assimilation. CO_2 can be fixed since ferredoxin is oxidized directly in the reductive TCA or citric acid (Krebs) cycle or indirectly via NADPH supplied to the reductive pentose phosphate pathway (Benson-Calvin cycle). Reduced ferredoxin can also transfer electrons to molecular nitrogen, hydrogen, and oxygen. Ferredoxin can additionally pass electrons back to P^+ through a cyclic pathway. The secondary donor to P^+ may be a cytochrome or a plastocyanin, in turn reduced by a donor represented by H_2A. Organic examples of H_2A are succinate, pyruvate, and acetate. Inorganic H_2A may be H_2, Fe^{2+}, Mn^{2+}, H_2S, or H_2O. In the case of H_2O, molecular oxygen is liberated and electrons are supplied through a second reaction center of type II, with its own primary donor, P, as depicted in Fig. 14.1

light-harvesting mechanism(s), biochemistry, and physiology. We might also then help to solve the mystery of a planetary revolution, the single most decisive step in biogeochemical, biological, and evolutionary history [61].

Acknowledgements I thank Nick Lane, William Martin, Wolfgang Nitschke, and Michael Russell for discussions on this and related topics.

References

1. Witt HT. Coupling of quanta, electrons, fields, ions and phosphorylation in the functional membrane of photosynthesis. Results by pulse spectroscopic methods. [Review]. Q Rev Biophys. 1971;4(4):365–477.
2. Hill R, Bendall F. Function of the two cytochrome components in chloroplasts: a working hypothesis. Nature. 1960;186(4719):136–7.

3. Johnston DT, Wolfe-Simon F, Pearson A, Knoll AH. Anoxygenic photosynthesis modulated Proterozoic oxygen and sustained Earth's middle age. Proc Natl Acad Sci U S A. 2009;106 (40):16925–9.
4. Nitschke W, Rutherford AW. Photosynthetic reaction centres: variations on a common structural theme? Trends Biochem Sci. 1991;16(7):241–5.
5. Cardona T, Sedoud A, Cox N, Rutherford AW. Charge separation in photosystem II: a comparative and evolutionary overview. BBA Bioenerg. 2012;1817(1):26–43.
6. Hohmann-Marriott MF, Blankenship RE. Evolution of photosynthesis. Annu Rev Plant Biol. 2011;62:515–48.
7. Rutherford AW, Osyczka A, Rappaport F. Back-reactions, short-circuits, leaks and other energy wasteful reactions in biological electron transfer: redox tuning to survive life in O-2. FEBS Lett. 2012;586(5):603–16.
8. Saito K, Rutherford AW, Ishikita H. Mechanism of proton-coupled quinone reduction in photosystem II. Proc Natl Acad Sci U S A. 2013;110(3):954–9.
9. Deisenhofer J, Epp O, Miki K, Huber R, Michel H. Structure of the protein subunits in the photosynthetic reaction center of rhodopseudomonas-viridis at 3a resolution. Nature. 1985;318 (6047):618–24.
10. Deisenhofer J, Michel H, Huber R. The structural basis of photosynthetic light reactions in bacteria. Trends Biochem Sci. 1985;10(6):243–8.
11. Schubert WD, Klukas O, Saenger W, Witt HT, Fromme P, Krauss N. A common ancestor for oxygenic and anoxygenic photosynthetic systems: a comparison based on the structural model of photosystem I. J Mol Biol. 1998;280(2):297–314.
12. Amunts A, Drory O, Nelson N. The structure of a plant photosystem I supercomplex at 3.4 A resolution. Nature. 2007;58–63.
13. Ben-Shem A, Frolow F, Nelson N. Crystal structure of plant photosystem I. Nature. 2003;426 (6967):630–5.
14. Hauska G, Schoedl T, Remigy H, Tsiotis G. The reaction center of green sulfur bacteria. BBA Bioenerg. 2001;1507(1–3):260–77.
15. Umena Y, Kawakami K, Shen JR, Kamiya N. Crystal structure of oxygen-evolving photosystem II at a resolution of 1.9 angstrom. Nature. 2011;473(7345):55–U65.
16. Raymond J, Blankenship RE. The evolutionary development of the protein complement of photosystem 2. BBA Bioenerg. 2004;1655(1–3):133–9.
17. Baymann D, Brugna M, Muhlenhoff U, Nitschke W. Daddy, where did (PS)I come from? BBA Bioenerg. 2001;1507(1–3):291–310.
18. Xiong J, Fischer WM, Inoue K, Nakahara M, Bauer CE. Molecular evidence for the early evolution of photosynthesis. Science. 2000;289(5485):1724–30.
19. Hall DO, Cammack R, Rao KK. Role for ferredoxins in origin of life and biological evolution. Nature. 1971;233(5315):136.
20. Russell MJ, Allen JF, Milner-White EJ. Inorganic complexes enabled the onset of life and oxygenic photosynthesis. In: Allen JF, Gantt E, Golbeck JH, Osmond B, editors. Photosynthesis 2007 Energy from the Sun Proceedings of the 14th international congress on photosynthesis. Heidelberg: Springer; 2008. p. 1187–92.
21. Bauer C, Elsen S, Swem LR, Swem DL, Masuda S. Redox and light regulation of gene expression in photosynthetic prokaryotes. Phil Trans Roy Soc Lond B. 2003;358(1429):147–54.
22. Marrs BL. Molecular-genetics studies of gene-expression and protein-structure function relationships in photosynthetic bacteria. FEMS Symp. 1990;53:1–4.
23. Allen JF. Redox homeostasis in the emergence of life. On the constant internal environment of nascent living cells. J Cosmol. 2010;10:3362–73.
24. Hill R, Bendall F. Function of the two cytochrome components in chloroplasts - a working hypothesis. Nature. 1960;186(4719):136–7.
25. Myers J. Enhancement studies in photosynthesis. Ann Rev Plant Physio. 1971;22:289.
26. Allen JF, Bennett J, Steinback KE, Arntzen CJ. Chloroplast protein-phosphorylation couples plastoquinone redox state to distribution of excitation-energy between photosystems. Nature. 1981;291(5810):25–9.

27. Pfannschmidt T, Nilsson A, Allen JF. Photosynthetic control of chloroplast gene expression. Nature. 1999;397(6720):625–8.
28. Allen JF, Santabarbara S, Allen CA, Puthiyaveetil S. Discrete redox signaling pathways regulate photosynthetic light-harvesting and chloroplast gene transcription. PLoS One. 2011;6(10):e26372.
29. Allen JF, Pfannschmidt T. Balancing the two photosystems: photosynthetic electron transfer governs transcription of reaction centre genes in chloroplasts. Phil Trans Roy Soc Lond Ser B Biol Sci. 2000;355(1402):1351–7.
30. Nisbet EG, Sleep NH. The habitat and nature of early life. Nature. 2001;409(6823):1083–91.
31. Mazor Y, Greenberg I, Toporik H, Beja O, Nelson N. The evolution of photosystem I in light of phage-encoded reaction centres. Phil Trans Roy Soc B Biol Sci. 2012;367(1608):3400–5.
32. Olson JM, Blankenship RE. Thinking about the evolution of photosynthesis. Photosynth Res. 2004;80(1–3):373–86.
33. Olson JM, Pierson BK. Evolution of reaction centers in photosynthetic prokaryotes. Int Rev Cytol. 1987;108:209–48.
34. Arnon DI, Chain RK. Role of oxygen in ferredoxin-catalyzed cyclic photophosphorylations. FEBS Lett. 1977;82(2):297–302.
35. Allen JF. Photosynthesis of ATP-electrons, proton pumps, rotors, and poise. Cell. 2002;110 (3):273–6.
36. Allen JF. Cyclic, pseudocyclic and noncyclic photophosphorylation: new links in the chain. Trends Plant Sci. 2003;8(1):15–9.
37. Allen JF. Oxygen reduction and optimum production of Atp in photosynthesis. Nature. 1975;256(5518):599–600.
38. Blankenship RE, Madigan MT, Bauer CE. Anoxygenic photosynthetic bacteria. Dordrecht: Kluwer; 1995.
39. Pierson BK, Castenholz RW. Ecology of thermophilic anoxygenic phototrophs. In: Blankenship RE, Madigan MT, Bauer CE, editors. Anoxygenic photosynthetic bacteria. Dordrecht: Kluwer; 1995. p. 87–103.
40. Johnston DT, Poulton SW, Fralick PW, Wing BA, Canfield DE, Farquhar J. Evolution of the oceanic sulfur cycle at the end of the Paleoproterozoic. Geochim Cosmochim Acta. 2006;70 (23):5723–39.
41. Li H, Sherman LA. A redox-responsive regulator of photosynthesis gene expression in the cyanobacterium Synechocystis sp. strain PCC 6803. J Bacteriol. 2000;182(15):4268–77.
42. Eraso JM, Kaplan S. From redox flow to gene regulation: role of the PrrC protein of Rhodobacter sphaeroides 2.4.1. Biochemistry. 2000;39(8):2052–62.
43. Wu J, Bauer CE. RegB kinase activity is controlled in part by monitoring the ratio of oxidized to reduced ubiquinones in the ubiquinone pool. MBio. 2010;1(5):e00272–10.
44. Georgellis D, Kwon O, Lin EC. Quinones as the redox signal for the ARC two-component system of bacteria. Science. 2001;292(5525):2314–6.
45. Green J, Scott C, Guest JR. Functional versatility in the CRP-FNR superfamily of transcription factors: FNR and FLP. Adv Microb Physiol. 2001;44:1–34.
46. Unden G, Bongaerts J. Alternative respiratory pathways of Escherichia coli: energetics and transcriptional regulation in response to electron acceptors. Biochim Biophys Acta Bioenerg. 1997;1320(3):217–34.
47. Alexeeva S, Hellingwerf KJ, Teixeira de Mattos MJ. Requirement of ArcA for redox regulation in Escherichia coli under microaerobic but not anaerobic or aerobic conditions. J Bacteriol. 2003;185(1):204–9.
48. Oren A, Padan E. Induction of anaerobic, photoautotrophic growth in the cyanobacterium Oscillatoria limnetica. J Bacteriol. 1978;133(2):558–63.
49. Sauer K, Yachandra VK. A possible evolutionary origin for the Mn4 cluster of the photosynthetic water oxidation complex from natural MnO2 precipitates in the early ocean. Proc Natl Acad Sci U S A. 2002;99(13):8631–6.

50. Dismukes GC, Klimov VV, Baranov SV, Kozlov YN, DasGupta J, Tyryshkin A. Special feature: the origin of atmospheric oxygen on Earth: the innovation of oxygenic photosynthesis. Proc Natl Acad Sci U S A. 2001;98(5):2170–5.
51. Khorobrykh A, Dasgupta J, Kolling DRJ, Terentyev V, Klimov VV, Dismukes GC. Evolutionary origins of the photosynthetic water oxidation cluster: bicarbonate permits Mn2+ photo-oxidation by anoxygenic bacterial reaction centers. Chembiochem. 2013;14 (14):1725–31.
52. Allen JF, Martin W. Evolutionary biology - out of thin air. Nature. 2007;445(7128):610–2.
53. Cheniae GM. Photosystem-II and O2 evolution. Ann Rev Plant Physio. 1970;21:467.
54. Allen JP, Olson TL, Oyala P, Lee WJ, Tufts AA, Williams JC. Light-driven oxygen production from superoxide by Mn-binding bacterial reaction centers. Proc Natl Acad Sci U S A. 2012;109(7):2314–8.
55. Johnson JE, Webb SM, Thomas K, Ono S, Kirschvink JL, Fischer WW. Manganese-oxidizing photosynthesis before the rise of cyanobacteria. Proc Natl Acad Sci. 2013;110(28):11238–43.
56. Kalman L, LoBrutto R, Allen JP, Williams JC. Manganese oxidation by modified reaction centers from Rhodobacter sphaeroides. Biochemistry. 2003;42(37):11016–22.
57. Rutherford AW, Boussac A. Biochemistry. Water photolysis in biology. Science. 2004;303 (5665):1782–4.
58. Rutherford AW, Faller P. Photosystem II: evolutionary perspectives. Philos Trans R Soc Lond B Biol Sci. 2003;358(1429):245–53.
59. Allen JF. A redox switch hypothesis for the origin of two light reactions in photosynthesis. FEBS Lett. 2005;579(5):963–8.
60. Allen JF, Puthiyaveetil S. Chloroflexus aurantiacus and the origin of oxygenic, two-light reaction photosynthesis in failure to switch between type I and type II reaction centres. In: van der Est A, Bruce D, editors. Photosynthesis: fundamental aspects to global perspectives. Lawrence, KS: Alliance Communications Group; 2005. p. 455–7.
61. Lane N. Oxygen. Oxford: Oxford University Press; 2002.
62. Tang KH, Barry K, Chertkov O, Dalin E, Han CS, Hauser LJ, et al. Complete genome sequence of the filamentous anoxygenic phototrophic bacterium Chloroflexus aurantiacus. BMC Genomics. 2011;29:12.
63. Arieli B, Padan E, Shahak Y. Sulfide-induced sulfide-quinone reductase activity in thylakoids of Oscillatoria limnetica. J Biol Chem. 1991;266(1):104–11.
64. Puthiyaveetil S, Kavanagh TA, Cain P, Sullivan JA, Newell CA, Gray JC, et al. The ancestral symbiont sensor kinase CSK links photosynthesis with gene expression in chloroplasts. Proc Natl Acad Sci U S A. 2008;105(29):10061–6.
65. Sousa FL, Shavit-Grievink L, Allen JF, Martin WF. Chlorophyll biosynthesis gene evolution indicates photosystem gene duplication, not photosystem merger, at the origin of oxygenic photosynthesis. Genome Biol Evol. 2013;5(1):200–16.
66. Dagan T, Roettger M, Stucken K, Landan G, Koch R, Major P, et al. Genomes of stigonematalean cyanobacteria (subsection v) and the evolution of oxygenic photosynthesis from prokaryotes to plastids. Genome Biol Evol. 2013;5(1):31–44.
67. Macalady JL, Schaperdoth I, Fulton JM, Freeman KH, Hanson TE. Microbial biogeochemistry of a meromictic blue hole. Geochim Cosmochim Acta. 2010;74(12):A651.
68. Maresca JA, Crowe SA, Macalady JL. Anaerobic photosynthetic ecosystems. Geobiology. 2012;10(3):193–5.
69. Gonzalez BC, Iliffe TM, Macalady JL, Schaperdoth I, Kakuk B. Microbial hotspots in anchialine blue holes: initial discoveries from the Bahamas. Hydrobiologia. 2011;677(1):149–56.
70. Sahl JW, Gary MO, Harris JK, Spear JR. A comparative molecular analysis of water-filled limestone sinkholes in north-eastern Mexico. Environ Microbiol. 2011;13(1):226–40.
71. Dietrich LEP, Tice MM, Newman DK. The co-evolution of life and Earth. Curr Biol. 2006;16 (11):R395–400.

Index

J. Golbeck and A. van der Est (eds.), *The Biophysics of Photosynthesis*, Biophysics for the Life Sciences 11, DOI 10.1007/978-1-4939-1148-6,

F